Department of Applied Geology

Deformation of Earth's Upper Mantle: Insights from Naturally Occurring Fabric Types

Erin M. Gray

This thesis is presented for the Degree of
Doctor of Philosophy
of
Curtin University

December 2013

Declaration

To the best of my knowledge and belief this thesis contains no material previously published by any other person except where due acknowledgement has been made.

This thesis contains no material which has been accepted for the award of any other degree or diploma in any university.

Signed E M Gray (ERIN GRAY)

Date 04/02/2013

Abstract

The Earth's upper mantle is comprised of ~70-80% olivine and therefore factors affecting the rheology of olivine are significant in terms of mantle flow dynamics. Crystal-plastic deformation of olivine in the upper mantle by dislocation creep produces an alignment of particular crystal directions (lattice preferred orientations, or LPOs). Recent experiments reveal that the presence of water is an important factor affecting the development of LPOs, such that different fabrics will develop under varying conditions of water fugacity, stress and temperature. It is known that the [100] axis of olivine controls the seismic fast axis, and so the main consequence of the development of different olivine fabrics is that interpretations of flow directions from seismic anisotropy will be non-unique and dependent on the dominant fabric type. Current controversy about trench-parallel [100] directions in supra-subduction zone mantle may reflect a number of possible scenarios including trench-parallel flow or the development of olivine fabrics associated with [001](010) slip (B-type fabrics) due to high water content and increased stress in the supra-subduction zone mantle wedge. Critical to discriminating between these possibilities is the formation and preservation of olivine B-type fabrics, however, there are few recorded examples of naturally occurring B-type fabrics.

Alpine-type peridotites from Japan and mantle xenoliths from Lihir are examined, which represent fragments of forearc mantle wedge exhumed along the margins of the SW Pacific plate, where trench-parallel seismic fast axes are observed (Buttles and Olson, 1998; Nakajima and Hasegawa, 2004; Hammond *et al.*,2010). Microstructural analysis using EBSD is integrated with FTIR and isotope analysis, in order to provide insights into the link between olivine deformation and hydrogen in the Earth's upper mantle.

Fabric analysis of the Lihir xenoliths reveals that the peridotites have a bulk olivine LPO slip direction of [100]. Slip consistent with three different slip systems is recorded by the intragrain microstructures in olivine: (010)[100], {0kl}[100] and (001)[100]. Japan samples have complicated LPO patterns, and record A-, B- and C-type fabrics, along with a fabric consistent with deformation by {hk0}[001]. Fabrics with [001] slip directions are interpreted to be localised to the mantle directly above

the slab, and therefore volumetrically insignificant in terms of seismic anisotropy. [100] slip directions are inconsistent with the B-type olivine fabric model for generating trench-parallel seismic fast axes, and thus requiring alternative models to explain the data. Examination of the transition between the fabric types in the Japan samples also provides further evidence for pre-existing LPOs controlling the activation of later slip systems.

Integration of detailed petrographic observations and FTIR analysis reveals a potential fluid-assisted brittle-ductile deformation mechanism operating in the mantle. This has large-scale implications for olivine fabric development and the subsequent interpretation of seismic anisotropy above the mantle wedge, as well as potential implications for fracture-induced anisotropy, partial melting of peridotite, and chemical exchange between fluids, melt and grain interiors.

This study also provides significant insights into the chemistry of the metasomatic fluids in the mantle wedge. FTIR analysis of Lihir peridotite suggests that conditions of metasomatism were oxidising in nature and had a high silica activity, consistent with fluids released by a subducting slab. Oxygen and magnesium isotope compositions of Japan peridotites also reflect melt depletion and metasomatism that occurred in the Higashi-Akaishi mantle wedge, with the overall variations observed in the oxygen and magnesium isotope compositions providing further evidence for the heterogeneity of the Earth's mantle. Integration of EBSD and isotope analysis reveals that the oxygen isotope composition of the Japan samples reflects the conditions of formation of the different LPO types, and is the first study of its' kind to link isotopic composition and olivine fabric development.

In this thesis, a number of empirical observations are presented that provide insights into the relationship between olivine deformation and geochemistry, with numerous implications for deformation in the Earth's mantle. These observations raise a number of questions and provide the basis for further investigations based on the integration of microstructural and geochemical approaches, which would progress our understanding of the link between crystal-plastic deformation, water and geochemistry.

Acknowledgements

First and foremost, I would like to acknowledge my family and close friends for all their invaluable support and patience over the past few years, I couldn't have done it without you. I would also like to thank my supervisors Prof. Steve Reddy and Dr. Nick Timms, both of whom have provided much support, guidance and patience throughout my time at Curtin University, and have played a pivotal role in the development of my research and ideas. Both Steve and Nick are wonderful researchers who have inspired me to aim for academic excellence and to maintain high standards of research quality.

I have had many helpful intellectual discussions with other researchers, namely Dr. Dave Healy and Dr. Katy Evans, who have often provided me with alternative perspectives and encouraged me to think outside the box. Dr. Katy Evans is also gratefully acknowledged for contributing her expertise to the collection of FTIR data from the Australian Synchrotron. Thank you also to my fellow PhD candidates, in particular Robert Madden, Fiona Mothersole and Qian Wang for support and friendship over the past 4 years.

I would like to acknowledge the use of equipment, scientific and technical assistance of the Curtin University Electron Microscope Facility, which is partially funded by the University, State and Commonwealth Governments. Thanks go out to the staff at the Curtin University Electron Microscope Facility, particularly Elaine Miller, Dr. Rob Hart and Will Rickard, who have provided invaluable technical assistance with sample analysis on the SEMs. Thanks also to Dr. Ljiljana Puskar and Dr. Mark Tobin at the Australian Synchrotron in Melbourne, for all your assistance with planning and running experiments on the IR beamline, and to Dr. John Cliff at the Centre for Microscopy at the University of Western Australia for assistance in successfully collecting and processing data from the Cameca ims 1280 ion probe.

This research was funded by ARC grant DP0878453. The Tubaf xenolith samples used in this study were collected during Cruise SO-94 of *RV Sonne* (Edison project), which was organized by Freiberg University of Mining and Technology and funded

by the German Federal Ministry for Research and Technology (BMFT grant 03G0094A to P. Herzig). FTIR analysis was made possible as a result of Australian Synchrotron access grant 739/859.

Throughout my PhD research I held an Australian Postgraduate Award (APA) and Curtin Research Scholarship (CRS), and received funding from the Minerals and Energy Research Institute of Western Australia (MERIWA). I would therefore like to thank the Australian Government, Curtin University and MERIWA for providing this support.

Publications included within this thesis:

Chapter 6.

Gray, E., Reddy, S., Healy, D., Timms, N. and McInnes, B. The relationship between bulk fabrics and low-angle boundaries in olivine: Microstructural evidence for [a] slip in supra-subduction zone mantle. *Submitted manuscript*.

Table of Contents

List of Figures

List of Tables

Chapter 1. Introduction

1.1. Background and overview

Mantle processes play a key role in the development and evolution of plate tectonic processes on Earth. Convection of mantle material is arguably the primary driving force behind plate motions (Hager and O'Connell, 1981; Anderson, 1982; Chase and Sprowl, 1983), affecting global heat flow, melt generation and volcanism, crustal growth, ore mineralisation and earthquake generation (Tackley, 2000; Schubert *et al*., 2001; Hoernle *et al*., 2008). Of particular interest in terms of plate motions and tectonic processes is the dynamics of the upper mantle.

The upper mantle extends to depths of 400 km and overlies the transition zone, which continues to a depth of 660 – 670 km (Bullen, 1954; Anderson *et al*., 1971; Dziewonski and Anderson, 1981; Zhou and Clayton, 1990). Compositionally, the primary rock type of the Earth's upper mantle is peridotite, which is dominated by the mineral olivine ($(Fe,Mg)_2SiO_4$). Olivine accounts for approximately 60 - 70% of the volume of the upper mantle. Other primary phases that may or may not be present (depending on pressure and temperature) include chromite, orthopyroxene, clinopyroxene, plagioclase, amphibole and garnet.

As olivine is the most abundant constituent of the mantle, the rheological properties of olivine largely control the way the mantle flows (Karato and Wu, 1993). Under upper mantle conditions, olivine deforms predominantly by dislocation creep-controlled processes related to large-scale convection, causing the development of fabrics called lattice preferred orientations (LPOs) (Karato and Wu, 1993; Savage, 1999). On a molecular level, defects in the crystal structure of mantle minerals systematically migrate due to the operation of slip systems, resulting in the widespread alignment of minerals with the kinematic reference frame of the deformation. Recent experimentally-derived developments in our understanding of olivine deformation include the discovery of several different olivine LPO types (different combinations of crystal axis alignments) that can develop as a result of variations in mantle conditions, such as stress, temperature, pressure and water

content (Zhang and Karato, 1995; Zhang *et al*., 2000; Jung and Karato, 2001; Katayama *et al*., 2004 and Jung *et al*., 2006).

Characterisation of the mantle flow direction is imperative for understanding the evolution of a subduction system, and modelling plate behaviour at convergent margins (Bercovici, 1993; Funiciello *et al*., 2004; Bercovici, 2003). Seismic anisotropy is generated when seismic waves propagate through anisotropic structures, and is commonly employed to infer flow directions in the upper mantle (Ribe, 1989; Mainprice and Silver, 1993; Russo and Silver, 1994; Park and Levin, 2002). In the past, seismic fast axes were inferred to reflect the direction of mantle flow. This assumption was based on the development of olivine LPOs associated with [100] slip, as the olivine [100] axis controls the seismic fast direction (Nicolas and Christensen, 1987; Zhang and Karato, 1995). However, in many subduction systems, seismic fast axes align parallel to the trench (Russo and Silver, 1994; Gledhill and Gubbins, 1996; Smith *et al*., 2001; Peyton *et al*., 2001; Nakajima and Hasegawa, 2004), leading to the development of flow models that invoke trench-parallel flow. This challenges the conventional understanding of mantle flow in supra-subduction environments, which is described by a corner flow model characterised by flow directions normal to the trench. One of the biggest geodynamic questions of the past decade has been whether or not these seismic fast axes truly represent the direction of mantle flow (therefore indicating trench-parallel or three-dimensional flow).

The ambiguity in the interpretation of these observations has arisen due to the large number of sources of seismic anisotropy within subduction zones that have been highlighted by recent studies. These include different olivine fabrics (Zhang and Karato, 1995; Zhang *et al*., 2000; Jung and Karato, 2001; Katayama *et al*., 2004; Jung *et al*., 2006), dehydration embrittlement (Faccenda *et al*., 2008; Healy *et al*., 2009) and serpentinisation (Katayama *et al*., 2009; Boudier *et al*., 2010). The presence of water plays a central role in most of these models, therefore elucidating the geochemical and microstructural interactions between water and deforming mantle rocks is crucial for advancing current understanding of mantle processes. The role of water in promoting hydrolytic weakening in other nominally anhydrous silicate minerals has been noted by several studies, including quartz (Griggs &

Blacic; 1964; Griggs & Blacic, 1965; Griggs 1967), clinopyroxene (Boland & Tullis, 2013) and albite (Tullis & Yund, 1980).

Several challenges still remain in studying mantle rocks. Firstly, the vast majority of samples are xenoliths, which have been volcanically extruded at the Earth's surface. From a structural perspective these samples are out of context, and if they lack any obvious macroscopic foliation, are currently not used for olivine fabric analysis since they cannot be linked to a kinematic reference frame. This means that many natural observations of olivine fabrics are made using rocks that have been exhumed during orogenesis and have been subjected to later episodes of deformation, which may overprint the structures formed during mantle deformation. Secondly, much of the evidence for olivine fabric development in peridotite is experimental, and thus further studies are required to bridge the gap between the experimental results and natural fabrics, highlighting the importance of further investigation of natural peridotite samples.

1.2. Aims and scope of the study

There is a complex interplay between the crust and upper mantle, which is most evident at subduction zones, where one tectonic plate sinks beneath another into the underlying mantle. At subduction zones, there is opportunity for chemical exchange between the mantle and the crust, with mobilisation of elements originally from the mantle due to interaction with fluids, and recycling of crustal material back into the mantle. Due to the global significance of processes that occur within and related to subduction zones, it is important to fully understand the tectonic and structural evolution of the setting and the geochemical processes that occur.

A significant amount of controversy around mantle flow patterns and seismic anisotropy in subduction zones still exists. It is evident that water plays a significant and multi-faceted role in mantle dynamics within subduction zones. The presence of water not only affects olivine fabric transitions, but also melt formation and magmatism (Schmidt and Poli, 1998) and facilitates the development of hydrous phases that influence seismic properties (Mainprice and Ildefonse, 2008).

The link between water and the deformation of nominally anhydrous olivine is still unclear. It is known that water enhances the deformation rates of olivine (Mei and Kohlstedt, 2000 a,b) and can change the dominant slip system (Jung and Karato, 2001; Jung *et al.,* 2006), with broader implications for interpretations of mantle flow directions. As well as the relationship between water and slip system development in olivine, hydrous mantle fluids also geochemically interact with deforming peridotite, and only a few investigations (e.g. Ando *et al*., 2001 and Plümper *et al*., 2012) have been undertaken which look at the nature and possible implications of these interactions.

The aim of this research was to provide insight into the effect of water on the deformation mechanisms and geochemistry of olivine in the upper mantle, and how these processes affect mantle geodynamics on a larger scale. Specifically, the aims of the project are to:

- **Characterise natural olivine fabric types in deformed upper mantle samples collected from an intra-oceanic supra-subduction zone** – samples were sourced from Shikoku (Japan) and Lihir Island (Papua New Guinea).
- **Investigate chemical heterogeneity (specifically hydrogen, magnesium and oxygen) in mantle olivine associated with deformation-related microstructures** – to identify the presence and spatial distribution of chemical and isotope variations with respect to olivine microstructure, and to determine mechanisms for hydrogen incorporation into olivine, which is a nominally anhydrous mineral.
- **Provide an explanation for the apparent link between fabric type & diffusion of hydrogen in nominally anhydrous olivine** – primarily to verify published experimental results linking hydrogen diffusion and olivine fabric development by looking at natural samples and to explain the nature of this relationship.
- **Outline the implications for mantle rheology, seismic anisotropy and broader tectonic processes** – to highlight the significance of the link between water and olivine in the upper mantle for large-scale deformation processes and the interpretation of mantle flow dynamics through the use of seismic anisotropy data.

This research is significant in specifically targeting the relationships between deformation, chemistry and hydrogen affinity in olivine to understand large-scale tectonic processes. To date, few quantitative studies on the role of crystal-plastic deformation (i.e. dislocation creep) in modifying olivine chemistry and/or hydrogen incorporation have been reported in the literature. Despite there being strong empirical evidence from experiments linking deformation fabrics and water fugacity (Jung *et al*., 2006), the nature of the relationship between these factors is largely unknown.

A broad overview of the layout of this thesis is as follows:
Chapter 2 provides an overview of supra-subduction mantle deformation and related processes, as well as a review of the published literature, highlighting topics that are currently contentious and require further research.

Chapter 3 is comprised of an overview of the field areas from which the peridotite samples used in this study were acquired (Shikoku, Japan and Lihir Island, Papua New Guinea), in terms of tectonic evolution and regional geology.

Chapter 4 documents the research methodologies and procedures that were used to analyse the peridotite samples, which include petrography, electron backscatter diffraction (EBSD) analysis, ion microprobe analysis and Fourier transform infrared (FTIR) analysis using Synchrotron radiation.

Chapter 5 is a summary of the petrographic observations of Shikoku and Lihir peridotite samples, with detailed petrographic descriptions and photomicrographs provided in appendix 1.

Chapters 6, 7 and **8** present the results of EBSD microstructural analysis. **Chapter 6** is based on a paper submitted for publication in the journal Terra Nova in 2012. In this chapter, EBSD results from Higashi-Akaishi olivine are presented that provide evidence for the existence of a systematic relationship between intragrain microstructures and bulk LPO. The nature of this systematic relationship is such that

it can be used to identify the mantle flow direction in samples that do not have a foliation or lineation, and was applied to EBSD data from Lihir xenoliths. Analysis of metasomatised Lihir peridotite xenoliths showed that the bulk slip direction is parallel to the olivine a-axis. Typically, 'wet' olivine fabrics are predicted to have c-axis slip directions, and given the relationship between seismic anisotropy and olivine deformation, these results have significant implications for the interpretation of seismic anisotropy above subduction zones. I am the first author of this paper, having undertaken the research and written the paper, and I have 3 co-authors (author contribution statements can be found in Appendix 1).

Chapter 7 presents a more thorough and detailed account of the analysis of Lihir peridotites, highlighting that the operation of numerous different slip systems is required to produce a tectonic fabric, and that grain orientation plays a role in slip system activation.

Chapter 8 presents the results of a detailed study of the olivine microstructure and fabrics of the Japan peridotites. The complex deformation history of the samples, which includes deformation in the mantle as well as later exhumation-related structural and mineralogical overprinting, provides an opportunity to examine the microstructural evolution of a deforming olivine aggregate and to examine the features of different fabrics.

Chapter 9 is a three-part investigation into the link between deformation and geochemistry in olivine, presenting the results from petrographic fluid inclusion studies, Synchrotron FTIR analysis and Mg and O isotope analysis. These studies provide valuable insights into the conditions and complex interactions between deformation and geochemical conditions in the mantle wedge.

Chapter 10 is a discussion chapter which examines the outcome of this research as a whole, placing these results within a broader tectonic context and highlighting the implications for mantle geodynamics.

The thesis concludes with **Chapter 11**, which summarises the main findings and implications, as well as potential areas for further research.

1.3. References

Anderson, D.L., Sammis, C. and Jordan, T. (1971) Composition and Evolution of the Mantle and Core, *Science*, v. 171 p. 1103-1112.

Anderson, D.L. (1982) Hotspots, polar wander, Mesozoic convection and the geoid, *Nature*, v. 297, p. 391-393.

Ando, J., Shibata, Y., Okajima, Y., Kanagawa, K., Furusho, M. and Tomioka, N. (2001) Striped iron zoning of olivine induced by dislocation creep in deformed peridotites, *Nature*, v. 414, p. 893-895.

Bercovici, D. (1993) A Simple Model of Plate Generation from Mantle Flow, *International Journal of Geophysics*., v. 114, p. 635-650.

Bercovici, D. (2003) The generation of plate tectonics from mantle convection, *Earth and Planetary Science Letters*, v. 205, p. 107-121.

Boland, J.N., and Tullis, T.E. (2013) Deformation Behavior of Wet and Dry Clinopyroxenite in the Brittle to Ductile Transition Region. In B.E. Hobbs & H.C. Heard (Eds.). *Mineral and Rock Deformation: Laboratory Studies: The Paterson Volume*, American Geophysical Union, p. 35-49.

Boudier, F.o., Baronnet, A. and Mainprice, D. (2010) Serpentine Mineral Replacements of Natural Olivine and their Seismic Implications: Oceanic Lizardite versus Subduction-Related Antigorite, *Journal of Petrology*, v. 51, p. 495-512.

Bullen, K.E. (1954) Introduction to the Theory of Seismology: New York, Cambridge University Press, 296 p.

Chase, C. G. and Sprowl, D. R. 1983. The modern geoid and ancient plate boundaries. *Earth and Planetary Science Letters,* 62**,** 314-320.

Dziewonski, A.M. and Anderson, D.L. (1981) Preliminary reference Earth model, *Physics of the Earth and Planetary Interiors*, v. 25, p. 297-356.

Faccenda, M., Burlini, L., Gerya, T.V. and Mainprice, D. (2008) Fault-induced seismic anisotropy by hydration in subducting oceanic plates, *Nature*, v. 455, p. 1097-1100.

Funiciello, F., Faccenna, C. and Giardini, D. (2004) Role of lateral mantle flow in the evolution of subduction systems: insights from laboratory experiments, *International Journal of Geophysics*, v. 157, p. 1393-1406

Gledhill, K. and Gubbins, D. (1996) SKS splitting and the seismic anisotropy of the mantle beneath the Hikurangi subduction zone, New Zealand, *Physics of the Earth and Planetary Interiors*, v. 95, p. 227-236.

Griggs, D.T. (1967) Hydrolitic Weakening of Quartz and Other Silicates. *Geophys. J. R. Ast. Soc*, v. 14, p. 19-31.

Griggs, D.T. and Blacic, J.D. (1964) The strength of quartz in the ductile regime. *Transactions American Geophysical Union*, v. 45, p. 102.

Griggs, D.T. and Blacic, J.D. (1965) Quartz: Anomalous weakness of synthetic crystals. *Science*, v. 147, p. 292 – 295.

Hager, B.H. and O'Connell, R.J. (1981) A Simple Global Model of Plate Dynamics and Mantle Convection, *Journal of Geophysical Research*, v. 86, p. 4843-4867.

Healy, D., Reddy, S.M., Timms, N.E., Gray, E.M. and Brovarone, A.V. (2009) Trench-parallel fast axes of seismic anisotropy due to fluid-filled cracks in subducting slabs, *Earth and Planetary Science Letters*, v. 283, p. 75-86.

Hoernle, K., Abt, D.L., Fischer, K.M., Nichols, H., Hauff, F., Abers, G.A., van den Bogaard, P., Heydolph, K., Alvarado, G., Protti, M. and Strauch, W. (2008)

Arc-parallel flow in the mantle wedge beneath Costa Rica and Nicaragua, *Nature*, v. 451, p. 1094-1098.

Jung, H. and Karato, S. (2001) Water-induced Fabric Transitions in Olivine, *Science*, v. 293, p. 1460-1463.

Jung, H., Katayama, I., Jiang, Z., Hiraga, T. and Karato, S. (2006) Effect of water and stress on the lattice-preferred orientation of olivine, *Tectonophysics*, v. 421, p. 1-22.

Karato, S. and Wu, P. (1993) Rheology of the Upper Mantle: A Synthesis, *Science*, v. 260, p. 771-778.

Katayama, I., Jung, H. and Karato, S. (2004) New type of olivine fabric from deformation experiments at modest water content and low stress, *Geology*, v. 32, p. 1045-1048.

Katayama, I., Hirauchi, K.-i., Michibayashi, K. and Ando, J.-i. (2009) Trench-parallel anisotropy produced by serpentine deformation in the hydrated mantle wedge, *Nature*, v. 461, p. 1114-1117.

Mainprice, D. and Ildefonse, B. (2009) Seismic Anisotropy of Subduction Zone Minerals–Contribution of Hydrous Phases, *in* Lallemand, S., and Funiciello, F. (eds.) Subduction Zone Geodynamics: Frontiers in Earth Sciences, Springer Berlin Heidelberg, p. 63-84.

Mainprice, D. and Silver, P.G. (1993) Interpretation of SKS-waves using samples from the subcontinental lithosphere, *Physics of the Earth and Planetary Interiors*, v. 78, p. 257-280.

Mei, S. and Kohlstedt, D.L. (2000a) Influence of water on plastic deformation of olivine aggregates: 1. Diffusion creep regime, *Journal of Geophysical Research*, v. 105, p. 21,457-21,469.

Mei, S. and Kohlstedt, D.L. (2000b) Influence of water on plastic deformation of olivine aggregates: 2. Dislocation creep regime, *Journal of Geophysical Research*, v. 105, p. 21,471-21,481.

Nakajima, J. and Hasegawa, A. (2004) Shear-wave polarisation anisotropy and subduction-induced flow in the mantle wedge of northeastern Japan, *Earth and Planetary Science Letters*, v. 225, p. 365-377.

Nicolas, A. and Christensen, N.I. (1987) Formation of anisotropy in upper mantle peridotites: A review, Composition, Structure and Dynamics of the Lithosphere-Asthenosphere System, Volume 16: Geodynamics Series, American Geophysical Union, Washington, DC, p. 111-123.

Park, J. and Levin, V. (2002) Seismic Anisotropy: Tracing Plate Dynamics in the Mantle, *Science*, p. 485-489.

Peyton, V., Levin, V., Park, J., Brandon, M., Lees, J., Gordeev, E. and Ozerov, A. (2001) Mantle Flow at a Slab Edge: Seismic Anisotropy in the Kamchatka Region, *Geophysical Research Letters*, v. 28, p. 379-382.

Plümper, O., King, H., Vollmer, C., Ramasse, Q., Jung, H. and Austrheim, H. (2012) The legacy of crystal-plastic deformation in olivine: high-diffusivity pathways during serpentinization, *Contributions to Mineralogy and Petrology*, v. 163, p. 701-724.

Ribe, N.M. (1989) Seismic Anisotropy and Mantle Flow, *Journal of Geophysical Research*, v. 94, p. 4213-4223.

Russo, R.M. and Silver, P.G. (1994) Trench-parallel Flow Beneath the Nazca Plate from Seismic Anisotropy, *Science*, v. 263, p. 1105-1111.

Savage, M.K. (1999) Seismic anisotropy and mantle deformation: What have we learned from shear wave splitting? *Reviews of Geophysics*, v. 37, p. 65-106.

Schmidt, M.W. and Poli, S. (1998) Experimentally based water budgets for dehydrating slabs and consequences for arc magma generation, *Earth and Planetary Science Letters*, v. 163, p. 361-379.

Schubert, G., Turcotte, D.L. and Olson, P. (2001) Mantle Convection in the Earth and Planets: Cambridge, Cambridge University Press, 912 p.

Smith, G.P., Wiens, D.A., Fischer, K.M., Dorman, L.M., Webb, S.C. and Hildebrand, J.A. (2001) A Complex Pattern of Mantle Flow in the Lau Backarc, *Science*, v. 292, p. 713-716.

Tackley, P. (2000) Mantle Convection and Plate Tectonics: Toward an Integrated Physical and Chemical Theory, *Science*, v. 288, p. 2002.

Tullis, J., and Yund, R.A. (1980) Hydrolytic weakening of experimentally deformed Westerly granite and Hale albite rock, Journal of Structural Geology, v. 2, p. 439-451.

Zhang, S. and Karato, S. (1995) Lattice preferred orientation of olivine aggregates deformed in simple shear, *Nature*, v. 375, p. 774-777.

Zhang, S., Karato, S., Fitz Gerald, J., Faul, U.H. and Zhou, Y. (2000) Simple shear deformation of olivine aggregates, *Tectonophysics*, v. 316, p. 133-152.

Zhou, H.-W. and Clayton, R.W. (1990) P and S Wave Travel Time Inversions for Subducting Slab Under the Island Arcs of the Northwest Pacific, *Journal of Geophysical Research*, v. 95, p. 6829-6851.

Chapter 2. Mantle flow and seismic anisotropy in the supra-subduction region

2.1. Introduction and background

Developing a comprehensive understanding of the mantle flow field and tectonic processes is critical for understanding how the Earth has changed over time, providing insight into the geodynamic and thermal evolution of the planet (Funiciello *et al*., 2004; Stadler *et al*., 2010). The geometry of mantle flow at convergent margins, particularly within the mantle wedge of subduction zones, is complicated and controversial despite the vast amount of research that has been undertaken in this field (Karato *et al*., 2008; Long and Silver, 2008; Wirth and Long, 2010).

The lack of understanding of flow in the mantle wedge can be partly attributed to the fact that direct observations of supra-subduction peridotites are limited to xenoliths and orogenically exhumed peridotites. Limitations in studying mantle xenoliths arise from the fact that they are structurally out of context once they have been separated from the host rock. A clear macroscopic foliation and lineation needs to be identified in order to interpret an LPO, and if this is lacking, fabrics cannot be reliably linked to the kinematic reference frame. Furthermore, fabric studies of orogenically exhumed peridotites are often complex and can be problematic if not approached systematically, as exhumation-related processes can result in the overprinting of mantle fabrics by later episodes of deformation, with the exception of small lenses or pockets where the later deformation is less intense (e.g. Enami and Mizukami, 2004; Mizukami and Wallis, 2005; Jung, 2009).

Conventional mantle flow is often described as two-dimensional corner flow, with flow occurring perpendicular to the trench and that is initially coupled with the overriding plate before coupling with the subducting slab (Figure 2.1; van Keken, 2003). However, due to the observation of trench-parallel seismic fast axes above the forearc mantle of many subduction zones (e.g. Nakajima and Hasegawa, 2004; Figure 2.2), a number of alternative models have been developed suggesting that mantle wedge flow also involves a trench-parallel component (Russo and Silver, 1994; Buttles and Olson, 1998; Mehl *et al*., 2003; Long and Silver, 2008).

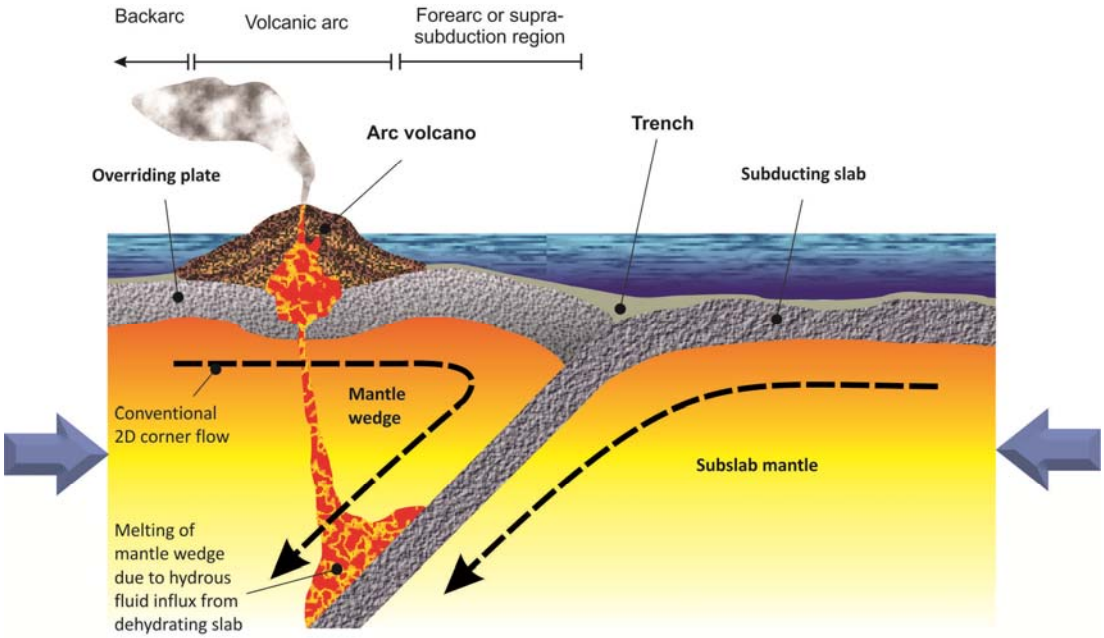

Figure 2.1. Schematic diagram illustrating the basic structure of a subduction zone, as well as the conventional understanding of mantle flow within subduction zones. Flow within the mantle wedge is usually described in terms of a two-dimensional corner wedge flow model, with the mantle flowing towards (and perpendicular to) the trench, before coupling with the subducting slab and descending into the mantle again.

One of the most controversial geodynamic questions of the past decade has been whether or not these seismic fast axes truly represent the direction of mantle flow (therefore indicating trench-parallel or three-dimensional flow). The ambiguity in the interpretation of these observations arises due to the large number of potential sources of seismic anisotropy within subduction zones. Seismic anisotropy can be generated by the alignment of olivine crystals in peridotite, which is how it has previously been linked to mantle flow directions and which can be modified by the addition of water during deformation (Jung and Karato, 2001; Jung *et al*., 2006). However, the presence of aligned hydrous minerals such as serpentine in the mantle wedge and subducting slab (Katayama *et al*., 2009; Boudier *et al*., 2010; Jung, 2011), dehydration-induced cracks (Healy *et al*., 2009) and brittle failure in the subducting slab (Faccenda *et al*., 2008) can also generate significant seismic anisotropy, and thus interpreting mantle flow directions from seismic anisotropy is not straightforward.

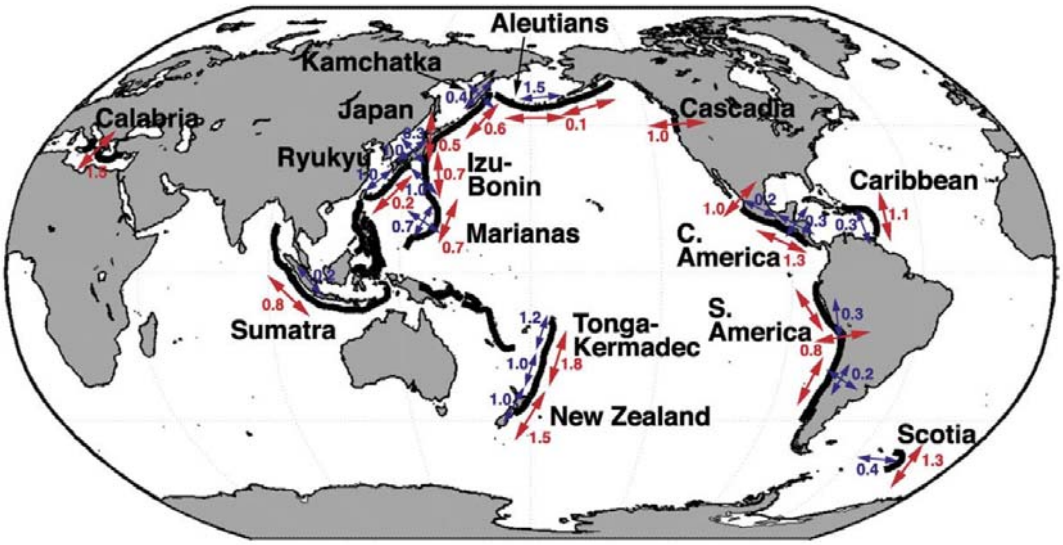

Figure 2.2. Shear wave splitting delay times and orientations for global subduction zones (Image from Long and Becker, 2010, and based on seismic anisotropy compilations from Long and Silver, 2008, 2009). Red arrows indicate fast directions for the sub-slab mantle and blue arrows indicate fast directions for the mantle wedge.

2.2. Olivine deformation in the mantle

The Earth's upper mantle is comprised of peridotite, with olivine making up approximately 60 – 70% of the rock. Mantle peridotite also contains other phases which may include orthopyroxene, clinopyroxene, spinel, chromite and garnet. As olivine is the most volumetrically significant mantle mineral, mantle flow is, therefore, controlled by the rheological properties of olivine (Russo and Silver, 1994; Karato and Jung, 2003). Olivine aggregates in the upper mantle deform by predominantly simple shear deformation (Tommasi *et al*., 1999) dominated by dislocation creep processes (Karato and Wu, 1993; Savage, 1999).

Dislocation creep has particular significance for understanding seismic anisotropy patterns, as it results in the development of olivine LPOs within the mantle. Early studies of olivine deformation and the development of olivine LPO in mantle rocks were undertaken by Turner (1942), Battey (1960), Raleigh (1963, 1968), Avé Lallemant and Carter (1970), Carter and Avé Lallemant (1970), Nicolas *et al*., (1971, 1973) and Avé Lallemant (1975). These studies established that olivine LPOs develop through crystal-plastic deformation by dislocation creep in the Earth's upper mantle, and that olivine [100] axes align parallel to mantle flow directions. More recent advances include work by Zhang and Karato (1995), Zhang *et al*. (2000), Jung

and Karato (2001), Jung and Karato (2001), Katayama *et al*. (2004) and Jung *et al*. (2006). The more recent studies have established the existence of several different fabric types that aren't necessarily characterised by olivine [100] slip directions, and lead to the current classification of olivine fabric types and associated mantle conditions.

Deformation by dislocation creep (both climb and glide) involves migration of defects along a particular crystallographic plane and in a particular crystallographic direction (i.e. the slip plane and slip direction), called a slip system. Experimental studies reveal that there are five different symmetrically distinct slip systems observed to operate in olivine at upper mantle conditions (Zhang and Karato, 1995; Zhang *et al*., 2000; Jung and Karato, 2001; Katayama *et al*., 2004 and Jung *et al*., 2006; Table 2.1), and each occur at different conditions of stress, temperature, water content and pressure. The orthorhombic symmetry of olivine means that each slip system consists of a family of two possible symmetric equivalents, with opposite slip directions. Individual crystals within a rock mass deforming by the operation of a particular slip system will align so that crystal axes are aligned in the same direction and plane, called a lattice preferred orientation (LPO), therefore the slip systems operating on a grain-scale will be reflected in the bulk fabric of the rock. According to the von Mises condition, five symmetrically different slip systems are required to accommodate the total strain within a deforming rock aggregate (von Mises, 1928), thus an LPO develops through the operation of a number of slip systems but generally reflects the operation of the slip system that has accommodated the most strain. Theoretically, the lineation direction of the bulk fabric will be sub-parallel to the slip direction, and the foliation plane will be sub-parallel to the slip plane.

The stability fields in terms of stress, temperature and water content for each of the different olivine fabrics (Table 2.1) is shown in Figure 2.3 (Jung *et al*., 2006). A- and D-type fabrics are produced through the operation of the (010)[100] and (0kl)[100] slip systems, respectively. Both are predicted to operate under relatively anhydrous conditions, with A-type fabrics occurring at lower stress than D-type fabrics.

Table 2.1. Slip systems that operate during deformation of olivine in the upper mantle, and the associated fabric/LPO type (◊Carter and Avé Lallemant, 1970; ◊Zhang and Karato, 1995; ◊Zhang *et al*., 2000; ◊Bystricky *et al*., 2001; *Jung and Karato, 2001; †Katayama *et al*., 2004; Jung *et al*., 2006). Slip system nomenclature is such that (slip plane)[slip direction].

Slip System	Rotation Axis	Associated Fabric Type
(010)[100]	[001]	A-type◊
(010)[001]	[100]	B-type*
(100)[001]	[010]	C-type*
(0kl)[100]	[011] or <110>	D-type◊
(001)[100]	[010]	E-type†

B-, C- and E-type fabrics (corresponding to the (010)[001], (100)[001] and (001)[100] slip systems, respectively) develop due to higher water content in the mantle. The transition from E- to C-type is dependent on water content, with C-type more stable at higher water content. Both E- and C-type fabrics occur at low to moderate stress, transitioning to B-type at higher stress conditions. B-type fabric is stable over a broad range of water contents, and the transition between B-type and C-type is sensitive to temperature (Katayama and Karato, 2006). These conditions are largely based on experimental observations however, and further work should be done to characterise the olivine fabrics and associated conditions of formation in natural peridotites.

The spatial distribution of different olivine fabric types within the mantle wedge is predicted by Kneller *et al*. (2005, 2008) and are expanded by Karato *et al*. (2008) to include the mantle in its' entirety (Figure 2.4). In the mantle wedge, E- or C-type olivine fabrics are predicted, with B-type fabrics forming in the upper tip of the wedge as a result of the high stress, hydrous conditions. A- and D-types are generally predicted to be restricted to the lithosphere, with the exception of a plume setting.

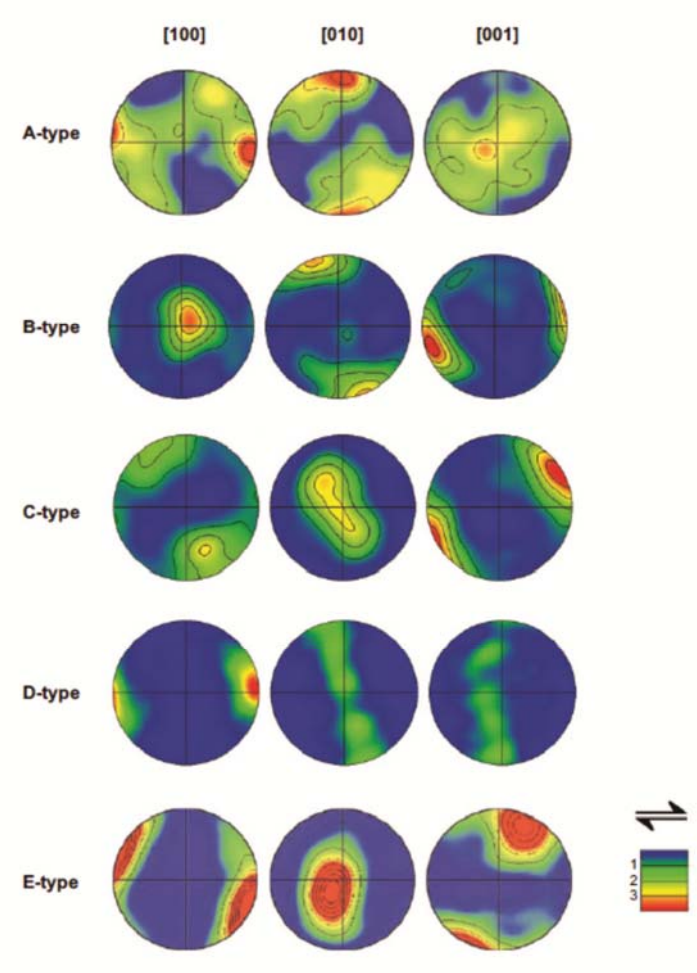

Figure 2.3 Pole figures of the different olivine fabric types showing the distribution of [100], [010] and [001] crystal axes with respect to the shear direction (x-axis) and shear plane (horizontal and projecting out of the page). This figure was taken from Karato *et al*. (2008) and was originally modified after Jung *et al*. (2006).

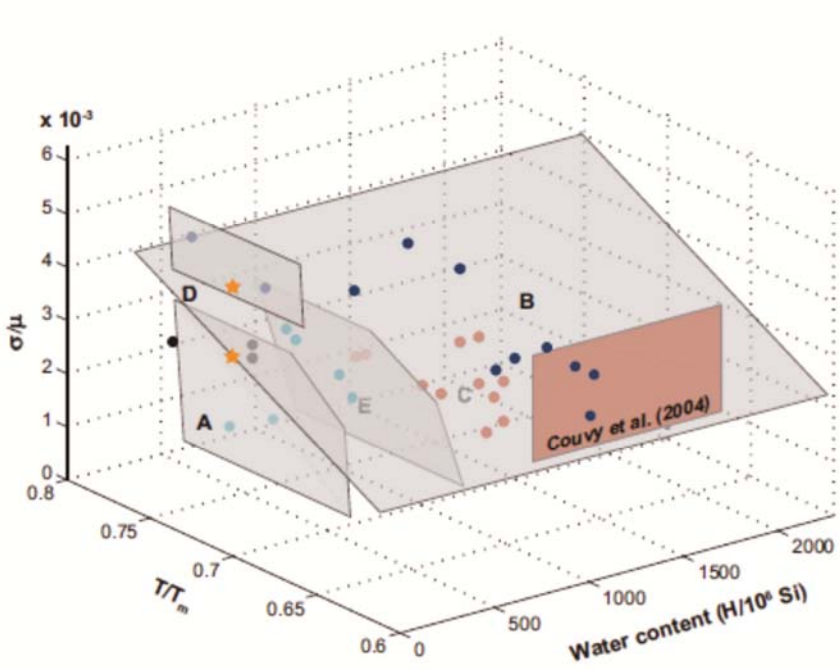

Figure 2.4. Graph illustrating the stability fields of the different olivine fabric types based on normalised water content, temperature and differential stress (vertical axis) taken from Karato *et al*. (2008). T = temperature; Tm = melting temperature; σ = deviatoric stress; μ = shear modulus.

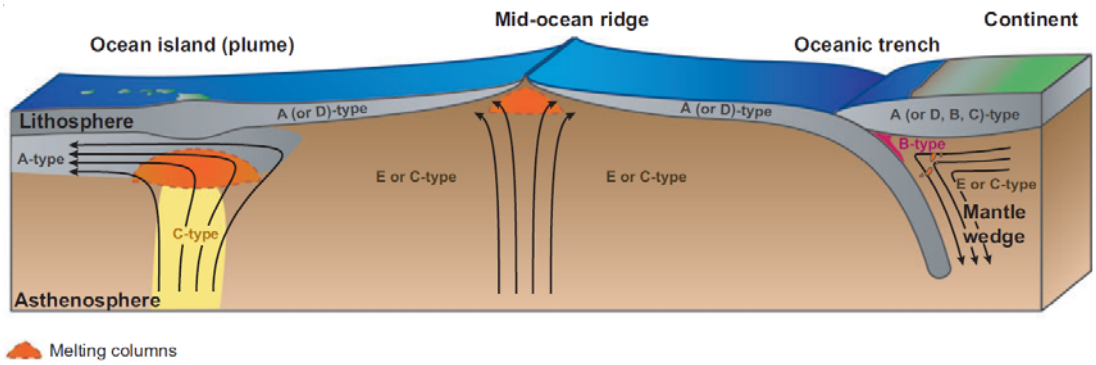

Figure 2.5. Predicted spatial distribution of olivine fabric types (taken from Karato *et al.*, 2008).

2.3. Seismic anisotropy patterns

Seismic anisotropy is a widespread tool that is used to determine the flow dynamics of the mantle (Ribe, 1989; Mainprice and Silver, 1993; Russo and Silver, 1994; Silver, 1996; Park and Levin, 2002). The velocity and properties of seismic waves are dependent on the elastic properties of the medium through which they travel (Silver, 1996). Both P- and S-waves can become polarised as they pass through anisotropic geological materials. When a wave becomes polarised, it splits into a fast ray or fast polarisation direction (ϕ) and a slow ray (Figure 2.6). There is also a delay time (δt) at the receiver station between the arrival of the fast and slow rays, which is usually expressed in seconds. Generally, the more anisotropic the material, the larger the delay time. For olivine, ϕ aligns with the [100] or a-axis (Nicolas and Christensen, 1987; Zhang and Karato, 1995). S-wave anisotropy (also called shear wave splitting) is most commonly used to infer the properties of the mantle flow field, and can be due to factors such as the alignment of minerals as a result of deformation or commonly oriented fractures and cracks that may also contain fluid (Russo and Silver, 1994; Silver, 1996).

Early work on seismic anisotropy and olivine LPO development in the mantle was undertaken by Hess (1964), Christensen (1966, 1971, 1984), Christensen and Crosson (1968), Francis (1969), Peselnick *et al.* (1974), Raitt *et al.* (1969), Lappin (1971), Crampin (1979) and Christensen and Salisbury (1979). These researchers established the existence of seismic anisotropy in the upper mantle and linked it to the preferred orientation of olivine due to mantle flow. The link between olivine [100] directions, seismic anisotropy and the spreading directions of mid-ocean ridges

was documented by Francis (1969) and Christensen (1984), who highlight the usefulness of this relationship for interpreting mantle flow dynamics.

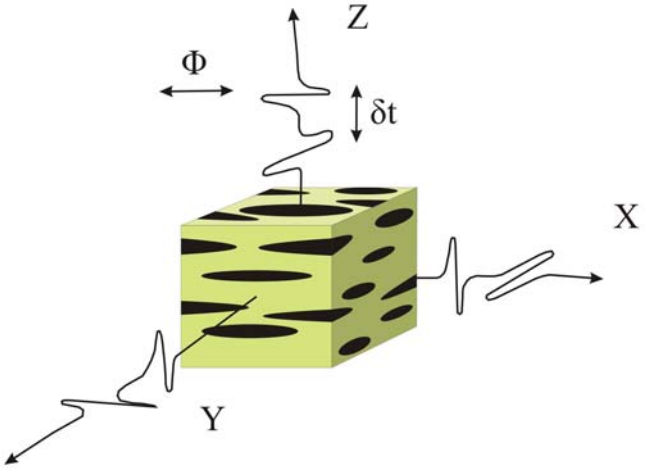

Figure 2.6. Splitting of a shear wave as it passes through an anisotropic material. The X, Y and Z axes are those of the structural framework, where X is the lineation, and XY is the foliation plane. δt is the time between fast and slow waves, and ϕ is the fast wave direction. Image taken from Gray (2008) and originally adapted from Silver (1996).

This relationship between olivine LPO and seismic anisotropy is often such that the seismic fast direction is parallel to the mantle flow direction, an observation which requires [100] slip directions (Hess, 1964; Zhang and Karato, 1995; Wolfe and Solomon, 1998; Wiens and Smith, 2003; Anderson *et al*., 2004). This is observed at spreading centres and plate interiors, where the direction of anisotropy is parallel to the direction of absolute plate motion (Hess, 1964; Wolfe and Solomon, 1998). However, seismic fast directions do not provide an unambiguous indication of upper mantle flow directions, as this relationship becomes complicated in a subduction zone setting. In subduction zones, the seismic fast axes observed commonly contradict the conventional mantle flow models (Figure 2.1), for both mantle wedge and sub-slab mantle (Russo and Silver, 1994; Gledhill and Gubbins, 1996; Smith *et al*., 2001; Peyton *et al*., 2001; Levin *et al*., 2004). The influence of factors such as complex flow geometries (due to the distribution of heterogeneous strain) and mantle wedge hydration have introduced complexity into interpretations.

The conventional model for flow within the mantle wedge is based on corner flow (Behn *et al*., 2007), in which the large-scale flow direction is perpendicular to the azimuth of the trench. The seismic fast axis alignment (ϕ) predicted to result from this kind of flow regime is normal to the trench. Trench-normal seismic fast axes have been observed along the Cascadia (Currie *et al*., 2004), Tonga (Fischer and Wiens, 1996) and Marianas subduction systems (Fouch and Fischer 1998), which is in agreement with the expected seismic response based on the mantle wedge corner

flow model. However, trench-parallel seismic fast axes have been observed in the supra-subduction region of many subduction systems, contradicting this flow model (Russo and Silver, 1994; Gledhill and Gubbins, 1996; Smith *et al*., 2001; Peyton *et al*., 2001; Nakajima and Hasegawa, 2004), suggesting that there may be some component of trench-parallel flow in the supra-subduction mantle (Russo and Silver, 1994; Hall *et al*., 2000; Smith *et al*., 2001; Mehl *et al*., 2003; Kneller and van Keken, 2007; Hoernle *et al*., 2008). Where trench-parallel seismic fast axes are observed, there is generally a common spatial pattern of alignment (Figure 2.7), with trench-perpendicular axes in the back-arc rotating to trench-parallel in the supra-subduction region between the arc and trench (e.g. Smith *et al*., 2001; Nakajima and Hasegawa, 2004).

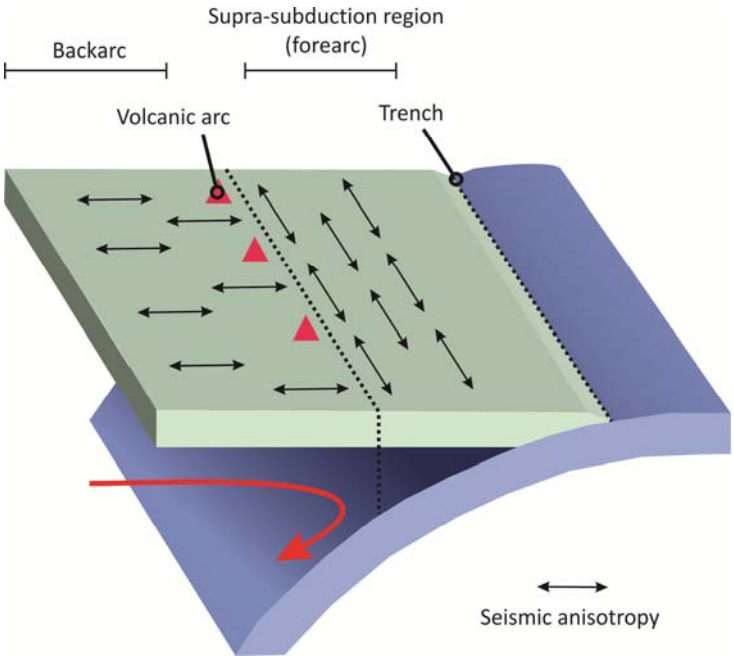

Figure 2.7. Commonly observed seismic fast axis orientations in a subduction setting (modified after Kneller *et al*., 2005). Seismic fast axes are trench-perpendicular until the forearc, where they are trench-parallel.

2.4. Generating Trench-parallel Seismic Anisotropy in the Mantle Wedge

Large-scale flow of the mantle in a subduction setting is characterised by flow towards the trench in the direction of absolute plate motion, with viscous coupling of the upper mantle and overlying plates. As illustrated in Figure 2.1, a simplified model describes a situation where mantle material in the wedge becomes coupled with the upper surface of the subducting slab. However in reality, flow geometries become more complicated and 3D in the approach to the subduction zone, and are

affected by a number of different factors. Models developed to explain the generation of trench-parallel seismic fast axes are discussed briefly here, however an in-depth discussion of the major models is provided in Chapter 10.

In the arc region, Behn *et al*. (2007) suggest that the foundering of dense arc crust may initiate small-scale convection, producing trench-parallel flow and other complicated flow patterns (Figure 2.8). It has also been suggested that there is a degree of small-scale convection in the mantle wedge, with a rotation axis perpendicular to the trench, and this may explain the shear-wave splitting delay times observed in nature through a weakening of the anisotropy produced by olivine LPO in the mantle wedge (Wirth and Korenaga, 2012). However, this theory is based on the assumption that flow in the mantle wedge is dominated by large-scale corner flow, and that there is no trench-parallel flow (e.g. Kneller and van Keken, 2007), which would destabilise the small-scale convection.

Trench-parallel seismic anisotropy in the mantle wedge may be a direct result of trench-parallel flow due to slab rollback (Russo and Silver, 1994; Smith *et al*., 2001; Long and Silver, 2008; Faccenda and Capitanio, 2012), oblique convergence (Smith *et al*., 2001), and along-strike variations in slab geometry (Kneller and van Keken, 2007) (Figure 2.8). However, the seismic anisotropy patterns could also be a result of a change in olivine fabric due to hydration of the mantle wedge, or other sources of anisotropy within the subduction system that are unrelated to the mantle flow regime.

Under anhydrous mantle conditions, olivine a-axes (the seismic fast direction) are predicted to align parallel to the large-scale flow direction, but hydration of olivine under fore-arc mantle conditions effects a change in the active slip systems (Lassak *et al*., 2006). Under the high stress and water-rich conditions expected in the mantle wedge, a B-type olivine fabric may develop such that the [001] or c-axis aligns parallel to the mantle flow direction and the [100] or a-axis aligns perpendicular to the shearing direction and parallel to the trench of the subduction zone (Figure 2.8) (Katayama *et al*., 2005; Jung *et al*., 2006; Lassak *et al*., 2006; Karato *et al*., 2008). A transition from a dominant flow direction of [100] to [001] between the backarc and forearc would explain the spatial distribution of trench-parallel seismic anisotropy above the mantle wedge (Kneller *et al*., 2005, 2007).

Fossil anisotropy from the subducting plate has also been proposed to explain trench-parallel seismic anisotropy (Long and Silver, 2008). However, no relationship between fossil spreading direction and seismic fast direction has been established and there is no correlation between increasing splitting time and increasing age, as would be expected with fossil anisotropy in the slab (Long and Silver, 2008). However, this does not rule out current subduction-related structures (e.g. cracks and fractures) as a source of trench-parallel seismic anisotropy. There is natural evidence for the presence of abundant fluid-filled cracks in the slab (Figure 2.8), which form as a result of the dehydration of hydrous metamorphic minerals (Healy *et al*., 2009). Modelling of the elastic properties of these structures predicts a seismic fast axis orientation that is parallel to the trench. Similarly, Faccenda *et al*. (2008) present a model in which the observed patterns in seismic anisotropy can be explained by the LPO of hydrous phases within steeply-dipping, serpentinised faults that occur in the uppermost part of the subducting slab (Figure 2.8).

The role of serpentinites in generating seismic anisotropy is not only restricted to the subducting slab. The LPO of serpentine that replaces olivine in the mantle wedge may also generate trench-parallel seismic anisotropy (Boudier *et al*., 2010; Katayama *et al*., 2009). Antigorite replacing primary mantle olivine inherits a preferred orientation from the host peridotite, and the S-wave fast polarisation direction predicted from this relationship is trench-parallel (Boudier *et al*., 2010). Katayama *et al*. (2009) present a similar theory, however they suggest that it is the deformation of the serpentine itself that is the source of the trench-parallel anisotropy.

The presence of melt in the mantle wedge may also play a role in generating trench-parallel seismic anisotropy (Holtzman *et al*., 2003). An experimental study done by Holtzman *et al*. (2003) provides evidence that the alignment of melt pockets can result in strain partitioning causing the olivine a-axes to orient perpendicular to the shearing direction, which could cause seismic fast axes to orient parallel to the trench (Figure 2.8).

Despite the vast amount of work that has been published surrounding the issue, the cause of trench parallel seismic anisotropy above the supra-subduction mantle is still

unclear. There may be a trench-parallel flow component, however there are numerous other factors that can influence the generation of seismic anisotropy and hence complicate the relationship between mantle flow and seismic fast axis alignment. One or many of these factors could be involved in producing trench parallel seismic anisotropy, reflecting a tectonically and geochemically complex system. It is evident, however, that nearly all of the factors that affect seismic anisotropy development at subduction zones are the result of the presence of water, highlighting the importance of understanding the link between water and tectonics.

The effect of water on plate tectonic processes is significant, and this relationship is primarily responsible for the environment and tectonics on Earth at the present day (Kaula *et al*., 1994; Regenauer-Lieb *et al*., 2001; Regenauer-Lieb and Kohl, 2003). The presence of water during deformation at subduction zones introduces geochemical and structural complexities into the system that influence the way that seismic waves interact with the rocks in this region of the Earth, resulting in the aforementioned ambiguity in seismic interpretations. Thus, comprehending the interactions between water and tectonics is critical for understanding many globally significant processes, including subduction initiation (Regenauer-Lieb *et al*., 2001) plate-mantle coupling (Becker and Faccena, 2009), asthenospheric and lithospheric strength (Becker and Faccena, 2009), arc volcanism (Wiens and Smith, 2003), melt generation and transport (Hirth and Kohlstedt, 1996; Abt *et al*., 2009), crustal growth (Doglioni *et al*., 2009) and orogenesis, ore mineralisation and earthquake generation.

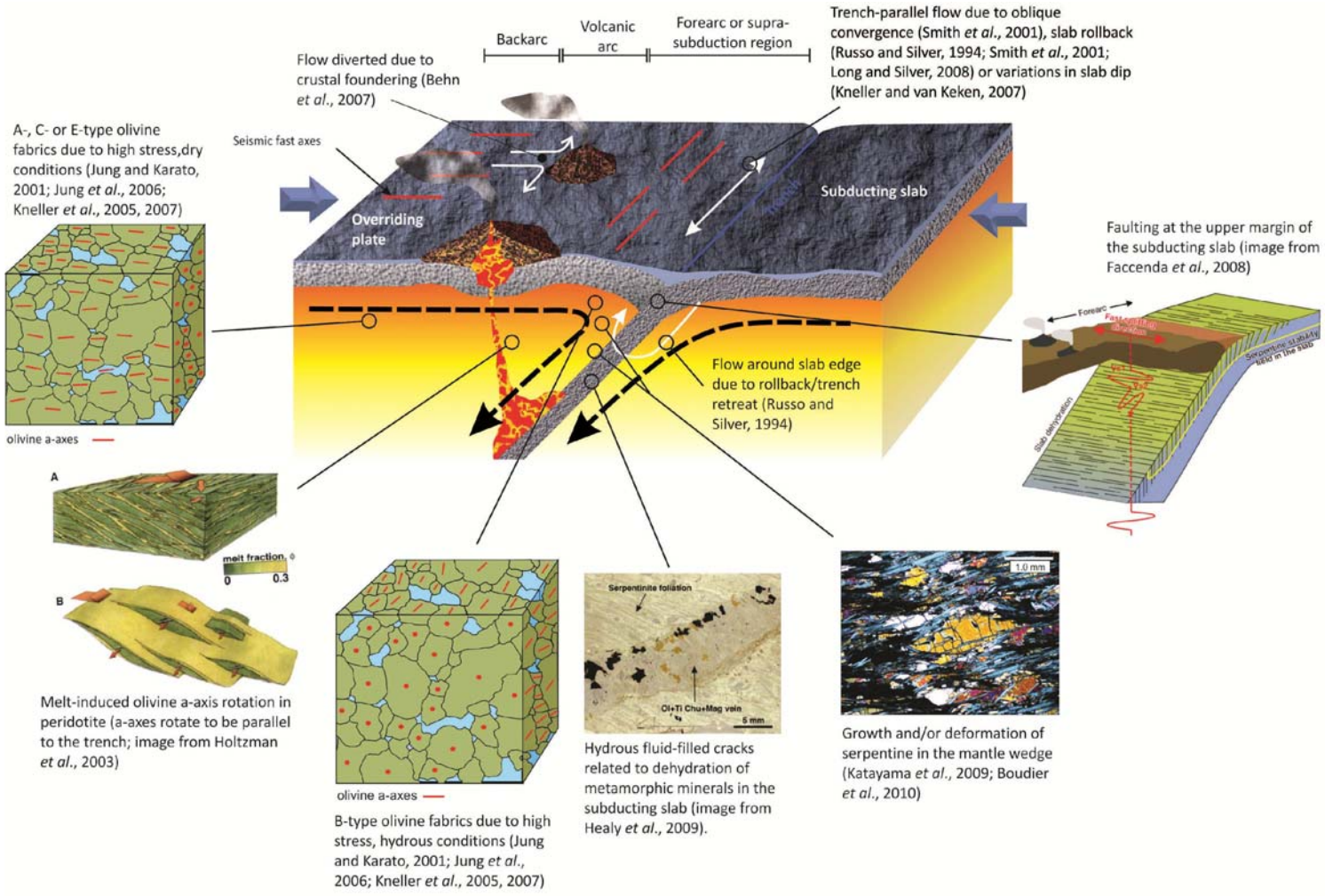

Figure 2.8. Schematic diagram illustrating the complex mantle flow dynamics and factors that can affect seismic anisotropy generation within a subduction zone. Large-scale flow towards and perpendicular to the trench still occurs, however there are a number of other factors that can affect flow patterns.

2.5. References

Abt, D.L., Fischer, K.M., Abers, G.A., Strauch, W., Protti, J.M. and Gonzalez, V. (2009) Shear wave anisotropy beneath Nicaragua and Costa Rica; implications for flow in the mantle wedge, *Geochemistry, Geophysics, Geosystems - G3*, v. 10, 26 p.

Anderson, M.L., Zandt, G., Triep, E., Fouch, M., and Beck, S. (2004) Anisotropy and mantle flow in the Chile-Argentina subduction zone from shear wave splitting analysis, *Geophysical Research Letters*, v. 31, 4 p.

Avé Lallemant, H.G. (1975) Mechanisms of preferred orientations of olivine in tectonite peridotite, *Geology*, v. 3, p. 653-656.

Ave'Lallemant, H.G. and Carter, N.L. (1970) Syntectonic Recrystallization of Olivine and Modes of Flow in the Upper Mantle, *Geological Society of America Bulletin*, v. 81, p. 2203-2220.

Battey, M.H. (1960) The relationship between preferred orientation of olivine in dunite and the tectonic environment, *American Journal of Science*, v. 258, p. 716-727.

Becker, T., Lallemand, S. and Funiciello, F. (2009) A review of the role of subduction dynamics for regional and global plate motions, Subduction Zone Geodynamics, Springer Berlin Heidelberg, 3-34 p.

Behn, M.D., Hirth, G. and Keleman, P.B. (2007) Trench-Parallel Anistropy Produced by Foundering of Arc Lower Crust, *Science*, v. 317, p. 108-111.

Boudier, F.O., Baronnet, A. and Mainprice, D. (2010) Serpentine Mineral Replacements of Natural Olivine and their Seismic Implications: Oceanic Lizardite versus Subduction-Related Antigorite, *Journal of Petrology*, v. 51, p. 495-512.

Carter, N.L. and Ave'Lallemant, H.G. (1970) High temperature flow of dunite and peridotite, *Geological Society of America Bulletin*, v. 81, p. 2181-2202.

Christensen, N.I. (1966) Shear Wave Velocities in Metamorphic Rocks at Pressures to 10 Kilobars, *Journal of Geophysical Research*, v. 71, p. 3549-3556.

Christensen, N.I. (1971) Shear Wave Propagation in Rocks, *Nature*, v. 229, p. 549-550.

Christensen, N.I. (1984) The magnitude, symmetry and origin of upper mantle anisotropy based on fabric analyses of ultramafic tectonites, *Geophysical Journal Royal Astronomical Society*, v. 76, p. 89-111.

Christensen, N.I., and Crosson, R.S. (1968) Seismic anisotropy in the upper mantle, *Tectonophysics*, v. 6, p. 93-107.

Christensen, N.I. and Salisbury, M.H. (1979) Seismic Anisotropy in the Oceanic Upper Mantle: Evidence From the Bay of Islands Ophiolite Complex, *Journal of Geophysical Research*, v. 84, p. 4601-4610.

Couvy, H., Frost, D. J., Heidelbach, F., Nyilas, K., Ungár, T., Mackwell, S., & Cordier, P. (2004) Shear deformation experiments of forsterite at 11 GPa - 1400°C in the multianvil apparatus. *European Journal of Mineralogy,* v. 16, p. 877-889.

Crampin, S. (1979) Seismic anisotropy in the upper mantle, *Tectonophysics*, v. 56, p. 131.

Currie, C.A., Cassidy, J.F., Hyndman, R.D. and Bostock, M.G. (2004) Shear wave anisotropy beneath the Cascadia subduction zone and western North American craton, *International Journal of Geophysics*, v. 157, p. 341-353.

Doglioni, C., Tonarini, S. and Innocenti, F. (2009) Mantle wedge asymmetries and geochemical signatures along W- and E–NE-directed subduction zones,

Lithos, v. 113, p. 179-189.

Faccenda, M., Burlini, L., Gerya, T.V. and Mainprice, D. (2008) Fault-induced seismic anisotropy by hydration in subducting oceanic plates, *Nature*, v. 455, p. 1097-1100.

Faccenda, M. and Capitanio, F.A. (2012) Development of mantle seismic anisotropy during subduction-induced 3-D flow, *Geophysical Research Letters*, v. 39, 5 p.

Fischer, K.M. and Wiens, D.A. (1996) The depth distribution of mantle anisotropy beneath the Tonga subduction zone, *Earth and Planetary Science Letters*, v. 142, p. 253-260.

Fouch, M.J. and Fischer, K.M. (1998) Shear wave anisotropy in the Mariana subduction zone, *Geophysical Research Letters*, v. 25, p. 1221-1224.

Francis, T.J.G. (1969) Generation of seismic anisotropy in the upper mantle along the mid-oceanic ridges, *Nature*, v. 221, p. 162-165.

Funiciello, F., Faccenna, C. and Giardini, D. (2004) Role of lateral mantle flow in the evolution of subduction systems: insights from laboratory experiments, *Geophysical Journal International*, v. 157, p. 1393-1406.

Gledhill, K. and Gubbins, D. (1996) SKS splitting and the seismic anisotropy of the mantle beneath the Hikurangi subduction zone, New Zealand, *Physics of the Earth and Planetary Interiors*, v. 95, p. 227-236.

Gray, E. (2008) Microstructural characterisation of olivine and implications for mantle geodynamics [Honours thesis], Curtin University of Technology, 104 p.

Hall, C.E., Fischer, K.M., Parmentier, E.M. and Blackman, D.K. (2000) The influence of plate motions on three-dimensional back arc mantle flow and

shear wave splitting, *Journal of Geophysical Research.*, v. 105, p. 28009-28033.

Healy, D., Reddy, S.M., Timms, N.E., Gray, E.M. and Brovarone, A.V. (2009) Trench-parallel fast axes of seismic anisotropy due to fluid-filled cracks in subducting slabs, *Earth and Planetary Science Letters*, v. 283, p. 75-86.

Hess, H.H. (1964) Seismic anisotropy of the uppermost mantle under oceans, *Nature*, v. 203, p. 629-631.

Hirth, G. and Kohlstedt, D.L. (1996) Water in the oceanic upper mantle: implications for rheology, melt extraction and the evolution of the lithosphere, *Earth and Planetary Science Letters*, v. 144, p. 93-108.

Hoernle, K., Abt, D.L., Fischer, K.M., Nichols, H., Hauff, F., Abers, G.A., van den Bogaard, P., Heydolph, K., Alvarado, G., Protti, M. and Strauch, W. (2008) Arc-parallel flow in the mantle wedge beneath Costa Rica and Nicaragua, *Nature*, v. 451, p. 1094-1098.

Holtzman, B.K., Kohlstedt, D.L., Zimmerman, M.E., Heidelbach, F., Hiraga, T. and Hustoft, J. (2003) Melt Segregation and Strain Partioning: Implications for Seismic Anisotropy and Mantle Flow, *Science*, v. 301, p. 1227-1230.

Jung, H. (2011) Seismic anisotropy produced by serpentine in mantle wedge, *Earth and Planetary Science Letters*, v. 307, p. 535-543.

Jung, H. and Karato, S. (2001) Water-induced Fabric Transitions in Olivine, *Science*, v. 293, p. 1460-1463.

Jung, H., Katayama, I., Jiang, Z., Hiraga, T. and Karato, S. (2006) Effect of water and stress on the lattice-preferred orientation of olivine, *Tectonophysics*, v. 421, p. 1-22.

Karato, S. and Jung, H. (2003) Effects of pressure on high-temperature dislocation

creep in olivine, *Philosophical Magazine*, v. 83, p. 401-414.

Karato, S., Jung, H., Katayama, I. and Skemer, P. (2008) Geodynamic Significance of Seismic Anisotropy of the Upper Mantle: New Insights from Laboratory Studies, *Annual Review of Earth and Planetary Sciences*, v. 36, p. 59-95.

Karato, S., and Wu, P. (1993) Rheology of the Upper Mantle: A Synthesis, *Science*, v. 260, p. 771-778.

Katayama, I., Hirauchi, K.-i., Michibayashi, K. and Ando, J.-i. (2009) Trench-parallel anisotropy produced by serpentine deformation in the hydrated mantle wedge, *Nature*, v. 461, p. 1114-1117.

Katayama, I., Jung, H. and Karato, S. (2004) New type of olivine fabric from deformation experiments at modest water content and low stress, *Geology*, v. 32, p. 1045-1048.

Katayama, I. and Karato, S. (2006) Effect of temperature on the B- to C-type olivine fabric transition and implication for flow pattern in subduction zones, *Physics of the Earth and Planetary Interiors*, v. 157, p. 33-45.

Katayama, I., Karato, S. and Brandon, M. (2005) Evidence of high water content in the deep upper mantle inferred from deformation microstructures, *Geology*, v. 33, p. 613-616.

Kaula, W.M., Owen, T., Runcorn, S.K., and Tozer, D.C. (1994) The Tectonics of Venus [and Discussion], *Philosophical Transactions of the Royal Society of London. Series A: Physical and Engineering Sciences*, v. 349, p. 345-355.

Kneller, E.A., Long, M.D. and van Keken, P.E. (2008) Olivine fabric transitions and shear wave anisotropy in the Ryukyu subduction system, *Earth and Planetary Science Letters*, v. 268, p. 268-282.

Kneller, E.A. and van Keken, P.E. (2007) Trench-parallel flow and seismic

anisotropy in the Mariana and Andean subduction systems, *Nature*, v. 450, p. 1222-1225.

Kneller, E.A., van Keken, P.E., Karato, S. and Park, J. (2005) B-type olivine fabric in the mantle wedge: Insights from high-resolution non-Newtonian subduction zone models, *Earth and Planetary Science Letters*, v. 237, p. 781-797.

Lappin, M.A. (1971) The Petrofabric Orientation of Olivine and Seismic Anisotropy of the Mantle, *Journal of Geology*, v. 79, p. 730-740.

Lassak, T.M., Fouch, M.J., Hall, C.E. and Kaminski, E. (2006) Seismic characterization of mantle flow in subduction systems: Can we resolve a hydrated mantle wedge?, *Earth and Planetary Science Letters*, v. 243, p. 632-649.

Levin, V., Droznin, D., Park, J. and Gordeev, E. (2004) Detailed mapping of seismic anisotropy with local shear waves in southeastern Kamchatka, *International Journal of Geophysics*, v. 158, p. 1009-1023.

Long, M.D. and Becker, T.W. (2010) Mantle dynamics and seismic anisotropy, *Earth and Planetary Science Letters*, v. 297, p. 341-354.

Long, M.D. and Silver, P.G. (2008) The Subduction Zone Flow Field from Seismic Anisotropy: A Global View, *Science*, v. 319, p. 315-319.

Mainprice, D. and Silver, P.G. (1993) Interpretation of SKS-waves using samples from the subcontinental lithosphere, *Physics of the Earth and Planetary Interiors*, v. 78, p. 257-280.

Mehl, L., Hacker, B.R., Hirth, G. and Keleman, P.B. (2003) Arc-parallel flow within the mantle wedge: Evidence from the accreted Talkeetna arc, south central Alaska, *Journal of Geophysical Research*, v. 108, p. ESE 4-1 - 4-18.

Nakajima, J. and Hasegawa, A. (2004) Shear-wave polarisation anisotropy and subduction-induced flow in the mantle wedge of northeastern Japan, *Earth and Planetary Science Letters*, v. 225, p. 365-377.

Nicolas, A., Bouchez, J.L., Boudier, F. and Mercier, J.C. (1971) Textures, structures and fabrics due to solid state flow in some European lherzolites, *Tectonophysics*, v. 12, p. 55-86.

Nicolas, A., Boudier, F. and Boullier, A. (1973) Mechanisms of flow in naturally and experimentally deformed peridotites, *American Journal of Science*, v. 273, p. 853-876.

Park, J. and Levin, V. (2002) Seismic Anisotropy: Tracing Plate Dynamics in the Mantle, *Science*, p. 485-489.

Peselnick, L., Nicolas, A. and Stevenson, P.R. (1974) Velocity anisotropy in a mantle peridotite from the Ivrea zone: application to upper mantle anisotropy, *Journal of Geophysical Research*, v. 79, p. 1175-1182.

Peyton, V., Levin, V., Park, J., Brandon, M., Lees, J., Gordeev, E. and Ozerov, A. (2001) Mantle Flow at a Slab Edge: Seismic Anisotropy in the Kamchatka Region, *Geophysical Research Letters*, v. 28, p. 379-382.

Raitt, R.W., Shor, G.G., Francis, T.J.G. and Morris, G.B. (1969) Anisotropy of the Pacific upper mantle, *Journal of Geophysical Research*, v. 74, p. 3095-3109.

Raleigh, C.B. (1963) Fabrics of naturally and experimentally deformed olivine, University of California, Los Angeles-Geology.

Raleigh, C.B. (1968) Mechanisms of Plastic Deformation of Olivine, *Journal of Geophysical Research*, v. 73, p. 5391-5406.

Regenauer-Lieb, K. and Kohl, T. (2003) Water solubility and diffusivity in olivine: its role in planetary tectonics, *Mineralogical Magazine*, v. 67, p. 697-715.

Regenauer-Lieb, K., Yuen, D.A. and Branlund, J. (2001) The Initiation of Subduction: Criticality by Addition of Water? *Science*, v. 294, p. 578-580.

Ribe, N.M. (1989) Seismic Anisotropy and Mantle Flow, *Journal of Geophysical Research*, v. 94, p. 4213-4223.

Russo, R.M. and Silver, P.G. (1994) Trench-parallel Flow Beneath the Nazca Plate from Seismic Anisotropy, *Science*, v. 263, p. 1105-1111.

Savage, M.K. (1999) Seismic anisotropy and mantle deformation: What have we learned from shear wave splitting? *Reviews of Geophysics*, v. 37, p. 65-106.

Silver, P.G. (1996) Seismic Anisotropy Beneath the Continents: Probing the Depths of Geology, *Annual Review of Earth and Planetary Sciences*, v. 24, p. 385-432.

Simpson, F. (2002) Intensity and direction of lattice-preferred orientation of olivine: are electrical and seismic anisotropies of the Australian mantle reconcilable? *Earth and Planetary Science Letters*, v. 203, p. 535-547.

Smith, G.P., Wiens, D.A., Fischer, K.M., Dorman, L.M., Webb, S.C. and Hildebrand, J.A. (2001) A Complex Pattern of Mantle Flow in the Lau Backarc, *Science*, v. 292, p. 713-716.

Stadler, G., Gurnis, M., Burstedde, C., Wilcox, L.C., Alisic, L. and Ghattas, O. (2010) The Dynamics of Plate Tectonics and Mantle Flow: From Local to Global Scales, *Science*, v. 329, p. 1033-1038.

Tommasi, A., Tikoff, B. and Vauchez, A. (1999) Upper mantle tectonics: three-dimensional deformation, olivine crystallographic fabrics and seismic properties, *Earth and Planetary Science Letters*, v. 168, p. 173-186.

Turner, F.J. (1942) Preferred orientation of olivine crystals in peridotites, with

special reference to New Zealand examples, *Transactions of the Royal Society of New Zealand*, v. 72, p. 280-300.

Wiens, D.A. and Smith, G.P. (2003) Seismological Constraints on Flow Patterns Within the Mantle Wedge, *Geophysical Monographs*, p. 48.

Wirth, E. and Long, M.D. (2010) Frequency-dependent shear wave splitting beneath the Japan and Izu-Bonin subduction zones, *Physics of the Earth and Planetary Interiors*, v. 181, p. 141-154.

Wirth, E.A. and Korenaga, J. (2012) Small-scale convection in the subduction zone mantle wedge, *Earth and Planetary Science Letters*, v. 357–358, p. 111-118.

Wolfe, C.J. and Solomon, S.C. (1998) Shear-Wave Splitting and Implications for Mantle Flow Beneath the MELT Region of the East Pacific Rise, *Science*, v. 280, p. 1230-1232.

Zhang, S. and Karato, S. (1995) Lattice preferred orientation of olivine aggregates deformed in simple shear, *Nature*, v. 375, p. 774-777.

Zhang, S., Karato, S., Fitz Gerald, J., Faul, U.H. and Zhou, Y. (2000) Simple shear deformation of olivine aggregates, *Tectonophysics*, v. 316, p. 133-152.

Chapter 3. Regional geology, tectonic evolution and sample localities

3.1. Introduction

In order to provide insight into the deformation of the Earth's upper mantle and the development of olivine fabrics, samples were acquired from two different field localities. The sample locations chosen for this study were Mt. Higashi-Akaishi, Japan, and Lihir Island, Papua New Guinea. Both localities lie on the Pacific plate boundary (Figure 3.1), which is dominated by trench-parallel seismic fast axes in the supra-subduction region (Figure 2.2; Long and Silver, 2008, 2009; Long and Becker, 2010).

Mt. Higashi-Akaishi is on Shikoku Island, a smaller island which lies southwest of Honshu and east of Kyushu, within the Besshi region. The rocks of this region are part of the Sanbagawa Belt and locally part of the Besshi Nappe complex (Kunigiza *et al*., 1986; Takasu, 1989), and include subduction-related mafic and ultramafic igneous bodies hosted within a metasedimentary sequence (Banno *et al*., 1978; Enami, 1982; Higashino, 1990). Alpine-type peridotites within the sequence are suggested to represent supra-subduction mantle (Tasaka *et al*., 2008; Hattori *et al*., 2010) and record B-type olivine fabrics (Mizukami *et al*., 2004; Mizukami and Wallis, 2005). Thus these peridotites provides a valuable opportunity to investigate the deformation processes occurring in the regions of the mantle suggested by some models (e.g. Jung *et al*., 2006) to be responsible for the generation of trench-parallel seismic anisotropy.

The Lihir samples are basalt-hosted peridotite xenoliths that were dredged from the seafloor surrounding the Tubaf seamount near Lihir Island (Gregoire *et al*., 2001; McInnes *et al*., 2001) by the RV Sonne research vessel. Sample location and petrology suggest that these xenoliths are also of supra-subduction mantle affinity (McInnes *et al*., 2001) and have undergone interaction with hydrous fluids. Thus the Lihir samples come from a region of the mantle consistent with conditions that are

predicted to cause B-type olivine fabrics, although there have been no B-type olivine fabrics observed in mantle xenoliths to date.

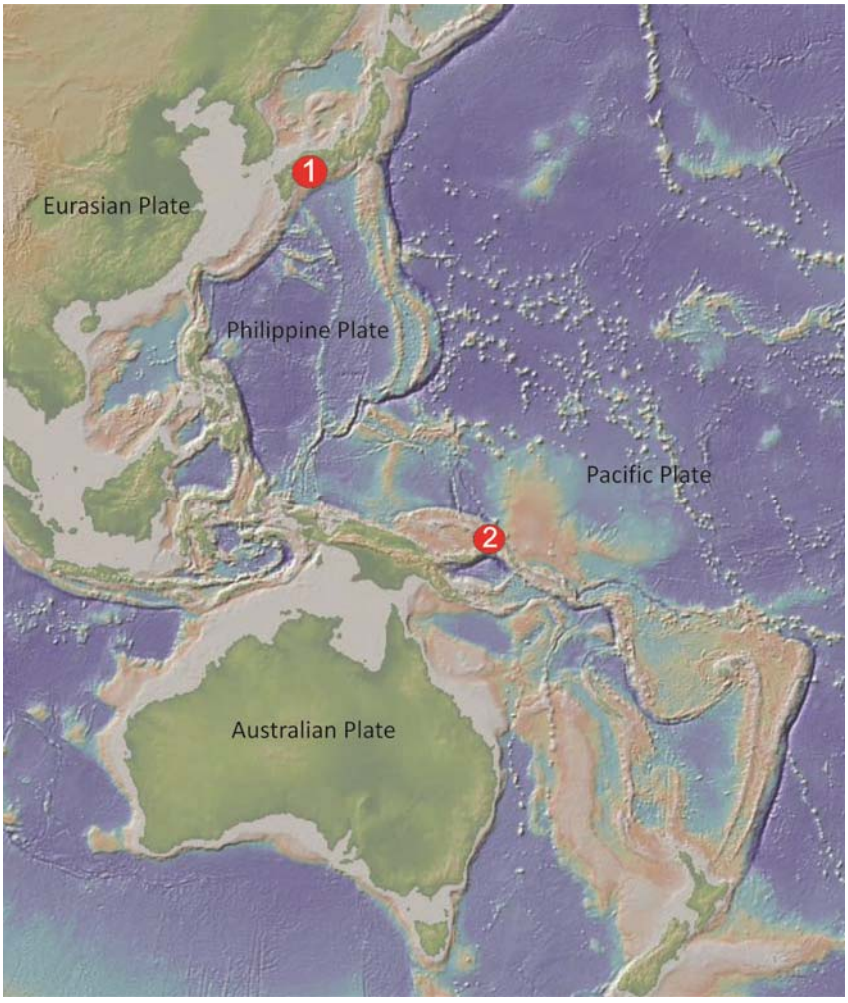

Figure 3.1. Map of the southwest Pacific region showing sample localities. 1) Higashi-Akaishi peridotite body, Shikoku, Japan; 2) Lihir Island, NE of Papua New Guinea. Both suites of samples are from the fore-arc region of subduction zones along the Pacific plate boundary (base map from GeoMapApp 2.3).

3.2. Shikoku, Japan

3.2.1. Tectonic Setting

The Japanese Islands have undergone a complex tectonic evolution that has involved the development of accretionary wedge complexes (Mizukami and Wallis, 2005; Enami, 2004; Takasu *et al*., 1994) that have later been exhumed within an orogenic metamorphic belt system, the Sanbagawa belt. The geology of the Sanbagawa belt represents the deepest parts of strongly-deformed Mesozoic accretionary complexes in the Japanese Island Arc formed during oceanic crustal subduction beneath the Eurasian continental margin during the Cretaceous (Enami, 2004; Mizukami and Wallis, 2005). To the North of the Sanbagawa Belt lies the Ryoke Belt, and these are

separated by the Median Tectonic Line (MTL), a major strike slip fault (Figure 3.2; Wallis *et al*., 2000; Enami, 2004; Takasu *et al*., 1994). To the South, the Sanbagawa Belt is bounded by the Mikabu Greenstone Complex (Takasu *et al*., 1994).

The Sanbagawa belt is divided into 3 distinct tectonochronological units and each have distinct metamorphic histories (Takasu *et al*., 1994, Wallis *et al*., 2000). The Kuma Nappe complex is the oldest unit. Muscovite yields $^{40}Ar/^{39}Ar$ ages of 109 and 116 Ma, and hornblende yields $^{40}Ar/^{39}Ar$ ages of 131 and 157 Ma for the Kuma Nappe complex (Takasu *et al*., 1994). The Kuma Nappe complex is now nearly completely eroded away, with the only remnants of the unit being clasts of high-grade epidote ampibolites in the Eocene Kuma Group Conglomerate (Takasu *et al*., 1994).

The Besshi Nappe complex is the highest-grade and most exposed unit in the Sanbagawa Belt (Takasu *et al*., 1994; Mizukami and Wallis, 2005), facing peak metamorphism at greenschist to epidote amphibolite facies. The Besshi Nappe complex and is divided into chlorite, garnet, albite-biotite, oligoclase-biotite zones based on metapelite paragenesis (Mizukami and Wallis, 2005, Takasu *et al*., 1994, Banno *et al*., 1978; Enami, 1983, Higashino, 1990). Ages for the Besshi Nappe complex are derived from whole rock $^{40}Ar/^{39}Ar$ isotopes of pelitic schists, yielding ages of 85 – 94 Ma (Takasu *et al*., 1994). The Besshi Nappe Complex has an apparent inverted thermal structure (Mizukami and Wallis, 2005, Takasu *et al*., 1994) and followed a series of clockwise P-T paths with a rise in temperature occurring subsequent to peak pressure at 0.6 – 1.1 Gpa (Higashino, 1990, Mizukami and Wallis, 2005, Enami *et al*., 1994). The lithologies of the Besshi Nappe Complex consist of metapelite with greenstones, minor chert and marble with local amphibolite and ultrabasic rocks in higher grade regions (Takasu *et al*., 1994). The Higashi-Akaishi and Imono Peridotite bodies form part of the Eclogite Unit within the Besshi Complex, which also includes the Iratsu Mass to the North and East of Higashi-Akaishi (Figure 3.3).

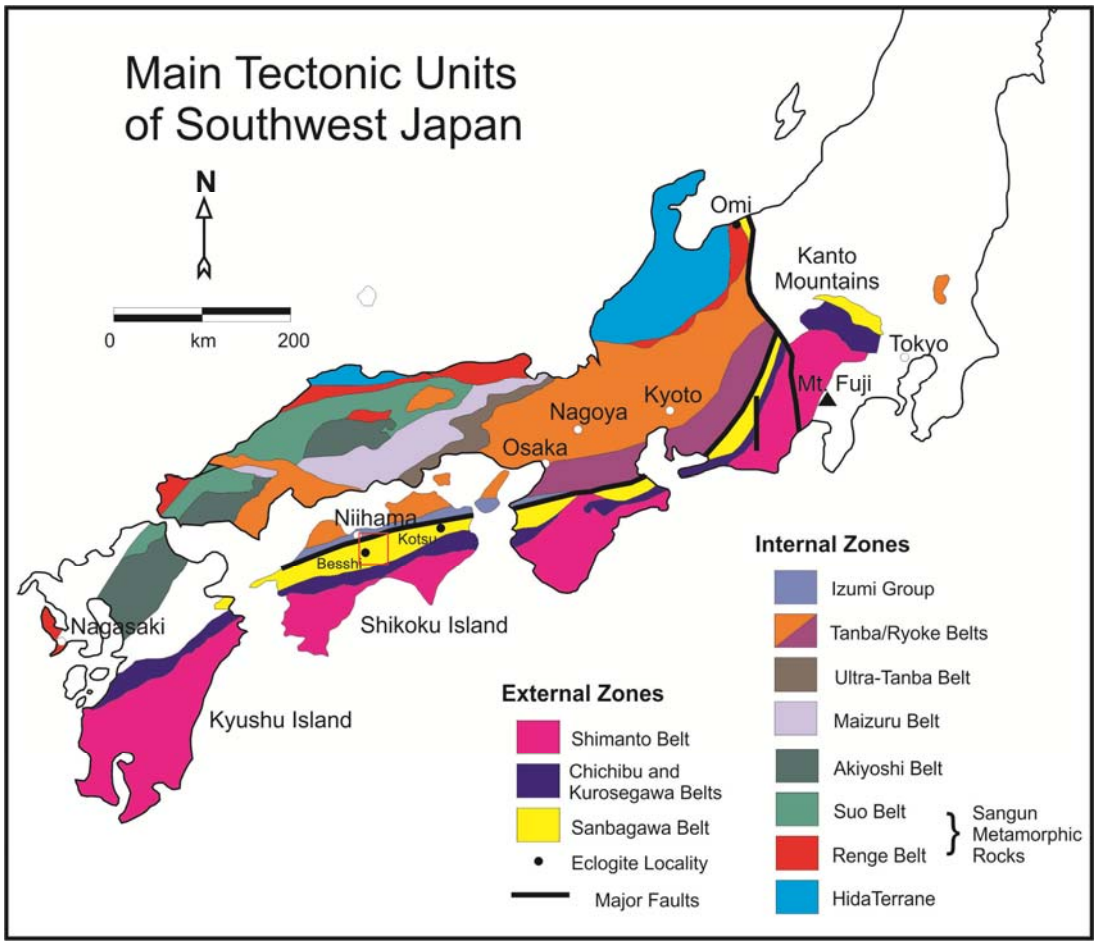

Figure 3.2. Map showing the major tectonic units of southwest Japan. The study area (the red box) lies within the Besshi Nappe Complex and is part of Sanbagawa Belt on Shikoku Island. Modified after Wallis *et al.*, 2000.

The Oboke Nappe Complex has whole rock $^{40}Ar/^{39}Ar$ ages of 70 – 77 Ma and is structurally overlain by the Besshi Nappe Complex (Takasu *et al*., 1994). The Oboke unit consists of psammitic and psephetic schists which include clasts of granite porphyry, quartz diorite, granite and rhyolite, and the sequence is metamorphosed to pumpellyite to actinolite facies (Takasu *et al*., 1994).

3.2.2. Regional geology and sampling

The Mt. Higashi-Akaishi (HA) region lies within the Cretaceous Sanbagawa belt. Geographically it is located on the western margin of the island of Shikoku, Japan (Figure 3.2) and it reaches an altitude of 1707m. Mt. Higashi-Akaishi is the largest of a number of ultramafic nappes that preserves the prograde evolution (Enami, 2004, Mizukami and Wallis, 2005) of a subduction sequence, including parts of the mantle wedge and subduction-related mafic and ultramafic igneous bodies. The nappes are

located within the Besshi Nappe complex, amongst a predominantly metasedimentary host rock (Figure 3.3).

The HA body itself has been subject to multiple deformation events (Figures 3.4 and 3.5). The initial event, or D_1, is related to a dry, high-temperature intra-plate mantle flow environment (Mizukami and Wallis, 2005) and resulting in the formation of an A-type olivine fabric. D_2 is related to mantle flow in a high-stress subduction environment within the mantle wedge and close to the subducting slab, with the presence of abundant fluids (Enami *et al*. 2004; Mizukami and Wallis 2005; Hattori *et al*., 2010). D_2 produced a porphyroclastic microstructure, with a foliation and lineation defined by olivine and chromite elongation, and an olivine fabric consistent with a B-type LPO. D_2 is generally split into 2 events, D_{2A} and D_{2B} (Mizukami and Wallis, 2005). During D_{2A}, antigorite was not stable and so does not contribute to the fabric, whereas a D_{2B} fabric is characterised by the presence of subordinate antigorite (Mizukami and Wallis 2005). The D_3 event is related to the exhumation of the HA peridotite, initiated by the density decrease associated with antigorite formation (Mizukami and Wallis, 2005). D_3 is characterised by a strong schistosity defined predominantly by alignment of platy antigorite (Mizukami and Wallis, 2005). D_4 is related to regional exhumation of the Sanbagawa belt due to the Pacific/Eurasian collision, and is associated with the uplift that produced the mountainous terrain currently present in the region (Mizukami and Wallis, 2005).

Samples were also taken from the Imono Peridotite Body, which lies approximately 5km to the east of Mt. Higashi-Akaishi (Tasaka *et al*., 2008). It is composed primarily of dunite and is serpentinised in places, preserving the earlier deformation events within the region (Tasaka *et al*., 2008). The foliations and lineations observed by Tasaka *et al*. (2008) are consistent with those measured throughout the Higashi-Akaishi peridotite body, and these authors conclude that the Imono peridotite preserves a B-type olivine fabric.

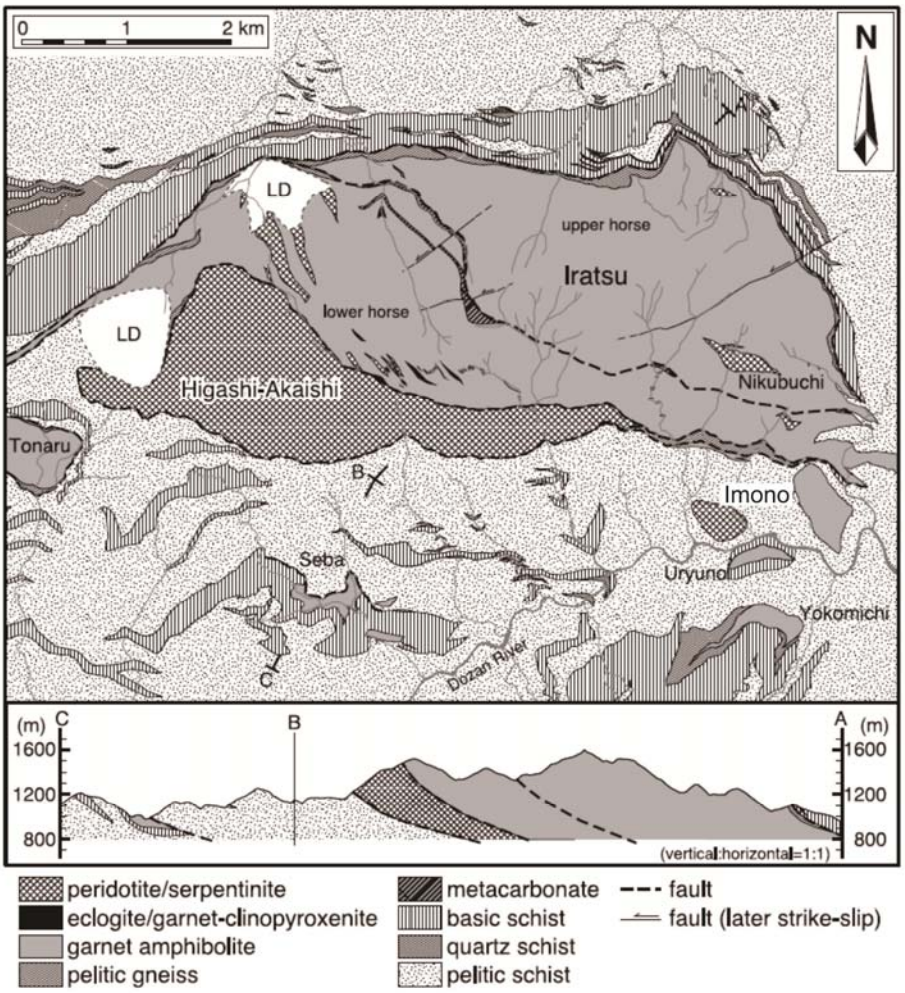

Figure 3.3. Geological map and cross section of the Besshi region, including the Higashi-Akaishi and Imono Peridotites and the Iratsu body. LD – Landslide deposit. Image from Ota *et al*. (2004).

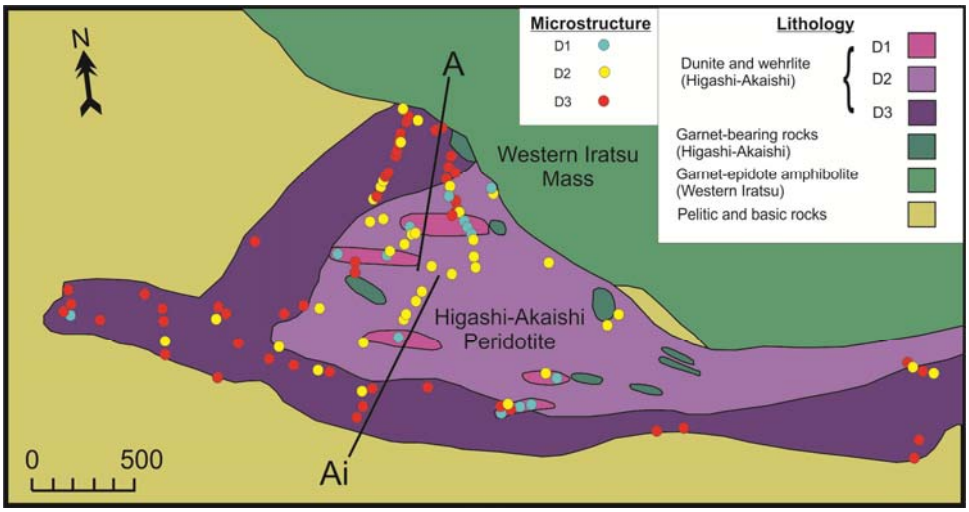

Figure 3.4. Geological map of the Higashi-Akaishi region within the Besshi Nappe Complex. The map shows localities within HA that have been associated with the deformation events D1-D3. Modified after Mizukami and Wallis (2005).

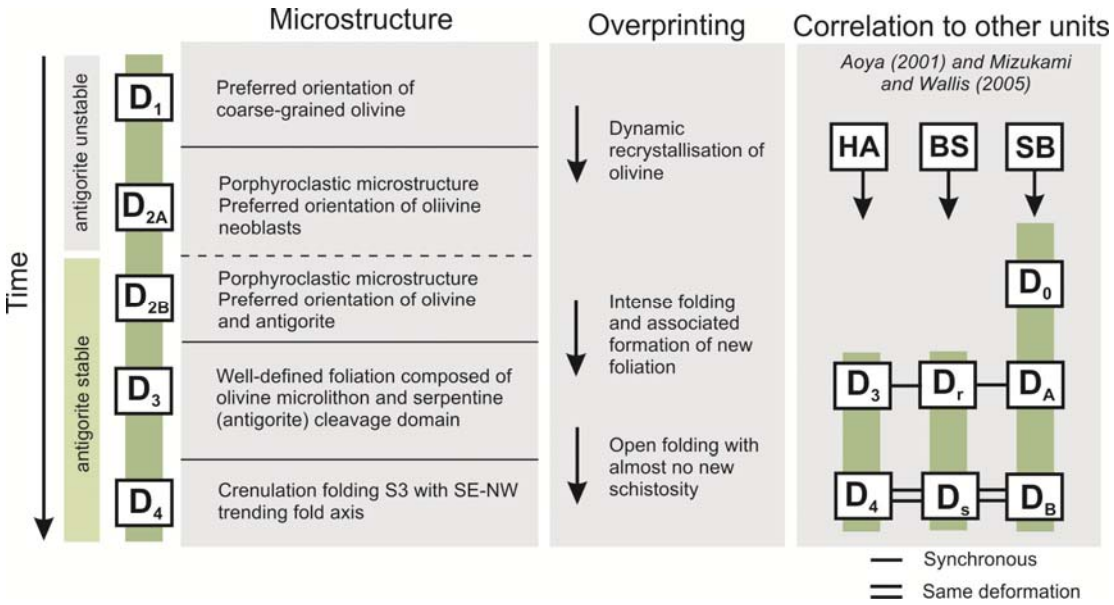

Figure 3.5. Schematic representation of the deformation events that have affected the Besshi region of Shikoku Island. Modified after Mizukami and Wallis (2005).

In terms of weathering, most of the dunites in the Besshi region are extensively weathered and are encrusted by a 1 – 2 cm thick layer of weathered material. Olivine-rich rocks tend to weather to a yellow/orange colour and these are often the most weathered lithologies (Figure 3.6). Compositional banding in the olivine-rich peridotite is easy to identify through different weathering patterns. Serpentine-rich bands/veins in peridotite are more weathered than the olivine-rich rocks which tend to stand out more (Figures 3.7 – 3.9). Weathering of the rocks has resulted in the development of small landslides, particularly within the Imono Peridotite body. Dunites and rocks in the upper (topographically) Higashi-Akaishi mass are quite weathered on the surface and form a distinctive weathering pattern with sections of soft yellow olivine-rich rock separated by more cohesive, resistant serpentine and/or chromite-rich rock. Underneath this weathered crust however, the dunites are extremely fresh (Figure 3.10).

The dunites exhibit distinctive compositional variations, with chromite-rich bands (Figure 3.11) and spatially variable serpentinisation. Serpentinisation occurs in two ways, replacing primary mantle minerals in the rock matrix, and veins cross-cutting the rock fabric. These veins are often sub-parallel and are up to 5 cm apart. Dunites towards the NE margin of the Higashi-Akaishi mass contain abundant sheared layers of chromite that still appear to preserve some compositional grading due to crystal

settling during initial peridotite formation (Figures 3.11 – 3.14). Chromite within these layers is quite coarse-grained (~1 – 3 mm) and the layers are ~0.5 – 1 cm thick. There are some intercalations and pods of relatively fresh clinopyroxenite within the dunite. The clinopyroxenite pods are deformed with the dunite and often boudinaged in places, and appear to be compositional variations related to the original igneous layered cumulate sequence (S_0; Figures 3.11, 3.13, 3.14). This is also suggested by Mizukami and Wallis (2005). There are two foliations that can be observed in the dunite. One is defined by the mineral alignment of olivine, serpentine and bands of streaky aligned chromite (e.g. Figure 3.7). This fabric doesn't appear to be very strong in general, but occasionally can be quite prominent and forms shear bands ~ 0.2 – 1 m wide (Figure 3.17). This foliation equates to the S_2 of Mizukami and Wallis (2005). There is a mineral lineation associated with this foliation that is defined by the alignment of antigorite and aggregates of fine-grained equant olivine. The S_2 foliation is cross-cut and crenulated by a second foliation that is quite widespread (Figures 3.15 and 3.16). This foliation is quite heterogeneous in distribution and also forms prominent shear bands. Further towards the centre of the Higashi-Akaishi mass and approaching from the northern side, the strain partitioning/shear zone development is very strong.

Maps of the sample localities from Imono and Higashi-Akaishi are provided in Figure 3.18. Stereographic projections of structural data collected from the Imono and Higashi-Akaishi peridotite bodies are provided in Figure 3.19. S_2 foliations in the Higashi-Akaishi peridotite strike roughly NW-SE and tend to be gently-dipping towards the NE. Mineral lineations from the same region are shallow to sub-horizontal and strike roughly E-W. Poles to S_2 from the Imono peridotite have a bimodal distribution, possibly due to the effects of folding. S_3 crenulation cleavages measured within both the Imono and Higashi-Akaishi peridotites are variable, which may also reflect the effects of later folding, possibly F_4 folds (Figure 3.18).

Figure 3.6. Field photograph of a D_2 peridotite outcrop in the Mt. Higashi-Akaishi region. The terrain is quite hilly and steep. The peridotites tend to weather to a yellowish-brown colour, but are reasonably fresh beneath the weathered crust.

Figure 3.7. A D_2 dunite outcrop in the Imono peridotite body (coin for scale). A foliation can be seen quite clearly on the weathered surfaces. There was a pervasive foliation similar to this throughout most of the Imono peridotite.

Figure 3.8. Compositional layering in a D_2 peridotite outcrop in the Imono region. Layers are comprised of coarse and fine olivine, as well as serpentine-rich bands that are more heavily weathered.

Figure 3.9. Penetrative S_2 foliation within dunite in the Imono peridotite body.

Figure 3.10. Fresh exposed surface of dunite in the Imono region. The dunite is foliated (S_2) with a weak crenulation (S_3).

Figure 3.11. Chromite layers in dunite from Higashi-Akaishi. The chromite layers are cross-cut and offset by a serpentine vein to the left of the image.

Figure 3.12. Aligned chromite within the matrix of a weakly-foliated dunite (S_2) from the Imono peridotite body.

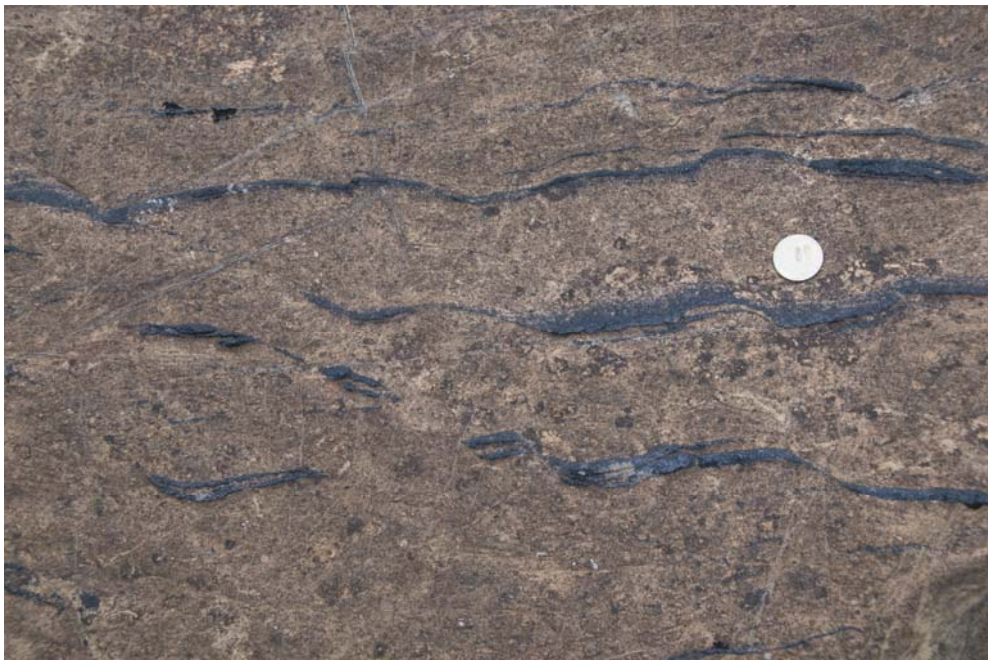

Figure 3.13. Compositional banding of chromite related to crystal settling within a magma. The chromite bands are sheared and boudinaged, and this is related to thin veins of serpentine cross-cutting the rock.

Figure 3.14. Compositional banding of chromite offset by shearing occurring along a thin veins of serpentine within a dunite from Mt. Higashi-Akaishi.

Figure 3.15. Multiple generations of foliation development in a dunite from Mt. Higashi-Akaishi. S_2 is the dominant foliation and S_3 is a weaker crenulation cleavage that has developed at a high angle to S_2.

Figure 3.16. Multiple generations of foliation development in a dunite from Mt. Higashi-Akaishi. S_2 is generally defined by the alignment of olivine, chromite and antigorite. S_3 crenulates S_2 and is generally defined by antigorite alignment.

Figure 3.17. Photo of a D_2 shear zone in Mt. Higashi-Akaishi. The finer-grained, more sheared region is richer in serpentine and more heavily-veined, whereas there is more fracturing and brittle behaviour in the coarser region to the top of the image.

A)

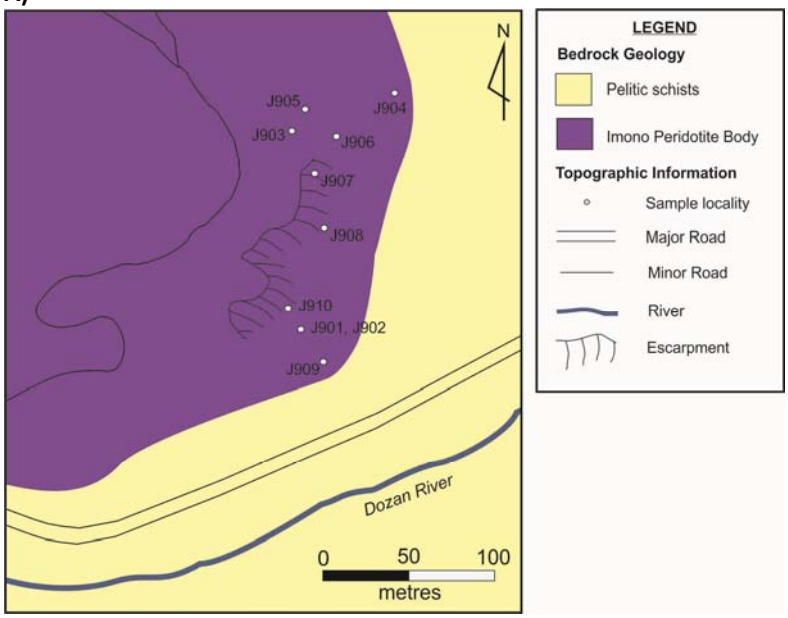

B)

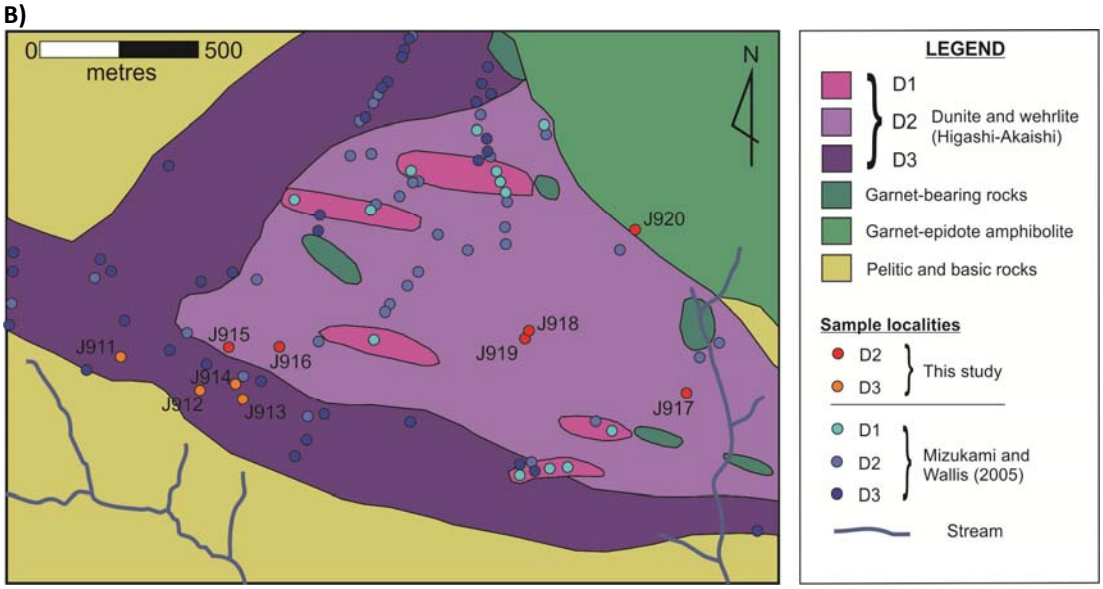

Figure 3.18. A) Map of the Imono peridotite body showing sample localities J901 – J910. Modified after Tasaka *et al*. (2008). B) Map of the Higashi-Akaishi peridotite showing sample localities J911 – J920. Modified after Mizukami and Wallis (2005).

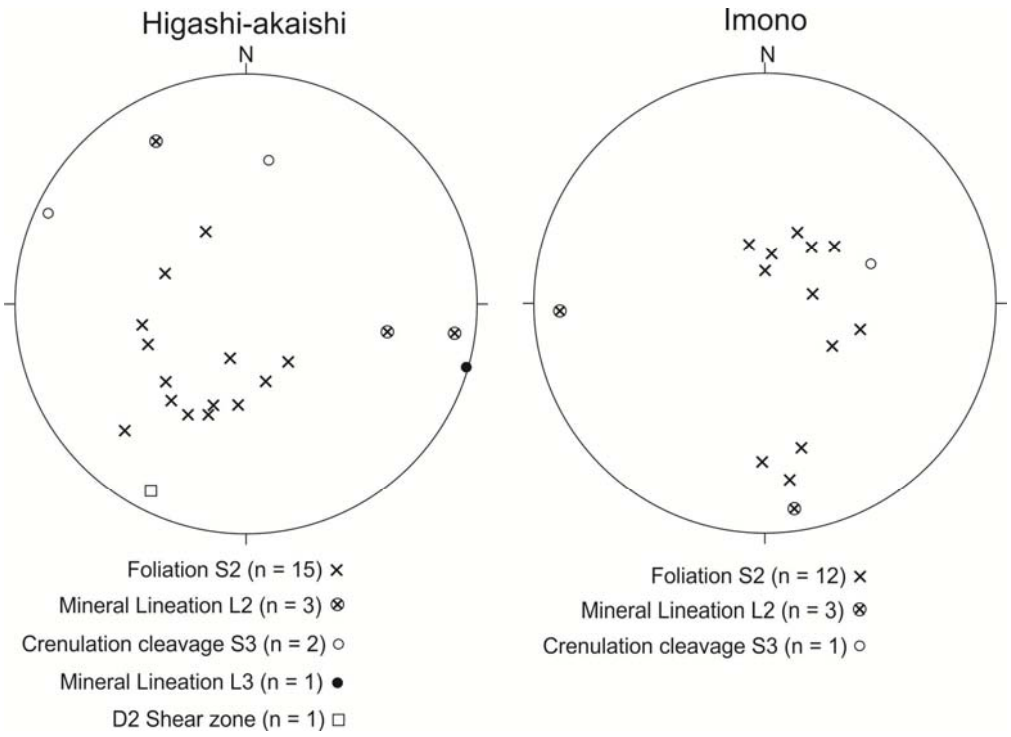

Figure 3.19. Structural data collected from the Higashi-Akaishi and Imono peridotite bodies, Japan.

3.3. Tubaf Seamount, Lihir Island, Papua New Guinea

3.3.1. Tectonic Setting

The xenoliths samples analysed in this study are sourced from the New Ireland Arc, an oceanic island arc located to the northeast of Papua New Guinea (Figure 3.20). This arc is comprised of the Tabar-Lihir-Tanga-Feni (TLTF) island chain, a series of islands above the supra-subduction region, and resulting from the collision of the Australian and Pacific plates. The volcanic arc associated with the Australian/Pacific plate boundary is presently characterised by silica-undersaturated, high potassium calc-alkaline volcanic rocks (McInnes and Cameron, 1994, McInnes *et al*., 2001), and is host to one of the richest and youngest gold deposits in the world (Luise Caldera on Lihir Island has 42.7 Moz of gold and is less than 1 million years old; (McInnes and Cameron, 1994) The region is located within the Bismarck Archipelago, including New Britain, New Ireland-New Hanover and the Solomons (McInnes and Cameron, 1994). Cenozoic tectonic evolution of the region has involved rapid northwards migration of the Australian plate since the Eocene, accompanied by subduction and collision events (Hall and Spakman, 2003). The

complexity of present tectonics in the SW Pacific reflects the extremely rapid motion along the Pacific and Australian plate boundaries (Hall and Spakman, 2003). A tectonic reconstruction of the SW Pacific (Figure 3.21.) by (Hall, 2002) suggests that at 55 Ma, the margin between the Australian and Pacific Plates was marked by a NE-dipping oceanic subduction zone.

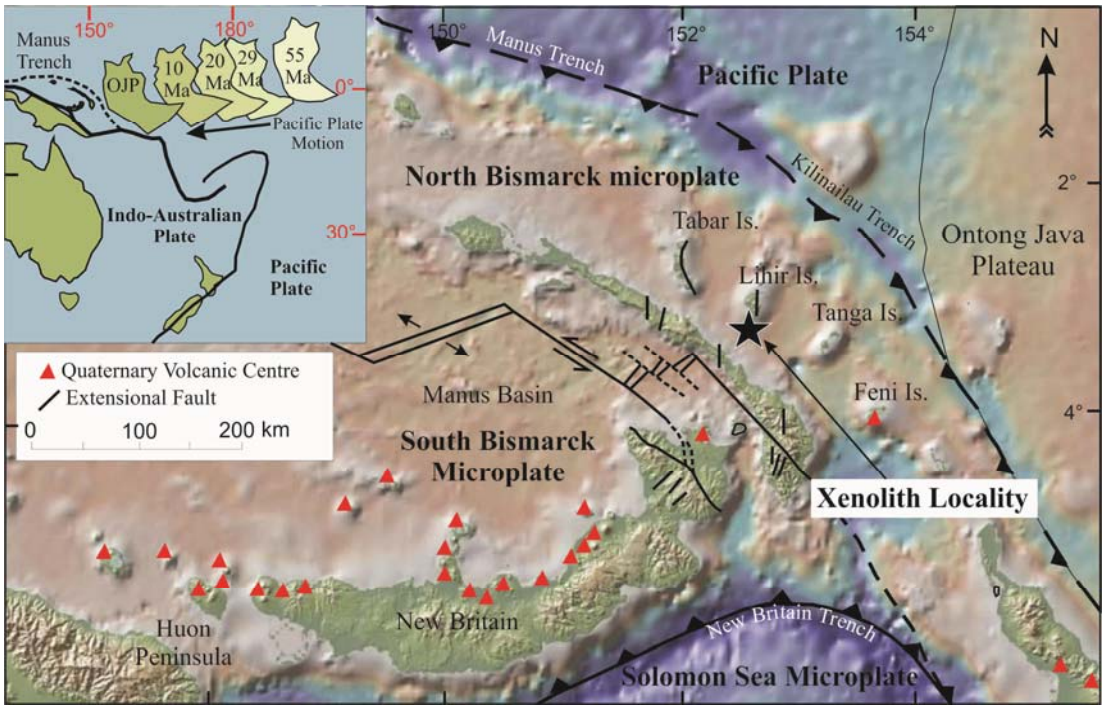

Figure 3.20. Locality map showing Lihir Island and surrounding tectonic setting. The green dot is the collection point of the xenoliths. Dotted lines are inferred faults/tectonic boundaries. The bathymetric base map was sourced from GeoMapApp. Adapted from (Gregoire *et al.*, 2001).

At 45 Ma, the collision between the Indian and Asian plates caused a major tectonic reorganisation, with the subduction polarity of the New Ireland Arc reversing from NE- to SW-dipping (Hall, 2002). At 25 Ma, the Australian Craton began to collide with the Ontong Java Plateau (OJP), beginning the so-called 'soft' phase of the collision, involving shortening of the leading edge of the OJP (Hall, 2002; Hall and Spakman, 2003; Hill and Hall, 2003)). Due to this collision, most of the voluminous, calc-alkaline arc volcanism, which initiated at 34 Ma, ceased in the early Miocene (Franz *et al.*, 2002; Hall, 2002), but was intermittent in some regions until the Pliocene (Hall, 2002). At 8 Ma, the onset of the 'hard' collisional phase occurred, where shortening of the OJP could no longer continue and the Solomons arc was thrust over the OJP, being completely transferred to the Pacific plate by the middle Miocene (Hall and Spakman, 2003). Regional volcanism resumed at 5.3 Ma (Hall,

2002) and initiation of high potassium calc-alkaline magmatism developed on Simberi Island at 3.6 Ma, migrating to the southeast to the Lihir, Tanga and Feni Islands (McInnes and Cameron, 1994). The New Britain-San Cristobal Trench to the south experienced a reversal of subduction polarity due to the onset of collision with the Ontong Java Plateau (OJP) on the seaward side of the subduction zone (McInnes and Cameron 1994; McInnes *et al*., 2001).

This collision resulted in the onset of a second generation of prolific calc-alkaline volcanism on New Britain, Bougainville and Solomon Islands, and caused the fragmentation of the Australian plate into the Bismarck and Solomon microplates, due to back-arc spreading and opening of the Manus Basin at 3.5 Ma (McInnes and Cameron, 1994). The proto-New Britain Island was transported to the south to its current position, overriding the Solomon Sea microplate (McInnes and Cameron, 1994). The western and eastern edges of proto-New Britain collided with Papua New Guinea and New Ireland, resulting in sinistral segmentation of the Manus spreading centre and NW-SE striking transform faulting of the Manus Basin, New Ireland and New Britain, as well as conjugate NNE-striking extensional faults extending into New Ireland and the New Ireland Basin (McInnes and Cameron, 1994). The current tectonic setting of Lihir Island is shown in Figure 3.22.

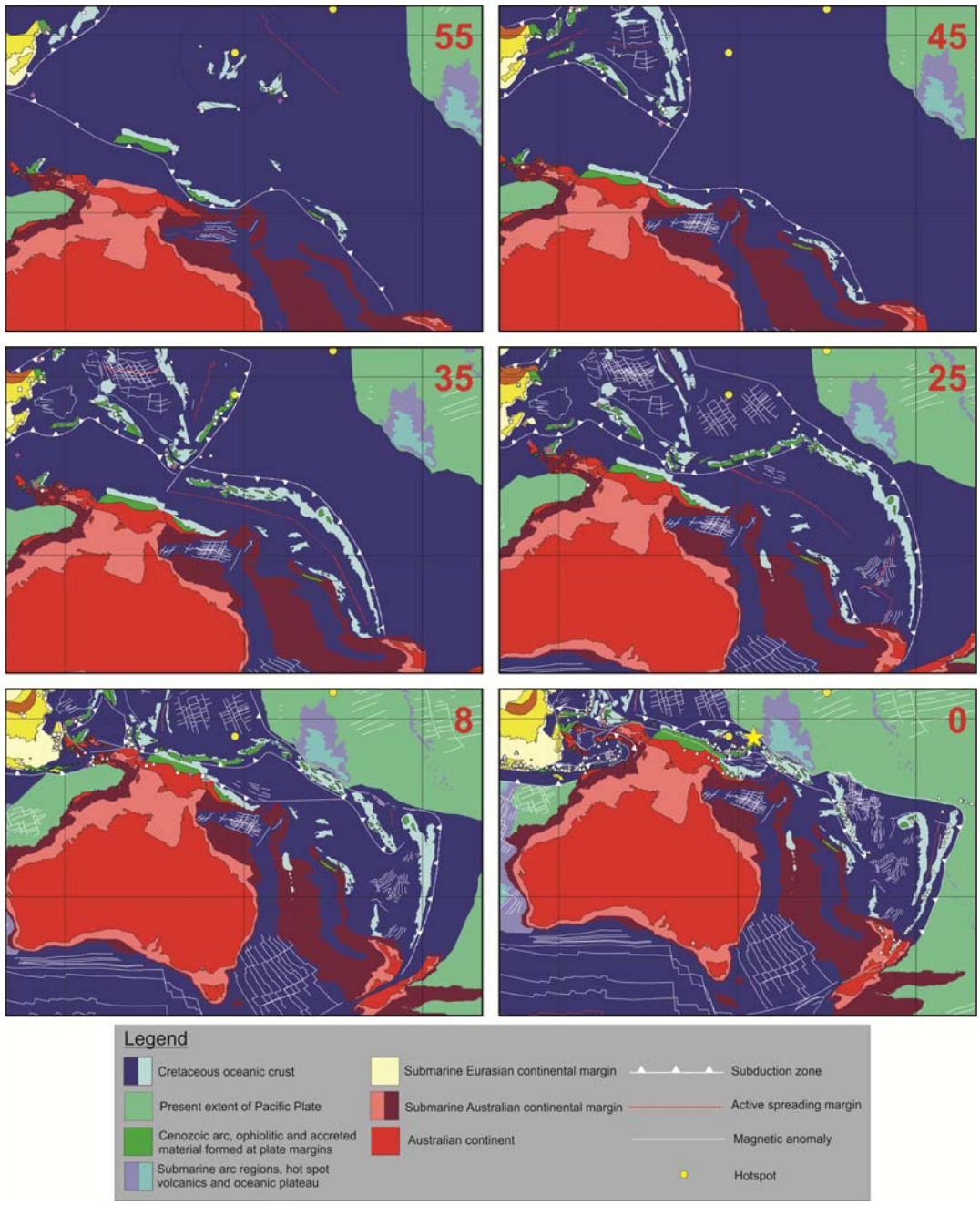

Figure 3.21. Series of maps showing the tectonic evolution of the SW Pacific between 55 Ma and the present day, modified after Hall 2002. The location of Lihir Island is marked by the yellow star.

3.3.2. Regional and local geology

The ultramafic samples acquired for this research were collected from cinder cones Tubaf and Edison, which are currently positioned in the supra-subduction region of the plate boundary. Xenoliths were collected by the CSIRO during the Sonne research cruise SO-94 (McInnes *et al*., 2001). The Tubaf and Edison cinder cones are 1.5 and 1.0 km in diameter, and rise 140 and 120 metres above the sea floor, respectively (McInnes *et al*., 2001). The ultramafic xenoliths are angular in shape, and range from 3-15 cm in diameter (McInnes *et al*., 2001).

Xenoliths are relatively pristine coarse-grained spinel peridotites from between 20 and 70 km depth and that show no post-eruption alteration (McInnes *et al*., 2001). They were erupted within a volatile-rich, hydrous alkali basalt (McInnes *et al*., 2001) with phlogopite, hornblende and augite phenocrysts in a very fine-grained, vesicular matrix. Aside from ultramafic mantle xenoliths, other xenoliths collected during the research cruise include a wide range of mineral assemblages similar to an ophiolite suite and that provide a representative stratigraphic section of the New Ireland supra-subduction oceanic lithosphere (Figure 3.3; McInnes *et al*., 2001).

As these samples are xenoliths, the structural context in which they belong was lost when they were removed from the host rock and exhumed. This makes it difficult to align LPO with flow directions and slip planes as these features cannot be constrained from the samples as there is no obvious foliation or lineation within the samples.

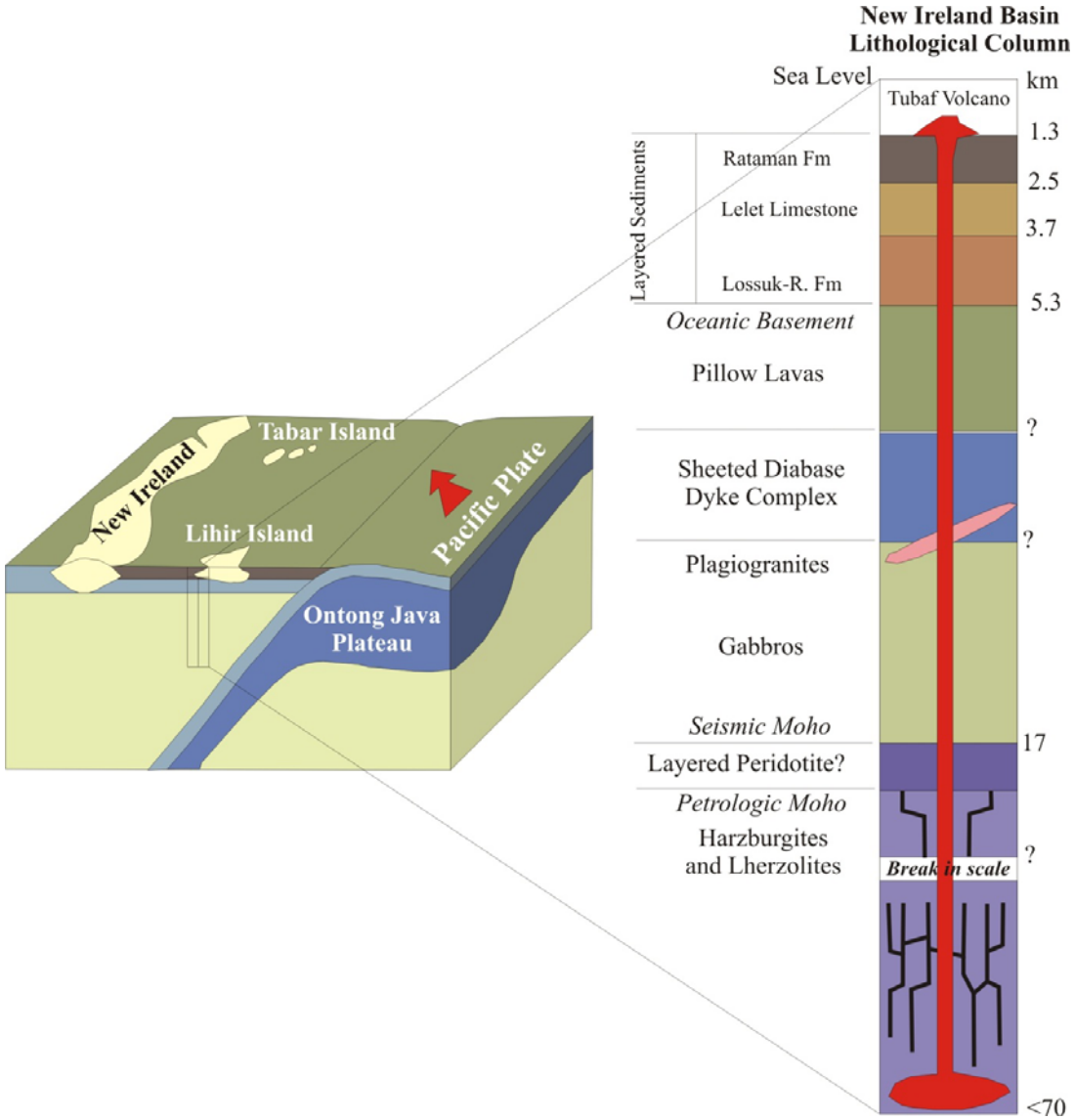

Figure 3.22. Lithostratographic column represented by the xenoliths found during the dredging of the Tubaf seamount. Modified after McInnes *et al*. (2001).

3.4. References

Banno, S., Higashino, T., Otsuki, M., Itaya, T. and Nakajima, T. (1978) Thermal structure of the Sambagawa metamorphic belt in central Shikoku, *J. Phys. Earth*, v. 26, p. 345-356.

Enami, M., 1982. Oligoclase–biotite zone of the Sanbagawa metamorphic terrain in the Besshi district, central Shikoku, Japan. *Journal of the Geological Society of Japan*, v. 88, p. 887–900 (in Japanese with English abstract).

Enami, M. and Mizukami, T. (2004) P-T-D Evolution of the Higashi-akaishi Ultramafic Mass in the Sanbagawa Belt, Central Shikoku, Japan: Subduction of Mantle Wedge Peridotite, *Journal of Geography*, v. 115, p. 317-632.

Enami, M., Wallis, S.R. and Banno, Y. (1994) Paragenesis of sodic pyroxene-bearing quartz schists: Implications for the P-T history of the Sanbagawa belt, *Contributions to Mineralogy and Petrology*, v. 116, p. 182-198.

Franz, L., Becker, K.-P., Kramer, W. and Herzig, P.M. (2002) Metasomatic Mantle Xenoliths from the Bismarck Microplate (Papua New Guinea)-Thermal Evolution, Geochemistry and Extent of Slab-induced Metasomatism, *Journal of Petrology*, v. 43, p. 315-343.

Gregoire, M., McInnes, B.I.A. and O'Reilly, S.Y. (2001) Hydrous metasomatism of oceanic sub-arc mantle, Lihir, Papua New Guinea: Part 2. Trace element characteristics of slab-derived fluids, *Lithos*, v. 59, p. 91-108.

Hall, R. (2002) Plate Tectonic Reconstructions: Southeast Asia, Southeast Asia Research Group. Accessed: October 13, 2009, from http://searg.rhul.ac.uk/current_research/plate_tectonics/index.html

Hall, R. and Spakman, W. (2003) Mantle structure and tectonic evolution of the

region north and east of Australia, Evolution and Dynamics of the Australian Plate, Geological Society of Australia Special Publication v. 22 and Geological Society of America Special Paper v. 372, p. 361-381.

Hattori, K., Wallis, S., Enami, M. and Mizukami, T. (2010) Subduction of mantle wedge peridotites: Evidence from the Higashi-akaishi ultramafic body in the Sanbagawa metamorphic belt, *Island Arc*, v. 19, p. 192-207.

Higashino, T. (1990) The higher-grade metamorphic zonation of the Sambagawa metamorphic belt in central Shikoku, Japan, *Journal of Metamorphic Geology*, v. 8, p. 413-423.

Hill, K.C. and Hall, R. (2003) Mesozoic-Cenozoic evolution of Australia's New Guinea margin in a west Pacific context, *Geological Society of America Special Papers*, v. 372, p. 265-290.

Jung, H., Katayama, I., Jiang, Z., Hiraga, T. and Karato, S. (2006) Effect of water and stress on the lattice-preferred orientation of olivine, *Tectonophysics*, v. 421, p. 1-22.

Kunugiza, K., Takasu, A. and Banno, S. (1986) The origin and metamorphic history of the ultramafic and metagabbro bodies in the Sanbagawa belt, *Geological Society of America Memoirs*, v. 164, p. 375–385.

Long, M.D. and Becker, T.W. (2010) Mantle dynamics and seismic anisotropy, *Earth and Planetary Science Letters*, v. 297, p. 341-354.

Long, M.D. and Silver, P.G. (2008) The Subduction Zone Flow Field from Seismic Anisotropy: A Global View, *Science*, v. 319, p. 315-319.

Long, M.D. and Silver, P.G. (2009) Shear Wave Splitting and Mantle Anisotropy: Measurements, Interpretations, and New Directions, *Surveys in Geophysics*, v. 30, p. 407-461.

McInnes, B.I.A. and Cameron, E.M. (1994) Carbonated, alkaline hybridizing melts from a sub-arc environment: Mantle wedge samples from the Tabar-Lihir-Tanga-Feni arc, Papua New Guinea, *Earth and Planetary Science Letters*, v. 122, p. 125-141.

McInnes, B.I.A., Gregoire, M., Binns, R.A., Herzig, P.M. and Hannington, M.D. (2001) Hydrous metasomatism of oceanic sub-arc mantle, Lihir, Papua New Guinea: petrology and geochemistry of fluid-metasomatised mantle wedge xenoliths, *Earth and Planetary Science Letters*, v. 188, p. 169-183.

Mizukami, T. and Wallis, S.R. (2005) Structural and petrological constraints on the tectonic evolution of the garnet-lherzolite facies Higashi-akaishi peridotite body, Sanbagawa belt, SW Japan, *Tectonics*, v. 24, p. 1-17.

Mizukami, T., Wallis, S.R. and Yamamoto, J. (2004) Natural examples of olivine lattice preferred orientation patterns with a flow-normal a-axis maximum, *Nature*, v. 427, p. 432-436.

Ota, T., Terabayashi, M. and Katayama, I. (2004) Thermobaric structure and metamorphic evolution of the Iratsu eclogite body in the Sanbagawa belt, central Shikoku, Japan, *Lithos*, v. 73, p. 95-126.

Takasu, A. (1989) P–T histories of peridotite and amphibolite tectonic blocks in the Sanbagawa metamorphic belt, Japan. In: Daly, J.S., Cliff, R.A., Yardley, B.W.D. (Eds.), Evolution in Metamorphic Belts. *Geological Society Special Publications*, v. 43, p. 533–536.

Takasu, A., Wallis, S.R., Banno, S. and Dallmeyer, R.D. (1994) Evolution of the Sambagawa metamorphic belt, Japan, *Lithos*, v. 33, p. 119-133.

Tasaka, M., Michibayashi, K. and Mainprice, D. (2008) B-type olivine fabrics developed in the fore-arc side of the mantle wedge along a subducting slab, *Earth and Planetary Science Letters*, v. 272, p. 747-757.

Wallis, S.R., Takasu, A., Enami, M. and Tsujimori, T. (2000) Eclogite and Related Metamorphism in the Sanbagawa Belt, Southwest Japan, *Bulletin of Research Institute of Natural Sciences*, v. 26, p. 3-17.

Chapter 4. Analytical techniques

Hydrous fluids play a vital role in tectonic processes, particularly in dynamic regions such as subduction zones, and are known to influence the development of slip systems in olivine deforming within the mantle (Mackwell *et al*., 1985; Karato, 1995). Recent evidence suggests that there is also a link between olivine deformation on a grain-scale and geochemistry (Ando *et al*., 2001; Murata *et al*., 2009; Plümper *et al*., 2012). The integration of microstructural analysis via EBSD with FTIR and isotope analysis, provides a unique opportunity to investigate this relationship between olivine deformation in the mantle and geochemical processes, and to infer conditions in the deforming mantle wedge.

4.1. Electron Backscatter Diffraction (EBSD)

4.1.1 Experimental Setup and Procedure

Electron backscatter diffraction (EBSD) was used to investigate the internal microstructures of deformed olivine grains in terms of their crystallographic and petrographic relationships to one another, and relationship to mesoscopic structures within the peridotites. EBSD is an important tool for investigating deformed rocks and minerals due to the fact that it enables collection of structural information. EBSD is a scanning electron microscope (SEM) technique, whereby a vertical electron beam is focussed on a sample tilted at 70°, producing backscattered electrons that are detected by a phosphor screen located below the sample in a specific geometric configuration. The electrons interact with the sample such that when these leave the sample as backscattered electrons, they travel in a trajectory controlled by the orientation of the crystallographic planes of that particular mineral. The backscattered electrons fluoresce when they make contact with the phosphor screen and produce a diffraction pattern known as an EBSP (electron backscatter pattern), comprised of several bands (Kikuchi bands) representing orientations and lattice spacings of the crystallographic planes (Oxford Instruments HKL, 2007) (Figure 4.1). For crystalline solids, EBSPs are unique to mineral phases and their orientation, and can be indexed using theoretical match units comprising a reference table of crystallographic planes responsible for Kikuchi bands (reflectors) and their relative

angular relationships. Match units are generated from established crystallographic parameters.

Automated collection and indexing of EBSPs by mapping on a grid over the sample surface enables the user to quantify the phase and its' crystallographic orientation of each point and thus any variations in phase and crystallographic orientation that may be present within the sample, and is used to identify specific minerals. Indexing enables the EBSP to be matched to a particular mineral according to how well the pattern fits the theoretical model. Pattern quality and indexing reliability depend on the number of Kikuchi bands that are can be detected from the EBSP, thus the acquisition of quality EBSPs is crucial. Key factors that affect EBSP quality are generally related to sample preparation, and include polish quality and flatness, but can also include the intrinsic crystallinity in the analytical volume of the beam. Operating parameters that can also influence EBSP quality include accelerating voltage, spot size, detector distance, sample tilt and sample charging. The optimisation of many of these variables is established for automated EBSD analysis, and consequently remain fixed during data collection.

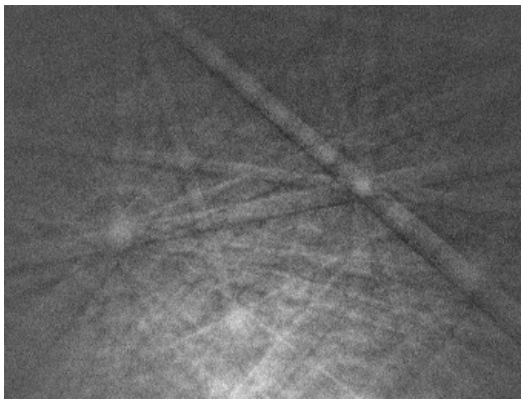

Figure 4.1. An example of an olivine EBSP (electron backscatter pattern) showing Kikuchi bands that are characteristic of the crystal structure of olivine.

Petrographic sections of selected samples were double polished with colloidal silica suspension (pH 9.8) for between 3 - 5 hours and EBSD data were collected from 3 Japan samples and 6 Lihir samples using a Philips XL30 FEG SEM, a Zeiss EVO 40XVP and a Zeiss Neon 40EsB FIBSEM at Curtin University. No inconsistencies were observed between the data collected from the different SEMs. Data acquisition was undertaken using Oxford Instruments (was HKL Technology) Channel 5.9 Flamenco software using an accelerating voltage of 20 kV on a carbon coated sample tilted at 70° under a vacuum of 4 x 10^{-5} Torr, with a working distance of 20 mm and EBSD detector distance of 149 mm.

The data was collected using automatic mapping mode. Settings used for automatic EBSD data collection are listed in Table 4.1. During automatic mapping, an EBSP is collected at each node of a user-defined grid, allowing the user to choose the spatial resolution of the resulting map (within the limitations of the SEM), as well as the size of the region of interest, with maps ranging from individual grains to entire petrographic thin sections. Each EBSP is indexed and the point is identified as a particular mineral, with data points only indexed if their mean angular deviation (MAD) from the theoretical match unit was less than 1°. EBSPs obtained from the olivine were automatically indexed to a theoretical match unit of forsterite, derived from crystallographic data obtained from the HKL database, which is similar to that of Hart (1978). Projection parameters were manually optimised for each individual map using the Channel 5.9 EBSD acquisition software 'Flamenco' to calibrate the beam-sample-detector geometry by manually checking the MAD for indexed points during setup mode. The signal to noise ratio of the EBSPs (and, therefore percentage of indexing) was improved during automatic data collection by subtracting a static background measurement (an average of 64 frames collected in scanning mode) from the EBSP acquired at each point, and binning the pixels on a 4x4 grid. This reduces the spatial resolution of the EBSPs but makes the Kikuchi bands clearer and easier to detect without significant loss of angular accuracy.

Table 4.1. EBSD collection and processing variables for EBSD maps**.**

SEM	Philips XL30 FEG/ Zeiss EVO 40XVP/ Zeiss Neon 40EsB FIBSEM						
EBSP collection time	60 ms						
Background	64 frames; binning 4 x 4; Low gain						
Hough resolution	60						
Band detection	5 (min); 7 (max)						
Noise reduction	'wildspike' and nearest neighbour zero solution extrapolation (4)						
Sample	**X steps**	**Y steps**	**Step size (µm)**	**Average mean angular deviation (MAD)**		**Zero solutions (%)**	
				Before processing	**After processing**	**Before processing**	**After processing**
136063	650	210	50	0.5692	0.5473	56.61	41.00
136065	750	105	50	0.6459	0.5858	55.03	42.42
136067	440	90	50	0.6629	0.5846	34.86	13.93
136069	700	70	50	0.6982	0.6141	57.49	40.73
136074	450	210	50	0.6724	0.6158	59.60	49.62
136090	700	175	50	0.7098	0.5858	58.10	42.76
J909C map 01	1014	125	20	0.7626	0.6642	74.92	69.78
J909C map 02	169	127	20	0.7329	0.6358	68.83	61.04
J909C map 03	516	64	40	0.7241	0.6338	66.16	59.47
J917 map	1476	92	15	0.6691	0.6338	78.96	75.69

J919B_1 map 02	785	292	9	0.7077	0.6552	44.37	31.34
J919B_1 map 05	815	186	4	0.6006	0.5494	37.84	27.21

4.1.2. Data Processing

Following data acquisition, noise reduction was undertaken by applying a "wildspike" correction followed by a 'zero solution extrapolation' (Figure 4.2) based on the values of neighbouring points (Reddy *et al*., 2007) whereby non-indexed points are assigned a phase and orientation. Zero solutions are points that cannot be indexed by the software, either due to the presence of a phase other than that specified or to an MAD that is greater than 1°. The degree of processing can be quantified by comparing the percentage of misindexing before and after applying the correction. In the example given in Figure 4.3, the percentage of misindexing in the raw data is 55.03%. Following a 4 nearest-neighbour zero solution extrapolation (which was the standard degree of extrapolation used to process the data) the percentage of misindexing was 42.42% and after demonstratively over-processing the data using a 1 nearest-neighbour extrapolation the misindexing was reduced to 24.21%. This highlights the fact that care needs to be taken to minimise processing artefacts, which can also have effects on further statistical analysis of the data, such as grain size distribution and grain shape.

Some of the software misindexing is related to the crystal symmetry of the mineral under investigation. Called systematic misindexing, this can be removed subsequent to zero solution extrapolation. Systematic misindexing generally occurs within the centre of well-indexed grains and is identified by the software as separate grains despite the fact that they belong to the host grain (Figure 4.3). In olivine, there is a pseudosymmetry around the [100] axis of 60°, resulting in apparent lattice rotations of 60° around either the <-100> or [100] axes even where there is no change in lattice orientation. To remove systematic misindexing, the software needs to be instructed to disregard 60° rotations around both [100] and <-100> when performing grain boundary detection. Once this has been done, the function for removal of systematic misindexing provided in the Channel 5 Tango module can be applied. For unknown reasons, this function is not entirely effective at removing misindexing and some misindexed points will remain in the data. In order to avoid the resulting statistical inaccuracies, individual grains smaller than 3 pixels in diameter (the metric length of which will vary between samples depending on the step size chosen) were

not included in any further analysis. Band contrast, texture and all Euler maps were produced using the Channel 5 software Tango module in order to highlight different microstructural features in the data:

- Band contrast maps - display contrast variations in the Kikuchi bands detected by the EBSD system. Band contrast is sensitive to crystallographic orientation as well as sample surface topography.
- Texture maps - display crystal lattice distortion within a grain and are thus useful for constraining intragrain deformation-related microstructure. Orientation variations are displayed relative to a user-defined reference point within the grain of interest. These are generally only useful in displaying individual grain data rather than grain aggregates.
- All Euler maps - show the orientation of the grain/s with respect to the sample geometry. The orientation of any data point can be described in terms of rotation around three axes – the Euler poles (φ_1, Φ and φ_2; Randle and Engler, 2000). The Euler poles are then assigned a colour-scale of red (φ_1), green (Φ) or blue (φ_2) and the grains are coloured accordingly (Figure 4.4).

Channel 5 'Mambo' software was used to produce pole figures showing the distribution of crystallographic and misorientation axes. Pole figures are equal area, lower hemisphere projections. The pole figures are presented within an X-Y reference framework corresponding to sample X and Y coordinates. The Lihir xenolith samples were recovered by dredging and show no obvious structural fabrics thus X-Y coordinates for these samples are arbitrarily assigned from thin section orientations. The Japan samples are collected from oriented outcrops and EBSD data were collected within the framework of the foliation and lineation orientations of the finite strain ellipsoid of the deformation, corresponding to the XZ and X directions, respectively. Bulk fabrics for the Japan samples were determined through comparison of the olivine LPO with the finite strain ellipsoid of the deformation. In order to compare the internal microstructure with the bulk fabric a more thorough approach was also applied. For both suites of samples, orientation mapping of numerous olivine grains was used to characterise the geometry of intragrain microstructures (low-angle boundaries).

The procedure for using EBSD data to interpret microstructure and the activation of different slip systems is described in detail by Boyle *et al*. (1998), Prior *et al*. (2002), Bestmann and Prior (2003) and Reddy and Buchan (2005). Orientation maps, crystal axis dispersion and misorientation analysis were used for slip system analysis assuming a tilt-boundary model for low-angle boundary formation (e.g. Figure 4.5). This assumption was tested using the EBSD data using the following method. Crystal axis dispersion is characteristic of rotation around one or more axes. For example, in Figure 4.5, [100] axes have dispersion patterns consistent with rotation around the [010] and [011] axes. Plots of misorientation/rotation axes are also consistent with rotation that is predominantly around [010] with minor [011]. The data are not consistent with a twist-boundary model for low-angle boundary formation, as the rotation axis does not lie within the plane perpendicular to the boundary trace (green dashed line on Figure 4.5), as would be expected for a twist-boundary. For all of the individual grains analysed, there was no evidence for twist-boundaries, thus the data were interpreted using the tilt-boundary model.

4.1.3. Acknowledgements

The author acknowledges the use of equipment, scientific and technical assistance of the Curtin University Electron Microscope Facility, which is partially funded by the University, State and Commonwealth Governments. In particular, Nick Timms, Rob Hart, Elaine Miller and Will Rickard are acknowledged for their invaluable technical assistance.

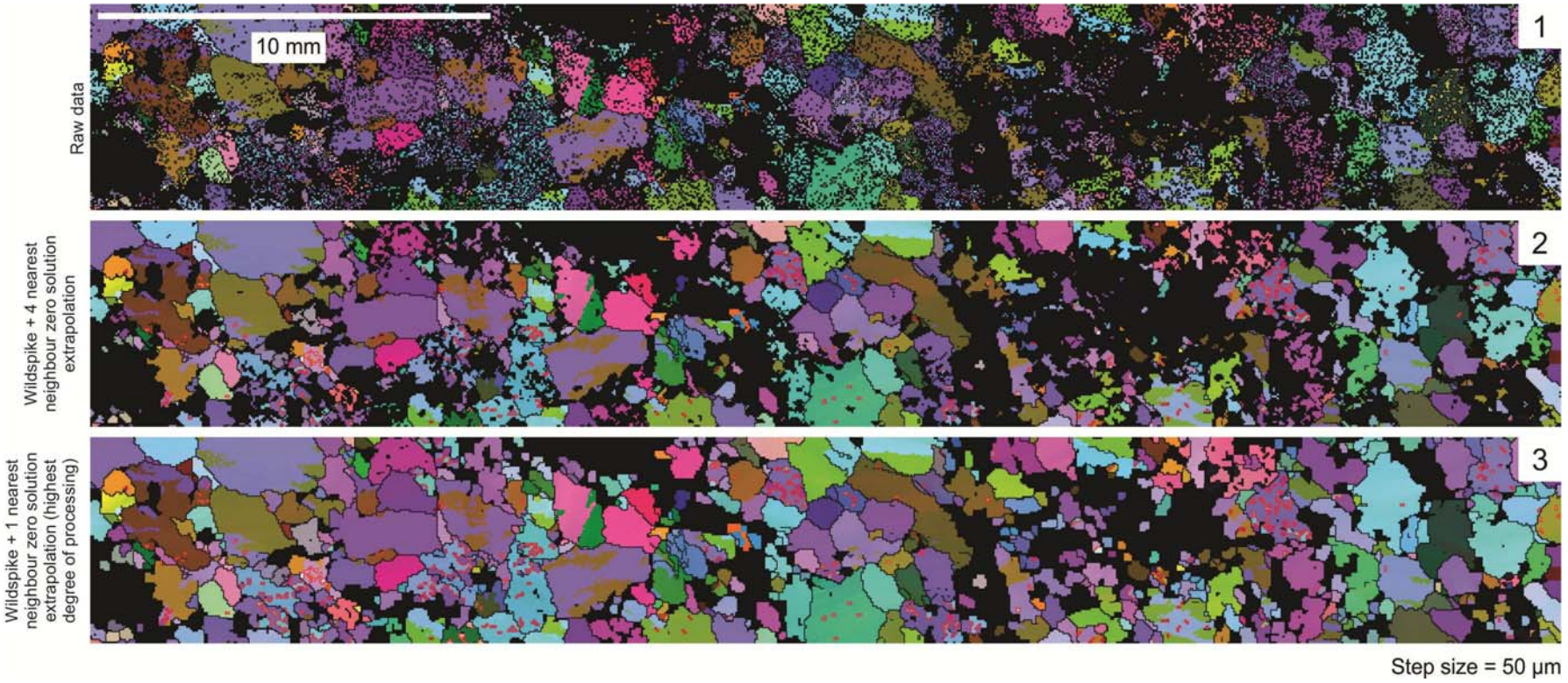

Figure 4.2. Application of noise correction procedures to EBSD data. Map 1 is the raw data, showing misindexing of points within grains as well as zero solutions (black). Map 2 shows the application of a wildspike noise correction with a 4 nearest neighbour zero solution extrapolation. This degree of processing was applied to all of the samples in this study. Map 3 shows excessive processing of the data through the application of a wildspike noise correction with a 1 nearest neighbour zero solution.

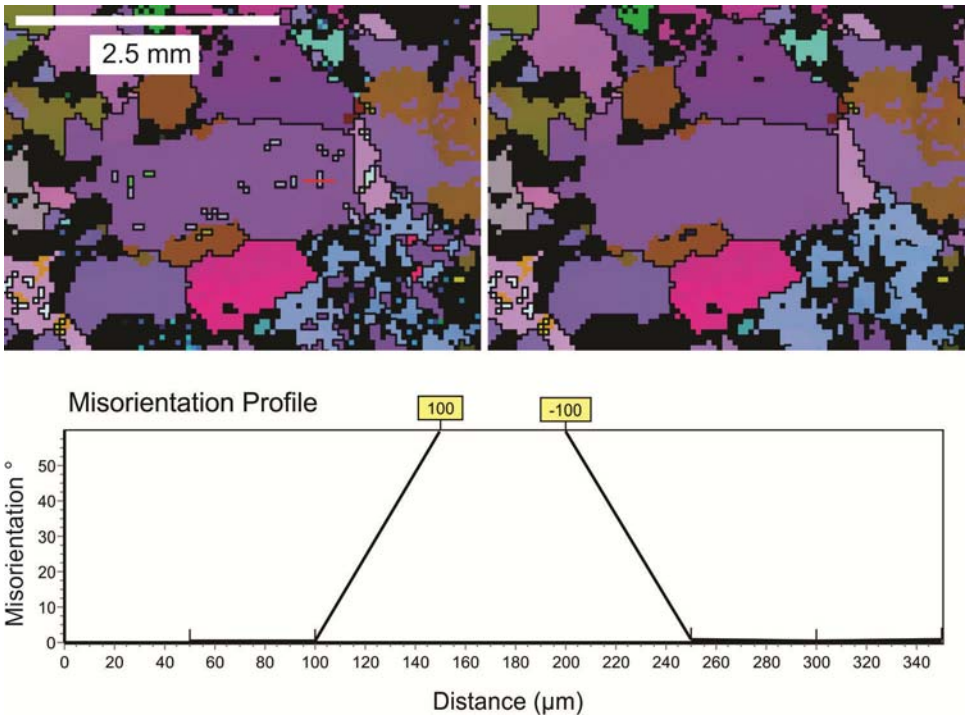

Figure 4.3. Removal of systematically misindexed points from olivine grains (post-zero solution extrapolation). The misorientation profile shows a transect along the red line in the left image. The software has indexed the blue pixel as forsterite (olivine) with a different orientation to the purple host grain (also forsterite). The pixels have the same orientation but have been indexed to have a lattice orientation that differs by a rotation of 60 ° around the [100] axis. If this is not corrected for, systematically misindexed points will be regarded as distinct grains, and will affect subsequent statistical analysis.

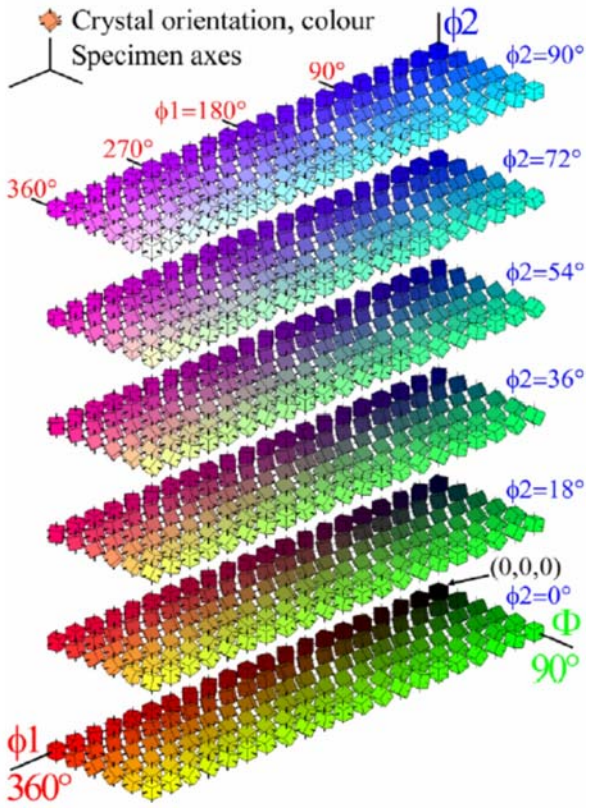

Figure 4.4. Legend for all Euler maps that are coloured with respect to the 3 Euler poles; ϕ_1 (red), Φ (green) or ϕ_2 (blue).

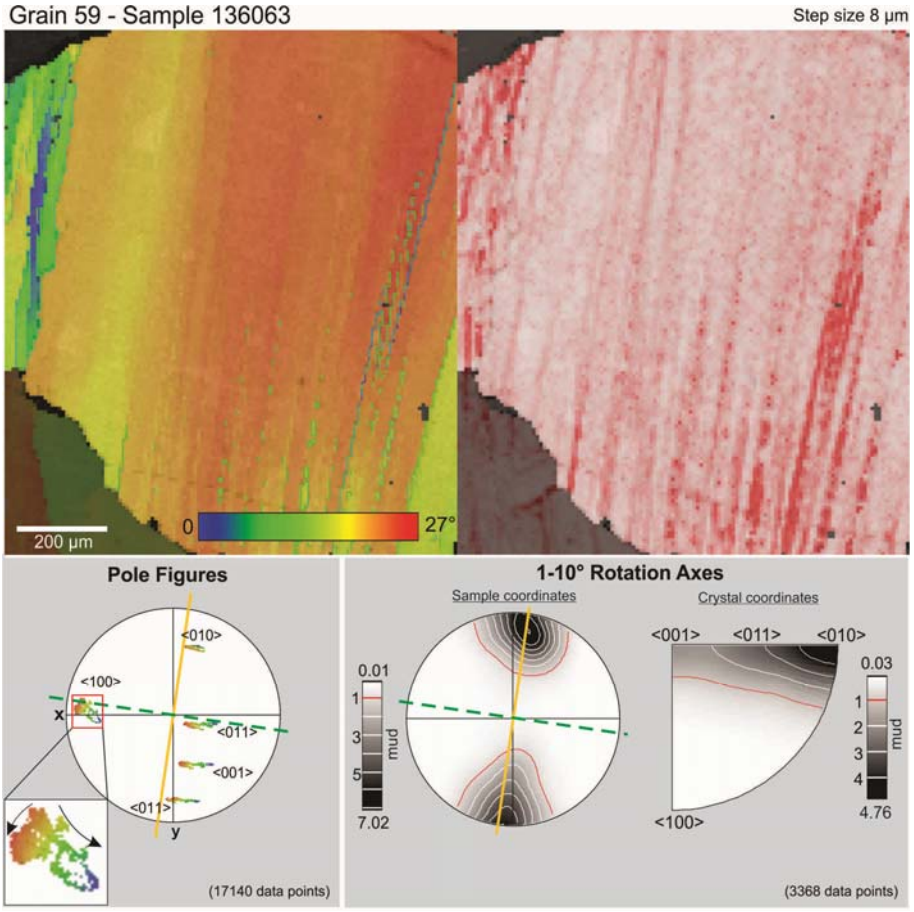

Figure 4.5. An example of the use of internal microstructure to interpret slip systems in olivine grains. The map to the left is a texture map with misorientation axes plotted over the top. The right map is a local misorientation plot showing the location and orientation of low-angle boundaries. The yellow line on the pole figures represents the low-angle boundary trace, and the green dashed line represents the plane perpendicular to the low-angle boundary trace. Rotation axes are contoured using a half width of 20°, and the units are multiples of unit density (mud). Pole figures are lower hemisphere equal area projections.

4.2. Synchrotron Fourier Transform Infrared Analysis (FTIR)

4.2.1. Experimental setup and procedure

Fourier Transform Infrared (FTIR) analysis is a particularly useful tool for investigating the presence and concentration of hydroxide in minerals, and can provide significant insight into the degree of hydrous fluid-rock interaction (Matveev *et al*., 2001). Olivine is nominally anhydrous, and so any water present within the crystal lattice is located at defect sites. The vibrational energy of structurally-bound water at these defect sites ranges from 3100 – 3650 cm^{-1} (Bai and Kohlstedt, 1993), and specific defect sites can be correlated with peaks in absorbance, making infrared (IR) light ideal for investigating water in olivine. In order to characterise the presence and location of water (in the form of structurally-bound hydroxyl) in supra-

subduction mantle olivine from Lihir peridotite sample 136063, Fourier Transform Infrared (FTIR) analysis was undertaken at the Australian Synchrotron in Melbourne, Australia (Figure 4.6).

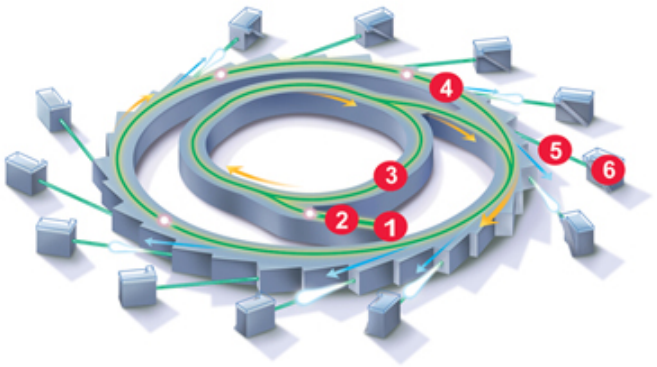

Figure 4.6. The Australian Synchrotron is a particle accelerator that extracts radiation generated from the interaction between electrons travelling at 99.9997% of the speed of light (Australian Synchrotron 2008) and magnetic fields around the perimeter of the storage ring. 1) Electron gun; 2) Linac; 3) Booster ring; 4) Storage ring; 5) Beamline and 6) End station. Image from Australian Synchrotron (2008).

The aim of this experiment was to ascertain the presence of hydroxide variations (OH^-) in olivine related to the presence of low-angle boundaries that are often separated by a distance of only a few µm, therefore synchrotron radiation was utilised due to the spatial resolution obtained from such a high-powered beam (3 µm, versus conventional FTIR of ~80 µm). Experiments were conducted using the infrared beamline, which extracts 58 (h) x 22 (v) milliradians of radiation from the storage ring (Creagh *et al.*, 2007) and has an energy range of between 10 cm^{-1} to 10,000 cm^{-1}. IR radiation is directed from the storage ring to a Bruker V80v FTIR spectrometer and Hyperion 3000 FTIR microscope with a liquid nitrogen-cooled detector, and is controlled by Opus 6.5 software (Figure 4.7).

Olivine grains were carefully selected for analysis based on observations under a polarised light microscope and microstructure highlighted by EBSD mapping. A double polished thick section (200 µm) of Lihir mantle xenolith 136063 was analysed using unpolarised light in transmission mode. Grid and line scans were undertaken over selected areas of the grains cutting across low-angle boundaries and other features of interest such as fluid inclusions and fractures, using a step size of 10 µm. FTIR absorbance between 1 – 4000 cm^{-1} was collected, with a spectral resolution of 4 cm^{-1}, and each spectrum comprises 128 sample scans.

Background measurements were made on a 200 μm thick glass slide (to remove the need to refocus the condenser between sample and background measurements) which had a low absorbance in the spectral region of interest between 3000 – 4000 cm^{-1}. Experiments were undertaken in an enclosed sample chamber (although not air-tight), with regular background measurements. There were some issues with the presence of molecular water, which exhibits a broad peak at ~3400 cm^{-1}. One sample was heated for 2 hours at 90^{o}C in an attempt to remove any molecular water adsorbed on the sample surface. However, spectra taken before and after heating showed no differences, leading to the conclusion that the broad water peak is an internal feature of the olivine, possibly due to the presence of fluid inclusions.

FTIR measurements were made using unpolarised light. Measurements made using polarised light can be used to quantify water content in olivine, and although useful, in this case the addition of a polariser substantially reduced the signal-to-noise ratio of the data such that they were unusable, and consequently was not used. Absorbance values presented in this study are dimensionless, as they are a ratio of incident to transmitted light.

4.2.2 Data processing

The processing methods used for polarised spectra are crucial for producing a reliable result for the concentration of hydroxide in olivine. However, the qualitative results obtained from unpolarised measurements are equally as sensitive to processing methods. The identification of peaks associated with structurally-bound hydroxyl in olivine is very much dependent on a number of parameters involved in processing, namely the baseline correction and noise reduction factor (Fourier self-deconvolution).

Bulk processing of each scan was undertaken using Bruker's Opus 7.0 software. Due to the length of line scans the number of spectra that required processing was high, meaning that manual processing of each scan was impractical. There were several corrections provided by the Opus software that were applied to the data in order to improve quality and peak resolution - a concave rubberband function was used as a baseline correction and a Fourier-self deconvolution was also applied to the data.

- *Baseline correction*

The baseline correction involves the removal of trends and broad peaks from spectra that are irrelevant and interfere with the identification of OH-bearing defects in olivine. The effect of removing unwanted peaks from a spectrum enables better resolution of smaller but more significant peaks (Figure 4.8). For example, the removal of a broad molecular H_2O peak between at ~3420 cm^{-1} corresponding to melt and fluid inclusions enables the detection of smaller, sharper peaks at wavenumbers that overlap the large peak (e.g. ~3350 cm^{-1} and ~3570 cm^{-1}), which represent structurally-bound water.

To process the data collected in this study, a concave rubberband baseline correction was applied. Manual selection of the baseline was unfeasible for the correction of numerous spectra (c. 3000 spectra in this case), we have used the standard concave rubberband option in Opus, using 200 baseline points. The major factor affecting the outcome of the concave rubberband correction is the number of iterations used. This depends on the amount of signal attributed to molecular water relative to the structurally-bound hydroxyl peaks. In some cases (as in Figure 4.8), the broad water peak associated with melt and fluid inclusions is so large that it entirely swamps the signal coming from nearby wavenumbers. The larger this molecular water peak, the more iterations are required to remove it from the spectrum. Figure 4.8 shows a detailed step-by-step removal of the molecular water peak using iterations at intervals of 5. In this study, the number of iterations has been optimised for each line scan (Table 4.2), so as to enable to the correct identification of peaks associated with structurally-bound hydroxyl. This was done at the expense of the ability to compare absorbance values between scans, which is limited for unpolarised spectra in any case.

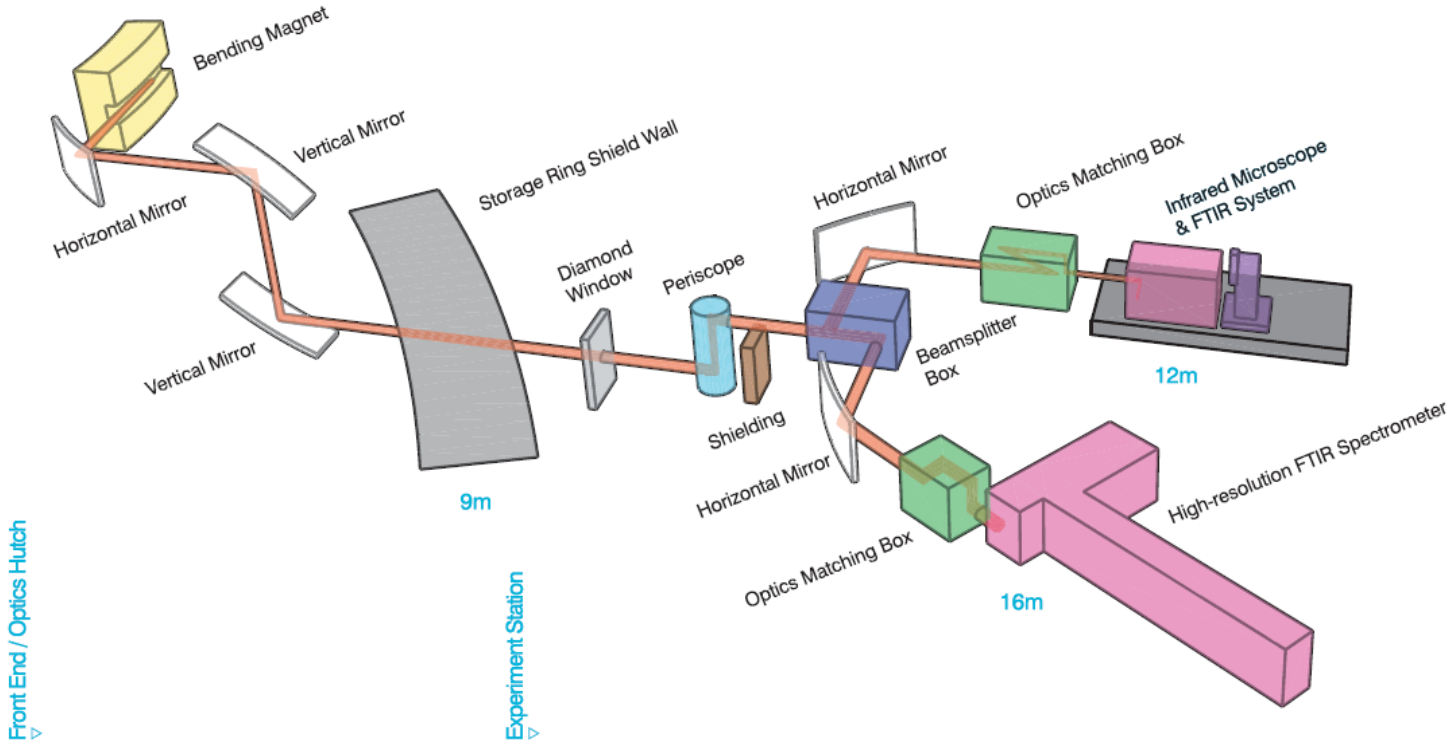

Figure 4.7. IR beamline setup at the Australian Synchrotron. The apparatus used during this experiment was the infrared microscope and FTIR system in the top right of the diagram. Image from Australian Synchrotron (2012).

- *Fourier self-deconvolution*

The purpose of the Fourier self-deconvolution function in Opus is to reduce the effects of interference fringing and noise on the spectra, in order to improve the peak resolution and quality of a spectrum (Kauppinen *et al*., 1981). There are a number of parameters that can be changed when applying a Fourier self-deconvolution, including the description of the peak shape (Gaussian or Lorentzian), the deconvolution factor and the noise reduction factor. This study used a Gaussian peak shape and a deconvolution factor of 2 for the processing of all scans. The factor that affected the outcome of the processed data most is the noise reduction factor. Like the number of iterations, this required optimisation for each individual scan. The optimisation process involved finding a compromise between the amount of noise reduction and the loss of peak height and shape (Figure 4.9). The removal of noise allows for the detection of small peaks that have the same amplitude and are on the same scale as the interference fringing or noise. However, too much noise reduction will reduce the size of peaks and degrade the quality of the spectral resolution such that peak information will be removed. The application of a Fourier self-deconvolution to FTIR data requires the careful selection of the correct noise reduction factor that will minimise noise but not degrade data quality. For very noisy scans, the deconvolution factor can be as low as 0.15 – 0.20 and for good quality scans, as high as 0.40.

- *Other processing issues*

The removal of noise can also be undertaken using the 'smooth' tool in Opus. This however, has the ability to degrade data quality, to the point of removing entire peaks of interest, and so it is suggested that an effective Fourier self-deconvolution is a more appropriate and reliable tool for noise removal.

The baseline correction applied to the data is extremely sensitive to the existing slope of a spectrum, and so extremely large peaks in the lower end of the spectrum will significantly affect the outcome of the baseline correction. An effective way of eliminating this effect is to crop the spectrum down to a range of wavelengths of interest prior to processing (this can be done using the crop tool in Opus). All structurally-bound hydroxide in olivine is contained within 3000 – 3650 cm^{-1} and

above 3650 cm^{-1} there are frequently large atmospheric water vapour peaks which will affect the baseline correction, so it is suggested that the scan be cropped to the region between 3000 – 3650 cm^{-1} to avoid these. The primary output following data processing was a series of FTIR absorbance maps of the OH^- stretching region in olivine (~3000 – 3650 cm^{-1}).

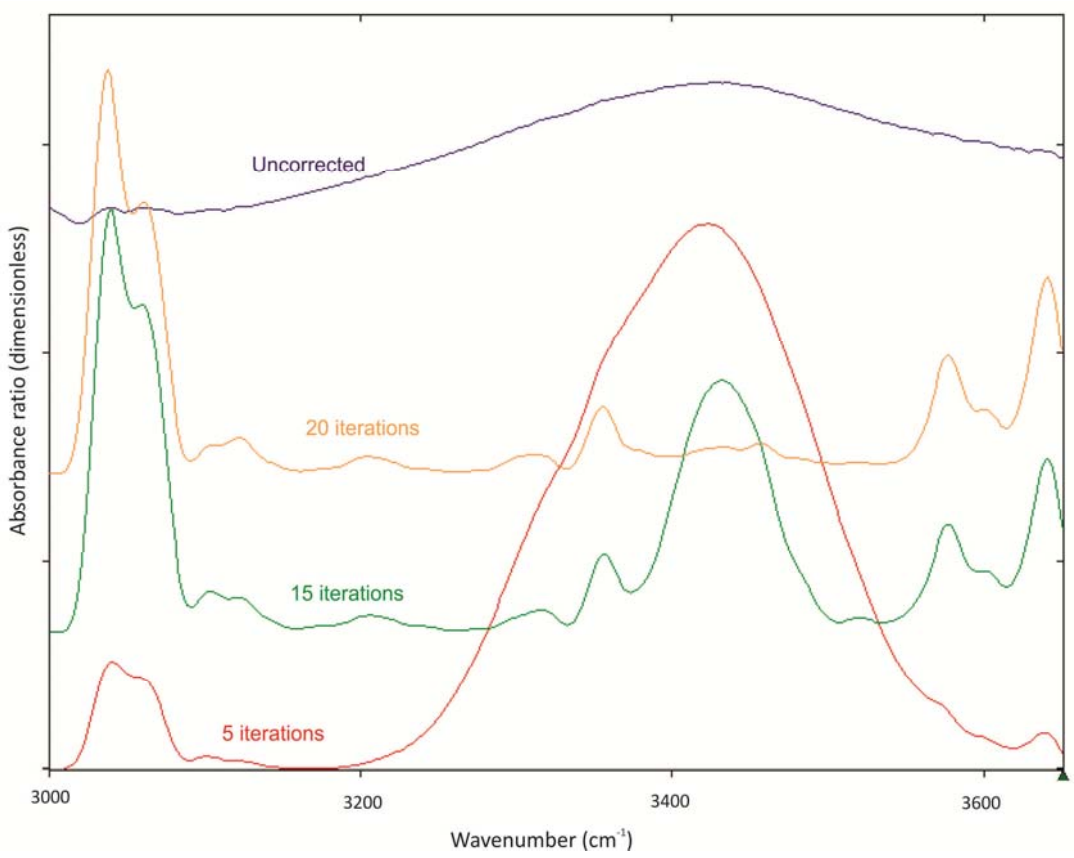

Figure 4.8. Example of the application of a concave rubberband baseline correction to an IR spectrum from olivine. The broad peak at 3420 cm^{-1} is due to the presence of molecular water, and as can be seen by increased number of iterations, can be processed out of the data to highlight smaller, sharper peaks. The noise reduction factor used on this data was 0.25.

Table 4.2. FTIR collection and processing parameters for sample 136063. All scans were corrected using a concave rubberband correction with 10 iterations.

Scan	Length (µm)	No. of Spectra	Baseline correction (no. of points)	Smoothing (no. of points)	Noise reduction factor
Grain 13A	1500	150	200	25	0.20
Grain 13B	660	66	200	25	0.25
Grain 13C	590	59	200	25	0.40
Grain 47	760	76	200	25	0.20
Grain 59A	500	50	200	25	0.20
Grain 59B	500	50	200	25	0.20
Grain 70	1000	100	200	25	0.20

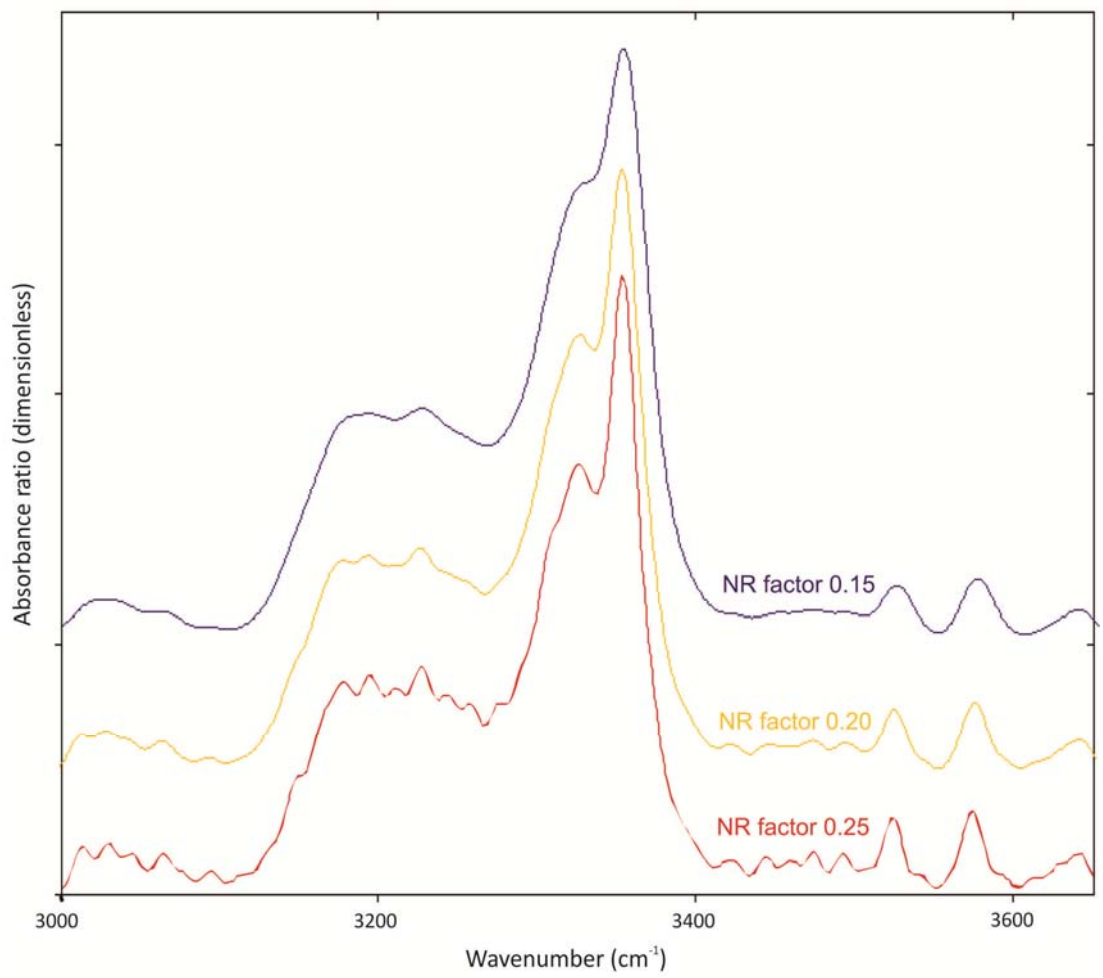

Figure 4.9. The effect of the noise reduction factor (NR) on FTIR spectra from olivine. The lower the NR factor applied during Fourier Self-deconvolution, the more information is lost from the spectrum, meaning that excessive processing can result in small but potentially significant peaks being processed out of the data.

4.2.3. Acknowledgements

Ljiljiana Puskar and Mark Tobin are gratefully acknowledged for their technical assistance during the collection of FTIR data at the IR beamline at the Australian Synchrotron in Melbourne, Australia. Katy Evans and Steve Reddy are also acknowledged for all their time and effort during data collection.

4.3. Ion Probe Isotope Analysis

The interaction between fluids and rocks can often leave an isotopic signature, thus isotope analysis can be a useful tool for determining the extent and nature of metasomatism. In order to shed light on the relationship between deformation and geochemistry in mantle olivine, analysis of the magnesium and oxygen isotopic composition of deformed mantle olivines from the Higashi-Akaishi and Imono peridotites was undertaken. Analysis was undertaken using a Cameca ims 1280 ion microprobe located at the Centre for Microscopy, Characterisation and Analysis (CMCA) at the University of Western Australia, Perth.

4.3.1. Experimental setup and procedure

Japan samples J909C (Imono Peridotite) and J917 (Higashi-Akaishi Peridotite) were mounted in 4 mm thick blocks of epoxy resin along with several chips of San Carlos olivine standard, polished and gold coated (Figures 4.10A and B). Care was taken during sample preparation and analysis to avoid fluid and mineral inclusions present in the San Carlos standard. Collection parameters are given in Table 4.3.

Table 4.3. Isotope data collection parameters. Parameters are different for the two datasets as they were collected on different days.

Parameters	Magnesium	Oxygen
Collection mode	Mono	Mono
Source	O+	Cs+
Primary beam current	~6.8 nA	~2.4 nA
Spot size	~7 µm	~7 µm

4.3.2. Data processing

A standard bracketing technique was used during data collection (Halicz *et al*., 1999). Measurements were repeatedly calibrated using analyses of San Carlos olivine as a standard (>5 San Carlos measurements were made in between ~15 unknown measurements). The precision was high, with the average $\delta^{18}O$ San Carlos measurement at 4.85‰ ± 0.13‰, which is consistent with published values for San Carlos of 4.88‰ ± 0.06‰ (Mattey and Macpherson, 1993) and 4.86‰ ± 0.18‰ (Chazot *et al*., 1997). $\delta^{26}Mg$ for San Carlos was -0.05‰ ± 0.16‰, which is similar to the published value for San Carlos of -0.06‰ ± 0.07‰ (Wiechert and Halliday,

2007), but different to those of Pearson *et al*. (2006) and Teng *et al*., (2007), who report a δ^{26}Mg value of -0.6‰, and Huang *et al*., (2009) who reports a value of -0.27‰ ± 0.14‰. The cause of variations in magnesium isotope composition between different laboratories is unresolved. However, in this study, the internal precision was high, thus variations in the isotope composition of the unknowns with respect to San Carlos are real, but it should be noted that comparison of measurements between laboratories should be approached with caution. Measurements that appeared to be outliers were repeated and in all cases were reproduced.

Repeated standard measurements identified the occurrence of primary beam drift in some of the datasets. A drift correction was required for both oxygen and magnesium isotope data from both samples. The following procedure has been applied to correct the observed time-dependent drift:

(1) On a plot of isotope ratio of the standard vs time, each point was projected back to the y-axis following the slope of the regression line fitted to the data;

(2) The same projection was applied to the unknowns, following the slope calculated from the standards bracketing the unknowns. The X variable coefficient of the standards was used to correct the unknown measurements using the following equation:

Drift corrected ratio = (uncorrected ratio – X variable coefficient) x (X variable)

The δ value of the unknowns relative to San Carlos olivine were then determined using the following equations:

1) $$\delta^{18}O_{SC} = \left[\left({}^{18}O/{}^{16}O\right)_{sample} / \left({}^{18}O/{}^{16}O_{SC}\right) - 1\right] \times 1000 \qquad \textit{(O isotopes)}$$

2) $$\delta^{n}Mg_{SC} = \left[\left({}^{n}Mg/{}^{24}Mg\right)_{sample} / \left({}^{n}Mg/{}^{24}Mg_{SC}\right) - 1\right] \times 1000 \quad \textit{(Mg isotopes)}$$

In equation 2, n refers to either 25 or 26. Corrected ^{25}Mg, ^{26}Mg and ^{18}O data are initially expressed as per mil (‰) deviation from the isotopic composition of San Carlos olivine. The final error on the unknown is the propagation of the analytical error and of the error on the average value of the standard. In order to make a comparison between these analyses and published values the Mg isotope data were corrected so that they could be expressed relative to standard DSM-3 (Dead Sea magnesium), which involved the subtraction of 0.58 ± 0.15 from $\delta^{26}Mg_{SC}$ and 0.28 ±

0.1 from $\delta^{25}Mg_{SC.}$ O isotope data were corrected to enable expression relative to Standard Mean Ocean Water (SMOW).

A)

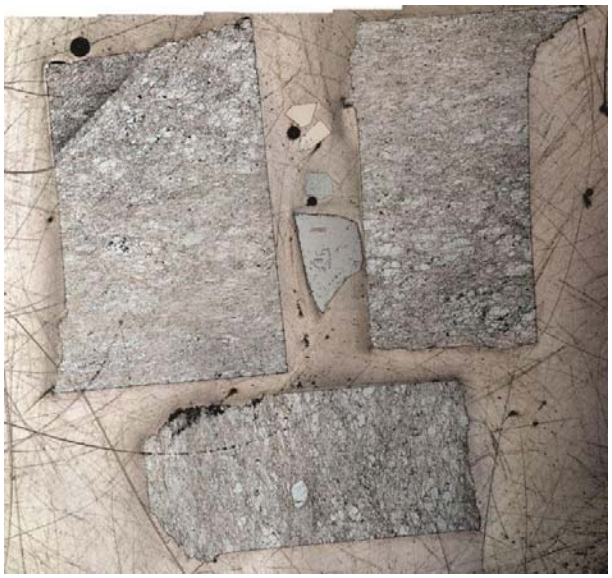

B)

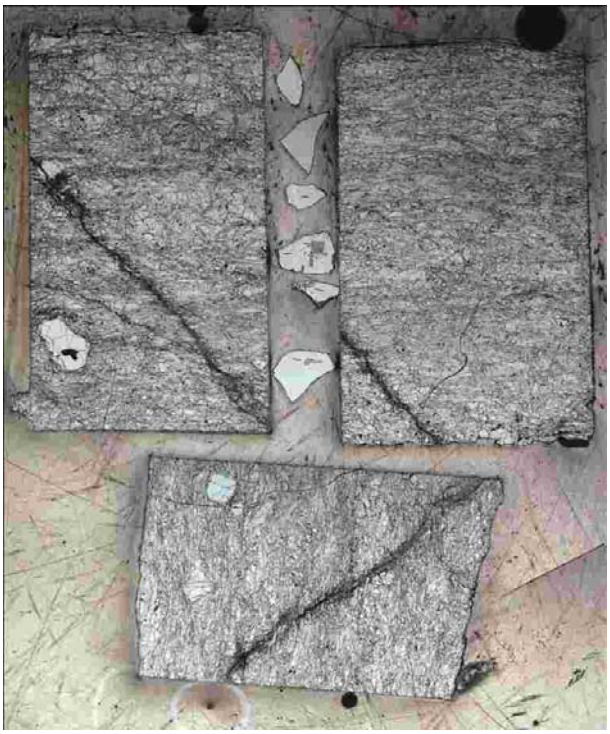

Figure 4.10. Photomicrographs of the J909C (A) and J917 (B) sample mounts. Blocks of mantle peridotite are located in the centre of the mounts and surround several grains of San Carlos olivine. Only the pristine, inclusion free San Carlos olivine was used for standard analyses.

4.3.3. Acknowledgements

The author gratefully acknowledges the assistance of John Cliff and the Centre for Microscopy, Characterisation and Analysis in preparing and analysing these samples.

4.4. References

Australian Synchrotron (2012) Infrared Spectroscopy (Fact Sheet), Accessed July 3, 2012, from http://www.synchrotron.org.au/index.php/aussyncbeamlines/beamline-fact-sheets

Bai, Q. and Kohlstedt, D.L. (1993) Effects of chemical environment on the solubility and incorporation mechanism for hydrogen in olivine, *Physics and Chemistry of Minerals*, v. 19, p. 460-471.

Bestmann, M. and Prior, D.J. (2003) Intragranular dynamic recrystallization in naturally deformed calcite marble: diffusion accommodated grain boundary sliding as a result of subgrain rotation recrystallization, *Journal of Structural Geology*, v. 25, p. 1597-1613.

Boyle, A.P., Prior, D.J., Banham, M.H. and Timms, N.E. (1998) Plastic deformation of metamorphic pyrite: new evidence from electron-backscatter diffraction and forescatter orientation-contrast imaging, *Mineralium Deposita*, v. 34, p. 71-81.

Chazot, G., Lowry, D., Menzies, M. and Mattey, D. (1997) Oxygen isotopic composition of hydrous and anhydrous mantle peridotites, *Geochimica et Cosmochimica Acta*, v. 61, p. 161-169.

Creagh, D., Tobin, M., Broadbent, A. and McKinlay, J. (2007) An Infrared Beamline at the Australian Synchrotron, *AIP Conference Proceedings - International Conference on Synchrotron Radiation Instrumentation, Daegu (Republic of Korea), 28 May - 2 Jun 2006,* v. 879, p. 615-618.

Halicz, L., Galy, A., S. Belshaw, N. and Keith O'Nions, R. (1999) High-precision measurement of calcium isotopes in carbonates and related materials by multiple collector inductively coupled plasma mass spectrometry (MC-ICP-MS), *Journal of Analytical Atomic Spectrometry*, v. 14, p. 1835-1838.

Hart, J.T. (1978) The structural morphology of olivine: II, A quantitative derivation, *The Canadian Mineralogist*, v. 16, p. 547-560.

Huang, F., Glessner, J., Ianno, A., Lundstrom, C. and Zhang, Z. (2009) Magnesium isotopic composition of igneous rock standards measured by MC-ICP-MS, *Chemical Geology*, v. 268, p. 15-23.

Kauppinen, J.K., Moffatt, D.J., Mantsch, H.H. and Cameron, D.G. (1981) Fourier self-deconvolution: a method for resolving intrinsically overlapped bands, *Applied Spectroscopy*, v. 35, p. 271-276.

Mattey, D.P. and Macpherson, C. (1993) High-precision oxygen isotope microanalysis of ferromagnesian minerals by laser-fluorination, *Chemical Geology*, v. 105, p. 305-318.

Matveev, S., O'Neill, H.S.C., Ballhaus, C., Taylor, W.R. and Green, D.H. (2001) Effect of Silica Activity on OH^- IR Spectra of Olivine: Implications for low $aSiO_2$ Mantle Metasomatism, *Journal of Petrology*, v. 42, p. 721-729.Oxford Instruments HKL A/S (2007) Channel 5 Manual, Denmark.

Pearson, N.J., Griffin, W.L., Alard, O. and O'Reilly, S.Y. (2006) The isotopic composition of magnesium in mantle olivine: Records of depletion and metasomatism, *Chemical Geology*, v. 226, p. 115-133.

Prior, D.J., Wheeler, J., Peruzzo, L., Spiess, R. and Storey, C. (2002) Some garnet microstructures: an illustration of the potential of orientation maps and misorientation analysis in microstructural studies, *Journal of Structural Geology*, v. 24, p. 999-1011.

Randle, V. and Engler, O. (2000) Introduction to Texture Analysis: Macrotexture, Microtexture and Orientation Mapping, Gordon and Breach Science Publishers, Amsterdam.

Reddy, S.M. and Buchan, C. (2005) Constraining kinematic rotation axes in high-

strain zones: a potential microstructural method? *Geological Society, London, Special Publications*, v. 243, p. 1-10.

Reddy, S.M., Timms, N.E., Pantleon, W. and Trimby, P. (2007) Quantitative characterisation of plastic deformation of zircon and geological implications, *Contributions to Mineralogy and Petrology*, v. 153, p. 625-645.

Teng, F.-Z., Wadhwa, M. and Helz, R.T. (2007) Investigation of magnesium isotope fractionation during basalt differentiation: Implications for a chondritic composition of the terrestrial mantle, *Earth and Planetary Science Letters*, v. 261, p. 84–92.

Wiechert, U. and Halliday, A.N. (2007) Non-chondritic magnesium and the origins of the inner terrestrial planets, *Earth and Planetary Science Letters*, v. 256, p. 360–371.

Chapter 5. Petrographic analysis of supra-subduction peridotites from Lihir, Papua New Guinea and Shikoku, Japan

This chapter provides a summary of the petrographic observations of thin sections made from samples collected from 1) Mt. Higashi-Akaishi and the surrounding area (Shikoku Island, Japan) and 2) Tubaf seamount, near Lihir Island (Papua New Guinea). The geological and tectonic setting of the samples is described in detail in Chapter 3. Observations were made under a polarised light microscope using plane-polarised light (PPL), cross-polarised light (XPL) and reflected light. For detailed petrographic descriptions and photomicrographs, the reader is referred to Appendix 2.

5.1. Shikoku Island, Japan

5.1.1. Sample descriptions and petrogenesis

Petrographic thin sections were made from 4 samples collected from the Imono Peridotite Body (Table 5.1; Figures 5.1A-D), and 5 samples collected from the Higashi-Akaishi Peridotite Body (Table 5.1; Figures 5.2A – E). Samples were cut such that the surface of the section represents the structural XZ plane, with the X direction parallel to the long axis of the section. Observation under a polarised light microscope reveals that the samples are porphyroclastic spinel dunites. Minerals observed include olivine, chromite, magnetite, pentlandite, antigorite and serpentine (possibly chrysotile or lizardite) in various proportions. Olivine in these samples is commonly bimodal in grain size, and includes porphyroclasts and neoblasts. Porphyroclasts are characterised by their relatively larger grain size and abundant preserved internal microstructure (e.g. low-angle boundaries) as well as the presence of common fluid and mineral inclusions. Neoblasts are smaller in size and have a relatively clean appearance, with no or very little internal microstructure or inclusions. Peridotites are classified with respect to relative proportions of olivine, orthopyroxene and clinopyroxene, and the latter two minerals are absent in these rocks, thus the peridotites are dunites. A detailed description of the petrography of each sample is provided below. Detailed petrographic descriptions and photomicrographs of each sample are provided in Appendix 2.

Table 5.1. Shikoku samples analysed in this study.	
Sample	**Description**
J902	Fine-grained metasomatised spinel dunite
J904A	Very fine-grained metasomatised spinel dunite
J908A	Very fine-grained metasomatised spinel dunite
J909C	Very fine-grained metasomatised spinel dunite
J915C	Fine-grained metasomatised spinel dunite
J917	Fine-grained metasomatised spinel dunite
J918B	Very fine-grained metasomatised spinel dunite
J919B_1	Very fine-grained metasomatised spinel dunite
J919B_2	Fine-grained spinel dunite

Imono Peridotites

J902:

Sample J902 is a metasomatised spinel dunite containing olivine, chromite, magnetite, antigorite and pentlandite. The rock has a porphyroclastic texture, with a weak, pervasive microscopic foliation and mineral lineation (Figure 5.1A). The foliation is predominantly defined by the alignment of antigorite fibres and bands of magnetite. The mineral lineation is defined by the alignment of antigorite fibres and long axes of chromite grains. The sample is cross-cut by a network of veins containing fine-grained antigorite, magnetite and pentlandite that appears to have slightly oxidised, possibly due to surficial weathering processes. Magnetite occurs towards the centre of these veins, overprinting the antigorite. Microlithons are defined by well-foliated, antigorite-rich and weakly-foliated, antigorite-poor domains. The antigorite-rich regions tend to contain larger and better preserved olivine porphyroclasts than the antigorite-poor microlithons. Microlithon boundaries are parallel to the foliation.

Primary olivine comprises approximately 70% of the rock, and the population of olivine grains can be subdivided into porphyroclasts (~10% of the rock) and neoblasts (~60% of the rock). Porphyroclastic olivine ranges in diameter from 0.5 – 1.5 mm, with an average grain size of 1.0 mm. Porphyroclasts are anhedral and slightly elongate in morphology, with irregular, curved grain boundaries with other olivine grains. Occasionally, olivine grain boundaries are very straight and regular,

parallel or sub-parallel to the internal microstructure. Porphyroclastic olivine is often elongate parallel to the lineation direction, and displays prominent internal microstructure in the form of low-angle boundaries as indicated by changes in extinction across the grains. Olivine porphyroclasts contain very fine (<1 μm) trails of fluid inclusions that are parallel to the low-angle boundaries. There are also coarser trails of fluid inclusions (~5 μm) that appear to connect to the finer inclusions. Grains show irregular, glassy fracture typical of olivine. Neoblastic olivine ranges from 0.05 – 0.30 mm in diameter, with an average grain size of ~0.07 mm. Neoblastic olivine grains often form triple junction grain boundaries with each other, have a subhedral to anhedral morphology and are equant in shape. Neoblastic olivine is clean in appearance with no inclusions or preserved internal microstructure, with a typical olivine fracture pattern as seen in the porphyroclasts. Olivine neoblasts have irregular and curved boundaries with olivine porphyroclasts.

Chromite comprises approximately 2% of the rock. Chromite grains range from 0.2 – 1.5 mm in diameter, with an average of ~0.3 mm. Grains are subhedral to euhedral, and tabular in shape with embayed grain boundaries, often rimmed by magnetite. Chromite grains are slightly elongate in the direction of the lineation. Antigorite occurs as a metasomatic mineral that replaces both populations of olivine grains and overprints chromite. Antigorite comprises ~27% of the rock, and grains are elongate to bladed and euhedral. Antigorite blades are 0.1 – 1.0 mm in length, and average ~0.3 mm. Magnetite comprises ~1% of the rock and ranges in grain size from 0.005 – 0.050 mm, with an average grain size of ~0.025 mm. Magnetite grains are subhedral to anhedral, and equant in shape, often forming rims surrounding the chromite. Trace amounts of pentlandite (0.01 – 0.05 mm, average 0.02 mm) occur in association with the magnetite.

J904A:

Sample J904A is a fine-grained, porphyroclastic, metasomatised spinel dunite with a prominent pervasive foliation and mineral lineation and a weak crenulation (Figure 9.1C). The rock contains porphyroclastic and neoblastic olivine, chromite, magnetite and pentlandite, and is metasomatically overprinted by antigorite. Both the foliation and weak crenulation are defined primarily by antigorite fibre alignment, with a

minor contribution to the dominant foliation from the long axes of lenticular olivine neoblasts. The foliation wraps around olivine and chromite porphyroclasts, with strain shadows forming around the clasts where neoblastic olivine tends to be more equant in shape, rather. There is also some evidence for weak microlithon development defined by varying amounts of olivine and antigorite. Although vague, the boundaries of these are sub-parallel to the dominant foliation.

Primary olivine comprises ~5% of the rock. The grains range in diameter from 0.75 – 2.1 mm, with an average grain size of 1.0 mm. Olivine porphyroclasts are anhedral and elongate in morphology. Grain boundaries with other porphyroclasts are irregular, and with neoblastic olivine are curved and irregular. Olivine porphyroclasts are usually fractured and are overprinted by coarse antigorite grains. There is some preservation of internal microstructure in the form of low-angle boundaries within the larger olivine grains, as well as fluid inclusions that often form trails parallel to the low-angle boundaries (Figure 9.1D). There are 2 types of fluid inclusions preserved within the olivine grains: 1) fine, vermicular trails and bubbles that are less than 1 μm in diameter, and 2) coarser spherical bubbles ~ 5 μm wide. Both of these types of fluid inclusions are spatially related to one another. Olivine neoblasts comprise 50% of the rock, with grains ranging from 0.025 – 0.5 mm in diameter and an average grain size of 0.3 mm. Neoblastic olivine is anhedral and lenticular in shape, but can be equant within strain shadows. Grain boundaries between olivine neoblasts tend to be straight and regular, often terminating at triple junctions. Boundaries with olivine porphyroclasts are curved and irregular. Neoblastic olivine is generally fairly clean in appearance, with no preservation of inclusions or internal microstructure.

Primary chromite is porphyroclastic and comprises ~2% of the rock, ranging in diameter from 0.2 – 1.5 mm with an average grain size of 1.0 mm. Grains are subhedral to anhedral and equant in morphology. Magnetite comprises ~1% of the rock, ranging from 0.05 – 0.2 mm in diameter with an average grain size of 0.1 mm. Grains are subhedral and equant in morphology. Magnetite cross-cuts antigorite, and tends to form around the rims of chromite grains. Associated with the magnetite are

small grains of pentlandite (0.01 – 0.05 mm, average 0.02 mm), which comprise less than 0.5% of the rock.

Antigorite is present in the rock as a secondary, metasomatic mineral and comprises 42% of the rock. It forms elongate, bladed and subhedral to euhedral grains that range in length from 0.1 – 1.0 mm, with an average length of 0.4 mm. Antigorite overprints primary olivine and chromite as well as olivine neoblasts. Antigorite appears to have played a role in olivine neoblast development through mechanical breakdown of the grains.

J908A:

J908A is a very fine-grained metasomatised spinel dunite comprising olivine, antigorite, chromite, magnetite and pentlandite. The pervasive foliation is defined primarily by the alignment of blades of antigorite and the mineral lineation by the long axes of lenticular olivine (Figure 9.1E). The antigorite foliation wraps olivine and chromite porphyroclasts. There is evidence for early olivine microlithon development and the sample is traversed by antigorite and magnetite-filled veins.

Olivine comprises 50% of the rock, and exhibits a continuous grain size change, ranging from 0.02 – 1.5 mm, with an average grain size of 0.5 mm. All olivine grains are anhedral and lenticular to equant, with the long axis of equant grains parallel to the structural x-direction. Coarser porphyroclastic grains are fractured and often preserve low-angle boundaries. Intragrain fractures often exhibit and orthogonal fracture geometry, forming both parallel and perpendicular to the low-angle boundaries. Porphyroclastic olivine is overprinted by coarse antigorite and is often wrapped by the foliation.

Chromite forms anhedral, equant porphyroclasts comprising 1% of the rock. Chromite grains range from 0.5 – 1 mm in diameter, with an average size of 0.9 mm. Chromite grains are often embayed at the edges and are surrounded by rims of magnetite and associated pentlandite.

Antigorite comprises 47% of the rock and forms elongate and bladed grains. Antigorite cross-cuts olivine and chromite and its' formation appears to be synchronous with olivine neoblast formation (Figure 9.1F). It appears to have played a role in olivine neoblast development by mechanically dismembering olivine grains. Antigorite is often fractured perpendicular to the length of the grain, and these fractures are commonly filled with fine magnetite.

Magnetite (ranging in size from 0.05 – 0.2 mm, average 0.1 mm) and pentlandite (ranging in size from 0.005 – 0.05 mm, average 0.025 mm) comprise 1.5 and <0.5% of the rock, respectively. Both are spatially associated with each other, and occur both as part of the rock matrix and forming rims around chromite. Magnetite and pentlandite overprint antigorite grains and are often found in veins traversing the sample.

J909C:

J909C is a fine-grained, sheared porphyroclastic spinel dunite that has been substantially metasomatised (Figure 5.1G). This sample comprises olivine, chromite, magnetite, pentlandite and metasomatic antigorite. The pervasive foliation is primarily defined by antigorite and the mineral lineation is defined by both elongation and alignment of deformed olivine (often forming clusters of grains resembling pods) and alignment of bladed antigorite. The thin section is divided into zones both rich and poor in antigorite (microlithons) corresponding to zones of strong and weak fabric, respectively. The antigorite-rich zone generally contains a finer fraction of olivine grains and the olivine within this region is predominantly neoblastic. Strain shadows have developed around porphyroclastic chromite grains. The foliation is slightly wavy, which indicates that there is a weak overprinting of this fabric by a later foliation.

Primary olivine is porphyroclastic, and comprises 57% of the rock. The grain size ranges from 0.5 – 2.0 mm, with an average grain size of 0.7 mm. Grains are anhedral, elongate and often lenticular in shape. Olivine porphyroclasts tend to preserve low-angle boundaries within grains, and often running parallel to these are

abundant sub-micron sized fluid inclusions. The fluid inclusions are spatially related to the presence of antigorite. Grain boundaries with other olivine porphyroclasts are straight and regular, whereas boundaries with olivine neoblasts are generally embayed and irregular. Olivine neoblasts comprise ~10% of the rock, and range from 0.05 – 0.4 mm in diameter, with an average grain size of 0.3 mm. Most neoblasts are anhedral to subhedral, and slightly elongate with a lenticular morphology, however grains that occur within lesser strained parts of the sample are more equant in shape. Neoblasts are relatively clean in appearance and do not contain any intragrain microstructures. Grain boundaries with other olivine neoblasts are often embayed (although in lower strain regions can terminate at triple junctions).

Chromite is porphyroclastic and comprises ~2% of the rock and grains range from 0.25 – 0.7 mm in diameter, with an average of 0.5 mm (Figure 5.1H). Grains are generally subhedral and equant to slightly elongate in shape. Large grains are wrapped by the foliation, with strain shadows developed at the margins of the grains. Some grain interiors tend to be spotted in appearance and occasionally contain small overgrowths of antigorite. Grain boundaries with both types of olivine are regular, but boundaries with other chromite grains tend to be embayed.

Magnetite comprises ~1% of the sample and the grain size ranges from 0.05 – 0.2 mm, with an average of 0.1 mm. Grains are anhedral to subhedral in morphology, and are equant to slightly elongate (with the long axis parallel to the X direction). Growth of magnetite appears to be a late feature, overgrowing antigorite and filling spaces in between antigorite grains. Often magnetite forms elongate aggregates parallel to the foliation appearing as ‘tails’ leading away from porphyroclasts. Magnetite and associated fine-grained pentlandite (ranging in size from 0.005 – 0.05 mm, average 0.025 mm) often forms around the rims of chromite.

Antigorite metasomatically replaces primary and secondary olivine in this sample and comprises 30% of the rock. Antigorite grains are elongate blades that range in length from 0.05 – 0.5 mm, with an average length of 0.3 mm. Antigorite generally has a uniform grain size and occurs in higher abundance in the higher strain regions of the thin section.

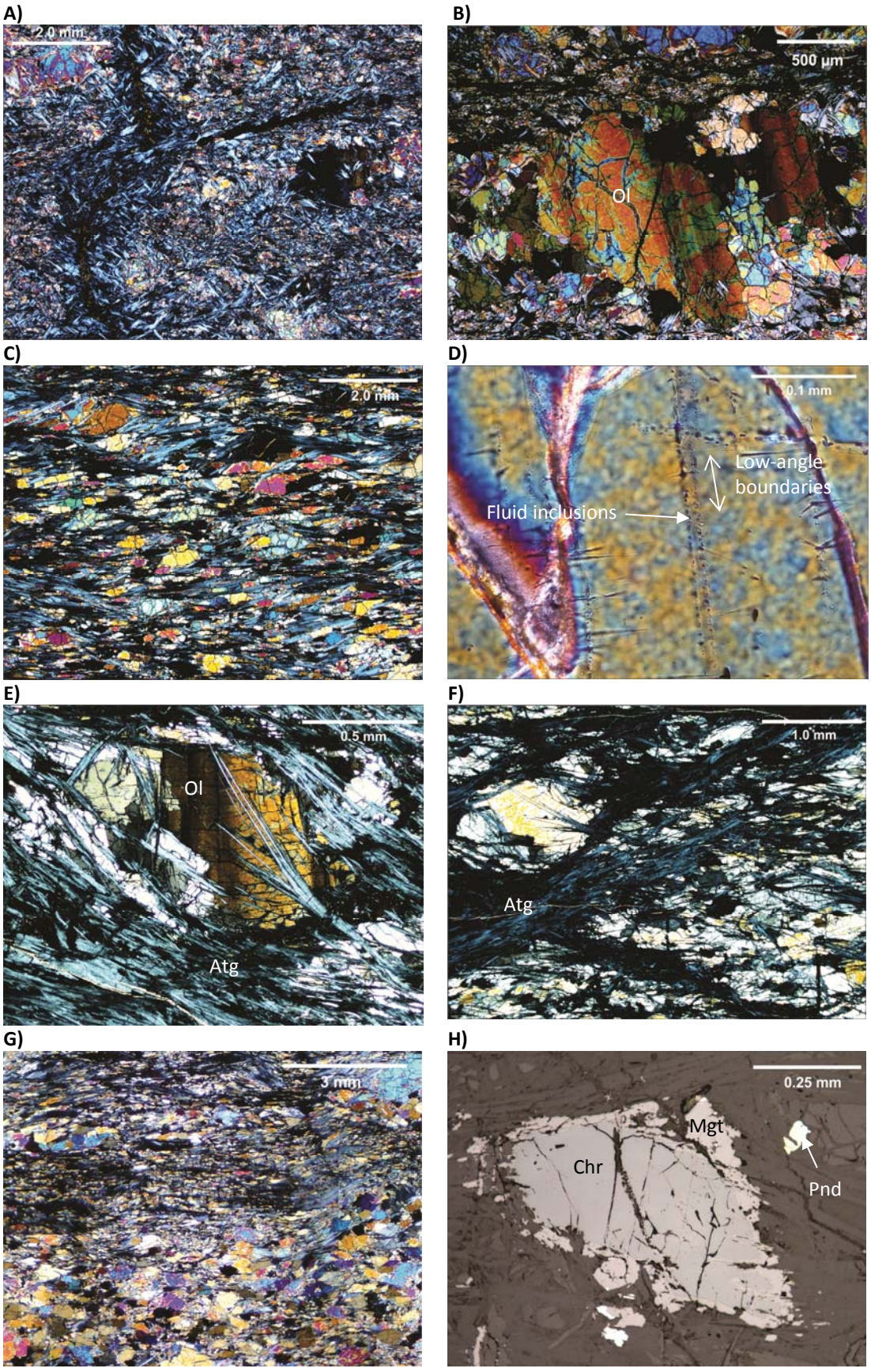

Figure 5.1. Photomicrographs of Imono Peridotite samples taken in a polarised light microscope. A) Overview of sample J902 under XPL showing the overall texture of the sample, including extensive antigorite replacement and cross-cutting vein. B) Olivine porphyroclast displaying low angle boundaries in J902. The grain displays dynamical recrystallisation by grain boundary migration, as shown by the population of neoblasts in the centre of the grain. C) The overall texture of sample J904A under XPL with a foliation defined by antigorite and alignment of lenticular olivine grains. D) Fluid inclusion trails running parallel to

low angle boundaries in an olivine porphyroclast in sample J904A (XPL). E) Coarse antigorite (grey) cross-cutting a deformed olivine porphyroclast showing relict internal microstructure (orange grain) in sample J908A (XPL). There is also some grain boundary migration recrystallisation occurring between the pale yellow olivine grain and the orange grain. F) Extensive antigorite replacement of primary mantle olivine in sample J908A (XPL image). G) Texture of sample J909C (XPL). The top half of the image is a well-foliated microlithon rich in antigorite, and the bottom half is olivine-rich with a weaker fabric. H) Chromite porphyroclast under reflected light (blue-grey in centre). Surrounding the grain is a rim of magnetite and there is also some pentlandite present (brighter yellow grains bottom middle and top).

Higashi-Akaishi Peridotites

J915C:

J915C is a fine-grained, porphyroclastic metasomatised spinel dunite with a weak pervasive foliation and mineral lineation (Figure 5.2A). The dunite is comprised of olivine, chromite, magnetite, pentlandite, antigorite and serpentine. The foliation is defined primarily by the alignment of coarse antigorite, with elongate olivine porphyroclasts aligned within the foliation parallel to the X structural direction. The sample is cross-cut by a network of veins containing aphanitic serpentine and magnetite, and these veins appear to have a conjugate relationship with the lineation direction. The serpentine within the veins is aligned oblique to the vein orientation, characteristic of the chrysotile or lizardite serpentine polymorphs. There appears to be evidence for multiple fluid flow episodes as there are several generations of magnetite and serpentine within these veins. There is some microboudinage of the coarse antigorite occurring, with the necks filled with fine-grained magnetite.

Porphyroclastic olivine forms anhedral and slightly elongate grains ranging from 0.4 – 0.75 mm in diameter (average 0.5 mm). These comprise 30% of the dunite and are highly fractured. Olivine porphyroclasts tend to contain both mineral and fluid inclusions on a sub-micron scale, which are particularly abundant in larger olivines. Fluid inclusions are generally spherical or form elongate trails, and often have a radial/stellate morphology. Very little internal microstructure preserved within the grains. Neoblastic olivines are relatively pristine grains that tend to surround the porphyroclasts. They form subhedral, equant grains 0.05 – 0.2 mm in diameter, averaging 0.1 mm.

Chromite is porphyroclastic and forms subhedral to anhedral, equant grains 0.06 – 0.58 mm in diameter (with an average of 0.2 mm). Chromite comprises 4% of the dunite. Grain boundaries are often embayed and grains are rimmed by magnetite and pentlandite.

Antigorite is a secondary, metasomatic mineral comprising 10% of the rock. It forms euhedral, acicular grains that cross-cut primary olivine and chromite. Coarse antigorite shows undulose extinction indicating deformation and contains small fractures perpendicular to the long axis of the grain, filled with magnetite (which appears to be associated with the fine serpentine). Antigorite is cross-cut by magnetite, pentlandite and fine serpentine.

Aphanitic serpentine (chrysotile or lizardite) comprises 15% of the sample and occurs along veins and in grain boundaries and fractures, replacing olivine. Within veins, olivines are completely replaced, although the relict grain boundary morphology can still be identified (Figure 5.2B). Associated with the veins of aphanitic serpentine are magnetite and pentlandite grains. Magnetite comprises 0.5% of the rock. It forms very fine grains (<0.001 mm) that occur along the grain boundaries of altered olivine grains, as well as being concentrated in the centre of serpentine veins. Magnetite also fills in the necks of microboudins of coarse antigorite. Pentlandite comprises <0.5% of the rock and is spatially related to magnetite. Pentlandite grains are <0.001 in diameter and is one of the latest minerals to form.

J917:

Sample J917 is a fine-grained metasomatised spinel dunite with a strong schistosity and mineral lineation (Figure 5.2C). The sample is comprised of porphyroclastic and neoblastic olivine, chromite, magnetite, pentlandite, antigorite and serpentine. Lens-like microlithons of porphyroclastic and neoblastic olivine are separated by domains of aligned coarse antigorite. Microlithon development is predominantly responsible for the spaced foliation. Parallel to the foliation are trails of fine-grained magnetite aggregates. The section is traversed by a few narrow veins (<0.5 mm wide) that post-date the coarse antigorite formation. The veins are filled with a very fine-grained/aphanitic serpentine, which is associated with fine-grained neoblastic magnetite and pentlandite.

Porphyroclastic olivine comprises 3% of the sample and grains are 0.4 – 0.9 mm in diameter, with an average of 0.7 mm. Grains are anhedral and slightly elongate, and

often contain very small fluid inclusions trails. Porphyroclasts also commonly exhibit distinct low-angle boundaries related to deformation of the olivine (Figure 5.2D). Neoblastic olivine comprises 64% of the sample and forms subhedral to euhedral, equant grains. Neoblastic olivine is clean in appearance and exhibits no evidence for internal microstructures. Grains commonly terminate at triple junction grain boundaries.

Primary chromite comprises 1% of the sample and is very amorphous at grain boundaries where it is often rimmed by magnetite. Grains range in size from 0.25 – 1 mm, with an average grain size of 0.4 mm. Often, more elongate chromite grains are aligned parallel to the foliation and have weak strain shadows.

Antigorite comprises 29% of the sample and defines the strong schistose foliation. Antigorite is euhedral and bladed, and replaces primary and neoblastic olivine. It is overprinted by a later very fine-grained serpentine mineral (chrysotile or lizardite) which comprises 1% of the sample. Fine serpentine is associated with a thin vein cross-cutting the section. Vein-fill also includes magnetite and pentlandite.

Magnetite comprises 1.5% of the rock and forms subhedral, rounded grains 0.01 – 0.09 mm in diameter (average 0.03 mm). It often occurs as aggregates less than 0.2 mm wide that form thin foliation-parallel layers. Magnetite also often occurs within strain shadows next to and rimming chromite as well as filling spaces between existing minerals. Pentlandite comprises <0.5% of the rock, forms subhedral grains and is often associated with magnetite.

J918B:

Sample J918B is a very fine-grained porphyroclastic metasomatised spinel dunite containing olivine, chromite, magnetite, antigorite, serpentine and chlorite. The sample has a weak pervasive foliation primarily defined by the alignment of olivine grains. The sample is characterised by a very heavily-veined, serpentine-rich region (Figure 5.2E) and a relatively pristine, olivine-rich region. Serpentine veining is related to extensive fracture development across the sample, with serpentine fibres aligning within the veins (Figure 5.2F). The serpentine veins run relatively sub-

parallel to each other and sub-parallel to the foliation, and cross-cut both generations of olivine. The sample is also cross-cut by a later set of serpentine veins at a high angle to the foliation. There is also an original chromite layer preserved that is at a high angle to the X direction.

Porphyroclastic olivine comprises 48% of the sample and forms subhedral to anhedral, slightly elongate grains. Grains range from 0.2 – 0.5 mm in diameter, with an average of 0.4 mm. Some internal microstructure related to deformation is preserved but this is not widespread. Most of the olivine (including neoblasts) is quite heavily fractured and replaced by fine serpentine. Olivine neoblasts comprise 12% of the sample and form subhedral to euhedral, equant grains <0.03 mm in diameter.

Chromite comprises 8% of the sample and forms grains 0.2 – 1 mm in diameter, with an average of 0.5. Chromite grains are fractured in appearance and form a thin layer across the sample, as well as occurring sporadically within the rock matrix. Larger chromite grains are often rimmed by magnetite.

Antigorite comprises only 5% of the sample, and grains are euhedral and bladed. Grains are relatively random in orientation and do not contribute to the fabric of the sample. Antigorite cross-cuts both primary and secondary olivine. Serpentine (either chrysotile or lizardite) comprises 25% of the sample and fills an extensive network of veins running parallel to the X direction (Figure 5.2F). Fibres are aligned within the veins and show multiple episodes of mineral growth indicating multiple episodes of fluid influx.

Magnetite comprises 1 % of the rock and is associated with the serpentine veins. Grains are 0.01 – 0.03 mm in diameter, with an average of 0.03, and often occur as rims around the chromite but also as isolated grains within the rock matrix. Very fine sub-micron sized magnetite grains occur within serpentine veins.

Chlorite comprises 1% of the rock and forms grains ranging in size from 0.2 – 0.5 mm in diameter (average of 0.4 mm). Chlorite exhibits birds eye maple extinction

characteristic of a mica. Grains are often bent and commonly occur as large strain shadows around porphyroclastic chromite grains. Chlorite overprints the fine serpentine, so is a late-forming phase.

J919B_1:

J919B_1 is a very fine-grained porphyroclastic metasomatised spinel dunite containing olivine, chromite, antigorite, serpentine, magnetite and pentlandite (Figure 5.2G). The dunite has a weak pervasive foliation and lineation. The foliation is defined primarily by chromite layers and elongation and alignment of deformed olivine, as well as alignment of acicular grains of antigorite although this is not significant. The mineral lineation is defined by alignment of the long axes of elongate chromite and olivine grains. The olivine in the sample is predominantly neoblastic. There are abundant veins of aphanitic serpentine that are generally oriented parallel to the foliation, but these are later structures as they also cross-cut the fabric and dissect sparse coarse antigorite grains. Large acicular antigorite tends to cross-cut olivine grains whilst the fine veil-fill serpentine tends to passively replace olivine along grain boundaries.

Porphyroclastic olivine forms anhedral and often lenticular grains that comprise 7% of the sample. Grains range in size from 0.4 – 0.8 mm, with an average diameter of 0.5 mm. Some olivine grains preserve internal microstructure related to deformation, and often contain abundant sub-micron sized fluid and mineral inclusions. Grain boundaries with neoblastic olivine are generally embayed, convex towards the neoblast. Olivine neoblasts comprise 58% of the sample and form anhedral to subhedral, slightly elongate to equant grains. Grains range in size from 0.06 – 0.1 mm, with an average of 0.09 mm. Neoblastic olivine grains are generally pristine with no internal microstructure.

Chromite forms subhedral to anhedral, rounded grains 0.05 – 1 mm in diameter (average 0.3 mm). Chromite comprises 5% of the rock and forms foliation parallel layers and appears to be overgrown by magnetite and pentlandite. Some grains are pitted in appearance and are cross-cut by fine veins of serpentine.

Antigorite comprises 5% of the rock and occurs as bladed to acicular, euhedral grains. Grains range in size from 0.1 – 0.3 mm, with an average of 0.25 mm. Antigorite cross-cuts olivine neoblasts and mainly occurs within the neoblastic olivine matrix. Finer and less abundant than that seen in other samples and does not contribute substantially to the fabric. Serpentine comprises 20% of the sample, and is aphanitic in grain size. Serpentine replaces olivine along grain boundaries and is generally found within veins cross-cutting foliation and coarse antigorite.

Magnetite comprises 3% of the sample and forms subhedral, equant grains 0.03 – 0.1 mm in diameter, with an average of 0.08 mm. Magnetite is generally associated with chromite and pentlandite. Pentlandite comprises 2% of the sample, forms subhedral to anhedral grains and appears to fill small spaces between other minerals. Pentlandite grains range in size from 0.01 – 0.05 mm, with an average grain size of 0.04 mm.

J919B_2:

Sample J919B_2 is a fine-grained, porphyroclastic spinel dunite containing olivine, chromite, antigorite, serpentine, magnetite and pentlandite (Figure 5.2H). Overall the sample is quite clean and massive in appearance. There are a few cross-cutting veins containing serpentine but these are not pervasive. Olivine is dominant in this sample and there is no real fabric apart from the presence of chromite layers related to crystal settling. Chromite grains often have tails and are boudinaged, indicating some shearing taking place but this is not evident in the olivine.

Porphyroclastic olivine comprises 10% of the rock and forms anhedral, equant grains. Grains are 0.5 – 1 mm in diameter, with an average of 0.8 mm. There is very little internal microstructure preserved inside the grains which are often dusty and contain abundant fluid inclusions. It is replaced in places by antigorite, as is neoblastic olivine. Neoblastic olivine comprises 72% of the sample. It is clean in appearance, and does not preserve any internal microstructures. Grains are subhedral and equant, with grain boundaries often terminating in triple junctions.

Chromite comprises 8.5% of the sample and forms subhedral, tabular to equant grains. Chromite grains are 0.25 – 1 mm in diameter, with an average of 0.7 mm. There are often tails emanating from the chromite grains composed of magnetite and trace amounts of pentlandite. Magnetite comprises 1% of the rock and forms anhedral, equant grains 0.05 – 0.2 mm in diameter (average 0.1 mm). Pentlandite comprises less than 0.5% of the sample and forms anhedral, equant grains 0.05 – 0.2 mm in diameter with an average size of 0.08 mm.

Antigorite is not in high abundance in this sample, comprising only 5% of the rock. Where it does occur grains are randomly oriented and do not contribute to the fabric. Antigorite forms euhedral blades 0.3 – 0.5 mm long (average 0.4 mm) that cross-cuts primary olivine. Serpentine comprises 3% of the sample and is mainly localised to thin veins cross-cutting the sample, and appears to be the latest mineral to form.

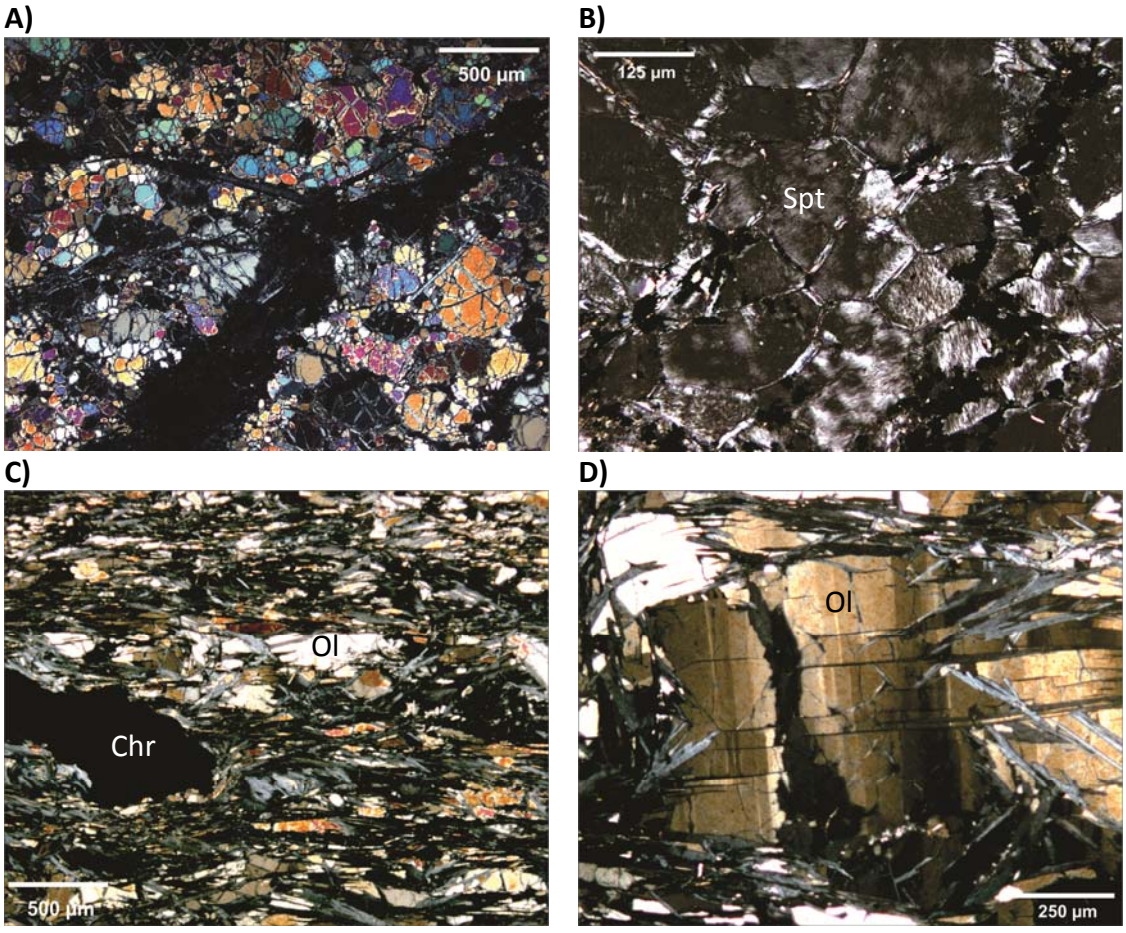

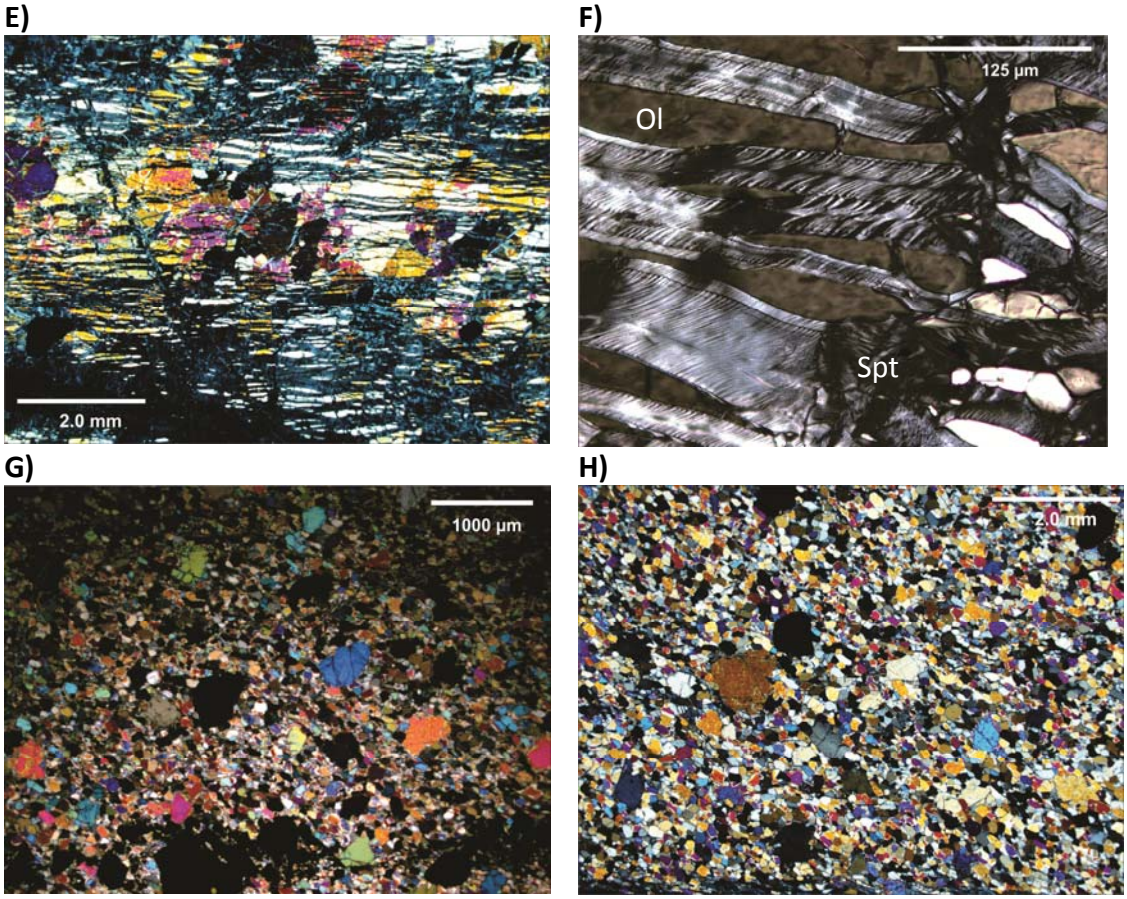

Figure 5.2. Photomicrographs of Higashi-Akaishi samples taken under XPL using a polarised light microscope. A) Overview showing overall texture of J915C. The multi-coloured grains are olivine and grey blades are antigorite. The section is cross-cut by a meandering fracture filled with very fine antigorite. B) Fine antigorite replacing olivine grains in sample J915C. The original grain boundaries are still observable. C) General overview of sample J917 showing foliation defined by grey blades of antigorite and lenticular olivine. The large black grain is a chromite porphyroclast. D) Olivine porphyroclast in sample J917 with relict internal microstructure as shown by the undulose extinction of the grain. E) Overview of the heavily-veined section of sample J918B where olivine grains (multi-coloured grains) are cross-cut by an extensive network of sub-parallel serpentine-filled fractures. F) Syntaxial antigorite fibres filling hydraulic fractures in sample J918B. Multiple generations of fibre growth suggest multiple episodes of fluid influx into the peridotite. G) Overview of the porphyroclastic and massive texture of olivine in sample J919B_1. H) Overall texture of sample J919B_2.

5.1.2. Sample suite petrogenesis and interpretation

The petrogenetic histories of the Imono and Higashi-Akaishi samples are extremely similar, so will be discussed together. The initial crystallisation sequence involved coarse-grained olivine and chromite. Aligned olivine porphyroclasts with an SPO that preserve internal microstructure suggest that the rocks were deformed by dislocation creep under mantle conditions. The overprinting of olivine and chromite by aligned antigorite forming a pervasive foliation indicates that the tectonic setting then transitioned to a hydrous environment. During this metamorphism, dislocation-creep dominated deformation was occurring resulting in dynamic recrystallisation of the olivine most likely by both grain boundary migration (GBM) and subgrain rotation (SR) resulting in the porphyroclastic texture of the sample.

Subsequently, veins cross-cut the samples and were filled with syntaxial antigorite fibres suggesting hydraulic fracturing of the peridotite. Multiple generations of fibre growth, similar to fibre growth during crack-seal processes described by Cox and Etheridge (1983), suggests multiple episodes of fluid influx (this is more evident in the Higashi-Akaishi samples). The nature of the fracturing and veining could be due to a systematic and progressive influx of hydrous fluid from the dehydrating slab and into the mantle wedge above.

Associated with the neoblastic chromite is a very bright mineral under reflected light that occurs in trace amounts, likely pentlandite (often shows iron staining under PPL). Pentlandite grains tend to cross-cut all mineral grains and infill cracks and gaps within the rock, and so is probably the most recent mineral to form.

The porphyroclastic microstructure of olivine and abundance of antigorite in most of the samples suggests that the microstructure reflects the deformation event D_{2B} (based on the classification of Mizukami and Wallis 2005; also refer to Fig. 3.8). In samples J904A and J909C, the S_{2B} foliation is also overprinted by a weak S_3 crenulation.

5.2. Lihir Island, Papua New Guinea

5.2.1. Sample descriptions

The following is a summary of the observations of petrographic thin sections collected from the Tubaf Seamount near Lihir Island, Papua New Guinea. Observations were made under a polarised light microscope using plane-polarised light (PPL), cross-polarised light (XPL) and reflected light. Detailed petrographic descriptions and photomicrographs of these samples have been provided in Appendix 2. Previous studies on these samples were also undertaken by Franz and Wirth (2000), Gregoire *et al.* (2001) and McInnes *et al.* (2001).

Petrographic thin sections of 9 xenolith samples (Table 5.2) were examined. Unlike the Higashi-Akaishi and Imono Peridotites, these samples are xenoliths and lack macroscopic foliations/lineations. As such, the orientation of the thin sections is

arbitrary and the samples cannot be examined within the context of a kinematic reference frame. Hand samples were not available for examination.

Table 5.2. Lihir xenolith samples analysed in this study.

Sample	Rock type
136062	Coarse-grained spinel lherzolite
136063	Coarse-grained spinel lherzolite
136065	Coarse-grained spinel harzburgite
136067	Coarse-grained spinel dunite
136068	Medium-grained spinel lherzolite
136069	Coarse-grained spinel dunite
136070	Coarse-grained spinel lherzolite
136074	Coarse-grained spinel lherzolite
136090	Coarse-grained metasomatised spinel dunite

136062:

Sample 136062 is a massive, coarse-grained (~2 mm) spinel lherzolite composed of olivine, enstatite, clinopyroxene and spinel (Figure 5.3A). The lherzolite has no obvious veins, large fractures or macroscopic foliation or lineation. The lherzolite is relatively pristine, with no replacement of the primary igneous minerals.

Olivine forms anhedral, equant grains that comprise 73% of the sample. Grains range in size from 0.4 – 3.4 mm, with an average diameter of 2.1 mm. Olivine is visibly deformed and shows widespread preservation of low-angle boundaries. Transgranular and intragranular cracks are often both parallel and perpendicular to low-angle boundaries, leading to a perpendicular fracture pattern. Many intragranular microcracks within the olivine are partially annealed, forming a network of fine (<1 μm in diameter) and coarse fluid inclusions (5 – 10 μm in diameter) that give the olivine a dusty appearance. Olivine-olivine boundaries often terminate at triple junctions but are generally curved and regular (infrequently these are also embayed). Olivine-enstatite and olivine-clinopyroxene boundaries are curved and regular, and olivine-spinel boundaries are curved and irregular, with spinel cross-cutting the olivine. Olivine also contains aligned inclusions of fine euhedral spinel (<1 μm) in diameter.

Clinopyroxene comprises 15% of the rock and occurs as subhedral to anhedral, prismatic grains that range in size from 1.2 – 4.2 mm, with an average of 2.1 mm. Clinopyroxene has a prominent cleavage and often shows undulose extinction suggesting deformation. Often contains inclusions of primary olivine. Clinopyroxene-clinopyroxene boundaries are curved and regular, as are those with olivine. Clinopyroxene-enstatite boundaries are curved and irregular.

Enstatite comprises 5% of the sample and forms subhedral, to anhedral and prismatic grains that range from 1.2 – 4.2 mm in diameter, with an average grain size of 2.1 mm. Enstatite has a weak cleavage and contains extensive clinopyroxene exsolution lamellae as well as fine fluid inclusions that appear to be controlled by the orientation of the lamellae. Enstatite-enstatite boundaries are not observed. Enstatite-spinel boundaries are curved and irregular, with spinel overprinting the enstatite.

Spinel comprises 7% of the lherzolite, and ranges in grain size from 0.01 – 0.85 mm, with an average grain size of 0.68 mm. Larger spinel grains form subhedral to anhedral, equant grains. Spinel-spinel boundaries are not observed. Often spinel contains inclusions of clinopyroxene. Sub-micron sized, euhedral and prismatic spinel grains also occur aligned inclusions in primary olivine.

136063:

Sample 136063 is a coarse-grained (~1.5 mm) spinel lherzolite, and consists of olivine, enstatite, clinopyroxene, spinel and trace amounts of pyrrhotite (Figure 5.3C). The rock has undergone a degree of metasomatism and primary mantle minerals are replaced by fibrous orthopyroxene (5% of the sample) within thin veins that cross-cut the section.

Olivine comprises 66% of the sample, and ranges in grain size from 0.25 – 3.0 mm, with an average grain size of 1.3 mm. Olivine is anhedral and equant, with glassy, irregular fracture pattern. Most grains preserve low-angle boundaries (Figure 5.3D) evident through parallel bands of undulose extinction. Fractures and microcracks are commonly oriented parallel to the low-angle boundaries (Figure 5.3D) and these are associated with abundant fluid inclusions. Both coarse (~10 μm) and fine (<1 μm) fluid inclusions are preserved within the olivine grains. Olivine-olivine boundaries

tend to be curved and irregular, but are occasionally straight. Olivine-enstatite boundaries are curved and irregular. Olivine-clinopyroxene boundaries are curved and irregular, and olivine-spinel boundaries are straight and regular. Olivine is cross-cut and overgrown by spinel.

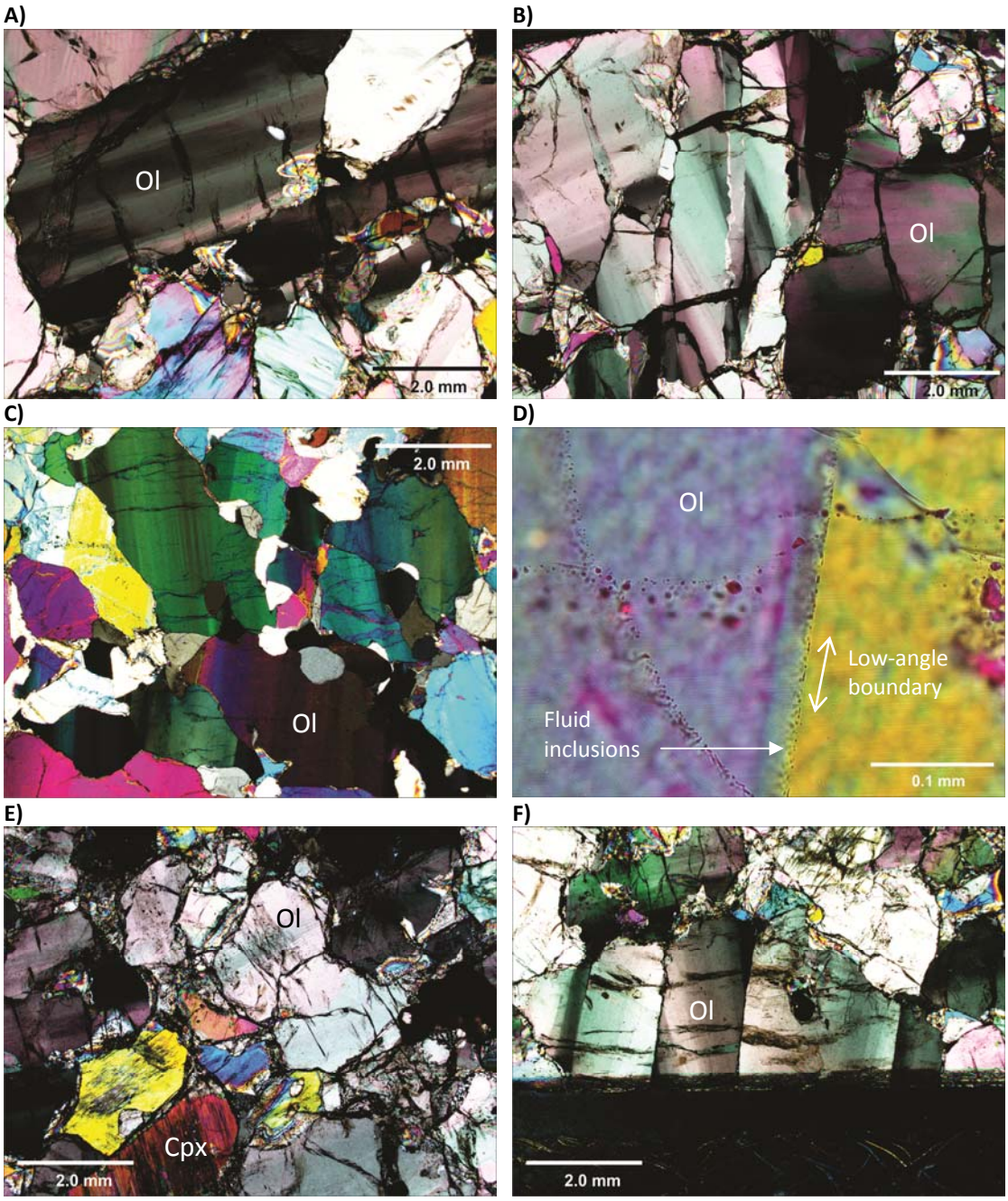

Figure 5.3. A) Overall texture of 136062 under XPL. Low-angle boundaries in olivine are prominent, as are partially annealed intragranular fractures. B) XPL image showing the complexity of low-angle boundaries preserved in the olivine grains in sample 136062. There are 2 orientations of low-angle boundaries in the centre grain ~15 - 20° apart. There is also subgrain rotation occurring around the vertical set of low-angle boundaries. C) Texture of 136063 under XPL. Olivine shows prominent low-angle boundaries but also irregular, curved grain boundaries. D) Fluid inclusion trails parallel to low-angle boundaries in olivine in 136063 (XPL). E) Dusty olivine and clinopyroxene in 136065 (XPL). F) Two generations of low-angle boundaries in olivine in 136065 (XPL).

Enstatite comprises 17% of the rock, and ranges in grain size from 0.5 – 3.0 mm, with an average grain size of 1.7 mm. Enstatite forms anhedral, slightly elongate grains with distinctive irregularly-shaped sub-parallel bands of undulose extinction. There are also well-formed exsolution lamellae that appear to have been deformed. Fluid inclusions are abundant. There is a well-developed cleavage in grains adjacent to major fractures and alteration zones. Enstatite is altered to fibrous orthopyroxene, and this is partially controlled by the orientation of both clinopyroxene lamellae and cleavage. Enstatite-enstatite boundaries are curved and regular. Enstatite-clinopyroxene boundaries are straight to curved and regular. Enstatite is overgrown by spinel, with straight, regular boundaries.

Fibrous orthopyroxene comprises 5% of the sample, forming subhedral to euhedral, elongate fibres less than 0.025 mm in length. Fibrous orthopyroxene replaces primary mantle olivine, clinopyroxene and enstatite, and cross-cuts all minerals. All grain boundaries are generally straight and regular.

Clinopyroxene forms anhedral, equant grains that comprise 5% of the rock. Grains range in size from 0.5 – 3.0 mm, with an average grain size of 1.7 mm. Often exhibits undulose extinction and is strongly fractured. Clinopyroxene-clinopyroxene boundaries are not observed, but clinopyroxene-spinel boundaries are curved and irregular.

Spinel comprises 3% of the rock, forming grains ranging in size from 0.1 – 1.0 mm (average of 2.0 mm). Spinel grains are subhedral to euhedral and prismatic, and are resistant to alteration. Spinel often contains inclusions of primary orthopyroxene and olivine. Spinel-spinel boundaries are not observed.

Pyrrhotite comprises 1% of the rock, and forms grains 0.1 – 1.0 mm in size (average 0.1 mm). Pyrrhotite is often associated with metasomatically altered regions in the thin section and is Fe-stained. Grain boundaries tend to be defined by the surrounding minerals.

136065

Sample 136063 is a relatively pristine coarse-grained spinel harzburgite containing olivine, enstatite, clinopyroxene and spinel, with no apparent structural fabric (Figure 5.3E).

Olivine comprises 84% of the sample and form anhedral, equant grains 0.1 – 2.0 mm in diameter (average 2.0 mm). The olivine grains in this sample have a glassy fracture/microcrack pattern that is commonly associated with low-angle boundaries preserved within the grains (Figure 5.3F). Associated with the fractures and microcracks are abundant fluid inclusions giving the olivine grains a dusty appearance under the microscope. Olivine is deformed with prominent low-angle boundaries evident through intragrain variations in extinction angle. The long axes of vermicular inclusions or trails of bubbles tend to form parallel to low-angle boundaries. Olivine contains inclusions of aligned, very fine-grained secondary spinel. Olivine-olivine boundaries are curved to straight and irregular (Figure 5.3F). Grain boundaries with all other minerals are curved and regular.

Enstatite comprises 8% of the sample, forming anhedral, slightly elongate grains that range in size from 0.1 – 1.2 mm (average 1.0 mm). Enstatite grains display undulose extinction across the grains and contain extensive deformed exsolution lamellae of clinopyroxene. Enstatite also generally has a weak cleavage. All grain boundaries are curved to straight and regular.

Clinopyroxene comprises 2% of the sample and forms anhedral, elongate grains 0.1 – 1.2 mm in diameter (average 1.0 mm). Clinopyroxene has a well-formed cleavage, and contains inclusions of primary olivine. Grain boundaries tend to be straight and regular.

Spinel comprises 2.5% of the sample forming subhedral to anhedral, equant grains that cross cut olivine, enstatite and clinopyroxene and are resistant to weathering. Spinel grains range in diameter from 0.01 – 0.9 mm, with an average grain size of 0.5 mm.

136067

Sample 136067 is a coarse-grained (~2 mm) spinel dunite containing olivine, and spinel. The sample is bimodal, with two populations of olivine. Olivine is extensively overgrown by small spinel grains, which often delineate olivine grain boundaries and give the thin section a spotted appearance. There is no obvious foliation, lineation or shape-preferred orientation.

Olivine comprises 89% of the sample, forming anhedral, equant grains 0.1 – 5.0 mm in diameter, with an average grain size of 2.0 mm. Grains are highly fractured and contain abundant sub-micron sized fluid and mineral inclusions. Olivine is deformed, with prominent low-angle boundaries evident through parallel bands of undulose extinction. Olivine-olivine boundaries are straight to curved, often terminating at triple junctions. Olivine is overgrown by spinel and these grain boundaries are generally curved and regular.

Spinel comprises 11% of the sample, forming larger equant, subhedral grains with an average grain size of 0.25 mm, and finer subhedral to euhedral and prismatic grains <0.01 mm in diameter. In the part of the sample dominated by finer olivine, coarse spinel is more scattered and located as inclusions within olivine and at olivine grain boundaries. In the part of the sample where coarser olivine dominates, spinel appears to be restricted to the olivine grain boundaries. Finer spinel grains occur as aligned inclusions in primary olivine.

136068:

136068 is a medium-grained (~0.75 mm) spinel lherzolite that consists of olivine, enstatite, orthopyroxene, clinopyroxene and spinel (Figure 5.4A). The sample is massive and contains some veins that cross-cut the thin section. There is no obvious foliation, lineation or shape-preferred orientation. Alteration of primary minerals to fibrous orthopyroxene occurs throughout the sample (Figure 5.4B), and is linked to the presence of fluid inclusions in olivine and pyroxenes.

Olivine comprises 81% of the sample, forming anhedral, equant grains 0.1 – 2.0 mm in diameter, with an average grain size of 0.5 mm. Olivine exhibits bands of parallel undulose extinction representing low-angle boundaries due to deformation. Highly

fractured grains are replaced by fibrous orthopyroxene within fractures. There are abundant sub-micron sized fluid inclusions present in the olivine. Olivine-olivine boundaries are curved and irregular. Grain boundaries with enstatite, spinel and clinopyroxene are curved and regular.

Enstatite comprises 6% of the sample, ranging in grain size from 0.5 – 3.0 mm, with an average grain size of 1.0 mm. Grains are anhedral and slightly elongate. There are sub-parallel bands of undulose extinction indicating deformation. Enstatite grains contain exsolution lamellae and a prominent cleavage. Abundant fluid inclusions form trails that run parallel to the cleavage. All grain boundaries tend to be straight and regular.

Fibrous orthopyroxene comprises 4% of the sample and forms subhedral to euhedral, acicular grains that cross-cut the other minerals (except spinel). Clinopyroxene comprises 4% of the sample, and forms grains 0.5 – 3.0 mm in diameter, with an average grain size of 1.0 mm. Clinopyroxene grains show undulose extinction, and have 2 weak cleavage planes. Clinopyroxene is also strongly fractured and is replaced in and near fractures by fibrous orthopyroxene.

Spinel comprises 4.5% of the sample and forms subhedral to euhedral, prismatic grains. Spinel grains range in size from 0.01 – 1.0 mm in diameter, with an average grain size of 0.5 mm.

136069:

Sample 136069 is a coarse-grained (~1.5 mm) spinel dunite containing olivine, enstatite, orthopyroxene, clinopyroxene and spinel (Figure 5.4C). The sample is massive with no obvious foliation, lineation or shape-preferred orientation. Olivine and enstatite are altered to fibrous orthopyroxene (Figure 5.4D). This alteration is controlled by two ~0.5 mm thick parallel fractures cutting across the thin section, and on a grain-scale is often controlled by low-angle boundaries in olivine.

Olivine comprises 85% of the sample, and forms anhedral, equant grains 0.1 – 2.0 mm in diameter (average 1.5 mm). Olivine is deformed, with prominent low-angle

boundaries highlighted by parallel undulose extinction under XPL. Olivine grains are highly fractured and altered to fibrous orthopyroxene along fractures and grain boundaries. Fluid inclusions are common close to fractures, and these are often parallel to low-angle boundaries. Olivine also contains very fine aligned spinel inclusions. Olivine-olivine boundaries are embayed to curved and irregular, but can be straight and parallel to low-angle boundaries on occasions. Grain boundaries that terminate in triple junctions are not uncommon. Olivine-enstatite boundaries are curved and regular, and olivine-clinopyroxene and olivine-spinel boundaries are straight and regular.

Enstatite comprises 3% of the sample, and forms subhedral to anhedral, slightly elongate to equant grains. Enstatite grains range in size from 0.5 – 2.0 mm, with an average grain size of 1.2 mm. There is a prominent widely spaced cleavage at ~90° and abundant exsolution lamellae controlling the orientation of open and annealed fractures. Enstatite grains are also deformed and show undulose, parallel extinction. Exsolution lamellae commonly show evidence for deformation. Orthopyroxene forms fibrous aggregates replacing primary mantle minerals, and comprises 6% of the sample. Clinopyroxene is rare and usually unaltered, comprising 1% of the sample. Clinopyroxene grains are subhedral to anhedral, equant and have a widely spaced cleavage.

Spinel is generally resistant to alteration, and is strongly fractured where it occurs near main alteration zones. Spinel forms subhedral to anhedral, prismatic grains that comprise 5% of the sample. Often these are included in primary olivine as very fine <0.1 mm inclusions.

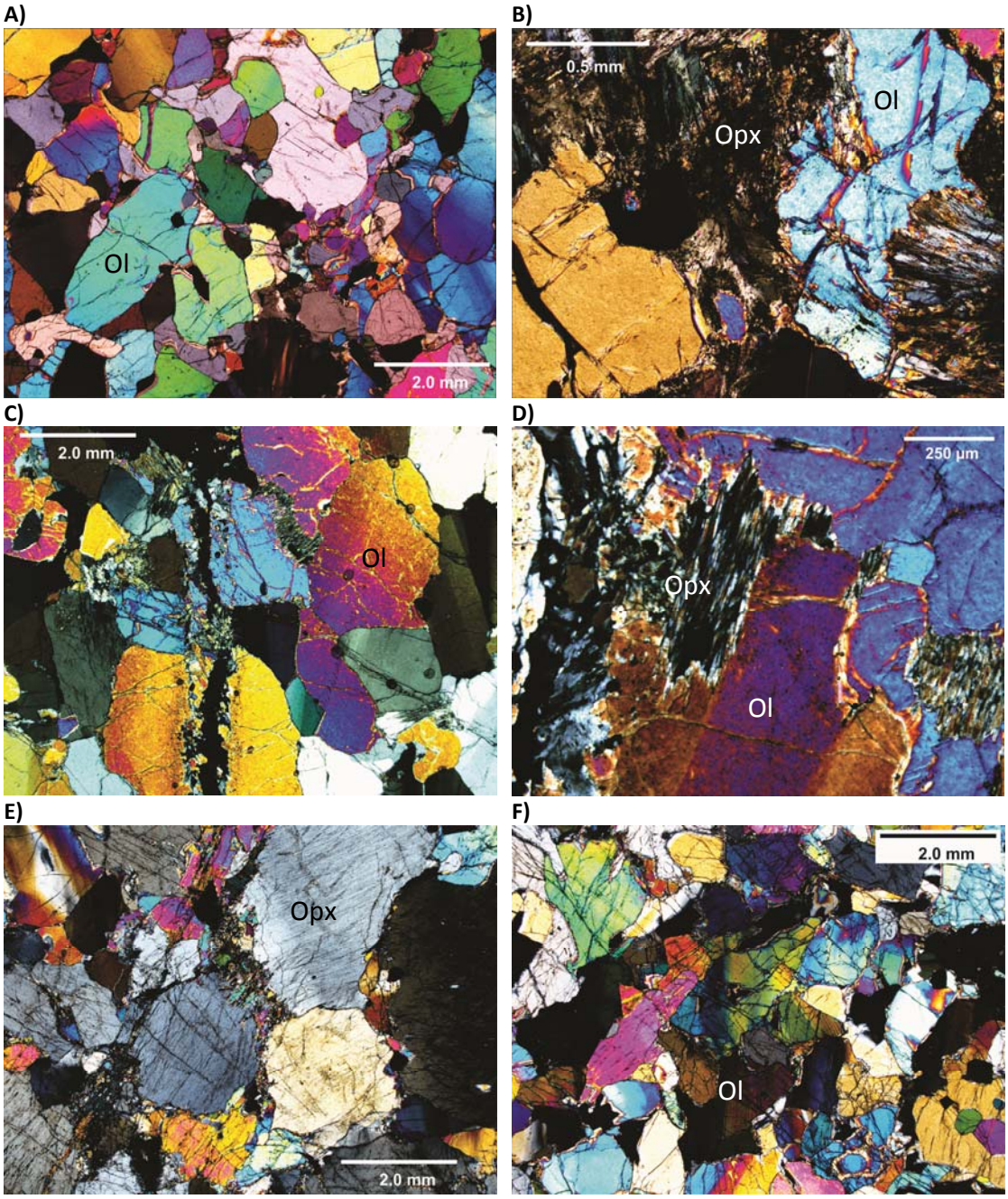

Figure 5.4. A) Overall texture of sample 136068 (XPL). B) Fibrous orthopyroxene replacing primary olivine in 136068 (XPL). C) Veins cross-cutting olivine in 136069. D) Replacement of olivine by fibrous orthopyroxene in 136069 (XPL). E) Pyroxene-rich region of sample 136070 (XPL). F) Olivine-rich region of 136070 (XPL).

136070:

Sample 136070 is a massive, coarse-grained (~1.5 mm) spinel lherzolite (Figures 5.4E, F) comprised of olivine, enstatite, spinel and fibrous orthopyroxene (1% of the sample). The sample has a layered cumulate texture, with parallel bands rich in pyroxene alternating with bands rich in olivine. Alteration of primary mantle minerals to fibrous orthopyroxene predominantly occurs around grain boundaries but

also within fractures. There is no apparent structural fabric in this sample when observed under a polarised light microscope.

Olivine comprises 66% of the sample, and forms subhedral to anhedral, equant grains ranging in diameter from 0.4 – 2.1 mm (average is 1.0 mm). Olivine grains preserve low-angle boundaries related to deformation. Fluid inclusions are also commonly preserved, often running parallel to the low-angle boundary orientation. Olivine-olivine boundaries are irregular and curved, and olivine-enstatite boundaries are straight and regular.

Enstatite comprises 30% of the sample, forming subhedral, equant grains 1.0 – 4.2 mm grains (average 2.1 mm). Enstatite often contains deformed clinopyroxene exsolution lamellae and is replaced in places by fine-grained orthopyroxene. Fluid inclusions occur in enstatite, and are associated with major fractures running through the sample. Enstatite grains contain inclusions of primary olivine (Figure 5.4F, bottom right).

Orthopyroxene replaces primary olivine and enstatite along grain boundaries and fractures, and comprises 1% of the sample. Orthopyroxene grains are fibrous and acicular, and cross-cut all the other minerals. Spinel comprises 3% of the sample, forming subhedral to euhedral, equant grains 0.25 – 1.0 mm in diameter (average 0.5 mm).

136074:

Sample 136074 is a massive, coarse-grained spinel lherzolite containing olivine, enstatite, orthopyroxene, clinopyroxene and spinel (Figure 5.5A). The sample is massive with occasional thin fractures traversing the section. There is no obvious foliation or lineation. Alteration of primary mantle minerals to fibrous orthopyroxene is associated with prominent fracturing and fractures are often controlled by low-angle boundary orientations in olivine. Fibrous orthopyroxene occurs in 0.5 mm veins cross-cutting the section, replacing olivine and primary orthopyroxene.

Olivine comprises 80% of the sample, forming anhedral, equant grains 0.5 – 3.0 mm in diameter (average 1.0 mm). Olivine is often highly fractured and deformed as shown by the prominent low-angle boundaries (Figure 5.5B), and contains abundant fluid inclusions that are oriented parallel to low-angle boundaries. Olivine also contains very small inclusions of aligned spinel. Olivine-olivine boundaries are straight and regular, often terminating at triple junctions. Grain boundaries with enstatite, clinopyroxene and spinel are curved and irregular.

Enstatite forms anhedral, equant grains that comprise 10% of the rock. Enstatite grains range in size from 0.5 – 4.0 mm, with an average grain size of 1.0 mm. Enstatite is often highly fractured with two prominent cleavages at ~90°, and is extensively altered in places and contains extensive exsolution lamellae. All grain boundaries tend to be curved and irregular. Orthopyroxene forms aggregates of very fine grains replacing primary mantle minerals (excluding spinel) and comprising 4% of the rock.

Clinopyroxene forms 4% of the rock, and grains range in size from 1.0 – 4.0 mm (average of 1.5 mm). Similar to the enstatite, clinopyroxene grains are highly fractured, grains with two prominent cleavages at ~90°. Highly altered in places to fibrous orthopyroxene and contain extensive exsolution lamellae.

Spinel forms subhedral to euhedral, prismatic grains that comprise 2% of the rock. Spinel grains range in size from 0.1 – 0.5 mm (average 0.35 mm) and clearly overgrow olivine and orthopyroxene.

136090:

Sample 136090 is a coarse-grained (~1.5 mm) metasomatised spinel dunite comprised of olivine, enstatite, clinopyroxene and spinel, with secondary metasomatic orthopyroxene (comprising ~10% of the sample) and trace amounts of pyrrhotite (Figures 5.5C, D). There is no obvious foliation, lineation or shape preferred orientation.

Olivine comprises 30% of the rock, and forms anhedral, equant grains that range in size from 0.5 – 2.0 mm (average 1.5 mm). Olivine grains are often deformed, exhibiting prominent low-angle boundaries. Abundant fluid inclusions are often oriented parallel to the low-angle boundaries, as are fractures. In general, olivine is extremely altered to fibrous orthopyroxene. Grain boundaries are curved and irregular.

Enstatite comprises 5% of the rock, forming anhedral, slightly elongate grains 0.5 – 1.0 mm in diameter (average 0.7 mm). Enstatite grains contain well-developed exsolution lamellae and two prominent cleavages at ~90°. Extensive fracturing in the olivine is controlled by the orientation of the exsolution lamellae. Grain boundaries are curved/scalloped and irregular. Fibrous orthopyroxene forms subhedral grains replacing primary mantle olivine, clinopyroxene and orthopyroxene, and comprises 10% of the sample. Orthopyroxene grains are generally less than 0.1 mm in length. Clinopyroxene forms anhedral, slightly elongate grains that comprise 3% of the rock. The clinopyroxene grains range in size from 0.1 – 0.5 mm (average 0.3 mm) and contain abundant fluid inclusions. Grain boundaries are curved and irregular. Spinel comprises 1.5% of the rock and forms dark red/brown subhedral to euhedral short prismatic grains <0.1 – 1 mm in size (average 0.3 mm in diameter). Spinel is generally resistant to alteration and overgrows primary olivine and pyroxene. Pyrrhotite occurs in trace amounts as individual grains 0.01 – 0.25 mm in diameter (average 0.1 mm). Grain boundaries are straight to curved and regular.

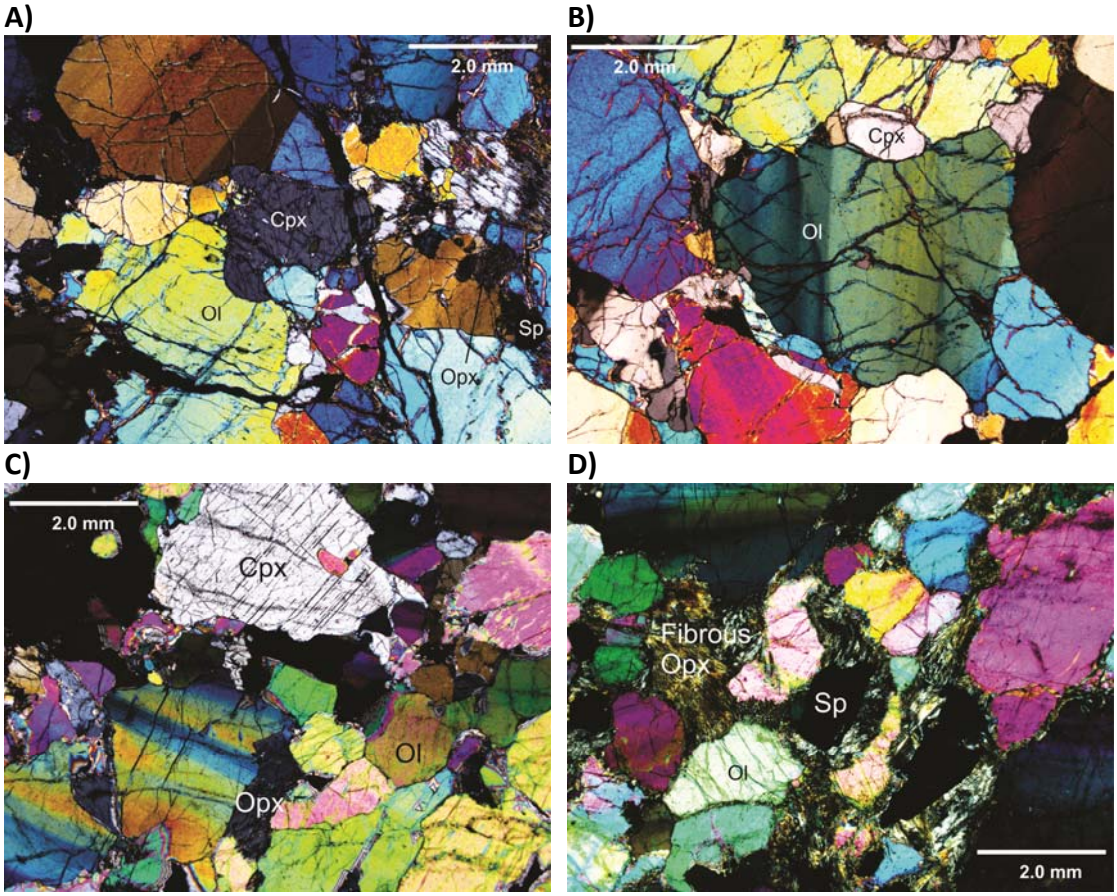

Figure 5.5. A) Overall texture of 136074 (XPL). B) Low-angle boundaries in olivine in sample 136074 (XPL). C) Texture of 136090 (XPL). D) Fibrous orthopyroxene replacing primary olivine in 136090 (XPL).

5.2.2 Sample suite petrogenesis and interpretation

Cross-cutting relationships between minerals indicate that the initial crystallisation sequence involved olivine and both clino- and orthopyroxenes followed by primary spinel. The presence of primary spinel in these samples indicates equilibration in the stability field of spinel peridotite. Exsolution lamellae in pyroxenes and the development of exsolved spinel grains in olivine (there is evidence for this event in all samples except 136068) suggest a subsequent pre-deformation cooling event. The exsolved spinel grains in the olivine are also observed in mantle olivines by Franz and Wirth (2000) and McInnes *et al.* (2001), and are interpreted to have formed in a cooling environment at a mid-ocean ridge (Franz and Wirth 2000).

After the cooling event, internal microstructures (including low-angle boundaries) preserved in olivine grains indicate that the samples were deformed in a dislocation creep-dominated upper mantle flow regime. Samples 136068 and 136069 show

evidence for an early period of fluid interaction, involving the development of dilational hydraulic fractures associated with mechanical breakdown of the surrounding peridotite. This was accompanied by extensive crystallisation of spinel indicating this event occurred within spinel peridotite facies conditions. All samples have undergone mantle metasomatism resulting in replacement of primary mantle minerals with orthopyroxene, equated by McInnes *et al.* (2001) with metasomatism due to the influx of H_2O-rich, alkalic, oxidising slab-derived fluids. Annealed microcracks/fractures that developed at the same time as the metasomatism indicate that ductile deformation and brittle failure due to fluid influx was synchronous, and occurred in the upper mantle. The presence of microcracks suggests that the samples were exhumed not long after the metasomatism occurred. The samples were exhumed in a silica-poor, vesicular, porphyritic hornblende-augite ± phlogopite basalt with zonation of both hornblende and augite indicating multiple stages of cooling.

5.3. References

Cox, S.F., and Etheridge, M.A. (1983) Crack-seal fibre growth mechanisms and their significance in the development of oriented layer silicate microstructures, *Tectonophysics*, v. 92, p. 147-170.

Franz, L. and Wirth, R. (2000) Spinel inclusions in olivine of peridotite xenoliths from TUBAF seamount (Bismarck Archipelago/Papua New Guinea): evidence for the thermal and tectonic evolution of the oceanic lithosphere, *Contributions to Mineralogy and Petrology*, v. 140, p. 283-295.

Gregoire, M., McInnes, B.I.A. and O'Reilly, S.Y. (2001) Hydrous metasomatism of oceanic sub-arc mantle, Lihir, Papua New Guinea: Part 2. Trace element characteristics of slab-derived fluids, *Lithos*, v. 59, p. 91-108.

McInnes, B.I.A., Gregoire, M., Binns, R.A., Herzig, P.M., and Hannington, M.D. (2001) Hydrous metasomatism of oceanic sub-arc mantle, Lihir, Papua New Guinea: petrology and geochemistry of fluid-metasomatised mantle wedge xenoliths, *Earth and Planetary Science Letters*, v. 188, p. 169-183.

Mizukami, T. and Wallis, S.R. (2005) Structural and petrological constraints on the tectonic evolution of the garnet-lherzolite facies Higashi-akaishi peridotite body, Sanbagawa belt, SW Japan, *Tectonics*, v. 24, p. 1-17

Chapter 6. The relationship between bulk fabrics and low-angle boundaries in olivine: Microstructural evidence for [a] slip in supra-subduction zone mantle

The contents of this chapter are based on a paper currently under review at the journal Terra Nova: Gray, E., Reddy, S., Healy, D. and McInnes, B. (2013) The relationship between bulk fabrics and low-angle boundaries in olivine: Microstructural evidence for [a] slip in supra-subduction zone mantle. In Review.

6.1. Introduction

Trench-parallel seismic fast axes observed above the mantle wedge of many subduction systems are inferred to reflect the alignment of olivine [100] axes in the mantle (Russo and Silver, 1994; Peyton *et al.*,2001; Lassak *et al.*,2006). Many models link the [100] direction to mantle flow directions (Russo and Silver, 1994; Buttles and Olson, 1998; Billen and Gurnis, 2001; Behn *et al.*,2007; Kneller and van Keken, 2007; Long and Silver, 2008). However, the relationship between LPO and mantle flow is more complicated because experimental studies display a range of olivine LPO types linked to the operation of different slip systems at different mantle conditions (Jung and Karato, 2001; Jung *et al.*,2006). Under normal upper mantle conditions, [100] aligns parallel to the flow direction (Russo and Silver, 1994; Peyton *et al.*,2001; Lassak *et al.*,2006). However, under high stress and hydrous mantle wedge conditions, [100] directions align perpendicular to mantle flow (B- and C-type fabrics), potentially explaining observations of trench-parallel seismic fast axes during corner-flow mantle convection.

Discriminating between these models is challenging because mantle xenoliths from forearc regions have poor foliations and lineations, hence the measured LPO is difficult to link to the principal finite strain directions associated with mantle flow. In this paper we present detailed analyses of the deformation microstructures and LPOs preserved in olivine from supra-subduction mantle peridotites from two areas (Figure 3.1) to establish a relationship between LPO and intragrain deformation

microstructures that overcomes the problems inherent in bulk fabric analysis of mantle xenoliths.

The samples represent fragments of forearc mantle wedge exhumed along the margins of the SW Pacific plate, where trench-parallel seismic fast axes are observed (Buttles and Olson, 1998; Nakajima and Hasegawa, 2004; Hammond *et al.*,2010). The Higashi-Akaishi Peridotite (HAP) (Japan) is one of a number of orogenically exhumed peridotite bodies exposed within the Cretaceous Sanbagawa Belt (Mizukami *et al.*,2004). The oriented Higashi-Akaishi sample (J917) is a metasomatised porphyroclastic spinel dunite containing a well-defined foliation and mineral lineation on both a hand specimen and microscopic scale. Mantle xenoliths from the Tubaf seamount (Lihir, SW Pacific) (McInnes *et al.*,2001) are texturally massive spinel peridotites with no obvious foliation or lineation that were acquired during dredging of the Tubaf seamount near the Pacific island of Lihir by the *RV Sonne* cruise SO-94 (Gregoire *et al.*,2001; McInnes *et al.*,2001). The xenoliths are found within a Pleistocene basaltic host (McInnes *et al.*,1999) and originated within the mantle wedge at depths of 20 - 70 km (McInnes *et al.*,2001). The peridotites record varying amounts of replacement of primary olivine by fibrous orthopyroxene, reflecting localised high-temperature metasomatism resulting from the influx of H_2O-rich, alkalic, oxidising slab-derived fluids (McInnes *et al.*,2001).

6.2. Methodology

Olivine microstructure and LPO was analysed using electron backscatter diffraction (EBSD) (see suPPLementary information; Prior *et al.*,1999). Bulk fabrics were determined using crystal axis orientations of multiple grains from each sample. In the case of the HAP sample (J917), the bulk fabric data were collected within the framework of the foliation and lineation orientations of the finite strain ellipsoid of the deformation, corresponding to the XZ and X directions, respectively. For both the HAP and Tubaf samples, orientation mapping of numerous olivine grains was used to characterise the geometry of intragrain microstructures (low-angle boundaries). Orientation maps, crystal axis dispersion and misorientation analysis were used for

slip system analysis assuming a tilt-boundary model for low-angle boundary formation. Much of the procedure for using EBSD data to interpret microstructure is described in detail by Boyle *et al.*(1998), Prior *et al.*(2002), Bestmann and Prior (2003) and Reddy and Buchan (2005). Key concepts of dislocation geometry are discussed in Sutton & Balluffi (1995), Lloyd *et al.*(1997) and Barrie *et al.*(2008). For consistency between LPO and slip system nomenclature, slip systems were labelled based on the LPO type that would be produced through deformation by a particular slip system (e.g. deformation by (010)[100] would produce an A-type LPO, and is hence referred to as an A-type slip system). Grains that have bimodal misorientation axes are labelled in terms of both slip systems (e.g. A/E-type results from slip along [100] and dispersion around both [001] and [010]), with the dominant slip system being the one which statistically has the most misorientation axes within the grain. The dominant system is stated first, followed by the subordinate slip system.

6.3. Results

Assessment of the intragrain deformation within individual olivine grains can be undertaken utilizing the coincidence of dispersion of crystallographic poles (and/or misorientation axes) and the geometry of the trace of low-angle boundaries within the grain. The first stage of analysis involves the recognition of crystallographic axes about which other poles are rotated. For example, in grain 01 of J917 a dispersion of [100] and [001] is observed around [010]. Two end-member scenarios need to then be considered in order to address the non-unique inversion of intra-grain distortions. Firstly, if the dispersion axis lies in the plane perpendicular to the boundary trace, then the data are consistent with either a tilt or twist boundary. In the case where the dispersion axis is not perpendicular to the boundary trace then the data are consistent only with a tilt boundary interpretation. In the situation here (Figure 6.1), no grains contain dispersion axes that are perpendicular to the boundary trace, and hence the data support a tilt boundary origin for the low-angle boundaries. In this case, the plane containing the dispersion axis and the low-angle boundary trace represent the orientation of the low-angle boundary and, for a tilt-boundary model, the pole to this

plane is the slip direction. The direction orthogonal to both the dispersion axis and the slip direction corresponds to the slip plane. Hence the slip system (plane and direction) associated with individual low-angle boundaries can be calculated. This approach has been automated in the weighted mean burgers vector approach (Wheeler *et al.*2009) which would be useful for future analyses of this kind.

Examination of the bulk pole figures of J917 (Figure 6.1) reveals alignment of [100] axes parallel to the lineation, and [010] axes with the pole to foliation - an A-type LPO according to the classification of Jung *et al.* (2006). Using the above approach, the EBSD analysis of deformed olivine porphyroclasts within HAP spinel dunite J917 reveals intragrain microstructures preserving evidence of deformation by (001)[100] (E-type) (Figure 6.1; grains 01, 08). Hence, in both cases, the slip direction associated with the low-angle boundaries is [100], and is identical to that inferred by the bulk fabric data. Hildyard *et al.* (2009) used a similar technique to analyse anhydrite (orthorhombic crystal symmetry, as with olivine) and also observe a consistency between intragrain slip system and bulk LPO. The interpretation of [100] slip at both the intragrain and bulk fabric scale in the HAP sample thus points to a systematic relationship between slip directions associated with dislocation creep and low-angle boundary formation in olivine, and the kinematic flow direction inferred from bulk fabric analysis.

The relationship outlined above has been investigated further by aPPLying the above methodology to a Tubaf xenolith sample (136063). In this case, all of the olivine grains within a single thin section (97 grains) were analysed. The bulk LPO pole figures show strongly clustered [100] axes and [010], [001] and [011] axes that are more dispersed and lie on a single girdle (Figure 6.2A). Low-angle misorientation axes associated with the bulk fabric show that the misorientation axes are perpendicular to [100], with a preferred orientation of [010] parallel to the misorientation axes (Figure 6.2A).

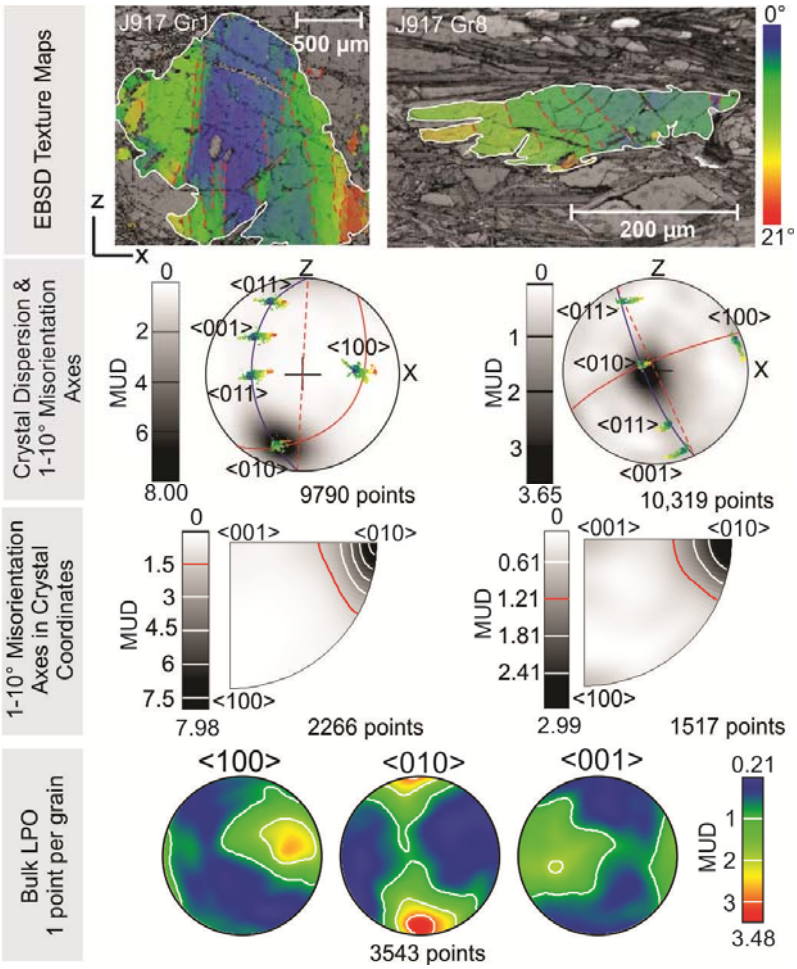

Figure 6.1. Bulk LPO and EBSD texture maps/pole figures of olivine grains from J917. Rotation axis contours for grains 01and 08 are based on 2266 and 1386 points, respectively. X = lineation and Z = pole to foliation. Bulk LPO colour scale is based on data point density with units in mud (multiples of uniform density), and contouring for all plots presented in this paper was calculated using a half width of 20° and cluster size of 3°. All pole figures are lower hemisphere equal area projections. Misorientation axes represent changes in orientation between neighbouring pixels. Dotted red lines on EBSD maps and pole figures represent low angle boundary traces and solid red lines represent the slip plane.

For all individual grains, dispersion and misorientation axes are not perpendicular to the trace of low-angle boundaries within the grains and hence the deformation cannot be interpreted in terms of twist boundaries. Using the previously eXPLained geometrical relationships between dispersion/misorientation axes and the boundary trace for tilt boundaries, the slip systems responsible for low-angle boundary formation were constrained for the 97 olivine grains. In this case, low-angle boundaries are best associated with the operation of several different slip systems. However, in all cases, all slip systems were characterized by [100] slip.

The distribution of different slip system types within the thin section are illustrated in Figure 6.2B and are seen to comprise (010)[100] A-type, {0kl}[100] D-type and (001)[100] E-type, with (001)[100] (the E-type slip system) being most common (43% of the grains analysed). Grains deforming by a combination of both the {0kl}[100] D-type and (001)[100] E-type slip systems are the second most abundant, comprising 23.7% of the total.

To more clearly identify the relationships between the crystallographic orientation and the slip system type, crystallographic pole figures for all collected diffraction patterns from all 97 grains (~46000 points) have been plotted to show the distributions of axes for different slip system type (Figure 6.2B). The data reveal that all low-angle boundary types have geometrically similar [100] axes (Fig. 2b). However, grains deforming by A-type, A/E-type, A/D-type and D-type slip systems tend to have differently oriented [010] and [001] axes compared to the grains deforming by E-type and D/E-type slip systems (Figure 6.2B). The distribution of these axes among the different slip systems is such that different parts of the [010] and [001] girdles are defined by olivine grains in similar orientations that are deforming by similar slip systems. The strong clustering of [100] axes and the evidence for slip along [100] for the different low-angle boundaries are consistent with the Tubaf LPO having developed by slip in the [100] direction. However, in detail, the bulk fabric is comprised of grains that have accommodated A-, D, & E-type slip.

It has been suggested that the dislocations preserved at low-angle boundaries in olivine grains represent the ‘hard’ slip systems (the slip systems that are least active and only accommodate small amounts of strain), whereas the bulk fabric reflects the operation of the most active or ‘easy’ slip system, and for this reason caution should be used when interpreting misorientation data (Tommasi *et al.*,2008; Soustelle *et al.*,2010; Falus *et al.*,2011).

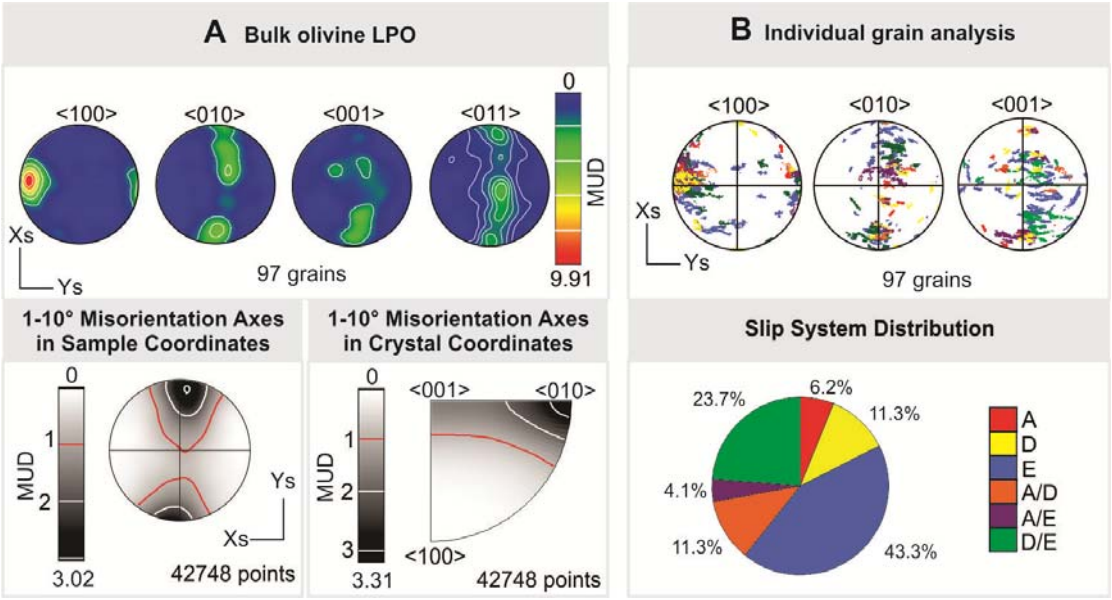

Figure 6.2. A) Rotation axes are dominated by [011] and [010]. Clustering of [100] orthogonal to a girdle defined by [010], [001] and [011] indicates a [100] slip direction, consistent with D-type LPO. B) Slip system analysis of 97 individual grains. Crystallographic orientations of each grain are coloured according to slip system. Xs and Ys correspond to arbitrary sample coordinates and do not reflect the structural framework of the xenoliths.

This theory is not unfeasible, however the observations presented here show that the slip directions inferred from both the intragrain microstructures and the corresponding bulk fabric are consistent ([100] slip), an observation that is not readily eXPLained by the interpretation of 'hard' and 'easy' slip systems with exactly the same slip direction. Based on the assumption that the 'hard' slip systems were preserved in the olivine grains and that most of the deformation was occurring by slip systems with [001] slip directions, it would also be expected to see a bulk slip direction of [001], which is inconsistent with the [100] bulk slip direction that was observed in the samples. This approach and interpretation is solely evidence-based, and there is a distinct lack of evidence for the operation of [001] slip on both an intragrain and bulk fabric scale. Thus it would be inappropriate to interpret a bulk [001] slip direction when there is no physical evidence for these slip systems.

Similar analyses on other variably-hydrated Tubaf samples have been undertaken with the same results (Figure 6.3). Despite the fact that these peridotites show a

range of metasomatic textures reflecting interaction with a large flux of slab-derived fluids in the supra-subduction environment (McInnes *et al.*,1999; Gregoire *et al.*,2001; McInnes *et al.*,2001), there is no evidence of deformation by [001] slip or any alteration-related trends.

In the past, the use of xenoliths to infer deformation kinematics from bulk fabric analysis of mantle wedge peridotites has been limited to xenoliths exhibiting clear mesoscopic foliations and lineations. This analysis of the preserved LPO and intragrain deformation microstructures of olivine reveals a new methodology for the inference of olivine deformation type. The results of this study illustrate that deformation of mantle wedge olivine is characterized by [100] slip, even in hydrated supra-subduction mantle where B-type olivine fabrics are predicted (Kneller *et al.*,2005). These results are consistent with other xenolith bulk LPO studies (Jung *et al.*,2009; Soustelle *et al.*,2010; Yang *et al.*,2010) which also fail to identify B-type olivine LPOs in mantle wedge xenoliths, and most natural observations of B-type fabrics are from tectonically complex orogenically-exhumed peridotites (Skemer *et al.*,2006; Tasaka *et al.*,2008; Jung, 2009; Webber *et al.*,2010) where preservation of primary mantle fabrics cannot be assumed.

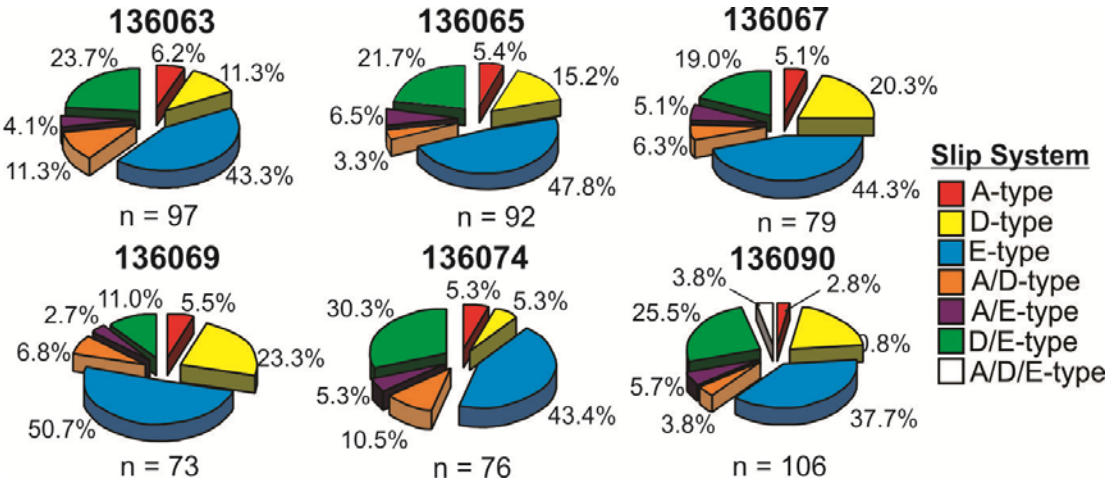

Figure 6.3. Pie charts showing the proportion of grains deformed by each slip system/combination of slip systems as a percentage of the total number of grains analysed.

6.4. Implications for forearc seismic anisotropy

Seismic anisotropy measurements along the Pacific plate to the north and south of Tubaf record trench-parallel fast directions (Nakajima and Hasegawa, 2004; Long and Silver, 2008; Hammond *et al.*,2010). If these seismic fast directions reflect the alignment of olivine [100] axes in the mantle (Russo and Silver, 1994; Peyton *et al.*,2001; Lassak *et al.*,2006), then extrapolation of these directions to Tubaf requires trench-parallel stretching to align olivine [100] axes parallel to the trench. This is consistent with several subduction zone mantle flow models (e.g. Billen and Gurnis, 2001; Behn *et al.*,2007; Kneller and van Keken, 2007; Manea and Gurnis, 2007; Long and Silver, 2008). Alternatively, a trench-parallel alignment of seismic fast directions may reflect a significant component of strongly anisotropic serpentinites in either the subducting slab (Healy *et al.*,2009) or in the mantle (Katayama, 2009; Katayama *et al.*,2009). In either case, the data from Tubaf provide no support for a model involving [001] slip.

6.5. Acknowledgements

The authors acknowledge the use of equipment, scientific and technical assistance of the Curtin University Electron Microscope Facility, which is partially funded by the University, State and Commonwealth Governments. In particular, Dr. Rob Hart and Will Rickard for assistance with SEM operation. Dr. Tom Mitchell is thanked for assistance with fieldwork and logistics, Dr. Nick Timms for comments and reviewers for comments and advice. This research was funded by ARC grant DP0878453. The Tubaf xenolith samples used in this study were collected during Cruise SO-94 of *RV Sonne* (Edison project), which was organized by Freiberg University of Mining and Technology and funded by the German Federal Ministry for Research and Technology (BMFT grant 03G0094A to P. Herzig).

6.6. References

Barrie, C. D., Boyle, A. P., Cox, S. F. and Prior, D. J. (2008) Slip systems and

critical resolved shear stress in pyrite: an electron backscatter diffraction (EBSD) investigation, *Mineralogical Magazine*, v. 72, no. 6, p. 1181-1199.

Behn, M.D., Hirth, G. and Keleman, P.B. (2007). Trench-Parallel Anisotropy Produced by Foundering of Arc Lower Crust, *Science*, v. 317, p. 108-111.

Bestmann, M. and Prior, D. J. (2003) Intragranular dynamic recrystallization in naturally deformed calcite marble: diffusion accommodated grain boundary sliding as a result of subgrain rotation recrystallization, *Journal of Structural Geology*, v. 25, no. 10, p. 1597-1613.

Billen, M.I. and Gurnis, M. (2001) A low viscosity wedge in subduction zones, *Earth and Planetary Science Letters*, v. 193, p. 227-236.

Boyle, A. P., Prior, D. J., Banham, M. H. and Timms, N. E. (1998) Plastic deformation of metamorphic pyrite: new evidence from electron-backscatter diffraction and forescatter orientation- contrast imaging, *Mineralium Deposita*, v. 34 no. 1, p. 71-81.

Buttles, J. and Olson, P. (1998) A laboratory model of subduction zone anisotropy, E*arth and Planetary Science Letters*, v. 164, p. 245-262.

Falus, G., Tommasi, A. and Soustelle, V. (2011) The effect of dynamic recrystallization on olivine crystal preferred orientations in mantle xenoliths deformed under varied stress condition, *Journal of Structural Geology*, v. 33, p. 1528 – 1540.

Gregoire, M., McInnes, B.I.A. and O'Reilly, S.Y. (2001) Hydrous metasomatism of oceanic sub-arc mantle, Lihir, Papua New Guinea: Part 2. Trace element characteristics of slab-derived fluids, *Lithos*, v. 59, p. 91-108.

Hammond, J.O.S., Wookey, J., Kaneshima, S., Inoue, H., Yamashina, T. and Harjardi, P. (2010) Systematic variation in anisotropy beneath the mantle wedge in the Java-Sumatra subduction system for shear-wave splitting, *Physics of the Earth and Planetary Interiors*, v. 178, p. 189-201.

Healy, D., Reddy, S.M., Timms, N.E., Gray, E.M. and Brovarone, A.V. (2009) Trench-parallel fast axes of seismic anisotropy due to fluid-filled cracks in subducting slabs, *Earth and Planetary Science Letters*, v. 283, p. 75-86.

Hildyard, R. C., Prior, D. J., Faulkner, D. R. and Mariani, E. (2009) Microstructural analysis of anhydrite rocks from the Triassic Evaporites, Umbria-Marche Apennines, Central Italy: An insight into deformation mechanisms and possible slip systems, *Journal of Structural Geology*, v. 31, no. 1, p. 92-103.

Jung, H. (2009) Deformation fabrics of olivine in Val Malenco peridotite found in Italy and implications for the seismic anisotropy in the upper mantle, *Lithos*, v. 109, p. 341-349.

Jung, H. and Karato, S. (2001) Water-induced Fabric Transitions in Olivine, *Science*, v. 293, p. 1460-1463.

Jung, H., Katayama, I., Jiang, Z., Hiraga, T. and Karato, S. (2006) Effect of water and stress on the lattice-preferred orientation of olivine, *Tectonophysics*, v. 421, p. 1-22.

Jung, H., Mo, W. and Choi, S.H. (2009) Deformation microstructures of olivine in peridotite from Spitsbergen, Svalbard and implications for seismic anisotropy, *Journal of Metamorphic Geology*, v. 27, p. 707-720.

Katayama, I. (2009) Thin anisotropic layer in the mantle wedge beneath northeast Japan, *Geology*, v. 37, p. 211-214.

Katayama, I., Hirauchi, K.-i., Michibayashi, K., and Ando, J.-i., 2009. Trench-parallel anisotropy produced by serpentine deformation in the hydrated mantle wedge. *Nature*, 461, 1114-1117.

Kneller, E.A., and van Keken, P.E., 2007. Trench-parallel flow and seismic anisotropy in the Mariana and Andean subduction systems. *Nature*, 450, 1222-1226.

Kneller, E.A., van Keken, P.E., Karato, S., and Park, J., 2005. B-type olivine fabric in the mantle wedge: Insights from high-resolution non-Newtonian subduction zone models. *Earth and Planetary Science Letters*, 237, 781-797.

Lassak, T.M., Fouch, M.J., Hall, C.E., and Kaminski, E., 2006. Seismic characterization of mantle flow in subduction systems: Can we resolve a hydrated mantle wedge? *Earth and Planetary Science Letters*, 243, 632-649.

Lloyd, G. E., Farmer, A. B., and Mainprice, D., 1997. Misorientation analysis and the formation and orientation of subgrain and grain boundaries. *Tectonophysics*, 279 (1-4), 55-78.

Long, M.D., and Silver, P.G., 2008. The Subduction Zone Flow Field from Seismic Anisotropy: A Global View. *Science*, 319, 315-319.

Manea, V., and Gurnis, M., 2007. Subduction zone evolution and low viscosity wedges and channels. *Earth and Planetary Science Letters*, 264, 22-45.

McInnes, B.I.A., Gregoire, M., Binns, R.A., Herzig, P.M., and Hannington, M.D., 2001. Hydrous metasomatism of oceanic sub-arc mantle, Lihir, Papua New Guinea: petrology and geochemistry of fluid-metasomatised mantle wedge xenoliths. *Earth and Planetary Science Letters,* 188, 169-183.

McInnes, B.I.A., McBride, J.S., Evans, N.J., Lambert, D.D., and Andrew, A.S., 1999. Osmium Isotope Constraints on Ore Metal Recycling in Subduction Zones. *Science*, 286, 512-516.

Mizukami, T., Wallis, S.R., and Yamamoto, J., 2004. Natural examples of olivine lattice preferred orientation patterns with a flow-normal a-axis maximum. *Nature*, 427, 432-436.

Nakajima, J., and Hasegawa, A., 2004. Shear-wave polarisation anisotropy and subduction-induced flow in the mantle wedge of northeastern Japan. *Earth and Planetary Science Letters*, 225, 365-377.

Peyton, V., Levin, V., Park, J., Brandon, M., Lees, J., Gordeev, E., and Ozerov, A., 2001. Mantle Flow at a Slab Edge: Seismic Anisotropy in the Kamchatka Region. *Geophysical Research Letters,* 28, 379-382.

Prior, D.J., Boyle, A.P., Brenker, F., Cheadle, M.C., Day, A., Lopez, G., Peruzzo, L., Potts, G.J., Reddy, S.M., Spiess, R., Timms, N.E., Trimby, P., Wheeler, J., and Zetterström, L., 1999. The aPPLication of electron backscatter diffraction and orientation contrast imaging in the SEM to textural problems in rocks: *American Mineralogist*, 84, 1741-1759.

Prior, D. J., Wheeler, J., Peruzzo, L., Spiess, R. and Storey, C. (2002) Some garnet

microstructures: an illustration of the potential of orientation maps and misorientation analysis in microstructural studies, *Journal of Structural Geology*, v. 24 no. 6-7, p. 999-1011.

Reddy, S.M. and Buchan, C. (2005) Constraining kinematic rotation axes in high-strain zones: a potential microstructural method? *Geological Society, London, Special Publications*, v. 243, p. 1-10.

Russo, R.M. and Silver, P.G. (1994) Trench-parallel Flow Beneath the Nazca Plate from Seismic Anisotropy, *Science*, v. 263, p. 1105-1111.

Skemer, P., Katayama, I. and Karato, S. (2006) Deformation fabrics of the Cima di Gagnone peridotite massif, Central Alps, Switzerland: evidence of deformation at low temperatures in the presence of water, *Contributions to Mineralogy and Petrology*, v. 152, p. 43-51.

Soustelle, V., Tommasi, A., Demouchy, S. and Ionov, D.A. (2010) Deformation and fluid-rock interaction in the supra-subduction mantle: Microstructures and water contents in peridotite xenoliths from the Avacha Volcano, Kamchatka, *Journal of Petrology*, v. 51, p. 363-394.

Sutton, A. P. and Balluffi, R. W. (1995) *Interfaces in crystalline materials*, Oxford Science Publications.

Tasaka, M., Michibayashi, K. and Mainprice, D. (2008) B-type olivine fabrics developed in the fore-arc side of the mantle wedge along a subducting slab, *Earth and Planetary Science Letters*, v. 272, p. 747-757.

Tommasi, A., Vauchez, A. and Ionov, D.A. (2008) Deformation, static recrystallization, and reactive melt transport in shallow subcontinental mantle

xenoliths (Tok Cenozoic volcanic field, SE Siberia), *Earth and Planetary Science Letters*, v. 272, p. 65-77.

Webber, C., Newman, J., Holyoke Iii, C.W., Little, T. and Tikoff, B. (2010). Fabric development in cm-scale shear zones in ultramafic rocks, Red Hills, New Zealand, *Tectonophysics*, v. 489, p. 55-75.

Wheeler, J., Mariani, E., Piazolo, S., Prior, D. J., Trimby, P. and Drury, M. R. (2009) The weighted Burgers vector: a new quantity for constraining dislocation densities and types using electron backscatter diffraction on 2D sections through crystalline materials, *Journal Of Microscopy*, v. 233, no. 3, p. 482-494.

Yang, K., Hidas, K., Falus, G., C., S., Nam, B., Kovács, I. and Hwang, B. (2010) Relation between mantle shear zone deformation and metasomatism in spinel peridotite xenoliths of Jeju Island (South Korea): Evidence from olivine CPO and trace elements, *Journal of Geodynamics*, v. 50, p. 424-440.

Chapter 7. Microstructural Characterisation and bulk fabric analysis of Lihir peridotite xenoliths

7.1. Introduction

Fabric and microstructural analysis of peridotite is crucial for understanding the deformation conditions within the upper mantle, and provides an indication of the upper mantle flow regime. Bulk fabric analysis is important for determining mantle flow directions and can give an indication of the pressure, temperature, stress and water conditions in the upper mantle (Jung *et al*., 2006). Microstructural analysis is an often overlooked aspect that can provide a great deal of information regarding the nature of the deformation, formation of fabrics and degree of recrystallisation.

Xenoliths remain an important source of information regarding mantle deformation that has not yet been utilised to its' full potential. As previously discussed, the lack of obvious foliation and lineation in many samples precludes their use for fabric analysis. The ability to use mantle xenoliths for fabric analysis would greatly enhance the current database of olivine fabric types, and provide substantially more information about the mantle than is currently available.

The data provided in Chapter 6 addressed the issues associated with the use of mantle xenoliths, and through examination of an oriented peridotite sample from Higashi-Akaishi, Japan, identified the nature of a systematic relationship that exists between bulk fabrics and microstructures preserved within individual olivine grains. Satsukawa and Michibayashi (2009) also present a preliminary study showing a potential link between intragrain slip systems and olivine LPO, although the dataset is limited. One of the main issues has been whether or not the olivine internal microstructure reflects the most active slip system preserved by the bulk fabric (Tommasi *et al.,* 2008; Soustelle *et al.,* 2010; Falus *et al.,* 2011). However, the data presented in Chapter 6 (Gray *et al*., in review) find that fabrics develop through the operation of a number of different slip systems, and that these different slip systems share a common slip direction with the bulk fabric, hence indicating the mantle flow

direction. This removes the necessity for a measured foliation and lineation to be present in order for the flow direction to be deduced. A thorough examination of the microstructure and bulk LPO should indicate the flow direction in absence of the foliation and lineation. This provides sufficient information to aid interpretations of seismic fast axes above the subduction zone mantle, which are sensitive to the [100] axis orientation in olivine.

The following chapter provides a comprehensive microstructural fabric analysis of olivine in 6 Lihir mantle xenoliths. The samples were analysed by EBSD, the analytical, noise reduction and processing procedures are outlined in chapter 4, along with sample preparation protocols. Bulk fabric data for these samples was initially presented by Gray (2008), as were individual thin section grain maps of samples 136063, 136067 and 136069. This data has been reprocessed and interpreted within the framework outlined in Chapter 6 (Gray *et al.*,in review). This new perspective, which has arisen due to the systematic relationship between bulk fabric and low-angle boundaries identified through analysis of the Higashi-Akaishi peridotite (Chapter 6), enabled a bulk slip direction to be assigned to the Lihir xenoliths. Subsequent slip system mapping has also been undertaken on samples 136065, 136074 and 136090, which provides substantially more data than was previously available.

7.2. Samples and methodology

The samples studied were 136063, 136065, 136067, 136069, 136074 and 136090. The samples are all spinel peridotites, and show varying degrees of alteration by metasomatism to fibrous orthopyroxene (Table 7.1; detailed petrography for the samples is provided in Chapter 5). Despite the lack of hydrous phases within the samples, McInnes *et al.* (2001) provide evidence that hydrous fluids were involved in metasomatising these samples. The high temperatures present at the time of metasomatism resulted in conditions in which hydrous minerals were not stable

despite the presence of water (Nakamura and Kushiro, 1974; Ryabchikov *et al*., 1982; Schneider and Eggler, 1986; McInnes *et al*. 2001).

Table 7.1. Lihir mantle xenolith samples and degree of alteration of primary mantle phases to fibrous orthopyroxene (OPX) as a result of hydrous fluid influx. Fibrous orthopyroxene was the main phase produced by this metasomatism, and is used as a proxy for the degree of alteration.

Sample	Rock Type	% Fibrous OPX
136063	Spinel Lherzolite	5%
136065	Spinel Harzburgite	0%
136067	Spinel Dunite	0%
136069	Spinel Dunite	6%
136074	Spinel Lherzolite	4%
136090	Spinel Dunite	10%

7.3 EBSD Structural Analysis

Bulk fabric data is presented in the form of maps, contoured bulk pole figures and contoured rotation axes plotted in both a sample coordinate and crystal coordinate reference frame. Most fabric classifications present only [100], [010] and [001] axes, however in this study the [011] axes appear to be significant, so these are also included.

Subsequent to bulk fabric analysis, the microstructure of individual grains within each peridotite was examined. The grains were subset out of the main dataset and examined in terms of low-angle boundary orientations, rotation axis orientations and crystal axis dispersion. Slip systems were interpreted according to the procedure outlined in chapters 4 and 6 (Figure 4.5). The data is presented as a series of maps, as providing the raw data for each grain was unfeasible (interpretation of each grain required 5 stereographic plots, which equates to approximately 2615 data plots for the 523 grains analysed). Numerous grains were not used for the analysis, either due to poor indexing or lack of internal microstructure. Many gaps in the maps represent phases other than olivine, such as orthopyroxene, clinopyroxene or spinel, as these were not indexed by the EBSD software.

Interpretation of the EBSD results is based on the assumption that the low-angle boundaries have a tilt boundary and not a twist boundary geometry. In general, twist boundaries are not common in mantle olivine, but this fact should not be ignored. This assumption was tested thoroughly for each grain (refer to the procedure shown in Figure 4.5 and the discussion in Chapter 6) and the data were found to be consistent with the tilt-boundary model.

Many of the grains were found to preserve microstructures consistent with the operation of two slip systems and are written as follows: e.g. (010)[100]/(001)[100], which corresponds to a grain comprising microstructures associated with (010)[100] and (001)[100].

136063

Pole figures showing the bulk fabric of sample 136063 (88856 data points, 97 olivine grains) reveal the presence of an obvious LPO (Figure 7.1). The LPO is characterised by a cluster of [100] axes, with [010] and [001] axes forming a girdle within the (100) plane. A plot of 1 - 10° misorientation axes preserved within olivine grains in sample coordinate geometry reveals that rotation axes are predominantly clustered, with some weak dispersion within the (100) plane. When examined on a crystal coordinate plot, these rotation axes are primarily clustered parallel to [010], with some minor dispersion towards [001] or [011]. This data indicates that most of the grains are deforming by a slip system consistent with a [010] rotation axis, or a combination of slip systems with [010], [011] and [001] rotation axes.

Mapping of the slip systems preserved within 97 individual grains (Figure 7.3) shows that despite the well-developed and clear fabric in the bulk pole figures, the individual grains were deforming by the operation of a number of slip systems. Most of the grains (43.3%) preserve microstructures consistent with (001)[100] slip (Figure 6.2). A further 23.7% of grains preserved microstructures consistent with deformation by both (001)[100] and {0kl}[100] slip within the same grain. The

remaining proportion of grains record structures associated with (010)[100]/{0kl}[100], {0kl}[100], (010)[100] and (010)[100]/(001)[100] (Figure 6.3). In this case, the rotation axis for {0kl}[100] observed in all grains deforming by this slip system was the [011] axis. Common to all of the inferred slip systems within all of the grains is a [100] slip direction.

Spatial distribution of the slip systems is variable, indicating that there are no specific regions that are deforming differently to the rest of the sample (Figure 7.3). Grain orientations are more systematic and show a pattern. [100] axes are clustered for all grains, however the [010] and [001] axes of grains deforming by slip within (001)[100] and (001)[100]/{0kl}[100] are clustered together, as are the [010] and [001] axes of the other grains. In comparison to the bulk fabric rotation axes, the [010] axes of grains deforming by (001)[100] and (001)[100]/{0kl}[100] cluster in a similar orientation to that of the bulk fabric rotation axes. The [010] axes of the other grain types cluster in the centre of the plot, in the weaker part of the girdle defined by the rotation axes. These observations are consistent with the statistical analysis of this sample, as the grains deforming by (001)[100] and (001)[100]/{0kl}[100] are also statistically dominant.

136065

Bulk pole figures of sample 136065 (35416 data points, 92 olivine grains) reveal that the sample has an LPO characterised by [100] axes that are clearly clustered. [010] and [001] axes are less so, and show a degree of dispersion within the (100) plane. 1 - 10° rotation axes plotted in terms of the sample coordinate reference frame are strongly clustered in the centre of the pole figure, parallel to the cluster of [010] axes. Rotation axes plotted in terms of the crystal coordinates confirm that most grains have [010] rotation axes, with some very minor dispersion towards [011]. This data is consistent with a slip system with a dominant [010] and minor [011] rotation axis.

Individual grain slip system mapping of 92 grains within the sample reveals that there are microstructures consistent with deformation by a number of different slip systems preserved within individual grains. This contrasts with the predominance of [010] rotation axes shown by the bulk fabric data. Statistical analysis of the slip systems within 136065 (Figure 6.2) reveals that 47.8% of the grains in the sample deformed by slip within (001)[100], followed by a combination of {0kl}[100] and (001)[100] slip comprising 21.7% of the sample. 15.2% of the grains within the sample were deforming by {0kl}[100] alone, 6.5% by a combination of (010)[100] and (001)[100], 5.4% by (010)[100] and 3.3% by both (010)[100] and {0kl}[100]. All of these slip systems have a common slip direction of [100]. [011] was the rotation axis for grains deforming by slip within {0kl}[100]. The slip system distribution map shows a scattered distribution of slip systems within the sample (Figure 7.3). Pole figures showing the orientations of grains coloured by slip system type (Figure 7.3) reveal that for sample 136065 there is no clear relationship between slip system activation and grain orientation.

136067

Bulk fabric pole figures (34084 data points, 79 grains) (Figure 7.1) show a distinct clustering of [100] axes with a girdle defined by [010] and [001] axes within the (100) plane. There is a small number of [100] axes within the girdle, and a small number of [001] axes in the same orientation as the cluster of [100]. 1 - 10° rotation axes plotted within a sample coordinate reference frame (Figure 7.1) are distinctly clustered in the x direction. Rotation axes plotted with respect to crystal coordinates show clustering parallel to [010], with some minor dispersion towards [011] or [001]. This data suggests that the fabric in this sample was produced by deformation by a slip system with a dominant [010] rotation axis, with some minor deformation within slip systems with [011] and [001] rotation axis.

Statistical analysis of the microstructures preserved within 79 olivine grains within sample 136067 shows that 44.3% of the grains are deforming by (001)[100], 20.3%

are deforming by {0kl}[100] and 19.0% are deforming by both {0kl}[100] and (001)[100] (Figure 6.2). A combination of (010)[100] and {0kl}[100], (010)[100] and (010)[100]/(001)[100] slip comprise 6.3%, 5.1% and 5.1% of the sample, respectively. The slip system distribution map (Figure 7.3) shows that grains deforming by different slip systems are scattered throughout the sample. There is a weak clustering of the [010] axes of grains deforming by (001)[100] (Figure 7.3), suggesting that slip system development might be linked to grain orientation in this sample.

136069

Bulk pole figures (29043 data points, 73 grains) (Figure 7.2) show an LPO defined by clustered [100], [010] and [001] axes. There is some minor dispersion of [010] and [001] within the bulk (100) plane that tends towards a girdle. 1 - 10° rotation axes define a girdle also within the bulk (100) plane. There is a clustering of rotation axes parallel to [010] and [011]. Examination of the rotation axes within a crystal reference frame show that [010] rotation axes are dominant, but there is a significant amount of dispersion towards [011] and [001]. The bulk fabric data suggests that this sample was likely deforming by multiple slip systems with [010], [011] and [001] rotation axes.

Statistically, 50.7% of the grains are deforming by (001)[100], 23.3% by {0kl}[100] and 11% by {0kl}[100]/(001)[100] (Figure 6.2). (010)[100]/{0kl}[100] slip, (010)[100] slip and (010)[100]/(001)[100] slip comprise 6.8%, 5.5% and 2.7% of the sample, respectively. Slip system distribution mapping of 73 individual olivine grains (Figure 7.4) shows that the spatial distribution of slip systems in 136069 are scattered. There is also no correlation between grain orientation and slip system, as can be seen in the pole figures in Figure 7.3.

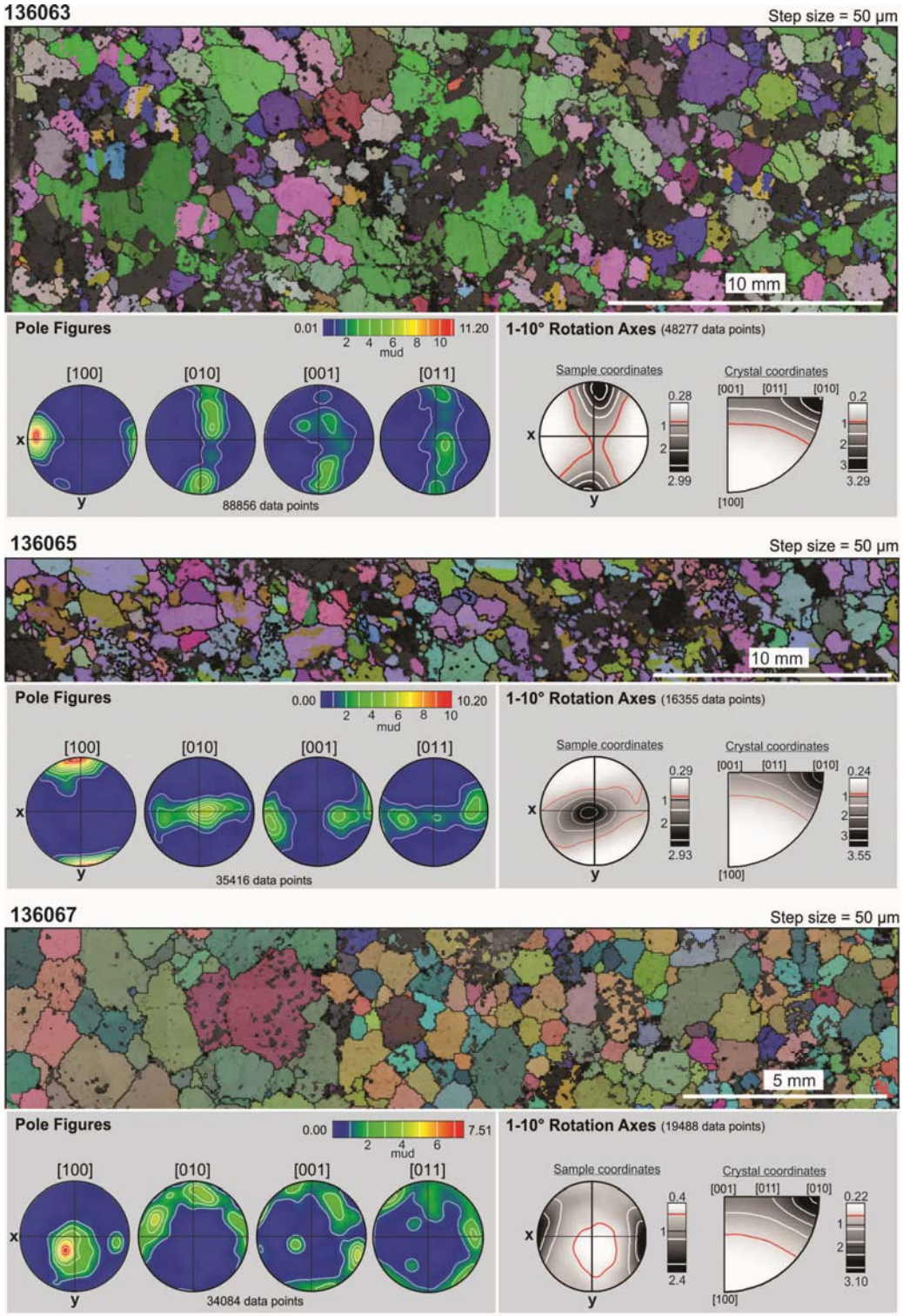

Figure 7.1. EBSD All Euler maps and pole figures and rotation axes of Lihir xenoliths 136063, 136065 and 136067. The pole figures are equal area, lower hemisphere projections and all contouring was using a half width of 20°. Contour intervals vary between plots and represent multiples of uniform density (mud). The figure also includes rotation axes plotted within a crystallographic framework to ease identification of the orientation of the rotation axis. The All Euler map legend is provided in Chapter 4 (Figure 4.5).

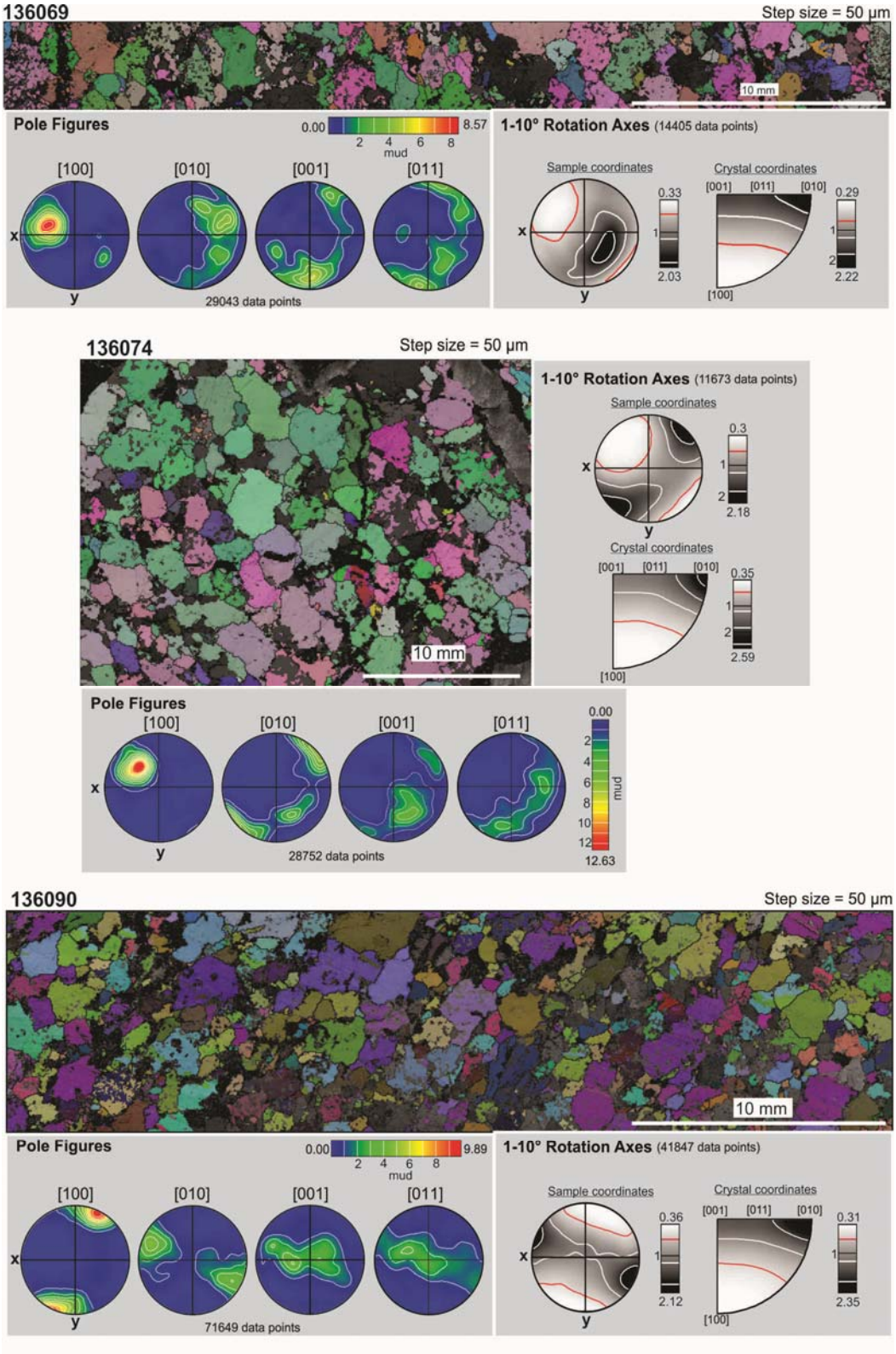

Figure 7.2. EBSD All Euler maps, pole figures and rotation axes of Lihir xenoliths 136069, 136074 and 136090.

136074

Bulk fabric analysis of sample 136074 (28752 data points, 76 grains) (Figure 7.4) shows an LPO defined by a strong clustering of [100] axes, with a double maxima of [010] and [001] axes within the bulk (100) plane. Examination of 1 - 10° rotation axes in a sample coordinate reference frame shows these are clustered parallel to the more horizontally-oriented [010] and [001] axes, with a slight dispersion defining a weak girdle, also within the bulk (100) plane. Rotation axes displayed in terms of the crystal coordinate reference frame show a clustering parallel to [010], with a weak dispersion towards [011] and [001]. This is consistent with a slip system with a [010] rotation axes, with minor deformation within slip systems with [011] and [001] rotation axes.

In terms of the distribution of slip systems within the sample, out of 76 grains, 43.4% of the grains preserved microstructures consistent with (001)[100] and 30.3% preserved microstructures consistent with a combination of {0kl}[100] and (001)[100] slip (Figure 6.2). (010)[100]/{0kl}[100] slip comprised 10.5% of the sample, and (010)[100], {0kl}[100] slip and (010)[100]/(001)[100] slip comprised 5.3% of the sample each. Maps of the spatial distribution of slip systems within the sample show a relatively scattered distribution (Figure 7.4). Most of the grains share a common [100] axis orientation, however the [010] axes of (001)[100] grains tend to cluster parallel to the bulk rotation axis orientation.

136090

Bulk fabric analysis of sample 136090 (71649 data points, 106 grains) (Figure 7.4) shows an LPO defined by a strong clustering of [100] axes, with clustered [010] and [001] axes within the bulk (100) plane. A plot of 1 – 10° rotation axes within a sample coordinate reference frame shows that rotation axes are clustered parallel to [010], with a weak girdle forming within the bulk (100) plane. Rotation axes displayed in terms of a crystal coordinate reference frame show clustering parallel to [010], with some dispersion towards [011] and [001]. This data is consistent with

deformation by slip within a slip system that has a [010] rotation axis, and minor deformation within a slip system with [011] and [001] rotation axes.

Out of 106 individual grains analysed, 37.7% were deforming by (001)[100], 25.5% were deforming by {0kl}[100]/(001)[100] and 20.8% were by {0kl}[100] (Figure 6.2). (010)[100]/(001)[100] slip comprised 5.7% of the sample and (010)[100]/{0kl}[100] slip and (010)[100] slip comprised 3.8% and 2.8% of the sample, respectively. 3.8% of the sample was comprised of grains that preserved microstructures consistent with three slip systems, (010)[100], {0kl}[100] and (001)[100]. Slip system mapping of these grains (Figure 7.4) shows a scattered slip system distribution. Pole figures showing the orientation of grains preserving evidence for different slip systems reveals that the [010] axes of grains deforming by (001)[100] tend to cluster parallel to the bulk fabric rotation axes, whereas the dispersion of rotation axes within the (100) plane is a result of grains deforming by {0kl}[100] and (001)[100] .

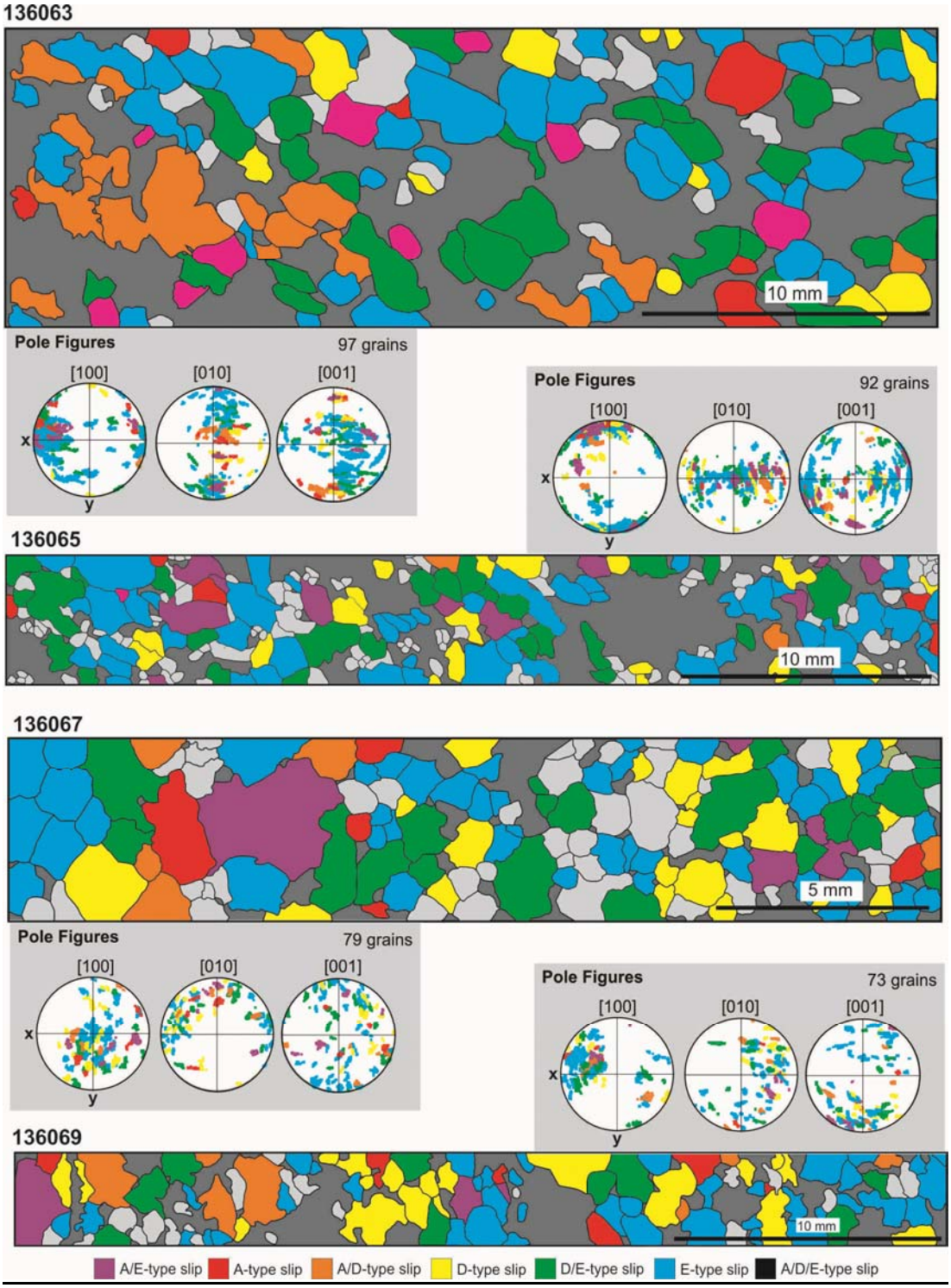

Figure 7.3. Slip system distribution maps of Lihir xenoliths 136063, 136065, 136067 and 136069. Each grain was analysed as part of a larger thin section map and individually examined to discern the slip systems operating within the grains. The pole figures are equal area, lower hemisphere projections, and both the maps and pole figures are coloured in terms of the slip system/s operating within each grain. Pale grey grains represent grains that did not preserve enough microstructure to analyse, and the dark grey regions are areas of the sample that were not indexed.

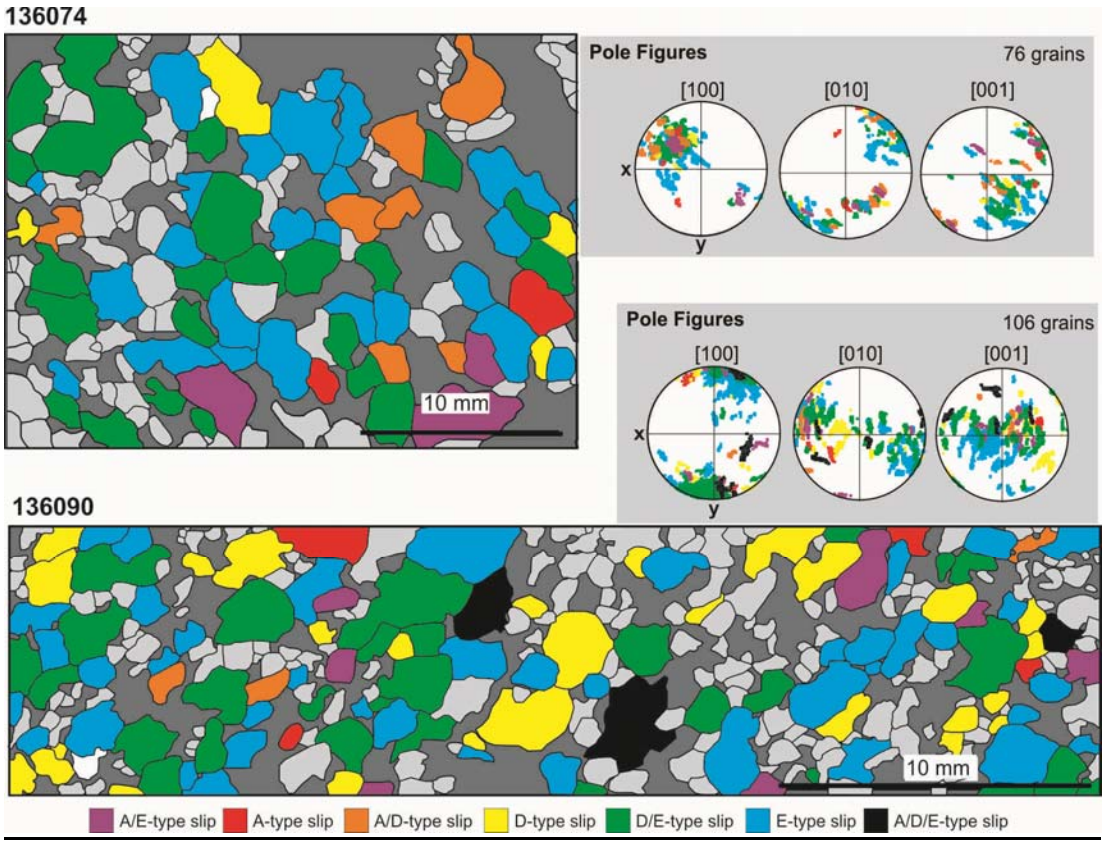

Figure 7.4. Slip system distribution maps of Lihir xenoliths 136074 and 136090 (parameters are the same as for Figure 7.3).

7.4. Interpretation and significance

All of the samples are deforming by slip within three different systems: (010)[100], {0kl}[100] and (001)[100]. There is no correlation between the active slip system and the degree of alteration, as all samples show similar results (Figure 6.3) despite being variably altered. Based on the olivine fabric classification of Jung *et al.*(2006) and the systematic link between olivine LPO and microstructure identified by in Chapter 6 (Gray *et al.*, in review), we can interpret the slip direction of the bulk fabric of the Lihir xenolith samples (Table 7.2). Deformation microstructures associated with (001)[100] slip dominate the samples, with subordinate amounts of {0kl}[100] slip. Contoured LPO plots appear to have patterns very similar to the published patterns for D- and E-type fabrics (Jung *et al.*, 2006). Due to the lack of a foliation plane, only the bulk slip direction can be determined with any certainty.

Olivine grains within the Lihir samples primarily contain rotation axes parallel to the [010] axis. The dispersion of these on the pole figures exhibit a weak girdle pattern with maxima parallel to [010], defining a plane that is orthogonal to the [100] direction (Figs. 7.1 and 7.2). This plane corresponds to the structural YZ plane (Fig. 7.4), the pole to which is the slip direction, in this case [100]. On a bulk scale, [100] is the only axis that is significantly clustered, a characteristic of the slip direction. Samples 136065 and 136090 have bulk slip directions of [100] and dominant rotation axis orientations of [010] with subordinate [011] rotation (determined from the internal microstructure), and are interpreted as E-type LPOs ((001)[100]). The LPO patterns of samples 136063, 136067, 136069 and 196074 show more dispersion of [010] and [001] axes, consistent with a D-type LPO, however the microstructure indicates dominant rotation around [010]. These interpretations are consistent with the statistical analysis of preserved internal microstructure of the grains (Figure 6.3).

Table 7.2. Summary of olivine fabric and microstructural analysis of Lihir xenoliths.

Sample	Bulk fabric slip direction	Bulk fabric rotation axes	Dominant slip system from grain mapping	Subordinate slip system from grain mapping
136063	[100]	[010], minor [011]	(001)[100]	Combination of (001)[100] and [011][100]
136065	[100]	[010], minor [011]	(001)[100]	Combination of (001)[100] and [011][100]
136067	[100]	[010], minor [011]	(001)[100]	[011][100]
136069	[100]	[010], minor [011]	(001)[100]	[011][100]
136074	[100]	[010], minor [011]	(001)[100]	Combination of (001)[100] and [011][100]
136090	[100]	[010], minor [011]	(001)[100]	Combination of (001)[100] and [011][100]

The consistency between intragrain microstructures and bulk fabrics allows us to infer that the flow direction of these samples is [100]. This is of particular significance in relation to the issue of trench-parallel seismic fast axes. A popular theory for the generation of trench-parallel seismic anisotropy is the existence of B-type olivine fabrics in the mantle wedge (Jung and Karato, 2001; Kneller *et al*., 2005, 2007). In a B-type olivine fabric the seismically fast [100] axis is aligned

perpendicular to the slip and hence mantle flow direction, resulting in a seismic anisotropy that is orthogonal rather than parallel to the flow direction. Many of the subduction zones around the Pacific plate boundary, including data from relatively close to Lihir Island, exhibit trench-parallel seismic anisotropy (Fig. 2.6). The lack of observations of B-type fabrics in the Lihir xenoliths, despite metasomatic alteration involving hydrous fluid, suggests that this model is an unlikely scenario and that there is most likely another explanation for the seismic anomaly, as was discussed in Chapter 6 and will be discussed in detail in Chapter 10.

Slip system distribution mapping (Fig. 7.3) shows that the distribution of slip systems is spatially relatively scattered. The clustering of similar slip systems on crystallographic pole figures for all collected diffraction patterns from individual grains (Figure 7.3) indicate that the orientation the grains may be a factor in slip system operation. This grain orientation effect has also been noted for olivine by Michibayashi and Mainprice (2004), Warren *et al*. (2008), Webber *et al*. (2010), calcite (Reddy and Buchan, 2005), ice (van der Veen & Whillans, 1994) and aluminium (Liu & Hansen, 1995; Hansen & Huang, 1998; Liu et al., 1998). Warren *et al*. (2008) report that the presence of an existing LPO potentially controls the slip systems that develop within a shear zone, such that the cluster of crystal axes that is more favourably oriented with respect to the rotation axis of the kinematic reference frame of the shear zone, will be more likely to become the rotation axis for the new slip system. For the Lihir olivine, it appears that the [010] and [011] axes are more favourably oriented to become rotation axes, as these dominate the intragrain microstructures and are differently oriented to the grains deforming by the subordinate slip systems.

It is evident that the Lihir bulk fabrics are produced by the operation of a number of different slip systems working in conjunction with each other, rather than a single slip system. According to the von Mises condition (von Mises, 1928), there must be deformation by multiple slip systems (five independent slip systems, including

symmetric equivalents) in order to accommodate the total amount of strain. This, however, can be relaxed with deformation by fracturing, diffusive mass transfer or grain boundary sliding that also accommodates some of the deformation (Boland and Hobbs, 1973). There is only evidence for the operation of three slip systems within the Lihir samples. This suggests that there are other mechanisms operating within the peridotites that are accommodating the deformation. Warren *et al*. (2008) suggest that additional phases such as orthopyroxene enhances the effect of dislocation accommodated grain boundary sliding, which relaxes the constraints on the von Mises condition. The Lihir peridotites contain up to 10% orthopyroxene, so this may be a significant factor. The samples are also pervasively fractured, thus brittle deformation may have accounted for the remainder of the strain. This has implications for the co-existence of brittle and ductile deformation in the mantle and there is a thorough discussion provided in Chapter 9.

LPO is generally thought to represent the final stage of deformation, and low-angle boundaries represent a transient increment of strain with only evidence for the 'hard' slip systems preserved, and thus are inherently inconsistent (Tommasi *et al.,* 2008; Soustelle *et al.,* 2010; Falus *et al.,* 2011). The fact that there is evidence for the consistency of the Lihir olivine LPO and low-angle boundaries preserved inside individual grains is significant, suggesting that these peridotites have achieved steady-state deformation. Alternatively, the relaxation of the von Mises condition by either brittle failure or grain boundary sliding may have negated the necessity for activation of the 'hard' slip system/s to accommodate strain, leading to the consistency between LPO and low-angle boundaries. In contrast with a situation where all five slip systems are required to deform the rock – the 'easy' slip system will accommodate strain until the 'hard' slip system is required at higher strains, which is likely to be temporally the latest active slip system and the one that is preserved by the low-angle boundaries (Karato, 2008).

7.5. Summary

- Lihir peridotites have a bulk olivine LPO slip direction of [100]. The [100] axis is seismically-fast, and thus these results have significant implications for the interpretation of seismic fast axes above supra-subduction mantle and resulting mantle flow models, which rely on natural observations of olivine LPO types.
- The presence of orthopyroxene in these samples along with the formation of brittle microcracks appears to have relaxed the von Mises condition, allowing the 'easy' slip systems to dominate the deformation of the sample and are thus responsible for both the low-angle boundaries preserved inside grains as well as the bulk fabric.
- Grain orientation may be a factor in determining the active slip system.

7.6. References

Boland, J.N., and Hobbs, B.E. (1973) Microfracturing processes in experimentally deformed peridotite, *International Journal of Rock Mechanics and Mining Sciences & Geomechanics Abstracts*, v. 10, p. 623-626.

Falus, G., Tommasi, A., and Soustelle, V. (2011) The effect of dynamic recrystallization on olivine crystal preferred orientations in mantle xenoliths deformed under varied stress conditions, *Journal of Structural Geology*, v. 33, p. 1528-1540.

Gray, E. (2008) Microstructural characterisation of olivine and implications for mantle geodynamics [Honours thesis], Curtin University of Technology.

Gray, E., Reddy, S., Healy, D., and McInnes, B. (In review) The relationship between bulk fabrics and low-angle boundaries in olivine: Microstructural

evidence for [a] slip in supra-subduction zone mantle, *Terra Nova*.

Hansen, N., and Huang, X. (1998) Microstructure and flow stress of polycrystals and single crystals, *Acta Materialia*, v. 46, p. 1827-1836.

Jung, H., and Karato, S. (2001) Water-induced Fabric Transitions in Olivine, *Science*, v. 293, p. 1460-1463.

Jung, H., Katayama, I., Jiang, Z., Hiraga, T., and Karato, S. (2006) Effect of water and stress on the lattice-preferred orientation of olivine, *Tectonophysics*, v. 421, p. 1-22.

Karato, S., Jung, H., Katayama, I., and Skemer, P. (2008) Geodynamic Significance of Seismic Anisotropy of the Upper Mantle: New Insights from Laboratory Studies, *Annual Reviews of the Earth and Planetary Sciences*, v. 36, p. 59-95.

Kneller, E.A., Long, M.D., and van Keken, P.E. (2008) Olivine fabric transitions and shear wave anisotropy in the Ryukyu subduction system, *Earth and Planetary Science Letters*, v. 268, p. 268-282.

Liu, Q. and Hansen, N. (1995) Deformation microstructure and orientation of F.C.C. crystals, *Physica Status Solidi (A) Applied Research*, v. 149, p. 187-199.

Liu, Q., Juul Jensen, D., and Hansen, N. (1998) Effect of grain orientation on deformation structure in cold-rolled polycrystalline aluminium, *Acta Materialia*, v. 46, p. 5819-5838.

McInnes, B.I.A., Gregoire, M., Binns, R.A., Herzig, P.M., and Hannington, M.D. (2001) Hydrous metasomatism of oceanic sub-arc mantle, Lihir, Papua New Guinea: petrology and geochemistry of fluid-metasomatised mantle wedge

xenoliths, *Earth and Planetary Science Letters*, v. 188, p. 169-183.

Michibayashi, K., and Mainprice, D. (2004) The Role of Pre-existing Mechanical Anisotropy on Shear Zone Development within Oceanic Mantle Lithosphere: an Example from the Oman Ophiolite, *Journal of Petrology*, v. 45, p. 405-414.

Nakamura, Y., and Kushiro, I. (1974) Composition of gas phase in Mg_2SiO_4-SiO_2-H_2O at 15 kbar, *Carnegie Institute Washington Yearbook* v. 73, p. 255-258.

Ryabchikov, I.D., Schreyer, W., and Abraham, K. (1982) Compositions of aqueous fluids in equilibrium with pyroxenes and olivines at mantle pressures and temperatures, *Contributions to Mineralogy and Petrology*, v. 79, p. 80-84.

Satsukawa, T., and Michibayashi, K. (2009) Determination of slip system in olivine based on crystallographic preferred orientation and subgrain-rotation axis: Examples from Ichinomegata peridotite xenoliths, Oga peninsula, Akita prefecture, *J. Geol. Soc. Jpn*, v. 115, p. 288-291.

Schneider, M.E., and Eggler, D.H. (1986) Fluids in equilibrium with peridotite minerals: Implications for mantle metasomatism, *Geochimica et Cosmochimica Acta*, v. 50, p. 711-724.

Soustelle, V., Tommasi, A., Demouchy, S., and Ionov, D.A. (2010) Deformation and Fluid-Rock Interaction in the Supra-subduction Mantle: Microstructures and Water Contents in Peridotite Xenoliths from the Avacha Volcano, Kamchatka, *Journal of Petrology*, v. 51, p. 363-394.

Tommasi, A., Vauchez, A., and Ionov, D.A. (2008) Deformation, static recrystallization, and reactive melt transport in shallow subcontinental mantle

xenoliths (Tok Cenozoic volcanic field, SE Siberia), *Earth and Planetary Science Letters*, v. 272, p. 65-77.

van der Veen, C.J. and Whillans, I.M. (1994) Development of fabric in ice, *Cold Regions Science and Technology*, v. 22, p. 171-195.

von Mises, R. (1928) Mechanik der plastischen Formandern von Kristallen, *Zeitschrift fur Angewandte Mathematik und Mechanik*, v. 8, p. 161-185.

Warren, J.M., Hirth, G., and Kelemen, P.B. (2008) Evolution of olivine lattice preferred orientation during simple shear in the mantle, *Earth and Planetary Science Letters*, v. 272, p. 501-512.

Webber, C., Newman, J., Holyoke Iii, C.W., Little, T. and Tikoff, B. (2010) Fabric development in cm-scale shear zones in ultramafic rocks, Red Hills, New Zealand, *Tectonophysics*, v. 489, p. 55-75.

Chapter 8. Olivine fabrics from the Higashi-Akaishi and Imono Peridotites: Insights into olivine fabric transitions

8.1. Introduction

One key aspect of olivine fabric development that needs to be more thoroughly understood is the evolution of olivine fabric types and the transition of one fabric to another. Recent studies by Lee *et al.*(2002), Warren *et al.*(2008), Webber *et al.*(2010) and Skemer *et al.*(2010, 2012) have focused on the evolution of olivine fabrics in peridotite, highlighting several important controls on the development of fabrics from aggregates with a pre-existing LPO. Significant factors include the reference frame in which the LPO is considered (Webber *et al.*,2010), the inference of shear sense from different fabrics (Skemer *et al.*,2012) and the potential change of deformation mechanism to grain-size sensitive deformation (Skemer *et al.*,2010).

The mutual consistency between intragrain deformation microstructures and bulk LPO highlighted in Chapters 6 and 7 has a useful application for analysing mantle xenoliths that lack a kinematic reference frame. This relationship however, can only be applied to peridotites that have achieved a steady-state of deformation. Peridotites within dynamic environments such as the mantle wedge are likely to be subject to geologically rapid changes in conditions, and thus the relationship between intragrain microstructure and LPO may be inconsistent. This inconsistency can provide a snapshot of a changing environment, and if carefully unraveled can also provide extremely useful information regarding the nature of deformation in the mantle wedge.

This chapter presents the results of EBSD analysis on two Japan peridotites that record evidence for a transition between two different fabric types. The Higashi-Akaishi and Imono peridotite bodies record a sequence of events related to the initial deformation of peridotite in the Earth's upper mantle and subsequent orogenic

exhumation as part of the Sanbagawa metamorphic belt and thus are ideal for investigating the development of olivine fabrics.

8.2. Samples and methodology

Samples J909C from the Imono peridotite body, and J919B_1 from the Higashi-Akaishi peridotite body were analysed using EBSD. The petrography of both samples was described in detail in Chapter 5 and Appendix 2, however for reference a short summary is provided below and in Table 8.1.

J909C is a very fine-grained, porphyroclastic, metasomatised spinel dunite with a pervasive foliation containing olivine, chromite, antigorite, magnetite and pentlandite. Porphyroclastic olivine comprises 57% of the rock and ranges in grain size from 0.5 – 2.0 mm, with an average of 0.7 mm. Neoblastic olivine comprises 10% of the rock and ranges in grain size from 0.05 – 0.4 mm, with an average grain size of 0.3 mm. The pervasive foliation is primarily defined by antigorite and the mineral lineation is defined by both SPO and alignment of deformed olivine (often forming clusters of grains resembling pods) and alignment of bladed antigorite. Microlithons are well-developed in this sample, comprised of antigorite-poor/olivine-rich and antigorite-rich/olivine-poor regions, the boundaries of which are parallel to the main foliation. The antigorite-rich zone contains predominantly neoblastic olivine with isolated porphyroclasts and has a very strong foliation, representing a D_3 fabric (Mizukami and Wallis, 2005). The olivine-rich region is noticeably coarser and more poorly foliated, potentially preserving an earlier D_{2B} fabric. The antigorite-rich zone in J909C also contains a crenulation cleavage at a high angle (~45°) to the dominant foliation.

J919B_1 is a very fine-grained, porphyroclastic, metasomatised spinel dunite containing olivine, chromite, antigorite, serpentine, magnetite and pentlandite. Porphyroclastic olivine comprises 7% of the rock and ranges in grain size from 0.4 – 0.8 mm, with an average of 0.5 mm. Neoblastic olivine comprises 58% of the rock

and ranges in grain size from 0.06 – 0.1 mm, with an average grain size of 0.09 mm. The dunite has a weak pervasive foliation and lineation defined primarily by chromite layers and elongation and alignment of deformed olivine, as well as alignment of acicular grains of antigorite although this is not significant. The mineral lineation is defined by alignment of the long axes of elongate chromite and olivine grains. Due to the sparseness of the antigorite and recrystallised nature of the olivine, the fabric of J919B_1 is consistent with that of the D_{2A} of Mizukami and Wallis (2005).

Table 8.1. Modal proportions of minerals in Japan dunites J909C and J919B_1.

	J909C	J919B_1
Olivine	67%	65%
Chromite	1.5%	5%
Magnetite	1%	3%
Pentlandite	0.5%	2%
Antigorite	30%	5%
Serpentine	-	20%

EBSD stage mapping of olivine at various resolutions was undertaken over regions of the oriented thin sections in order to characterise the bulk fabrics of the peridotites. The procedure for EBSD mapping is described in detail, and acquisition and processing parameters are given in Chapter 4.

8.3 EBSD Results

8.3.1. J909C

Three regions of sample J909C were mapped using EBSD (Figure 8.1), including one map in the olivine-rich microlithon (Figure 8.1, Map 3), and two maps in the crenulated antigorite-rich zone (Figure 8.1, Maps 1 and 2).

The EBSD data from map 1 shows that the olivine within the antigorite-rich region has an LPO (Figure 8.2). The LPO pattern is complicated and relatively scattered. The complex dataset shows [001] axes parallel to X and [010] and [100] forming a girdle in the (001) plane. Inverse pole figures (IPFs) show that [001] is aligned

parallel to the shear direction, with [010] and [100] axes showing dispersion in terms of the shear plane normal.

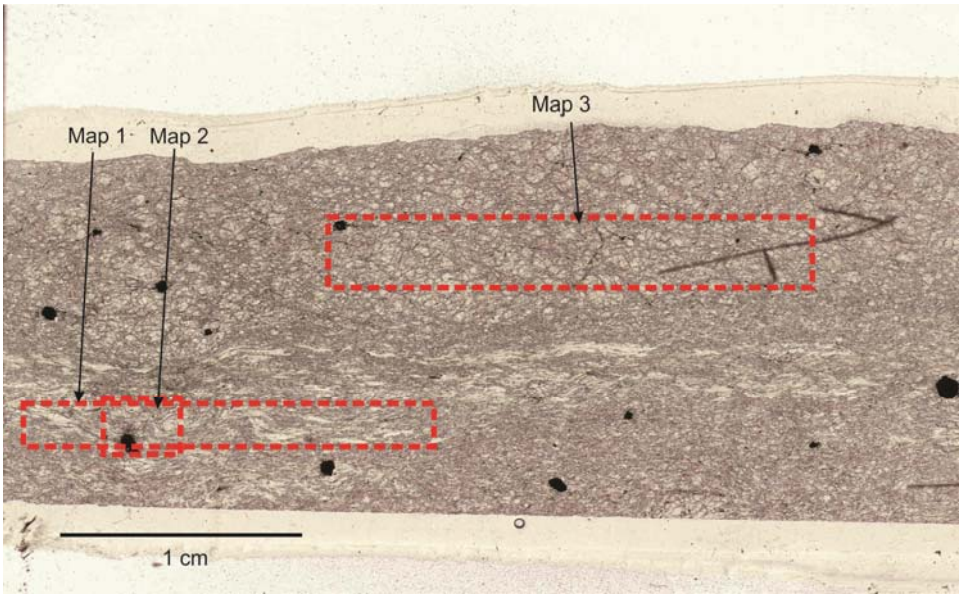

Figure 8.1. Locations of EBSD stage maps on sample J909C. The top half of the section is the coarse olivine-rich region, and the bottom half is the more sheared antigorite-rich region. The lineation direction is E-W and the foliation is horizontal and coming out of the page (this is the same for all of the samples).

The alignment of [001] parallel to X indicates that the fabric is either a B- or C-type, however the girdle formed by the [100] and [010] axes in both the pole figures and IPFs is inconsistent with any known fabric types. It is consistent with a slip system defined by pencil glide (*hk*0) with [001] slip (Carter and Avé Lallemant, 1970; Karato *et al.*,2008), which on a bulk scale appears to have a similar LPO pattern to the D-type olivine LPO, but with [001] parallel to X. This could potentially represent a previously unidentified olivine fabric type. An examination of the low-angle 1 - 10° rotation axes reveals that these are strongly clustered parallel to [100], which is associated with a B-type fabric. With respect to the kinematic reference frame, the rotation axes are unexpectedly clustered parallel to Z, when for simple shear these are expected to be parallel to Y. Thus the low-angle rotation axes, which reflect the operation of slip systems on a grain scale, are inconsistent with the bulk LPO.

The porphyroclastic grains in this sample (Figure 8.2, map 2) have a different orientation to that of the bulk fabric. [100] axes are parallel to Z, [010] axes are sub-parallel to X and [001] axes are parallel to Y. The orientations of the grains suggest that within the given kinematic reference frame, [010] is the slip direction and (100) is the slip plane. This is inconsistent with any known slip systems, thus it is likely that this reference frame is incorrect for these grains as they represent a different deformation event. There are relatively very few low-angle rotation axes preserved inside grain 1 (246 points) and these are very scattered (Figure 8.2). There is an abundance of rotation axes preserved within grain 2 (1271 points), which are parallel to [100], consistent with slip within (010)[001]. However, these are not systematically arranged into low-angle boundaries, and thus there is no tilt-boundary trace to strengthen this interpretation.

The EBSD data in the coarser olivine-rich region (map 3; Figure 8.2) shows that the olivine has a strong LPO. The [001] axes are parallel to X, the [010] axes are sub-parallel to Y and the [100] axes are sub-parallel to Z. This LPO pattern is consistent with a B-type fabric. IPFs show that [001] is parallel to the shear direction, with [010] parallel to the shear plane normal, also indicating slip by (010)[001], a B-type fabric. The low-angle 1 – 10° rotation axes however, show that rotation is primarily occurring around [010], and to a lesser degree [100] and [001]. The rotation axes for a B-type fabric is the [100] axis and thus the internal microstructure and LPO are inconsistent. As observed in map 1, the low-angle rotation axes are also clustered parallel to Z instead of Y, as would be expected.

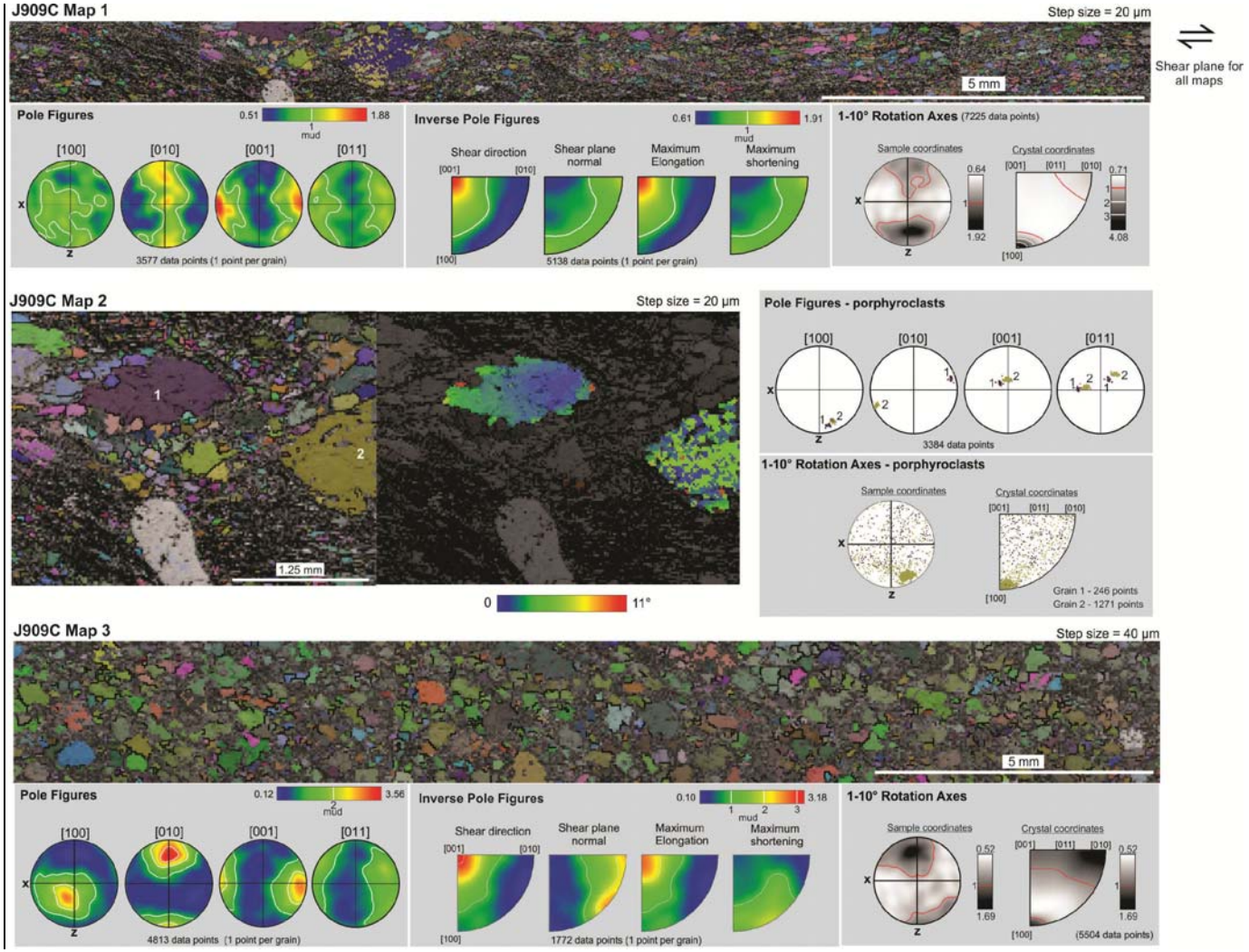

Figure 8.2. EBSD All Euler maps, pole figures, inverse pole figures and rotation axes for Imono sample J909C. The pole figures are equal area, lower hemisphere projections and all contouring was using a half width of 20°. Inverse pole figures are equal area upper hemisphere projections, and show the crystallographic axes with respect to the kinematic framework. Contour intervals vary between plots and represent multiples of uniform density (mud). The figure also includes rotation axes plotted within a crystallographic framework to ease identification of the orientation of the rotation axis. The All Euler map legend is provided in Chapter 4 (Figure 4.5). There is also a texture map of the porphyroclasts provided, showing the intragrain orientation variations with respect to an arbitrarily defined reference point. The large pale grey grain in maps 1 and 2 is chromite. The All Euler maps are underlain by band contrast maps.

8.3.2. J919B_1

Two regions of sample J919B_1 were mapped (Figure 8.3). There is little difference between the two regions, both contain neoblastic olivine and are cross-cut by serpentine-filled fractures. Pole figures of olivine grains in J919B_1 map 2 (Figure 8.4) show a distinct LPO. [001] is strongly clustered parallel to X, indicating that this is the bulk slip direction. [100] is clustered sub-parallel to Y and [010] is clustered sub-parallel to Z, although both [100] and [010] are show some weak dispersion within the (001) plane. These appear to be consistent with a C-type bulk LPO ((100)[001]), although the dispersion suggests there could also be a component of slip within {hk0}[001]. IPFs show [001] alignment with the shear direction, but the shear plane normal shows dispersion between the [100] and [010] axes, consistent with the {hk0}[001] slip system. Examination of the low-angle 1 - 10° rotation axes reveal clustering parallel to [100], consistent with a B-type LPO ((010)[001]), which is inconsistent with both the bulk fabric and the IPFs. Rotation axes are clustered parallel to the Z direction of the kinematic framework.

Pole figures of J919B_1 map 5 (Figure 8.4) show a weaker olivine LPO, with [001] parallel to X. [100] and [010] are dispersed and show a girdle pattern within the (001) plane. The IPFs are similar to those in map 2, with alignment of [001] and dispersion of [100] and [010] with respect to the shear plane normal. This is also seen in J909C and is only consistent with deformation within (*hk*0)[001] at low temperature and high strain rate (Carter and Avé Lallemant, 1970; Karato *et al.*,2008). However, low-angle 1 – 10° rotation axes show evidence for predominant rotation around [100], which is associated with a B-type LPO. As observed in the other maps, the rotation axes are parallel to Z.

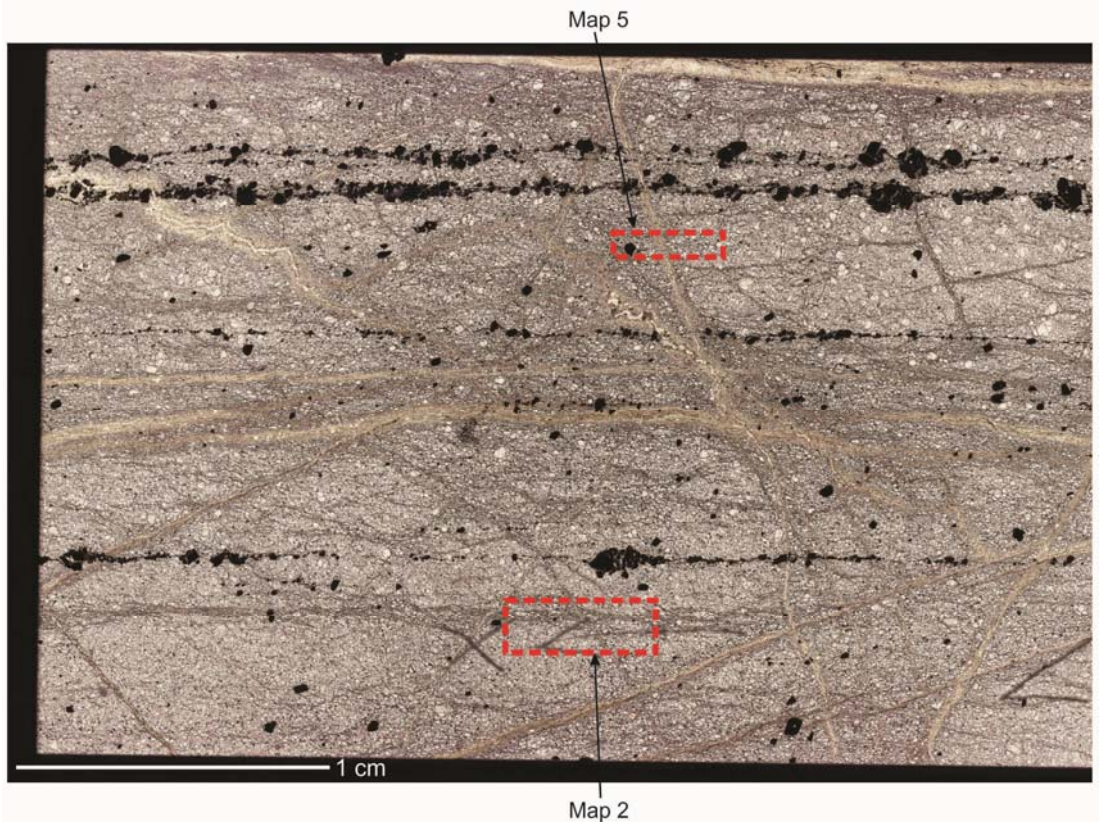

Figure 8.3. Location of the EBSD stage maps on sample J919B_1.

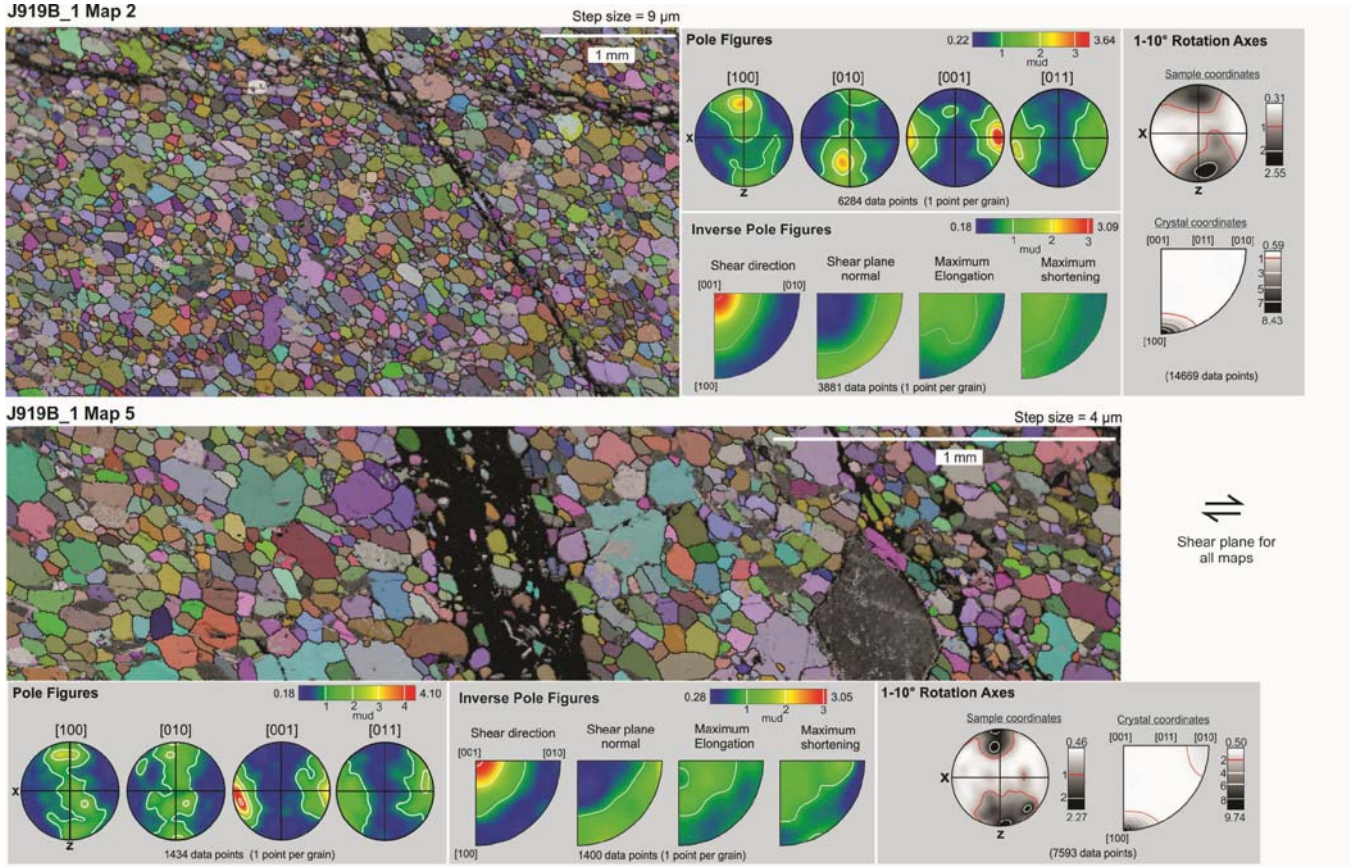

Figure 8.4. EBSD All Euler maps, pole figures, inverse pole figures and rotation axes for Higashi-Akaishi sample J919B. The pole figures are equal area, lower hemisphere projections and all contouring was using a half width of 20°. Contour intervals vary between plots and represent multiples of uniform density (mud). The figure also includes rotation axes plotted within a crystallographic framework to ease identification of the orientation of the rotation axis. The All Euler map legend is provided in Chapter 4 (Figure 4.5). The All Euler maps are underlain by band contrast maps.

8.4. Interpretation and discussion

8.4.1. Olivine fabric types and transitions

EBSD data reveals complexity in the LPO patterns of the Japan peridotites. Both J909C and J919B_1 have LPOs consistent with deformation by {hk0}[001], (010)[001] and (100)[001]. The olivine in the olivine-rich microlithon in J909C exhibits a clear B-type LPO (map 3, Figure 8.2), and map 2 of J919B_1 exhibits a C-type LPO (Figure 8.4). The rotation axes for the C-type and {hk0}[001] fabrics (J909C map 1, J919B_1 maps 2 and 5) plot parallel to the [100] axis, which is consistent with a B-type fabric ((010)[001]). The rotation axes for the B-type fabric (map 3) plot parallel to the [010] axis, which is consistent with either a C-((100)[001]) or E-type fabric ((001)[100]). All of the slip systems interpreted using the low-angle rotation axes are characterised by [001] slip, which is consistent with the bulk fabric slip direction of [001]. This provides further evidence for the systematic relationship between the bulk fabric and intragrain slip directions observed in the Lihir data (Chapters 6 and 7), and indicates that this is a reasonably reliable method for estimating the slip direction in unoriented peridotite xenoliths. However, it appears that the slip planes indicated by the bulk fabric and intragrain rotation axes may not share this systematic relationship. The slip systems interpreted using the low-angle rotation axes are not consistent with the slip system interpreted from the LPO. The 1 - 10° rotation axes of both samples are inconsistent with the olivine LPOs in terms of two key aspects, which provide further information regarding the deformation history of the sample: 1) the rotation axes plotted in terms of crystallographic axes align parallel to a crystallographic axis that is inconsistent with the bulk LPO slip system; 2) rotation axes plotted in terms of the kinematic reference frame are aligned with Z, when for simple shear, these should align with Y.

There are two potential reasons for this disparity: 1) The rotation axes are very recent and linked to a late overprinting of the older (010)[001], (100)[001] and {hk0}[001] fabrics, with a new kinematic reference frame imposed on the peridotite. 2) The

rotation axes may represent the activation of the ‘hard’ slip systems, whereas the LPO records the activation of the ‘easy’ slip systems.

LPO is generally thought to represent the final stage of deformation, and low-angle boundaries represent a transient increment of strain with only evidence for the ‘hard’ slip systems preserved, and thus are inherently inconsistent (Tommasi *et al.,* 2008; Soustelle *et al.,* 2010; Falus *et al.,* 2011). It is possible that this is the case for these samples, although this does not explain why consistency between slip directions is observed in both the Japan and Lihir peridotites. It is more likely that the inconsistency reflects an overprinting relationship and marks a transition between two fabric types: the LPOs when observed with respect to the current dominant foliation and lineation preserve an old LPO, but the grains are deforming by different slip systems associated with a new kinematic reference frame.

The low-angle rotation axes of both Japan samples plot sub-parallel to the Z direction of the kinematic reference frame. For deformation dominated by simple shear, the Y direction should act as the rotation axis (Figure 8.5). Reddy and Buchan (2005) observe a coincidence between the bulk rotation axis, misorientation axes associated with low-angle boundaries and rotation axes associated with crystallographic dispersion in calcite, such that the kinematic framework controls the activation of slip systems. The implication of these observations is that the intragrain microstructure reflects the bulk kinematic rotation axis, Y. In contrast to this, the Japan EBSD data may have formed as a result of general shear, reflecting a combination of pure and simple shear, for which the bulk kinematic rotation axis is not necessarily parallel to Y.

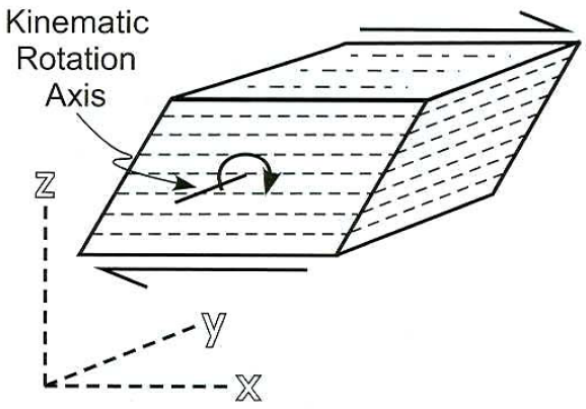

Figure 8.5. The standard kinematic reference frame for deformation by simple shear. The X direction lies parallel to the stretching lineation, the XY plane represents the foliation plane, and the Y direction is the kinematic rotation axis. Figure from Reddy and Buchan (2005).

Alternatively, the bulk rotation axes of the Japan samples appear to be consistent with a vertically oriented foliation plane roughly parallel to the XZ plane of the old kinematic reference frame. Geographically, this would correspond to a steeply-dipping to sub-vertical E-W trending foliation. Foliation data from J909C are folded, with the fold axial plane on an orientation that is consistent with the orientation of both the steep to sub-vertical S_3 foliation measured in the field (Chapter 3 and by Mizukami and Wallis, 2005), or F_4 axial planes measured by Mizukami and Wallis (2005) (Figures 8.6a and 8.7d, f). The data seem to fit the S_3 foliation better than the F_4 axial planes. However, the rotation axes of both J909C and J919B_1 indicate that both samples are affected by this new kinematic reference frame and J919B_1 shows no petrographic evidence for overprinting by S_3, which is characterised by a pervasive, well-developed antigorite schistosity. The D_4 deformation is characterised by open folding of the earlier fabrics, with SE-NW trending fold axes and the lack of development of a new schistosity (Mizukami and Wallis, 2005). The lack of D_4 schistosity development explains why there is no foliation on this orientation observed in the Japan samples, particularly in J919B_1. Based on this information, the low-angle rotation axes in these samples are interpreted to correspond to the Y direction of the F_4 axial plane, however it is possible that these are related to D_3. This provides further evidence for the inconsistent rotation axes discussed earlier being caused by a different deformation event, rather than representing the 'hard' slip system.

Recent studies have observed that a pre-existing LPO will control the development of a subsequent LPO (Michibayashi and Mainprice, 2004; Warren *et al.*, 2008; Webber *et al.*, 2010). In the study done by Warren *et al.* (2008), the kinematic reference frame of the shear zone with respect to the existing LPO was differently oriented, and the crystallographic axes sub-parallel to the Y direction of the shear zone were favourably oriented to become the rotation axes, thus controlling the active slip system. Applying this concept to the Japan samples, the D_2 deformation event of Mizukami and Wallis (2005) is characterised by a B-type fabric, with [010] maxima parallel to Z, as seen in J909C map 3. The 1 - 10° rotation axes however, plot parallel to [010]. The D_4 kinematic reference frame has a foliation plane sub-parallel to the S_2 XZ plane, thus the [010] axes of the B-type fabric are oriented parallel to the new Y direction and are thus favourably oriented to accommodate rotation within the new reference frame (Figures 8.7b and 8.8). For the C-type fabric with [100] maxima sub-parallel to Z, in terms of the D_4 kinematic reference frame this becomes the new rotation axis (Figure 8.8), consistent with rotation axes plotting parallel to [100] on a crystal axis coordinate plot. The {hk0}[001] fabrics have a girdle of both [010] and [100], which results in both of these axes accommodating rotation within the new reference frame, which is why rotation axes cluster parallel to both [010] and [100] on crystal coordinate plots, albeit with [100] dominant (Figure 8.8).

a)

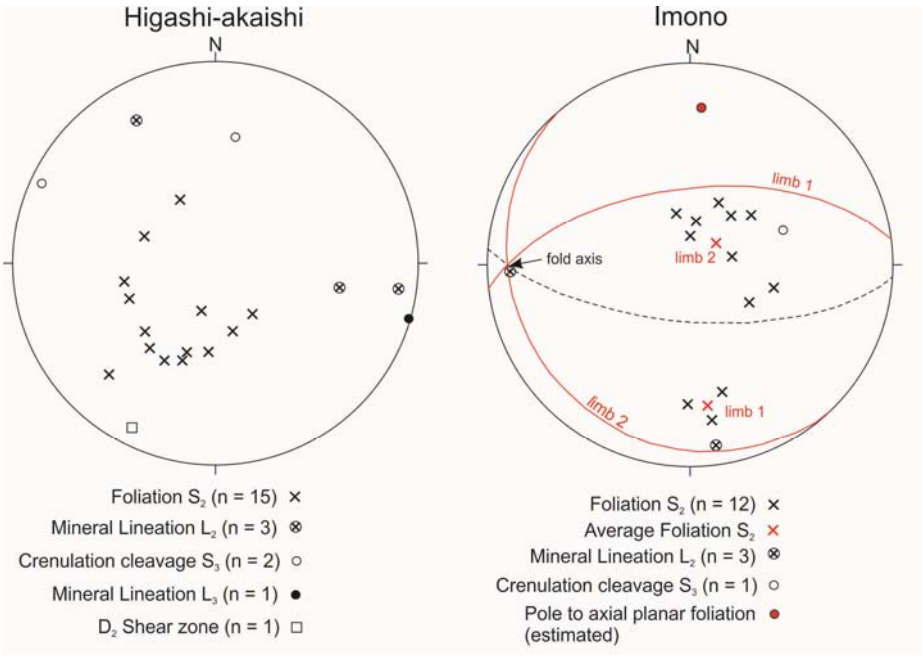

b)

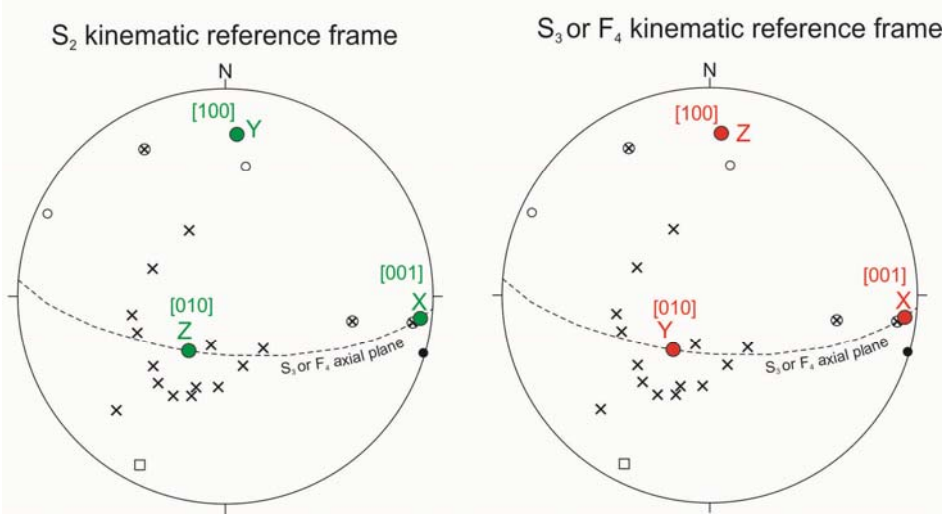

Figure 8.6. a) Structural measurements from the Higashi-Akaishi and Imono peridotites. There is no obvious folding of S_2 in the Higashi-Akaishi region, but the S_2 foliations measured in the Imono peridotites cluster in two distinct orientations, suggesting these have been folded. The axial planar foliation estimated from these fold limbs has an orientation similar to the S_3 crenulation cleavage measured in Higashi-Akaishi, and is also similarly oriented to the S_3 measurements of Mizukami and Wallis (2005) (Figure 8.7d). Within error, the axial planar foliation may also be consistent with the F_4 axial planes measured by Mizukami and Wallis (2005) (Figure 8.7f). b) Comparing the new kinematic reference frame with the D_2 structural data from Higashi-Akaishi, the XY plane of the new reference frame is parallel to the XZ plane of S_2, with poles to foliation showing the S_2 Z direction, and L_2 mineral lineations showing the X direction, which are sub-parallel to the fold axis, within error. All pole figures are lower hemisphere equal area projections.

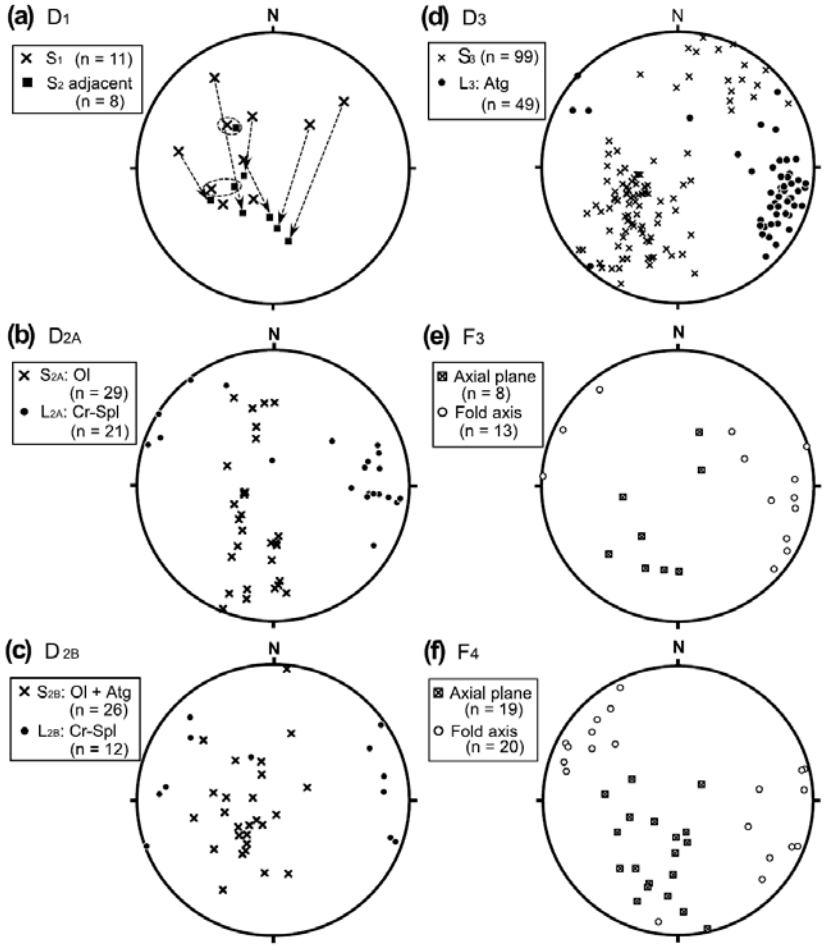

Figure 8.7. Orientations of the foliations and lineations corresponding to each deformation event to affect the Higashi-Akaishi peridotite. Figure from Mizukami and Wallis (2005).

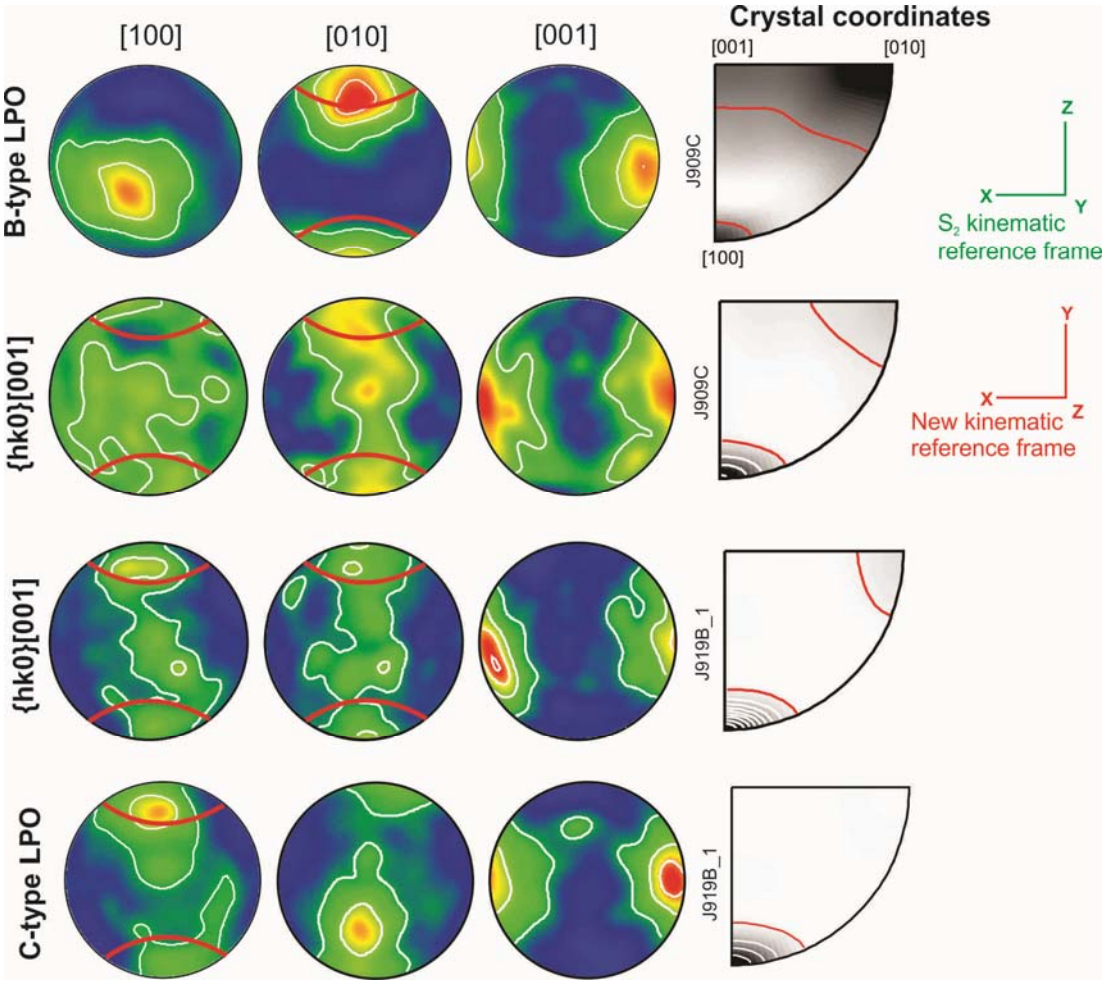

Figure 8.8. Schematic diagram showing that the inconsistency between the bulk fabrics and rotation axes in the Japan data can be explained by examining the rotation axes within the kinematic reference frame of a later deformation event, with a foliation plane parallel to the old XZ plane. The red small circles in the coloured pole figures represent the new rotation axis. If the D_2 Z direction is assumed to be the new Y direction, the rotation axes plotted in terms of crystal coordinates can be interpreted in a new light, and show good agreement with the bulk rotation axis of the new reference frame.

This also enables the interpretation of the fabric types associated with the new kinematic reference frame. Structural data suggests that X is common to both the new and old reference frames, thus the slip direction for the new fabrics is [001]. Both the {hk0}[001] fabrics are interpreted to remain the same, that in both reference frames they are characterised by a [001] parallel to the lineation, and a girdle of [100] and [010] within the (001) plane. The new fabric corresponding to the B-type LPO is interpreted to be a C-type fabric ((100)[001]), with [010] parallel to the Y direction of the kinematic framework. Conversely, the C-type LPO re-interpreted within the later reference frame is consistent with a B-type LPO, with [100] parallel

to X. This data highlights that there is a strong control of the existing LPO on new fabric development.

The EBSD data from both Lihir and Japan samples are in good agreement with the observations of Michibayashi and Mainprice (2004), Warren *et al*. (2008) and Webber *et al*. (2010) who highlight that the activation of slip systems appears to be controlled by the existing orientation of the grains. The data also provide an explanation for the inconsistencies between the rotation axes of individual grains and the bulk fabrics in terms of both orientation and their corresponding crystallographic axis. Thus while the intragrain slip directions are systematically linked to the bulk LPO and can be used to estimate the bulk slip direction where there is no macroscopic lineation, the slip plane and therefore rotation axis orientations are not systematic and vary as a result of fabric overprinting.

8.4.2. Implications for supra-subduction zone deformation conditions

The LPO patterns of both samples are complicated, as a result of the complex deformation history of the Higashi-Akaishi region. In J909C, there are two different olivine fabrics preserved within the different regions of the sample. The coarser, olivine-rich microlithon is interpreted to preserve an LPO related to the D_{2B} deformation event of Mizukami and Wallis (2005). D_{2B} is related to deformation and serpentinisation due to influx of slab fluids within the mantle wedge above a subduction zone (Mizukami *et al.,* 2004; Mizukami and Wallis, 2005; Tasaka *et al.*,2008; Hattori *et al*., 2009). EBSD analysis of this region indicates a B-type LPO, consistent with observations of a B-type LPO in the Imono peridotite body by Tasaka *et al.* (2008). The antigorite-rich region is a later exhumation-related overprint representing D_3, and olivine LPO patterns have not been reported in the literature for this deformation event. These results show that the LPO in this region is consistent with an {hk0}[001] fabric, which was not reported as one of the main olivine fabrics by Jung *et al*. (2006), but is associated with low-temperatures and a high strain rate (Carter and Avé Lallemant, 1970; Karato *et al.*,2008). Dynamic recrystallisation also

has considerably weakened the LPO in antigorite-rich region, consistent with the observations of Lee *et al.* (2002) and Skemer *et al.* (2010).

The foliation, lineation and mineralogy of J919B_1 are consistent with the D_{2A} fabric of Mizukami and Wallis (2005), which is characterised by a B-type LPO. Similar olivine LPO patterns are observed in J919B_1 as in J909C, although the fabric types are not organised into distinct microstructural domains as in J909C, nor are the different LPOs restricted to certain grain size populations. The LPO pattern in map 5 is consistent with an {hk0}[001] fabric, as with the antigorite-rich zone in J909C. Map 2 has a C-type olivine LPO, with weak dispersion of [100] and [010].

The olivine LPO patterns in both J909C and J919B_1 are thus interpreted to reflect the overprinting of B- and C-type fabrics developed in the mantle wedge with one or more exhumation-related fabrics dominated by {hk0}[001] slip (either D_3 or D_4, or both), which are controlled by the existing LPO (as discussed in 8.4.1).

C-type olivine fabrics are thought to develop under hydrous, low to moderate stress conditions and B-type fabrics under hydrous, high stress conditions (Jung *et al.,* 2006), consistent with conditions predicted for the forearc mantle wedge (e.g. Kneller *et al*, 2007; Karato, 2008). The observation of a B-type LPO in mantle fabrics has implications for seismic anisotropy above the mantle wedge, and the significance of this will be discussed in Chapter 10. The {hk0}[001] fabric observed represents low temperature, high strain conditions (Carter and Avé Lallemant, 1970; Karato *et al.,*2008), which although can be attributed to the pre-existing LPO, is also consistent with exhumation of the peridotite.

8.5. Summary

- Japan samples J909C (Imono peridotite) and J919B_1 (Higashi-Akaishi peridotite) are comprised of complicated LPO patterns. J909C records a B-type fabric in the region of the sample consistent with mantle deformation

during D_2. The serpentinised region of J909C records an {hk0}[001] fabric Different regions of J919B_1 record both an {hk0}[001] fabric and a C-type fabric. B- and C-type fabrics are consistent with deformation in the forearc mantle wedge, and the {hk0}[001] fabric is interpreted to reflect exhumation-related deformation.

- The pre-existing LPO appears to provide a strong control on the activation of later slip systems, with the crystal axes aligned with the new kinematic reference frame Y direction more likely to act as low-angle rotation axes for the new slip system.

8.6. References

Carter, N.L. and Ave'Lallemant, H.G. (1970) High temperature flow of dunite and peridotite, *Geological Society of America Bulletin*, v. 81, p. 2181-2202.

Escartín, J., Hirth, G. and Evans, B. (2001) Strength of slightly serpentinized peridotites: Implications for the tectonics of oceanic lithosphere, *Geology*, v. 29, p. 1023-1026.

Hermann, J., Müntener, O. and Scambelluri, M. (2000) The importance of serpentinite mylonites for subduction and exhumation of oceanic crust, *Tectonophysics*, v. 327, p. 225-238.

Jung, H., Katayama, I., Jiang, Z., Hiraga, T. and Karato, S. (2006) Effect of water and stress on the lattice-preferred orientation of olivine, *Tectonophysics*, v. 421, p. 1-22.

Karato, S., Jung, H., Katayama, I. and Skemer, P. (2008) Geodynamic Significance of Seismic Anisotropy of the Upper Mantle: New Insights from Laboratory Studies, *Annual Reviews of the Earth and Planetary Sciences*, v. 36, p. 59-95.

Lee, K.-H., Jiang, Z. and Karato, S. (2002) A scanning electron microscope study of the effects of dynamic recrystallization on lattice preferred orientation in olivine, *Tectonophysics*, v. 351, p. 331-341.

Michibayashi, K., and Mainprice, D. (2004) The Role of Pre-existing Mechanical Anisotropy on Shear Zone Development within Oceanic Mantle Lithosphere: an Example from the Oman Ophiolite, *Journal of Petrology*, v. 45, p. 405-414.

Mizukami, T., and Wallis, S.R. (2005) Structural and petrological constraints on the tectonic evolution of the garnet-lherzolite facies Higashi-akaishi peridotite body, Sanbagawa belt, SW Japan, *Tectonics*, v. 24, p. 1-17.

Mizukami, T., Wallis, S.R. and Yamamoto, J. (2004) Natural examples of olivine lattice preferred orientation patterns with a flow-normal a-axis maximum, *Nature*, v. 427, p. 432-436.

Reddy, S.M. and Buchan, C. (2005) Constraining kinematic rotation axes in high-strain zones: a potential microstructural method?, *Geological Society, London, Special Publications*, v. 243, p. 1-10.

Skemer, P., Warren, J.M. and Hirth, G. (2012) The influence of deformation history on the interpretation of seismic anisotropy, *Geochemistry Geophysics Geosystems*, v. 13, p. Q03006.

Skemer, P., Warren, J.M. and Kelemen, P.B. (2010) Microstructural and rheological evolution of a mantle shear zone, *Journal of Petrology*, v. 51, p. 43-53.

Tasaka, M., Michibayashi, K. and Mainprice, D. (2008) B-type olivine fabrics developed in the fore-arc side of the mantle wedge along a subducting slab,

Earth and Planetary Science Letters, v. 272, p. 747-757.

Warren, J.M., Hirth, G. and Kelemen, P.B. (2008) Evolution of olivine lattice preferred orientation during simple shear in the mantle, *Earth and Planetary Science Letters*, v. 272, p. 501-512.

Webber, C., Newman, J., Holyoke Iii, C.W., Little, T. and Tikoff, B. (2010) Fabric development in cm-scale shear zones in ultramafic rocks, Red Hills, New Zealand, *Tectonophysics*, v. 489, p. 55-75.

Chapter 9. Deformation microstructure, fluid-rock interaction and isotope geochemistry

Fluids play a key role in the tectonic and metamorphic evolution of the Earth's lithosphere, particularly in dynamic regions such as subduction zones, where a cold, wet slab is juxtaposed with a hot, dry mantle. Hydrous fluids are responsible for initiating melting at subduction zones (Gaetani and Grove, 1998), facilitating chemical exchange and mass transfer (including transport and deposition of metals such as gold and copper; McInnes *et al*., 1999), and the development of olivine fabrics (Jung and Karato, 2001; Jung *et al*., 2006) in the mantle.

The link between mantle deformation, fluids and geochemistry is of particular interest. Recent evidence suggests that there is a link between olivine deformation on a grain-scale and geochemistry (Ando *et al*., 2001; Murata *et al*., 2009; Plümper *et al*., 2012), with observations of Fe and Mg interdiffusion along low-angle boundaries in olivine. Low-angle boundaries may also act as pathways for the migration of hydrous fluids, providing a means for water to enter the olivine crystal structure. Water affects the slip system type by which mantle olivine deforms through preferentially enhancing c- (or [001]) slip (Mackwell *et al*., 1985; Karato, 1995). On a larger scale this leads to the development of different olivine fabric types, which may change the alignment of seismic fast axes and thus influence interpretations of mantle flow directions from seismic anisotropy.

This chapter will examine this relationship in detail, using observations and analysis of natural mantle olivine from both Lihir and Japan. Section 9.1 is an investigation into the geometry of grain-scale fractures and fluid inclusions within mantle olivine. The observations shed light on the grain-scale mechanisms for fluid migration and the incorporation of water into the olivine structure, and the implications for co-existing brittle and ductile deformation. Sections 9.2 and 9.3 present the results of FTIR and Mg and O isotope analysis, revealing the nature of metasomatic fluids in the mantle, identifying melt extraction processes and highlighting a compelling link between geochemistry, fluids and deformation. Section 9.4 provides a discussion of

the results from Sections 9.1 – 9.3, with a more detailed discussion and broader implications discussed in Chapter 10.

9.1. Fluid inclusion morphology and intragrain microstructure

9.1.1. Overview

Fluid inclusion studies provide valuable insight into the processes that occur at depth in the Earth. Inclusions that remain pristine and closed to late-stage processes are chemical repositories that yield valuable information that can be used to establish the nature of environments deep in the Earth's mantle. These regions are otherwise difficult to sample and are clearly inaccessible to direct observation, other than through large-scale remote methods such as seismic studies.

One of the earliest comprehensive studies of fluid inclusions in mantle minerals, including olivine, was undertaken by Roedder (1965), who found CO_2 to be a major phase preserved in inclusions from a wide range of environments. Since then, there have been many studies that have looked at the geochemistry of preserved fluids in mantle minerals (e.g. Roedder, 1965, 1984; Bergman and Dubessy, 1984; Rosenbaum *et al*., 1996; Anderson and Neumann, 2001 and references therein; Frezzotti *et al*., 2012), through techniques such as Raman spectroscopy (Burke, 2001). However, there have been fewer studies on the structure and morphology of fluid inclusions. Green and Radcliffe (1975) observe fluid inclusions and bubbles decorating defects in mantle olivine. Fluid inclusion trails are thought to represent annealed microcracks/fractures in minerals (Green and Radcliffe, 1975; Simmons and Richter, 1976; Wanamaker *et al*., 1990) and provide direct evidence for the role of fluid during deformation (Van den Kerkhof and Hein, 2001). Kranz (1983) provided a thorough review of the literature surrounding microcrack development to that point in time, and highlight that dislocations play a significant role in microcrack development above 500°C. Van den Kerkhof and Hein (2001) and Andersen and Neuman (2001) both provide useful overviews of the petrographic study of fluid inclusions in rocks.

This study focuses on the morphology of fluid inclusions in deformed mantle olivine, and in particular, the relationship between fluid inclusion trails and intragrain microstructure. Petrographic observations enable the identification of a spatial

relationship between fracture geometry, fluid inclusion morphology and low-angle boundaries in olivine.

9.1.2. Sampling and fluid inclusion observations

Thorough descriptions of these samples are provided in Chapter 5 and in Appendix 2 and the descriptions below focus on fluid inclusion morphology and related features in olivine. Intragranular microcracks and fluid inclusions associated with fluid influx were observed in 7 peridotite xenoliths from Lihir with varying degrees of metasomatism (136062, 136063, 136065, 136068, 136069, 136070 and 136090). The fluid inclusions within 4 Alpine-type Japanese peridotites (J902, J904, J908A and J917) were also investigated. A summary of the different types of fluid inclusions observed is provided in Table 9.1.

Table 9.1. Summary of fine and coarse fluid inclusions observed in mantle olivine.

	Fluid Inclusions	
	Coarse	**Fine**
Morphology	Amorphous or spherical	• Strings of spherical bubbles • Vermicular/tubular with "bridge" structures
Size	Average 5-10 µm, range from ~5 – 100 µm	Average ~1 µm
Relationship to internal microstructure	Most commonly randomly oriented. Occasionally seen parallel to low-angle boundaries.	Frequently parallel to low-angle boundaries.

Lihir, Papua New Guinea

- ***136062***

Sample 136062 is a coarse-grained spinel lherzolite with no obvious structural fabric. It consists of olivine, enstatite, clinopyroxene and spinel. The lherzolite is relatively pristine, with no replacement of the primary igneous minerals. Olivine grains show some evidence for dynamic recrystallisation by both grain boundary migration and subgrain rotation. The olivine in sample 136062 is visibly deformed and preserves low-angle boundaries associated with deformation. Many intragranular microcracks within the olivine are partially annealed, forming a network of fine and coarse fluid

inclusions. Small microcracks within these olivine grains are parallel to the low-angle boundaries observed under cross-polarised light (Figure 9.1A). Fine fluid inclusions have a diameter of 1 – 2 μm and form both small circular bubbles and tubular voids that are vermicular in character (Figure 9.1B, C). The long axes of the tubes are frequently observed to run parallel to low-angle boundaries in deformed olivine, and are 'bridged' or connected by shorter tubular structures (Figure 9.1C). Coarse inclusions (~5 μm in diameter) are less common, and are generally amorphous or spherical.

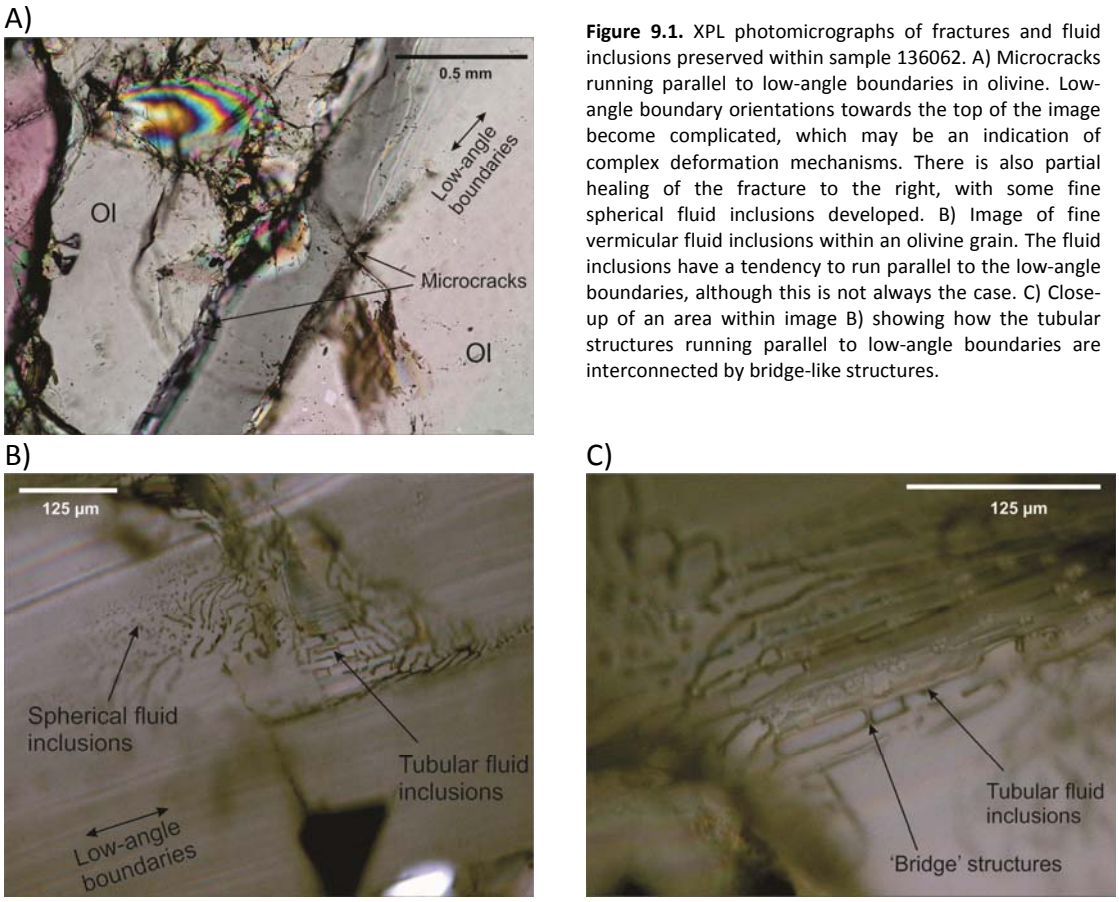

Figure 9.1. XPL photomicrographs of fractures and fluid inclusions preserved within sample 136062. A) Microcracks running parallel to low-angle boundaries in olivine. Low-angle boundary orientations towards the top of the image become complicated, which may be an indication of complex deformation mechanisms. There is also partial healing of the fracture to the right, with some fine spherical fluid inclusions developed. B) Image of fine vermicular fluid inclusions within an olivine grain. The fluid inclusions have a tendency to run parallel to the low-angle boundaries, although this is not always the case. C) Close-up of an area within image B) showing how the tubular structures running parallel to low-angle boundaries are interconnected by bridge-like structures.

- ***136063***

Sample 136063 is a coarse-grained spinel lherzolite, and consists of olivine, enstatite, clinopyroxene, spinel and trace amounts of pyrrhotite. The rock has undergone a degree of metasomatism and primary mantle minerals are replaced by fibrous orthopyroxene (5% of the sample) within thin veins that cross-cut the section. Olivine has a glassy, irregular fracture pattern and most grains preserve low-angle

boundaries (Figure 9.2A). Fractures and microcracks are commonly oriented parallel to the low-angle boundaries (Figure 9.2A) and associated with these are abundant fluid inclusions within the olivine. The fluid inclusions are more abundant in regions of the sample that have undergone more metasomatism. Both coarse and fine fluid inclusions are preserved within the olivine grains (Figure 9.2B). Coarse fluid inclusions are spherical and approximately 5-6 μm in diameter. These are usually randomly oriented and not aligned with any structures within the grains. The fine fluid inclusions (~1 μm in diameter) are very prominent and are vermicular in appearance forming tubular structures as well as strings of spherical bubbles. Commonly both the tubular structures and trails of bubbles are aligned with low-angle boundaries within the olivine grains (Figure 9.2A). There are no 'bridge' structures as seen in sample 136062.

- ***136065***

Sample 136063 is a relatively pristine coarse-grained spinel harzburgite containing olivine, enstatite, clinopyroxene and spinel, with no apparent structural fabric. The olivine grains in this sample have a glassy fracture/microcrack pattern that commonly follows low-angle boundaries preserved within the grains (Figure 9.3A). Associated with the fractures and microcracks are abundant fluid inclusions giving the olivine grains a dusty appearance under the microscope. Amorphous coarse fluid inclusions are very common, and range from 50 – 100 μm in diameter (Figure 9.3B). Associated with these are very fine (<2 μm in diameter) inclusions often vermicular in morphology or forming small spherical bubbles (Figure 9.3B). The long axes of vermicular inclusions or trails of bubbles tend to form parallel to low-angle boundaries (Figure 9.3C).

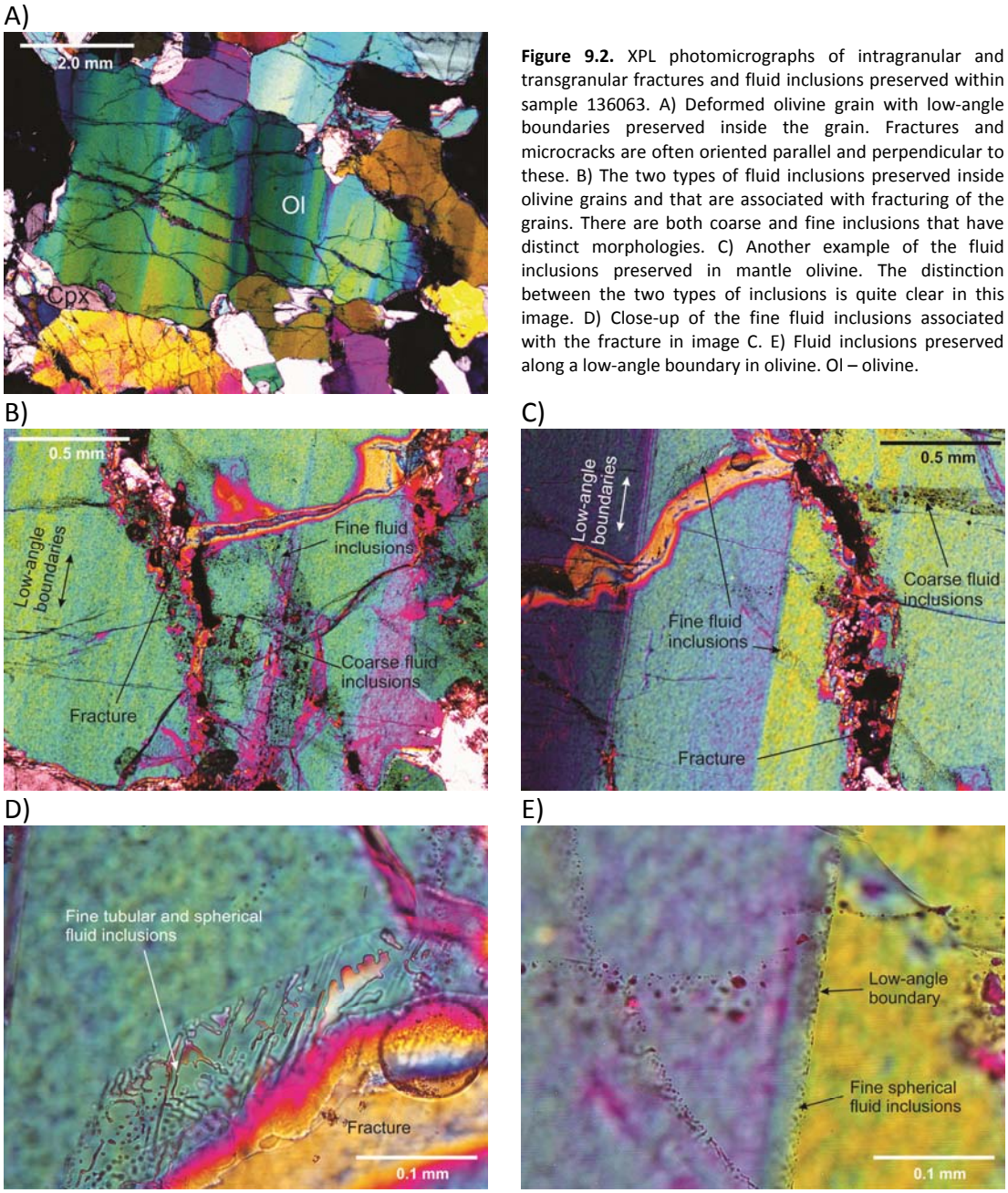

Figure 9.2. XPL photomicrographs of intragranular and transgranular fractures and fluid inclusions preserved within sample 136063. A) Deformed olivine grain with low-angle boundaries preserved inside the grain. Fractures and microcracks are often oriented parallel and perpendicular to these. B) The two types of fluid inclusions preserved inside olivine grains and that are associated with fracturing of the grains. There are both coarse and fine inclusions that have distinct morphologies. C) Another example of the fluid inclusions preserved in mantle olivine. The distinction between the two types of inclusions is quite clear in this image. D) Close-up of the fine fluid inclusions associated with the fracture in image C. E) Fluid inclusions preserved along a low-angle boundary in olivine. Ol – olivine.

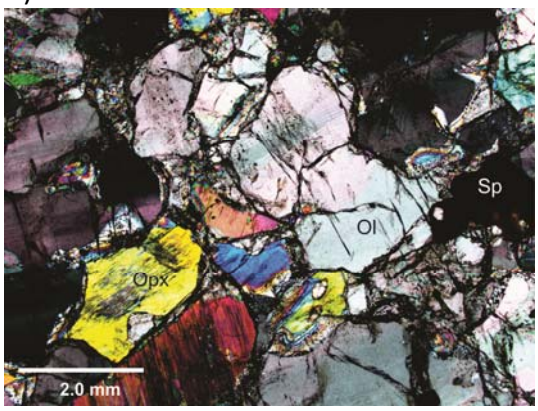

Figure 9.3. XPL images of olivine in sample 136065. A) Low-angle boundaries preserved in olivine. The olivines also have a dusty appearance due to the abundance of fluid inclusions contained within the grains. B) Close-up of fluid inclusions within a deformed olivine grain. Coarse inclusions are very common in this sample and are generally larger than in other samples, reaching up to 100 µm in diameter. Fine vermicular inclusions and spherical bubbles can also be seen in this grain. The vermicular inclusions commonly run parallel to the low-angle boundaries. Exsolved spinel grains are also visible in this image. C) A tubular fluid inclusion trail following a low-angle boundary in olivine. Ol – olivine, Opx – orthopyroxene, Sp – spinel.

B)

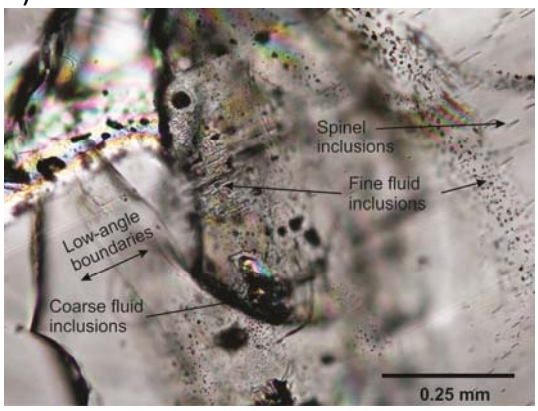

C)

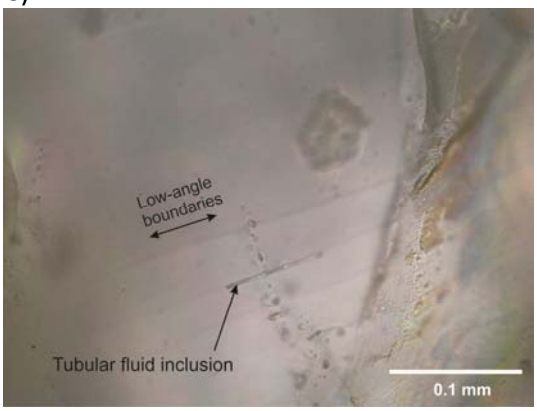

- ***136068***

Sample 136068 is a coarse-grained spinel lherzolite containing olivine, enstatite, clinopyroxene and spinel, and these have been metasomatically overprinted by fibrous orthopyroxene, which comprises 4% of the rock (Figure 9.4A). The section is traversed by some thin veins of orthopyroxene but is otherwise massive, with no apparent foliation or lineation. Low-angle boundaries are commonly preserved in olivine grains within this sample. Fracturing in the olivine is glassy and is commonly seen to form along low-angle boundaries (although not always), as well as perpendicular to the low-angle boundaries, forming a perpendicular geometry (Figure 9.4A). Transgranular fractures and microcracks are both open and annealed/partially healed. Annealed microcracks appear as trails of coarse, spherical bubbles (on average ~5 μm in diameter) and fine spherical and vermicular fluid inclusions (Figure 9.4B and C). The finer inclusions are approximately 1 μm wide and frequently form trails of bubbles that often decorate and delineate low-angle boundaries (Figure 9.4C).

- ***136069***

Sample 136069 is a massive, coarse-grained spinel dunite containing olivine, enstatite, clinopyroxene and spinel with replacement of primary mantle minerals by orthopyroxene (6% of the rock). There is no apparent structural fabric when observed under a polarised light microscope. Alteration of the sample is concentrated around 2 large parallel fractures ~0.5 mm thick. As observed in the previous samples, olivine has well-preserved low-angle boundaries (Figure 9.5A). Open and partially-healed transgranular fractures frequently run parallel to these, and are associated with coarse (5 – 10 μm) and fine (<1 μm) fluid inclusions (Figure 9.5B). Microcrack propagation

along low-angle boundaries is more prominent in this sample compared to the other samples. The fine inclusions are less abundant than in other samples and tend to form strings of bubbles, also parallel to the low-angle boundaries.

- ***136070***

Sample 136070 is a massive, coarse-grained spinel lherzolite (Figure 9.6A) comprised of olivine, enstatite, spinel and secondary metasomatic orthopyroxene (1% of the sample). The sample has a layered cumulate texture, with parallel bands rich in pyroxene alternating with bands rich in olivine. Alteration of primary mantle minerals to fibrous orthopyroxene predominantly occurs around grain boundaries but also within fractures. There is no apparent structural fabric in this sample when observed under a polarised light microscope. The olivine in this sample has prominent low-angle boundaries that are often the site of propagation for fractures and microcracks. Some microcracks are partially healed, presenting as trails of both coarse (~7 μm) and fine fluid inclusions (<1 μm) (Figure 9.6B). The finer inclusions are vermicular in morphology and mainly form tubular structures and strings of bubbles with few bridging structures in between the trails.

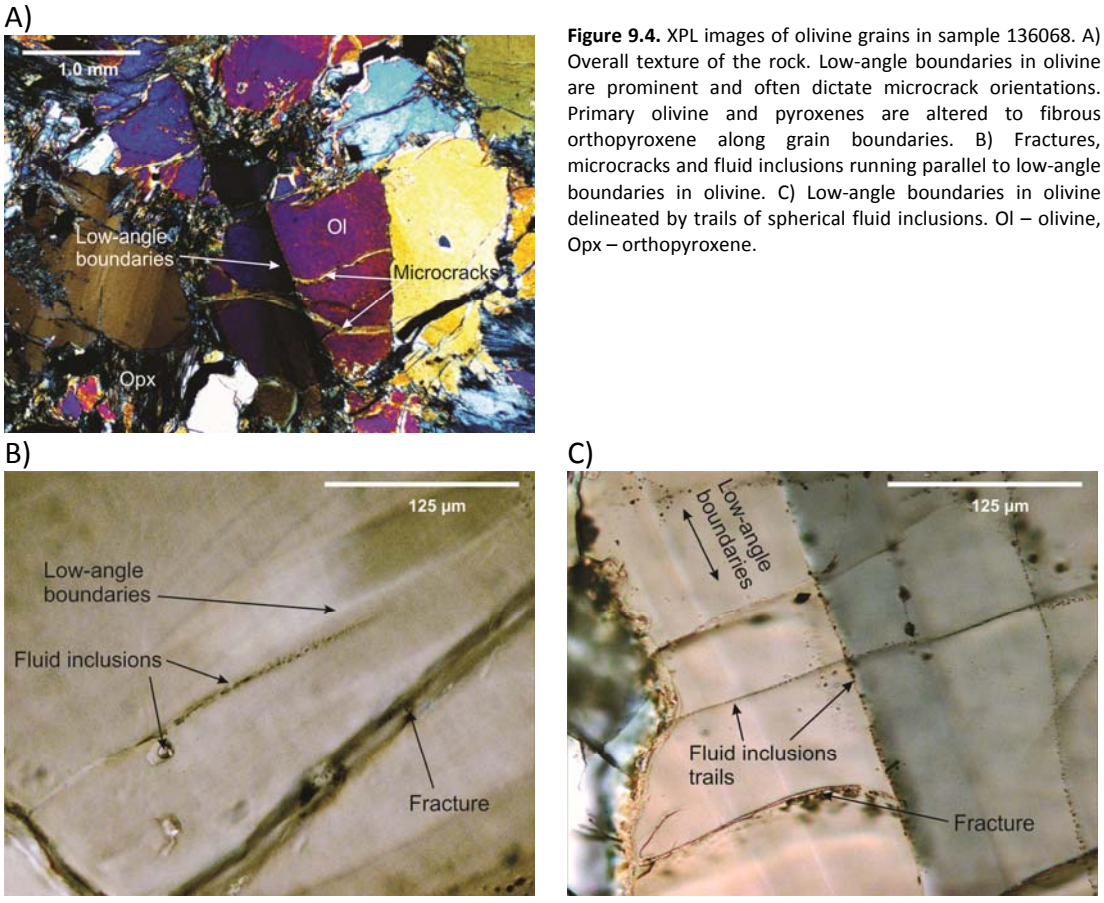

Figure 9.4. XPL images of olivine grains in sample 136068. A) Overall texture of the rock. Low-angle boundaries in olivine are prominent and often dictate microcrack orientations. Primary olivine and pyroxenes are altered to fibrous orthopyroxene along grain boundaries. B) Fractures, microcracks and fluid inclusions running parallel to low-angle boundaries in olivine. C) Low-angle boundaries in olivine delineated by trails of spherical fluid inclusions. Ol – olivine, Opx – orthopyroxene.

There is no clear relationship between the orientation of fine bubble strings or tube structures with low-angle boundaries in this sample as seen in the others. The coarse inclusions form trails of amorphous bubbles that are often parallel to low-angle boundaries (Figure 9.6C).

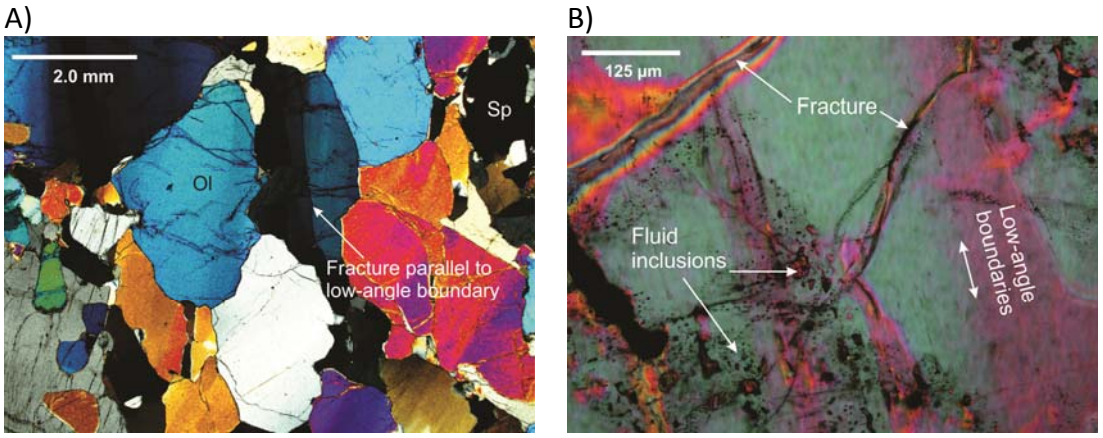

Figure 9.5. XPL images of olivine grains in sample 136069. A) Overall texture of the sample showing prominent low-angle boundaries in olivine that often dictate fracture orientations. Primary olivine and pyroxenes are altered to fibrous orthopyroxene along grain boundaries. B) Fractures, microcracks and fluid inclusions in olivine. Ol – olivine, Sp – spinel.

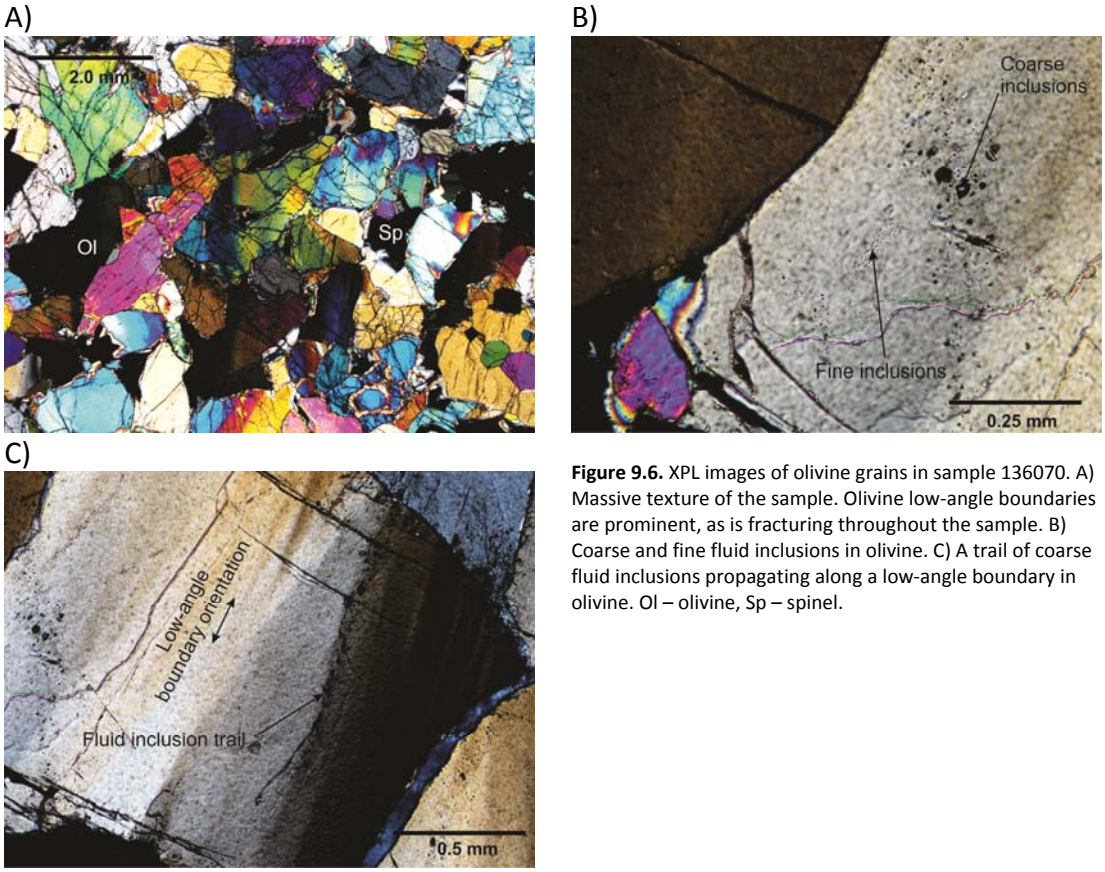

Figure 9.6. XPL images of olivine grains in sample 136070. A) Massive texture of the sample. Olivine low-angle boundaries are prominent, as is fracturing throughout the sample. B) Coarse and fine fluid inclusions in olivine. C) A trail of coarse fluid inclusions propagating along a low-angle boundary in olivine. Ol – olivine, Sp – spinel.

- ***136090***

Sample 136090 is a coarse-grained metasomatised spinel dunite comprised of olivine, enstatite, clinopyroxene and spinel, with secondary metasomatic orthopyroxene (comprising ~10% of the sample) and trace amounts of pentlandite. There is no obvious foliation or lineation. As with the other samples, there are low-angle boundaries associated with deformation preserved inside the olivine grains. There is abundant fracturing and microcrack development parallel to the low-angle boundaries (Figure 9.7A). Many fractures are annealed to form strings of coarse and fine bubbles. Fine vermicular inclusions (<1 μm wide) are common. Coarse amorphous inclusions are common in this sample and are generally larger than in the other samples (up to 10 – 20 μm in diameter). There is a strong perpendicular microcrack pattern associated with the low-angle boundaries. There appears to be more inclusions with a spherical morphology than tubular structures in the olivine in this sample, and low-angle boundaries are often delineated by fluid inclusions (Figure 9.7B).

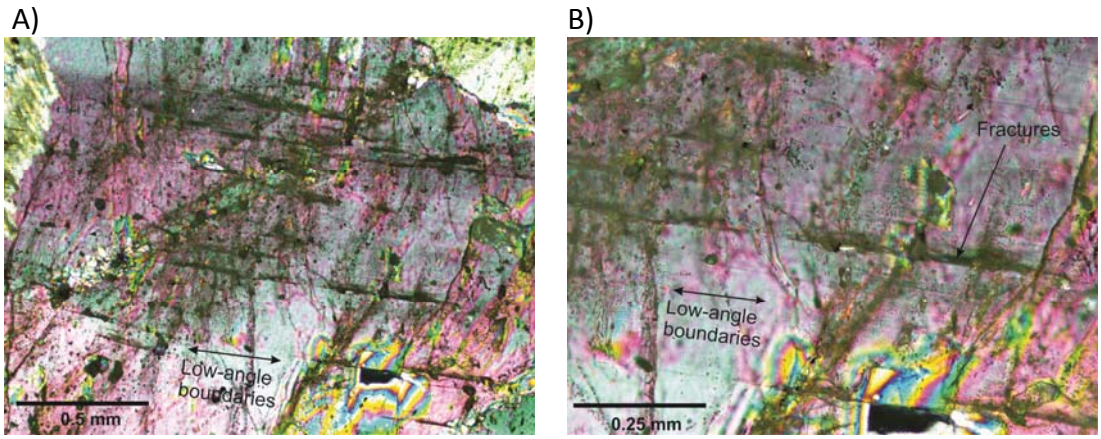

Figure 9.7. XPL images of olivine grains in sample 136090. A) Close-up of an olivine grain showing microcrack development parallel to low-angle boundaries and the 'dusty' appearance of olivines in this sample as a result of fluid inclusions. B) Close-up of the grain in B.

Higashi-Akaishi and Imono region, Japan

- ***J902***

J902 is a porphyroclastic spinel peridotite with a weak foliation and pervasive lineation. Sample J902 contains olivine, chromite, magnetite, antigorite and pentlandite. The foliation is predominantly defined by the alignment of antigorite

fibres and the mineral lineation is defined by chromite and antigorite alignment. Olivine porphyroclasts tend to be elongate and also contribute to the fabric. Neoblastic olivine is relatively equant in form and has no shape-preferred orientation. The sample is cross-cut by a network of veins containing fine-grained antigorite and magnetite.

Visibly deformed olivine porphyroclasts appear dusty and contain very fine trails of fluid inclusions (<1 μm, average size ~0.5 μm), often forming tube structures that are parallel to low-angle boundaries (Figure 9.8A - C). There are also coarser trails of fluid inclusions (ranging from 2 – 6 μm) contained within the porphyroclastic olivine (but not the neoblastic grains) that are likely to represent annealed microcracks, however the smaller inclusion trails frequently branch off from these and so are interpreted to be linked to the same fluid influx event. Microcracks in olivine grains also tend to show the orthogonal pattern observed in the Lihir samples (Figure 9.8C).

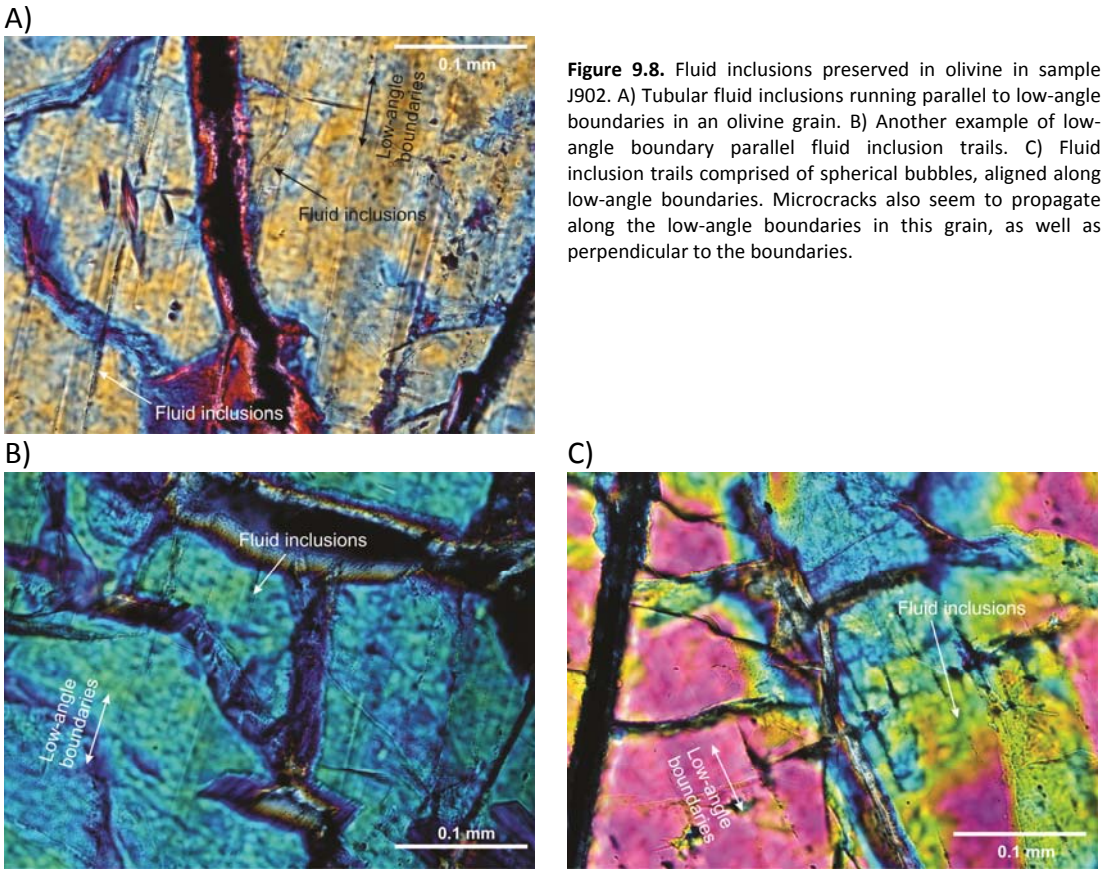

Figure 9.8. Fluid inclusions preserved in olivine in sample J902. A) Tubular fluid inclusions running parallel to low-angle boundaries in an olivine grain. B) Another example of low-angle boundary parallel fluid inclusion trails. C) Fluid inclusion trails comprised of spherical bubbles, aligned along low-angle boundaries. Microcracks also seem to propagate along the low-angle boundaries in this grain, as well as perpendicular to the boundaries.

- ***J904***

Sample J904 is a well-foliated and lineated porphyroclastic spinel dunite, containing porphyroclastic and neoblastic olivine, chromite, antigorite, magnetite and pentlandite. The foliation is defined primarily by the alignment of antigorite and the long axes of lenticular olivine, and wraps olivine and chromite porphyroclasts. Sample J904 also has weak olivine microlithon development and a very weak crenulation cleavage. Olivine porphyroclasts commonly preserve some internal microstructure and fine fluid inclusions (<1 μm, average size ~0.5 μm) that form trails running parallel to the low-angle boundaries (Figure 9.9 A, B). The fine fluid inclusions form spherical bubbles, and there are no 'bridging' or tube structures observed in the inclusions in this sample.

- ***J908A***

Sample J908A is a well-foliated and lineated porphyroclastic spinel dunite, containing olivine, chromite, antigorite, magnetite and pentlandite. Porphyroclastic and neoblastic olivine are extensively altered to bladed antigorite, which primarily defines the foliation along with the shape-preferred orientation of olivine. This sample is traversed by veins filled with fibrous antigorite and magnetite. Porphyroclastic olivine preserves internal microstructure in the form of low-angle boundaries related to mantle deformation. There are very fine fluid inclusion trails (<1 μm) frequently observed in these porphyroclastic grains that run parallel to the low-angle boundaries (Figure 9.10A). There are also abundant microcracks preserved in the olivine, commonly perpendicular to low-angle boundaries.

- ***J917***

Sample J917 is a well-foliated spinel dunite containing pods of porphyroclastic olivine surrounded by a matrix of neoblastic olivine, antigorite, serpentine, chromite, magnetite and pentlandite. There is a strong planar fabric/schistosity defined by antigorite alignment. Lens-like microlithons of porphyroclastic and neoblastic olivine are separated by domains of aligned coarse antigorite, and this is predominantly responsible for the spaced foliation. Olivine porphyroclasts commonly preserve intragrain microstructures associated with deformation. Porphyroclastic olivine often contains very small fluid inclusions that often form trails parallel to low-angle

boundaries (average ~2 μm in diameter), but these are not as extensive as in other samples (Figure 9.10B).

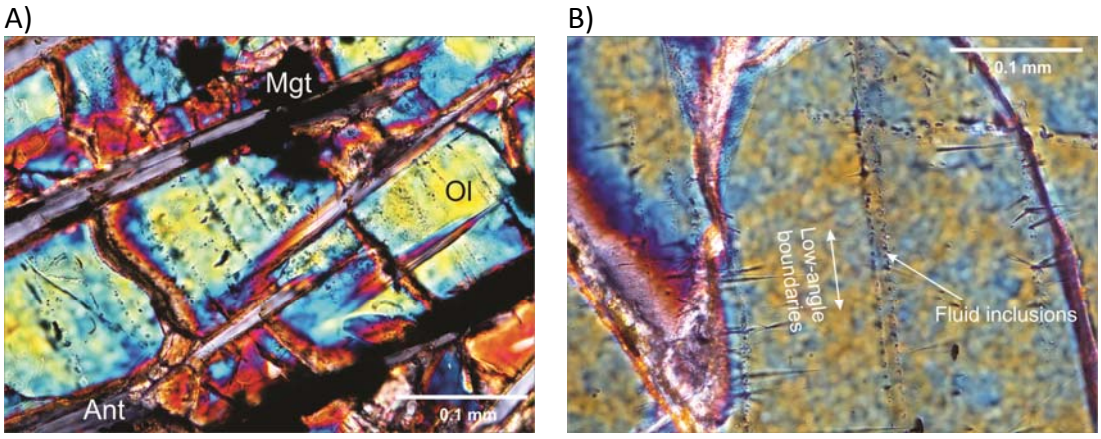

Figure 9.9. Fluid inclusions preserved in olivine grains in sample J904A. A) Spherical fluid inclusion trails aligned within olivine neoblasts. B) Spherical fluid inclusions running along low-angle boundaries in an olivine grain. Ol – olivine, Ant – antigorite, Mgt - magnetite.

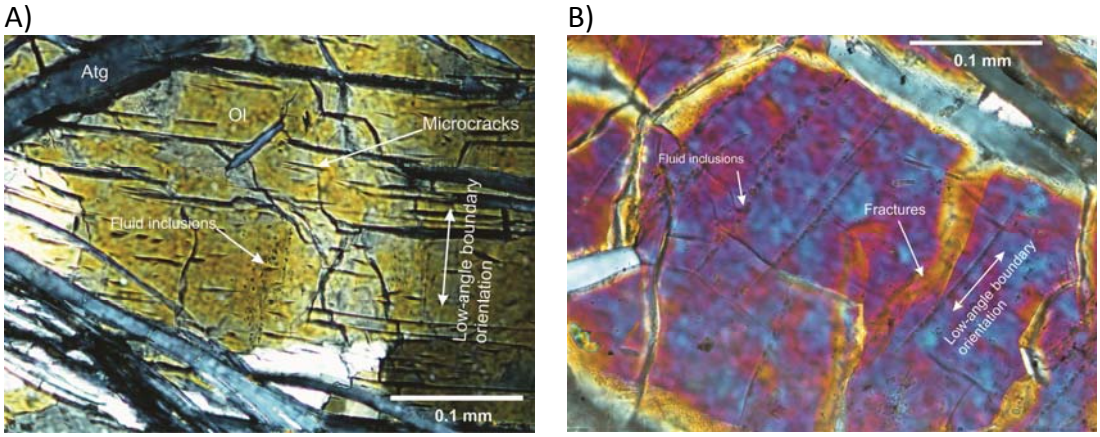

Figure 9.10. Fluid inclusions preserved in olivine grains in samples J908A and J917. There were appreciably less fluid inclusions preserved in both of these samples compared to the others. A) Microcracks and fluid inclusions in olivine in J908A. B) Microcracks and fluid inclusions in olivine in J917.

9.2. Hydroxide incorporation and distribution in mantle olivine: Insights from Synchrotron FTIR analysis

9.2.1. Overview

It is well-established that olivine and other nominally anhydrous minerals (NAMs) can contain trace amounts of water in the form of hydroxyl (OH^-), which affects the physical properties of these minerals and the rocks they comprise (e.g. Bai and Kohlstedt, 1992). Hydroxyl distribution in nominally anhydrous minerals can be investigated using X-ray diffraction, Fourier transform infrared (FTIR) and Raman

spectroscopy and proton-NMR spectroscopy (Libowitsky and Beran, 2006). Fourier transform infrared (FTIR) analysis is a particularly useful tool for investigating the presence and concentration of hydroxide in minerals, and can provide significant insight into the degree of hydrous fluid-rock interaction (Matveev *et al*., 2001). The application of IR spectroscopy methods to NAMs such as olivine has been undertaken for over three decades (e.g. Beran and Putnis, 1983; Miller *et al*., 1987; Rossman 1988). More recent advances have enabled quantitative analysis of hydroxide concentration (e.g. Bell *et al*. 2003; Kovács *et al*., 2008; Kovács *et al*., 2010) and the identification of the particular defect types involved in hydroxide incorporation in olivine (Libowitzky and Rossman, 1996; Matveev *et al*., 2001; Lemaire *et al*., 2004; Berry *et al*., 2005, 2007; Libowitzky and Beran, 2006).

Recently, studies have focussed on understanding the mechanisms that introduce hydroxide into the olivine crystal structure, with the aim of elucidating the modes of fluid percolation through mantle peridotite. The observations of a microstructural control on microcrack development and fluid flow in mantle olivine discussed in Chapter 9.1 suggest that hydroxide is introduced into the olivine crystal structure through brittle deformation related to strain hardening during dislocation creep. To date, very few FTIR studies have examined the link between hydrogen diffusion and deformation in olivine. Beran and Putnis (1983) observe an FTIR peak at 3400 cm^{-1} that correlated with the presence of low-angle boundaries. Sommer *et al*. (2008) present preliminary data showing that small variations in FTIR absorbance are found within pristine olivine grain interiors, although the limitations of this study are that the increased areas of absorbance have not been emphatically linked to the presence of internal microstructure, and the variations observed fall within the error margin of the water content calculations. Nonetheless, these studies indicate that there is a link between microstructural deformation and geochemistry, and sets the stage for further investigation.

This chapter presents the results of qualitative FTIR analysis of mantle olivine from Lihir. Although no water contents were calculated due to the fact that unpolarised light was used (Chapter 4), qualitative FTIR data provides information on the sites that host hydroxide within the olivine crystal lattice and the spatial distribution of structurally-bound hydroxide, from which we can infer conditions of fluid flow

processes in the mantle wedge. A detailed description of the procedure followed during FTIR data analysis and processing is provided in Chapter 4. FTIR analysis was undertaken at the Australian Synchrotron in Melbourne, Australia using the IR beamline. A spreadsheet of the data is provided in Appendix 3.

9.2.2. Sample description and methodology

One peridotite was analysed - 136063 (see Chapter 5 and Appendix 2 for a detailed description). It is a coarse-grained spinel lherzolite, comprised of olivine, enstatite, clinopyroxene, spinel and pyrrhotite. The rock has undergone metasomatism and primary mantle minerals are replaced by fibrous orthopyroxene (5% of the sample) within thin veins that cross-cut the section. The olivine in sample 136063 is deformed and contains abundant fluid inclusions (see Section 9.1).

A range of features occur within the grains analysed that may be related to structurally-bound hydroxide in olivine and therefore cause FTIR absorbance between 3100 – 3650 cm^{-1}. These include fluid inclusions, mineral inclusions, low-angle boundaries and fractures/cracks.

Low-angle boundaries, produced during deformation due to dislocation creep and associated with the operation of slip systems, are widespread in the olivine within sample 136063 (Figure 9.11). Fractures that traverse the grain interior can also be seen in Figure 9.11, and these are linked to fluid flow, potentially introducing hydroxide into the olivine crystal structure. Inclusions of spinel are also observed within the olivine grains in this sample. There are two types of spinel inclusions: 1) exsolved spinel inclusions produced during cooling that are aligned parallel to <010> (Franz and Wirth, 2000); and 2) larger, unaligned spinel inclusions (Figure 9.12). During the data processing, there has been no distinction between these two types of spinel inclusions, as they are not expected to significantly contribute greatly to the total amount of hydroxide in olivine.

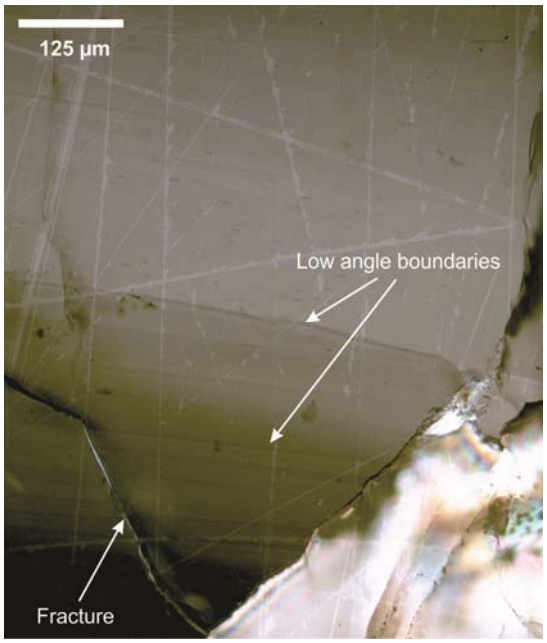

Figure 9.11. Photomicrograph (taken under XPL) of low-angle boundaries observed in grain 70 (peridotite sample 136063). Low-angle boundaries are produced as a result of plastic deformation by dislocation creep.

There are also two types of fluid inclusions observed (Figure 9.13), the characteristics of which are described in Section 9.1. Coarse fluid inclusions are morphologically similar to fractures cross-cutting the grains (Figure 9.13A), and are assumed to represent poorly healed fractures that occurred during mantle deformation. Fine sub-micron scale fluid inclusions and fluid inclusion trails/microtubules occur on a much smaller scale than the coarse inclusions, yet are often spatially-related (Figures 9.13B and C).

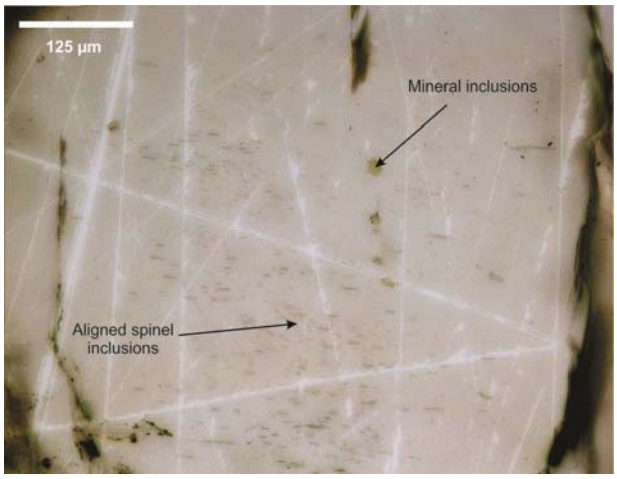

Figure 9.12. Photomicrograph (taken under XPL) of the types of mineral inclusions observed in Lihir olivine grains (peridotite sample 136063). Spinel inclusions aligned parallel to <010> are an exsolution feature (Franz and Wirth, 2000). These occur alongside larger and randomly oriented spinel and other mineral inclusions. (Note: The white lines in the image are scratches in the carbon coat, which was applied to the sample in order to perform EBSD analysis).

Highly detailed FTIR analysis was undertaken on four grains in sample 136063 (grains 13, 47, 59 and 70). During FTIR analysis, both molecular and structurally-bound water was observed to occur in these grains. Molecular water (in the form of H_2O) was observed within structures such as fluid inclusions/fractures as well as water vapour in the air. Molecular water produces a large broad peak with a maxima at approximately 3420 cm^{-1}. Efforts were made to reduce the effect of water vapour on the spectra during data collection by purging the air within the sample chamber before beginning acquisition, however this introduced significant and variable noise

into the signal. Instead, regular background measurements were taken to ensure that the water vapour signal was consistent, and the H_2O peak was processed out of the spectra post-acquisition. Structurally-bound hydroxide produces absorbance peaks that are relatively sharp and isolated, so these types can be distinguished from the broad H_2O peak by examination of the spectrum (Figure 4.8). This study focuses primarily on the structurally-bound water in the form of OH^- occupying defect sites in the olivine crystal lattice, and thus variations in molecular water will not be addressed.

Data processing involved manual selection of peaks, and correlation with intragrain features that occur close to the line scans. Absorbance values, where presented, are given in terms of relative absorbance I/Io, where I is the absorbance of the peak and Io is the total absorbance of the scan. This is to allow for comparison between scans, due to the fact that the values collected during acquisition are absorbance ratios that are specific to each scan and are not absolute values. Overall, a large number of FTIR absorbance peaks were observed (Table 9.1), suggesting a high level of complexity within the data. An overview and sketch maps of the grains are provided in Figures 9.16 – 9.19. More detailed photomicrographs are provided in Figures 9.18 – 9.24. The primary output of this analysis is a series of maps of each of the scans (Figures 9.25 – 9.31) and peaks are also plotted in Figures 9.32 and 9.35.

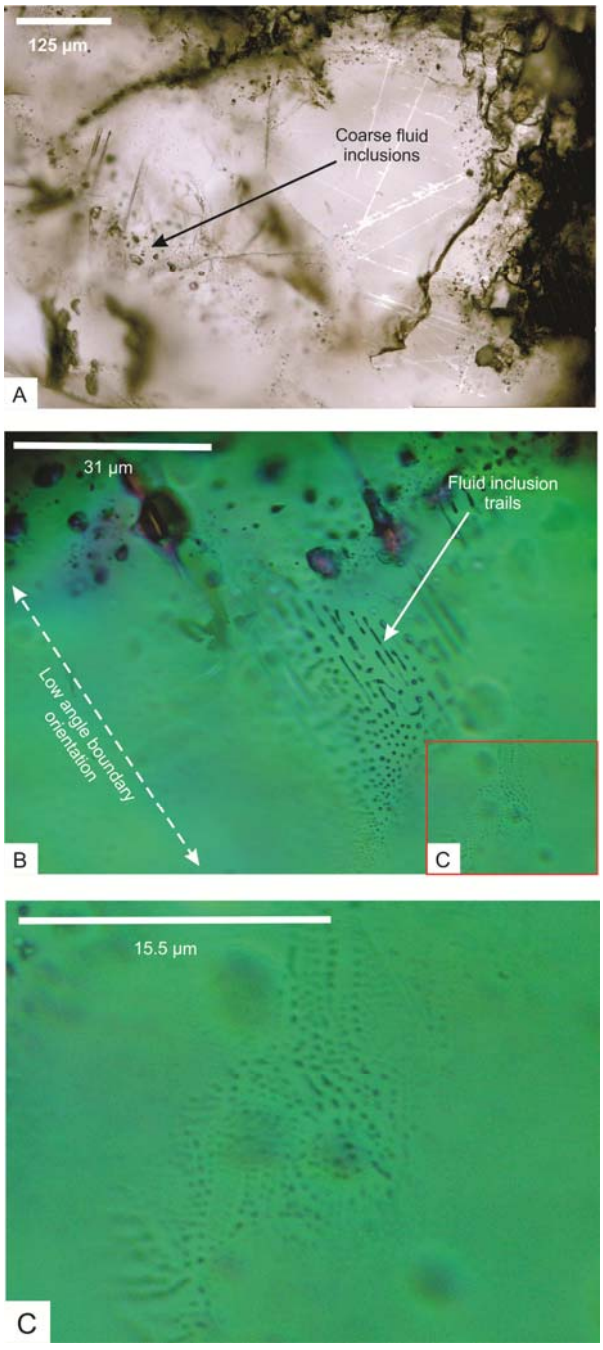

Figure 9.13. Photomicrographs of olivine within sample 136063 showing the different types of fluid inclusions observed. A) PPL image of coarse fluid inclusions observed in the Lihir olivine grains. These represent poorly healed fractures that occurred in the mantle. B) An XPL photomicrograph of the fine fluid inclusion trails that are also observed in the Lihir olivine. Often these are parallel to the low-angle boundary orientation (but this is not always the case). These fluid inclusions appear are spatially related to the coarser annealed fluid inclusions but are represent more completely healed fractures and have a distinctly different morphology. C) Close-up of the bottom-right corner of B, showing that the fine fluid inclusions also occur on a sub-micron scale.

9.2.3. FTIR Results

Table 9.2. FTIR peaks observed in Lihir peridotite olivine (sample 136063).

Wavenumber (cm^{-1})	Associated lattice site	References
3149	Probably a hydrated Mg vacancy similar to 3159	
3159	Hydrated Mg Vacancy	Lemaire *et al*. (2004); Berry *et al*. (2005)
3174 - 3176		Matsyuk and Langer (2004)
3184 - 3185		
3200		

3220	Hydrated Mg vacancy	Matsyuk and Langer (2004), Lemaire *et al*. (2004), Berry *et al*. (2005)
3228		Miller *et al*. (1987), Matsyuk and Langer (2004)
3233 -3235		Miller *et al*. (1987), Matsyuk and Langer (2004)
3241 - 3244		Matsyuk and Langer (2004)
3246		Matsyuk and Langer (2004)
3250 - 3254		Matsyuk and Langer (2004)
3269		Miller *et al*. (1987); Matsyuk and Langer (2004)
3297		Miller *et al*. (1987); Matsyuk and Langer (2004)
3313		
3319	Ti-clinohumite (Miller *et al* 1987)	Miller *et al*. (1987)
3325 - 3326	Trivalent impurities (e.g. Fe^{3+})	Miller *et al*. (1987); Matsyuk and Langer (2004), Berry *et al*. (2005, 2007)
3353 - 3356	Trivalent impurities (e.g. Fe^{3+})	Miller *et al*. (1987); Matsyuk and Langer (2004), Berry *et al*. (2005, 2007)
3398		Miller *et al*. (1987); Matsyuk and Langer (2004)
3409 - 3413	Ti-clinohumite planar defect	Kitamura *et al*. (1987); Miller *et al*. (1987); Liu *et al*., 2003; Matsyuk and Langer (2004)
3417		Matsyuk and Langer (2004)
3420 - 3422		Matsyuk and Langer (2004)
3426 - 3427		Matsyuk and Langer (2004)
3434		Miller *et al*. (1987)
3437		Matsyuk and Langer (2004)
3442 - 3443		
3450		
3456		Miller *et al*. (1987); Matsyuk and Langer (2004)
3470		Miller *et al*. (1987); Matsyuk and Langer (2004)
3483 - 3488		Miller *et al*. (1987); Matsyuk and Langer (2004)
3501 - 3504		Miller *et al*. (1987); Matsyuk and Langer (2004)
3514		Libowitsky and Beran (1995); Matsyuk and Langer (2004)
3517 - 3522		
3525 - 3528	Ti-clinohumite-type point and planar defects	Kitamura *et al*. (1987); Miller *et al*. (1987); Libowitsky and Beran (1995); Matsyuk and Langer (2004)
3536 - 3537		Libowitsky and Beran (1995); Matsyuk and Langer (2004)
3544 - 3546		Miller *et al*. (1987)
3567 - 3570	Hydrated Si vacancy	Miller *et al*. (1987); Libowitsky and Beran (1995); Matveev *et al*., (2001); Lemaire *et al*. (2004); Matsyuk and Langer (2004); Berry *et al*. (2007)
3572 - 3574	Ti-clinohumite-type point and planar defects	Kitamura *et al*. (1987); Miller *et al*. (1987); Matsyuk and Langer (2004); Berry *et al*. (2005)
3576	Ti-clinohumite-type point defects	Miller *et al*. (1987); Matsyuk and Langer (2004); Berry *et al*. (2005, 2007)
3600 - 3604		Miller *et al*. (1987); Libowitsky and Beran (1995); Matsyuk and Langer (2004)
3619 - 3621		Matsyuk and Langer (2004)
3625 - 3626		Miller *et al*. (1987); Libowitsky and Beran (1995); Matsyuk and Langer (2004)
3629 - 3632		Matsyuk and Langer (2004)
3636 - 3640	Serpentine inclusions	Miller *et al*. (1987); Libowitsky and Beran (1995); Matsyuk and Langer (2004)
3644		Miller *et al.* (1987); Libowitsky and Beran (1995); Matsyuk and Langer (2004)

Grain 13

Scan A

The FTIR absorbance map of scan 13A (Figure 9.25) shows regions of moderate to high absorbance at 3355, 3572 and 3637 cm^{-1}. The peaks at 3572 and 3637 cm^{-1} are isolated and are spatially related to each other, with the 3572 cm^{-1} peak consistently weaker in intensity than the 3637 cm^{-1} peak. These two peaks appear to behave as a pair and are associated with the same features. The peak at 3355 cm^{-1} is uniformly present across the length of the scan, with only minor variations in absorbance. There are also some very small peaks at ~3320 cm^{-1}.

Scan B

The FTIR absorbance map of scan 13B (Figure 9.26) shows a larger number of peaks than are observed in the 13A scan. Peaks are observed at 3319, 3420, 3525, 3572 and 3638 cm^{-1}. This scan has more background noise than 13A. Below 3100 cm^{-1} there are two peaks present that are unrelated to OH^- in olivine. These are cyanoacrylate (superglue) peaks, due to the presence of residual adhesive previously used to secure the sample to a glass slide. The most prominent peaks in this sample are 3355 and 3420 cm^{-1}. The 3355 and 3572 cm^{-1} peaks are consistently present across the length of the scan, whereas peaks at 3420 cm^{-1} are sporadic. As observed in scan 13A, the peaks at 3572 and 3638 cm^{-1} appear to behave as a pair, however in this situation 3572 cm^{-1} is more highly absorbing than 3638 cm^{-1}. The 3525 cm^{-1} peak also tends to occur at the same positions as the paired peaks. It may be important to note that the orientations of scans 13A and 13B are different – these are almost orthogonal (Figure 9.14), which may explain the relative differences in absorbance between 3572 and 3638 cm^{-1} peaks.

Scan C

The FTIR absorbance map of scan 13C (Figure 9.27) shows moderate to highly absorbing peaks at 3355, 3567, 3572 and 3638 cm^{-1}. As observed in 13A and B, the 3572 and 3638 cm^{-1} peaks are paired, with 3638 cm^{-1} peak higher in intensity than 3572 cm^{-1}. Unlike the other scans, the 3355 cm^{-1} peak in this sample is subordinate to the other peaks, and is not consistently present across the length of the scan.

A plot of all the manually selected peaks observed in Grain 13 (all scans combined) and the features these correlate with (Figure 9.32), highlights that FTIR absorbance occurs between wavelengths of 3319 – 3638 cm^{-1}. Some peaks correlate with the presence of fractures and coarse fluid inclusions but many peaks do not appear to correlate to any visible features inside the grain (pristine grain interior). The most highly absorbing peaks correlate to fractures and pristine grain interiors at 3355, 3420 and 3639 cm^{-1}.

Grain 47

The FTIR absorbance map of grain 47 (Figure 9.28) is relatively noisy compared with the other scans. The main peaks observed are at 3354, 3421, 3572 and 3638 cm^{-1}, with numerous smaller peaks between 3150 – 3350 cm^{-1}. In this scan, all the peaks appear to be spatially related, and are probably caused by the same intragrain features. The 3355 cm^{-1} peak is generally consistently present across the scan but varies in intensity, whereas the other peaks are spatially more sporadic.

A plot of the manually selected peaks observed in Grain 47 and the related intragrain features (Figure 9.32) show that the peaks in this grain correlate with pristine grain interiors, mineral inclusions and both types of fluid inclusions. The highest intensity absorbance correlates to the presence of both types of fluid inclusions, as well as the pristine grain interior.

Grain 59

Scan A

The FTIR absorbance map of scan 59A (Figure 9.29) shows major peaks at 3355, 3567, 3572, and 3637 cm^{-1}, with minor peaks at 3426 and 3320 cm^{-1}. As in most of the other scans, the 3355 cm^{-1} peak is consistently present across the scan but varies in intensity. Peaks at 3567, 3572 and 3637 cm^{-1} occur at the x positions across the scan, as observed in other grains. At x position 39, there has been a data 'drop out' (during acquisition), with a row of null values.

Scan B

The FTIR absorbance map of scan 59B (Figure 9.30) is more complicated than the other maps and shows major peaks at 3354, 3421, ~3517, 3567, 3572-73, ~3600 and 3638 cm^{-1}. The 3354 cm^{-1} peak is not as dominant in this scan as observed in the others.

Looking at grain 59 as a whole, the grain is quite complicated in terms of FTIR absorbance peaks (Figure 9.32). Absorbance occurs in the range of 3159 – 3638 cm^{-1}, with major peaks at 3325, 3355, 3526, 3573, 3600, 3625 and 3638 cm^{-1}, and many smaller peaks present. All of the potentially absorbing structures are observed in grain 59, however the highest intensity absorbance correlates with the presence of pristine grain interiors (i.e. no observable features) and low-angle boundaries.

Grain 70

FTIR absorbance in grain 70 occurs in the region between 3220 – 3640 cm^{-1} (Figure 9.31). The dominant peaks are 3355, ~3570 and 3640 cm^{-1}, and the latter 2 peaks are again paired in nature. There is some absorbance at 3567 cm^{-1} along with some smaller peaks at 3220, 3319 and between 3470 and 3546 cm^{-1}. The 3355 cm^{-1} peak is consistently present across the scan but varies in intensity. A plot of the peaks observed in grain 70 and the features these correlate with, shows that the peaks with the highest absorbance appear to correlate with pristine grain interiors and low-angle boundaries (Figure 9.32).

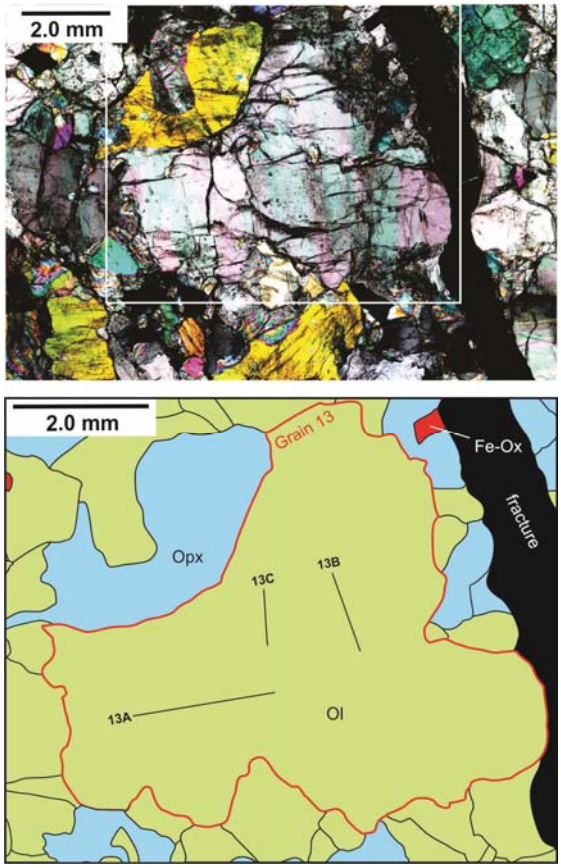

Figure 9.14. Photomicrograph (XPL) and sketch of olivine grain 13 in peridotite sample 136063. The green represents olivine grains, the blue primary orthopyroxene and the red is Fe-Ni oxide. The black region is a fracture. The locations and orientations of FTIR line scans 13A, B and C are indicated on the sketch map.

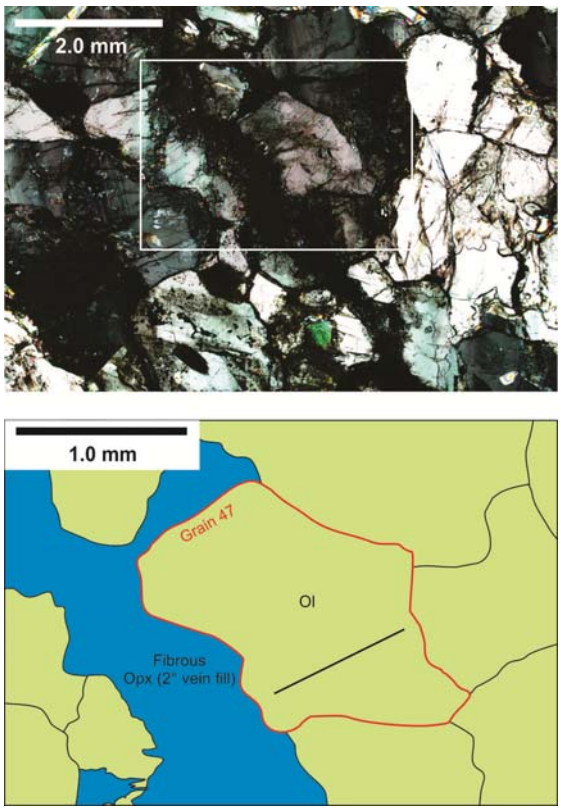

Figure 9.15. Photomicrograph (taken under XPL) and sketch of olivine grain 47 in peridotite sample 136063. The green represents olivine and the blue secondary orthopyroxene. The locations and orientation of the FTIR line scan is indicated on the sketch map.

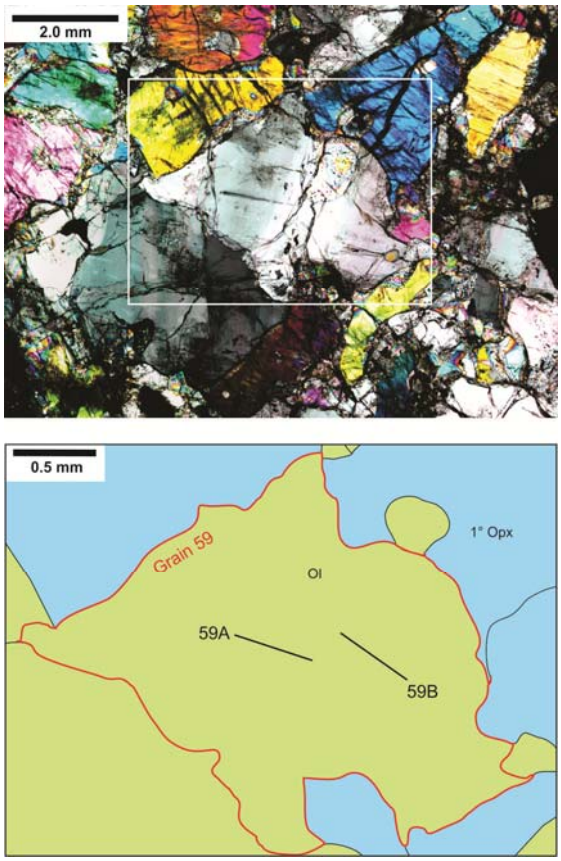

Figure 9.16. Photomicrograph (taken under XPL) and sketch of olivine grain 59 in peridotite sample 136063. The green represents olivine and the blue primary orthopyroxene. The locations and orientation of the FTIR line scans 59A and 59 B are indicated on the sketch map.

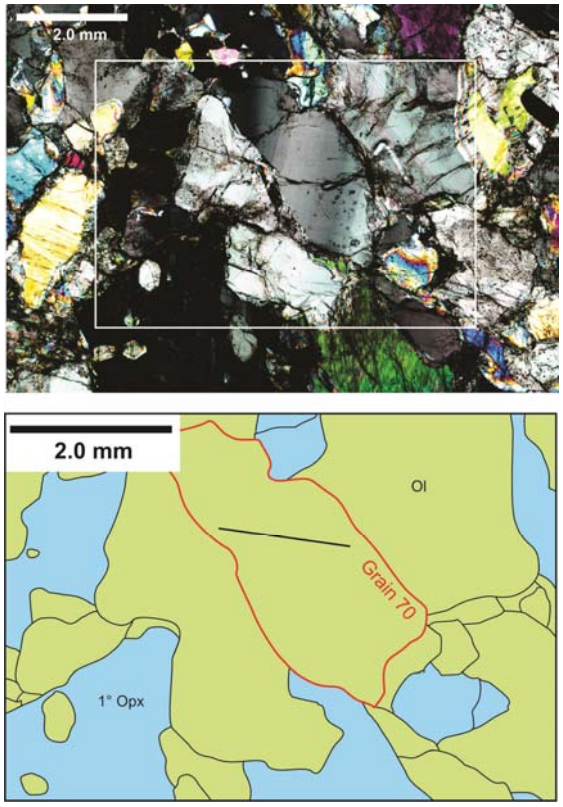

Figure 9.17. Photomicrograph (taken under XPL) and sketch of olivine grain 70 in peridotite sample 136063. The green represents olivine and the blue primary orthopyroxene. The locations and orientation of the FTIR line scan is indicated on the sketch map.

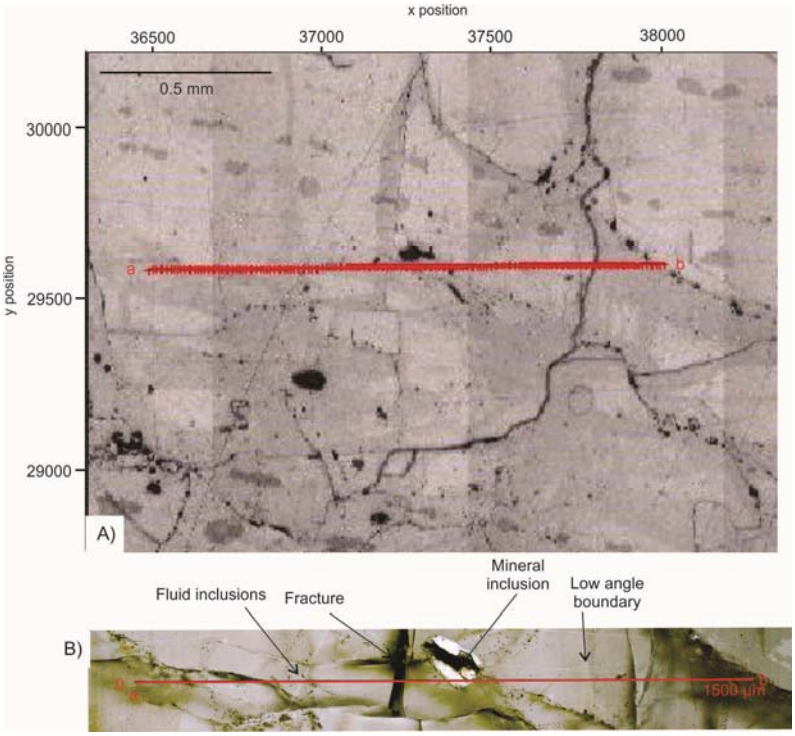

Figure 9.18. A) Reflected light image of line scan 13A taken during data acquisition. B) Photomicrograph taken under XPL of scan 13A, showing the scan cutting across the internal microstructure of the grain (low-angle boundaries), as well as features such as fractures and fluid/mineral inclusions. Scan 13A is 1500 µm long, with a spectrum collected every 1 µm.

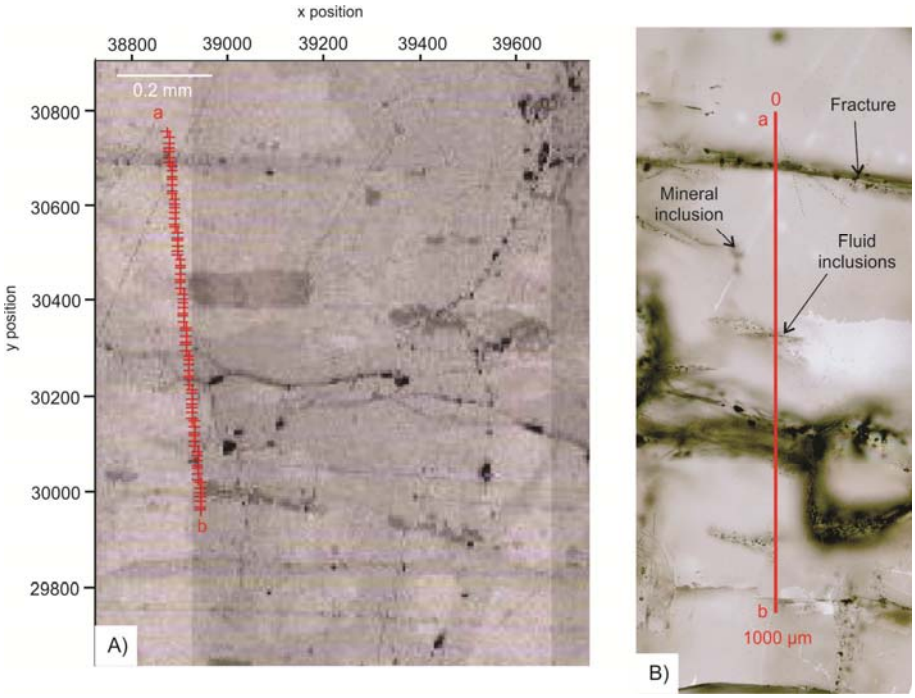

Figure 9.19. A) Reflected light image of line scan 13B taken during data acquisition. B) Photomicrograph taken under PPL of scan 13B, showing fractures and fluid/mineral inclusions within the grain. The scan runs sub-parallel to the low-angle boundaries so does not cross these and none are observed under XPL. Scan 13B is 1000 µm long, with a spectrum collected every 1 µm.

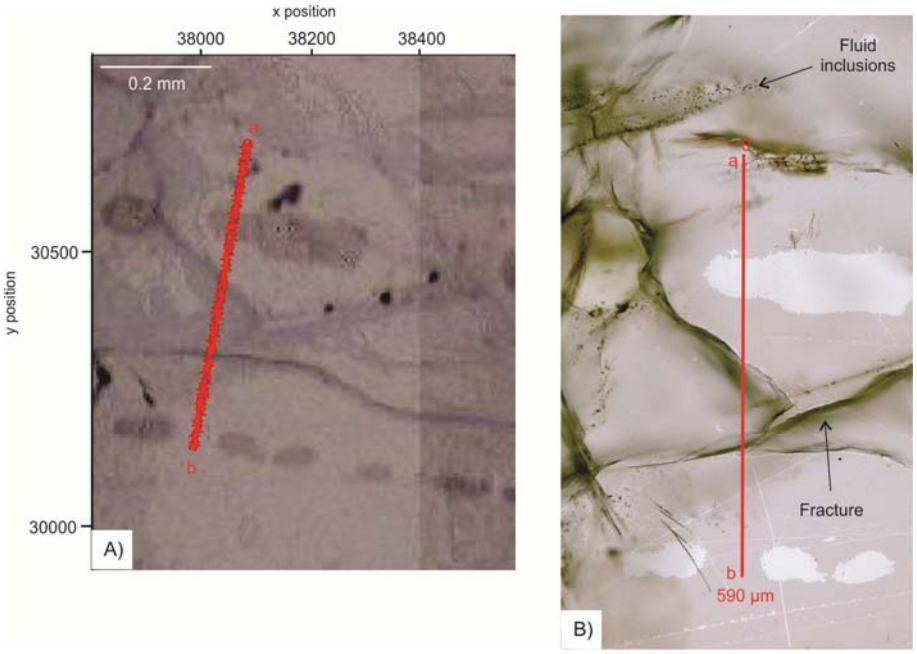

Figure 9.20. A) Reflected light image of line scan 13C taken during data acquisition. B) Photomicrograph taken under PPL of scan 13C, showing the features within the grain including fractures and fluid inclusions. As with 13B, scan 13C is parallel to the low-angle boundary orientation (thus no boundaries can be seen under XPL) and is 590 µm long, with a spectrum collected every 1 µm.

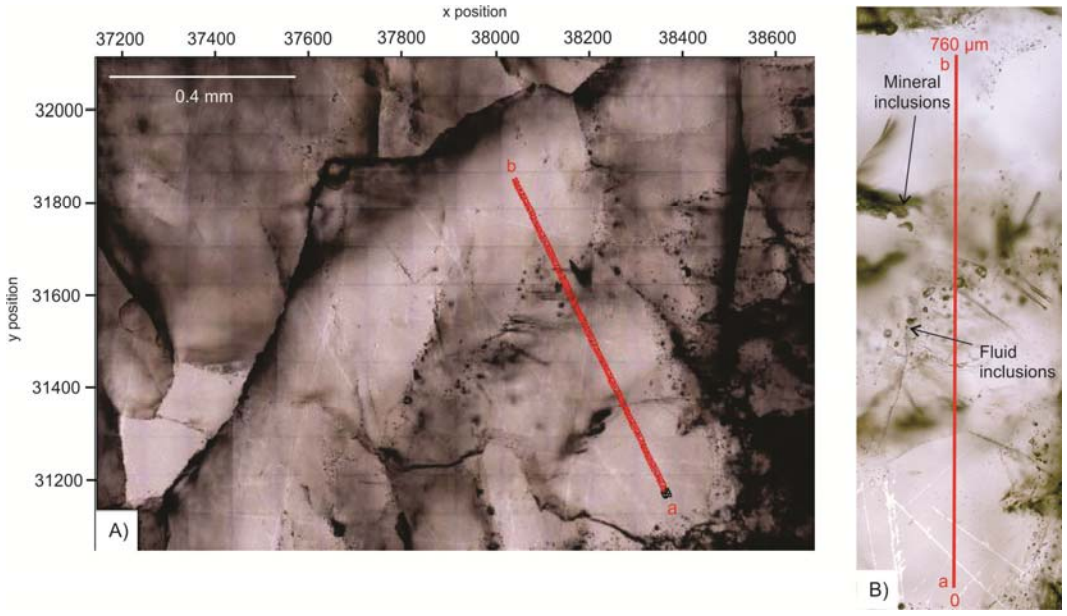

Figure 9.21. A) Transmitted light image of line scan 47 taken during data acquisition. B) Photomicrograph taken under PPL of scan 47, showing the intragrain features such as fluid and mineral inclusions. In this case, there were no observable low-angle boundaries under XPL. Scan 47 is 760 µm long, with a spectrum collected every 1 µm.

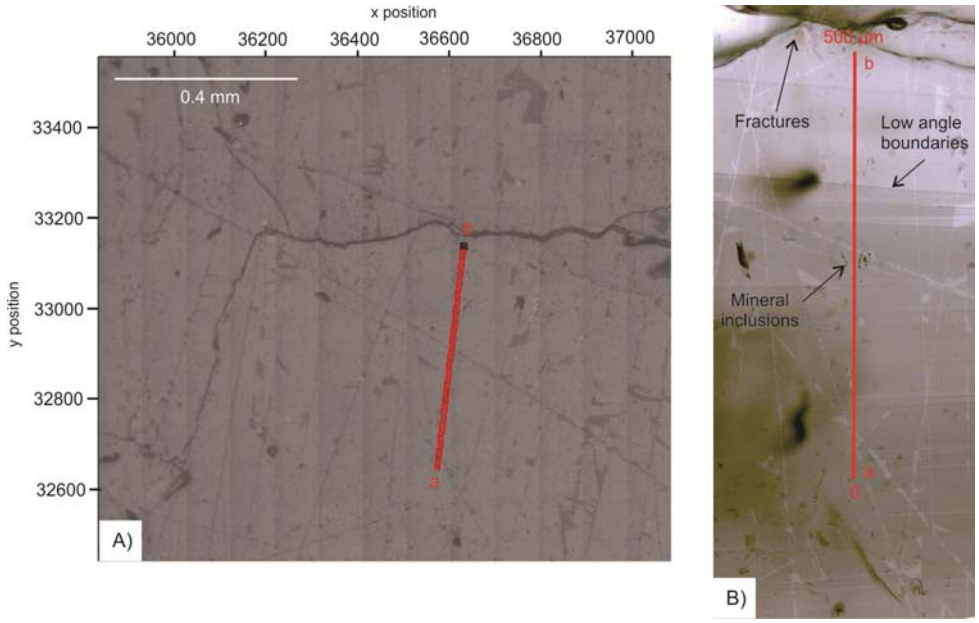

Figure 9.22. A) Reflected light image of line scan 59A taken during data acquisition. B) Photomicrograph taken under XPL of scan 59A, showing the scan cutting across intragrain features such as low-angle boundaries, fractures and mineral inclusions. Scan 59A is 500 µm long, with a spectrum collected every 1 µm.

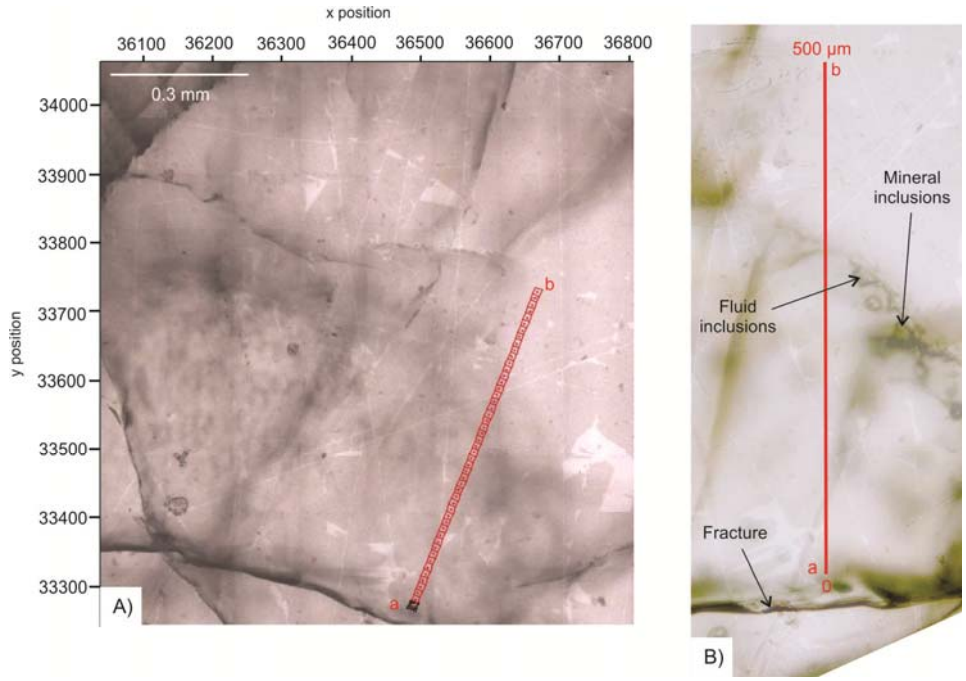

Figure 9.23. A) Transmitted light image of line scan 59B taken during data acquisition. B) Photomicrograph taken under PPL of scan 59B, showing the intragrain features such as fractures, fluid and mineral inclusions. In this case, there were no observable low-angle boundaries under XPL. The scan is 500 µm long, with a spectrum collected every 1 µm.

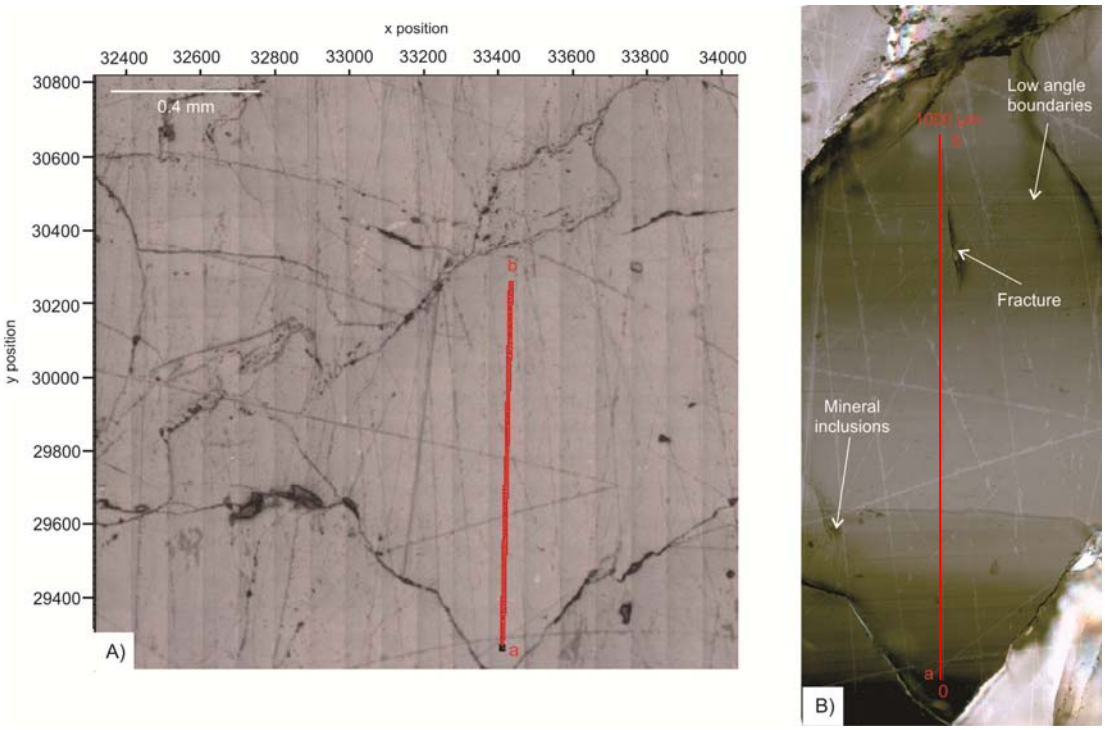

Figure 9.24. A) Transmitted light image of line scan 70 taken during data acquisition. B) Photomicrograph taken under PPL of scan 70, showing the intragrain features such as fractures, mineral inclusions and prominent low-angle boundaries. The scan is 1000 µm long, with a spectrum collected every 1 µm.

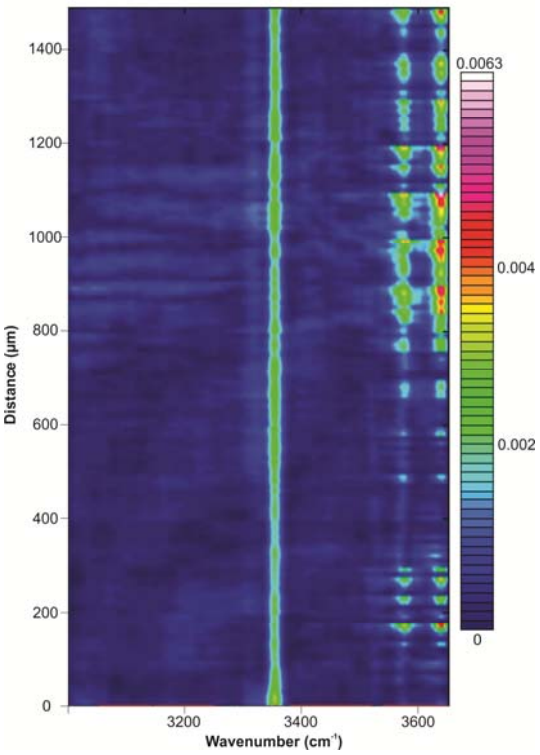

Figure 9.25. FTIR absorbance map of scan 13A.

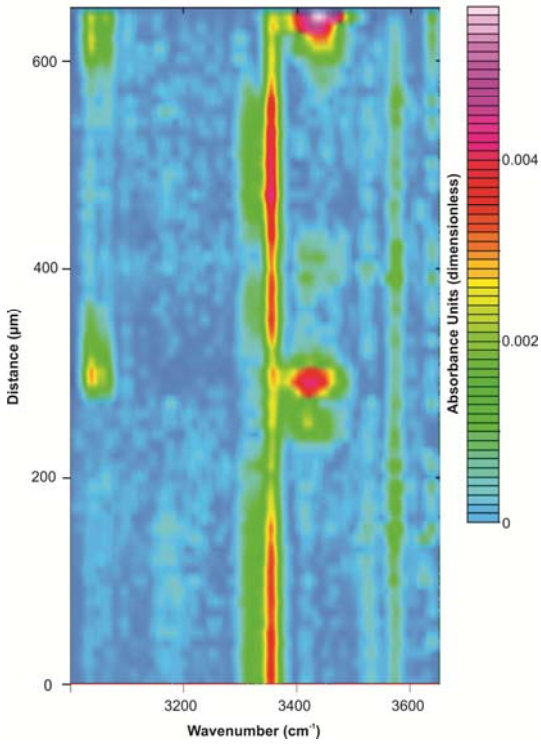

Figure 9.26. FTIR absorbance map of scan 13B.

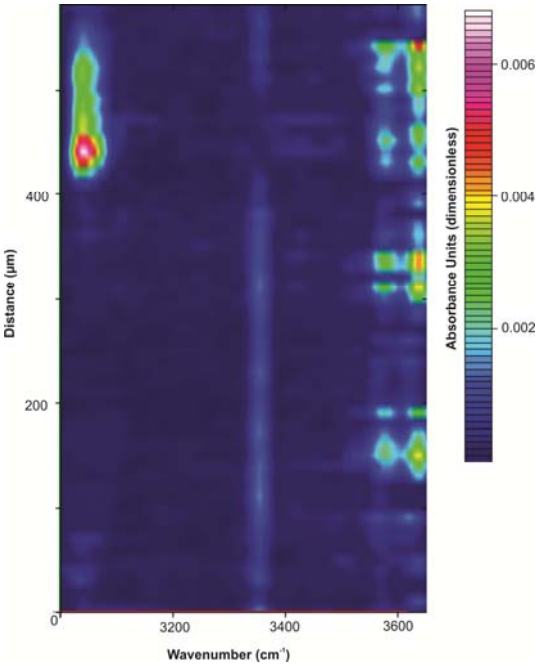

Figure 9.27. FTIR absorbance map of scan 13C.

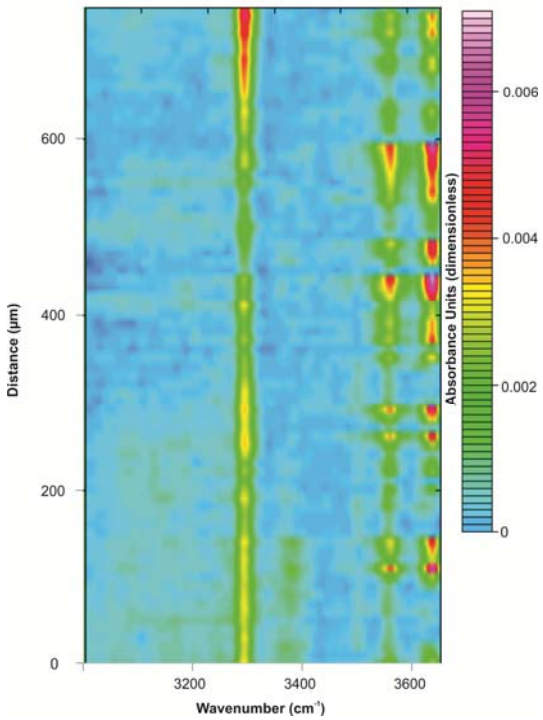

Figure 9.28. FTIR absorbance map of scan 47.

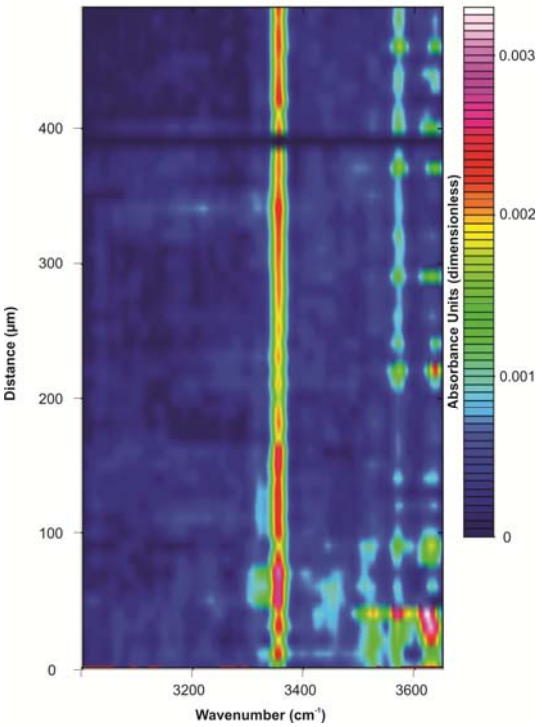

Figure 9.29. FTIR absorbance map of scan 59A.

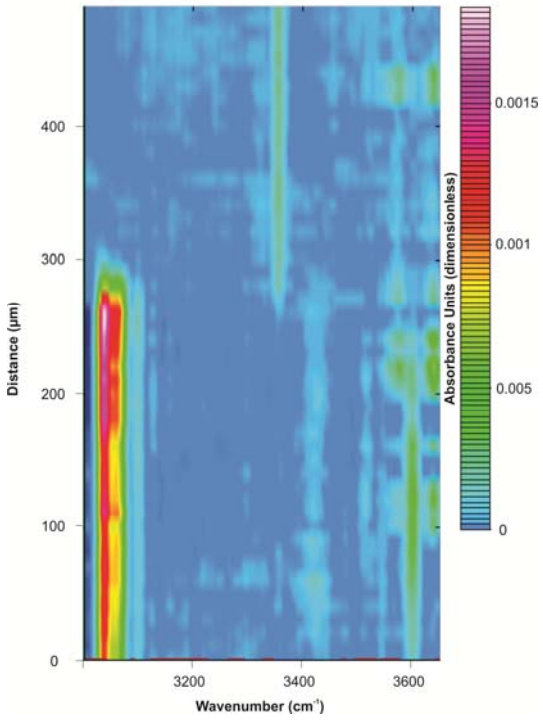

Figure 9.30. FTIR absorbance map of scan 59B.

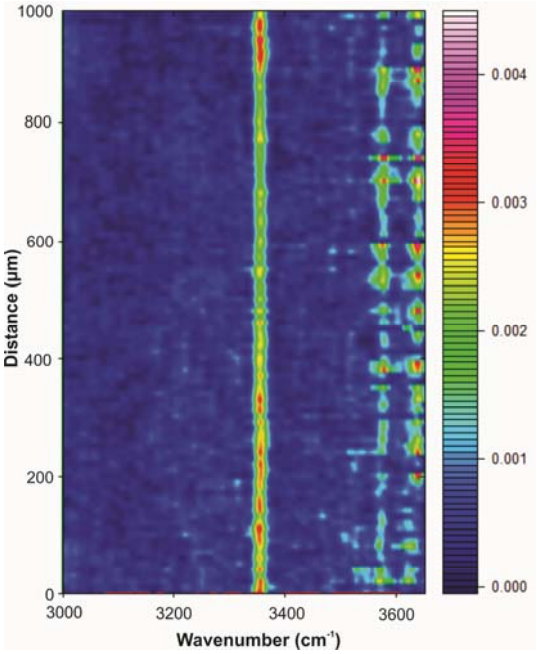

Figure 9.31. FTIR absorbance map of scan 70.

9.2.4. EBSD results

EBSD mapping of the areas of grains 13 and 59 that contained scans 13A and 15A was undertaken in order to further investigate the link between deformation microstructures and hydroxide incorporation. EBSD texture and local misorientation maps were produced, along with pole figure showing the orientation of crystallographic axes and rotation axes with respect to both the sample coordinates and crystal coordinates (Figures 9.33 and 9.34). The crystallographic axis dispersion of grain 13A and clustering of rotation axes in terms of both sample and crystal coordinates suggests a rotation axis of [001], consistent with (010)[100] slip. The crystallographic axis dispersion of grain 59A and clustering of rotation axes in terms of both sample and crystal coordinates suggests a rotation axis of [010], consistent with either (001)[100] slip or (100)[001] slip. The weak dispersion of rotation axes within the YZ plane suggests a [100] slip direction, which is consistent with (001)[100] slip. Both of these slip systems are consistent with the olivine LPO and microstructure observations presented in Chapter 6.

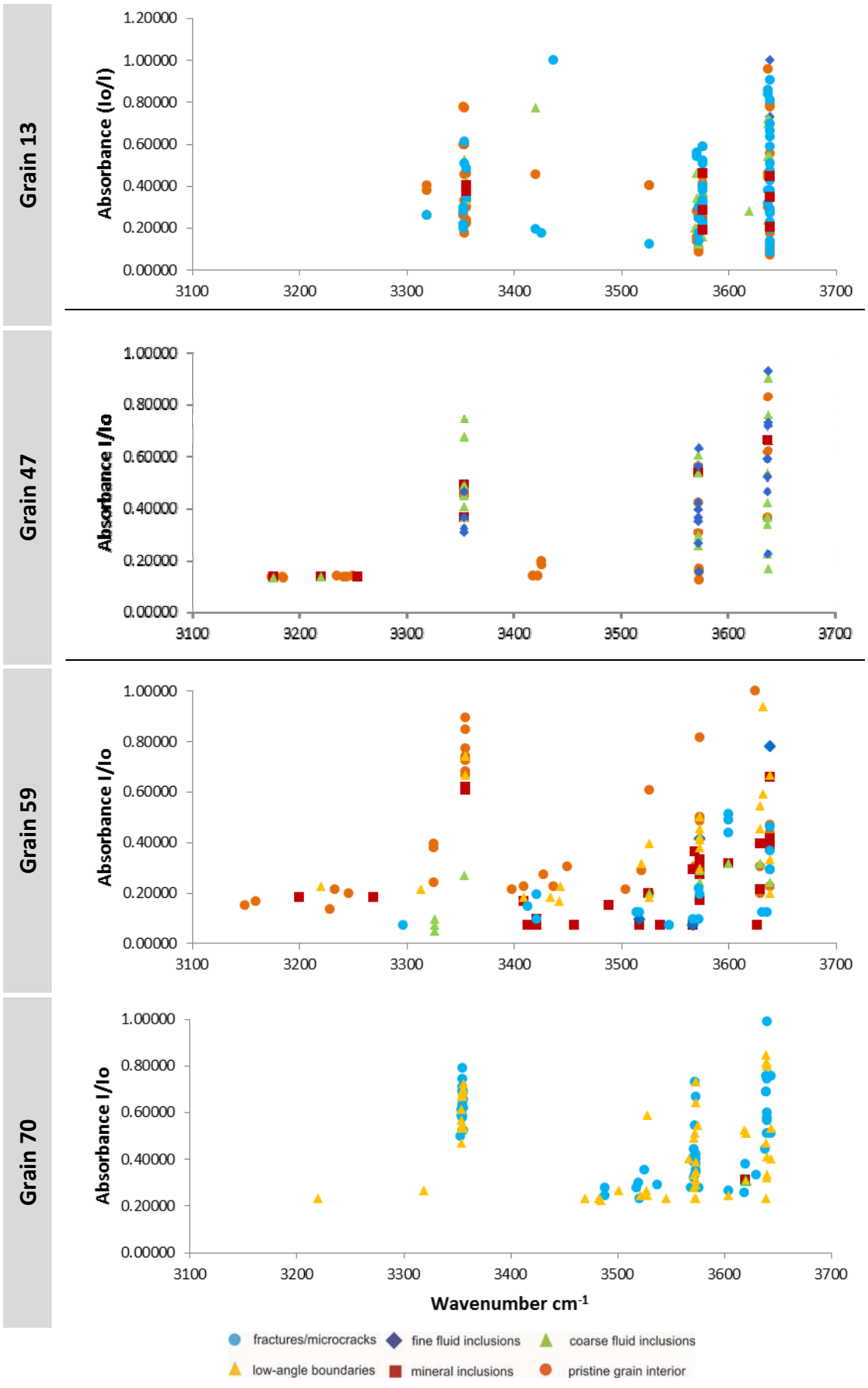

Figure 9.32. Correlation of FTIR absorbance peaks with intragrain features in 136063 grains 13, 47, 59 and 70.

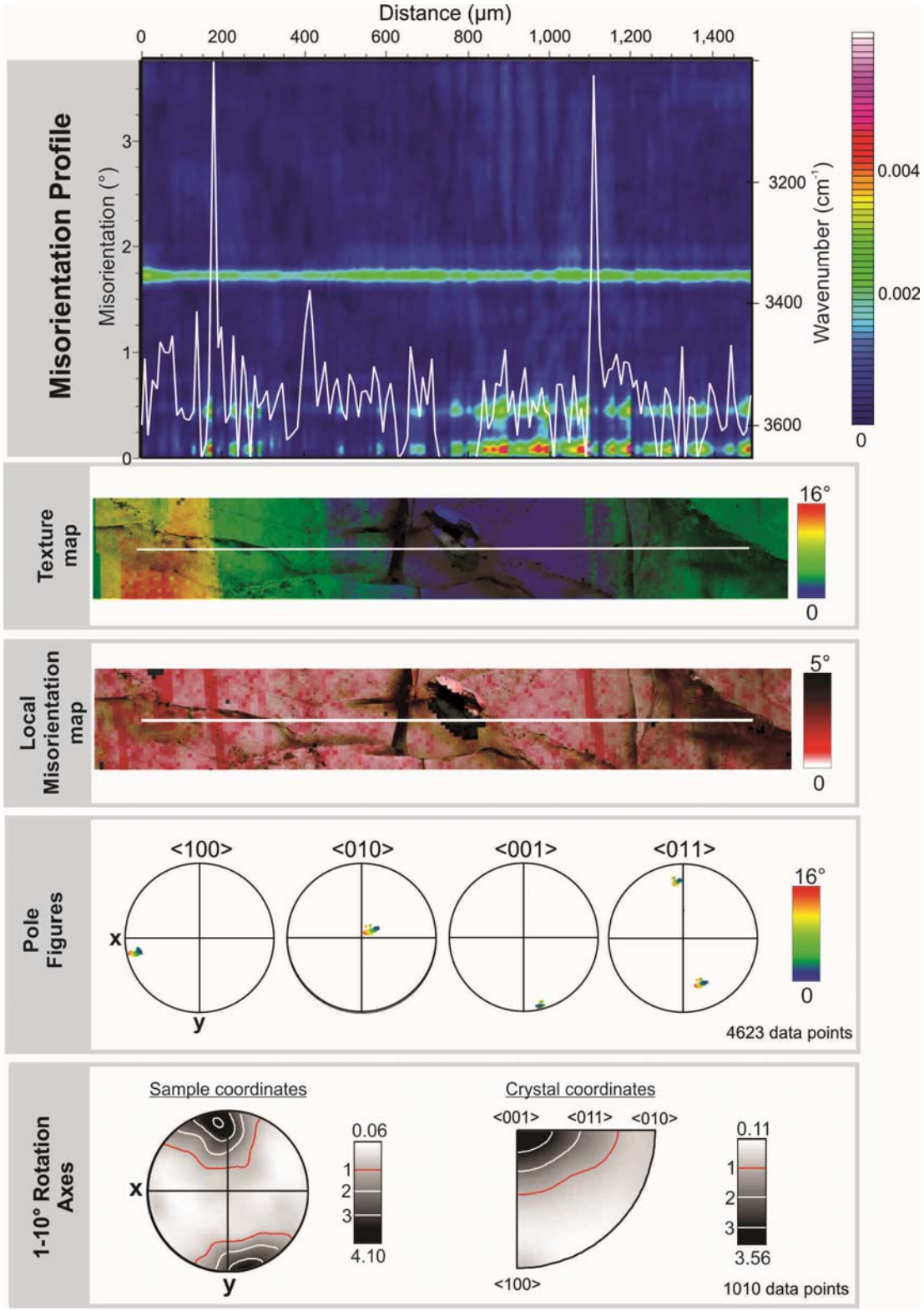

Figure 9.33. A comparison of the misorientation profile (relative to previous point) across scan 13A obtained from EBSD analysis with the FTIR absorbance between 3000 and 3650 cm^{-1}. EBSD texture and local misorientation maps are also provided, along with crystallographic pole figures and rotation axes. Pole figures are equal area lower hemisphere projections.

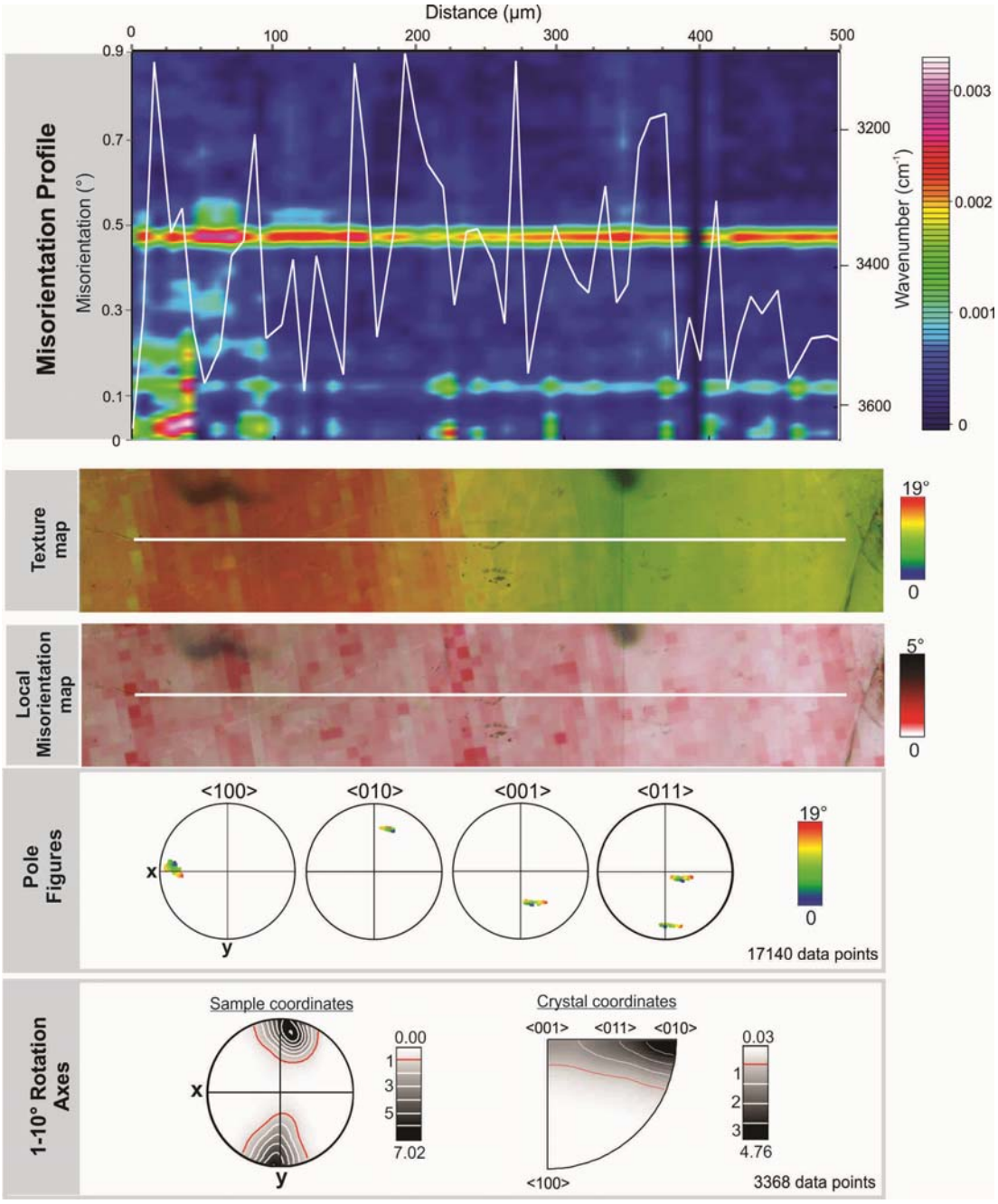

Figure 9.34. A comparison of the misorientation profile (relative to previous point) across scan 59A obtained from EBSD analysis with the FTIR absorbance between 3100 and 3650 cm^{-1}. EBSD texture and local misorientation maps are also provided, along with crystallographic pole figures and rotation axes. Pole figures are equal area lower hemisphere projections.

Figure 9.33 shows a comparison between the FTIR absorbance and misorientation profile across scan 13A. Peaks at ~3640, ~3572 and to a lesser degree ~3355 cm^{-1} are linked to the presence of low-angle boundaries, with the frequency of the peaks showing a moderate degree of correlation with the frequency of low-angle boundaries. Low-angle boundaries with a misorientation angle of <1° correlate moderately well with the FTIR peaks, although this relationship is also made

complicated by the presence of fluid inclusions within the olivine grain. This relationship is also observed in scan 59A (Figure 9.34), with peaks at ~3640 and ~3572 cm-1 correlating with the presence of low-angle boundaries. This relationship is not as strong in grain 59A, despite the lack of any other absorbing features such as fluid inclusions or fractures.

In some cases, there is a slight offset between FTIR peaks and low-angle boundaries. This can be attributed to either another absorbing feature, or error in matching of the EBSD and FTIR results. Matching low-resolution Synchrotron images, EBSD maps and high resolution photomicrographs was undertaken manually and was a difficult process, given the lack of reference points in the images. Thus there is likely to be a degree of uncertainty between the spatial correlation of the data.

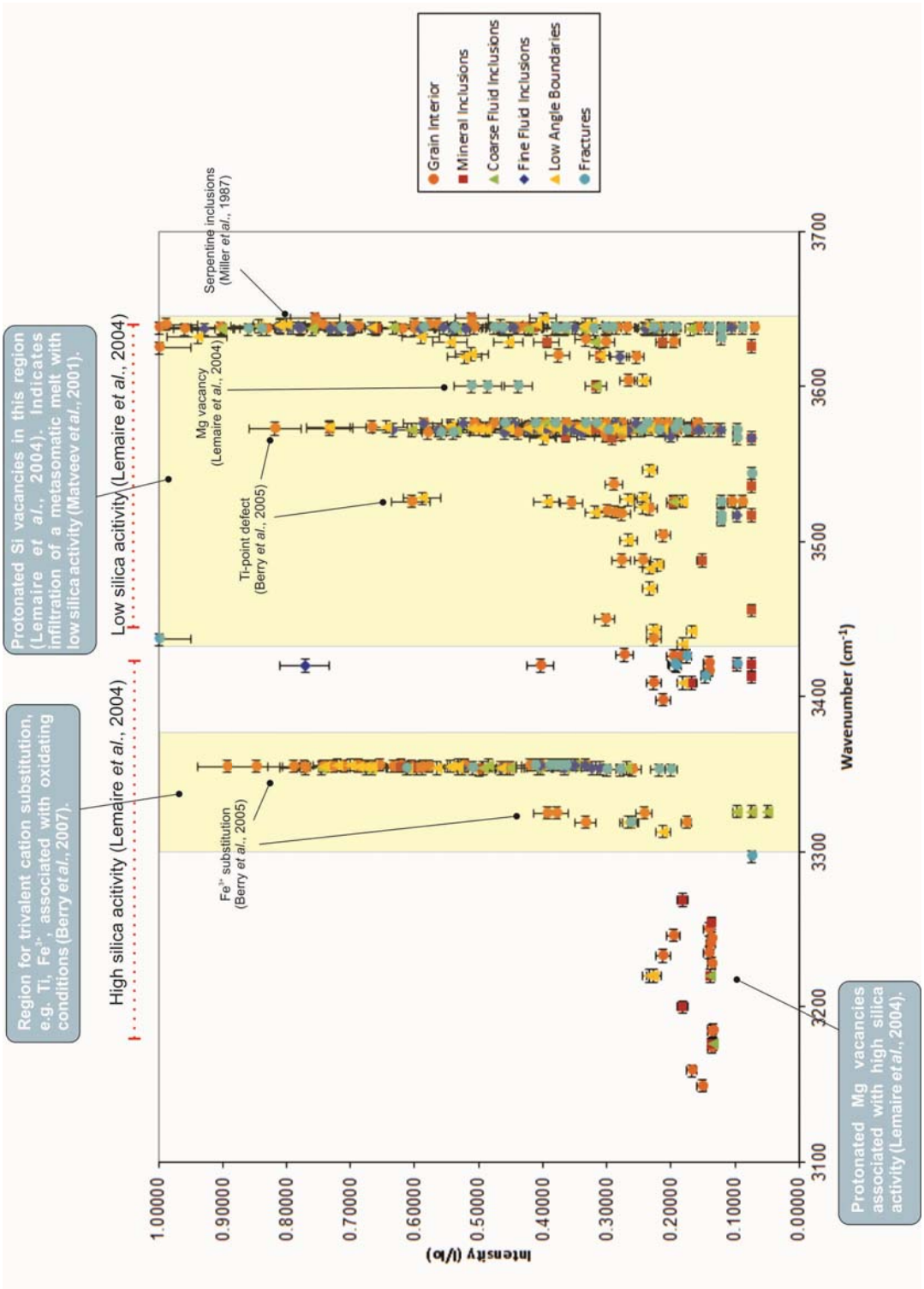

Figure 9.35. A summary of the FTIR peaks observed in olivine grains within Lihir sample 136063, and the features that these correlate with. The plot is annotated to show the associations between FTIR peaks and different hydroxyl incorporation conditions from the literature.

9.3. Stable isotope exchange in deformed mantle olivine

9.3.1. Introduction

Variations in the isotopic compositions of minerals can provide evidence for the nature of planetary and tectonic phenomena, and isotope analysis is a particularly powerful tool for identifying both large- and small-scale processes in rocks. Both oxygen and magnesium isotopes may act as a potential tracer of geochemical processes (Pearson *et al*., 2006), and have been employed to investigate a wide range of geological phenomena, from sedimentary processes (Galy *et al*., 2002) to fluid-rock interaction in the mantle (Kempton *et al*., 1988; Chazot *et al*., 1997; Zhang *et al*., 2001; Pearson *et al*., 2006) and meteorite formation (Clayton, 1993; Galy *et al*., 2000; Clayton, 2003; Wiechert and Halliday, 2007).

The purpose of this study was to characterise the oxygen and magnesium isotopic signature of supra-subduction mantle from peridotites from the Imono and Higashi-Akaishi, and to investigate the relationship between olivine microstructure and isotope variations, in order to gain insight into metasomatic processes in the mantle wedge.

9.3.2. Previous work

Oxygen

Early studies on the oxygen isotope composition of the Earth's mantle (e.g. Clayton and Mayeda, 1963; Borthwick and Harmon, 1982) highlighted variations in $\delta^{18}O$, that were attributed to the interactions between peridotite, melt and fluids (Mattey *et al*., 1994). Most studies analysed the bulk rock $\delta^{18}O$ (e.g. Taylor, 1968; Kyser *et al*., 1981, 1982) with later studies focussing on analysis of constituent minerals, including olivine (e.g. Harmon *et al*., 1986; Kempton *et al*., 1988; Kyser, 1990). In the early nineties, advances in analytical techniques such as laser fluorination (Sharp, 1990, 1992; Mattey and Macpherson, 1993), enabled analysis of very small amounts of material and in-situ samples (Chazot *et al*., 1997). In contrast to these earlier studies, Mattey *et al*. (1994) published a comprehensive dataset of oxygen isotope measurements on olivine, and found homogeneity in $\delta^{18}O$ despite the wide variety of samples analysed. Mattey *et al*. (1994) also found a $\delta^{18}O$ value for the bulk mantle of 5.5 ± 0.2‰. Chazot *et al*. (1997) and Dobosi *et al*. (1998) present similar findings. There has been a large amount of research undertaken on the oxygen isotope

composition of mantle olivine, with many more studies on basalts assumed to have inherited oxygen isotope compositions from the mantle. Despite this, there is still no general consensus regarding the variability of oxygen isotopes in mantle olivine, although it has been suggested that samples containing variations are rare and unrepresentative of the mantle as a whole (Eiler *et al*., 2011).

Magnesium

Most of the work undertaken into the Mg isotope composition of olivine has been focussed on the differentiation of basalts (e.g. Teng *et al*., 2007). Mg isotope studies have also been utilised in order to identify mantle metasomatism events (e.g. O'Reilly *et al*., 1988), but these tend to focus on features of pyroxene rather than olivine. The development of high precision analytical methods (Galy *et al*., 2001) and theoretical foundations of mass-dependent fractionation (Young *et al*., 2002) using MC-ICPMS (multiple collector inductively coupled plasma source mass spectrometry) provided the basis for further investigation of Mg isotopes as a potential tracer for geochemical processes. Galy *et al*. (2001) noted that the mass-dependent fractionation of Mg isotopes in terrestrial materials plots along a curve (slope = 0.5118x ± 0.038) termed the terrestrial fractionation curve (TFC). Young and Galy (2004) summarised these advances, highlighting areas for future development.

In the last 6 years, the Mg isotope composition of terrestrial mantle olivine has been utilised to identify different processes affecting the mantle (Pearson *et al*., 2006; Teng *et al*., 2007; Gray, 2008; Handler *et al*., 2009; Young *et al*., 2009; Yang *et al*., 2009; Chakrabarti and Jacobsen, 2010; Huang *et al*., 2011; Pogge von Strandmann *et al*., 2011; Xie *et al*., 2011), including metasomatism and basalt differentiation, with a view to identifying if the mantle is chondritic in terms of its Mg isotope composition. Despite this, there is still no consensus regarding the nature and variability of Mg isotopes in the terrestrial upper mantle. Several comprehensive studies reveal little or no variation, suggesting that Mg isotopes in the mantle are homogeneous (Teng *et al*., 2007; Handler *et al*., 2009; Young *et al*., 2009; Yang *et al*., 2009; Chakrabarti and Jacobsen, 2010; Huang *et al*., 2011; Pogge von Strandmann *et al*., 2011; Xie *et al*., 2011). However an extensive in-situ LA-ICPMS study done by Pearson *et al.* (2006) shows that there is significant heterogeneity in ^{25}Mg and ^{26}Mg, with large

ranges in δMg values of both ^{25}Mg and ^{26}Mg isotopes, and a trend towards a heavier isotopic composition in metasomatised olivine from the upper mantle. Pearson *et al*. (2006) also identify intragrain variations in isotope composition. An in-situ SIMS study of mantle olivine from metasomatised spinel peridotites from Lihir Island by Gray (2008) also identify significant variation in δMg values, with most of the variation found within single deformed olivine grains. It is currently argued whether these variations are real and only found at a very small intragrain scale that cannot be detected by bulk sampling, or the result of unresolved analytical issues (Handler *et al*., 2009).

9.3.3. Analytical techniques and samples

SIMS analysis was undertaken using a Cameca ims 1280 ion microprobe located at the Centre for Microscopy, Characterisation and Analysis (CMCA) at the University of Western Australia, Perth. The analytical procedure is explained in detail in Chapter 4 but is summarised below. A standard bracketing technique was used to enable identification and correction of time-dependent drift (Halicz *et al*., 1999). Measurements were repeatedly calibrated using analyses of San Carlos olivine as a standard (>5 San Carlos measurements were made in between ~15 unknown measurements). A spot size of ~7 μm was used during magnesium isotope analysis. A drift correction was applied to both oxygen and magnesium isotope data from both samples. The precision was high, with the average δ^{18}O San Carlos measurement at 4.85‰ ± 0.13‰, δ^{25}Mg -0.03‰ ± 0.09‰ and δ^{26}Mg -0.05‰ ± 0.16‰. Measurements that appeared to be outliers were repeated and in all cases were reproduced.

Japan samples J909C (Imono Peridotite) and J917 (Higashi-Akaishi Peridotite) were analysed. Samples J909C and J917 have been described extensively in Chapter 5, as well as throughout the preceding text, so will not be repeated here. Both dunites are porphyroclastic, deformed and contain abundant antigorite. The two samples were chosen for isotope analysis as a result of their contrasting olivine fabrics and interesting microstructural characteristics. Olivine in sample J909C (Imono peridotite body) was found to have two different LPOs, a B-type in the low-strain, olivine-rich microlithon, and a combination of B- and C-type in the high-strain antigorite-rich microlithon (Chapter 8). J917 (Higashi-Akaishi peridotite body) has an A-type

olivine LPO (Chapter 6). Due to the lack of internal microstructure preserved in many of the olivine grains, it was not possible to correlate the internal microstructure directly with the results from the isotope analysis.

9.3.4. Results

Oxygen

Figures 9.36 and 9.37 are plots of the measurements made on J909C and J917, as well as the San Carlos standard measurements used to bracket the data. The San Carlos data points show the high reproducibility of the measurements. The $\delta^{18}O_{V\text{-}SMOW}$ of all the olivine in J909C has an average value of 4.94 ± 0.29‰. The data ranges from 4.26 – 5.81‰, with a total variation of 1.56‰. All of the measurements are provided in Tables 9.2 and 9.3, with uncertainty to 2 standard deviations.

At a more detailed level, the olivine located within the B-type fabric, low-strain zone is comprised of both porphyroclasts and neoblasts. Neoblastic olivine has an average $\delta^{18}O_{V\text{-}SMOW}$ of 5.05 ± 0.30‰, within error of the sample average, and the data ranges from 4.26 – 5.48‰, with a total variation of 1.22‰. Porphyroclastic olivine has an average of 4.77 ± 0.30‰, which is slightly lower than the sample average but this is not statistically significant. The porphyroclastic olivine has a range of $\delta^{18}O_{V\text{-}SMOW}$ from 4.26 – 4.77‰, with a total variation of 0.51‰. Neoblastic olivine from within the high-strain, B-/C-type LPO region has an average of 5.19 ± 0.27‰. The values range from 4.27 – 5.18‰, with a total variation of 0.91‰. In comparison, both generations of neoblasts have a higher average and variation of $\delta^{18}O_{V\text{-}SMOW}$ than the porphyroclastic olivine.

Olivine in J917 has an average value of 4.46 ± 0.24‰, ranging from 4.17 – 4.70‰, with a total variation in $\delta^{18}O_{V\text{-}SMOW}$ of 0.53‰. J917 olivine is also comprised of porphyroclasts and neoblasts. Neoblastic olivine has an average $\delta^{18}O_{V\text{-}SMOW}$ of 4.43 ± 0.24‰, with a range of 4.17 – 4.70‰ and a total variation of 0.53‰. The average is slightly lower than that of the sample, but the variation is identical. The porphyroclastic olivine has an average of 4.49 ± 0.24‰, which is slightly higher than that of the sample. The data ranges from 4.20 – 4.65‰, and the total variation is 0.45‰.

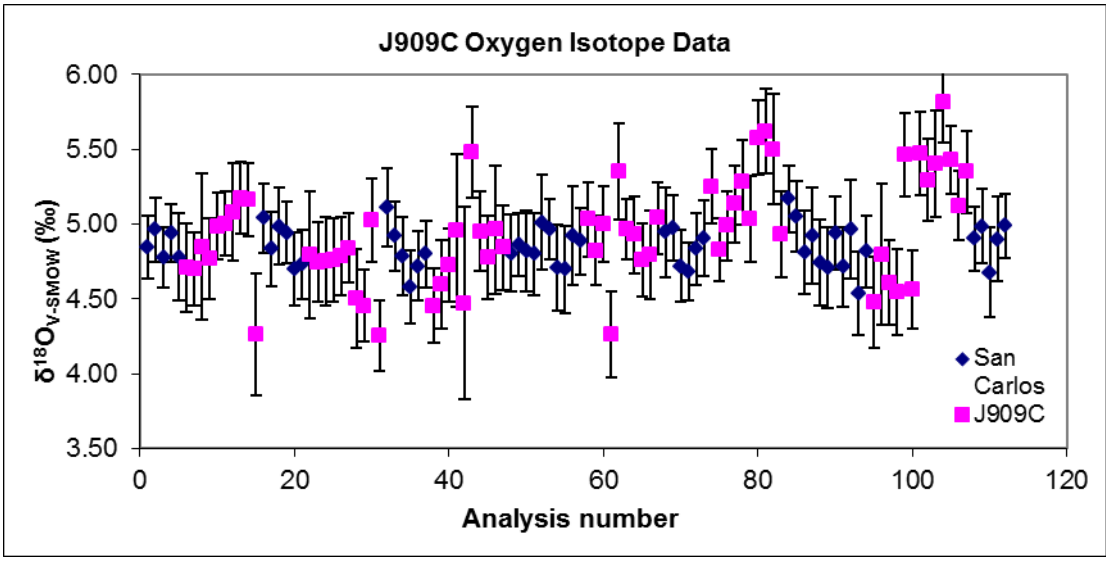

Figure 9.36. Plot of J909C olivine $\delta^{18}O$ relative to V-SMOW. Errors are reported as 2σ.

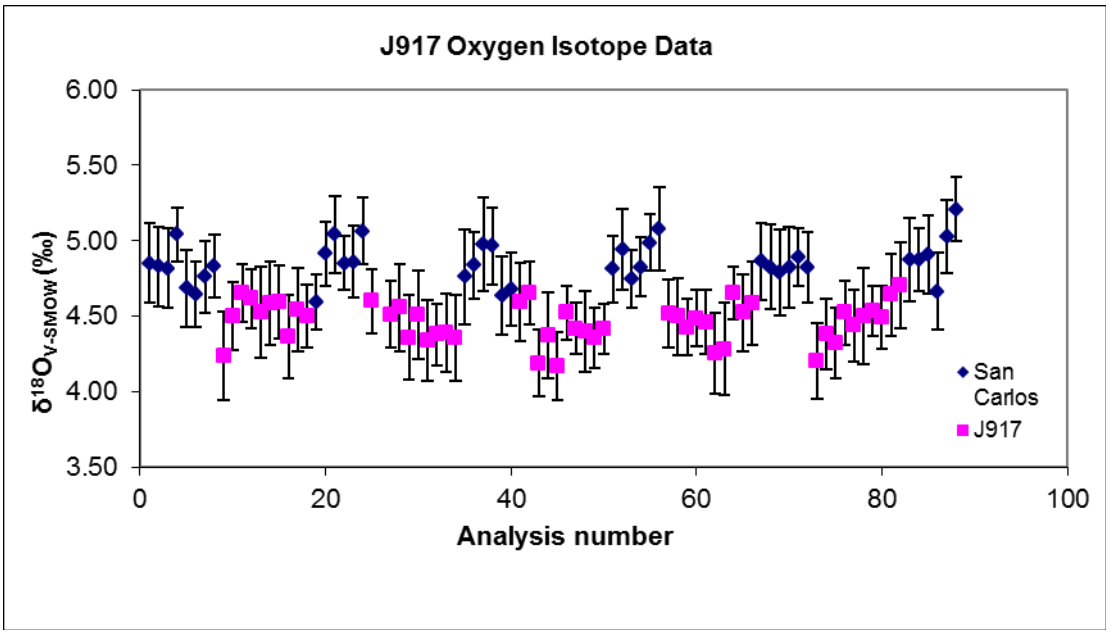

Figure 9.37. Plot of J917 olivine $\delta^{18}O$ relative to V-SMOW. Errors are reported as 2σ.

Table 9.3. Oxygen isotope data from sample J909C, corrected for instrumental drift and expressed relative to Standard Mean Ocean Water (SMOW). The $\delta^{18}O$ values are coloured to enable comparison to the pole figures in Figure 9.42.

Spot Name	Grain type	Comments	Grain area	$\delta^{18}O_{V\text{-}SMOW}$	Uncertainty (2σ)
J909C_Ol@01	Porphyroclast	Same grain	280000	4.71	0.15
J909C_Ol@2	Porphyroclast		280000	4.70	0.12
J909C_Ol@3	Porphyroclast		280000	4.85	0.24
J909C_Ol@4	Porphyroclast		280000	4.77	0.13
J909C_Ol@5	Porphyroclast		280000	4.99	0.11
J909C_Ol@6	Porphyroclast		280000	5.00	0.11
J909C_Ol@7	Porphyroclast		280000	5.08	0.16

J909C_Ol@8	Neoblast	Same grain	36800	5.18	0.12
J909C_Ol@9	Neoblast		36800	5.16	0.12
J909C_Ol@10	Neoblast		22500	4.26	0.20
J909C_Ol@11	Neoblast		9000	4.80	0.21
J909C_Ol@12	Porphyroclast	Same grain	45500	4.75	0.13
J909C_Ol@13	Porphyroclast		45500	4.75	0.15
J909C_Ol@14	Porphyroclast	Same grain	630000	4.76	0.14
J909C_Ol@15	Porphyroclast		630000	4.79	0.13
J909C_Ol@16	Porphyroclast		630000	4.84	0.11
J909C_Ol@17	Porphyroclast		630000	4.50	0.16
J909C_Ol@18	Porphyroclast		630000	4.45	0.12
J909C_Ol@19	Porphyroclast		630000	5.03	0.14
J909C_Ol@20	Porphyroclast		630000	4.26	0.12
J909C_Ol@21	Porphyroclast		630000	4.45	0.12
J909C_Ol@22	Porphyroclast		630000	4.60	0.15
J909C_Ol@23	Porphyroclast		630000	4.72	0.12
J909C_Ol@24	Porphyroclast		630000	4.96	0.26
J909C_Ol@25	Porphyroclast		630000	4.47	0.32
J909C_Ol@26	Neoblast		9000	5.48	0.15
J909C_Ol@27	Neoblast		10000	4.95	0.13
J909C_Ol@28	Porphyroclast	Same grain	30000	4.78	0.14
J909C_Ol@29	Porphyroclast		30000	4.96	0.21
J909C_Ol@30	Porphyroclast	Same grain	240000	4.84	0.14
J909C_Ol@31	Porphyroclast		240000	5.03	0.12
J909C_Ol@32	Porphyroclast		240000	4.82	0.12
J909C_Ol@33	Porphyroclast		240000	5.00	0.13
J909C_Ol@34	Neoblast		1600	4.27	0.14
J909C_Ol@35	Neoblast	Same grain	500	5.35	0.16
J909C_Ol@36	Neoblast		500	4.97	0.10
J909C_Ol@37	Porphyroclast	Same grain	165000	4.93	0.13
J909C_Ol@38	Porphyroclast		165000	4.76	0.12
J909C_Ol@39	Porphyroclast		165000	4.80	0.15
J909C_Ol@40	Porphyroclast		165000	5.04	0.12
J909C_Ol@41	Neoblast		1000	5.25	0.12
J909C_Ol@42	Neoblast	Same grain	2400	4.83	0.10
J909C_Ol@43	Neoblast		2400	4.99	0.12
J909C_Ol@44	Neoblast		2400	5.13	0.13
J909C_Ol@45	Neoblast	Same grain	3200	5.28	0.14
J909C_Ol@46	Neoblast		3200	5.04	0.14
J909C_Ol@47	Neoblast	Same grain	1800	5.58	0.13
J909C_Ol@48	Neoblast		1800	5.62	0.14
J909C_Ol@49	Neoblast		6000	5.50	0.18
J909C_Ol@50	Neoblast		4000	4.93	0.14
J909C_Ol@10_rerun	Neoblast		22500	4.47	0.15
J909C_Ol@17rerun	Porphyroclast	Same grain	630000	4.80	0.24
J909C_Ol@18rerun	Porphyroclast		630000	4.61	0.14
J909C_Ol@20rerun	Porphyroclast		630000	4.55	0.14
J909C_Ol@26rerun	Neoblast		9000	5.46	0.14
J909C_Ol@34rerun	Neoblast		1600	4.56	0.13
J909C_Ol@35rerun	Neoblast		500	5.47	0.14
J909C_Ol@47rerun	Neoblast	Same grain	1800	5.30	0.14
J909C_Ol@48rerun	Neoblast		1800	5.40	0.18
J909C_Ol@49_rerun	Neoblast		6000	5.81	0.14
J909C_Ol_near-47-49@1	Neoblast		1800	5.43	0.11
J909C_Ol_near-47-49@2	Neoblast		800	5.12	0.12
J909C_Ol_near-47-49@3	Neoblast		1800	5.35	0.14

Table 9.4. Oxygen isotope data from sample J917, expressed relative to Standard Mean Ocean Water (SMOW). The $\delta^{18}O$ values are coloured to enable comparison to the pole figures in Figure 9.43.

Spot Name	Grain type	Comments	Grain area	$\delta^{18}O_{V\text{-}SMOW}$	Uncertainty (2σ)
J917_Ol@01	Porphyroclast		16900	4.23985	0.146653
J917_Ol@2	Porphyroclast		22500	4.500987	0.11132
J917_Ol@3	Neoblast		33600	4.649428	0.095612
J917_Ol@4	Porphyroclast	Same grain	877500	4.615669	0.09754
J917_Ol@5	Porphyroclast		877500	4.523824	0.151636
J917_Ol@6	Porphyroclast		877500	4.586874	0.139182
J917_Ol@7	Porphyroclast		877500	4.593825	0.119487
J917_Ol@8	Porphyroclast		877500	4.365454	0.138422
J917_Ol@9	Porphyroclast		877500	4.541697	0.136999
J917_Ol@10	Porphyroclast		877500	4.499498	0.104749
J917_Ol@11	Porphyroclast		877500	4.599286	0.106995
J917_Ol@13	Porphyroclast		877500	4.510916	0.111053
J917_Ol@14	Porphyroclast		877500	4.557583	0.14403
J917_Ol@15	Porphyroclast		80000	4.359496	0.141303
J917_Ol@16	Neoblast		9000	4.508434	0.145575
J917_Ol@17	Neoblast		10000	4.337652	0.132347
J917_Ol@18	Neoblast		23000	4.379851	0.101911
J917_Ol@19	Neoblast		7350	4.387794	0.130814
J917_Ol@20	Neoblast		5400	4.352546	0.142813
J917_Ol@21	Neoblast		10000	4.594818	0.130878
J917_Ol@22	Neoblast		4000	4.651414	0.103959
J917_Ol@23	Neoblast		5400	4.189707	0.109446
J917_Ol@24	Neoblast		24000	4.371908	0.141044
J917_Ol@25	Neoblast		17600	4.170842	0.11312
J917_Ol@26	Neoblast	Same grain	25000	4.52432	0.088682
J917_Ol@27	Neoblast		25000	4.419071	0.085253
J917_Ol@28	Neoblast		25000	4.397724	0.134009
J917_Ol@29	Neoblast		6500	4.354532	0.098623
J917_Ol@30	Neoblast		12600	4.412617	0.082222
J917_Ol@31	Porphyroclast	Same grain	138000	4.517867	0.111712
J917_Ol@32	Porphyroclast		138000	4.498008	0.128182
J917_Ol@33	Porphyroclast		138000	4.425525	0.093364
J917_Ol@34	Porphyroclast		138000	4.487086	0.094244
J917_Ol@35	Porphyroclast		49500	4.460774	0.106822
J917_Ol@36	Neoblast	Same grain	31500	4.25524	0.135196
J917_Ol@37	Neoblast		31500	4.282545	0.154427
J917_Ol@38	Porphyroclast	Same grain	495000	4.6534	0.08579
J917_Ol@39	Porphyroclast		495000	4.522831	0.126138
J917_Ol@40	Porphyroclast		495000	4.585385	0.137943
J917_Ol@41	Porphyroclast		495000	4.201126	0.126039
J917_Ol@42	Porphyroclast		495000	4.379355	0.116931
J917_Ol@43	Porphyroclast		495000	4.321765	0.118448
J917_Ol@44	Porphyroclast	Same grain	44000	4.523328	0.105146
J917_Ol@45	Porphyroclast		44000	4.43893	0.118306
J917_Ol@46	Porphyroclast		13000	4.497512	0.159274
J917_Ol@47	Porphyroclast		12100	4.53425	0.083525
J917_Ol@48	Porphyroclast		13000	4.492051	0.103346
J917_Ol@49	Porphyroclast		16000	4.641485	0.137323
J917_Ol@50	Porphyroclast		15400	4.704038	0.144216

The two samples have similar means, although there is a substantially larger variation observed in $\delta^{18}O_{V\text{-}SMOW}$ in J909C than J917. The variations observed within

neoblastic olivine in the high-strain region (B-/C-type olivine LPO) of J909C show significantly more variation than has been observed in the most of the literature thus far, with the exception of a recent in-situ SIMS study by Eiler *et al*. (2011) (Figure 9.38). Other significant variations have been observed in coarse-grained metasomatised spinel peridotites from Lihir Island (McInnes *et al*., 1999), coarse-grained garnet harzburgites from Sierra Leone (Deines and Haggerty, 2000), coarse-grained spinel and garnet from Vitim (Ionov *et al*., 1994), anhydrous spinel peridotite from West Germany (Kempton *et al*., 1988), anhydrous spinel lherzolite from North-Central Mongolia (Harmon *et al*., 1986) and porphyroclastic olivine from the Kaapvaal Craton (Zhang *et al*., 2003). The variations observed in J917 are comparable to that of much of the published literature (e.g. Mattey *et al*., 1994; Chazot *et al*., 1997).

Analytical considerations

There are several potential causes behind the variations in $\delta^{18}O_{V\text{-}SMOW}$ that need to be addressed including standard variations, grain size, grain orientation and natural variability as a result of geochemical processes. There has been some controversy over the use of SIMS to analyse for oxygen isotopes, particularly in terms of the effects of instrumental mass fractionation (Eiler *et al*., 1997; Hartley *et al*., 2012). However the findings of a recent study by Eiler *et al*. (2011) show agreement between results from both laser fluorination (LF) and SIMS techniques, and that current SIMS techniques are precise and accurate enough to detect small variations in the oxygen isotope composition of silicates. The analytical procedure of Valley and Kita (2009) was followed in the current study, including standard bracketing techniques and centrally-mounted standards and unknowns, therefore it is not expected that instrumental mass fractionation related to SIMS is a significant factor in producing variations in oxygen isotope composition.

The variations in $\delta^{18}O_{V\text{-}SMOW}$ of San Carlos are on the order of those observed in sample J917, and thus may explain the spread of the J917 measurements. The variations observed in J909C are larger than those of San Carlos, so are interpreted to be significant.

Zhang *et al*. (2000) observe a positive correlation between grain size and oxygen isotope ratio, with neoblastic olivine showing more evidence for isotopic exchange with fluids and melt than larger grains. In order to examine this effect on the Japan samples, $\delta^{18}O_{V\text{-}SMOW}$ was plotted relative to grain area (Figure 9.39). There was no significant effect of grain size on oxygen isotope ratio, except for the fact that neoblastic olivine in sample J909C tended to be more variable in composition, which may or may not be a function of the grain size.

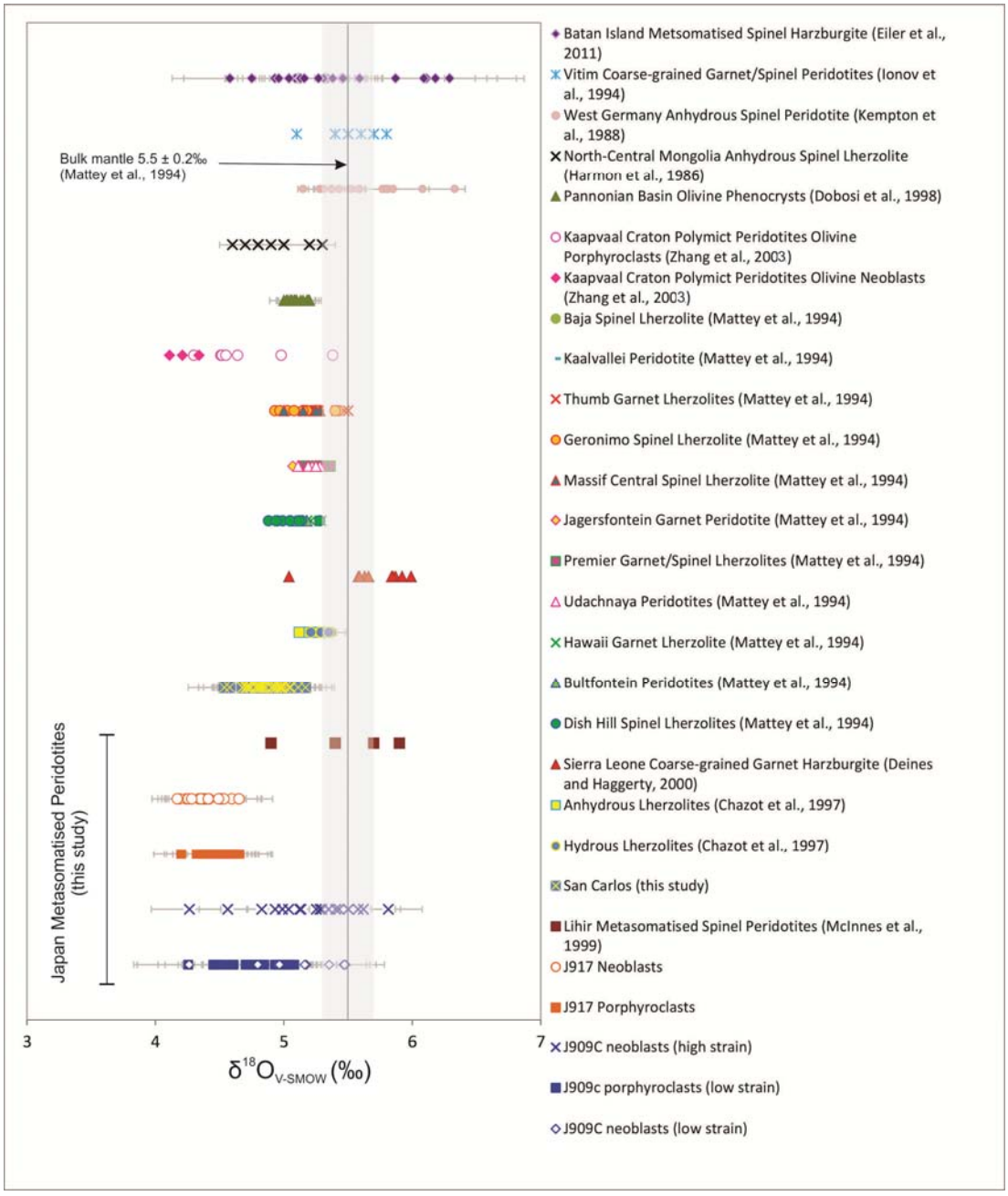

Figure 9.38. Comparison of oxygen isotope data for olivine from the Japanese dunites of this study to published literature on natural mantle olivine. The titles in the legend are in the same order as the data points, for ease of comparison.

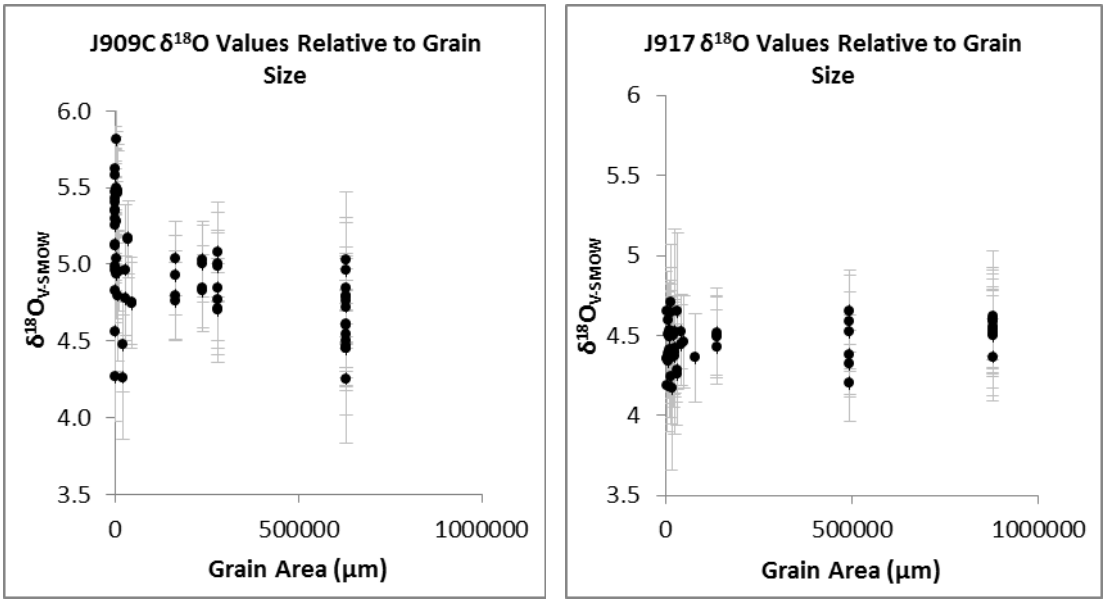

Figure 9.39. Plot of $\delta^{18}O_{SMOW}$ relative to grain size, showing that there is no apparent link between the area of the grain and the absolute oxygen isotope ratio. The largest variations are found in the smallest grains, which may reflect higher diffusion rates in smaller grains.

A grain orientation effect on oxygen isotope fractionation in magnetite (Lyon *et al*., 1998; Huberty *et al*., 2010) and hematite (Huberty *et al*., 2010) has been reported during SIMS analysis. In order to examine this as a potential cause of oxygen isotope variations in the Japan olivine, numerous grains from each sample were analysed using EBSD (see Chapter 4 for methodology). Pole figures of the grain populations are presented in Figures 9.40 and 9.41. These plots show that there is no clear systematic link between the orientation of a grain and the oxygen isotope variations.

Magnesium

Data is provided in Tables 9.4 and 9.5. On a three-isotope plot of the Mg isotope ratios (showing ^{25}Mg and ^{26}Mg relative to ^{24}Mg; Figures 9.42 and 9.43), in-situ analyses of Japan olivine plot on the terrestrial fractionation curve (slope of 0.521 from Galy *et al*., 2001; Young and Galy, 2004). In sample J909C, the δ^{25} Mg of olivine ranges from -0.80 to -0.24‰, with a total variation of 0.56‰ (Table 9.4). δ^{26} Mg ranges from -1.54 to -0.46‰, with a total variation of 1.08‰. The average values for δ^{25} Mg and δ^{26} Mg are -0.54 ± 0.04‰ and -1.03 ± 0.08‰, respectively. A closer examination of the different grain size populations reveals that both porphyroclastic

and neoblastic olivine have similar ranges in δ^{25} Mg but the neoblastic olivine shows slightly more variation in δ^{26} Mg than the porphyroclasts.

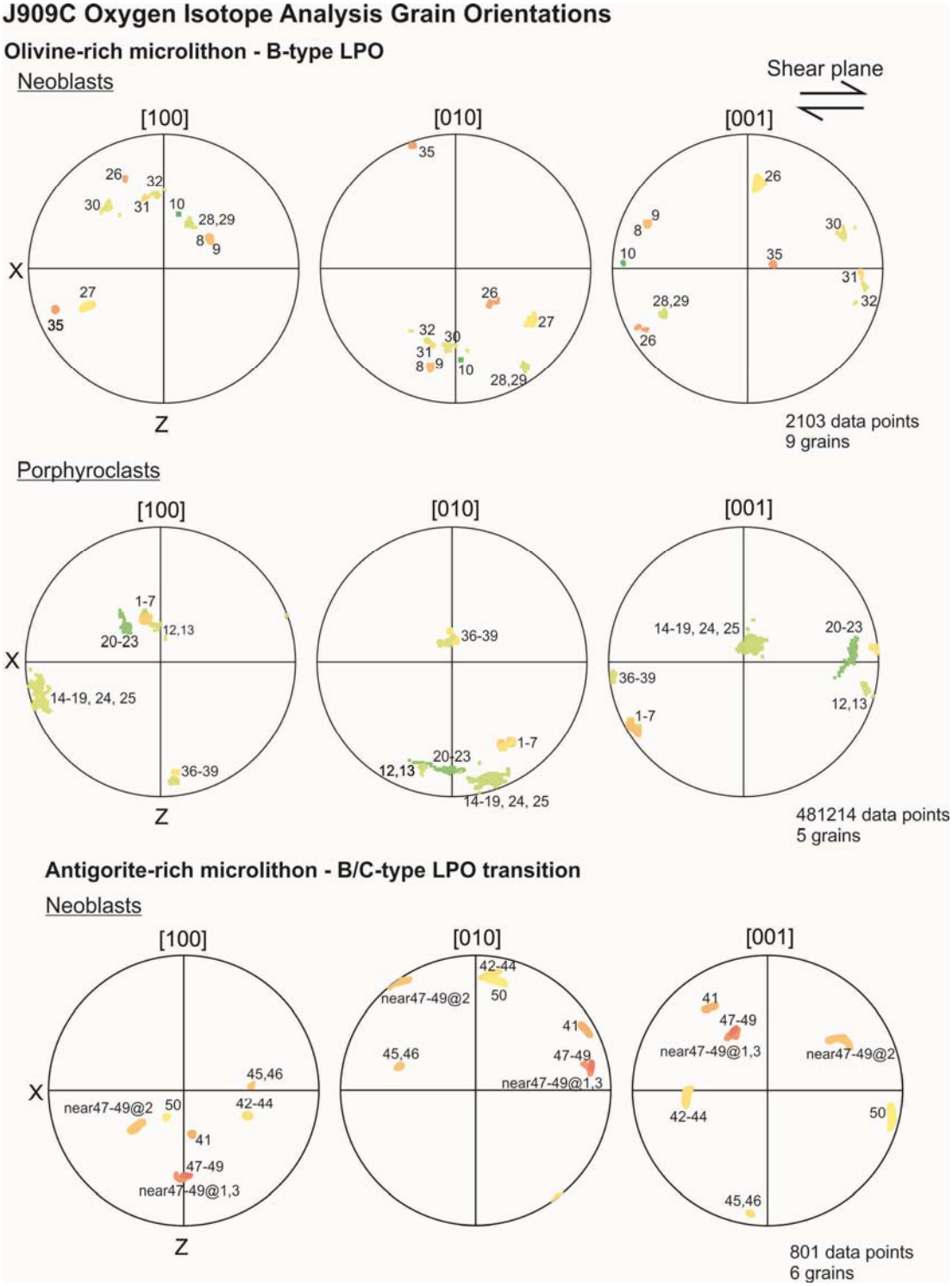

Figure 9.40. Orientations of olivine grains in sample J909C analysed for oxygen isotopes. The grains are coloured by isotope ratio using the same colour scale as table 9.2. Where there are multiple analyses for a single grain an average is value is applied. There is no obvious link between grain orientation and oxygen isotope ratio, therefore the isotopic variations are not caused by grain orientation effects. The shear plane is represented by the XY plane, and the lineation direction is the X direction. Pole figures are equal area, lower hemisphere projections.

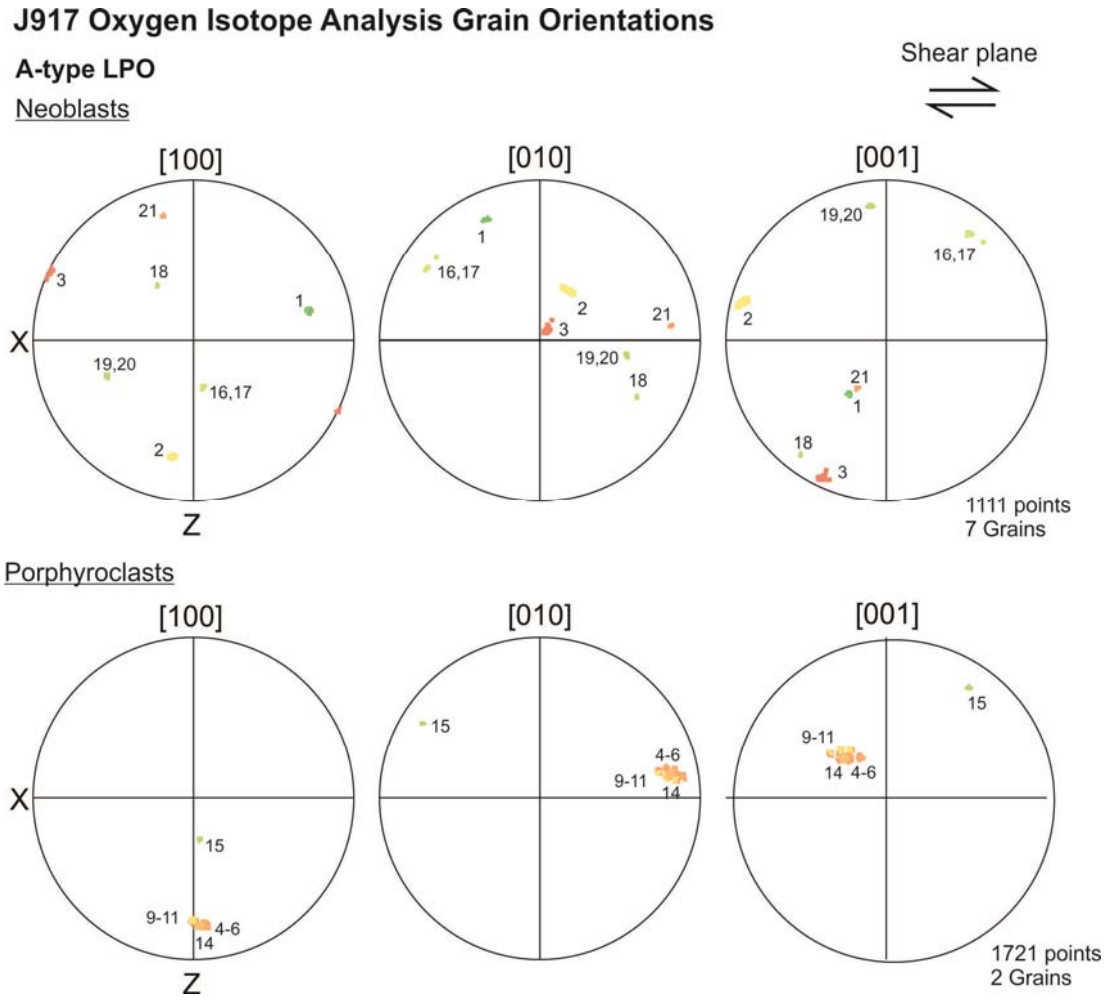

Figure 9.41. Orientations of olivine grains in sample J917 analysed for oxygen isotopes. The grains are coloured by isotope ratio using the same colour scale as table 9.3. Where there are multiple analyses for a single grain an average is value is applied. There is no systematic relationship between grain orientation and oxygen isotope ratio, therefore the isotopic variations are not caused by grain orientation effects. The shear plane is represented by the XY plane, and the lineation direction is the X direction. Pole figures are equal area, lower hemisphere projections.

The average values also show that neoblastic olivine is more depleted in both ^{25}Mg and ^{26}Mg compared to the porphyroclastic olivine (Table 9.6 and Figure 9.43). There was a small amount of intragrain variation identified in porphyroclastic olivine within J909C. Three porphyroclasts were analysed, and two were found to contain internal variations in δ^{26} Mg of 0.48‰ and 0.58‰. This is over half the variation observed for the entire sample, however is not much larger than the uncertainty.

In sample J917, the δ^{25} Mg of olivine ranges from -0.61 to -0.13‰, with a total variation of 0.49‰ (Table 9.6). δ^{26} Mg ranges from -1.26 to -0.26‰, with a total variation of 1.00‰. The average values for δ^{25} Mg and δ^{26} Mg are -0.40 ± 0.10‰ and -0.80 ± 0.16‰, respectively. The average δ^{25} Mg and δ^{26} Mg values for

porphyroclasts and neoblasts shows that there is little variation between the two populations of grains in J917 (Table 9.6).

Analytical considerations

The careful analysis of these samples using standard bracketing techniques and centrally-mounted standards and unknowns enabled the correction of time-dependent drift. Thus the effect of instrumental mass fractionation during SIMS analysis on magnesium isotope ratio is not expected to be significant in this data. In the past, concern has also been raised regarding the effects of variations in olivine chemistry on magnesium isotope ratio, however variations in Ca and Ti content have been found to be negligible for Mg-rich olivine (Young *et al*., 2002; Pearson *et al*., 2006).

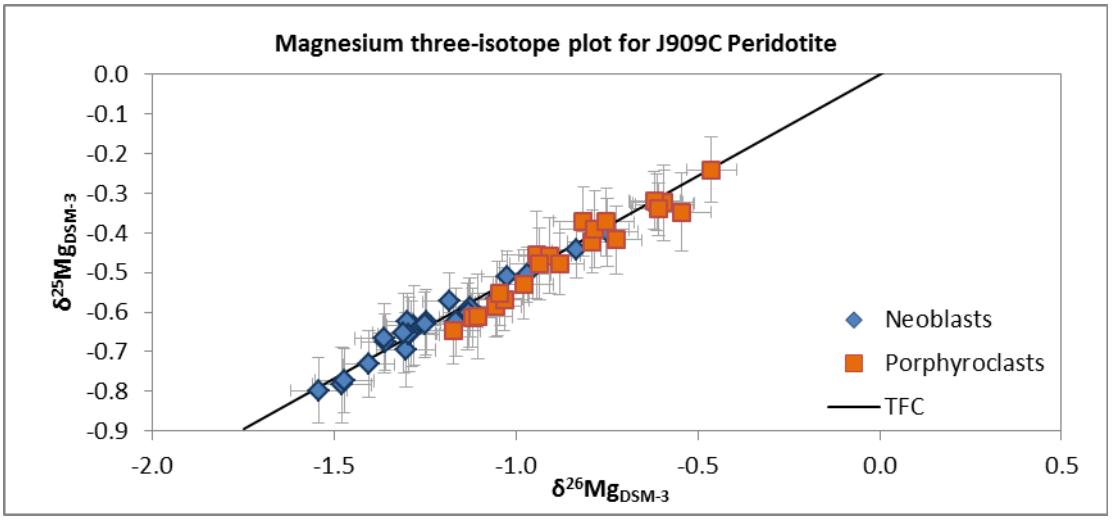

Figure 9.42. Magnesium three-isotope plot for olivine in sample J909C. Uncertainty is reported to 2σ. The data plot on the terrestrial fractionation curve (TFC) defined by Galy *et al*. (2000).

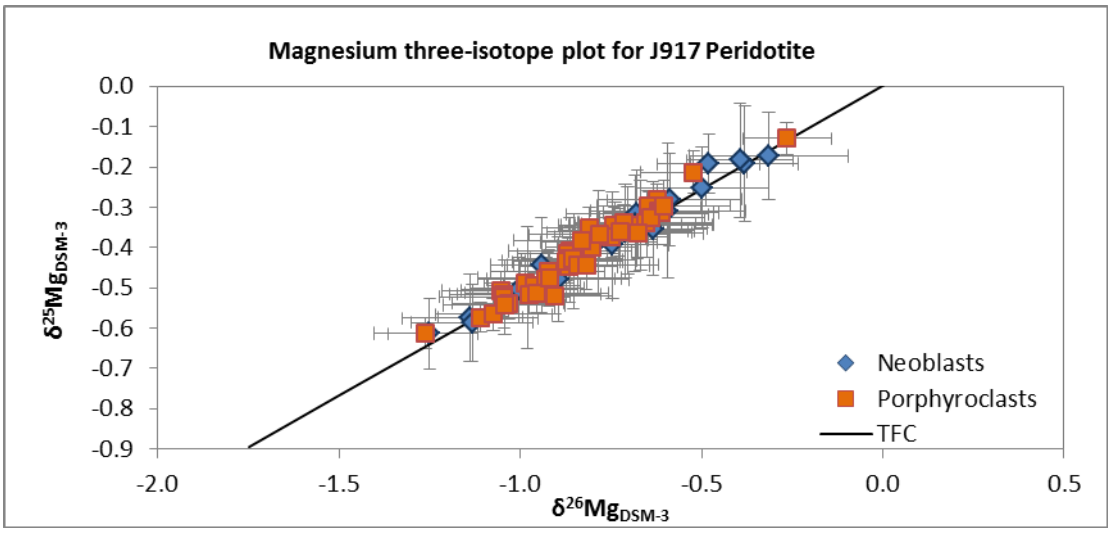

Figure 9.43. Magnesium three-isotope plot for olivine in sample J917. Uncertainty is reported to 2σ. The data plot on the terrestrial fractionation curve (TFC) defined by Galy *et al*. (2000).

In order to rule out the effects of orientation on δMg, the orientation of a number of grains that were analysed using SIMS was determined using EBSD. Figure 9.47 shows that for sample J909C there is no significant relationship between δMg and grain orientation (there were not enough grains from sample J917 analysed using EBSD to produce a meaningful diagram for the data).

Table 9.5. Magnesium isotope data from sample J909C, corrected for instrumental drift and expressed relative to DSM-3.

Spot Name	Grain type	Grain area	Comments	$\delta^{25}Mg_{DSM-3}$	Uncertainty (2σ)	$\delta^{26}Mg_{DSM-3}$	Uncertainty (2σ)
J909C-NB@1	Neoblast	5000		-0.63	0.05	-1.28	0.07
J909C-NB@2	Neoblast	3500		-0.57	0.04	-1.18	0.07
J909C-NB@3	Neoblast	6000		-0.65	0.04	-1.29	0.07
J909C-NB@4	Neoblast	7150		-0.62	0.03	-1.30	0.07
J909C-NB@5	Neoblast	21000		-0.68	0.04	-1.36	0.07
J909C-NB@6	Neoblast	21000	Same grain	-0.51	0.03	-1.02	0.07
J909C-NB@7	Neoblast	21000		-0.59	0.04	-1.13	0.06
J909C-NB@8	Neoblast	4500		-0.44	0.04	-0.83	0.07
J909C-NB@9	Neoblast	4000		-0.57	0.05	-1.05	0.07
J909C-NB@10	Neoblast	6500		-0.61	0.04	-1.13	0.08
J909C-NB@11	Neoblast	8000	Same grain	-0.80	0.04	-1.54	0.08
J909C-NB@12	Neoblast	8000		-0.78	0.05	-1.48	0.08
J909C-NB@13	Neoblast	5000		-0.33	0.04	-0.59	0.08
J909C-NB@14	Neoblast	6300		-0.60	0.04	-1.13	0.07
J909C-NB@15	Neoblast	5500		-0.77	0.04	-1.47	0.08
J909C-NB@16	Neoblast	80000		-0.62	0.04	-1.25	0.07
J909C-NB@17	Neoblast	80000		-0.51	0.04	-0.97	0.07
J909C-NB@18	Neoblast	80000	Same grain	-0.63	0.04	-1.25	0.07
J909C-NB@19	Neoblast	80000		-0.67	0.04	-1.36	0.08
J909C-NB@20	Neoblast	80000		-0.69	0.05	-1.30	0.08
J909C-NB@21	Neoblast	80000		-0.63	0.04	-1.16	0.08
J909C-NB@22	Neoblast	37500	Same grain	-0.73	0.04	-1.40	0.07
J909C-NB@23	Neoblast	37500		-0.40	0.04	-0.75	0.08
J909C-NB@24	Neoblast	4500		-0.66	0.05	-1.29	0.08
J909C-NB@25	Neoblast	9500		-0.65	0.05	-1.31	0.09
J909C-PC@1	Porphyroclast	100000		-0.46	0.06	-0.94	0.09
J909C-PC@02	Porphyroclast	100000		-0.37	0.04	-0.81	0.08
J909C-PC@03	Porphyroclast	100000	Same grain	-0.46	0.05	-0.91	0.09
J909C-PC@04	Porphyroclast	100000		-0.32	0.04	-0.61	0.07
J909C-PC@05	Porphyroclast	100000		-0.24	0.04	-0.46	0.07
J909C-PC@06	Porphyroclast	100000		-0.48	0.04	-0.88	0.07
J909C-PC@07	Porphyroclast	630000		-0.42	0.04	-0.79	0.07
J909C-PC@08	Porphyroclast	630000		-0.61	0.04	-1.12	0.06
J909C-PC@09	Porphyroclast	630000		-0.59	0.04	-1.06	0.07
J909C-PC@10	Porphyroclast	630000		-0.65	0.04	-1.17	0.08
J909C-PC@11	Porphyroclast	630000		-0.57	0.04	-1.03	0.07
J909C-PC@12	Porphyroclast	630000	Same grain	-0.39	0.05	-0.78	0.10
J909C-PC@13	Porphyroclast	630000		-0.48	0.05	-0.94	0.08
J909C-PC@14	Porphyroclast	630000		-0.32	0.05	-0.59	0.08
J909C-PC@15	Porphyroclast	630000		-0.32	0.04	-0.62	0.07
J909C-PC@16	Porphyroclast	630000		-0.37	0.04	-0.75	0.08
J909C-PC@17	Porphyroclast	45500	Same grain	-0.42	0.04	-0.73	0.07
J909C-PC@18	Porphyroclast	45500		-0.34	0.03	-0.61	0.08
J909C-PC@19	Porphyroclast	17000		-0.35	0.05	-0.54	0.08

J909C-PC@20	Porphyroclast	90000		-0.53	0.04	-0.98	0.08
J909C-PC@21	Neoblast	30000	Same grain	-0.55	0.04	-1.04	0.09
J909C-PC@22	Neoblast	30000		-0.61	0.05	-1.11	0.09

Table 9.6. Magnesium isotope data from sample J909C, corrected for instrumental drift and expressed relative to DSM-3.

Spot Name	Grain type	Grain area	Comments	δ^{25} Mg_{DSM-3}	Uncertainty (2σ)	δ^{26} Mg_{DSM-3}	Uncertainty (2σ)
J917-NB@1	Neoblast	36000	Same grain	-0.5048	0.040963	-1.00345	0.080206
J917-NB@02	Neoblast	36000		-0.61412	0.043985	-1.25033	0.056511
J917-NB@03	Neoblast	15750		-0.43193	0.05264	-0.86341	0.092604
J917-NB@04	Neoblast	8400		-0.5753	0.054371	-1.13844	0.093713
J917-NB@05	Neoblast	9100		-0.47866	0.053308	-0.89589	0.098437
J917-NB@06	Neoblast	12600		-0.17291	0.054691	-0.31478	0.110188
J917-NB@07	Neoblast	15400		-0.31707	0.05479	-0.67716	0.098631
J917-NB@08	Neoblast	12100		-0.58639	0.047742	-1.13267	0.083821
J917-NB@09	Neoblast	6600		-0.35985	0.057809	-0.71109	0.086422
J917-NB@10	Neoblast	11000		-0.35826	0.054343	-0.70387	0.092786
J917-NB@11	Neoblast	21000	Same grain	-0.25133	0.049782	-0.49886	0.091298
J917-NB@12	Neoblast	21000		-0.34163	0.041349	-0.64901	0.091665
J917-NB@13	Neoblast	6300		-0.52223	0.046101	-1.04243	0.090569
J917-NB@14	Neoblast	5400		-0.344	0.056174	-0.66778	0.099003
J917-NB@15	Neoblast	11900		-0.27984	0.057432	-0.58765	0.098643
J917-NB@16	Neoblast	6000		-0.35291	0.058213	-0.63366	0.074412
J917-NB@17	Neoblast	22000	Same grain	-0.44279	0.058642	-0.94188	0.069533
J917-NB@18	Neoblast	22000		-0.49941	0.076063	-0.98097	0.079387
J917-NB@19	Neoblast	13600		-0.19174	0.071424	-0.38074	0.074278
J917-NB@20	Neoblast	11200		-0.18342	0.070516	-0.39385	0.073868
J917-NB@21	Neoblast	8000		-0.43407	0.059031	-0.85288	0.067313
J917-NB@22	Neoblast	7500		-0.39408	0.066515	-0.74549	0.076708
J917-NB@23	Neoblast	20000		-0.38655	0.064112	-0.78385	0.080376
J917-NB@24	Neoblast	10500		-0.34022	0.059671	-0.68367	0.084284
J917-NB@25	Neoblast	4000		-0.30814	0.083214	-0.59215	0.106112
GRAIN-1@5	Neoblast	80000	Same grain	-0.1931	0.036663	-0.47956	0.070925
GRAIN-1RERUN@7	Neoblast	80000		-0.50756	0.04827	-1.05409	0.080736
GRAIN-1RERUN@8	Porphyroclast	877500	Same grain	-0.3436	0.054911	-0.7394	0.074214
GRAIN-1RERUN@9	Porphyroclast	877500		-0.28261	0.040072	-0.62319	0.06843
GRAIN-1@6	Porphyroclast	877500		-0.40855	0.061253	-0.86282	0.085496
GRAIN-1@7	Porphyroclast	877500		-0.44657	0.042867	-0.86715	0.06709
GRAIN-1@8	Porphyroclast	877500		-0.29766	0.037163	-0.64557	0.071153
GRAIN-1@9	Porphyroclast	877500		-0.35231	0.051413	-0.80941	0.066355
GRAIN-1@10	Porphyroclast	877500		-0.34518	0.045474	-0.74156	0.075564
GRAIN-2@1	Porphyroclast	495000	Same grain	-0.61291	0.039042	-1.26123	0.071651
GRAIN-2@2	Porphyroclast	495000		-0.34439	0.03093	-0.70114	0.073222
GRAIN-2@3	Porphyroclast	495000		-0.48934	0.041164	-0.98624	0.057391
GRAIN-2@4	Porphyroclast	495000		-0.41647	0.038904	-0.86859	0.069487
GRAIN-2@5	Porphyroclast	495000		-0.33884	0.04657	-0.71413	0.062165
GRAIN-2@6	Porphyroclast	495000		-0.42677	0.040351	-0.86498	0.053337
GRAIN-2@7	Porphyroclast	495000		-0.39825	0.040898	-0.80363	0.063857
GRAIN-2@8	Porphyroclast	495000		-0.51548	0.036555	-1.04615	0.074772
GRAIN-2@9	Porphyroclast	495000		-0.31033	0.050693	-0.61814	0.075506
GRAIN-2@10	Porphyroclast	495000		-0.46083	0.050135	-0.92417	0.077953
GRAIM-3@1	Porphyroclast	60000	Same grain	-0.43548	0.044959	-0.87292	0.074646
GRAIM-3@02	Porphyroclast	60000		-0.2129	0.052211	-0.52142	0.073188
GRAIM-3@03	Porphyroclast	60000		-0.31271	0.05133	-0.61092	0.079781
GRAIM-3@04	Porphyroclast	225000		-0.49489	0.032692	-0.96098	0.064179

GRAIM-3@05	Porphyroclast	225000		-0.52261	0.048667	-1.04759	0.086971
GRAIM-3@06	Porphyroclast	225000		-0.57331	0.036994	-1.11038	0.057924
GRAIM-3@07	Porphyroclast	225000		-0.12894	0.039339	-0.26447	0.061297
GRAIM-3@08	Porphyroclast	225000		-0.56538	0.040023	-1.07429	0.080411
GRAIM-3@09	Porphyroclast	225000		-0.37211	0.051098	-0.74878	0.078896
GRAIM-3@10	Porphyroclast	225000		-0.53845	0.038757	-1.03243	0.076873
GRAIM-3@11	Porphyroclast	225000		-0.38162	0.042195	-0.83106	0.092891
GRAIM-3@12	Porphyroclast	225000		-0.42835	0.035544	-0.85632	0.070072
GRAIN-3TRANS@1	Porphyroclast	225000	Same grain	-0.33884	0.053105	-0.65351	0.093939
GRAIN-3TRANS@2	Porphyroclast	225000		-0.32696	0.051353	-0.63979	0.073527
GRAIN-3TRANS@3	Porphyroclast	225000		-0.54241	0.058096	-1.04398	0.083666
GRAIN-3TRANS@4	Porphyroclast	225000		-0.51548	0.04966	-0.97541	0.098514
GRAIN-3TRANS@5	Porphyroclast	225000		-0.51865	0.046083	-0.9054	0.079818
GRAIN-3TRANS@6	Porphyroclast	225000		-0.36182	0.058787	-0.7264	0.099237
GRAIN-6@1	Porphyroclast	240000		-0.47746	0.052113	-0.9285	0.094504
GRAIN-6@2	Porphyroclast	240000		-0.36815	0.05873	-0.78126	0.097073
GRAIN-6@3	Porphyroclast	240000		-0.51311	0.048876	-0.95448	0.099177
GRAIN-6@4	Porphyroclast	240000	Same grain	-0.29607	0.062083	-0.6037	0.091591
GRAIN-6@5	Porphyroclast	240000		-0.47588	0.068965	-0.92056	0.099122
GRAIN-6@6	Porphyroclast	240000		-0.3634	0.061299	-0.67516	0.090183
GRAIN-6@7	Porphyroclast	240000		-0.4434	0.056781	-0.84044	0.098078
GRAIN-6@8	Porphyroclast	240000		-0.44261	0.061655	-0.81807	0.099436

Table 9.7. Summary of magnesium isotope results for both Japan samples. Errors are reported to 2σ.

Sample		$\delta^{25}Mg_{DSM-3}$ (‰)	$\delta^{26}Mg_{DSM-3}$ (‰)
J909C	*All olivine*		
	Average	-0.54 ± 0.04	-1.03 ± 0.08
	Range	-0.80 to -0.24	-1.54 to -0.46
	Total variation	0.56	1.08
	Porphyroclastic olivine		
	Average	-0.43 ± 0.04	-0.82 ± 0.08
	Range	-0.65 to -0.24	-1.17 to -0.46
	Total variation	0.41	0.71
	Neoblastic olivine		
	Average	-0.61 ± 0.04	-1.19 ± 0.08
	Range	-0.80 to -0.33	-1.54 to -0.59
	Total variation	0.47	0.95
J917	*All olivine*		
	Average	-0.40 ± 0.10	-0.80 ± 0.16
	Range	-0.61 to -0.13	-1.26 to -0.26
	Total variation	0.49	1.00
	Porphyroclastic olivine		
	Average	-0.40 ± 0.10	-0.83 ± 0.16
	Range	-0.61 to -0.13	-1.26 to -0.26
	Total variation	0.48	1.00
	Neoblastic olivine		
	Average	-0.38 ± 0.11	-0.75 ± 0.17
	Range	-0.61 to -0.17	-1.25 to -0.31
	Total variation	0.44	0.94

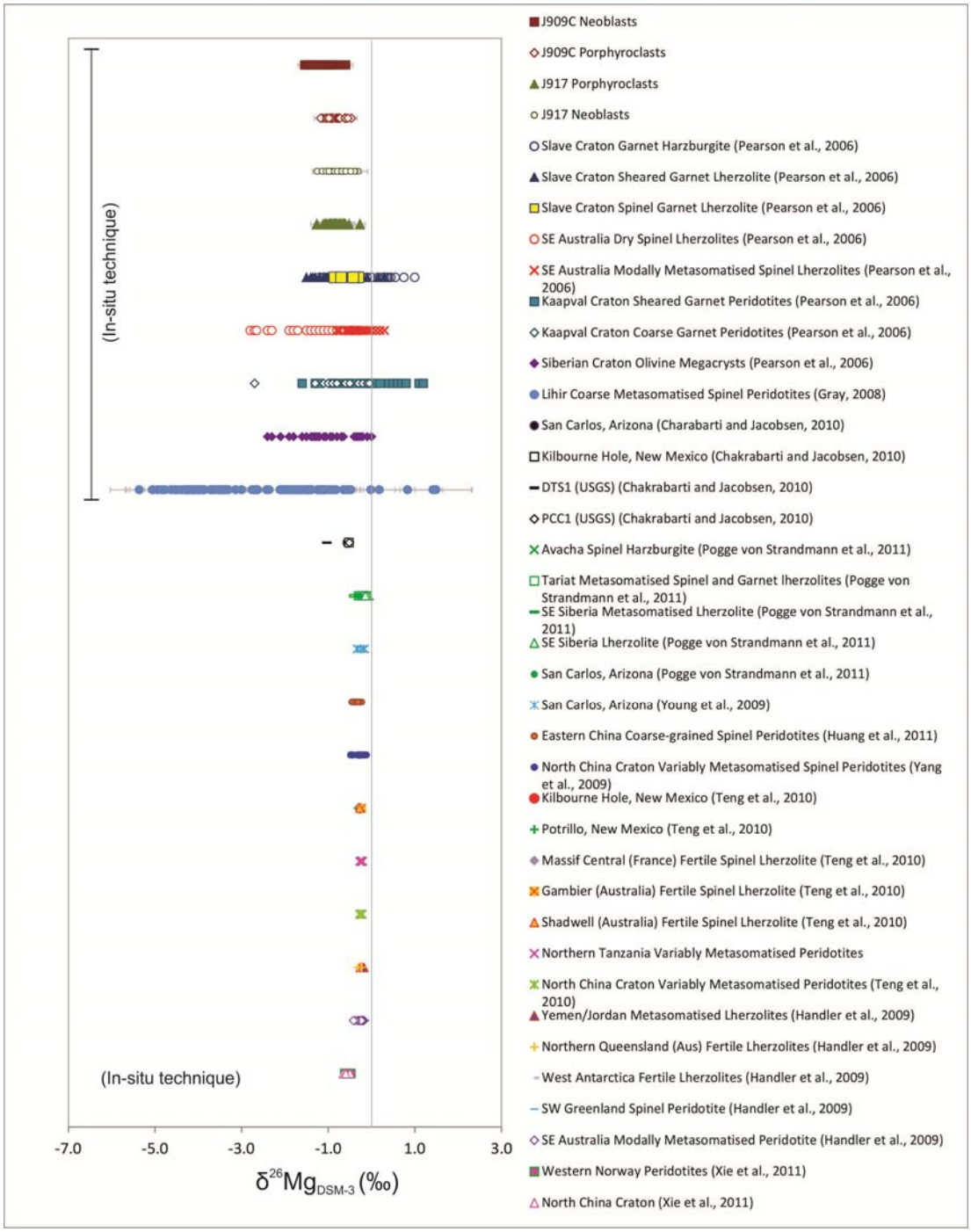

Figure 9.44. Comparison of magnesium isotope data for olivine from the Japanese dunites of this study to published literature. The grey vertical line represents the chondritic reservoir of 0.00‰ (Galy and O'Nions, 2000 *in* Young and Galy, 2004).

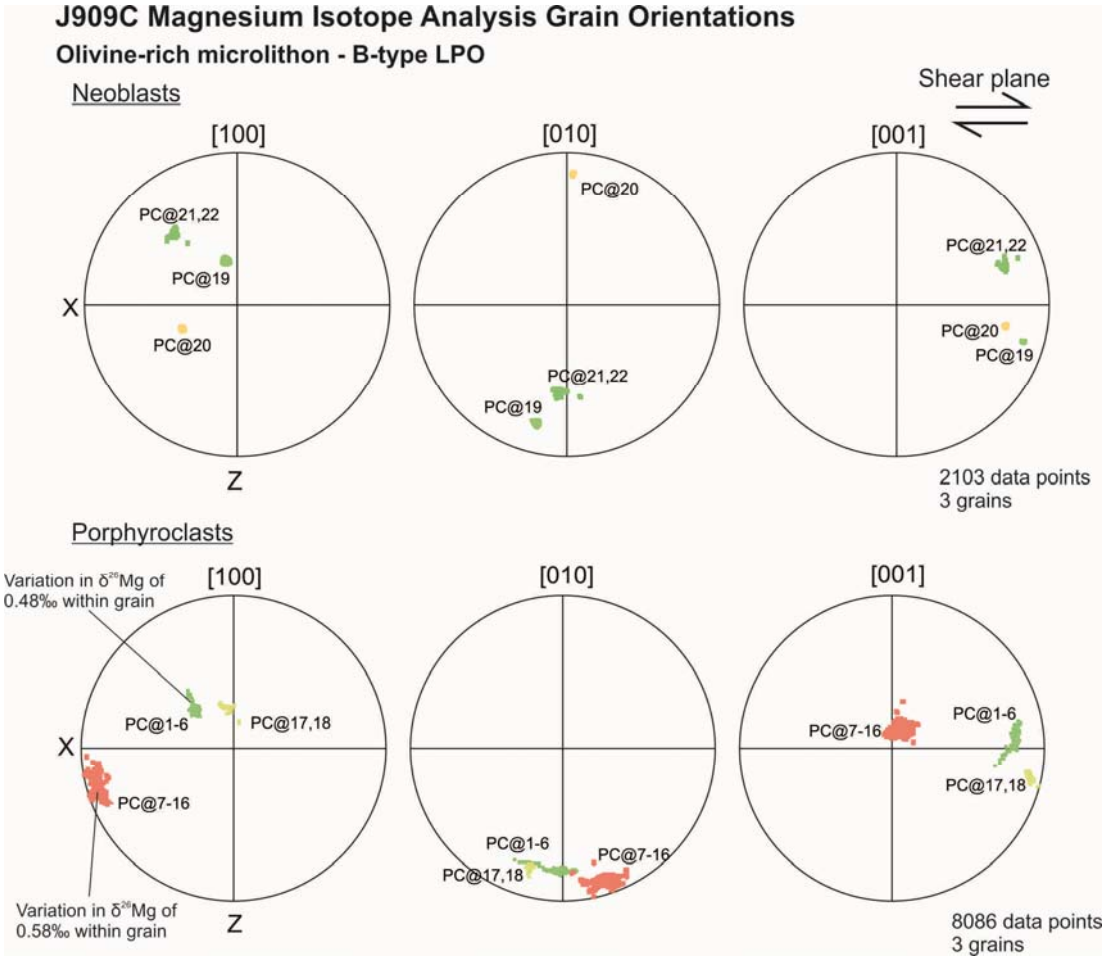

Figure 9.45. Orientations of olivine grains in sample J909C analysed for magnesium isotopes. The grains are coloured by isotope ratio using the same colour scale as table 9.4. For the three olivine porphyroclasts, the grains were coloured to reflect the maximum value, as an average was unrepresentative given the wide range of variation observed in these individual grains. There is no obvious link between grain orientation and oxygen isotope ratio, therefore the isotopic variations are not caused by grain orientation effects. The shear plane is represented by the XY plane, and the lineation direction is the X direction. Plots are lower hemisphere, equal area projections.

Variations in the δ^{26} Mg values of mantle olivine from Japan identified through SIMS analysis provide further evidence for heterogeneity in the upper mantle Mg isotopic composition. Pearson *et al*. (2006) also identify significant variations in Mg isotopic composition using laser ablation/MC-ICPMS techniques (range in δ^{25} Mg of 2.10‰ and δ^{26} Mg of 4.04‰).

These results contradict the results of a recent extensive investigation into the Mg isotopic composition of the upper mantle undertaken by Handler *et al*. (2009), in which variations in δ^{25} Mg and δ^{26} Mg of only 0.140‰ and 0.269‰, respectively, were identified. It is proposed by Handler *et al*. (2009) that unresolved analytical issues associated with LA-MC-ICP-MS are the cause of the large, intragrain

variations in Mg isotope composition observed by Pearson *et al*. (2006). The Mg isotope composition of Lihir olivine (Gray, 2008) was analysed using SIMS techniques and also identified significant variations, with much of the variations on an intragranular scale. Therefore it is likely that the variations observed by Pearson *et al*. (2006) are a natural feature of the olivine. It is possible, however, that the variations are a transient feature of the upper mantle (Handler *et al*. 2009), only occurring in regions where processes such as melt extraction and metasomatism are occurring.

9.4. Discussion

Fluid inclusion morphology and the link to deformation microstructures

A common observation in both Lihir and Japan peridotites is the orthogonal pattern of fracture and microcrack development, characterised by fractures oriented both parallel and normal to low-angle boundaries in olivine. Orthogonal microcrack patterns are more prominent in smaller intragrain fractures than larger ones, and are related to the presence of both coarse and fine fluid inclusions. Both types of fluid inclusions observed are secondary and were trapped within the olivine after initial crystallisation. Schmatz and Urai (2011) also observe fluid inclusions contained within subgrain boundaries in quartz, and interpret these as being related to interactions between fluid and migrating grain boundaries. However, due to the close spatial relationship between the inclusions and visible fractures in the olivine grains, it is highly likely that the fluid inclusions are related to brittle deformation and not grain boundary migration, and formed during the same event.

According to the classification of Vollbrecht (1989) (after Simmons and Richter, 1976, and Kranz, 1983 in Van der Kerkhof and Hein, 2001), the fine fluid inclusion trails are intragranular and decorate deformation bands and low-angle boundaries. The morphology of the fine fluid inclusions is comparable to those in the crack healing model described by Wanamaker *et al*. (1990) (Figure 9.46), and fluid inclusions that form trails are considered to represent healed microcracks (Van den Kerkhof and Hein, 2001). Thus the fine fluid inclusions observed in Lihir and Japan olivine are interpreted to be cracks that formed under mantle conditions and subsequently healed. During the healing process, cracks initially form

tubes/cylindrical structures, which are interconnected with the crack tip by small 'bridging' tubes. As healing progresses, the tubes close by way of the 'zipper' mechanism described by Renard *et al*. (2009), leaving trails of bubbles and residual tubes as seen in this study. The coarse fluid inclusions are interpreted as microcracks that are in the early stages of closure, and as such are poorly healed.

The tubular structures observed in the olivine grains in this study and described by Wanamaker *et al*. (1990) and Renard *et al*. (2009) are consistent with the microtubes described by Richter and Simmons (1977). Richter and Simmons (1977) suggest that microtubes can form by three processes; partial annealing of fractures, natural etching of dislocations or primary inclusion of fluid during crystallisation.

The microtubes observed in Lihir and Japan olivine grains are mainly consistent with formation due to fracture annealing, however there are some inclusions (e.g. Figure 9.47) that have a morphology typical of the Chelmsford granite microtubes (Richter and Simmons, 1977). These are characterised by the protrusion of a long needle-like microtube from the initial fluid inclusion and are interpreted to be an etching of crystal defects/dislocations.

According to Kranz (1983), microcracks normal to low-angle boundaries or deformation lamellae have also been observed in quartz (Heard and Carter, 1968; Carter and Kirby, 1978), microcline (Tullis and Yund, 1977) and plagioclase (Marshall and McLaren, 1977). Observations of low-angle boundary controlled microcracks in natural mantle olivine have been made by Green and Radcliffe (1974) and Boudier *et al*. (2010).

The link between fluid inclusions and crystal defects has been observed in other studies. Green and Radcliffe (1975) observe CO_2-rich bubbles attached to deformation-related crystal defects in mantle olivine and Drury (1991) observe fluid inclusions associated with dislocations in olivine. Hydrous mineral phases along low-angle boundaries in olivine have also been observed by Boudier *et al*. (2010) and Plümper *et al*. (2012), implying that hydrous fluid has been able to flow along the boundaries. Murata *et al*. (2009) infer fluid flow along low-angle boundaries in

olivine from variations in Fe and Mg content in regions linked to the replacement of olivine by antigorite.

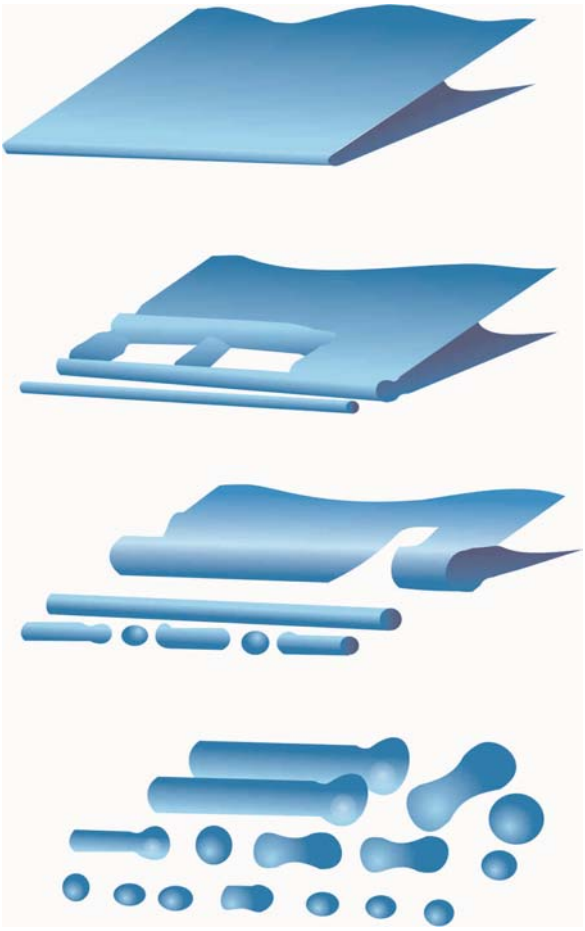

Figure 9.46. Progressive stages of microcrack healing (modified after Wanamaker *et al*., 1990). Cracks initially form microtubes, which are interconnected with the crack tip by small 'bridging' tubes (Richter and Simmons, 1977). As healing progresses, the tubes close by way of the 'zipper' mechanism described by Renard *et al*. (2009), leaving trails of bubbles and residual microtubes.

Fluid inclusions represent healed fractures, and fracture healing requires conditions that enable the grains to actively recover, such as the high temperatures found in the mantle. It is likely that the fracturing of the olivine grains developed in the mantle, and occurred simultaneously with the ductile deformation of olivine, due to the apparent interaction between low-angle boundaries and microcrack orientations. It is important to note that cracking/fracturing is not solely constrained by the internal microstructure of the olivine grains – there is also a large amount of irregular fracturing patterns that are meandering and unrelated to the crystal structure or orientation of the grain. This suggests temperatures are such that intragrain microstructure plays a role in controlling fracture development (for dislocations to influence intragrain fracture development, temperatures must be greater than 500°C; Kranz, 1983), but it is not the only influence.

Brittle deformation of olivine within the mantle below 30 – 40 km is generally unexpected, and rarely observed (Precigout *et al*., 2007) in exhumed mantle samples. However, both the Lihir (~30 – 70 km depth) and Japan (~100 km depth) peridotite samples are extensively fractured. Fracture development parallel to low-angle boundaries and the coexistence of brittle and ductile deformation in mantle olivine

from depths below 40 km raises a number of questions: 1) How is fracturing initiated along low-angle boundaries? 2) What is the mechanism allowing brittle deformation to occur where it is otherwise unexpected? and 3) How do co-existing ductile and brittle processes interact? The following discussion expands on the issues involved with some of these questions.

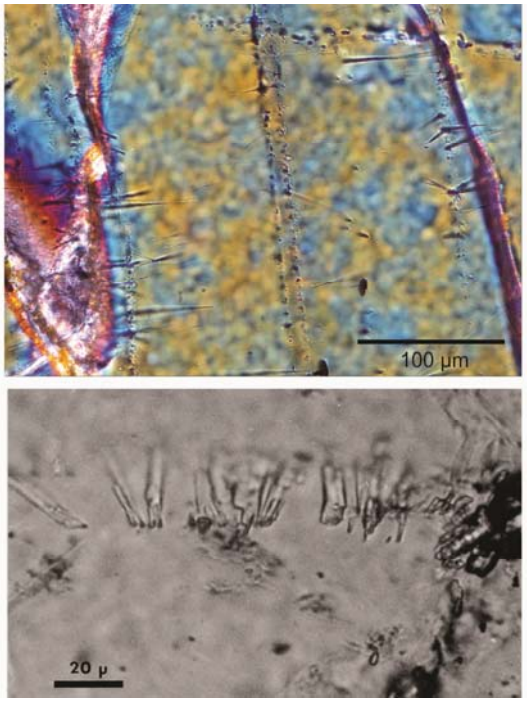

Figure 9.47. Microtubules in olivine in sample J904A (top) and the Chelmsford Granite microtubules after Richter and Simmons (1977) (bottom).

Microcrack formation and ductile deformation processes

For dislocation creep processes to fully accommodate strain in rocks, five independently operating slip systems are required, this is termed the Von Mises condition (Von Mises, 1928). EBSD analysis (Chapters 6 and 7) of Lihir olivine identifies the operation of only three slip systems, which does not satisfy the Von Mises condition. The observation of co-existing brittle and ductile deformation in these rocks is consistent with the observations of Boland and Hobbs (1973), who suggest that brittle deformation acts to accommodate the remainder of the strain in the olivine that cannot be accommodated through ductile processes. Thus, three slip systems operating in conjunction with 2 sets of fractures may be sufficient to satisfy the Von Mises condition.

Kranz (1983) states that microcracks can be produced by a number of different mechanisms, with the most relevant to this study being the release of stored energy associated with low-angle boundaries. This stored energy could develop as a result of strain hardening in mantle olivine deforming by dislocation creep.

Here it is proposed that microcrack development is due to dislocation creep-related strain hardening in mantle olivine. The migration of defects towards low-angle boundaries during dislocation creep results in dislocation entanglement and

subsequently strain hardening at the boundary (Carter and Kirby, 1978), inhibiting the ability of the olivine to accommodate strain through ductile deformation. This results in a local build-up of stress and coupled with a relatively high pore-fluid pressure (due to the influx of water, e.g. from dehydration of metamorphic minerals within a subducting slab), results in the development of microcracks in olivine. Microcracks development occurs parallel and normal to (Kranz, 1983) the defect-rich (and therefore structurally weaker) low-angle boundaries. Water would then able to infiltrate the boundary and defect sites are hydrated. Subsequently, local stress is relaxed and the fracture closes and begins to anneal due to the high temperatures in the mantle, leaving behind trails of fluid inclusions. It is widely understood that the addition of hydroxyl to defect sites enhances the ability for the defects to migrate, particularly in olivine (Mackwell *et al*., 1985; Karato, 1995; Mei and Kohlstedt, 2000). Thus the hydration of defect sites could potentially overcome the effects of strain hardening, allowing dislocation creep to proceed. A similar process operating in crustal rocks has been observed by Brander *et al*. (2012).

The implications for this process are broad and may be significant for mantle flow processes. The presence of water in the olivine crystal structure not only enhances deformation rates, but also has the ability to change the dominant slip system in olivine, preferentially enhancing slip within systems with [001] burgers vectors (Jung and Karato, 2001). It is proposed that microcrack development due to strain hardening in the presence of hydrous fluid, is the grain-scale mechanism that results in the change from anhydrous to hydrous slip systems, and initiates hydrous fabric development (B-, C- and E-type fabrics). The dominant olivine slip system in the Lihir samples is (001)[100] (Chapters 6 and 7), which is associated with conditions of low to moderate stress and moderate water content (Katayama *et al*., 2004; Jung *et al*., 2006). Japan sample J917 has an A-type bulk LPO, but with grains deforming by (001)[100], reflecting the interaction between individual olivine grains and water. These results provide further evidence for low-angle boundary assisted hydration. This also has important implications for the development of seismic anisotropy above the supra-subduction mantle, which is discussed in detail in Chapter 10.

Geochemistry of fluids in the mantle wedge

Table 9.1 and Figure 9.35 present the FTIR absorbance peaks observed in this study. Of the peaks observed, 3149, 3159, 3220, ~3600 cm^{-1} can be attributed to hydrated magnesium vacancies indicating high silica activity (Figure 9.35) (Lemaire *et al*., 2004; Berry *et al*., 2005). The stability of hydrothermally-grown enstatite in the Lihir samples also indicates a high SiO_2/MgO ratio (Schneider and Eggler, 1986; Nakamura and Kushiro, 1974; Ryabchikov *et al*., 1982; McInnes *et al*. 2001). This is consistent with observations of peaks at ~3160, ~3220 and ~3600 cm^{-1} associated with protonated Mg vacancies, which are indicative of the influx of hydrous fluids with a high silica activity ($a SiO_2$) (Lemaire *et al*., 2004).

Peaks at 3409 - 3413, 3319, 3525 and ~3570 cm^{-1} are assumed to be related to Ti-clinohumite defects (Figure 9.35) (Kitamura *et al*., 1987; Miller *et al*., 1987; Berry *et al*., 2005). Peaks at ~3480 cm^{-1} are interpreted to be associated with hydration of silica vacancies reflecting low silica activity (Lemaire *et al*., 2004) and have also been observed by Miller *et al*. (1987), Libowitsky and Beran (1995) and Matsyuk and Langer (2004). The peaks at 3325 – 3326 cm^{-1} are related to the substitution of trivalent cations (e.g. Fe^{3+}) into the crystal lattice (Berry *et al*., 2005). Relatively high absorbance at ~3355 cm^{-1} also reflects the presence of trivalent impurities and Fe^{3+} related point defects arising from Fe loss and oxidation (Berry *et al*., 2005).

A very prominent peak at ~3640 cm^{-1} is interpreted to reflect the presence of sub-microscopic serpentine inclusions within the olivine (Miller *et al*., 1987). There was also high absorbance at peaks at 3440 and ~3630 cm^{-1}, however these are not associated with any lattice defects in the literature. There are many peaks observed in this study that have not yet been attributed to a particular defect site in the olivine lattice or a particular environment (Table 9.1).

The results of this study provide significant insights into the chemistry of the metasomatic fluids responsible for alteration of the Lihir peridotite. The formation of Ti-clinohumite inclusions in olivine is linked to hydrous metasomatism (Wirth *et al*., 2001), as is serpentine formation (Hyndman and Peacock, 2003; Boudier *et al*., 2010). The observation of apparent pairing of these peaks is most likely due to the fact that they both act as markers for the degree of hydrous metasomatism of the

peridotite. This is supported by McInnes *et al*., (2001) who report hydrous metasomatism of Lihir peridotite, despite the fact that there are no hydrous phases as part of the mineral assemblage. Temperatures during metasomatism of the Lihir peridotite reached 700 – 1000°C, resulting in the growth of enstatite as a stable hydrothermal precipitate (Schneider and Eggler, 1986; Nakamura and Kushiro, 1974; Ryabchikov *et al*., 1982; McInnes *et al*. 2001). In light of this, the presence of serpentine inclusions in olivine is unexpected, as serpentine is only a stable metasomatic mineral at temperatures less than 620°C (Hyndman and Peacock, 2003). This may indicate that the serpentine is either metastable, or that the Lihir peridotite underwent a degree of cooling in the mantle before exhumation.

Trace element analysis and petrographic investigation of the Lihir peridotites (Gregoire *et al*., 2001; McInnes *et al*., 2001) reveal that the peridotites were metasomatised by a high-density, hydrous fluid with a substantial component of alkali aluminosilicate melt, aqueous carbon and sulphur. The magnetite-pyrrhotite-water mineral assemblages observed in the Lihir peridotites are also indicative of oxidising conditions (McInnes *et al*., 2001). The oxidising, Si-rich and hydrous nature of the metasomatic fluid involved in alteration of the Lihir peridotite is consistent with fluids derived from the subducting slab (Manning, 2004). These results are consistent, and thus the FTIR data from these olivine grains are both useful and reliable for inferring metasomatic conditions in the mantle.

The link between low-angle boundaries and FTIR absorbance evident from the EBSD results provides indicates that there may be a degree of serpentine growth along low-angle boundaries in Lihir olivine. Petrographically, there is no evidence for this, however the serpentine inclusions may not be large enough to be observed under a petrographic microscope. If this is the case, this also strengthens the case for the influx of hydrous fluids along low-angle boundaries as observed in Section 9.1. This fluid influx event was clearly preserved inside the olivine grains and hydrogen was not completely lost during re-equilibration within the host magma and ascent of the xenoliths. The preservation of this structurally-bound hydroxide provides insight into the chemistry of hydrous mantle fluids and conditions in the mantle wedge associated with the serpentinisation process.

The water content of the Earth's upper mantle

Berry *et al*. (2007), state that hydroxide incorporation related to oxidation (indicated by absorbance at ~3325 and 3355 cm^{-1}) does not occur under mantle conditions, and that this peak should be omitted from estimates of water content. The presence of peaks at 3355 cm^{-1} associated with the presence of trivalent cations, notably Fe^{3+}, often spatially correlates with the presence of low-angle boundaries in the Lihir olivine, indicating that hydroxide was incorporated into these defect sites within the mantle. The fact that this peak is not uniform across scans, varying within the pristine grain interior and does not correlate specifically with proximity to grain boundaries and fractures as would be expected with a late-stage process, also suggests that incorporation of hydroxide at these sites was not exhumation-related. This has significant implications for the estimation of the water contents of the upper mantle. Whilst these oxidising conditions may not be normal for the majority of the relatively anhydrous, intraplate upper mantle, conditions within the proximity of a subducting slab are likely to be vastly different. As indicated by geochemical studies of the Lihir olivine, oxidising conditions are a likely consequence of the release of subduction-related fluids into the mantle wedge. Recent interest in linking olivine LPO development and water content means that more studies are investigating the anomalous processes occurring in the mantle wedge close to a dehydrating slab. Omission of the 3325 and 3355 cm^{-1} peaks from water calculations would result in a value significantly less than the true water content, especially given the high absorbance of the 3355 cm^{-1} peak relative to most other defect sites.

Metasomatism and melt extraction processes

J917 forms a discrete group of data points that is substantially depleted in $\delta^{18}O$ relative to the bulk mantle of Mattey *et al*. (1994) (Figures 9.38 and 9.48). J909C shows a continuous range between that of the bulk mantle and a more depleted $\delta^{18}O$ composition. This is likely to reflect the operation of both melt extraction, which drives the $\delta^{18}O$ to lower values, and metasomatism, which results in an increase in $\delta^{18}O$. The lack of metasomatic signature observed in J917 olivine is unexpected, as the primary olivine in the sample is heavily replaced by antigorite. However, EBSD analysis of J917 (Chapters 5 and 6) reveal that the sample has an A-type LPO, reflecting the deformation of olivine under dry conditions (Jung *et al*., 2006). The lack of metasomatic signature in the oxygen isotopes is consistent with this fabric

type, reflecting the lack of interaction between olivine grains and hydrous fluid, despite the presence of antigorite suggesting hydrous conditions. J909C is comprised of microlithons characterised by a B-type olivine LPO in the olivine-rich region, and a transitional B-/C-type olivine LPO in the serpentinised region. Both of these olivine fabrics are characteristic of deformation in the presence of significant amounts of hydrous fluid phase. The metasomatic $\delta^{18}O$ variations are consistent with both of these fabrics. The neoblastic olivine from both microlithons in J909C show ranges in $\delta^{18}O$ that reflects both melt extraction and metasomatic processes, while the olivine porphyroclasts in the B-type region record only the melt extraction. It is likely that the neoblasts are more susceptible to isotope exchange due to their smaller grain size and therefore record both processes. It is also possible that the neoblasts represent conditions at the time of recrystallisation, potentially indicating that metasomatism was concurrent with dynamic recrystallisation.

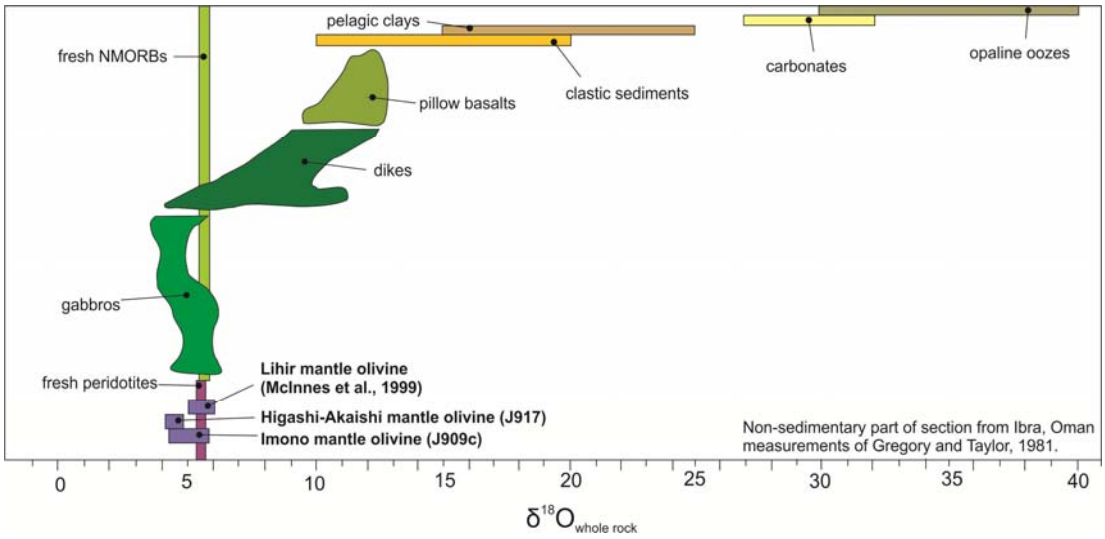

Figure 9.48. Whole rock oxygen isotope composition for terrestrial materials (modified after Eiler, 2001). The Higashi-Akaishi and Imono peridotites are significantly depleted in δ^{18} O relative to fresh peridotites and NMORBs, reflecting melt extraction processes.

The slight depletion of $\delta^{26}Mg$ relative to the chondritic reservoir (Figure 9.44) observed in both J909C and J917 is indicative of melt extraction from the peridotite (Pearson *et al*., 2006). Thus the Mg isotope data from this study complements the oxygen isotope results, providing further evidence for melt extraction processes in the mantle represented by the Higashi-Akaishi and Imono peridotites.

The depletion of δ^{26}Mg in the J909C neoblastic olivine (-1.19 ± 0.08‰) relative to the porphyroclastic population (-0.82 ± 0.08‰) suggests that the neoblastic olivine is more open to isotopic exchange. This was also observed in the oxygen isotope data and similarly, is likely due to the decreased grain size and increased interaction with surrounding melt and fluid. Although there is less variation observed than in Pearson *et al*. (2006) and Gray (2008), the variations are still significant and provide further evidence for Mg isotope heterogeneity in the Earth's mantle. One limitation of this study is the inability to examine if there is a relationship between the isotope composition and the internal microstructure of the olivine. It would be useful to look at how aspects such as dislocation density influence the isotopic composition within individual grains.

9.5. Summary

- Microcrack development recorded by the preservation of fluid inclusions in mantle olivine from Lihir and Japan provides further evidence for a link between intragrain deformation microstructures and grain-scale brittle failure. It is proposed that the ingression of fluid along low-angle boundaries associated with the development of microcracks within mantle olivine may be a mechanism for olivine defect hydration and therefore hydrolytic weakening of the olivine, with potential to effect a change in the dominant slip system from [100] to [001] slip. This has large-scale implications for olivine fabric development and the subsequent interpretation of seismic anisotropy above the mantle wedge.

- The strain hardening of olivine as a result of dislocation entanglement at low-angle boundaries provides a mechanism for fracturing and therefore fluid migration through a peridotite. This has potential implications for fracture-induced anisotropy and partial melting of peridotite, as well as for chemical exchange between fluids, melt and grain interiors.

- FTIR peaks correlate with a range of features within olivine grains, including fluid inclusions, fractures and mineral inclusions, but also pristine grain interiors and low-angle boundaries. The observation of FTIR absorbance

directly linked to low-angle boundaries has not yet been reported in the literature.

- FTIR peaks in olivine from Lihir peridotite sample 136063 indicate that conditions of metasomatism were oxidising in nature and had a high silica activity, consistent with fluids released by a subducting slab. The omission of peaks at ~3325 and 3355 cm^{-1} from water content calculations as suggested by Berry *et al*. (2007) may result in a value significantly lower than the true value. These peaks need not necessarily be omitted from water content calculations - the FTIR spectra should be examined within the context of the sample and geological setting in order to discern which peaks are appropriate to use in the calculation.
- Oxygen and magnesium isotope analysis of Japan samples J909C and J917 reveal that these samples record melt depletion and metasomatic events that occurred in the mantle wedge. The overall variations observed in the isotopic composition of both samples provides further evidence for the heterogeneity of the Earth's mantle with respect to both oxygen and magnesium. The oxygen isotope composition of both the samples reflects the conditions of formation of the different LPO types, and is the first study of its' kind to link isotopic composition and olivine fabric development.

- There is much scope for further investigation into the interaction between brittle and ductile processes in the mantle. In particular, it would be useful to investigate if certain low-angle boundary types (produced by the operation of different slip systems in olivine) are more or less likely to act as nucleation sites for microcracks and hence hydration of olivine. This may progress our understanding of the link between slip system operation and water in olivine deformation. Further investigations into the integrated effect of microcrack geometry and olivine LPO on the seismic properties of peridotite would also be useful and have important implications for seismic anisotropy interpretations.

9.6. References

Andersen, T. and Neumann, E.-R. (2001) Fluid inclusions in mantle xenoliths, *Lithos*, v. 55, p. 301-320.

Ando, J., Shibata, Y., Okajima, Y., Kanagawa, K., Furusho, M. and Tomioka, N. (2001) Striped iron zoning of olivine induced by dislocation creep in deformed peridotites, *Nature*, v. 414, p. 893-895.

Bai, W. and Kohlstedt, D.L. (1992) Substantial hydrogen solubility in olivine and implications for water storage in the mantle, *Nature*, v. 357, p. 672-674.

Bell, D.R., Rossman, G.R., Maldener, J., Endisch, D. and Rauch, F. (2003) Hydroxide in olivine: A quantitative determination of the absolute amount and calibration of the IR spectrum, *Journal of Geophysical Research*, v. 108, p. 8-1 - 8-9.

Beran, A. (1983) A model of the OH positions in olivine, derived from infrared-spectroscopic investigations, *Physics and Chemistry of Minerals*, v. 9, p. 57-60.

Bergman, S.C. and Dubessy, J. (1984) CO_2-CO fluid inclusions in a composite peridotite xenolith: implications for upper mantle oxygen fugacity, *Contributions to Mineralogy and Petrology*, v. 85, p. 1-13.

Berry, A.J., Hermann, J., O'Neill, H.S.C. and Foran, G.J. (2005) Fingerprinting the water site in mantle olivine, *Geology*, v. 33, p. 869-872.

Berry, A.J., O'Neill, H.S.C., Hermann, J. and Scott, D.R. (2007) The infrared signature of water associated with trivalent cations in olivine, *Earth and Planetary Science Letters*, v. 261, p. 134–142.

Boland, J.N. and Hobbs, B.E. (1973) Microfracturing processes in experimentally deformed peridotite, *International Journal of Rock Mechanics and Mining*

Sciences & Geomechanics Abstracts, v. 10, p. 623-626.

Borthwick, J. and Harmon, R.S. (1982) A note regarding CIF3 as an alternative to BrF5 for oxygen isotope analysis, *Geochimica et Cosmochimica Acta*, v. 46, p. 1665-1668.

Boudier, F.o., Baronnet, A. and Mainprice, D. (2010) Serpentine Mineral Replacements of Natural Olivine and their Seismic Implications: Oceanic Lizardite versus Subduction-Related Antigorite, *Journal of Petrology*, v. 51, p. 495-512.

Brander, L. (2012) Brittle-plastic deformation in initially dry rocks at fluid-present conditions: transient behaviour of feldspar at mid-crustal levels, *Contributions to Mineralogy and Petrology*, v. 163, p. 403-425.

Burke, E.A.J. (2001) Raman microspectrometry of fluid inclusions, *Lithos*, v. 55, p. 139-158.

Carter, N. and Kirby, S. (1978) Transient creep and semibrittle behavior of crystalline rocks, *pure and applied geophysics*, v. 116, p. 807-839.

Chakrabarti, R. and Jacobsen, S.B. (2010) The isotopic composition of magnesium in the inner Solar System, *Earth and Planetary Science Letters*, v. 293, p. 349-358.

Chazot, G., Lowry, D., Menzies, M. and Mattey, D. (1997) Oxygen isotopic composition of hydrous and anhydrous mantle peridotites, *Geochimica et Cosmochimica Acta*, v. 61, p. 161-169.

Clayton, R.N. (1993) Oxygen Isotopes in Meteorites, *Annual Review of Earth and Planetary Sciences*, v. 21, p. 115-149.

Clayton, R.W. (2003) Oxygen isotopes in the solar system, *Space Science Reviews*, v. 106, p. 19-32.

Clayton, R.W. and Mayeda, T.K. (1963) The use of bromine pentafluoride in the extraction of oxygen from oxides and silicates for isotope analysis, *Geochimica et Cosmochimica Acta*, v. 27, p. 43-52.

Deines, P. and Haggerty, S.E. (2000) Small-scale oxygen isotope variations and petrochemistry of ultradeep (>300 km) and transition zone xenoliths, *Geochimica et Cosmochimica Acta*, v. 64, p. 117–131.

Dobosi, G., Downes, H., Mattey, D.P. and Embey-Isztin, A. (1998) Oxygen isotope ratios of phenocrysts from alkali basalts of the Pannonian basin: Evidence for an O-isotopically homogeneous upper mantle beneath a subduction-influenced area, *Lithos*, v. 42, p. 213-223.

Drury, M.R. (1991) Hydration-induced climb dissociation of dislocations in naturally deformed mantle olivine, *Physics and Chemistry of Minerals*, v. 18, p. 106-116.

Eiler, J. (2001) Oxygen Isotope Variations of Basaltic Lavas and Upper Mantle Rocks, *Reviews in Mineralogy and Geochemistry*, v. 43, p. 319–364.

Eiler, J., Stolper, E.M. and McCanta, M.C. (2011) Intra- and Intercrystalline Oxygen Isotope Variations in Minerals from Basalts and Peridotites, *Journal of Petrology*, v. 52, p. 1393-1413.

Franz, L. and Wirth, R. (2000) Spinel inclusions in olivine of peridotite xenoliths from TUBAF seamount (Bismarck Archipelago/Papua New Guinea): evidence for the thermal and tectonic evolution of the oceanic lithosphere, *Contributions to Mineralogy and Petrology*, v. 140, p. 283-295.

Frezzotti, M.L., Ferrando, S., Tecce, F. and Castelli, D. (2012) Water content and nature of solutes in shallow-mantle fluids from fluid inclusions, *Earth and Planetary Science Letters*, v. 351–352, p. 70-83.

Gaetani, G.A. and Grove, T.L. (1998) The influence of water on melting of mantle peridotite, *Contributions to Mineralogy and Petrology*, v. 131, p. 323-346.

Galy, A. and O'Nions, R.K. (2000) Is there a CHUR for Mg? Goldschmidt 2000, 424, *in* Young, E.D., and Galy, A. (2004) The Isotope Geochemistry and Cosmochemistry of Magnesium, *Reviews in Mineralogy and Geochemistry*, v. 55, p. 197-230.

Galy, A., Bar-Matthews, M., Halicz, L. and O'Nions, R.K. (2002) Mg isotopic composition of carbonate: insight from speleothem formation, *Earth and Planetary Science Letters*, v. 201, p. 105-115.

Galy, A., Young, E.D., Ash, R.D., and O'Nions, R.K. (2000) The Formation of Chondrules at High Gas Pressures in the Solar Nebula, *Science*, v. 290, p. 1751-1753.

Gray, E. (2008) Microstructural characterisation of olivine and implications for mantle geodynamics [Honours thesis], Curtin University of Technology.

Green, H.W., and Radcliffe, S.V. (1975) Fluid Precipitates in Rocks from the Earth's Mantle, *Geological Society of America Bulletin*, v. 86, p. 846-852.

Gregoire, M., McInnes, B.I.A. and O'Reilly, S.Y. (2001) Hydrous metasomatism of oceanic sub-arc mantle, Lihir, Papua New Guinea: Part 2. Trace element characteristics of slab-derived fluids, *Lithos*, v. 59, p. 91-108.

Harmon, R.S., Kempton, P.D., Stosch, H.G., Hoefs, J., Kovalenko, V.I. and Eonov, D. (1986) $^{18}O/^{16}O$ ratios in anhydrous spinel lherzolite xenoliths from the Shavaryn-Tsaram volcano, Mongolia, *Earth and Planetary Science Letters*, v. 81, p. 193-202.

Hartley, M.E., Thordarson, T., Taylor, C., Fitton, J.G. and Eimf (2012) Evaluation of the effects of composition on instrumental mass fractionation during SIMS oxygen isotope analyses of glasses, *Chemical Geology*, v. 334, p. 312-323.

Heard, H.C. and Carter, N.L. (1968) Experimentally induced 'natural' intragranular flow in quartz and quartzite, *American Journal of Science*, v. 266, p. 1-42.

Huang, F., Zhang, Z., Lundstrom, C.C. and Zhi, X. (2011) Iron and magnesium isotopic compositions of peridotite xenoliths from Eastern China, *Geochimica et Cosmochimica Acta*, v. 75, p. 3318-3334.

Huberty, J.M., Kita, N.T., Kozdon, R., Heck, P.R., Fournelle, J.H., Spicuzza, M.J., Xu, H. and Valley, J.W. (2010) Crystal orientation effects in $\delta^{18}O$ for magnetite and hematite by SIMS, *Chemical Geology*, v. 276, p. 269-283.

Hyndman, R.D. and Peacock, S.M. (2003) Serpentinization of the fore-arc mantle, *Earth and Planetary Science Letters*, v. 212, p. 417-432.

Ionov, D.A., Harmon, R.S., France-Lanord, C., Greenwood, P.B., and Ashchepkov, I.V. (1994) Oxygen isotope composition of garnet and spinel peridotites in the continental mantle: Evidence from the Vitim xenolith suite, southern Siberia, *Geochimica et Cosmochimica Acta*, v. 58, p. 1463-1470.

Jung, H., and Karato, S. (2001) Water-induced Fabric Transitions in Olivine, *Science*, v. 293, p. 1460-1463.

Jung, H., Katayama, I., Jiang, Z., Hiraga, T., and Karato, S. (2006) Effect of water and stress on the lattice-preferred orientation of olivine, *Tectonophysics*, v. 421, p. 1-22.

Karato, S. (1995) Effects of Water on Seismic Wave Velocities in the Upper Mantle, *Proceedings of the Japan Academy. Ser. B: Physical and Biological Sciences*, v. 71, p. 61-66.

Kempton, P.D., Harmon, R.S., Stosch, H.G., Hoefs, J., and Hawkesworth, C.J. (1988) Open-system O-isotope behaviour and trace element enrichment in the sub-Eifel mantle, *Earth and Planetary Science Letters*, v. 89, p. 273-287.

Kitamura, M., Kondoh, S., Morimoto, N., Miller, G.H., Rossman, G.R., and Putnis, A. (1987) Planar OH-bearing defects in mantle olivine, *Nature*, v. 328, p. 143-145.

Kovács, I., Hermann, J., O'Neill, H.S.C., Fitz Gerald, J.D., Sambridge, M., and Horvath, G. (2008) Quantitative absorbance spectroscopy with unpolarized light: Part II. Experimental evaluation and development of a protocol for quantitative analysis of mineral IR spectra, *Americal Mineralogist*, v. 93, p. 765–778.

Kovács, I., O'Neill, H.S.C., Hermann, J., and Hauri, E.H. (2010) Site-specific infrared O-H absorption coefficients for water substitution into olivine, *Americal Mineralogist*, v. 95, p. 292-299.

Kranz, R.L. (1983) Microcracks in rocks: A review, *Tectonophysics*, v. 100, p. 449-480.

Kyser, T.K., O'Neil, J., and Carmichael, I.E. (1981) Oxygen isotope thermometry of basic lavas and mantle nodules, *Contributions to Mineralogy and Petrology*, v. 77, p. 11-23.

Kyser, T.K., O'Neil, J.R., and Carmichael, I.S.E. (1982) Genetic relations among basic lavas and ultramafic nodules: evidence from oxygen isotope compositions, *Contributions to Mineralogy and Petrology*, v. 81, p. 88-102.

Lemaire, C., Kohn, S.C., and Brooker, R.A. (2004) The effect of silica activity on the incorporation mechanisms of water in synthetic forsterite: a polarised infrared spectroscopic study, *Contributions to Mineralogy and Petrology*, v. 147, p. 48-57.

Libowitsky, E., and Beran, A. (2006) The Structure of Hydrous Species in Nominally Anhydrous Minerals: Information from Polarized IR Spectroscopy, *Reviews in Mineralogy & Geochemistry*, v. 62, p. 29-52.

Lyon, I.C., Saxton, J.M., and Cornah, S.J. (1998) Isotopic fractionation during secondary ionisation mass spectrometry: Crystallographic orientation effects in magnetite, *International Journal of Mass Spectrometry and Ion Processes*, v. 172, p. 115-122.

Mackwell, S.J. (1985) The role of water in the deformation of olivine single crystals, *Journal of Geophysical Research*, v. 90, p. 11319.

Manning, C.E. (2004) The chemistry of subduction-zone fluids, *Earth and Planetary Science Letters*, v. 223, p. 1-16.

Marshall, D.B., and McLaren, A.C. (1977) Deformation mechanisms in experimentally deformed plagioclase feldspars, *Physics and Chemistry of Minerals*, v. 1, p. 351-370.

Matsyuk, S.S., and Langer, K. (2004) Hydroxyl in olivines from mantle xenoliths in kimberlites of the Siberian platform, *Contributions to Mineralogy and Petrology*, v. 147, p. 413-437.

Mattey, D.P., Lowry, D., and Macpherson, C. (1994) Oxygen isotope composition of mantle peridotite, *Earth and Planetary Science Letters*, v. 128, p. 231-241.

Mattey, D.P., and Macpherson, C. (1993) High-precision oxygen isotope microanalysis of ferromagnesian minerals by laser-fluorination, *Chemical Geology*, v. 105, p. 305-318.

Matveev, S., O'Neill, H.S.C., Ballhaus, C., Taylor, W.R., and Green, D.H. (2001) Effect of Silica Activity on OH^- IR Spectra of Olivine: Implications for low $aSiO_2$ Mantle Metasomatism, *Journal of Petrology*, v. 42, p. 721-729.

McInnes, B.I.A., Gregoire, M., Binns, R.A., Herzig, P.M., and Hannington, M.D. (2001) Hydrous metasomatism of oceanic sub-arc mantle, Lihir, Papua New Guinea: petrology and geochemistry of fluid-metasomatised mantle wedge

xenoliths, *Earth and Planetary Science Letters*, v. 188, p. 169-183.

Mei, S., and Kohlstedt, D.L. (2000) Influence of water on plastic deformation of olivine aggregates: 2. Dislocation creep regime, *Journal of Geophysical Research*, v. 105, p. 21,471-21,481.

Miller, G.H., Rossman, G.R., and Harlow, G.E. (1987) The natural occurrence of hydroxide in olivine, *Physics and Chemistry of Minerals*, v. 14, p. 461-472.

Murata, K., Maekawa, H., Ishii, K., Mohammad, Y.O., and Yokose, H. (2009) Iron-rich stripe patterns in olivines of serpentinized peridotites from Mariana forearc seamounts, western Pacific, *Journal of Mineralogical and Petrological Sciences*, v. 104, p. 199-203.

Nakamura, Y., and Kushiro, I. (1974) Composition of gas phase in Mg_2SiO_4-SiO_2-H_2O at 15 kbar, *Carnegie Institute Washington Yearbook*, v. 73, p. 255-258.

O'Reilly, S.Y., and Griffin, W.L. (1988) Mantle metasomatism beneath Victoria, Australia I: metasomatic processes in Cr-diopside lherzolites, *Geochimica et Cosmochimica Acta*, v. 52, p. 433– 437.

Pearson, N.J., Griffin, W.L., Alard, O., and O'Reilly, S.Y. (2006) The isotopic composition of magnesium in mantle olivine: Records of depletion and metasomatism, *Chemical Geology*, v. 226, p. 115-133.

Plümper, O., King, H., Vollmer, C., Ramasse, Q., Jung, H., and Austrheim, H. (2012) The legacy of crystal-plastic deformation in olivine: high-diffusivity pathways during serpentinization, *Contributions to Mineralogy and Petrology*, v. 163, p. 701-724.

Pogge von Strandmann, P.A.E., Elliott, T., Marschall, H.R., Coath, C., Lai, Y.-J., Jeffcoate, A.B., and Ionov, D.A. (2011) Variations of Li and Mg isotope ratios in bulk chondrites and mantle xenoliths, *Geochimica et Cosmochimica Acta*, v. 75, p. 5247-5268.

Precigout, J., Gueydan, F., Gapais, D., Garrido, C.J., and Essaifi, A. (2007) Strain localisation in the subcontinental mantle - a ductile alternative to the brittle mantle, *Tectonophysics*, v. 445, p. 318-336.

Renard, F., Dysthe, D., Feder, J., and Jamtveit, B. (2002) Healing of fluid-filled microcracks, *Poromechanics II*, p. 925-931.

Richter, D., and Simmons, G. (1977) Microscopic tubes in igneous rocks, *Earth and Planetary Science Letters*, v. 34, p. 1-12.

Roedder, E. (1965) Liquid CO_2 inclusions in olivine-bearing nodules and phenocrysts from basalts, *American Mineralogist*, v. 50, p. 1746-1782.

Roedder, E. (1984) Fluid Inclusions: Reviews in Mineralogy, *Mineralogical Society of America*, v. 12.

Rosenbaum, J.M., Zindler, A., and Rubenstone, J.L. (1996) Mantle fluids: Evidence from fluid inclusions, *Geochimica et Cosmochimica Acta*, v. 60, p. 3229-3252.

Rossman, G.R. (1988) Vibrational spectroscopy of hydrous components, *Rev. Mineral.*, v. 18, p. 193-206.

Ryabchikov, I.D., Schreyer, W., and Abraham, K. (1982) Compositions of aqueous fluids in equilibrium with pyroxenes and olivines at mantle pressures and temperatures, *Contributions to Mineralogy and Petrology*, v. 79, p. 80-84.

Schmatz, J. and Urai, J.L. (2011) The interaction of migrating grain boundaries and fluid inclusions in naturally deformed quartz: A case study of a folded and partly recrystallized quartz vein from the Hunsrück Slate, Germany, *Journal of Structural Geology*, v. 33, p. 468-480.

Schneider, M.E., and Eggler, D.H. (1986) Fluids in equilibrium with peridotite

minerals: Implications for mantle metasomatism, *Geochimica et Cosmochimica Acta*, v. 50, p. 711-724.

Sharp, Z.D. (1990) A laser based microanalytical method for the in situ determination of oxygen isotope ratios of silicates and oxides, *Geochimica et Cosmochimica Acta*, v. 54, p. 1353-1357.

Sharp, Z.D. (1992) In situ laser microprobe techniques for stable isotope analysis, *Chemical Geology*, v. 101, p. 3-19.

Simmons, G., and Richter, D. (1976) Microcracks in rocks. In: Strens, R. G. J. (ed) The Physics and Chemistry of Minerals and Rocks, p. 105 – 137, John Wiley, New York.

Sommer, H., Regenauer-Lieb, K., Gasharova, B., and Siret, D. (2008) Grain boundaries: a possible water reservoir in the Earth's mantle? *Mineralogy and Petrology*, v. 94, p. 1-8.

Taylor, H., Jr. (1968) The oxygen isotope geochemistry of igneous rocks, *Contributions to Mineralogy and Petrology*, v. 19, p. 1-71.

Teng, F.-Z., Wadhwa, M., and Helz, R.T. (2007) Investigation of magnesium isotope fractionation during basalt differentiation: Implications for a chondritic composition of the terrestrial mantle, *Earth and Planetary Science Letters*, v. 261, p. 84–92.

Tullis, J., and Yund, R.A. (1977) Experimental deformation of dry Westerly granite, *J. Geophys. Res.*, v. 82, p. 5705-5718.

Valley, J.W., and Kita, N.T. (2009) In situ oxygen isotope geochemistry by ion microprobe, *Mineralogical Association of Canada Short Course*, v. 41, p. 19-63.

Van den Kerkhof, A.M., and Hein, U.F. (2001) Fluid inclusion petrography, *Lithos*,

v. 55, p. 27-47.

Vollbrecht, A., 1989. Mikroriß-Analyse im KTB — Datenerhebung U-Tisch Mikroskopie. Unpublished report IGDL, Go¨ttingen, *in* Van den Kerkhof, A.M., and Hein, U.F. (2001) Fluid inclusion petrography, *Lithos*, v. 55, p. 27-47. (No translation available)

von Mises, R. (1928) Mechanik der plastischen Formänderung von Kristallen, *Zeitschrift für Angewandte Mathematik und Mechanik*, v. 8, p. 161-185. (No translation available)

Wanamaker, B., Wong, T.F., and Evans, B. (1990) Decrepitation and crack healing of fluid inclusions in San Carlos olivine, *Journal of Geophysical Research*, v. 95, p. 15623-15,641.

Wiechert, U., and Halliday, A.N. (2007) Non-chondritic magnesium and the origins of the inner terrestrial planets, *Earth and Planetary Science Letters*, v. 256, p. 360–371.

Wirth, R., Dobrzhinetskaya, L.F., and Green, H.W. (2001) Electron microscope study of the reaction olivine + H_2O + TiO_2 → titanian clinohumite + Titanian chondrodite synthesized at 8 GPa, 1300 K, *American Mineralogist*, v. 86, p. 601-610.

Xie, L.-W., Yin, Q.-Z., Yang, J.-H., Wu, F.-Y., and Yang, Y.-H. (2011) High precision analysis of Mg isotopic composition in olivine by laser ablation MC-ICP-MS, *Journal of Analytical Atomic Spectrometry*, v. 26, p. 1773-1780.

Young, E.D., and Galy, A. (2004) The Isotope Geochemistry and Cosmochemistry of Magnesium, *Reviews in Mineralogy and Geochemistry*, v. 55, p. 197-230.

Young, E.D., Tonui, E., Manning, C.E., Schauble, E., and Macris, C.A. (2009) Spinel-olivine magnesium isotope thermometry in the mantle and

implications for the Mg isotopic composition of Earth, *Earth and Planetary Science Letters*, v. 288, p. 524–533.

Zhang, H.F., Mattey, D.P., Grassineau, N., Lowry, D., Brownless, M., Gurney, J.J., and Menzies, M.A. (2000) Recent fluid processes in the Kaapvaal Craton, South Africa: coupled oxygen isotope and trace element disequilibrium in polymict peridotites, *Earth and Planetary Science Letters*, v. 176, p. 57-72.

Zhang, H.F., Menzies, M.A., and Mattey, D.P. (2003) Mixed mantle provenance: diverse garnet compositions in polymict peridotites, Kaapvaal craton, South Africa, *Earth and Planetary Science Letters*, v. 216, p. 329-346.

Chapter 10. Discussion

10.1. Olivine fabrics in the supra-subduction zone mantle and implications for seismic anisotropy interpretations

EBSD analysis of the fabrics and microstructures of olivine from Lihir and Japan peridotites (Chapters 6, 7 and 8) provides numerous insights into the deformation processes affecting the supra-subduction zone mantle. Fabrics associated with [100] slip directions along with deformation by (010)[100], {0kl}[100] and (001)[100] were observed in the Lihir peridotite xenoliths. A-, B- and C-type fabrics along with bulk olivine deformation by {hk0}[001] (which is inconsistent with any known fabric types) were observed in Alpine-type peridotites from Higashi-Akaishi and Imono, Japan 9 (Chapters 6 and 8).

Volcanic-hosted peridotite xenoliths are likely to provide information on the backarc and central forearc mantle due to these being the regions tapped by volcanic activity. Olivine fabric data collected from previous studies on peridotite xenoliths show A-, D- and E-type LPOs (Arai *et al*., 2004; Michibayashi *et al*., 2006; Konc *et al*., 2010; Soustelle *et al*., 2010). The fabrics observed in the xenoliths reported in the literature are in good agreement with the intragrain slip systems of (001)[100], {0kl}[100] and (010)[100] observed in the Lihir peridotites (Chapters 6 and 7). In conjunction with previously published xenolith fabric data from both the backarc and forearc mantle (Table 10.1), these results suggest that the upper mantle in these regions is deforming by predominantly [100] slip and relatively dry conditions (according to the classification of Jung *et al*., 2006).

Table 10.1. A summary of the olivine fabric types observed in subduction zone mantle peridotites.

Subduction Zone Mantle Xenoliths		
Location	**Olivine Fabric**	**Reference**
Lihir Island, PNG	[100] bulk slip directions with intragrain slip systems of (010)[100], {0kl}[100] and (001)[100]	This study
Avacha Volcano, Kamchatka	D-type	Soustelle *et al*. (2010)
Iraya Volcano, Philippines	A-type	Arai *et al*. (2004)
Ichinomegata, Japan	D-type (back-arc)	Michibayashi *et al*. (2006)
SE Iberian Volcanic Province, Spain	D-type (back-arc)	Konc *et al*. (2010)

Alpine-type Peridotites		
Higashi-Akaishi, Japan	A-/B-/C-type/{hk0}[001]	Mizukami *et al*. (2004); This study
Imono, Japan	B-type/{hk0}[001]	Tasaka *et al*. (2008); This study
Talkeetna Arc, Alaska	E-type	Hacker *et al*. (2008)
Hokkaido, Japan	A-/D-/E-type	Sawaguchi (2004)
Josephine Peridotite, SW Oregon	A-/E-type	Warren *et al*. (2008); Skemer *et al*. (2009)
Val Malenco, Italy	A-/B-/E-type	Jung (2009)
Cima di Gagnone, Italy	C-type/B-type	Frese *et al*. (2003); Skemer *et al*. (2006)
Red Hills, NZ	D/B-type	Webber *et al*. (2010)
Khoy Ophiolite, NW Iran	E-type	Monsef *et al*. (2010)
Southern Mariana Trench	A/B-type	Michibayashi *et al*. (2007)
Ronda Peridotite, SW Spain	A/D-type	Van Der Wal and Vissers (1996)
Almklovdalen Peridotite, S Norway	D-type/{110}[001]	Cordellier *et al*. (1981)
Norwegian Caledonides	A/C-type	Katayama *et al*. (2005)

The Japan peridotites represent forearc mantle wedge material that became entrained in the Sanbagawa subduction channel (Hattori *et al*., 2010) and are therefore likely to represent mantle that was situated relatively close to the subducting slab. When examined in the context of earlier olivine fabric observations (Table 10.1), constraints can be placed on the olivine fabric distribution in the mantle wedge, allowing us to infer the deformation conditions of this region of the mantle. Alpine-type peridotites are likely to provide information on regions of the mantle wedge close to the subducting slab, as peridotites directly adjacent to the slab are the most likely to be exhumed during orogenic uplift. There have been a number of olivine fabric analyses done on Alpine-type peridotites yielding a wide variety of olivine LPOs. All the olivine fabric types have been observed in Alpine-type peridotites. Most notably however, are the observations of B- and C-type fabrics, which are significantly absent from observations of olivine fabric data from xenoliths. This suggests that the conditions that favour B- and C-type olivine fabric development are restricted to regions of the mantle wedge close to the slab, and within localised shear zones in the mantle (e.g. Webber *et al*., 2010) where both stresses and water contents are high, and that these may not be a widespread feature of the forearc mantle wedge. Even in many of the studies that identify [001] slip in olivine in Alpine-type peridotites, there are still olivine fabrics observed with a bulk slip direction of [100]. Thus regions where B- and C-type fabrics do develop are unlikely to be homogeneous in terms of LPO distribution. Based on these observations, the contribution of B- and C-type fabrics to the seismic properties of the mantle wedge is likely to be volumetrically insignificant.

Seismic anisotropy data is not available for the Lihir region, however seismic anisotropy measurements along the Pacific plate to the north and south of Lihir record trench-parallel fast directions (Figure 2.6; Nakajima and Hasegawa, 2004; Long and Silver, 2008; Hammond *et al*., 2010). If olivine fabrics are assumed to be responsible for seismic anisotropy above the mantle wedge, extrapolation of these directions to Lihir, combined with the requirement for deformation by [100] slip requires trench-parallel stretching to align olivine [100] axes parallel to the trench. The data presented here are inconsistent with B-type olivine fabric models that aim to explain the generation of trench-parallel anisotropy above the forearc mantle through a hydration-induced slip system transition in olivine, thus an alternative explanation is needed. B-type fabrics may play a role in generating trench-parallel seismic anisotropy associated with corner flow in some subduction systems. However natural observations suggest that the global propensity of trench-parallel seismic fast axes cannot be explained by B-type olivine fabric development. Furthermore, in subduction systems where B-type olivine fabrics were proposed to play a major role in the development of seismic anisotropy above the forearc mantle (e.g. the Ryuku subduction system, Japan), the magnitude of shear-wave splitting is too large to be attributed solely to olivine LPO, requiring a significant component of slab or crustal anisotropy (Kneller *et al*., 2008).

The results presented in this study are consistent with several models for the generation of trench-parallel seismic anisotropy that do not involve B-type olivine fabrics (Table 10.2). Existing models proposed to account for trench-parallel seismic fast axes can be divided into 3 broad categories: trench-parallel flow, heterogeneous strain distribution and mantle wedge or slab-sourced anisotropy not associated with olivine LPO (also see Figure 2.8).

Trench-parallel flow models require modification of the current corner wedge flow model, and lateral flow of supra-subduction and subslab mantle linked to slab-rollback has been suggested as a process by which ubiquitous trench-parallel flow could be accommodated (Russo and Silver, 1994; Buttles and Olson, 1998; Long and Silver, 2008). However, using an Indo-Atlantic hotspot reference frame (Schellart *et al*., 2008), trench-parallel fast directions are found above slabs that show little retreat

along their length (e.g. Russo and Silver, 1994). Trench-parallel fast directions are difficult to explain by 3D flow around slab-edges in these areas (cf. Long and Silver, 2008). Slab-rollback is generally thought to be responsible for trench-parallel seismic fast axes in subduction systems where the origin of the seismic anisotropy is beneath the slab (Long and Silver, 2008). However this cannot account for trench-parallel anisotropy generated in the mantle wedge.

Oblique subduction has been proposed to explain trench-parallel seismic fast axes in some subduction systems, whereby the flow field can be described by both trench-parallel and trench-perpendicular components (Mehl *et al*., 2003). This has been found to have minimal impact on the existence of trench-parallel seismic anisotropy in some cases, with the orthogonally converging Ryuku subduction system displaying trench-parallel seismic fast axes (Long and van der Hilst 2005; Kneller *et al*. 2008).

A number of models for seismic anisotropy originating in the mantle wedge involve the development of heterogeneous strain distribution. These include the foundering of lower arc crust (Behn *et al*., 2007), strain partioning related to melt segregation (Holtzman *et al*., 2003) and variations in the geometry of the subducting slab (Kneller and van Keken, 2007).

Table 10.2. A summary of models from the published literature that have been proposed to explain observations of trench-parallel seismic fast axes above the mantle wedge.

Model	Type	Reference
Oblique convergence	Trench-parallel flow	Mehl *et al*. (2003)
Slab rollback	Trench-parallel flow	Russo and Silver (1994); Buttles and Olson (1998); Long and Silver (2008)
Crustal foundering	Heterogeneous strain distribution	Behn *et al*. (2007)
Slab geometry variations	Heterogeneous strain distribution	Kneller and van Keken (2007)
Melt segregation	Heterogeneous strain distribution	Holtzman *et al*. (2003)
B-type olivine LPO	Olivine fabric distribution	Kneller *et al*. (2005, 2007); Jung *et al*, (2006)
Hydrated faults in the subducting slab	Dehydration embrittlement	Faccenda *et al*. (2008)
Dehydration-induced cracks in the subducting slab	Dehydration embrittlement	Healy *et al*. (2009)
Serpentine deformation and growth in the mantle wedge	Serpentine LPO	Katayama *et al*. (2009); Boudier *et al*. (2010)

The foundering of crust in the arc region has been suggested to act as a physical barrier to flow, diverting flow such that a significant trench-parallel component develops (Behn *et al*., 2007). Trench-parallel seismic fast axes are laterally extensive along most subduction zones (Figure 2.6), thus a change in flow orientation of this magnitude would require similar scales of crustal foundering. There is likely to be along-arc variations in the composition and density of the crust, resulting in regions that potentially founder to a lesser degree than other parts or not at all. Also, the composition and density of arc crust is likely to vary among different subduction systems, therefore crustal foundering may not occur in all systems. Thus, the crustal foundering model has the potential to explain localised variations in the flow field but cannot be reliably extrapolated to explain the global-scale of trench-parallel seismic fast axes.

The results of an experimental study by Holtzman *et al.* (2003) suggest that the presence of oriented melt pockets can alter the olivine fabric from A-type to B-type without a change of slip system. This is attributed to the fact that components of strain normal to the shear direction are larger in the presence of melt causing a rotation of [100] and [001] axes. However, it is unlikely that the formation of melt-related anisotropic structures can cause significant trench-parallel seismic anisotropy, as there is no such partial melt-induced anisotropy observed at mid-ocean ridges, where melting is prolific (Wolfe and Solomon, 1998; Katayama and Karato, 2006).

Along-strike variations in the geometry of subducting slabs, for example in the Mariana and Andean subduction systems, have also been proposed to generate a component of 3D flow within the mantle wedge (Kneller and van Keken, 2007). Irregularities in slab dip and curvature are likely to exist for many subduction systems and this model has the potential to explain trench-parallel seismic fast axis patterns. However these geometric variations and their effects on the mantle flow field are likely to vary largely between subduction systems.

Heterogeneous strain models (Holtzman *et al*., 2003; Behn *et al*., 2007, Kneller and van Keken, 2007) can account for local anisotropy variations but do not readily account for the global propensity of trench-parallel fast directions above subduction zones. An alternative approach to interpreting trench-parallel seismic anisotropy that

is consistent with the presence of olivine fabrics dominated by [100] slip in the mantle wedge is to have a significant non-flow related, trench-parallel component of anisotropy generated in either the subducting slab (e.g. Faccenda *et al*., 2008; Healy *et al*., 2009) or in the mantle wedge (e.g. Katayama, 2009; Boudier *et al*., 2010). Anisotropy contributions from the slab have largely been dismissed (e.g. Long and Silver, 2008), principally because the seismic anisotropy of the slab has been assumed to be inherited from the down-going plate rather than having developed during the subduction process.

Trench-parallel seismic fast axes can be generated by dehydration-induced crack development in the subducting slab (Healy *et al*., (2009). This model provides a strong basis for the generation of seismic anisotropy in subducting slabs rather than the mantle wedge, showing that seismic anisotropy generated by transient, fluid-filled cracks (the intersections of which align and will cause the seismic fast axes to align parallel to the trench) is much larger than that produced by deformation-induced olivine fabrics. This model has the potential to explain the spatial distribution of observed seismic anisotropy (involving rotation of seismic fast axes from trench-perpendicular in the back-arc to parallel in the fore-arc; Figure 2.7) without requiring the presence of a B-type LPO fabric as suggested by Jung *et al*. (2006) and Kneller *et al*. (2005).

Microcrack development in peridotites in the mantle wedge may also play a role in generating seismic anisotropy. Intragrain crack development is identified in olivine within peridotites from both Japan and Lihir (Chapter 9, Section 9.1), and these cracks are often parallel to low-angle boundaries. Crack annealing leaving behind residual fluid inclusions suggests that brittle deformation was occurring in the mantle, concurrently with deformation. Fluid-filled cracks along low-angle boundaries associated with the formation of olivine fabrics by dislocation creep in the upper mantle will be oriented perpendicular to the flow direction. On a mesoscopic scale, aggregates of olivine grains with this crack pattern will potentially result in a significant change to the way seismic waves propagate through the peridotite. If these fluid-filled crack observations are widespread in the mantle wedge, this provides a mechanism for generating trench-parallel seismic fast axis alignments without changing the dominant slip system in olivine or invoking a

component of trench-parallel flow. Obvious questions with respect to this theory still remain, including the time-scale at which these cracks develop and anneal, the crack density and orientations in terms of the volume of the rock, and the magnitude and orientation of the resulting anisotropy. Further investigation is required to validate this theory and explore the effects of fluid-filled cracks on seismic anisotropy in the mantle, which is another aspect for consideration when interpreting seismic fast axes above the forearc mantle wedge.

Recent research provides evidence that serpentinite deformation also plays a key role in producing seismic anisotropy in subduction zones (Faccenda *et al*., 2008; Katayama *et al*., 2009; Boudier *et al*., 2010). Models of slab anisotropy show that deformation of the subducting slab can lead to significant delay times with a trench-parallel seismic fast direction, particularly when the slab contains dehydrating and deforming serpentinites (Faccenda *et al*., 2008). A recent study investigating the influence of faulting near the upper surface of the slab finds that the LPO of both serpentine and talc within the faults is sufficient to produce seismic fast axis orientations and delay times consistent with natural observations (Faccenda *et al*., 2008). Furthermore, this study also links the orientations of major fault sets and seismic fast axis orientations around the globe, therefore this model has the potential to explain observed patterns of seismic anisotropy above subduction zones. Other studies provide evidence for the link between serpentine LPO within the mantle wedge (Katayama *et al*., 2009; Boudier *et al*., 2010). However, the absence of serpentine in the Lihir peridotites suggests that serpentine is not volumetrically significant throughout the entire mantle wedge, and this therefore may not be sufficient to explain seismic fast axis alignments above the forearc region.

It is clear from previous studies that the presence of serpentine and other hydrous phases such as talc can have extensive effects on seismic anisotropy, however it is probable that the seismic anisotropy measured at the surface is a result of the combined effects of a number of structures within a subduction zone.

The delay times (δt) between fast and slow waves predicted by deformed serpentinites are substantially higher than observed values of ~0.5 – 2 seconds (Long and Silver, 2008). However the combined effect of a slab component (approximately

6-8 seconds (Faccenda *et al*., 2008)) with a trench-parallel azimuth and overlying wedge comprising trench-perpendicular A-, D- or E-type fabrics, could be smaller delay times on the order of those observed in nature (Figure 10.1). In this model, the magnitude and direction of the measured supra-subduction seismic anisotropy will depend upon the thickness and deformation state of the slab, and will lead to complexity that is apparent in real seismic data. A slab component of trench-parallel fast directions may also account for the measured "sub-slab" trench-parallel anisotropy component that has previously been assigned to mantle flow (Long and Silver, 2008). However, it is proposed that the orientation and magnitude of observed seismic anisotropy above supra-subduction regions is due to the combined effects of olivine LPO in the mantle wedge, with a significant component associated with deformation in the subducting slab. There is also likely to be a contribution from serpentine LPO in the mantle wedge, however the nature of this contribution would depend on the amount and extent of serpentinisation.

The corner flow model itself is largely oversimplified and flow is actually influenced by a large number of parameters, such as slab characteristics (speed, evolution and geometry), overlying plate characteristics, lithosphere-asthenosphere boundary conditions, slab-wedge coupling and mantle wedge rheology (van Keken, 2003). Thus in some subduction systems, particularly near slab edges and where slab rollback is a major, the flow field is likely to deviate from the corner flow model. In other subduction systems where convergence is predominantly oblique and slab rollback is negligible, the corner flow model is likely to be a reasonable approximation of the flow field. These aspects all need to be considered when approaching the interpretation of seismic anisotropy above subduction zones. Interpretations need to incorporate natural observations of olivine and serpentine fabrics, as well as numerical modelling of factors including thermal and rheological characteristics of the subduction system, and should also differentiate between different anisotropic source regions in order to generate a model that is specific to a subduction system.

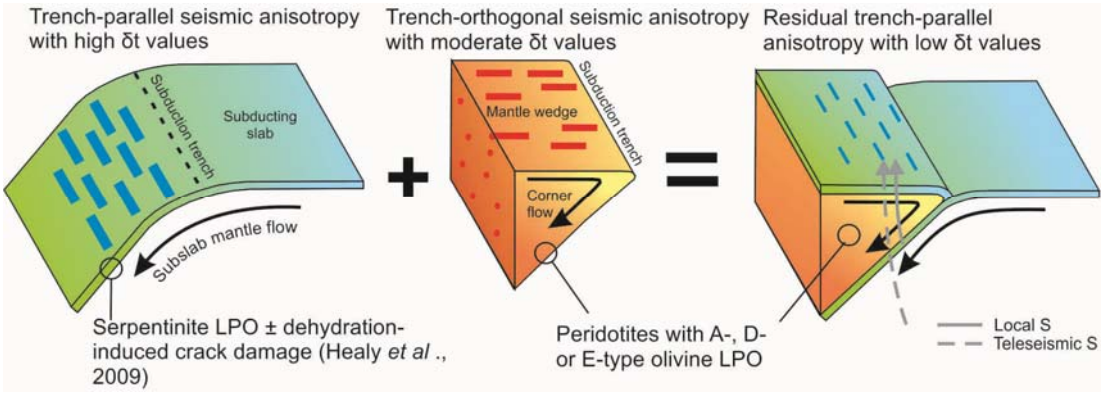

Figure 10.1. Schematic illustration of the influence of seismic anisotropy from both the mantle wedge and subducting slab. The resulting shear wave splitting patterns and delay times are likely to be on the order of those observed in nature. The red and blue lines represent the orientation of seismic fast axes and the thickness of the lines represents the predicted magnitude. δt is the delay time (the difference in arrival times between fast and slow waves).

10.2. Microstructural control on fluid influx and chemical changes – simultaneous brittle-ductile deformation

Studies on supra-subduction zone mantle peridotites not only provide a wealth of information regarding the nature of deformation in the mantle, but also shed light on the dynamic geochemical processes occurring in this region of the Earth. As highlighted earlier, there is a complex relationship between water and the deformation of peridotite, and this extends beyond influencing fabric development through a change in slip system. Microcrack development recorded by the preservation of fluid inclusions in mantle olivine from Lihir and Japan, provides evidence for a link between intragrain deformation microstructures generated through dislocation creep, and grain-scale brittle failure. This suggests that rather than being discrete, brittle and ductile deformation processes interact in a complex way. The strain hardening of olivine as a result of dislocation entanglement at low-angle boundaries during dislocation creep provides a mechanism for fracturing and therefore fluid migration through a peridotite. This process is similar to a fluid-assisted deformation mechanism observed in feldspar at mid-crustal levels (Brander *et al*., 2012), and it is proposed here that a similar process is operating within olivine in the upper mantle.

There is much scope for further investigation into the interaction between brittle and ductile processes in the mantle. In particular, it would be useful to investigate if certain low-angle boundary types (produced by the operation of different slip

systems in olivine) are more or less likely to act as nucleation sites for microcracks and hence hydration of olivine. Also, further work is required primarily to establish the pressure, temperature and stress conditions under which this fluid-assisted deformation mechanism operates, and the potential influence on fabric evolution in peridotites.

The implications of fluid influx facilitated by brittle low-angle boundary behaviour extend beyond influencing deformation mechanisms. The brittle failure of olivine deforming by predominantly ductile processes provides a means of chemical exchange between fluids, melt and olivine, such that olivine from the mantle preserves a vast amount of information regarding the geochemical nature of fluids and melt in the supra-subduction mantle.

Understanding the nature of metasomatic fluids, melt formation and migration in the mantle wedge has numerous applications, and provides insights into the development of processes such as arc magmatism and the genesis of subduction-related porphyry-epithermal copper-gold deposits, e.g. Lihir Island, Papua New Guinea (McInnes and Cameron, 1994). These ore deposits are related to alkalic magmatism (Kamenov *et al*., 2005) generated by the influx of hydrous fluid into the mantle wedge, and the hydrous fluids are responsible for transport and deposition of the ore metals. The source region for gold hosted by the Ladolam gold deposit on Lihir Island is the underlying forearc mantle (McInnes *et al*., 1999), thus, understanding how mantle fluids migrate through and interact with peridotites in the forearc mantle has significant implications for ore deposit formation.

FTIR absorbance associated with low-angle boundaries preserves evidence for the influx of hydrous fluids into olivine grains from Lihir peridotite. The preservation of structurally-bound hydroxide along these low-angle boundaries and within other features inside olivine grains provides insight into the chemistry of hydrous mantle fluids and conditions in the Lihir forearc mantle wedge. FTIR absorbance peaks reveal that conditions of metasomatism were oxidising in nature and had a high silica activity, consistent with fluids released by a subducting slab with a component of partial melt. This is supported by trace element and petrographic studies of the Lihir peridotites by Gregoire *et al*. (2001) and McInnes *et al*. (2001). This places further

constraints on the chemistry of fluids responsible for mobilisation of ore metals such as gold and copper.

Isotope studies can also provide insights into metasomatism and partial melting in the mantle. Oxygen and magnesium isotope analysis of Japan samples J909C and J917 record melt depletion and metasomatic events that occurred in the forearc mantle wedge. The overall variations observed in the isotopic composition of Japan peridotites provides further evidence for the heterogeneity of the Earth's mantle with respect to both oxygen and magnesium.

The results highlight a compelling link between olivine fabric type and isotopic composition that provides further evidence for the operation of a fluid-assisted deformation mechanism and the interaction between deforming olivine, hydrous fluids and melt. The oxygen isotope composition of both samples reflect the conditions of formation of the different LPO types, and as far as the author is aware, is the first study of its' kind to link isotopic composition and olivine fabric development. The A-type fabric in J917 has an isotopic signature that only reflects melt extraction from the peridotites, despite petrographic evidence for hydrous metasomatism. B-type and {hk0}[001] fabrics in J909C record both the melt extraction and hydrous metasomatism, indicating that there is isotopic exchange occurring between fluids/melt and the olivine grains with [001] slip directions, but not the olivine grains with [100] slip directions. This suggests that low-angle boundaries associated with the development of hydrous olivine fabrics have had more interaction with water, and this is likely to be through fluid-assisted deformation mechanisms. Serpentinisation was widespread in both of the samples analysed, despite the fact that one of the peridotites had an anhydrous olivine fabric (sample J917) and the other had hydrous olivine fabrics (sample J909C). As serpentine needs water to form, this suggests that water may be present around olivine grain boundaries in peridotite but needs to interact with the internal structure of olivine grains in order to affect the deformation within individual grains. This appears to be facilitated by the utilization of low-angle boundaries as pathways for chemical exchange between fluids and the crystal structure. This also suggests that water at grain boundaries does not penetrate the grain interior and is not sufficient to hydrate the crystal structure of olivine without brittle failure of the grains.

10.3. References

Arai, S., Takada, S., Michibayashi, K. and Kida, M. (2004) Petrology of Peridotite Xenoliths from Iraya Volcano, Philippines, and its Implication for Dynamic Mantle-Wedge Processes, *Journal of Petrology*, v. 45, p. 369-389.

Behn, M.D., Hirth, G. and Keleman, P.B. (2007) Trench-Parallel Anistropy Produced by Foundering of Arc Lower Crust, *Science*, v. 317, p. 108-111.

Boudier, F.o., Baronnet, A. and Mainprice, D. (2010) Serpentine Mineral Replacements of Natural Olivine and their Seismic Implications: Oceanic Lizardite versus Subduction-Related Antigorite, *Journal of Petrology*, v. 51, p. 495-512.

Brander, L. (2012) Brittle-plastic deformation in initially dry rocks at fluid-present conditions: transient behaviour of feldspar at mid-crustal levels, *Contributions to Mineralogy and Petrology*, v. 163, p. 403-425.

Buttles, J. and Olson, P. (1998) A laboratory model of subduction zone anisotropy, *Earth and Planetary Science Letters*, v. 164, p. 245-262.

Cordellier, F., Boudier, F. and Boullier, A. (1981) Structural study of the Almklovdalen peridotite massif (southern Norway), *Tectonophysics*, v. 77, p. 257-281.

Faccenda, M., Burlini, L., Gerya, T.V. and Mainprice, D. (2008) Fault-induced seismic anisotropy by hydration in subducting oceanic plates, *Nature*, v. 455, p. 1097-1100.

Frese, K., Trommsdorff, V., and Kunze, K. (2003) Olivine [100] normal to foliation: lattice preferred orientation in prograde garnet peridotite formed at high H 2 O activity, Cima di Gagnone (Central Alps), *Contributions to Mineralogy and Petrology*, v. 145, p. 75-86.

Gregoire, M., McInnes, B.I.A. and O'Reilly, S.Y. (2001) Hydrous metasomatism of oceanic sub-arc mantle, Lihir, Papua New Guinea: Part 2. Trace element characteristics of slab-derived fluids, *Lithos*, v. 59, p. 91-108.

Hacker, B.R., Mehl, L., Keleman, P.B., Rioux, M., Behn, M.D. and Luffi, P. (2008) Reconstruction of the Talkeetna intraoceanic arc of Alaska through thermobarometry, *Journal of Geophysical Research*, v. 113, p. 1-16.

Hammond, J.O.S., Wookey, J., Kaneshima, S., Inoue, H., Yamashina, T. and Harjadi, P. (2010) Systematic variation in anisotropy beneath the mantle wedge in the Java-Sumatra subduction system from shear-wave splitting, *Physics of the Earth and Planetary Interiors*, v. 178, p. 189-201.

Hattori, K., Wallis, S., Enami, M. and Mizukami, T. (2010) Subduction of mantle wedge peridotites: Evidence from the Higashi-akaishi ultramafic body in the Sanbagawa metamorphic belt, *Island Arc*, v. 19, p. 192-207.

Healy, D., Reddy, S.M., Timms, N.E., Gray, E.M. and Brovarone, A.V. (2009) Trench-parallel fast axes of seismic anisotropy due to fluid-filled cracks in subducting slabs, *Earth and Planetary Science Letters*, v. 283, p. 75-86.

Holtzman, B.K., Kohlstedt, D.L., Zimmerman, M.E., Heidelbach, F., Hiraga, T. and Hustoft, J. (2003) Melt Segregation and Strain Partioning: Implications for Seismic Anisotropy and Mantle Flow, *Science*, v. 301, p. 1227-1230.

Jung, H. (2009) Deformation fabrics of olivine in Val Malenco peridotite found in Italy and implications for the seismic anisotropy in the upper mantle, *Lithos*, v. 109, p. 341-349.

Jung, H., Katayama, I., Jiang, Z., Hiraga, T. and Karato, S. (2006) Effect of water and stress on the lattice-preferred orientation of olivine, *Tectonophysics*, v. 421, p. 1-22.

Kamenov, G.D., Perfit, M.R., Jonasson, I.R. and Mueller, P.A. (2005) High-

precision Pb isotope measurements reveal magma recharge as a mechanism for ore deposit formation: Examples from Lihir Island and Conical seamount, Papua New Guinea, *Chemical Geology*, v. 219, p. 131-148.

Katayama, I., Hirauchi, K.-i., Michibayashi, K. and Ando, J.-i. (2009) Trench-parallel anisotropy produced by serpentine deformation in the hydrated mantle wedge, *Nature*, v. 461, p. 1114-1117.

Katayama, I., and Karato, S. (2006) Effect of temperature on the B- to C-type olivine fabric transition and implication for flow pattern in subduction zones, *Physics of the Earth and Planetary Interiors*, v. 157, p. 33-45.

Katayama, I., Karato, S., and Brandon, M. (2005) Evidence of high water content in the deep upper mantle inferred from deformation microstructures, *Geology*, v. 33, p. 613-616.

Kneller, E.A., Long, M.D., and van Keken, P.E. (2008) Olivine fabric transitions and shear wave anisotropy in the Ryukyu subduction system, *Earth and Planetary Science Letters*, v. 268, p. 268-282.

Kneller, E.A., and van Keken, P.E. (2007) Trench-parallel flow and seismic anisotropy in the Mariana and Andean subduction systems, *Nature*, v. 450, p. 1222-1225.

Kneller, E.A., van Keken, P.E., Karato, S., and Park, J. (2005) B-type olivine fabric in the mantle wedge: Insights from high-resolution non-Newtonian subduction zone models, *Earth and Planetary Science Letters*, v. 237, p. 781-797.

Konc, Z., Garrido, C.J., Tommasi, A., Hidas, K., Szabo, C., and Marchesi, C., 2010 (Deformation study on alkaline basalt hosted upper mantle xenoliths from SE Iberian Volcanic Province (Spain), EGU General Assembly Conference Abstracts, Volume 12, p. 9043.

Long, M.D., and Silver, P.G. (2008) The Subduction Zone Flow Field from Seismic Anisotropy: A Global View, *Science*, v. 319, p. 315-319.

Long, M.D., and van der Hilst, R.D. (2005) Upper mantle anisotropy beneath Japan from shear wave splitting, *Physics of the Earth and Planetary Interiors*, v. 151, p. 206-222.

McInnes, B.I.A., and Cameron, E.M. (1994) Carbonated, alkaline hybridizing melts from a sub-arc environment: Mantle wedge samples from the Tabar-Lihir-Tanga-Feni arc, Papua New Guinea, *Earth and Planetary Science Letters*, v. 122, p. 125-141.

McInnes, B.I.A., Gregoire, M., Binns, R.A., Herzig, P.M., and Hannington, M.D. (2001) Hydrous metasomatism of oceanic sub-arc mantle, Lihir, Papua New Guinea: petrology and geochemistry of fluid-metasomatised mantle wedge xenoliths, *Earth and Planetary Science Letters*, v. 188, p. 169-183.

McInnes, B.I.A., McBride, J.S., Evans, N.J., Lambert, D.D., and Andrew, A.S. (1999) Osmium Isotope Constraints on Ore Metal Recycling in Subduction Zones, *Science*, v. 286, p. 512-516.

Mehl, L., Hacker, B.R., Hirth, G., and Keleman, P.B. (2003) Arc-parallel flow within the mantle wedge: Evidence from the accreted Talkeetna arc, south central Alaska, *Journal of Geophysical Research*, v. 108, p. ESE 4-1 - 4-18.

Michibayashi, K., Ina, T., and Kanagawa, K. (2006) The effect of dynamic recrystallization on olivine fabric and seismic anisotropy: Insight from a ductile shear zone, Oman ophiolite, *Earth and Planetary Science Letters*, v. 244, p. 695-708.

Michibayashi, K., Tasaka, M., Ohara, Y., Ishii, T., Okamoto, A., and Fryer, P. (2007) Variable microstructure of peridotite samples from the southern Mariana Trench: Evidence of a complex tectonic evolution, *Tectonophysics*, v. 444, p. 111-118.

Mizukami, T., Wallis, S.R., and Yamamoto, J. (2004) Natural examples of olivine lattice preferred orientation patterns with a flow-normal a-axis maximum, *Nature*, v. 427, p. 432-436.

Monsef, I., Rahgoshay, M., Mohajjel, M., and Shafaii Moghadam, H. (2010) Peridotites from the Khoy Ophiolitic Complex, NW Iran: Evidence of mantle dynamics in a supra-subduction-zone context, *Journal of Asian Earth Sciences*, v. 38, p. 105-120.

Nakajima, J., and Hasegawa, A. (2004) Shear-wave polarisation anisotropy and subduction-induced flow in the mantle wedge of northeastern Japan, *Earth and Planetary Science Letters*, v. 225, p. 365-377.

Russo, R.M., and Silver, P.G. (1994) Trench-parallel Flow Beneath the Nazca Plate from Seismic Anisotropy, *Science*, v. 263, p. 1105-1111.

Sawaguchi, T. (2004) Deformation history and exhumation process of the Horoman Peridotite Complex, Hokkaido, Japan, *Tectonophysics*, v. 379, p. 109-126.

Schellart, W., Stegman, D., and Freeman, J. (2008) Global trench migration velocities and slab migration induced upper mantle volume fluxes: Constraints to find an Earth reference frame based on minimizing viscous dissipation, *Earth-Science Reviews*, v. 88, p. 118-144.

Skemer, P., Katayama, I., and Karato, S. (2006) Deformation fabrics of the Cima di Gagnone peridotite massif, Central Alps, Switzerland: evidence of deformation at low temperatures in the presence of water, *Contributions to Mineralogy and Petrology*, v. 152, p. 43-51.

Skemer, P., Warren, J.M., Kelemen, P.B., and hirth, G. (2009) Microstructural and Rheological Evolution of a Mantle Shear Zone, *Journal of Petrology*.

Soustelle, V., Tommasi, A., Demouchy, S., and Ionov, D.A. (2010) Deformation and

Fluid-Rock Interaction in the Supra-subduction Mantle: Microstructures and Water Contents in Peridotite Xenoliths from the Avacha Volcano, Kamchatka, *Journal of Petrology*, v. 51, p. 363-394.

Tasaka, M., Michibayashi, K., and Mainprice, D. (2008) B-type olivine fabrics developed in the fore-arc side of the mantle wedge along a subducting slab, *Earth and Planetary Science Letters*, v. 272, p. 747-757.

Van der Wal, D., and Vissers, R.L.M. (1996) Structural petrology of the Ronda peridotite, SW Spain: deformation history, *Journal of Petrology*, v. 37, p. 23-43.

van Keken, P.E. (2003) The structure and dynamics of the mantle wedge, *Earth and Planetary Science Letters*, v. 215, p. 323-338.

Warren, J.M., Hirth, G., and Kelemen, P.B. (2008) Evolution of olivine lattice preferred orientation during simple shear in the mantle, *Earth and Planetary Science Letters*, v. 272, p. 501-512.

Webber, C., Newman, J., Holyoke Iii, C.W., Little, T., and Tikoff, B. (2010) Fabric development in cm-scale shear zones in ultramafic rocks, Red Hills, New Zealand, *Tectonophysics*, v. 489, p. 55-75.

Wolfe, C.J., and Solomon, S.C. (1998) Shear-Wave Splitting and Implications for Mantle Flow Beneath the MELT Region of the East Pacific Rise, *Science*, v. 280, p. 1230-1232.

Chapter 11. Conclusions, recommendations and further work

Japan and Lihir peridotites represent fragments of forearc mantle wedge exhumed along the margins of the SW Pacific plate, where trench-parallel seismic fast axes are observed (Buttles and Olson, 1998; Nakajima and Hasegawa, 2004; Hammond *et al.*,2010). Detailed analyses of the deformation microstructures and LPOs preserved in olivine from supra-subduction mantle peridotites have highlighted a relationship between LPO and intragrain deformation microstructures that overcomes the problems inherent in bulk fabric analysis of mantle xenoliths. The nature of this relationship is such that the slip direction of the bulk fabric and that of individual grains is consistent, and thus can be used to infer the mantle flow direction.

Fabric analysis of the Lihir xenoliths reveals that the peridotites have a bulk olivine LPO slip direction of [100]. Slip consistent with three different slip systems is recorded by the intragrain microstructures in olivine: (010)[100], {0kl}[100] and (001)[100]. The [100] axis is seismically-fast, and thus these results have significant implications for the interpretation of seismic fast axes above supra-subduction mantle and resulting mantle flow models, which rely on natural observations of olivine LPO types. [100] slip directions are inconsistent with the B-type fabric model for generating trench-parallel seismic anisotropy, requiring an alternative explanation, such as serpentine and crack development in the subducting slab and/or wedge.

Japan samples have complicated LPO patterns, and record A-, B- and C-type fabrics, along with a fabric consistent with deformation by {hk0}[001]. B- and C-type fabrics are consistent with deformation in the forearc mantle wedge, but within the context of fabric observations published in the literature, are interpreted to represent a volumetrically insignificant region of the mantle wedge in terms of seismic anisotropy. The {hk0}[001] fabric is interpreted to reflect exhumation-related deformation. Examination of the transition between these fabric types provides further evidence for pre-existing LPOs controlling the activation of later slip

systems, with crystal axes that are aligned with the new kinematic reference frame Y direction more likely to act as low-angle rotation axes for the new slip system.

Detailed petrographic observation reveals that the relationship between crystal-plastic deformation in olivine and water extends beyond influencing the active slip system. Microcrack development recorded by the preservation of fluid inclusions in mantle olivine from Lihir and Japan provides evidence for a link between intragrain deformation microstructures and grain-scale brittle failure, suggesting that there is a fluid-assisted deformation mechanism operating in the mantle. The strain hardening of olivine as a result of dislocation entanglement at low-angle boundaries during dislocation creep provides a potential mechanism for 'dynamic' fracturing and therefore fluid migration through a peridotite.

FTIR analysis reveals peaks associated with structurally-bound hydroxide in olivine can be directly linked to the presence of low-angle boundaries. The ingression of fluid along low-angle boundaries associated with the development of microcracks within mantle olivine is likely to be a mechanism for olivine defect hydration and therefore hydrolytic weakening of the olivine, with potential to effect a change in the dominant slip system from [100] to [001] slip. This fluid-assisted brittle-ductile deformation mechanism has large-scale implications for olivine fabric development and the subsequent interpretation of seismic anisotropy above the mantle wedge, as well as potential implications for fracture-induced anisotropy, partial melting of peridotite, and chemical exchange between fluids, melt and grain interiors.

There is much scope for further investigation into the interaction between brittle and ductile processes in the mantle. In particular, it would be useful to investigate if certain low-angle boundary types (produced by the operation of different slip systems in olivine) are more or less likely to act as nucleation sites for microcracks and hence hydration of olivine. Also, further work is required primarily to establish the pressure, temperature and stress conditions under which this fluid-assisted brittle-ductile deformation mechanism operates, and the potential influence on fabric evolution in peridotites.

The results of this study also provide significant insights into the chemistry of the metasomatic fluids in the mantle wedge. FTIR analysis of Lihir peridotite suggests that conditions of metasomatism were oxidising in nature and had a high silica activity, consistent with fluids released by a subducting slab. Oxygen and magnesium isotope compositions of Japan peridotites also reflect melt depletion and metasomatism that occurred in the Higashi-Akaishi mantle wedge. The overall variations observed in the isotopic composition of both samples provides further evidence for the heterogeneity of the Earth's mantle with respect to both oxygen and magnesium. Integration of EBSD and isotope analysis reveals that the oxygen isotope composition of the Japan samples reflects the conditions of formation of the different LPO types, and is the first study of its' kind to link isotopic composition and olivine fabric development.

This study presents a number of empirical observations that provide insights into the relationship between olivine deformation and geochemistry, with numerous implications for deformation in the Earth's mantle. These observations raise a number of questions and provide the basis for further investigations based on the integration of microstructural and geochemical approaches, which would progress our understanding of the link between crystal-plastic deformation, water and geochemistry.

Bibliography

Abt, D.L., Fischer, K.M., Abers, G.A., Strauch, W., Protti, J.M. and Gonzalez, V. (2009) Shear wave anisotropy beneath Nicaragua and Costa Rica; implications for flow in the mantle wedge, *Geochemistry, Geophysics, Geosystems - G3*, v. 10, 26 p.

Andersen, T. and Neumann, E.-R. (2001) Fluid inclusions in mantle xenoliths, *Lithos*, v. 55, p. 301-320.

Anderson, M.L., Zandt, G., Triep, E., Fouch, M., and Beck, S. (2004) Anisotropy and mantle flow in the Chile-Argentina subduction zone from shear wave splitting analysis, *Geophysical Research Letters*, v. 31, 4 p.

Anderson, D.L., Sammis, C. and Jordan, T. (1971) Composition and Evolution of the Mantle and Core, *Science*, v. 171 p. 1103-1112.

Anderson, D.L. (1982) Hotspots, polar wander, Mesozoic convection and the geoid, *Nature*, v. 297, p. 391-393.

Ando, J., Shibata, Y., Okajima, Y., Kanagawa, K., Furusho, M. and Tomioka, N. (2001) Striped iron zoning of olivine induced by dislocation creep in deformed peridotites, *Nature*, v. 414, p. 893-895.

Arai, S., Takada, S., Michibayashi, K. and Kida, M. (2004) Petrology of Peridotite Xenoliths from Iraya Volcano, Philippines, and its Implication for Dynamic Mantle-Wedge Processes, *Journal of Petrology*, v. 45, p. 369-389.

Australian Synchrotron (2012) Infrared Spectroscopy (Fact Sheet), Accessed July 3, 2012, from http://www.synchrotron.org.au/index.php/aussyncbeamlines/beamline-fact-sheets

Avé Lallemant, H.G. (1975) Mechanisms of preferred orientations of olivine in tectonite peridotite, *Geology*, v. 3, p. 653-656.

Ave'Lallemant, H.G. and Carter, N.L. (1970) Syntectonic Recrystallization of Olivine and Modes of Flow in the Upper Mantle, *Geological Society of America Bulletin*, v. 81, p. 2203-2220.

Bai, W. and Kohlstedt, D.L. (1992) Substantial hydrogen solubility in olivine and implications for water storage in the mantle, *Nature*, v. 357, p. 672-674.

Bai, Q. and Kohlstedt, D.L. (1993) Effects of chemical environment on the solubility and incorporation mechanism for hydrogen in olivine, *Physics and Chemistry of Minerals*, v. 19, p. 460-471.

Banno, S., Higashino, T., Otsuki, M., Itaya, T. and Nakajima, T. (1978) Thermal structure of the Sambagawa metamorphic belt in central Shikoku, *J. Phys. Earth*, v. 26, p. 345-356.

Barrie, C. D., Boyle, A. P., Cox, S. F. and Prior, D. J. (2008) Slip systems and critical resolved shear stress in pyrite: an electron backscatter diffraction (EBSD) investigation, *Mineralogical Magazine*, v. 72, no. 6, p. 1181-1199.

Battey, M.H. (1960) The relationship between preferred orientation of olivine in dunite and the tectonic environment, *American Journal of Science*, v. 258, p. 716-727.

Becker, T., Lallemand, S. and Funiciello, F. (2009) A review of the role of subduction dynamics for regional and global plate motions, Subduction Zone Geodynamics, Springer Berlin Heidelberg, 3-34 p.

Behn, M.D., Hirth, G. and Keleman, P.B. (2007) Trench-Parallel Anistropy Produced by Foundering of Arc Lower Crust, *Science*, v. 317, p. 108-111.

Bell, D.R., Rossman, G.R., Maldener, J., Endisch, D. and Rauch, F. (2003) Hydroxide in olivine: A quantitative determination of the absolute amount and calibration of the IR spectrum, *Journal of Geophysical Research*, v. 108,

p. 8-1 - 8-9.

Beran, A. (1983) A model of the OH positions in olivine, derived from infrared-spectroscopic investigations, *Physics and Chemistry of Minerals*, v. 9, p. 57-60.

Bercovici, D. (1993) A Simple Model of Plate Generation from Mantle Flow, *International Journal of Geophysics*., v. 114, p. 635-650.

Bercovici, D. (2003) The generation of plate tectonics from mantle convection, *Earth and Planetary Science Letters*, v. 205, p. 107-121.

Bergman, S.C. and Dubessy, J. (1984) CO_2-CO fluid inclusions in a composite peridotite xenolith: implications for upper mantle oxygen fugacity, *Contributions to Mineralogy and Petrology*, v. 85, p. 1-13.

Berry, A.J., Hermann, J., O'Neill, H.S.C. and Foran, G.J. (2005) Fingerprinting the water site in mantle olivine, *Geology*, v. 33, p. 869-872.

Berry, A.J., O'Neill, H.S.C., Hermann, J. and Scott, D.R. (2007) The infrared signature of water associated with trivalent cations in olivine, *Earth and Planetary Science Letters*, v. 261, p. 134–142.

Bestmann, M. and Prior, D.J. (2003) Intragranular dynamic recrystallization in naturally deformed calcite marble: diffusion accommodated grain boundary sliding as a result of subgrain rotation recrystallization, *Journal of Structural Geology*, v. 25, p. 1597-1613.

Billen, M.I. and Gurnis, M. (2001) A low viscosity wedge in subduction zones, *Earth and Planetary Science Letters*, v. 193, p. 227-236.

Boland, J.N., and Hobbs, B.E. (1973) Microfracturing processes in experimentally deformed peridotite, *International Journal of Rock Mechanics and Mining Sciences & Geomechanics Abstracts*, v. 10, p. 623-626.

Boland, J.N., and Tullis, T.E. (2013) Deformation Behavior of Wet and Dry Clinopyroxenite in the Brittle to Ductile Transition Region. In B.E. Hobbs & H.C. Heard (Eds.). *Mineral and Rock Deformation: Laboratory Studies: The Paterson Volume*, American Geophysical Union, p. 35-49.

Borthwick, J. and Harmon, R.S. (1982) A note regarding CIF3 as an alternative to BrF5 for oxygen isotope analysis, *Geochimica et Cosmochimica Acta*, v. 46, p. 1665-1668.

Boudier, F.O., Baronnet, A. and Mainprice, D. (2010) Serpentine Mineral Replacements of Natural Olivine and their Seismic Implications: Oceanic Lizardite versus Subduction-Related Antigorite, *Journal of Petrology*, v. 51, p. 495-512.

Boyle, A.P., Prior, D.J., Banham, M.H. and Timms, N.E. (1998) Plastic deformation of metamorphic pyrite: new evidence from electron-backscatter diffraction and forescatter orientation-contrast imaging, *Mineralium Deposita*, v. 34, p. 71-81.

Brander, L. (2012) Brittle-plastic deformation in initially dry rocks at fluid-present conditions: transient behaviour of feldspar at mid-crustal levels, *Contributions to Mineralogy and Petrology*, v. 163, p. 403-425.

Bullen, K.E. (1954) Introduction to the Theory of Seismology: New York, Cambridge University Press, 296 p.

Burke, E.A.J. (2001) Raman microspectrometry of fluid inclusions, *Lithos*, v. 55, p. 139-158.

Buttles, J. and Olson, P. (1998) A laboratory model of subduction zone anisotropy, E*arth and Planetary Science Letters*, v. 164, p. 245-262.

Carter, N.L. and Ave'Lallemant, H.G. (1970) High temperature flow of dunite and

peridotite, *Geological Society of America Bulletin*, v. 81, p. 2181-2202.

Carter, N. and Kirby, S. (1978) Transient creep and semibrittle behavior of crystalline rocks, *pure and applied geophysics*, v. 116, p. 807-839.

Chakrabarti, R. and Jacobsen, S.B. (2010) The isotopic composition of magnesium in the inner Solar System, *Earth and Planetary Science Letters*, v. 293, p. 349-358.

Chase, C. G. and Sprowl, D. R. 1983. The modern geoid and ancient plate boundaries. *Earth and Planetary Science Letters,* 62**,** 314-320.

Chazot, G., Lowry, D., Menzies, M. and Mattey, D. (1997) Oxygen isotopic composition of hydrous and anhydrous mantle peridotites, *Geochimica et Cosmochimica Acta*, v. 61, p. 161-169.

Christensen, N.I. (1966) Shear Wave Velocities in Metamorphic Rocks at Pressures to 10 Kilobars, *Journal of Geophysical Research*, v. 71, p. 3549-3556.

Christensen, N.I. (1971) Shear Wave Propagation in Rocks, *Nature*, v. 229, p. 549-550.

Christensen, N.I. (1984) The magnitude, symmetry and origin of upper mantle anisotropy based on fabric analyses of ultramafic tectonites, *Geophysical Journal Royal Astronomical Society*, v. 76, p. 89-111.

Christensen, N.I., and Crosson, R.S. (1968) Seismic anisotropy in the upper mantle, *Tectonophysics*, v. 6, p. 93-107.

Christensen, N.I. and Salisbury, M.H. (1979) Seismic Anisotropy in the Oceanic Upper Mantle: Evidence From the Bay of Islands Ophiolite Complex, *Journal of Geophysical Research*, v. 84, p. 4601-4610.

Clayton, R.N. (1993) Oxygen Isotopes in Meteorites, *Annual Review of Earth and*

Planetary Sciences, v. 21, p. 115-149.

Clayton, R.W. (2003) Oxygen isotopes in the solar system, *Space Science Reviews*, v. 106, p. 19-32.

Clayton, R.W. and Mayeda, T.K. (1963) The use of bromine pentafluoride in the extraction of oxygen from oxides and silicates for isotope analysis, *Geochimica et Cosmochimica Acta*, v. 27, p. 43-52.

Cordellier, F., Boudier, F. and Boullier, A. (1981) Structural study of the Almklovdalen peridotite massif (southern Norway), *Tectonophysics*, v. 77, p. 257-281.

Couvy, H., Frost, D. J., Heidelbach, F., Nyilas, K., Ungár, T., Mackwell, S., & Cordier, P. (2004) Shear deformation experiments of forsterite at 11 GPa - 1400°C in the multianvil apparatus. *European Journal of Mineralogy,* v. 16, p. 877-889.

Cox, S.F., and Etheridge, M.A. (1983) Crack-seal fibre growth mechanisms and their significance in the development of oriented layer silicate microstructures, *Tectonophysics*, v. 92, p. 147-170.

Crampin, S. (1979) Seismic anisotropy in the upper mantle, *Tectonophysics*, v. 56, p. 131.

Creagh, D., Tobin, M., Broadbent, A. and McKinlay, J. (2007) An Infrared Beamline at the Australian Synchrotron, *AIP Conference Proceedings - International Conference on Synchrotron Radiation Instrumentation, Daegu (Republic of Korea), 28 May - 2 Jun 2006,* v. 879, p. 615-618.

Currie, C.A., Cassidy, J.F., Hyndman, R.D. and Bostock, M.G. (2004) Shear wave anisotropy beneath the Cascadia subduction zone and western North American craton, *International Journal of Geophysics*, v. 157, p. 341-353.

Deines, P. and Haggerty, S.E. (2000) Small-scale oxygen isotope variations and petrochemistry of ultradeep (>300 km) and transition zone xenoliths, *Geochimica et Cosmochimica Acta*, v. 64, p. 117–131.

Dobosi, G., Downes, H., Mattey, D.P. and Embey-Isztin, A. (1998) Oxygen isotope ratios of phenocrysts from alkali basalts of the Pannonian basin: Evidence for an O-isotopically homogeneous upper mantle beneath a subduction-influenced area, *Lithos*, v. 42, p. 213-223.

Doglioni, C., Tonarini, S. and Innocenti, F. (2009) Mantle wedge asymmetries and geochemical signatures along W- and E–NE-directed subduction zones, *Lithos*, v. 113, p. 179-189.

Drury, M.R. (1991) Hydration-induced climb dissociation of dislocations in naturally deformed mantle olivine, *Physics and Chemistry of Minerals*, v. 18, p. 106-116.

Dziewonski, A.M. and Anderson, D.L. (1981) Preliminary reference Earth model, *Physics of the Earth and Planetary Interiors*, v. 25, p. 297-356.

Eiler, J. (2001) Oxygen Isotope Variations of Basaltic Lavas and Upper Mantle Rocks, *Reviews in Mineralogy and Geochemistry*, v. 43, p. 319–364.

Eiler, J., Stolper, E.M. and McCanta, M.C. (2011) Intra- and Intercrystalline Oxygen Isotope Variations in Minerals from Basalts and Peridotites, *Journal of Petrology*, v. 52, p. 1393-1413.

Enami, M., 1982. Oligoclase–biotite zone of the Sanbagawa metamorphic terrain in the Besshi district, central Shikoku, Japan. *Journal of the Geological Society of Japan*, v. 88, p. 887–900 (in Japanese with English abstract).

Enami, M. and Mizukami, T. (2004) P-T-D Evolution of the Higashi-akaishi Ultramafic Mass in the Sanbagawa Belt, Central Shikoku, Japan: Subduction of Mantle Wedge Peridotite, *Journal of Geography*, v. 115, p. 317-632.

Enami, M., Wallis, S.R. and Banno, Y. (1994) Paragenesis of sodic pyroxene-bearing quartz schists: Implications for the P-T history of the Sanbagawa belt, *Contributions to Mineralogy and Petrology*, v. 116, p. 182-198.

Escartín, J., Hirth, G. and Evans, B. (2001) Strength of slightly serpentinized peridotites: Implications for the tectonics of oceanic lithosphere, *Geology*, v. 29, p. 1023-1026.

Faccenda, M., Burlini, L., Gerya, T.V. and Mainprice, D. (2008) Fault-induced seismic anisotropy by hydration in subducting oceanic plates, *Nature*, v. 455, p. 1097-1100.

Faccenda, M. and Capitanio, F.A. (2012) Development of mantle seismic anisotropy during subduction-induced 3-D flow, *Geophysical Research Letters*, v. 39, 5 p.

Falus, G., Tommasi, A. and Soustelle, V. (2011) The effect of dynamic recrystallization on olivine crystal preferred orientations in mantle xenoliths deformed under varied stress condition, *Journal of Structural Geology*, v. 33, p. 1528 – 1540.

Fischer, K.M. and Wiens, D.A. (1996) The depth distribution of mantle anisotropy beneath the Tonga subduction zone, *Earth and Planetary Science Letters*, v. 142, p. 253-260.

Fouch, M.J. and Fischer, K.M. (1998) Shear wave anisotropy in the Mariana subduction zone, *Geophysical Research Letters*, v. 25, p. 1221-1224.

Francis, T.J.G. (1969) Generation of seismic anisotropy in the upper mantle along the mid-oceanic ridges, *Nature*, v. 221, p. 162-165.

Franz, L., Becker, K.-P., Kramer, W. and Herzig, P.M. (2002) Metasomatic Mantle

Xenoliths from the Bismarck Microplate (Papua New Guinea)-Thermal Evolution, Geochemistry and Extent of Slab-induced Metasomatism, *Journal of Petrology*, v. 43, p. 315-343.

Franz, L. and Wirth, R. (2000) Spinel inclusions in olivine of peridotite xenoliths from TUBAF seamount (Bismarck Archipelago/Papua New Guinea): evidence for the thermal and tectonic evolution of the oceanic lithosphere, *Contributions to Mineralogy and Petrology*, v. 140, p. 283-295.

Frese, K., Trommsdorff, V., and Kunze, K. (2003) Olivine [100] normal to foliation: lattice preferred orientation in prograde garnet peridotite formed at high H 2 O activity, Cima di Gagnone (Central Alps), *Contributions to Mineralogy and Petrology*, v. 145, p. 75-86.

Frezzotti, M.L., Ferrando, S., Tecce, F. and Castelli, D. (2012) Water content and nature of solutes in shallow-mantle fluids from fluid inclusions, *Earth and Planetary Science Letters*, v. 351–352, p. 70-83.

Funiciello, F., Faccenna, C. and Giardini, D. (2004) Role of lateral mantle flow in the evolution of subduction systems: insights from laboratory experiments, *International Journal of Geophysics*, v. 157, p. 1393-1406

Gaetani, G.A. and Grove, T.L. (1998) The influence of water on melting of mantle peridotite, *Contributions to Mineralogy and Petrology*, v. 131, p. 323-346.

Galy, A., Bar-Matthews, M., Halicz, L. and O'Nions, R.K. (2002) Mg isotopic composition of carbonate: insight from speleothem formation, *Earth and Planetary Science Letters*, v. 201, p. 105-115.

Galy, A. and O'Nions, R.K. (2000) Is there a CHUR for Mg? Goldschmidt 2000, 424, *in* Young, E.D., and Galy, A. (2004) The Isotope Geochemistry and Cosmochemistry of Magnesium, *Reviews in Mineralogy and Geochemistry*, v. 55, p. 197-230.

Galy, A., Young, E.D., Ash, R.D., and O'Nions, R.K. (2000) The Formation of Chondrules at High Gas Pressures in the Solar Nebula, *Science*, v. 290, p. 1751-1753.

Gledhill, K. and Gubbins, D. (1996) SKS splitting and the seismic anisotropy of the mantle beneath the Hikurangi subduction zone, New Zealand, *Physics of the Earth and Planetary Interiors*, v. 95, p. 227-236.

Gray, E. (2008) Microstructural characterisation of olivine and implications for mantle geodynamics [Honours thesis], Curtin University of Technology, 104 p.

Gregoire, M., McInnes, B.I.A. and O'Reilly, S.Y. (2001) Hydrous metasomatism of oceanic sub-arc mantle, Lihir, Papua New Guinea: Part 2. Trace element characteristics of slab-derived fluids, *Lithos*, v. 59, p. 91-108.

Green, H.W., and Radcliffe, S.V. (1975) Fluid Precipitates in Rocks from the Earth's Mantle, *Geological Society of America Bulletin*, v. 86, p. 846-852.

Griggs, D.T. (1967) Hydrolitic Weakening of Quartz and Other Silicates. Geophys. J. R. Ast. Soc, v. 14, p. 19-31.

Griggs, D.T. and Blacic, J.D. (1964) The strength of quartz in the ductile regime. Transactions American Geophysical Union, v. 45, p. 102.

Griggs, D.T. and Blacic, J.D. (1965) Quartz: Anomalous weakness of synthetic crystals. Science, v. 147, p. 292 – 295.

Hacker, B.R., Mehl, L., Keleman, P.B., Rioux, M., Behn, M.D. and Luffi, P. (2008) Reconstruction of the Talkeetna intraoceanic arc of Alaska through thermobarometry, *Journal of Geophysical Research*, v. 113, p. 1-16.

Hager, B.H. and O'Connell, R.J. (1981) A Simple Global Model of Plate Dynamics and Mantle Convection, *Journal of Geophysical Research*, v. 86, p. 4843-

4867.

Halicz, L., Galy, A., S. Belshaw, N. and Keith O'Nions, R. (1999) High-precision measurement of calcium isotopes in carbonates and related materials by multiple collector inductively coupled plasma mass spectrometry (MC-ICP-MS), *Journal of Analytical Atomic Spectrometry*, v. 14, p. 1835-1838.

Hall, R. (2002) Plate Tectonic Reconstructions: Southeast Asia, Southeast Asia Research Group. Accessed: October 13, 2009, from http://searg.rhul.ac.uk/current_research/plate_tectonics/index.html

Hall, C.E., Fischer, K.M., Parmentier, E.M. and Blackman, D.K. (2000) The influence of plate motions on three-dimensional back arc mantle flow and shear wave splitting, *Journal of Geophysical Research.*, v. 105, p. 28009-28033.

Hall, R. and Spakman, W. (2003) Mantle structure and tectonic evolution of the region north and east of Australia, Evolution and Dynamics of the Australian Plate, Geological Society of Australia Special Publication v. 22 and Geological Society of America Special Paper v. 372, p. 361-381.

Hammond, J.O.S., Wookey, J., Kaneshima, S., Inoue, H., Yamashina, T. and Harjardi, P. (2010) Systematic variation in anisotropy beneath the mantle wedge in the Java-Sumatra subduction system for shear-wave splitting, *Physics of the Earth and Planetary Interiors*, v. 178, p. 189-201.

Hansen, N., and Huang, X. (1998) Microstructure and flow stress of polycrystals and single crystals, *Acta Materialia*, v. 46, p. 1827-1836.

Harmon, R.S., Kempton, P.D., Stosch, H.G., Hoefs, J., Kovalenko, V.I. and Eonov, D. (1986) $^{18}O/^{16}O$ ratios in anhydrous spinel lherzolite xenoliths from the Shavaryn-Tsaram volcano, Mongolia, *Earth and Planetary Science Letters*, v. 81, p. 193-202.

Hart, J.T. (1978) The structural morphology of olivine: II, A quantitative derivation, *The Canadian Mineralogist*, v. 16, p. 547-560.

Hartley, M.E., Thordarson, T., Taylor, C., Fitton, J.G. and Eimf (2012) Evaluation of the effects of composition on instrumental mass fractionation during SIMS oxygen isotope analyses of glasses, *Chemical Geology*, v. 334, p. 312-323.

Hattori, K., Wallis, S., Enami, M. and Mizukami, T. (2010) Subduction of mantle wedge peridotites: Evidence from the Higashi-akaishi ultramafic body in the Sanbagawa metamorphic belt, *Island Arc*, v. 19, p. 192-207.

Healy, D., Reddy, S.M., Timms, N.E., Gray, E.M. and Brovarone, A.V. (2009) Trench-parallel fast axes of seismic anisotropy due to fluid-filled cracks in subducting slabs, *Earth and Planetary Science Letters*, v. 283, p. 75-86.

Heard, H.C. and Carter, N.L. (1968) Experimentally induced 'natural' intragranular flow in quartz and quartzite, *American Journal of Science*, v. 266, p. 1-42.

Hermann, J., Müntener, O. and Scambelluri, M. (2000) The importance of serpentinite mylonites for subduction and exhumation of oceanic crust, *Tectonophysics*, v. 327, p. 225-238.

Hess, H.H. (1964) Seismic anisotropy of the uppermost mantle under oceans, *Nature*, v. 203, p. 629-631.

Higashino, T. (1990) The higher-grade metamorphic zonation of the Sambagawa metamorphic belt in central Shikoku, Japan, *Journal of Metamorphic Geology*, v. 8, p. 413-423.

Hildyard, R. C., Prior, D. J., Faulkner, D. R. and Mariani, E. (2009) Microstructural analysis of anhydrite rocks from the Triassic Evaporites, Umbria-Marche Apennines, Central Italy: An insight into deformation mechanisms and possible slip systems, *Journal of Structural Geology*, v. 31, no. 1, p. 92-103.

Hill, K.C. and Hall, R. (2003) Mesozoic-Cenozoic evolution of Australia's New Guinea margin in a west Pacific context, *Geological Society of America Special Papers*, v. 372, p. 265-290.

Hirth, G. and Kohlstedt, D.L. (1996) Water in the oceanic upper mantle: implications for rheology, melt extraction and the evolution of the lithosphere, *Earth and Planetary Science Letters*, v. 144, p. 93-108.

Hoernle, K., Abt, D.L., Fischer, K.M., Nichols, H., Hauff, F., Abers, G.A., van den Bogaard, P., Heydolph, K., Alvarado, G., Protti, M. and Strauch, W. (2008) Arc-parallel flow in the mantle wedge beneath Costa Rica and Nicaragua, *Nature*, v. 451, p. 1094-1098.

Holtzman, B.K., Kohlstedt, D.L., Zimmerman, M.E., Heidelbach, F., Hiraga, T. and Hustoft, J. (2003) Melt Segregation and Strain Partioning: Implications for Seismic Anisotropy and Mantle Flow, *Science*, v. 301, p. 1227-1230.

Huang, F., Glessner, J., Ianno, A., Lundstrom, C. and Zhang, Z. (2009) Magnesium isotopic composition of igneous rock standards measured by MC-ICP-MS, *Chemical Geology*, v. 268, p. 15-23.

Huang, F., Zhang, Z., Lundstrom, C.C. and Zhi, X. (2011) Iron and magnesium isotopic compositions of peridotite xenoliths from Eastern China, *Geochimica et Cosmochimica Acta*, v. 75, p. 3318-3334.

Huberty, J.M., Kita, N.T., Kozdon, R., Heck, P.R., Fournelle, J.H., Spicuzza, M.J., Xu, H. and Valley, J.W. (2010) Crystal orientation effects in $\delta^{18}O$ for magnetite and hematite by SIMS, *Chemical Geology*, v. 276, p. 269-283.

Hyndman, R.D. and Peacock, S.M. (2003) Serpentinization of the fore-arc mantle, *Earth and Planetary Science Letters*, v. 212, p. 417-432.

Ionov, D.A., Harmon, R.S., France-Lanord, C., Greenwood, P.B., and Ashchepkov, I.V. (1994) Oxygen isotope composition of garnet and spinel peridotites in

the continental mantle: Evidence from the Vitim xenolith suite, southern Siberia, *Geochimica et Cosmochimica Acta*, v. 58, p. 1463-1470.

Jung, H. (2009) Deformation fabrics of olivine in Val Malenco peridotite found in Italy and implications for the seismic anisotropy in the upper mantle, *Lithos*, v. 109, p. 341-349.

Jung, H. (2011) Seismic anisotropy produced by serpentine in mantle wedge, *Earth and Planetary Science Letters*, v. 307, p. 535-543.

Jung, H. and Karato, S. (2001) Water-induced Fabric Transitions in Olivine, *Science*, v. 293, p. 1460-1463.

Jung, H., Katayama, I., Jiang, Z., Hiraga, T. and Karato, S. (2006) Effect of water and stress on the lattice-preferred orientation of olivine, *Tectonophysics*, v. 421, p. 1-22.

Jung, H., Mo, W. and Choi, S.H. (2009) Deformation microstructures of olivine in peridotite from Spitsbergen, Svalbard and implications for seismic anisotropy, *Journal of Metamorphic Geology*, v. 27, p. 707-720.

Kamenov, G.D., Perfit, M.R., Jonasson, I.R. and Mueller, P.A. (2005) High-precision Pb isotope measurements reveal magma recharge as a mechanism for ore deposit formation: Examples from Lihir Island and Conical seamount, Papua New Guinea, *Chemical Geology*, v. 219, p. 131-148.

Karato, S. (1995) Effects of Water on Seismic Wave Velocities in the Upper Mantle, *Proceedings of the Japan Academy. Ser. B: Physical and Biological Sciences*, v. 71, p. 61-66.

Karato, S. and Jung, H. (2003) Effects of pressure on high-temperature dislocation creep in olivine, *Philosophical Magazine*, v. 83, p. 401-414.

Karato, S., Jung, H., Katayama, I. and Skemer, P. (2008) Geodynamic Significance

of Seismic Anisotropy of the Upper Mantle: New Insights from Laboratory Studies, *Annual Review of Earth and Planetary Sciences*, v. 36, p. 59-95.

Karato, S., and Wu, P. (1993) Rheology of the Upper Mantle: A Synthesis, *Science*, v. 260, p. 771-778.

Katayama, I. (2009) Thin anisotropic layer in the mantle wedge beneath northeast Japan, *Geology*, v. 37, p. 211-214.

Katayama, I., Hirauchi, K.-i., Michibayashi, K. and Ando, J.-i. (2009) Trench-parallel anisotropy produced by serpentine deformation in the hydrated mantle wedge, *Nature*, v. 461, p. 1114-1117.

Katayama, I., Jung, H. and Karato, S. (2004) New type of olivine fabric from deformation experiments at modest water content and low stress, *Geology*, v. 32, p. 1045-1048.

Katayama, I. and Karato, S. (2006) Effect of temperature on the B- to C-type olivine fabric transition and implication for flow pattern in subduction zones, *Physics of the Earth and Planetary Interiors*, v. 157, p. 33-45.

Katayama, I., Karato, S. and Brandon, M. (2005) Evidence of high water content in the deep upper mantle inferred from deformation microstructures, *Geology*, v. 33, p. 613-616.

Kaula, W.M., Owen, T., Runcorn, S.K., and Tozer, D.C. (1994) The Tectonics of Venus [and Discussion], *Philosophical Transactions of the Royal Society of London. Series A: Physical and Engineering Sciences*, v. 349, p. 345-355.

Kauppinen, J.K., Moffatt, D.J., Mantsch, H.H. and Cameron, D.G. (1981) Fourier self-deconvolution: a method for resolving intrinsically overlapped bands, *Applied Spectroscopy*, v. 35, p. 271-276.

Kempton, P.D., Harmon, R.S., Stosch, H.G., Hoefs, J., and Hawkesworth, C.J.

(1988) Open-system O-isotope behaviour and trace element enrichment in the sub-Eifel mantle, *Earth and Planetary Science Letters*, v. 89, p. 273-287.

Kitamura, M., Kondoh, S., Morimoto, N., Miller, G.H., Rossman, G.R., and Putnis, A. (1987) Planar OH-bearing defects in mantle olivine, *Nature*, v. 328, p. 143-145.

Kneller, E.A., van Keken, P.E., Karato, S., and Park, J., 2005. B-type olivine fabric in the mantle wedge: Insights from high-resolution non-Newtonian subduction zone models. *Earth and Planetary Science Letters*, 237, 781-797.

Kneller, E.A., Long, M.D. and van Keken, P.E. (2008) Olivine fabric transitions and shear wave anisotropy in the Ryukyu subduction system, *Earth and Planetary Science Letters*, v. 268, p. 268-282.

Kneller, E.A. and van Keken, P.E. (2007) Trench-parallel flow and seismic anisotropy in the Mariana and Andean subduction systems, *Nature*, v. 450, p. 1222-1225.

Kneller, E.A., van Keken, P.E., Karato, S. and Park, J. (2005) B-type olivine fabric in the mantle wedge: Insights from high-resolution non-Newtonian subduction zone models, *Earth and Planetary Science Letters*, v. 237, p. 781-797.

Konc, Z., Garrido, C.J., Tommasi, A., Hidas, K., Szabo, C., and Marchesi, C., 2010 (Deformation study on alkaline basalt hosted upper mantle xenoliths from SE Iberian Volcanic Province (Spain), EGU General Assembly Conference Abstracts, Volume 12, p. 9043.

Kovács, I., Hermann, J., O'Neill, H.S.C., Fitz Gerald, J.D., Sambridge, M., and Horvath, G. (2008) Quantitative absorbance spectroscopy with unpolarized light: Part II. Experimental evaluation and development of a protocol for quantitative analysis of mineral IR spectra, *Americal Mineralogist*, v. 93, p. 765–778.

Kovács, I., O'Neill, H.S.C., Hermann, J., and Hauri, E.H. (2010) Site-specific infrared O-H absorption coefficients for water substitution into olivine, *Americal Mineralogist*, v. 95, p. 292-299.

Kranz, R.L. (1983) Microcracks in rocks: A review, *Tectonophysics*, v. 100, p. 449-480.

Kunugiza, K., Takasu, A. and Banno, S. (1986) The origin and metamorphic history of the ultramafic and metagabbro bodies in the Sanbagawa belt, *Geological Society of America Memoirs*, v. 164, p. 375–385.

Kyser, T.K., O'Neil, J., and Carmichael, I.E. (1981) Oxygen isotope thermometry of basic lavas and mantle nodules, *Contributions to Mineralogy and Petrology*, v. 77, p. 11-23.

Kyser, T.K., O'Neil, J.R., and Carmichael, I.S.E. (1982) Genetic relations among basic lavas and ultramafic nodules: evidence from oxygen isotope compositions, *Contributions to Mineralogy and Petrology*, v. 81, p. 88-102.

Lappin, M.A. (1971) The Petrofabric Orientation of Olivine and Seismic Anisotropy of the Mantle, *Journal of Geology*, v. 79, p. 730-740.

Lassak, T.M., Fouch, M.J., Hall, C.E. and Kaminski, E. (2006) Seismic characterization of mantle flow in subduction systems: Can we resolve a hydrated mantle wedge?, *Earth and Planetary Science Letters*, v. 243, p. 632-649.

Lee, K.-H., Jiang, Z. and Karato, S. (2002) A scanning electron microscope study of the effects of dynamic recrystallization on lattice preferred orientation in olivine, *Tectonophysics*, v. 351, p. 331-341.

Lemaire, C., Kohn, S.C., and Brooker, R.A. (2004) The effect of silica activity on the incorporation mechanisms of water in synthetic forsterite: a polarised infrared

spectroscopic study, *Contributions to Mineralogy and Petrology*, v. 147, p. 48-57.

Levin, V., Droznin, D., Park, J. and Gordeev, E. (2004) Detailed mapping of seismic anisotropy with local shear waves in southeastern Kamchatka, *International Journal of Geophysics*, v. 158, p. 1009-1023.

Libowitsky, E., and Beran, A. (2006) The Structure of Hydrous Species in Nominally Anhydrous Minerals: Information from Polarized IR Spectroscopy, *Reviews in Mineralogy & Geochemistry*, v. 62, p. 29-52.

Liu, Q. and Hansen, N. (1995) Deformation microstructure and orientation of F.C.C. crystals, *Physica Status Solidi (A) Applied Research*, v. 149, p. 187-199.

Liu, Q., Juul Jensen, D., and Hansen, N. (1998) Effect of grain orientation on deformation structure in cold-rolled polycrystalline aluminium, *Acta Materialia*, v. 46, p. 5819-5838.

Lloyd, G. E., Farmer, A. B., and Mainprice, D., 1997. Misorientation analysis and the formation and orientation of subgrain and grain boundaries. *Tectonophysics*, 279 (1-4), 55-78.

Long, M.D. and Becker, T.W. (2010) Mantle dynamics and seismic anisotropy, *Earth and Planetary Science Letters*, v. 297, p. 341-354.

Long, M.D. and Silver, P.G. (2008) The Subduction Zone Flow Field from Seismic Anisotropy: A Global View, *Science*, v. 319, p. 315-319.

Long, M.D. and Silver, P.G. (2009) Shear Wave Splitting and Mantle Anisotropy: Measurements, Interpretations, and New Directions, *Surveys in Geophysics*, v. 30, p. 407-461.

Long, M.D., and van der Hilst, R.D. (2005) Upper mantle anisotropy beneath Japan from shear wave splitting, *Physics of the Earth and Planetary Interiors*, v.

151, p. 206-222.

Lyon, I.C., Saxton, J.M., and Cornah, S.J. (1998) Isotopic fractionation during secondary ionisation mass spectrometry: Crystallographic orientation effects in magnetite, *International Journal of Mass Spectrometry and Ion Processes*, v. 172, p. 115-122.

Mackwell, S.J. (1985) The role of water in the deformation of olivine single crystals, *Journal of Geophysical Research*, v. 90, p. 11319.

Mainprice, D. and Ildefonse, B. (2009) Seismic Anisotropy of Subduction Zone Minerals–Contribution of Hydrous Phases, *in* Lallemand, S., and Funiciello, F. (eds.) Subduction Zone Geodynamics: Frontiers in Earth Sciences, Springer Berlin Heidelberg, p. 63-84.

Mainprice, D. and Silver, P.G. (1993) Interpretation of SKS-waves using samples from the subcontinental lithosphere, *Physics of the Earth and Planetary Interiors*, v. 78, p. 257-280.

Manea, V., and Gurnis, M., 2007. Subduction zone evolution and low viscosity wedges and channels. *Earth and Planetary Science Letters*, 264, 22-45.

Manning, C.E. (2004) The chemistry of subduction-zone fluids, *Earth and Planetary Science Letters*, v. 223, p. 1-16.

Marshall, D.B., and McLaren, A.C. (1977) Deformation mechanisms in experimentally deformed plagioclase feldspars, *Physics and Chemistry of Minerals*, v. 1, p. 351-370.

Matsyuk, S.S., and Langer, K. (2004) Hydroxyl in olivines from mantle xenoliths in kimberlites of the Siberian platform, *Contributions to Mineralogy and Petrology*, v. 147, p. 413-437.

Mattey, D.P., Lowry, D., and Macpherson, C. (1994) Oxygen isotope composition of

mantle peridotite, *Earth and Planetary Science Letters*, v. 128, p. 231-241.

Mattey, D.P., and Macpherson, C. (1993) High-precision oxygen isotope microanalysis of ferromagnesian minerals by laser-fluorination, *Chemical Geology*, v. 105, p. 305-318.

Matveev, S., O'Neill, H.S.C., Ballhaus, C., Taylor, W.R. and Green, D.H. (2001) Effect of Silica Activity on OH^- IR Spectra of Olivine: Implications for low $aSiO_2$ Mantle Metasomatism, *Journal of Petrology*, v. 42, p. 721-729.Oxford Instruments HKL A/S (2007) Channel 5 Manual, Denmark.

McInnes, B.I.A. and Cameron, E.M. (1994) Carbonated, alkaline hybridizing melts from a sub-arc environment: Mantle wedge samples from the Tabar-Lihir-Tanga-Feni arc, Papua New Guinea, *Earth and Planetary Science Letters*, v. 122, p. 125-141.

McInnes, B.I.A., Gregoire, M., Binns, R.A., Herzig, P.M. and Hannington, M.D. (2001) Hydrous metasomatism of oceanic sub-arc mantle, Lihir, Papua New Guinea: petrology and geochemistry of fluid-metasomatised mantle wedge xenoliths, *Earth and Planetary Science Letters*, v. 188, p. 169-183.

McInnes, B.I.A., McBride, J.S., Evans, N.J., Lambert, D.D., and Andrew, A.S., 1999. Osmium Isotope Constraints on Ore Metal Recycling in Subduction Zones. *Science*, 286, 512-516.

Mehl, L., Hacker, B.R., Hirth, G. and Keleman, P.B. (2003) Arc-parallel flow within the mantle wedge: Evidence from the accreted Talkeetna arc, south central Alaska, *Journal of Geophysical Research*, v. 108, p. ESE 4-1 - 4-18.

Mei, S. and Kohlstedt, D.L. (2000a) Influence of water on plastic deformation of olivine aggregates: 1. Diffusion creep regime, *Journal of Geophysical Research*, v. 105, p. 21,457-21,469.

Mei, S. and Kohlstedt, D.L. (2000b) Influence of water on plastic deformation of

olivine aggregates: 2. Dislocation creep regime, *Journal of Geophysical Research*, v. 105, p. 21,471-21,481.

Michibayashi, K., and Mainprice, D. (2004) The Role of Pre-existing Mechanical Anisotropy on Shear Zone Development within Oceanic Mantle Lithosphere: an Example from the Oman Ophiolite, *Journal of Petrology*, v. 45, p. 405-414.

Michibayashi, K., Ina, T., and Kanagawa, K. (2006) The effect of dynamic recrystallization on olivine fabric and seismic anisotropy: Insight from a ductile shear zone, Oman ophiolite, *Earth and Planetary Science Letters*, v. 244, p. 695-708.

Michibayashi, K., Tasaka, M., Ohara, Y., Ishii, T., Okamoto, A., and Fryer, P. (2007) Variable microstructure of peridotite samples from the southern Mariana Trench: Evidence of a complex tectonic evolution, *Tectonophysics*, v. 444, p. 111-118.

Miller, G.H., Rossman, G.R., and Harlow, G.E. (1987) The natural occurrence of hydroxide in olivine, *Physics and Chemistry of Minerals*, v. 14, p. 461-472.

Mizukami, T. and Wallis, S.R. (2005) Structural and petrological constraints on the tectonic evolution of the garnet-lherzolite facies Higashi-akaishi peridotite body, Sanbagawa belt, SW Japan, *Tectonics*, v. 24, p. 1-17.

Mizukami, T., Wallis, S.R. and Yamamoto, J. (2004) Natural examples of olivine lattice preferred orientation patterns with a flow-normal a-axis maximum, *Nature*, v. 427, p. 432-436.

Monsef, I., Rahgoshay, M., Mohajjel, M., and Shafaii Moghadam, H. (2010) Peridotites from the Khoy Ophiolitic Complex, NW Iran: Evidence of mantle dynamics in a supra-subduction-zone context, *Journal of Asian Earth Sciences*, v. 38, p. 105-120.

Murata, K., Maekawa, H., Ishii, K., Mohammad, Y.O., and Yokose, H. (2009) Iron-rich stripe patterns in olivines of serpentinized peridotites from Mariana forearc seamounts, western Pacific, *Journal of Mineralogical and Petrological Sciences*, v. 104, p. 199-203.

Nakajima, J. and Hasegawa, A. (2004) Shear-wave polarisation anisotropy and subduction-induced flow in the mantle wedge of northeastern Japan, *Earth and Planetary Science Letters*, v. 225, p. 365-377.

Nakamura, Y., and Kushiro, I. (1974) Composition of gas phase in Mg_2SiO_4-SiO_2-H_2O at 15 kbar, *Carnegie Institute Washington Yearbook* v. 73, p. 255-258.

Nicolas, A., Bouchez, J.L., Boudier, F. and Mercier, J.C. (1971) Textures, structures and fabrics due to solid state flow in some European lherzolites, *Tectonophysics*, v. 12, p. 55-86.

Nicolas, A., Boudier, F. and Boullier, A. (1973) Mechanisms of flow in naturally and experimentally deformed peridotites, *American Journal of Science*, v. 273, p. 853-876.

Nicolas, A. and Christensen, N.I. (1987) Formation of anisotropy in upper mantle peridotites: A review, Composition, Structure and Dynamics of the Lithosphere-Asthenosphere System, Volume 16: Geodynamics Series, American Geophysical Union, Washington, DC, p. 111-123.

O'Reilly, S.Y., and Griffin, W.L. (1988) Mantle metasomatism beneath Victoria, Australia I: metasomatic processes in Cr-diopside lherzolites, *Geochimica et Cosmochimica Acta*, v. 52, p. 433– 437.

Ota, T., Terabayashi, M. and Katayama, I. (2004) Thermobaric structure and metamorphic evolution of the Iratsu eclogite body in the Sanbagawa belt, central Shikoku, Japan, *Lithos*, v. 73, p. 95-126.

Park, J. and Levin, V. (2002) Seismic Anisotropy: Tracing Plate Dynamics in the

Mantle, *Science*, p. 485-489.

Pearson, N.J., Griffin, W.L., Alard, O. and O'Reilly, S.Y. (2006) The isotopic composition of magnesium in mantle olivine: Records of depletion and metasomatism, *Chemical Geology*, v. 226, p. 115-133.

Peselnick, L., Nicolas, A. and Stevenson, P.R. (1974) Velocity anisotropy in a mantle peridotite from the Ivrea zone: application to upper mantle anisotropy, *Journal of Geophysical Research*, v. 79, p. 1175-1182.

Peyton, V., Levin, V., Park, J., Brandon, M., Lees, J., Gordeev, E. and Ozerov, A. (2001) Mantle Flow at a Slab Edge: Seismic Anisotropy in the Kamchatka Region, *Geophysical Research Letters*, v. 28, p. 379-382.

Plümper, O., King, H., Vollmer, C., Ramasse, Q., Jung, H. and Austrheim, H. (2012) The legacy of crystal-plastic deformation in olivine: high-diffusivity pathways during serpentinization, *Contributions to Mineralogy and Petrology*, v. 163, p. 701-724.

Pogge von Strandmann, P.A.E., Elliott, T., Marschall, H.R., Coath, C., Lai, Y.-J., Jeffcoate, A.B., and Ionov, D.A. (2011) Variations of Li and Mg isotope ratios in bulk chondrites and mantle xenoliths, *Geochimica et Cosmochimica Acta*, v. 75, p. 5247-5268.

Precigout, J., Gueydan, F., Gapais, D., Garrido, C.J., and Essaifi, A. (2007) Strain localisation in the subcontinental mantle - a ductile alternative to the brittle mantle, *Tectonophysics*, v. 445, p. 318-336.

Prior, D.J., Boyle, A.P., Brenker, F., Cheadle, M.C., Day, A., Lopez, G., Peruzzo, L., Potts, G.J., Reddy, S.M., Spiess, R., Timms, N.E., Trimby, P., Wheeler, J., and Zetterström, L., 1999. The application of electron backscatter diffraction and orientation contrast imaging in the SEM to textural problems in rocks: *American Mineralogist*, 84, 1741-1759.

Prior, D.J., Wheeler, J., Peruzzo, L., Spiess, R. and Storey, C. (2002) Some garnet microstructures: an illustration of the potential of orientation maps and misorientation analysis in microstructural studies, *Journal of Structural Geology*, v. 24, p. 999-1011.

Raitt, R.W., Shor, G.G., Francis, T.J.G. and Morris, G.B. (1969) Anisotropy of the Pacific upper mantle, *Journal of Geophysical Research*, v. 74, p. 3095-3109.

Raleigh, C.B. (1963) Fabrics of naturally and experimentally deformed olivine, University of California, Los Angeles-Geology.

Raleigh, C.B. (1968) Mechanisms of Plastic Deformation of Olivine, *Journal of Geophysical Research*, v. 73, p. 5391-5406.

Randle, V. and Engler, O. (2000) Introduction to Texture Analysis: Macrotexture, Microtexture and Orientation Mapping, Gordon and Breach Science Publishers, Amsterdam.

Reddy, S.M. and Buchan, C. (2005) Constraining kinematic rotation axes in high-strain zones: a potential microstructural method? *Geological Society, London, Special Publications*, v. 243, p. 1-10.

Reddy, S.M., Timms, N.E., Pantleon, W. and Trimby, P. (2007) Quantitative characterisation of plastic deformation of zircon and geological implications, *Contributions to Mineralogy and Petrology*, v. 153, p. 625-645.

Regenauer-Lieb, K. and Kohl, T. (2003) Water solubility and diffusivity in olivine: its role in planetary tectonics, *Mineralogical Magazine*, v. 67, p. 697-715.

Regenauer-Lieb, K., Yuen, D.A. and Branlund, J. (2001) The Initiation of Subduction: Criticality by Addition of Water? *Science*, v. 294, p. 578-580.

Renard, F., Dysthe, D., Feder, J., and Jamtveit, B. (2002) Healing of fluid-filled microcracks, *Poromechanics II*, p. 925-931.

Ribe, N.M. (1989) Seismic Anisotropy and Mantle Flow, *Journal of Geophysical Research*, v. 94, p. 4213-4223.

Richter, D., and Simmons, G. (1977) Microscopic tubes in igneous rocks, *Earth and Planetary Science Letters*, v. 34, p. 1-12.

Roedder, E. (1965) Liquid CO_2 inclusions in olivine-bearing nodules and phenocrysts from basalts, *American Mineralogist*, v. 50, p. 1746-1782.

Roedder, E. (1984) Fluid Inclusions: Reviews in Mineralogy, *Mineralogical Society of America*, v. 12.

Rosenbaum, J.M., Zindler, A., and Rubenstone, J.L. (1996) Mantle fluids: Evidence from fluid inclusions, *Geochimica et Cosmochimica Acta*, v. 60, p. 3229-3252.

Rossman, G.R. (1988) Vibrational spectroscopy of hydrous components, *Rev. Mineral.*, v. 18, p. 193-206.

Russo, R.M. and Silver, P.G. (1994) Trench-parallel Flow Beneath the Nazca Plate from Seismic Anisotropy, *Science*, v. 263, p. 1105-1111.

Ryabchikov, I.D., Schreyer, W., and Abraham, K. (1982) Compositions of aqueous fluids in equilibrium with pyroxenes and olivines at mantle pressures and temperatures, *Contributions to Mineralogy and Petrology*, v. 79, p. 80-84.

Satsukawa, T., and Michibayashi, K. (2009) Determination of slip system in olivine based on crystallographic preferred orientation and subgrain-rotation axis: Examples from Ichinomegata peridotite xenoliths, Oga peninsula, Akita prefecture, *J. Geol. Soc. Jpn*, v. 115, p. 288-291.

Savage, M.K. (1999) Seismic anisotropy and mantle deformation: What have we learned from shear wave splitting? *Reviews of Geophysics*, v. 37, p. 65-106.

Sawaguchi, T. (2004) Deformation history and exhumation process of the Horoman Peridotite Complex, Hokkaido, Japan, *Tectonophysics*, v. 379, p. 109-126.

Schellart, W., Stegman, D., and Freeman, J. (2008) Global trench migration velocities and slab migration induced upper mantle volume fluxes: Constraints to find an Earth reference frame based on minimizing viscous dissipation, *Earth-Science Reviews*, v. 88, p. 118-144.

Schmatz, J. and Urai, J.L. (2011) The interaction of migrating grain boundaries and fluid inclusions in naturally deformed quartz: A case study of a folded and partly recrystallized quartz vein from the Hunsrück Slate, Germany, *Journal of Structural Geology*, v. 33, p. 468-480.

Schmidt, M.W. and Poli, S. (1998) Experimentally based water budgets for dehydrating slabs and consequences for arc magma generation, *Earth and Planetary Science Letters*, v. 163, p. 361-379.

Schneider, M.E., and Eggler, D.H. (1986) Fluids in equilibrium with peridotite minerals: Implications for mantle metasomatism, *Geochimica et Cosmochimica Acta*, v. 50, p. 711-724.

Schubert, G., Turcotte, D.L. and Olson, P. (2001) Mantle Convection in the Earth and Planets: Cambridge, Cambridge University Press, 912 p.

Sharp, Z.D. (1990) A laser based microanalytical method for the in situ determination of oxygen isotope ratios of silicates and oxides, *Geochimica et Cosmochimica Acta*, v. 54, p. 1353-1357.

Sharp, Z.D. (1992) In situ laser microprobe techniques for stable isotope analysis, *Chemical Geology*, v. 101, p. 3-19.

Silver, P.G. (1996) Seismic Anisotropy Beneath the Continents: Probing the Depths of Geology, *Annual Review of Earth and Planetary Sciences*, v. 24, p. 385-

432.

Simmons, G., and Richter, D. (1976) Microcracks in rocks. In: Strens, R. G. J. (ed) The Physics and Chemistry of Minerals and Rocks, p. 105 – 137, John Wiley, New York.

Simpson, F. (2002) Intensity and direction of lattice-preferred orientation of olivine: are electrical and seismic anisotropies of the Australian mantle reconcilable? *Earth and Planetary Science Letters*, v. 203, p. 535-547.

Skemer, P., Katayama, I. and Karato, S. (2006) Deformation fabrics of the Cima di Gagnone peridotite massif, Central Alps, Switzerland: evidence of deformation at low temperatures in the presence of water, *Contributions to Mineralogy and Petrology*, v. 152, p. 43-51.

Skemer, P., Warren, J.M. and Hirth, G. (2012) The influence of deformation history on the interpretation of seismic anisotropy, *Geochemistry Geophysics Geosystems*, v. 13, p. Q03006.

Skemer, P., Warren, J.M. and Kelemen, P.B. (2010) Microstructural and rheological evolution of a mantle shear zone, *Journal of Petrology*, v. 51, p. 43-53.

Skemer, P., Warren, J.M., Kelemen, P.B., and Hirth, G. (2009) Microstructural and Rheological Evolution of a Mantle Shear Zone, *Journal of Petrology*.

Smith, G.P., Wiens, D.A., Fischer, K.M., Dorman, L.M., Webb, S.C. and Hildebrand, J.A. (2001) A Complex Pattern of Mantle Flow in the Lau Backarc, *Science*, v. 292, p. 713-716.

Sommer, H., Regenauer-Lieb, K., Gasharova, B., and Siret, D. (2008) Grain boundaries: a possible water reservoir in the Earth's mantle? *Mineralogy and Petrology*, v. 94, p. 1-8.

Soustelle, V., Tommasi, A., Demouchy, S. and Ionov, D.A. (2010) Deformation and

fluid-rock interaction in the supra-subduction mantle: Microstructures and water contents in peridotite xenoliths from the Avacha Volcano, Kamchatka, *Journal of Petrology*, v. 51, p. 363-394.

Stadler, G., Gurnis, M., Burstedde, C., Wilcox, L.C., Alisic, L. and Ghattas, O. (2010) The Dynamics of Plate Tectonics and Mantle Flow: From Local to Global Scales, *Science*, v. 329, p. 1033-1038.

Sutton, A. P. and Balluffi, R. W. (1995) *Interfaces in crystalline materials*, Oxford Science Publications.

Tackley, P. (2000) Mantle Convection and Plate Tectonics: Toward an Integrated Physical and Chemical Theory, *Science*, v. 288, p. 2002.

Takasu, A. (1989) P–T histories of peridotite and amphibolite tectonic blocks in the Sanbagawa metamorphic belt, Japan. In: Daly, J.S., Cliff, R.A., Yardley, B.W.D. (Eds.), Evolution in Metamorphic Belts. *Geological Society Special Publications*, v. 43, p. 533–536.

Takasu, A., Wallis, S.R., Banno, S. and Dallmeyer, R.D. (1994) Evolution of the Sambagawa metamorphic belt, Japan, *Lithos*, v. 33, p. 119-133.

Tasaka, M., Michibayashi, K. and Mainprice, D. (2008) B-type olivine fabrics developed in the fore-arc side of the mantle wedge along a subducting slab, *Earth and Planetary Science Letters*, v. 272, p. 747-757.

Taylor, H., Jr. (1968) The oxygen isotope geochemistry of igneous rocks, *Contributions to Mineralogy and Petrology*, v. 19, p. 1-71.

Teng, F.-Z., Wadhwa, M. and Helz, R.T. (2007) Investigation of magnesium isotope fractionation during basalt differentiation: Implications for a chondritic composition of the terrestrial mantle, *Earth and Planetary Science Letters*, v. 261, p. 84–92.

Tommasi, A., Tikoff, B. and Vauchez, A. (1999) Upper mantle tectonics: three-dimensional deformation, olivine crystallographic fabrics and seismic properties, *Earth and Planetary Science Letters*, v. 168, p. 173-186.

Tommasi, A., Vauchez, A. and Ionov, D.A. (2008) Deformation, static recrystallization, and reactive melt transport in shallow subcontinental mantle xenoliths (Tok Cenozoic volcanic field, SE Siberia), *Earth and Planetary Science Letters*, v. 272, p. 65-77.

Tullis, J. and Yund, R.A. (1977) Experimental deformation of dry Westerly granite, *J. Geophys. Res.*, v. 82, p. 5705-5718.

Tullis, J. and Yund, R.A. (1980) Hydrolytic weakening of experimentally deformed Westerly granite and Hale albite rock, Journal of Structural Geology, v. 2, p. 439-451.

Turner, F.J. (1942) Preferred orientation of olivine crystals in peridotites, with special reference to New Zealand examples, *Transactions of the Royal Society of New Zealand*, v. 72, p. 280-300.

Valley, J.W., and Kita, N.T. (2009) In situ oxygen isotope geochemistry by ion microprobe, *Mineralogical Association of Canada Short Course*, v. 41, p. 19-63.

Van den Kerkhof, A.M., and Hein, U.F. (2001) Fluid inclusion petrography, *Lithos*, v. 55, p. 27-47.

van der Veen, C.J. and Whillans, I.M. (1994) Development of fabric in ice, *Cold Regions Science and Technology*, v. 22, p. 171-195.

Van der Wal, D., and Vissers, R.L.M. (1996) Structural petrology of the Ronda peridotite, SW Spain: deformation history, *Journal of Petrology*, v. 37, p. 23-43.

van Keken, P.E. (2003) The structure and dynamics of the mantle wedge, *Earth and Planetary Science Letters*, v. 215, p. 323-338.

Vollbrecht, A., 1989. Mikroriß-Analyse im KTB — Datenerhebung U-Tisch Mikroskopie. Unpublished report IGDL, Go¨ttingen, *in* Van den Kerkhof, A.M., and Hein, U.F. (2001) Fluid inclusion petrography, *Lithos*, v. 55, p. 27-47. (No translation available)

von Mises, R. (1928) Mechanik der plastischen Formänderung von Kristallen, *Zeitschrift für Angewandte Mathematik und Mechanik*, v. 8, p. 161-185. (No translation available)

Wallis, S.R., Takasu, A., Enami, M. and Tsujimori, T. (2000) Eclogite and Related Metamorphism in the Sanbagawa Belt, Southwest Japan, *Bulletin of Research Institute of Natural Sciences*, v. 26, p. 3-17.

Wanamaker, B., Wong, T.F., and Evans, B. (1990) Decrepitation and crack healing of fluid inclusions in San Carlos olivine, *Journal of Geophysical Research*, v. 95, p. 15623-15,641.

Warren, J.M., Hirth, G., and Kelemen, P.B. (2008) Evolution of olivine lattice preferred orientation during simple shear in the mantle, *Earth and Planetary Science Letters*, v. 272, p. 501-512.

Webber, C., Newman, J., Holyoke Iii, C.W., Little, T. and Tikoff, B. (2010). Fabric development in cm-scale shear zones in ultramafic rocks, Red Hills, New Zealand, *Tectonophysics*, v. 489, p. 55-75.

Wheeler, J., Mariani, E., Piazolo, S., Prior, D. J., Trimby, P. and Drury, M. R. (2009) The weighted Burgers vector: a new quantity for constraining dislocation densities and types using electron backscatter diffraction on 2D sections through crystalline materials, *Journal Of Microscopy*, v. 233, no. 3, p. 482-494.

Wiechert, U. and Halliday, A.N. (2007) Non-chondritic magnesium and the origins of the inner terrestrial planets, *Earth and Planetary Science Letters*, v. 256, p. 360–371.

Wiens, D.A. and Smith, G.P. (2003) Seismological Constraints on Flow Patterns Within the Mantle Wedge, *Geophysical Monographs*, p. 48.

Wirth, R., Dobrzhinetskaya, L.F., and Green, H.W. (2001) Electron microscope study of the reaction olivine + H_2O + TiO_2 → titanian clinohumite + Titanian chondrodite synthesized at 8 GPa, 1300 K, *American Mineralogist*, v. 86, p. 601-610.

Wirth, E.A. and Korenaga, J. (2012) Small-scale convection in the subduction zone mantle wedge, *Earth and Planetary Science Letters*, v. 357–358, p. 111-118.

Wirth, E. and Long, M.D. (2010) Frequency-dependent shear wave splitting beneath the Japan and Izu-Bonin subduction zones, *Physics of the Earth and Planetary Interiors*, v. 181, p. 141-154.

Wolfe, C.J. and Solomon, S.C. (1998) Shear-Wave Splitting and Implications for Mantle Flow Beneath the MELT Region of the East Pacific Rise, *Science*, v. 280, p. 1230-1232.

Xie, L.-W., Yin, Q.-Z., Yang, J.-H., Wu, F.-Y., and Yang, Y.-H. (2011) High precision analysis of Mg isotopic composition in olivine by laser ablation MC-ICP-MS, *Journal of Analytical Atomic Spectrometry*, v. 26, p. 1773-1780.

Yang, K., Hidas, K., Falus, G., C., S., Nam, B., Kovács, I. and Hwang, B. (2010) Relation between mantle shear zone deformation and metasomatism in spinel peridotite xenoliths of Jeju Island (South Korea): Evidence from olivine CPO and trace elements, *Journal of Geodynamics*, v. 50, p. 424-440.

Young, E.D., and Galy, A. (2004) The Isotope Geochemistry and Cosmochemistry of Magnesium, *Reviews in Mineralogy and Geochemistry*, v. 55, p. 197-230.

Young, E.D., Tonui, E., Manning, C.E., Schauble, E., and Macris, C.A. (2009) Spinel-olivine magnesium isotope thermometry in the mantle and implications for the Mg isotopic composition of Earth, *Earth and Planetary Science Letters*, v. 288, p. 524–533.

Zhang, S. and Karato, S. (1995) Lattice preferred orientation of olivine aggregates deformed in simple shear, *Nature*, v. 375, p. 774-777.

Zhang, S., Karato, S., Fitz Gerald, J., Faul, U.H. and Zhou, Y. (2000) Simple shear deformation of olivine aggregates, *Tectonophysics*, v. 316, p. 133-152.

Zhang, H.F., Mattey, D.P., Grassineau, N., Lowry, D., Brownless, M., Gurney, J.J., and Menzies, M.A. (2000) Recent fluid processes in the Kaapvaal Craton, South Africa: coupled oxygen isotope and trace element disequilibrium in polymict peridotites, *Earth and Planetary Science Letters*, v. 176, p. 57-72.

Zhang, H.F., Menzies, M.A., and Mattey, D.P. (2003) Mixed mantle provenance: diverse garnet compositions in polymict peridotites, Kaapvaal craton, South Africa, *Earth and Planetary Science Letters*, v. 216, p. 329-346.

Zhou, H.-W. and Clayton, R.W. (1990) P and S Wave Travel Time Inversions for Subducting Slab Under the Island Arcs of the Northwest Pacific, *Journal of Geophysical Research*, v. 95, p. 6829-6851.

Every reasonable effort has been made to acknowledge the owners of copyright material. I would be pleased to hear from any copyright owner who has been omitted or incorrectly acknowledged.

Appendix 1. Co-author Contribution Statement

Statement of Contribution of Others

To Whom It May Concern
I, Erin Gray, contributed to all aspects of the research publication, including, but not limited to, primary data collection, data processing and analysis, figure drafting and writing of the publication entitled 'The relationship between bulk fabrics and low-angle boundaries in olivine: Microstructural evidence for <a> slip in supra-subduction zone mantle'.

A realistic breakdown of the contribution by each author is as follows:

Erin Gray	85%
Prof. Steve Reddy	10%
Dr. David Healy	3%
Prof. Brent McInnes	2%

I, as a Co-Author, endorse that the level of contributions indicated above are accurate.

Prof. Steve Reddy

Dr. David Healy

Prof. Brent McInnes

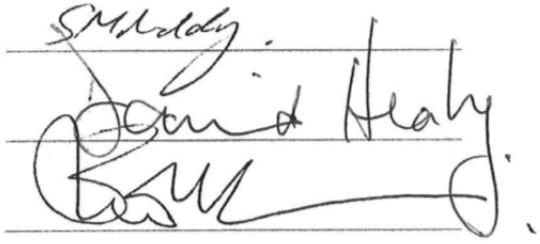

Appendix 2. Thin section descriptions and photomicrographs

Sample	Rock type	Locality	Analysis undertaken
J902	Fine-grained metasomatised spinel dunite	Imono Peridotite, Japan	Petrography
J904A	Very fine-grained metasomatised spinel dunite	Imono Peridotite, Japan	Petrography
J908A	Very fine-grained metasomatised spinel dunite	Imono Peridotite, Japan	Petrography
J909C	Very fine-grained metasomatised spinel dunite	Imono Peridotite, Japan	Petrography, EBSD, Mg/O isotopes
J915C	Fine-grained metasomatised spinel dunite	Higashi-akaishi Peridotite, Japan	Petrography
J917	Fine-grained metasomatised spinel dunite	Higashi-akaishi Peridotite, Japan	Petrography, EDS, EBSD, Mg/O isotopes
J918B	Very fine-grained metasomatised spinel dunite	Higashi-akaishi Peridotite, Japan	Petrography, EBSD
J919B_1	Very fine-grained metasomatised spinel dunite	Higashi-akaishi Peridotite, Japan	Petrography
J919B_2	Fine-grained spinel dunite	Higashi-akaishi Peridotite, Japan	Petrography
136062	Coarse-grained spinel lherzolite	Tubaf seamount, Lihir, Papua New Guinea	Petrography
136063	Coarse-grained spinel lherzolite	Tubaf seamount, Lihir, Papua New Guinea	Petrography, EBSD, FTIR
136065	Coarse-grained spinel harzburgite	Tubaf seamount, Lihir, Papua New Guinea	Petrography, EBSD
136067	Coarse-grained spinel dunite	Tubaf seamount, Lihir, Papua New Guinea	Petrography, EBSD
136068	Medium-grained spinel lherzolite	Tubaf seamount, Lihir, Papua New Guinea	Petrography
136069	Coarse-grained spinel dunite	Tubaf seamount, Lihir, Papua New Guinea	Petrography, EBSD
136070	Coarse-grained spinel lherzolite	Tubaf seamount, Lihir, Papua New Guinea	Petrography
136074	Coarse-grained spinel lherzolite	Tubaf seamount, Lihir, Papua New Guinea	Petrography, EBSD
136090	Coarse-grained metasomatised spinel dunite	Tubaf seamount, Lihir, Papua New Guinea	Petrography, EDS, EBSD

List of Abbreviations used	
Atg	Antigorite
Chr	Chromite
Cpx	Clinopyroxene
Mgt	Magnetite
Ol	Olivine
Opx	Orthopyroxene
Pnd	Pentlandite

Spt	Serpentine
Sp	Spinel
PC	Porphyroclast
NB	Neoblast
XPL	Cross-polarised light
PPL	Plane-polarised light

THIN SECTION	**J902**	**OVERALL GRAIN SIZE:** Bimodal - 0.05 micron matrix with porphyroclasts ~ 0.5 - 1.5 microns in diameter
ROCK NAME	Spinel dunite	
SAMPLE LOCATION	Imono Peridotite Body, Shikoku, Japan	
HAND SAMPLE	Dark grey in colour (melanocratic) with a penetrative foliation and pervasive lineation defined by elongated clusters of chromite and antigorite. Contains porphyroclasts of chromite within a groundmass of fine-grained equigranular olivine that is pale green in colour and elongate needles of dark grey antigorite (<1mm in size). The mineral lineation is defined by the alignment of olivine and the penetrative foliation is defined by the alignment of deformed chromite porphyroclasts with tails. Typically weathered to a yellow-brown colour.	
Section was cut with respect to the X and Z structural directions - lineation (X) is the long axis of the section, and the section is looking along the foliation plane.		

Mineral	%	Size (mm)			Morphology	Grain boundaries	Comments
		min.	max.	av.			
Olivine (porphyroclasts)	10	0.5	1.5	1	Anhedral, elongate	Irregular curved boundaries with olivine neoblasts. Cross-cut/overgrown by antigorite fibres. No boundaries with chromite observed. Boundaries with magnetite are amoeboid/embayed and irregular.	Olivine is clear and colourless in PPL, and up to 2nd order pink interference colours in XPL. High relief. Porphyroclastic olivine is often elongated parallel to the lineation. Well-preserved internal microstructure, displaying heterogeneous extinction characteristic of low-angle boundaries associated with deformation. Porphyroclasts contain very fine, vermicular trails of fluid inclusions that are parallel to low-angle boundaries (<1 micron in diameter). There are also coarser trails of spherical fluid inclusions (~5 microns in diameter) and the finer inclusion trails branch off from these. Grains show fracturing typical of mantle olivine - irregular and somewhat glassy.
Olivine (neoblasts)	60	0.05	0.3	0.05 - 0.075	Subhedral to anhedral, equant	Often form triple junctions with other olivine neoblasts. Irregular boundaries with other olivine neoblasts. Cross-cut by blades of fine-grained antigorite, boundaries are straight and regular. Irregular and curved boundaries with olivine porphyroclasts. Irregular and embayed boundaries with magnetite.	Clear and colourless in PPL, up to 2nd order pink interference colours in XPL. Generally equant in shape with no shape preferred orientation. Grains are clean in appearance with no inclusions or internal microstructure, and generally cross-cut by fine antigorite grains. Grains show fracturing typical of mantle olivine.

Antigorite	27	0.1	1	0.3	Elongate, bladed, euhedral	Straight and regular with most other minerals except for magnetite - directly overprints these minerals.	Clear and colourless in PPL, grey in XPL. Low relief. Antigorite is widespread throughout this sample and defines the foliation. Also forms veins that traverse the thin section and cross-cut the foliation.
Chromite	2	0.2	1.5	0.3	Subhedral to euhedral, tabular	No self-boundaries. Embayed boundaries with olivine neoblasts. Irregular boundaries with magnetite. Rimmed by magnetite and overprinted by antigorite.	Edges are embayed and magnetite (lighter under reflected light) occurs along the edges of the grains. Grains are slightly elongated in the direction of the lineation.
Magnetite	1	0.005	0.05	0.025	Equant and subhedral to anhedral in shape	Overprint all other minerals and so grain boundaries are usually irregular and curved. Self-boundaries are straight and regular and form triple junctions.	Brighter under reflected light than chromite. One of the most recent minerals to form; overprints antigorite in the centre of cross-cutting veins. Weathers to a brown/red colour. Often forms rims around the chromite grains.
Pentlandite	<0.5	0.01	0.05	0.02	Subhedral to anhedral, equant	Boundaries with magnetite are straight and regular. Boundaries with other minerals are not commonly observed.	Very bright under reflected light, and pale yellow in colour. Occurs in trace amounts and is usually associated with magnetite.
Overall Texture and Alteration :	This sample is porphyroclastic (primarily due to the bimodal grain size of olivine), with a weak foliation and lineation. The foliation is predominantly defined by the alignment of antigorite fibres and the mineral lineation by chromite and antigorite. There are of bands of fine-grained magnetite that are sub-parallel to the foliation. Olivine porphyroclasts have a tendency to be elongate and are aligned parallel to the antigorite foliation/lineation. The sample is cross-cut by a network of veins containing fine-grained antigorite and magnetite that appear to have oxidised, probably due to weathering at the surface. Antigorite is widespread throughout the sample but there are microlithons containing domains that are olivine-rich/antigorite-poor and olivine-poor/antigorite-rich. The foliation is stronger in the antigorite-rich microlithon, which also tends to contain larger and better preserved olivine porphyroclasts. Microlithon boundaries are parallel to the foliation.						
Petrogenesis:	Initial synchronous crystallisation of olivine and chromite under spinel peridotite facies. These were deformed (olivine porphyroclasts have preserved internal microstructure, are aligned and have an SPO) before undergoing dynamic recrystallisation by grain boundary migration to produce neoblastic olivine. Subsequently, there was an influx of hydrous fluid as shown by the overprinting of chromite and both generations of olivine by aligned antigorite. Following the initial fluid influx event, the sample was cross-cut by veins filled with fine-grained antigorite, magnetite and trace amounts of pentlandite.						

Sample J902 Photomicrographs

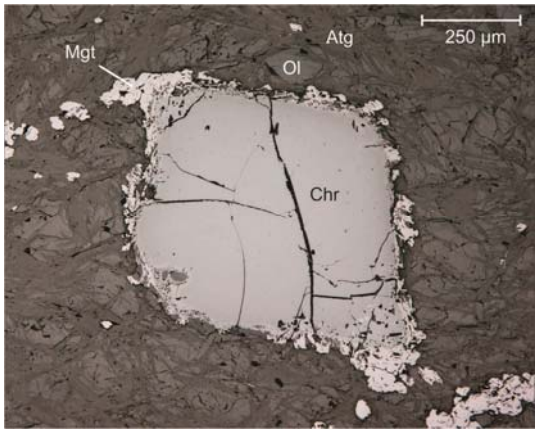

Reflected light image of a primary chromite grain surrounded by a rim of magnetite. The magnetite grains form an asymmetric trail leading away from the chromite porphyroclast. Olivine and antigorite are also visible in this image and are part of the rock matrix.

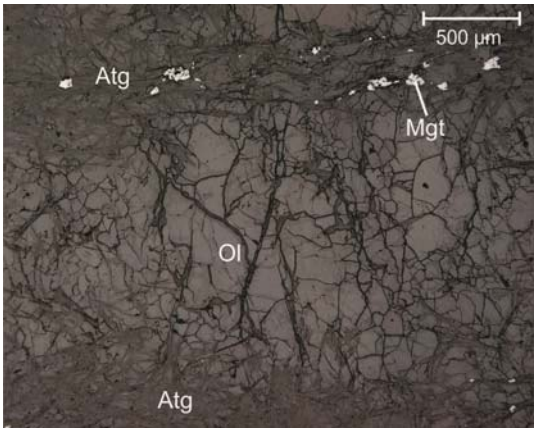

Reflected light image showing fine-grained magnetite (bright white grains) contained within an antigorite-rich region of the sample.

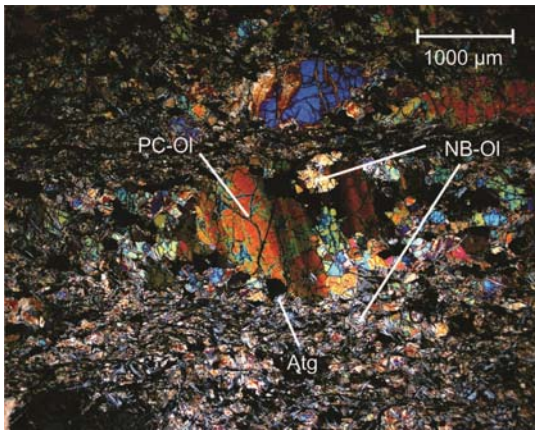

XPL image showing a deformed porphyroclastic olivine grain within a fine matrix of antigorite and neoblastic olivine. There are also neoblastic olivine grains occurring at the edges of the olivine porphyroclasts.

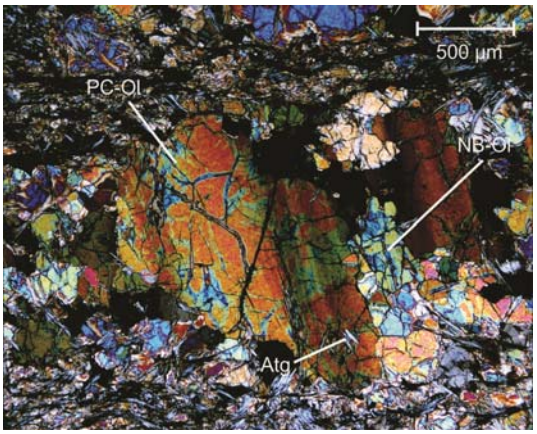

Close-up of the olivine porphyroclast in the previous XPL image, showing the development of neoblasts around the grain boundaries of the porphyroclast, as well as the low-angle boundaries preserved inside the porphyroclast.

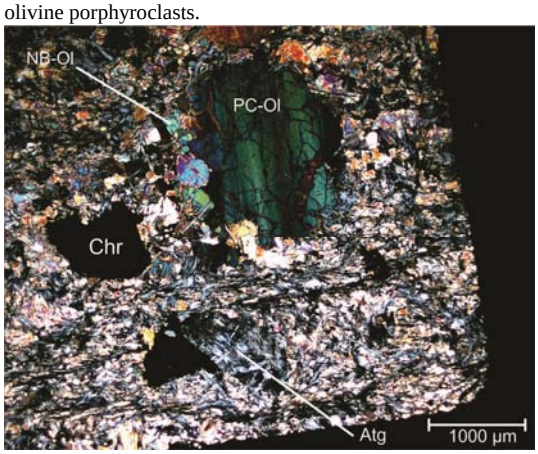

XPL image of a deformed olivine porphyroclasts, showing the neoblastic olivine-antigorite matrix and neoblastic olivine development surrounding the porphyroclast.

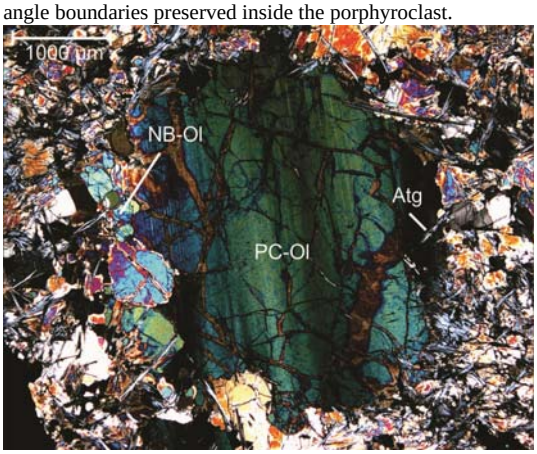

Close-up of the XPL image to the left. Low-angle boundaries are prominent in this grain.

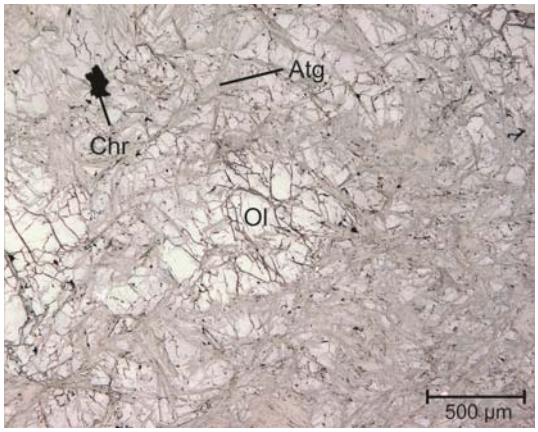

PPL image of sample J902, showing relief contrast between olivine (high) and antigorite (low). There is also a chromite grain visible in this image.

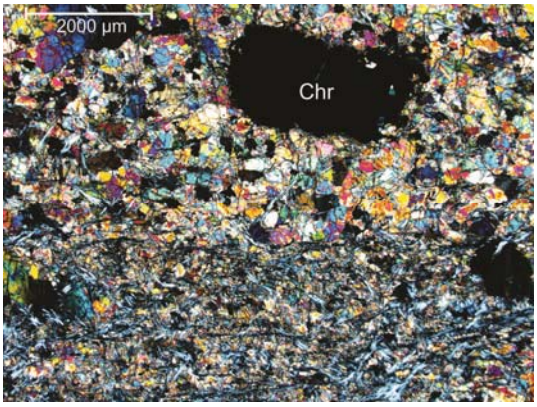

XPL image showing the strongly-foliated antigorite-rich region to the bottom of the thin section, and the olivine-rich microlithon to the top.

THIN SECTION	**J904A**	**OVERALL GRAIN SIZE:** Bimodal but overall is very fine-grained (~0.5 mm)
ROCK NAME	Spinel dunite	
SAMPLE LOCATION	Imono Peridotite Body, Shikoku, Japan	
HAND SAMPLE	Fine-grained, porphyroclastic, well-foliated spinel peridotite. Moderately weathered to a yellow-brown colour. Fresh surfaces are dark grey and melanocratic. Foliated and lineated with a weak crenulation approximately 45 degrees away from the main foliation. The main foliation is defined by the alignment of elongate and sheared porphyroclasts of chromite. The crenulation cleavage is wavy and is more obvious on the weathered surfaces. Contains olivine, chromite and needles of a pale acicular mineral (<0.5 mm in length). Most of the mineral is too aphanitic to analyse the mineral proportions.	
Section was cut with respect to the X and Z structural directions - lineation (X) is the long axis of the section, and the section is looking along the foliation plane.		

Mineral	**%**	**Size (mm)**			**Morphology**	**Grain boundaries**	**Comments**
		min.	**max.**	**av.**			
Olivine (porphyroclasts)	5	0.75	2.1	1	Anhedral and elongate.	Self-boundaries are irregular. Boundaries with fine olivine are curved and irregular. Boundaries between porphyroclasts, antigorite and chromite are straight and regular.	Clear in PPL, up to 2nd order blue/green interference colours in XPL. High relief. Usually overprinted by coarse antigorite. These usually preserve some internal microstructure and fluid inclusions (<1 micron in diameter) that form trails parallel to the low-angle boundaries. Olivine porphyroclasts are wrapped by the foliation.
Olivine (neoblasts)	50	0.025	0.5	0.3	Anhedral and lenticular in shape but can be equant around strain shadows.	Self-boundaries are straight and regular and often form triple junctions. Boundaries with coarse olivine are curved and irregular. Boundaries between neoblasts, antigorite and chromite are straight and regular.	Clear in PPL, 2nd order green/blue interference colours. High relief. The neoblastic olivine comprises most of the sample and contributes to the foliation, with the long axis of most grains parallel to the lineation direction. Grains are fairly clean in appearance.
Antigorite	42	0.1	1	0.4	Elongate, bladed, subhedral to euhedral.	Boundaries with olivine are straight and regular. Boundaries with chromite are curved and irregular.	Clear in PPL, low relief, grey in XPL. Antigorite defines the structural fabric in the sample. It cross-cuts primary olivine and chromite and appears to be synchronous with olivine neoblast development.
Chromite	2	0.2	1.5	1	Subhedral to anhedral, equant.	No self-boundaries observed. Boundaries with magnetite are curved and irregular, as are those with antigorite. Boundaries with olivine are straight and regular.	Opaque mineral, high relief. Does not appear to contribute to the fabric of the sample. Often rimmed by magnetite grains.

Magnetite	<1	0.05	0.2	0.1	Subhedral and equant	Self-boundaries are irregular and tend to be defined by the surrounding minerals.	Opaque, similar in appearance to chromite grains but brighter in reflected light. Cross-cuts and so formed later than antigorite. Tends to form around the boundaries of chromite grains.
Pentlandite	<0.5	0.01	0.05	0.02	Subhedral to anhedral, equant	Boundaries with magnetite are straight and regular. Boundaries with other minerals are not commonly observed.	Very bright under reflected light (brighter than magnetite), and pale yellow in colour. Occurs in trace amounts and is usually associated with magnetite.
Overall Texture and Alteration :	Porphyroclastic texture. The foliation is defined primarily by the alignment of blades of antigorite and the long axes of lenticular olivine. The foliation wraps olivine and chromite porphyroclasts with associated strain shadows developing at the margins of the porphyroclasts, where neoblastic olivine tends to be more equant in shape. The sample shows evidence for weak olivine microlithon development. Antigorite appears to have played a role in neoblast development by mechanically dismembering grains.						
Petrogenesis:	Initial synchronous crystallisation of olivine and chromite under spinel peridotite facies in the mantle. Olivine grains show evidence for deformation (preserved intragrain microstructures) in the presence of hydrous fluids, as shown by the overprinting of olivine and chromite by aligned antigorite, as well as the presence of low angle boundary-parallel fluid inclusions in olivine porphyroclasts. Neoblasts were formed through dynamic recrystallisation of primary olivine by predominantly grain boundary migration, as shown by the curved and irregular grain boundaries between olivine porphyroclasts and neoblasts. Subsequently, magnetite and pentlandite formed, cross-cutting the other mineral grains and infilling cracks and gaps within the rock, and so is probably the most recent mineral to form.						

Sample J904A Photomicrographs

XPL overview image of the texture of sample J904A. There are porphyroclasts of olivine and chromite within a sheared neoblastic olivine, antigorite and magnetite matrix.

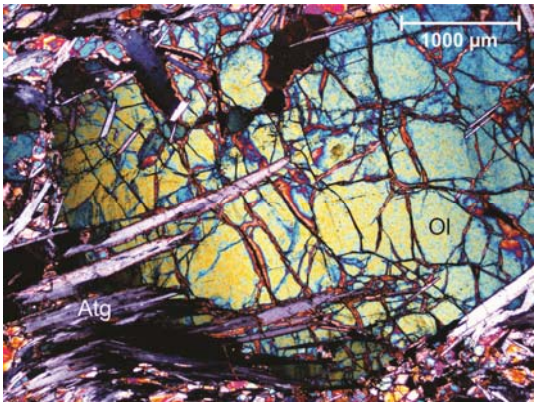

XPL image showing antigorite overpriting a deformed olivine porphyroclast. There is also some recrystallisation by grain boundary migration of the olivine occurring towards the top of the image.

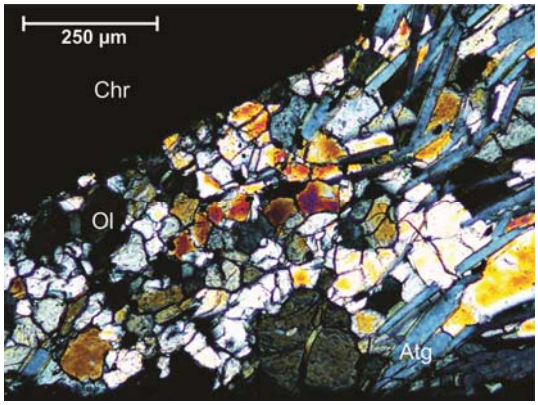

XPL image of the equant olivine neoblasts below the chromite porphyroclast shown above.

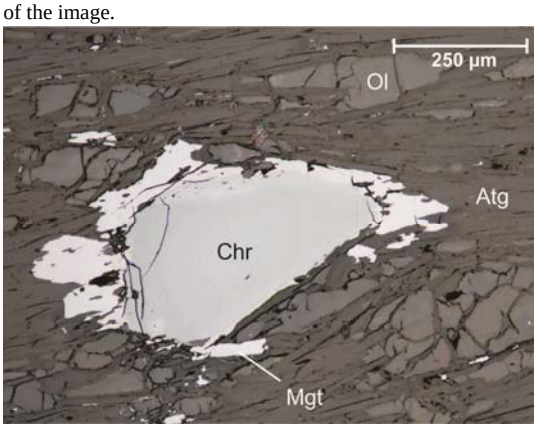

Reflected light image of a chromite porphyroclast surrounded by a rim of magnetite.

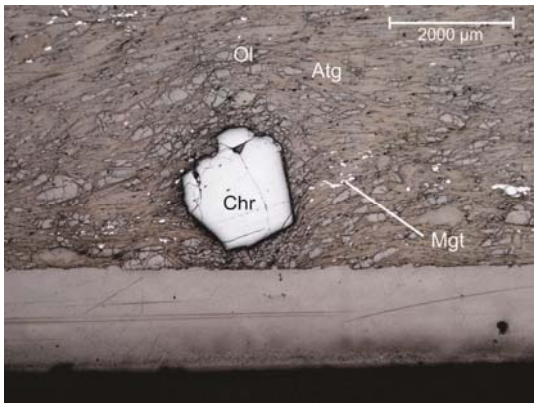

Reflected light image of a chromite porphyroclast within a matrix of sheared olivine, antigorite and magnetite.

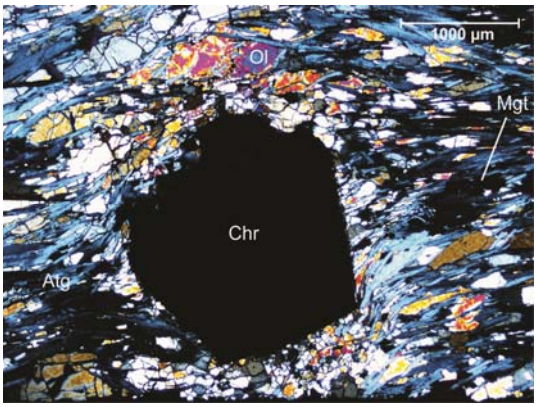

XPL image of the chromite grain to the left wrapped by the antigorite foliation. Olivine is also lenticular to the left and right of the grain, but is finer and more equant to the top and bottom where there appears to be less strain.

THIN SECTION	**J908A**	**OVERALL GRAIN SIZE:** Very fine-grained
ROCK NAME	Spinel dunite	
SAMPLE LOCATION	Imono Peridotite Body, Shikoku, Japan	
HAND SAMPLE	Very fine-grained with porphyroclasts of chromite. Reasonably well-foliated and lineated, fabric primarily defined by pale acicular mineral (antigorite?) Creamy-brown colour on weathered surfaces. Dark-grey to black on fresh surfaces. Contain abundant dark grey veins of an aphanitic material. The foliation is penetrative and defined by the alignment of antigorite and dark, wispy vein structures. The mineral lineation is defined by the alignment of olivine porphyroclasts and chromite. These are often rotated and have strain shadows. Veins cross-cutting the sample contain an oxidised Fe-bearing ore mineral.	
Section was cut with respect to the X and Z structural directions - lineation (X) is the long axis of the section, and the section is looking along the foliation plane.		

Mineral	**%**	**Size (mm)**			**Morphology**	**Grain boundaries**	**Comments**
		min.	**max.**	**av.**			
Olivine	50	0.02	1.5	0.5	Anhedral and lenticular to equant	Self-boundaries are irregular. Boundaries with fine olivine are curved and irregular. Boundaries between porphyroclasts, antigorite and coarse chromite are straight and regular.	High relief, up to pale yellow interference colours in XPL, clear in PPL. Porphyroclasts are fractured and usually overprinted by coarse antigorite. These usually preserve some internal microstructure. Olivine porphyroclasts are wrapped by the foliation. Olivine is often highly fractured, with a perpendicular fracture geometry. There appears to be a continuous range in grain size from neoblast to porphyroclast, as opposed to two distinct populations. Difficult to assess grain boundary relationships of the finer grain fraction. The long axis of the grains is usually parallel to the foliation direction.
Antigorite	47	0.1	1.5	1.1	Elongate, bladed to fibrous, subhedral to euhedral.	Boundaries with olivine are straight and regular. Boundaries with chromite are curved and irregular.	Clear in PPL, low relief. Antigorite defines the structural fabric in the sample. It cross-cuts primary olivine and chromite, and appears to be synchronous with olivine neoblast development. Antigorite appears to have played a role in olivine neoblast development by mechanically dismembering grains. Grains are often fractured perpendicular to the length of the grain, and these fractures are often filled with

							fine magnetite.
Chromite	1	0.5	1	0.9	Anhedral, equant	Grain boundaries are generally highly embayed.	Very dark brown to opaque. Occurs as isolated grains. Pale to mid-grey under reflected light. This is the dullest opaque mineral in the sample. Often rimmed by fine magnetite grains.
Magnetite	1.5	0.05	0.2	0.1	Anhedral	Self-boundaries are irregular and usually determined by the surrounding minerals.	Cross-cuts and so formed later than antigorite. Tends to form around the boundaries of larger chromite grains. Brighter under reflected light than chromite but duller pentlandite.
Pentlandite	<0.5	0.005	0.05	0.025	Equant and subhedral to anhedral in shape	Morphology tends to be controlled by the surrounding mineralogy.	Often associated with magnetite and is the latest mineral to form. High reflectance under reflected light and often quite yellow in appearance.
Overall Texture and Alteration :	The foliation is defined primarily by the alignment of blades of antigorite and the long axes of lenticular olivine. The foliation wraps olivine and chromite porphyroclasts. The sample is porphyroclastic, although the porphyroclasts are much less abundant than in other samples. The sample is also starting to develop olivine microlithons. The sample is traversed by antigorite and magnetite-filled veins.						
Petrogenesis:	Initial synchronous crystallisation of olivine and chromite. Olivine grains show evidence for subsequent deformation (preserved intragrain microstructures) before dynamic recrystallisation by both grain boundary migration and subgrain rotation as indicated by curved boundaries between olivine neoblasts and porphyroclasts. Olivine neoblast development was synchronous with hydrous fluid influx indicated by the overprinting of olivine and chromite by aligned antigorite, as well as the presence of low-angle boundary-parallel fluid inclusions in olivine porphyroclasts. Primary chromite is unstable under these conditions, appearing to be reacting at the grain boundaries to magnetite. Associated with the magnetite is trace amounts of pentlandite. Pentlandite grains tend to cross-cut all mineral grains and infill cracks and gaps within the rock, and so is probably the most recent mineral to form.						

Sample J908A Photomicrographs

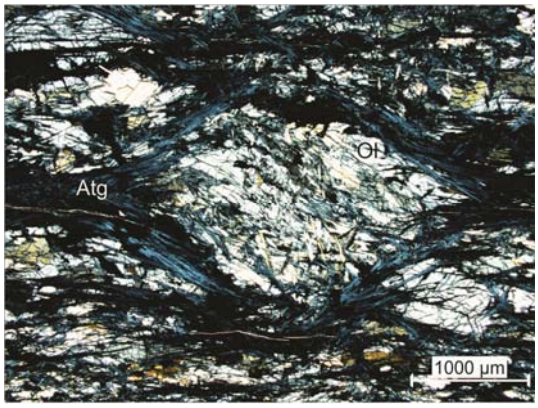

XPL image showing an antigorite foliation wrapping the remains of an olivine porphyroclast that has been recrystallised and heavily altered to antigorite.

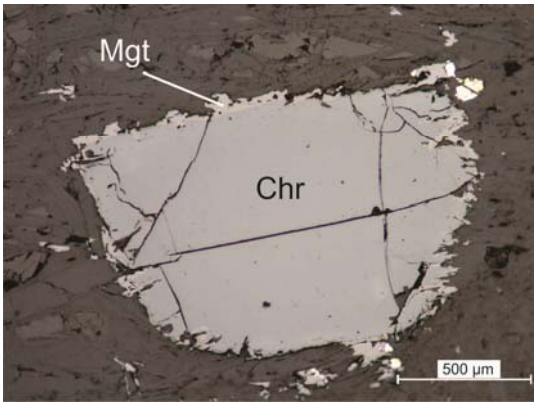

Chromite grain surrounded by a rim of magnetite and associated pentlandite (reflected light).

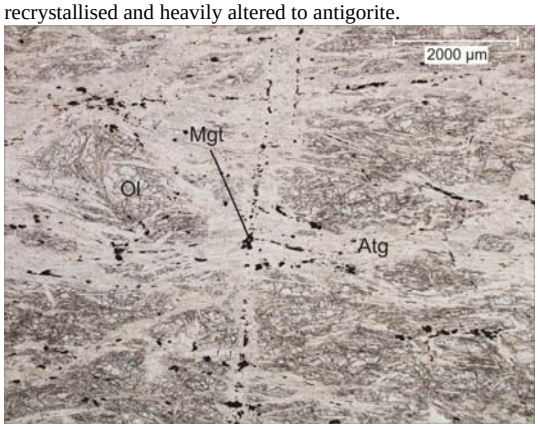

PPL image of antigorite-magnetite veins cross-cutting the olivine-antigorite matrix.

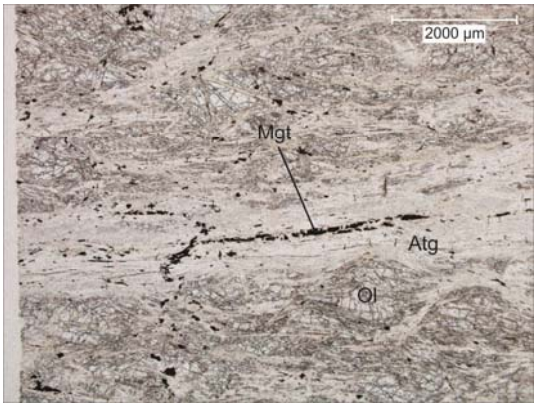

PPL image of magnetite replacing antigorite at the centre of veins that cross-cut the sample.

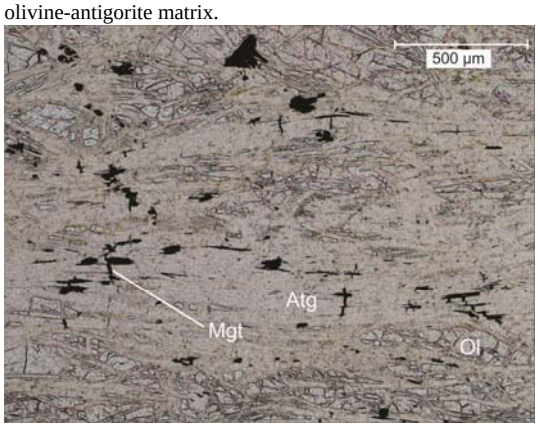

PPL image showing magnetite filling cracks in antigorite grains.

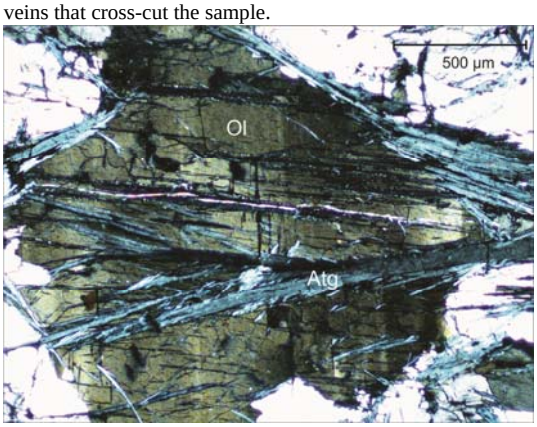

Low-angle boundaries preserved in an olivine porphyroclast with some replacement by antigorite (XPL).

THIN SECTION	**J909C** **OVERALL GRAIN SIZE:** Phaneritic fine-grained to aphanitic
ROCK NAME	Spinel dunite
SAMPLE LOCATION	Imono Peridotite Body, Shikoku, Japan
HAND SAMPLE	Extremely sheared, heterogeneously deformed, foliated and lineated; seriate to porphyroclastic in places. Contains olivine and chromite, both of which are porphyroclastic, as well as fine needles of antigorite. Melanocratic on fresh surfaces, yellow-brown in colour on weathered surfaces. The foliation is pervasive and defined by needles of antigorite and chromite. The mineral lineation is defined by the alignment of chromite porphyroclasts.
Section was cut with respect to the X and Z structural directions - lineation (X) is the long axis of the section, and the section is looking along the foliation plane.	

Mineral	%	Size (mm)			Morphology	Grain boundaries	Comments
		min.	max.	av.			
Olivine (porphyroclasts)	57	0.5	2	0.7	Anhedral, elongate and often lenticular in shape, sub-parallel or parallel to the lineation.	Self-boundaries are straight and regular. Boundaries between neoblasts and porphyroclasts are generally embayed - neoblast is convex, porphyroclast is concave.	Clear in PPL, up to 2nd order blues in XPL. High relief. Tend to preserve some deformation microstructures. Replaced by acicular antigorite grains and wrapped by the foliation. Porphyroclasts often contain abundant sub-micron sized fluid and mineral inclusions. The fluid inclusions are spatially related to antigorite overgrowth/cross-cutting.
Olivine (neoblasts)	10	0.05	0.4	0.3	Neoblasts in the high strain zone are anhedral to subhedral and slightly elongate (often lenticular). Grains in the low strain zone are equant and subhedral.	Neoblasts have embayed self-boundaries but often form triple junctions in the low strain zone.	High relief, clear in PPL and up to 2nd order blue in XPL. Overprinted by antigorite. Neoblasts do not preserve any intragrain microstructure and are generally clean in appearance.
Antigorite	30	0.05	0.5	0.3	Elongate subhedral blades.	Self-boundaries are straight and regular.	Clear in PPL, grey in XPL, low relief. Uniform grain size. In higher abundance in the high strain zone. Cross-cuts primary and secondary olivine and

							chromite.
Chromite	1.5	0.25	0.7	0.5	Generally equant to slightly elongate subhedral grains.	Self-boundaries are embayed. Regular boundaries with olivine and irregular boundaries with antigorite.	Opaque mineral that is wrapped by the foliation, with strain shadows developed. Some grain interiors tend to be pitted/spotted in appearance and occasionally contain small overgrowths of antigorite.
Magnetite	1	0.05	0.2	0.1	Anhedral to subhedral, equant to slightly elongate parallel to the foliation	Self-boundaries irregular. Tends to fill in spaces between grains so grain boundary interactions tend to be based on the shape of surrounding minerals.	Opaque. Very fine-grained. Appears to be a late feature, overgrowing antigorite and filling in spaces between antigorite grains. Often forms elongate aggregates parallel to the foliation - trails of magnetite leading away from chromite porphyroclasts. Often accumulated around the grain boundaries of porphyroclastic chromite.
Pentlandite	<0.5	0.005	0.05	0.025	Equant and subhedral to anhedral in shape	Morphology tends to be controlled by the surrounding mineralogy.	High reflectance under reflected light and often quite yellow in appearance.
Overall Texture and Alteration :	The foliation is defined by both elongation and alignment of deformed olivine (forming pods) and alignment of acicular grains of antigorite. The section is divided (parallel to x) into zones or microlithons that are rich and poor in antigorite, corresponding to zones of strong and weak fabric, respectively. The antigorite-rich zone (~50% antigorite) has a stronger fabric and generally contains a finer fraction of olivine grains. The lesser foliated antigorite-poor (~10% antigorite), olivine-rich zone contains coarser olivines but also sees the development of neoblasts. The olivine dominating the strongly foliated zone is predominantly neoblastic. Strain shadows have developed around porphyroclastic chromite grains. The foliation is slightly wavy, possibly suggesting that there is a later deformation fabric overprinting the foliation.						
Petrogenesis:	Initial crystallisation of olivine and chromite occurred under spinel peridotite facies and this was followed by deformation indicated by the presence of a foliation and lineation, as well as the intragrain microstructures preserved within the porphyroclasts. Subsequently, this sample interacted with a hydrous fluid during deformation, as shown by the presence of fluid inclusions in olivine and the development and alignment of antigorite fibres to produce a pervasive foliation. This deformation also resulted in dynamic recrystallisation of olivine by grain boundary migration as indicated by the embayed nature of the olivine porphyroclast/neoblast grain boundaries. This fabric was then overprinted by a weak crenulation and growth of magnetite and pentlandite.						

Sample J909C Photomicrographs

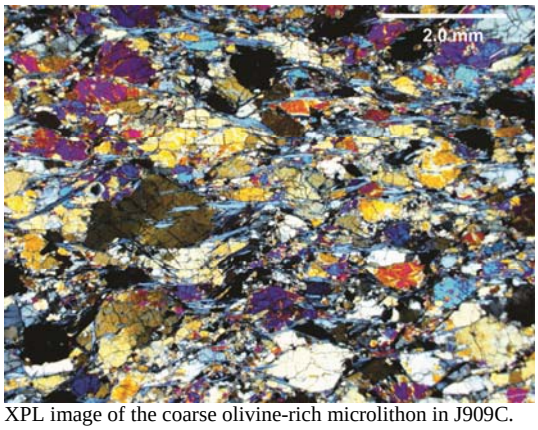

XPL image of the coarse olivine-rich microlithon in J909C.

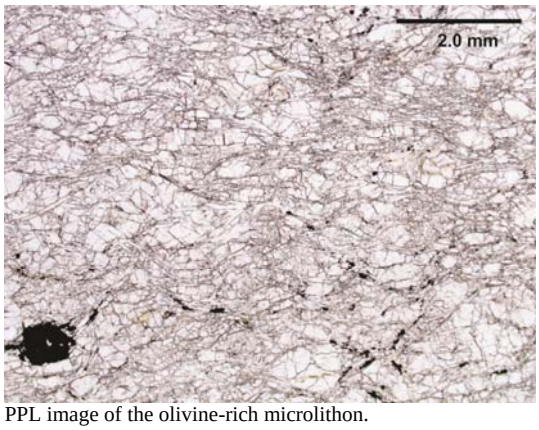

PPL image of the olivine-rich microlithon.

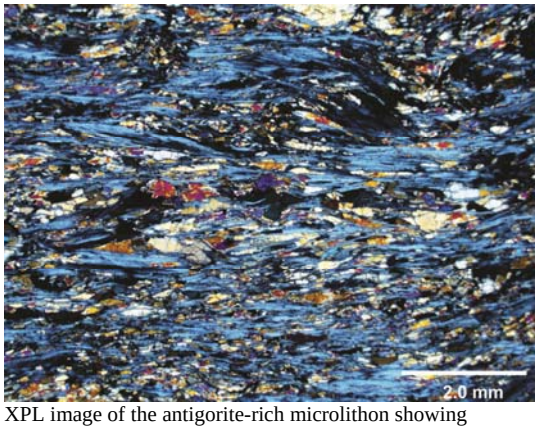

XPL image of the antigorite-rich microlithon showing extensive antigorite growth and alignment parallel to the lineation direction (E-W).

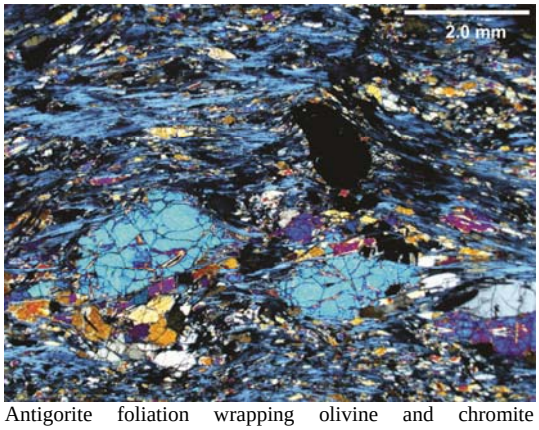

Antigorite foliation wrapping olivine and chromite porphyroclasts (XPL).

Porphyroclastic olivine in a pervasively foliated matrix of antigorite and neoblastic olivine.

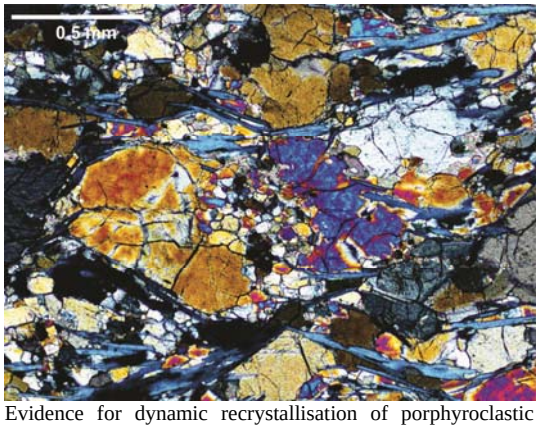

Evidence for dynamic recrystallisation of porphyroclastic olivine in the olivine-rich microlithon by grain boundary migration. There is a cluster of small equant neoblastic grains in between two embayed porphyroclasts (XPL).

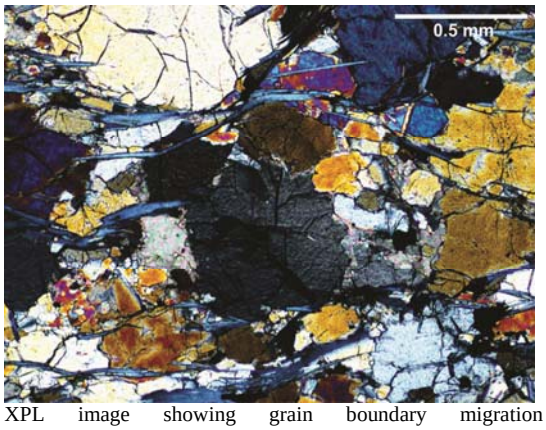

XPL image showing grain boundary migration recrystallisation of porphyroclastic olivine in the olivine-rich microlithon.

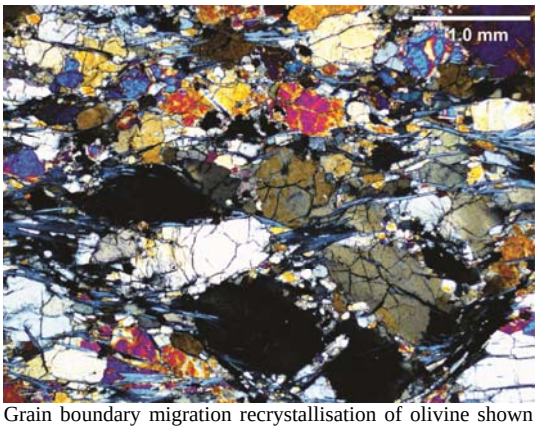

Grain boundary migration recrystallisation of olivine shown by the aggregates of small equant olivines concentrated around the grain boundaries of olivine porphyroclasts (XPL).

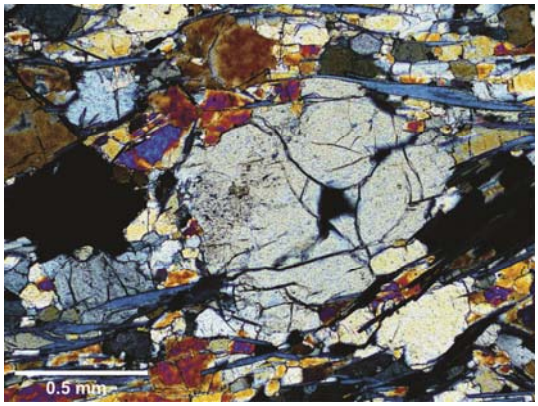

Grain boundary migration recrystallisation of olivine in J909C (XPL).

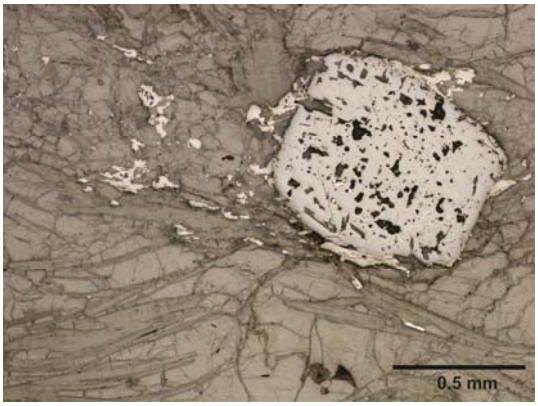

Irregular, spotted appearance of primary chromite rimmed by fine magnetite (reflected light).

THIN SECTION	**J915C** **OVERALL GRAIN SIZE:** Fine- to medium-grained
ROCK NAME	Spinel dunite
SAMPLE LOCATION	Higashi-akaishi Peridotite Body, Shikoku, Japan
HAND SAMPLE	Weakly-foliated, chromite-bearing spinel peridotite. Cohesive with a high specific gravity. Melanocratic. Fresh surface is dark-green grey in colour. Weathered to a yellow-brown colour. Spotted in appearance due to small (<1 mm) grains of chromite. Contains small, pale shiny needles (<0.5 mm long) and mm-wide veins of a dark aphanitic material. The weak foliation is defined by the alignment of elongate chromite and shiny acicular mineral. The acicular mineral also defines a mineral lineation. Contains fine (aphanitic) and coarse-grained olivine (>1.0 mm) that is green in colour. Also contains porphyroclasts and neoblasts of chromite.
Section was cut with respect to the X and Z structural directions - lineation (X) is the long axis of the section, and the section is looking along the foliation plane.	

Mineral	**%**	**Size (mm)**			**Morphology**	**Grain boundaries**	**Comments**
		min.	**max.**	**av.**			
Olivine (porphyroclasts)	30	0.4	0.75	0.5	Anhedral, slightly elongate	Porphyroclast self-boundaries are irregular and amoeboid.	Clear in ppl, high relief, up to 2nd order green in xpl. Highly fractured and tends to contain both mineral and fluid inclusions on a sub-micron scale, which are particularly abundant in larger olivines. These often have a radial/stellate morphology. Where fluid inclusions are present (less abundant than mineral inclusions), they are aligned and elongate. Very little internal microstructure preserved.
Olivine (neoblasts)	40	0.05	0.2	0.1	Subhedral, equant.	Curved to straight and regular, forming triple junctions in places.	Clear in ppl, high relief, up to 2nd order green in xpl. Relatively pristine grains that tend to surround the porphyroclasts.
Antigorite	10	0.12	0.8	0.25	Euhedral, acicular to prismatic	All grain boundaries (both self and interphase) are fairly straight and regular.	Clear in PPL, pale grey in XPL, low relief. Cross-cuts olivine grains; appears to be earlier than the fine serpentine along fractures and in grain boundaries. Coarse antigorite shows undulose extinction indicating deformation. Contains small fractures perpendicular to the long axis of the grain, filled with magnetite (which appears to be associated with the fine serpentine). There appears to be multiple serpentinisation events recorded in this section, with the finer serpentine representing the youngest event.

Serpentine	15	Aphanitic			Too fine to be distinguished under the microscope	N/A – Too fine to distinguish	Clear to very pale green in PPL, low relief, grey in XPL. Fine serpentine occurs along veins and in grain boundaries and fractures, replacing olivine. Within veins, olivines are completely replaced, although the relict grain boundary morphology can still be identified.
Chromite	4	0.06	0.58	0.2	Subhedral to anhedral although some crystal faces are still visible.	Rare self-boundaries. Interphase boundaries with olivine are regular and straight. Boundaries with fine serpentine are irregular and embayed but straight and regular with coarse antigorite.	Opaque in PPL. Grains are often rimmed by magnetite, which is slightly brighter under reflected light.
Magnetite	0.5	<0.001	<0.001	<0.001	Unable to observe	N/A – Too fine to distinguish	Opaque mineral that is very similar in appearance to chromite, but is brighter under reflected light. Magnetite occurs along the grain boundaries of olivines that have been completely replaced by fine serpentine. Magnetite is concentrated into the centre of serpentine-filled veins as well as in the necks of microboudins of coarse antigorite.
Pentlandite	<0.5	<0.001	<0.001	<0.001	Unable to observe	N/A – Too fine to distinguish	Opaque mineral that is found in trace amounts in this sample. Associated with magnetite and overprints chromite. Substantially brighter under reflected light than either magnetite or chromite and has a pale yellow colour.
Overall Texture :	This sample is porphyroclastic. Olivine porphyroclasts are slightly elongate and aligned parallel to the foliation, although the foliation is defined primarily by the alignment of coarse antigorite. The sample is cross-cut by a network of veins containing aphanitic serpentine and magnetite, and these veins appear to have a conjugate relationship with the lineation direction. The serpentine within the veins is aligned oblique to the vein orientation, indicating these may be pull-apart structures. There appears to be evidence for multiple fluid flow episodes as there are several generations of magnetite and serpentine within these veins. There is some microboudinage of the coarse antigorite occurring, with the necks filled with magnetite, indicating that this is the most recent recorded by the sample.						
Petrogenesis:	Initial crystallisation of olivine and chromite grains under spinel peridotite facies was followed by dislocation-creep deformation producing low-angle boundaries in olivine. Subsequently the olivine underwent dynamic recrystallisation by grain boundary migration to produce neoblasts. Following this, the sample was subject to influx of hydrous fluids resulting in the replacement of primary and neoblastic olivine by coarse antigorite. Subsequently, there was an influx of large amounts of fluid associated with extensive fracturing of the peridotite, with fine serpentine (possibly chrysotile due to the fibre orientations) replacing olivine along grain boundaries and fractures. The formation of magnetite rims around chromite and pentlandite formation is also linked to this latest metasomatism event.						

Sample J915C Photomicrographs

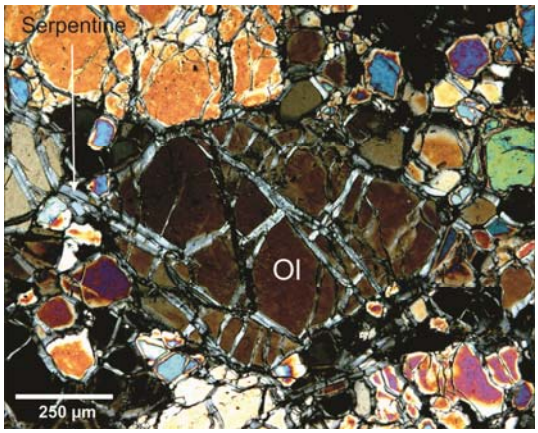

Photomicrograph showing a porphyroclastic olivine grain surrounded by neoblastic olivine. The grains are traversed by abundant fractures filled with fine serpentine. Image taken under XPL.

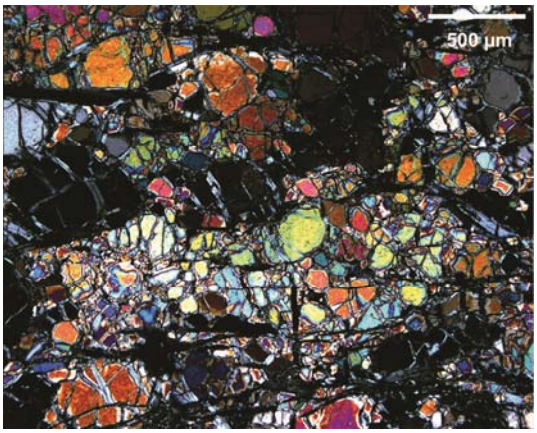

XPL image showing the porphyroclastic texture of the sample.

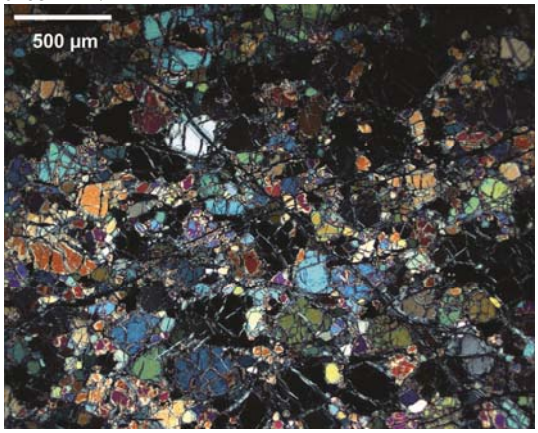

Thin conjugate fractures filled with fine serpentine traverse the thin section (XPL).

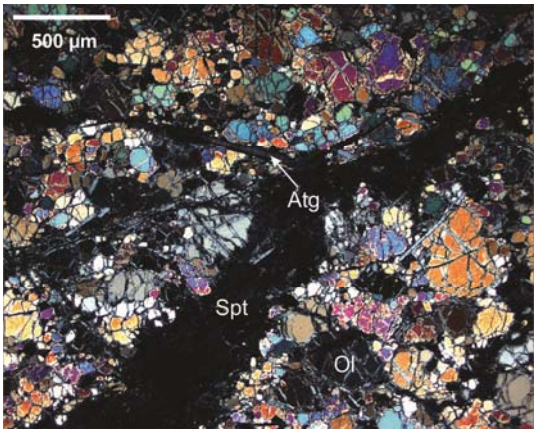

Thick serpentine vein cross-cutting the peridotite (XPL).

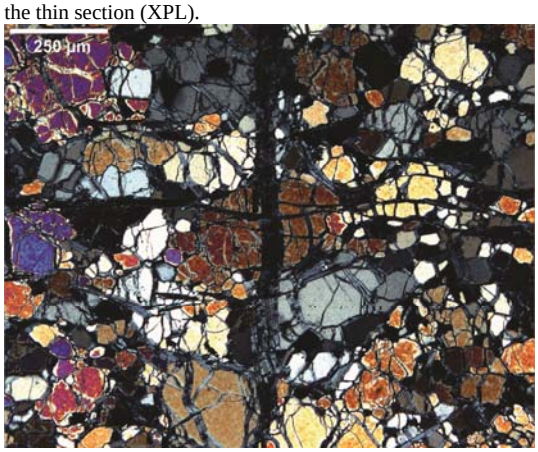

Serpentine-filled fractures cross-cutting olivine porphyroclasts and neoblasts (XPL).

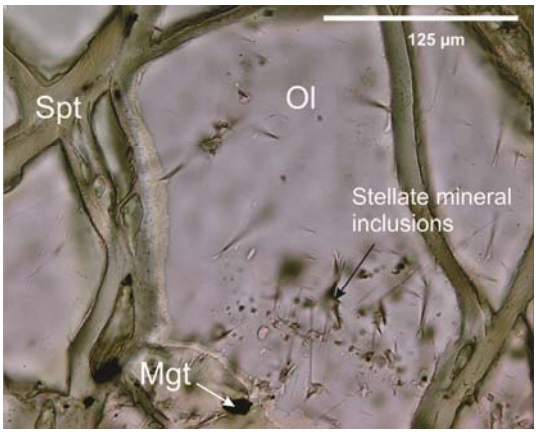

Stellate mineral inclusions and fluid inclusions trails in olivine (PPL).

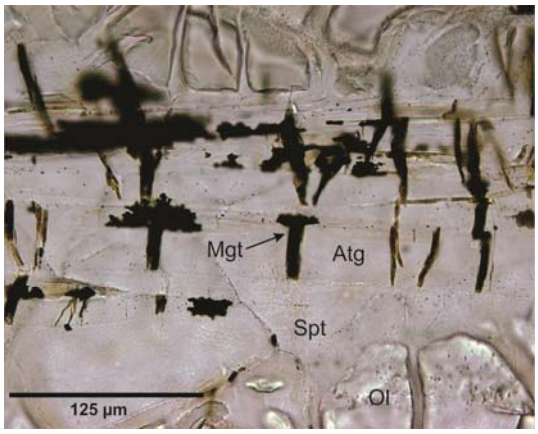

PPL image of very fine magnetite filling in the necks of microboudins in antigorite grains. The magnetite grains are clustered forming dendritic structures, but are also scattered as very small grains within the serpentine veins.

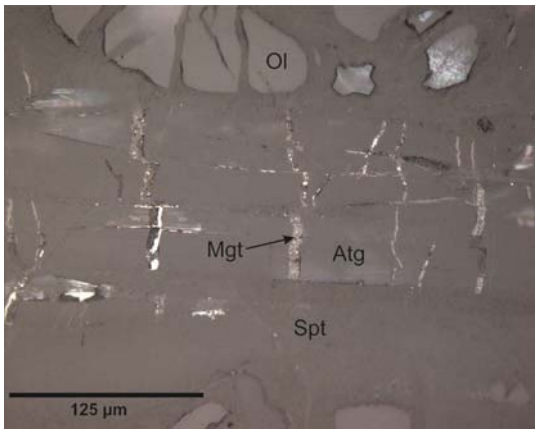

Reflected light image of the area to the left.

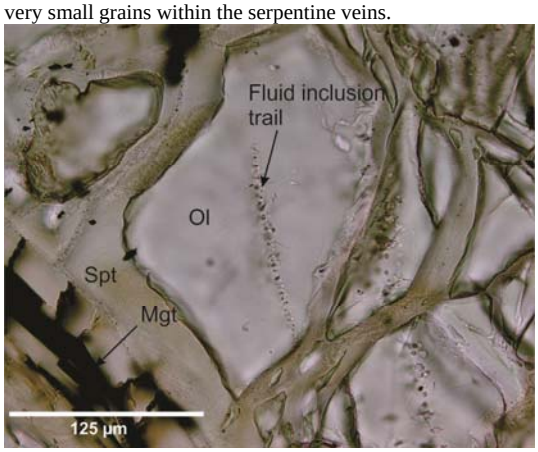

PPL image of a fluid inclusion trail in olivine.

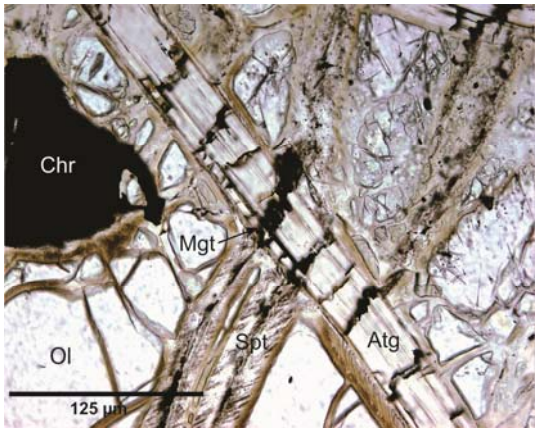

PPL image of an antigorite grain cross-cut by serpentine-magnetite veins.

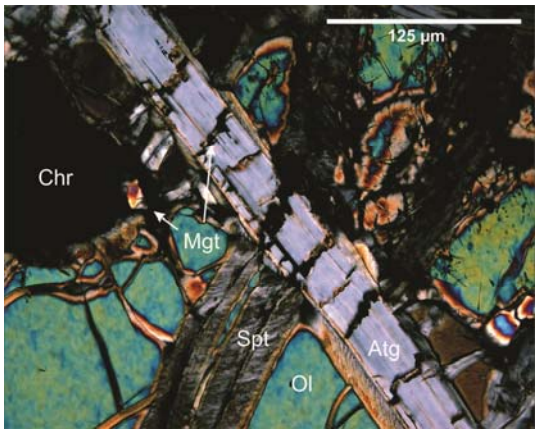

XPL image of the region above. Segregation of the serpentine-magnetite veins is clear in this image, with magnetite concentrated towards the centre of the veins.

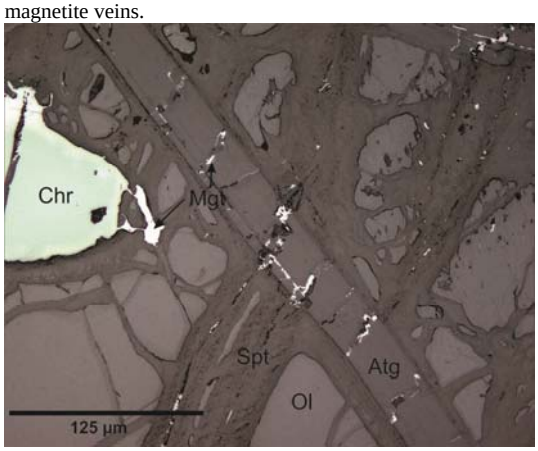

Reflected light image of the image to the left.

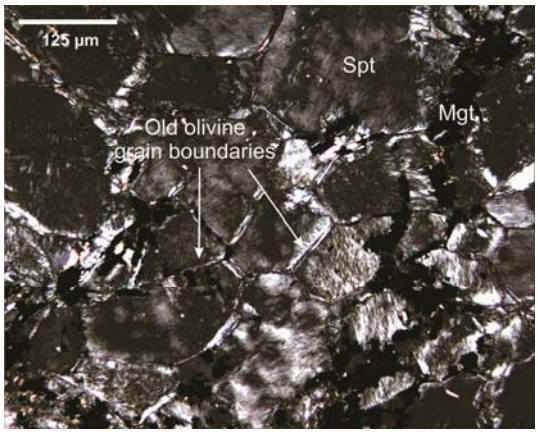

XPL image showing complete static replacement of olivine by fine serpentine and magnetite. The relict olivine grain boundaries are still visible.

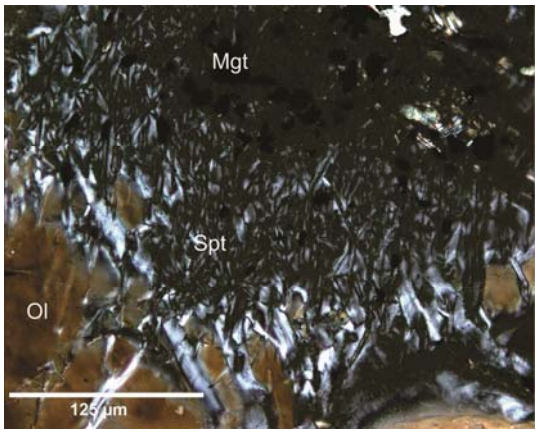

XPL image of serpentine and magnetite replacing olivine. The serpentine forms a spinifex-like texture.

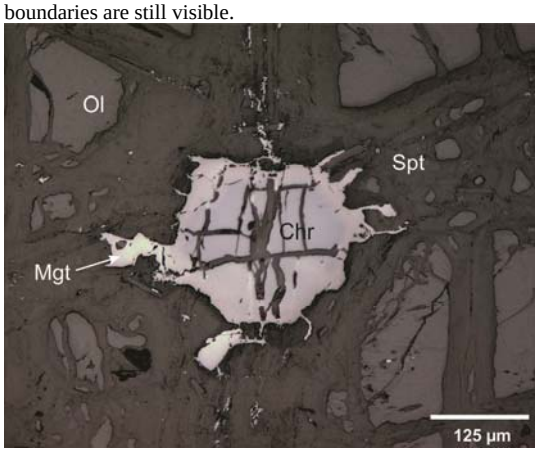

Magnetite forming an anhedral rim around a primary chromite grain cross-cut by fine serpentine veins. Image taken under reflected light.

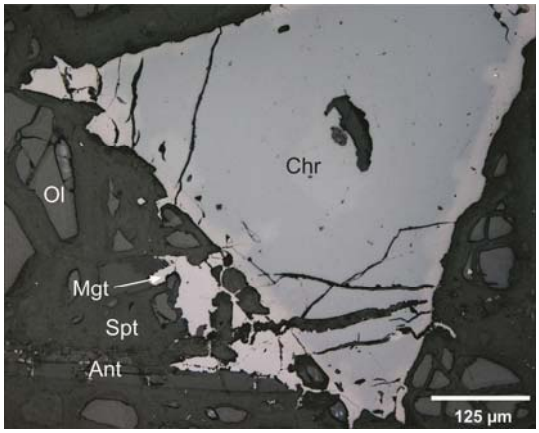

Reflected light image showing primary chromite rimmed by magnetite. The transition between chromite to magnetite seems to be gradual, suggestive of a chemical reaction between the chromite and a surrounding fluid.

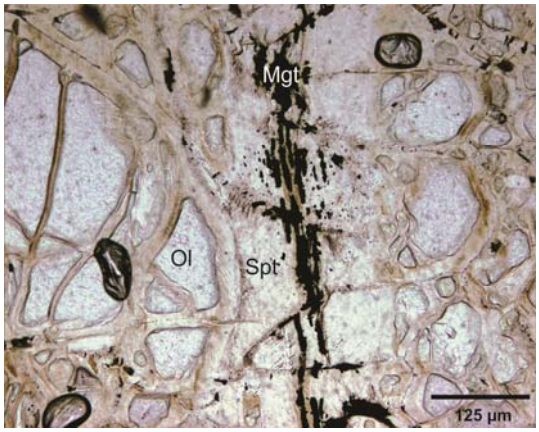

PPL image of multiple generations of magnetite within a serpentine vein.

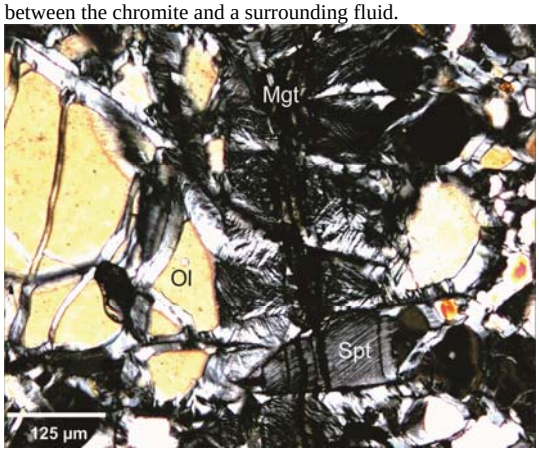

XPL image of a serpentine-magnetite vein. The serpentine fibres are aligned within the veins.

THIN SECTION	**J917** **OVERALL GRAIN SIZE:** Medium-grained
ROCK NAME	Spinel dunite
SAMPLE LOCATION	Higashi-akaishi Peridotite Body, Shikoku, Japan
HAND SAMPLE	Coarse-grained porphyroclastic peridotite containing olivine, chromite and a fine acicular mineral. Coarse-grained dark green olivine (1 – 3 mm in diameter) occurs in a fine melanocratic groundmass containing fine olivine, the pale-coloured acicular mineral (<0.5 mm in length) and porphyroclasts of chromite (0.5 – 1 mm). The rock contains a pervasive foliation defined by the alignment of lenticular olivine porphyroclasts and the acicular mineral. The rock is cross-cut by fine veins filled with a melanocratic, aphanitic material.
Section was cut with respect to the X and Z structural directions - lineation (X) is the long axis of the section, and the section is looking along the foliation plane.	

Mineral	**%**	**Size (mm)**			**Morphology**	**Grain boundaries**	**Comments**
		min.	**max.**	**av.**			
Olivine (porphyroclasts)	3	0.4	0.9	0.7	Anhedral, slightly elongate.	Self-boundaries are varied in nature. Some tend to be straight and regular, whilst others are lobate. Boundaries with antigorite are straight and regular as with magnetite. Porphyroclastic chromite boundaries with olivine (coarse and fine) are embayed and irregular.	Clear in ppl, up to 2nd order blue in XPL, high relief. Often contain very small fluid inclusions and trails of fluid inclusions, but these are not widespread. Porphyroclasts commonly exhibit distinct low-angle boundaries. Overprinted by antigorite.
Olivine (neoblasts)	64	0.04	0.2	0.06	Subhedral to euhedral, equant crystals.	Self-boundaries are straight and regular, often triple junctions. Boundaries with antigorite and magnetite are straight and regular.	Clear in ppl, up to 2nd order blue in XPL, high relief. Fairly clean in appearance, show no evidence for internal microstructures, and commonly exhibit triple junction boundaries.
Antigorite	29	0.4	1.5	1	Acicular, euhedral blades.	Straight and regular grain boundaries with all phases.	Defines the strong schistose foliation and lineation. Replaces primary and neoblastic olivine.
Serpentine	1	Aphanitic			Too fine to be distinguished under the microscope	N/A – Too fine to distinguish	Clear to very pale green in PPL, low relief, grey in XPL. Fine serpentine generally occurs within a thin vein cutting across the section. Associated with magnetite.
Chromite	1	0.25	1	0.4	Anhedral, slightly elongate.	Boundaries with all other minerals are irregular and embayed.	Opaque, pale blue-grey under reflected light. Primary chromite is very amorphous at grain boundaries where it is often rimmed by magnetite. Often more elongate chromite grains are aligned parallel to the

							foliation and have weak strain shadows.
Magnetite	1.5	0.01	0.09	0.03	Difficult to assess, grains very small. Appear to be rounded and subhedral to anhedral.	Difficult to assess due to size, however appear to be in equilibrium with all except primary chromite.	Opaque mineral, pale grey, slightly brighter under reflected light than chromite. Forms aggregates less than 0.2 mm in diameter and form thin foliation-parallel layers. Often forms within strain shadows next to and forms rims around chromite. Also seems to fill 'gaps' between minerals.
Pentlandite	<0.5	0.01	0.09	0.03	Subhedral	N/A – too small to observe.	Opaque mineral that is substantially brighter than both chromite and magnetite, and has a pale yellow colour under reflected light. Occurs in trace amounts in the sample and is often associated with magnetite.
Overall Texture and Alteration:	Lens-like microlithons of porphyroclastic and neoblastic olivine are separated by domains of aligned coarse antigorite. Microlithon development is predominantly responsible for the spaced foliation, which is almost a schistosity. Parallel to the foliation are trails of aggregated, fine magnetite. Olivine porphyroclasts commonly preserve intragrain microstructures and neoblasts are undeformed, displaying triple point junctions. There are often sub-grains formed from porphyroclasts with grain boundaries parallel to the low-angle boundaries. This indicates dynamic recrystallisation by subgrain rotation. There is also evidence for grain boundary migration recrystallisation, with highly irregular and often bulging grain boundaries of porphyroclastic olivine. The section is traversed by a few narrow veins (<0.5 mm wide) that post-date/cross-cut the coarse antigorite and chromite. Veins are filled with a very fine-grained/aphanitic serpentine, which is associated with fine-grained neoblastic magnetite.							
Petrogenesis:	Initial crystallisation involved olivine and chromite under spinel peridotite facies in the mantle, followed by deformation under a predominantly dislocation creep regime to produce low-angle boundaries. Fluid inclusion trails and annealed fluid-filled fractures preserved inside the porphyroclastic olivine suggest that this phase of deformation involved some fluid interaction. Subsequently, the olivine began to dynamically recrystallise, involving both grain boundary migration and subgrain rotation mechanisms, leaving only a small number of coarse olivine grains as porphyroclasts. During recrystallisation, the olivine was overprinted by abundant coarse antigorite as a result of interaction with hydrous fluids, which aligned to form the current foliation. The sample was then cross-cut by a fracture which was filled with fine antigorite, magnetite and pentlandite.							

Sample J917 Photomicrographs

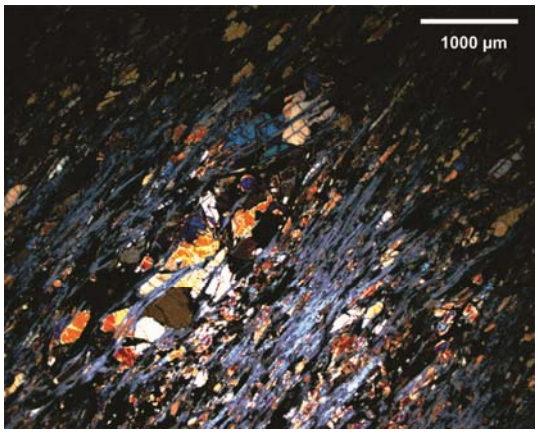

XPL image showing the texture of sample J917. The rock is strongly foliated, with microlithons of olivine interspersed with domains rich in aligned antigorite defining a spaced foliation.

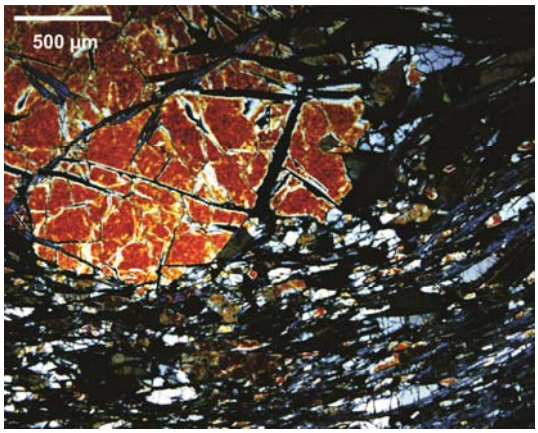

XPL image of an olivine porphyroclast within a sheared matrix of neoblastic olivine, antigorite, chromite and magnetite.

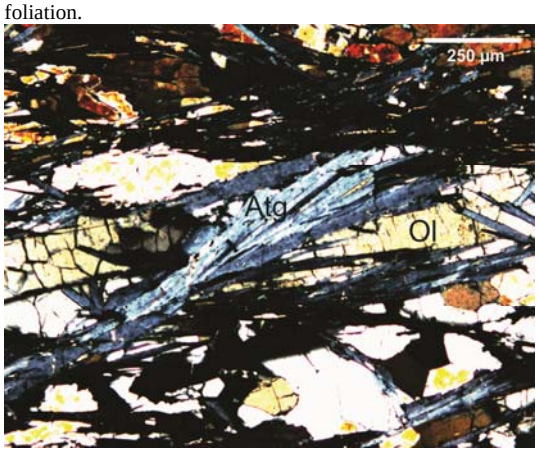

Coarse antigorite blades cross-cutting an olivine grain (XPL).

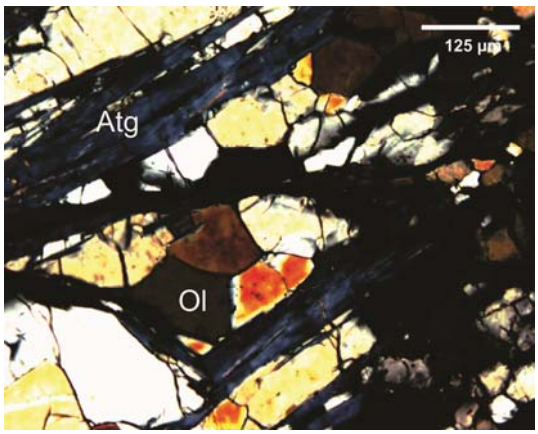

An aggregate of olivine neoblasts between thin layers of antigorite and magnetite (XPL).

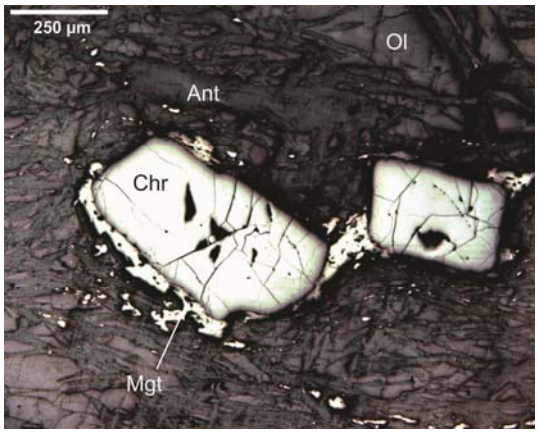

A reflected light image showing chromite porphyroclasts surrounded by rims of magnetite within a sheared olivine-antigorite matrix.

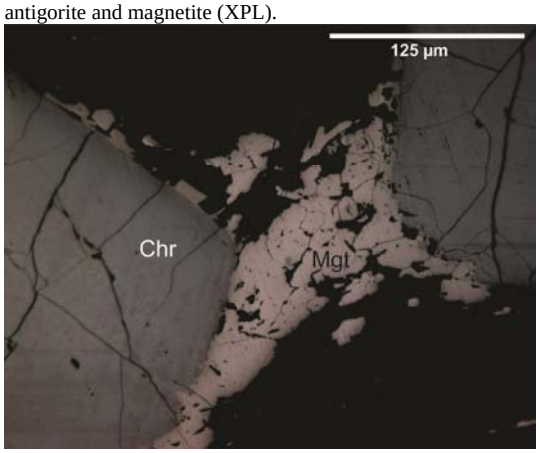

A close-up of the region between the chromite porphyroclasts above (reflected light image). Magnetite grains form in the strain shadow between the two grains.

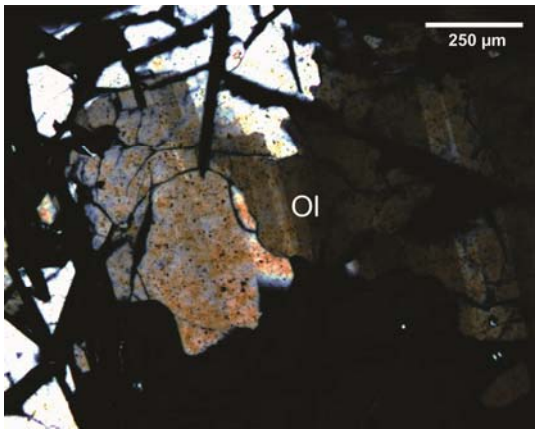

Evidence for dynamic recrystallisation by subgrain rotation in olivine (XPL).

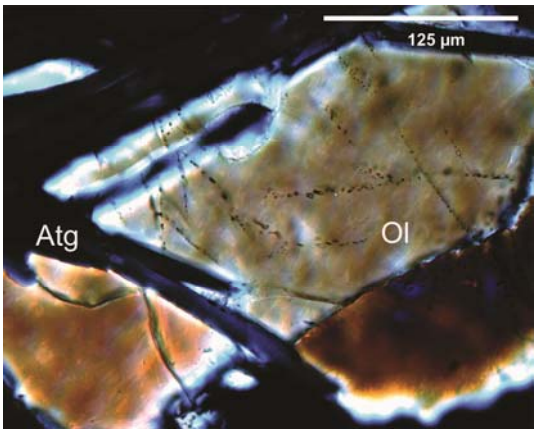

Fluid inclusion trails in olivine (XPL).

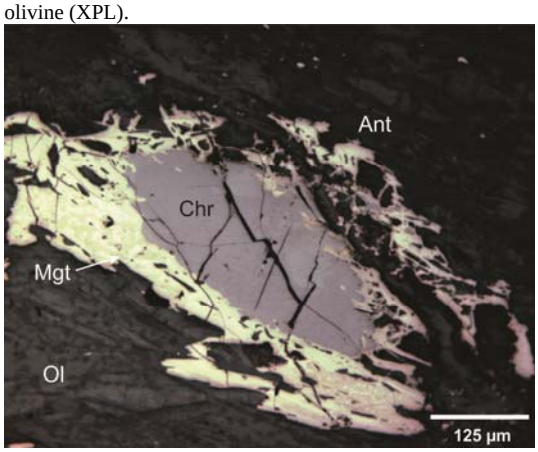

Magnetite rimming a primary chromite grain (under reflected light).

THIN SECTION	**J918B**	**OVERALL GRAIN SIZE:** Fine- to medium-grained
ROCK NAME	Spinel dunite	
SAMPLE LOCATION	Higashi-akaishi Peridotite Body, Shikoku, Japan	
HAND SAMPLE	Strongly foliated, aphanitic peridotite. Fresh surfaces are very dark grey to black in colour (melanocratic) and weather to a yellow-brown colour. The rock contains olivine (<1 mm in diameter), chromite (<0.5 mm in diameter) and a pale grey, aphanitic material. Striped in appearance. The penetrative foliation is defined by elongate aggregates of olivine and the alignment of chromite (which also defines a mineral lineation). Cross-cut by very thin veins (<1 mm wide) containing the pale, aphanitic material.	
Section was cut with respect to the X and Z structural directions - lineation (X) is the long axis of the section, and the section is looking along the foliation plane.		

Mineral	**%**	**Size (mm)**			**Morphology**	**Grain boundaries**	**Comments**
		min.	**max.**	**av.**			
Olivine (porphyroclasts)	48	0.2	0.5	0.4	Subhedral to anhedral.	Self-boundaries are embayed and irregular, and often grain boundaries are frequently dotted with neoblastic olivine. Porphyroclastic olivine is cross-cut by coarse antigorite and boundaries are fairly straight and regular. Where large olivine grains are in contact with chromite, the boundary is serrated and irregular.	Clear in ppl, up to 2nd order blue in xpl, high relief. The section is dominated by porphyroclastic olivine, unlike many of the other samples. Some internal microstructure is preserved but this is not widespread. Most of the olivine (including neoblasts) is quite heavily fractured and replaced by fine serpentine.
Olivine (neoblasts)	12	<0.03	<0.03	<0.03	Subhedral to euhedral.	Self-boundaries are straight and regular, frequently forming triple junctions. Boundaries with antigorite and chromite are seldom observed.	Clear in ppl, up to 2nd order blue in xpl, high relief. Similar in appearance and character to the porphyroclastic olivine. Also replaced by serpentine.
Antigorite	5	0.2	1	0.3	Bladed and elongate. Euhedral.	Boundaries with all minerals are straight and regular.	Clear to pale green in ppl, grey in xpl. Not abundant in this sample. There are isolated grains occurring that are relatively random in orientation and do not contribute to the fabric. Where it does occur, it generally cross-cuts primary and secondary olivine.
Serpentine	25	Aphanitic			Acicular	Too small to determine.	Low relief, pale green in ppl, dark grey in xpl. Fills an extensive network of veins running parallel to the X direction. Fibres are aligned within the veins and show multiple episodes of mineral growth indicating multiple episodes of fluid influx. Possible chrysotile.

Chromite	8	0.2	1	0.5	Subhedral to anhedral, equant	Boundaries with olivine porphyroclasts are serrated and irregular. Straight and regular with coarse antigorite and self-boundaries are irregular.	Opaque, blue-grey under reflected light. Fractured in appearance. Forms a thin layer through the sample. As with other samples. Rimmed by magnetite.
Magnetite	1	0.01	0.03	0.03	Subhedral to anhedral, equant	Self-boundaries are irregular and curved.	Opaque, pale grey under reflected light. Brighter than chromite. Often occurs as rims around the chromite but also as isolated grains.
Chlorite	1	0.2	0.5	0.4	Euhedral to subhedral, platy	Straight and regular	Moderate relief, clear in ppl, greyish-olive green in xpl and exhibits birds eye maple extinction characteristic of a mica. Grains are often bent and commonly occur forming large strain shadows around porphyroclastic chromite grains. Overprints the fine serpentine, so is a very late phase.
Overall Texture and Alteration :	The sample is characterised by a very heavily veined antigorite-rich region and a relatively pristine, olivine-rich region. Serpentine veining is related to appears to be related to extensive fracture development across the sample, with serpentine fibres aligning within the veins. The serpentine veins run relatively parallel to each other and parallel to the foliation, and cross-cut both generations of olivine. The sample is also cross-cut by a later set of veins at a high angle to the foliation. There is also an original chromite layer preserved that is approximately 20 degrees off the X direction.						
Petrogenesis:	The initial sequence of crystallisation involved olivine and chromite under spinel peridotite facies in the mantle. Subsequently the rock was deformed by dislocation creep resulting in the development of low-angle boundaries in olivine. Following this, the olivine underwent dynamic recrystallisation primarily by grain boundary migration (as shown by the nature of the olivine grain boundaries and relationship between neoblasts and porphyroclasts). Antigorite then formed as a result of interaction with hydrous fluid. This was then followed by a period of extensive fluid influx into the sample associated with fracturing of the peridotite and resulting in the development of an extensive network of very fine serpentine-filled veins. The sample then was subject to a late stage of very fine serpentine veining that cross-cuts all the other structures.						

Sample J918B Photomicrographs

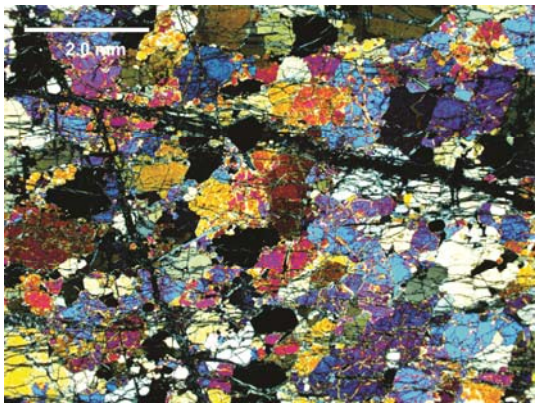

Texture of the more pristine region of sample J918B (XPL).

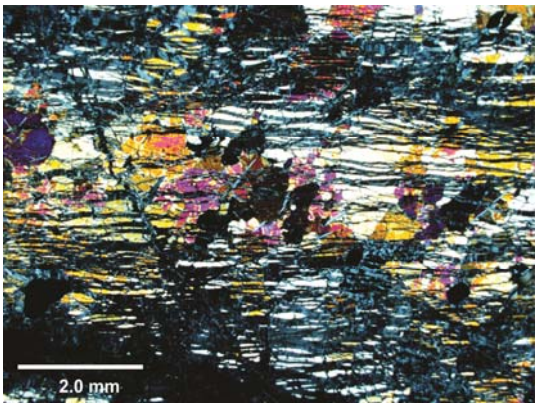

Region of J918B that has been extensively serpentinised by foliation-parallel veins that cross-cut primary olivine (XPL).

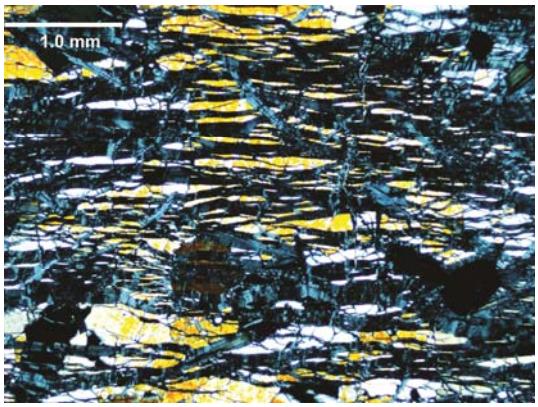

Extensive serpentine veins cross-cutting olivine (XPL).

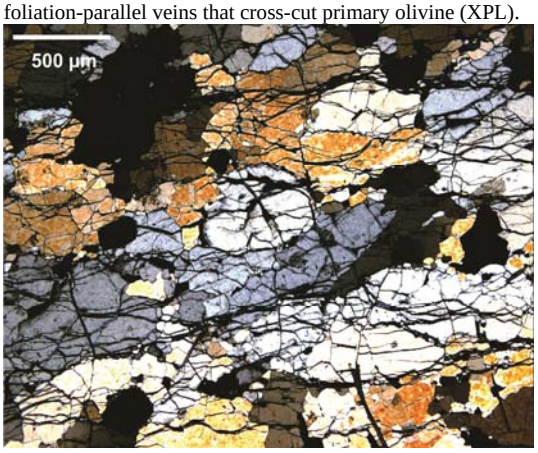

Olivine porphyroclasts and neoblasts in the pristine region of the thin section (XPL).

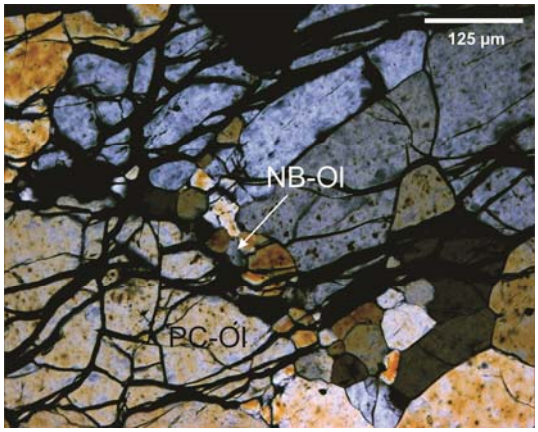

Close-up of the relationship between porphyroclastic and neoblastic olivine (XPL).

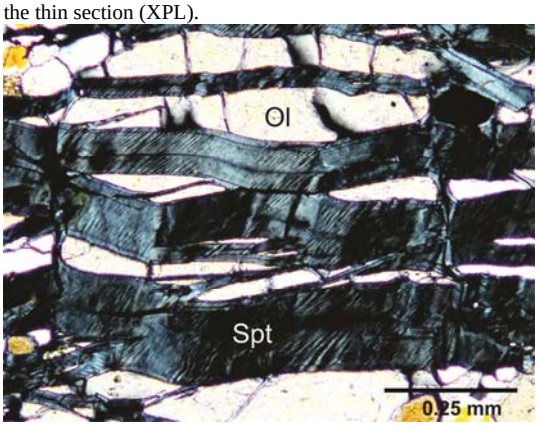

Aligned serpentine fibres within veins (XPL).

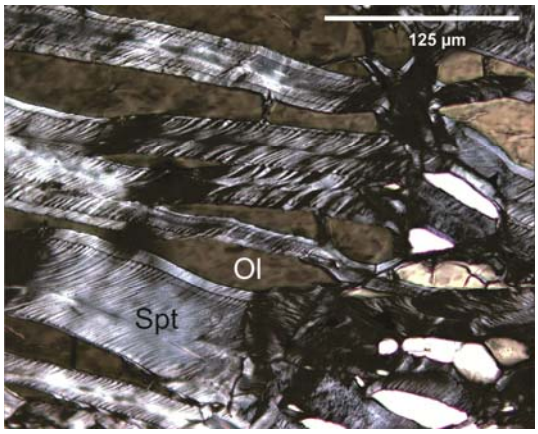

Aligned serpentine fibres within veins (XPL).

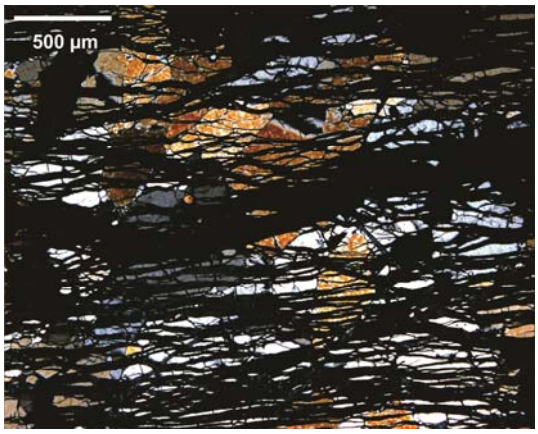

Extensive veining of a region of the thin section (XPL).

THIN SECTION	**J919B_1**	**OVERALL GRAIN SIZE:** Fine- to medium-grained
ROCK NAME	Spinel dunite	
SAMPLE LOCATION	Higashi-akaishi Peridotite Body, Shikoku, Japan	
HAND SAMPLE	Very fine-grained, sheared peridotite containing olivine, chromite and a pale acicular mineral. Intermediate in colour (light greenish grey) with bands of shiny black chromite. High specific gravity and weathers to a distinctive yellow-brown. There is a very strong foliation in places and deformation is segregated into regions of high and low shear. The more undeformed parts of the sample have a knobbly weathered texture and tend to be more resistant to the weathering than the sheared regions. The foliation and lineation are defined by the elongation of aggregates of chromite as well as the tails of rotated chromite porphyroclasts. Original chromite layers are strung out and highly sheared. Within one of the shear bands there also appears to be a region rich in the pale acicular mineral (antigorite?).	
Section was cut with respect to the X and Z structural directions - lineation (X) is the long axis of the section, and the section is looking along the foliation plane.		

Mineral	**%**	**Size (mm)**			**Morphology**	**Grain boundaries**	**Comments**
		min.	**max.**	**av.**			
Olivine (porphyroclastic)	7	0.4	0.8	0.5	Anhedral, often lenticular	Self-boundaries are curved and irregular. Boundaries between neoblasts and porphyroclasts are generally embayed - neoblast is convex, porphyroclast is concave.	Clear in ppl, high relief, up to 2nd order yellow in xpl. Preserves some internal microstructures. Replaced by acicular serpentine grains. Porphyroclasts often contain abundant sub-micron sized fluid and mineral inclusions.
Olivine (neoblastic)	58	0.06	0.1	0.1	Anhedral to subhedral, equant to slightly elongate	Curved self-boundaries but often form triple junctions. Curved and irregular boundaries with chromite and magnetite.	Clear in ppl, high relief, up to 2nd order yellow in XPL. Pristine grains with no internal microstructure.
Antigorite	5	0.1	0.3	0.25	Bladed and acicular euhedral grains	Boundaries with olivine neoblasts are straight and regular although the antigorite cross cuts the olivine. No boundaries observed with olivine or chromite porphyroclasts.	Clear in ppl, low relief, grey in XPL. Cross-cuts olivine neoblasts and mainly occurs within the neoblastic olivine matrix. Finer and less abundant than that seen in other samples and does not contribute substantially to the fabric.
Serpentine	20	Aphanitic			N/A	N/A	Pale green in ppl, low relief, dark grey in XPL. Replaces olivine along grain boundaries. Generally found within veins cross-cutting foliation and coarse antigorite. Probably the last mineral to form. There is some evidence for mineral alignment orthogonal to

							the orientation of veins. Possibly chrysotile.
Chromite	5	0.05	1	0.3	Subhedral to anhedral, often rounded in shape.	Usually curved and irregular.	Opaque, dull grey under reflected light. Forms foliation parallel layers and associated with magnetite and pentlandite. Some grains are full of holes and are cross-cut by fine veins of serpentine.
Magnetite	3	0.03	0.1	0.08	Subhedral to anhedral, equant.	Straight to curved and irregular	Opaque, pale grey under reflected light but brighter than chromite. Generally associated with chromite and pentlandite.
Pentlandite	2	0.01	0.05	0.04	Subhedral to anhedral. Morphology appears to be controlled by the surrounding minerals.	Straight to curved and irregular.	Opaque. Yellower and substantially brighter under reflected light than the magnetite. Occurs with chromite and magnetite, within the layers parallel to the foliation. Seems to fill small gaps in between grains.
Overall Texture and Alteration:	The foliation is defined primarily by chromite layers and elongation and alignment of deformed olivine, as well as alignment of acicular grains of antigorite although this is not significant. The section is divided (parallel to x) into zones rich and poor in antigorite. The antigorite-rich zone has a stronger fabric and generally contains a finer fraction of olivine grains. The lesser foliated antigorite-poor, olivine-rich zone contains coarser olivines but also sees the development of olivine neoblasts from porphyroclasts. The olivine dominating the foliated zone is predominantly neoblastic. There are abundant veins of aphanitic serpentine that are generally oriented parallel to the foliation, but are later structures as these also cross-cut the fabric and dissect coarse antigorite grains. Large acicular antigorite tends to cross-cut grains whilst the fine veil-fill serpentine tends to replace olivine along grain boundaries.						
Petrogenesis:	Initial mineral assemblage was olivine and chromite, which crystallised under spinel peridotite facies in the mantle. This was then deformed by dislocation creep dominated processes to produce internal microstructure within olivine porphyroclasts. Subsequently, there was an influx of fluid into the rock preserved in the form of fluid inclusions within olivine porphyroclasts. This was followed by formation of coarse antigorite and the dynamic recrystallisation of olivine predominantly by grain boundary migration (as indicated by the nature of the olivine grain boundaries). Subsequently, the sample was dissected by a network of fine veins filled with aphanitic serpentine, the fibres of which are approximately orthogonal to the lineation direction of the sample.						

Sample J919B_1 Photomicrographs

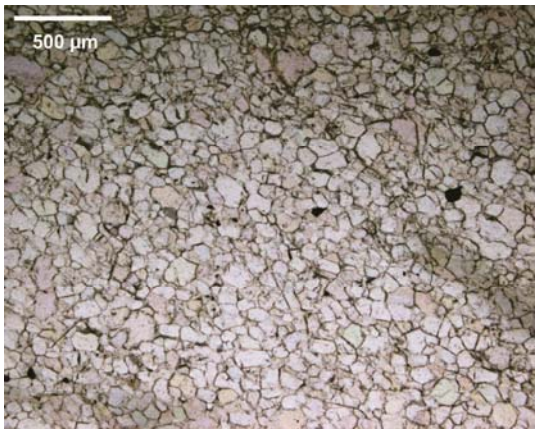

PPL image of olivine in sample J919B_1.

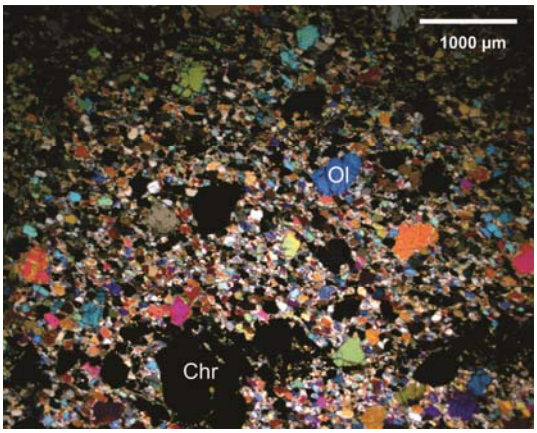

Porphyroclastic olivine and chromite within a matrix of neoblastic olivine (XPL).

Porphyroclastic olivine and within a matrix of neoblastic olivine cross-cut by a fine serpentine vein (XPL).

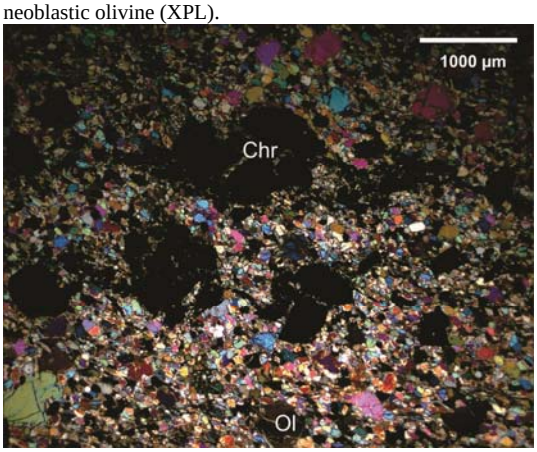

Porphyroclastic olivine and chromite within a matrix of neoblastic olivine (XPL).

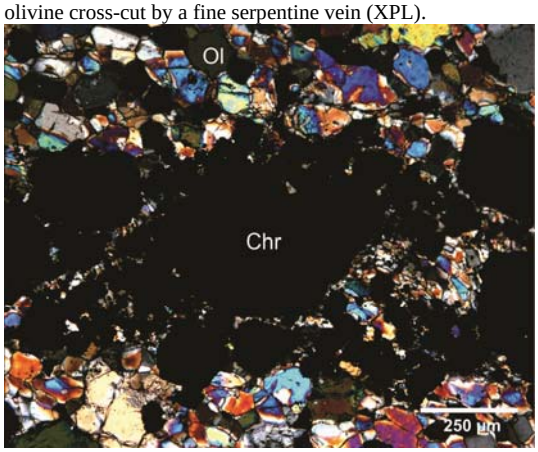

Close-up image showing chromite and magnetite layer in the sample. The porphyritic chromites are surrounded by smaller chromite and magnetite grains (XPL).

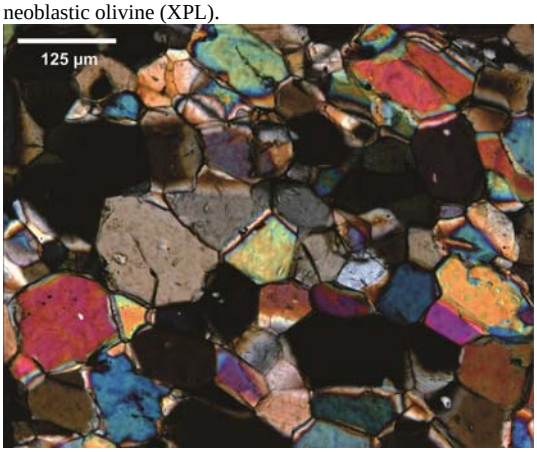

XPL image showing the equant nature of neoblastic olivine. Many of the grain boundaries terminate at triple junctions.

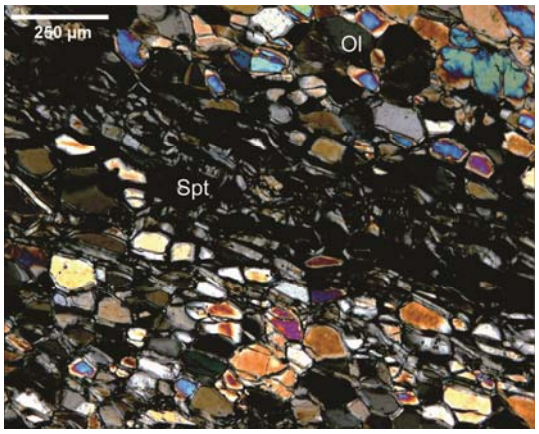

Fine serpentine replacing neoblastic olivine along grain boundaries (XPL).

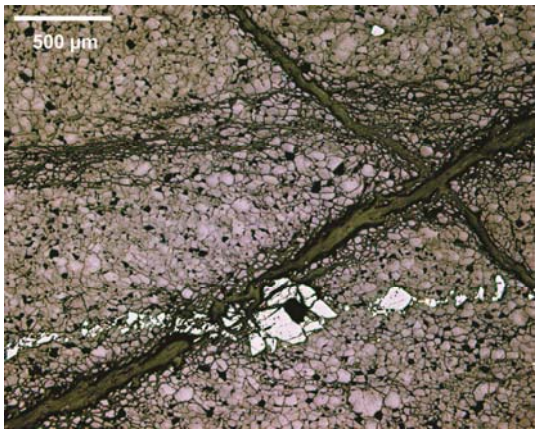

Reflected light image of fine serpentine veins cross-cutting the primary fabric of the rock.

THIN SECTION	**J919B_2** **OVERALL GRAIN SIZE:** Fine- to medium-grained
ROCK NAME	Spinel dunite
SAMPLE LOCATION	Higashi-akaishi Peridotite Body, Shikoku, Japan
HAND SAMPLE	Very fine-grained, peridotite containing olivine, chromite and a pale acicular mineral. Intermediate in colour (light greenish grey) and contains bands of shiny black chromite. High specific gravity and weathers to a distinctive yellow-brown. This sample is fairly massive in appearance. The foliation and lineation are weak but are defined by the elongation of aggregates of chromite and olivine.
Section was cut with respect to the X and Z structural directions - lineation (X) is the long axis of the section, and the section is looking along the foliation plane.	

Mineral	%	Size (mm)			Morphology	Grain boundaries	Comments
		min.	max.	av.			
Olivine (porphyroclastic)	10	0.5	1	0.8	Anhedral, equant	Boundaries with neoblasts are embayed and irregular. Boundaries with antigorite are straight and regular, and with chromite are curved and regular.	High relief, clear in ppl, up to 2nd order blue in XPL. Very little internal microstructure preserved. Often dusty and containing abundant fluid inclusions. Replaced in places by antigorite.
Olivine (neoblastic)	72	0.03	0.4	0.2	Subhedral, equant	Often forms triple junctions with other neoblastic olivine. Embayed boundaries with olivine porphyroclasts. Straight boundaries with antigorite.	High relief, clear in ppl, up to 2nd order blue in XPL. Comprises most of the sample. Clean in appearance, does not preserve any internal microstructures.
Antigorite	5	0.3	0.5	0.4	Euhedral, bladed	Grain boundaries are straight and regular.	Low relief, clear in ppl, pale grey in XPL. Not in high abundance in this sample, randomly oriented and does not contribute to the fabric. Cross-cuts all olivine in the sample.
Serpentine	3	Aphanitic			N/A	N/A	Pale green in ppl, low relief, dark grey in XPL. Mainly localised to thin veins cross-cutting the sample. Probably the latest mineral to form. Possibly

							chrysotile.
Chromite	8.5	0.25	1	0.7	Subhedral, tabular to equant	Curved and regular with olivine. Irregular self-boundaries.	Opaque, pale blue-grey under reflected light. Forms thin layers parallel to x. Often has tails or finer chromite and magnetite.
Magnetite	1	0.05	0.2	0.1	Anhedral, equant	Curved and irregular	Opaque, pale grey under reflected light but slightly brighter than chromite. Generally associated with the larger chromite grains, forming the 'tails' around rotating porphyroclasts.
Pentlandite	<0.5	0.05	0.2	0.08	Anhedral, equant	Curved and irregular	Opaque, very bright, light yellow under reflected light. Occurs in trace amounts, often with magnetite, and also infilling spaces between grains.
Overall Texture and Alteration:	Overall the sample is quite clean and massive in appearance. There are a few cross-cutting veins with antigorite but these are not pervasive. Olivine is dominant in this sample and there is no real fabric apart from the presence of chromite layers. Chromites often have tails and are boudinaged, indicating some shearing taking place but this is not evident in the olivine.						
Petrogenesis:	Initial crystallisation sequence involved olivine followed by chromite, which formed thin parallel layers under spinel peridotite facies in the mantle. A subsequent change in conditions resulted in the dynamic recrystallisation of olivine to a finer grain size by grain boundary migration (as indicated by the nature of olivine grain boundaries). This was followed by the development of small antigorite grains indicating the presence of a hydrous fluid. The sample was then cross-cut by a dispersed network of veins containing very fine serpentine. Growth of magnetite and pentlandite appears to be a late feature associated with the serpentine veins.						

Sample J919B_2 Photomicrographs

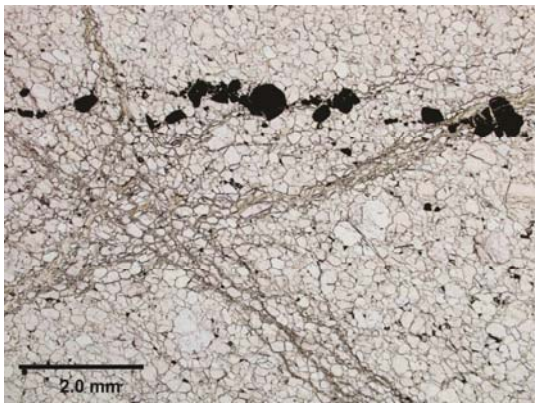

PPl image of a chromite layer within a matrix of neoblastic olivine. Both are cross-cut by veins of fine serpentine.

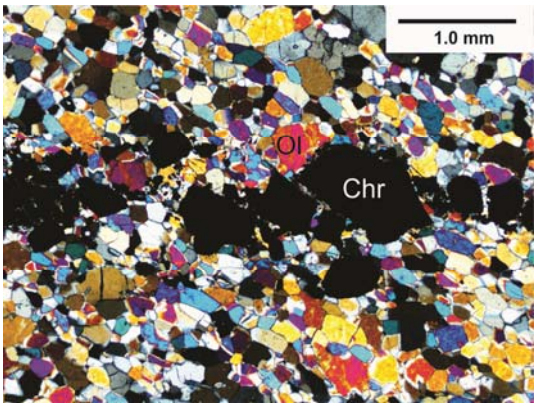

Chromite grains within a neoblastic olivine matrix (XPL).

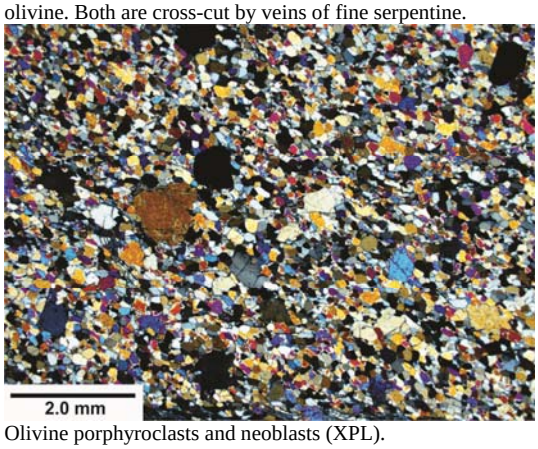

Olivine porphyroclasts and neoblasts (XPL).

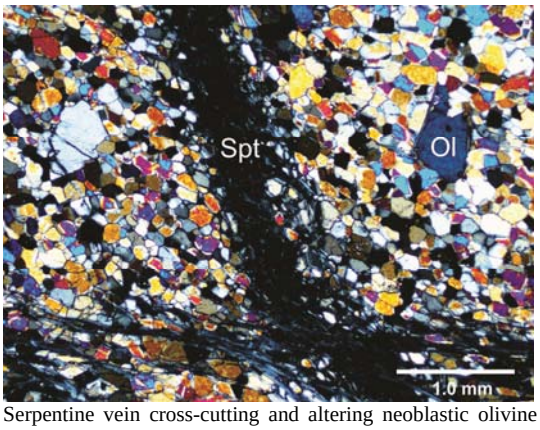

Serpentine vein cross-cutting and altering neoblastic olivine along grain boundaries (XPL).

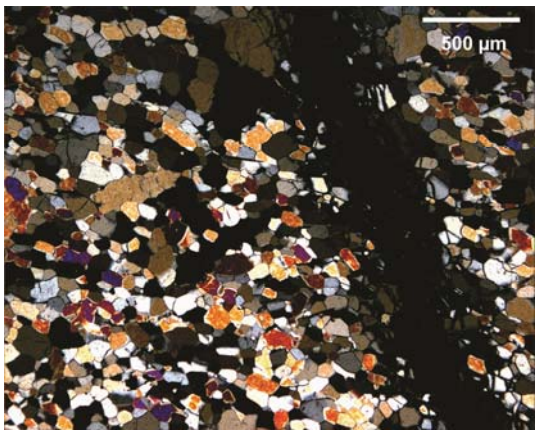

Serpentine vein cross-cutting the sample (XPL).

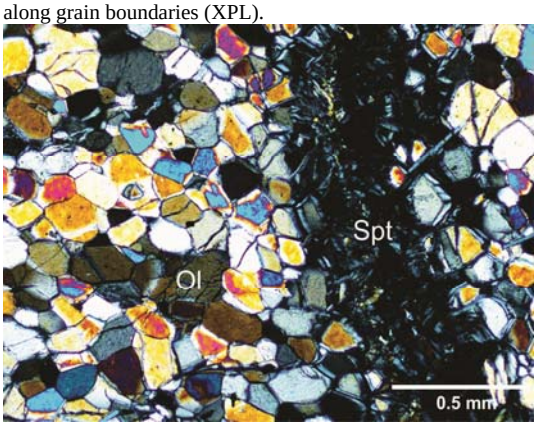

Serpentine replacement of neoblastic olivine grains (XPL).

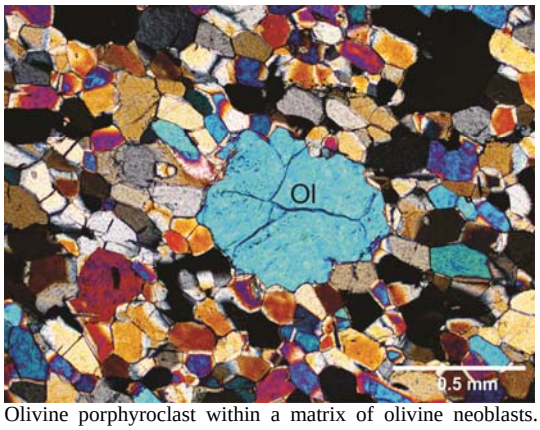

Olivine porphyroclast within a matrix of olivine neoblasts. The grain boundaries of the porphyroclast are embayed and concave towards the porphyroclast (XPL).

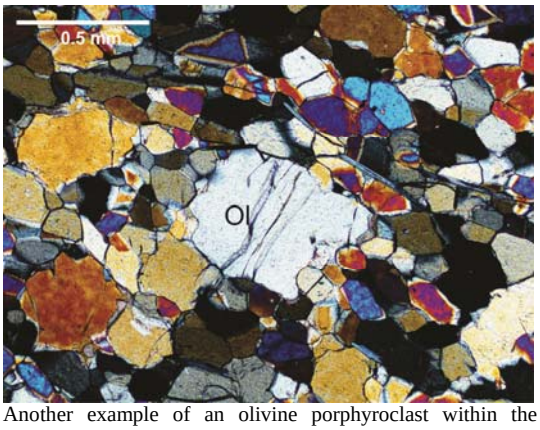

Another example of an olivine porphyroclast within the neoblastic olivine matrix (XPL).

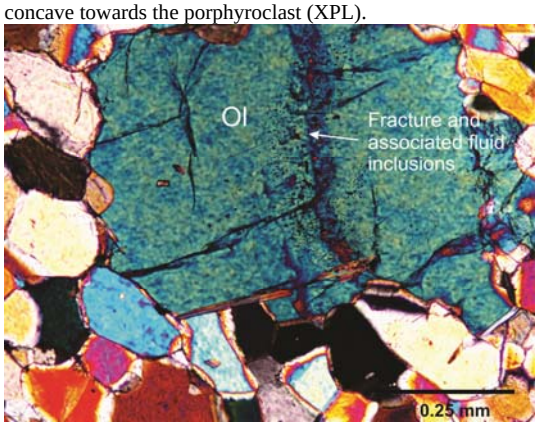

Fluid inclusions within an olivine porphyroclast associated with a cross-cutting fracture (XPL).

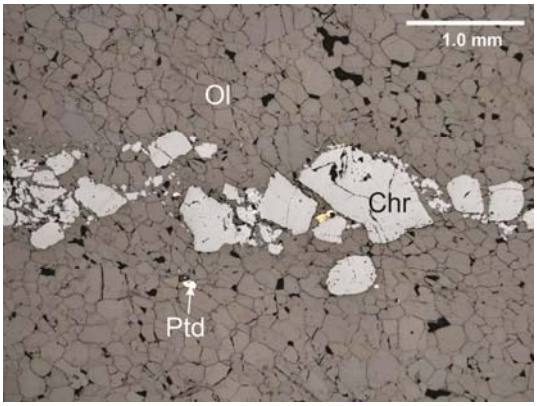

Reflected light image of a chromite layer with minor magnetite and pentlandite.

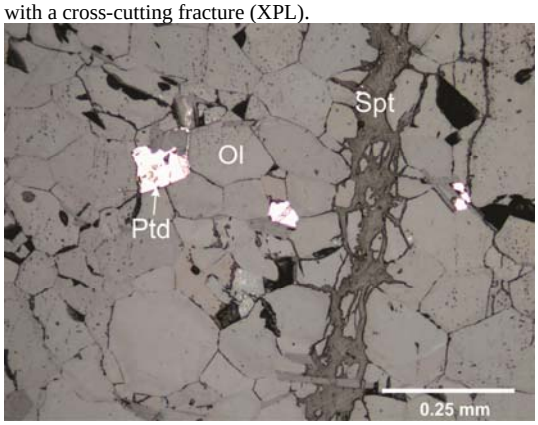

Reflected light image showing grains of pentlandite within the sample.

THIN SECTION	**136062**	**OVERALL GRAIN SIZE:** Coarse-grained
ROCK NAME	Coarse-grained spinel lherzolite	
SAMPLE LOCATION	Tubaf seamount, Lihir Island, Papua New Guinea	
HAND SAMPLE	None available	

Mineral	%	Size (mm)			Morphology	Grain boundaries	Comments
		min.	max.	av.			
Olivine	73	0.4	3.4	2.1	Anhedral, equant	Self-boundaries often form triple junctions, but are usually curved and regular. Some boundaries are curved and embayed. Boundaries with enstatite and clinopyroxene are curved and regular, and with spinel are curved and irregular, with spinel cross-cutting the olivine.	Clear in PPL, moderate birefringence up to 2nd order colours in XPL. Undulose extinction defines low-angle boundaries indicating grains are deformed. Grains often appear dusty due to the presence of fluid inclusions. There are two types of fluid inclusions preserved within the olivine: 1) Coarse bubbles ~5-10 µm in diameter; 2) Fine, vermicular to dendritic inclusions (<2-3 µm wide) often parallel to low-angle boundaries (but not always). Olivine grains are also fractured, with a typical glassy olivine fracture as well as a fracture pattern that is geometrically linked to the presence of low-angle boundaries. Aligned euhedral spinel inclusions are also present (<1 µm in diameter) within olivine.
Clinopyroxene	15	1.2	4.2	2.1	Subhedral to anhedral, prismatic	Self-boundaries are curved and regular, as are those with olivine. Boundaries with enstatite are curved and irregular. Clinopyroxene is overprinted by spinel and so these grain boundaries are curved and irregular.	Clear to very pale green pleochroism in PPL, with 2nd to 3rd order interference colours in XPL. Inclined extinction that is sometimes undulose indicating deformation. Prominent cleavage and contains inclusions of primary olivine.
Enstatite	5	1.2	4.2	2.1	Subhedral to anhedral, prismatic	Self-boundaries are not observed. Boundaries with spinel are curved and irregular, with spinel overprinting the enstatite.	Clear to pale green pleochroism in PPL, with 2nd order interference colours in XPL. Straight extinction and contains a weak cleavage. Contains extensive clinopyroxene exsolution lamellae and fine fluid

							inclusions that are controlled by the lamellae.
Spinel	7	0.01	0.85	0.68	Subhedral to anhedral, equant	Self-boundaries are not observed.	Dark red/brown in colour in PPL. Isotropic in XPL. Contains inclusions of clinopyroxene.
Spinel	trace	<0.01		<0.01	Euhedral, prismatic	Boundaries with olivine are straight and regular.	Dark red/brown in colour in PPL. Isotropic in XPL. Occur as very fine aligned inclusions within primary olivine.
Overall Texture and Alteration:	Massive coarse-grained spinel lherzolite. No obvious veins, large fractures or structural fabric.						
Petrogenesis:	Grain boundary and cross-cutting relationships suggest initial crystallisation of olivine, followed by clinopyroxene, enstatite and lastly the coarser spinel grains under spinel peridotite facies conditions in the mantle. Clinopyroxene exsolution lamellae in enstatite and exsolved spinel grains in olivine (Franz and Wirth, 2000) suggest that there was a decompression event subsequent to crystallisation. Undulose extinction in both olivine and clinopyroxene suggest that the sample has been deformed to some degree by dislocation creep. Multiple sets of low-angle boundary geometries (see Figures below) suggest that the deformation of this sample was complex. The nature of olivine grain boundaries suggests a degree of dynamic recrystallisation by grain boundary migration, although the relative timing of this is recrystallisation is unclear. Fracturing and fluid inclusions developed syn-deformation, as the fluid inclusions represent annealed fracture planes, and such annealing can only happen at depth where pressure and temperature conditions permit. The last event to occur was the exhumation of the sample to the Earth's surface through volcanic activity in a forearc volcano.						

Sample 136062 Photomicrographs

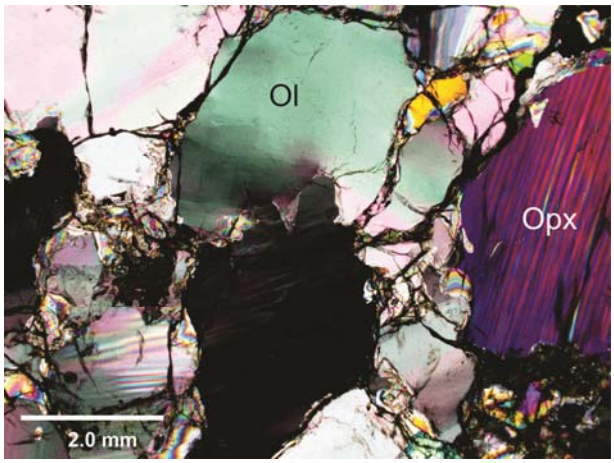

XPL image of the massive structure of sample 136062. Olivine grains are deformed and preserve low-angle boundaries. There appears to be some grain boundary migration between the top and bottom olivine grains in the centre of the image. Orthopyroxene contains clinopyroxene exsolution lamellae that are often bent, indicating deformation.

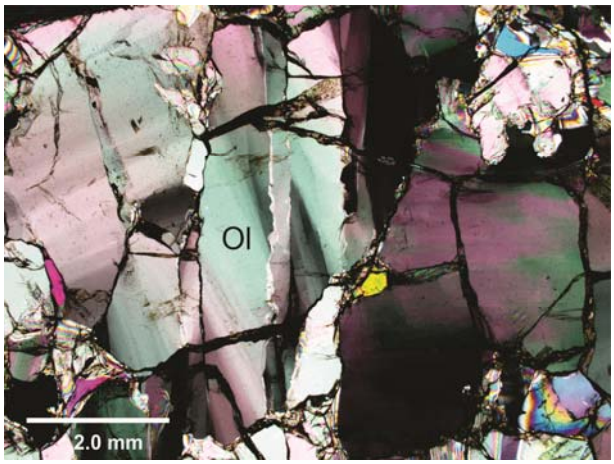

XPL image showing the complexity of low-angle boundaries preserved in the olivine grains in sample 136062. There are 2 orientations of low-angle boundaries in the centre grain ~15 - 20° apart. There is also subgrain rotation occurring around the vertical set of low-angle boundaries.

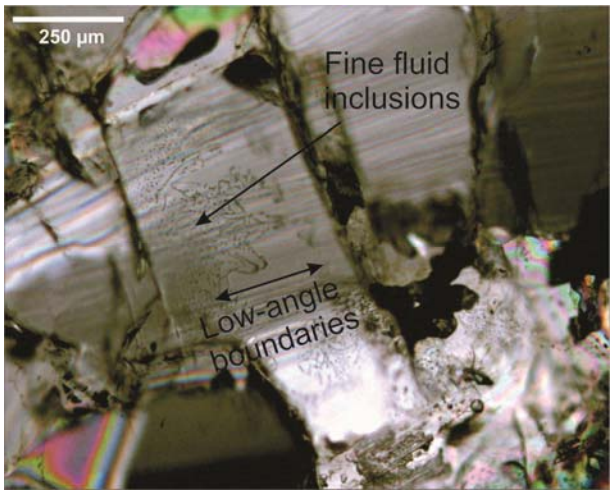

XPL image of fine fluid inclusions within an olivine grain.

THIN SECTION	**136063**	**OVERALL GRAIN SIZE:** Coarse-grained
ROCK NAME	Coarse-grained spinel lherzolite	
SAMPLE LOCATION	Tubaf seamount, Lihir Island, Papua New Guinea	
HAND SAMPLE	None available	

Mineral	%	Size (mm)			Morphology	Grain boundaries	Comments
		min.	max.	av.			
Olivine	66	0.25	3	1.3	Anhedral, equant	Grain boundaries with enstatite grains are curved and irregular. Self-boundaries also tend to be curved and irregular, but are occasionally straight. Boundaries with clinopyroxene are curved and irregular, with spinel are straight and regular. Olivine is cross-cut and overgrown by spinel.	Clear in PPL, with 2nd - 3rd order interference colours. Typical glassy olivine fracture, with fractures also forming an orthogonal geometry both parallel and perpendicular to low-angle boundaries preserved within the grains. Low-angle boundaries are prominent and defined by parallel bands of undulose extinction. Contains abundant fine fluid inclusion trails (sub-µm sized) frequently oriented parallel to the low-angle boundaries. These are associated with annealed and open fractures, and are more frequent in the vicinity of major alteration zones. Also contains aligned inclusions of spinel, often associated with more strongly altered zones and often appears to coincide with the parts of grains that contain fluid inclusions. These mineral inclusions contain abundant holes/cavities and are contained within planar features. Olivine is altered to fibrous orthopyroxene.
Enstatite	17	0.5	3	1.7	Anhedral, slightly elongate	Self-boundaries are curved and regular. Boundaries with clinopyroxene are straight to curved and regular. Enstatite is overgrown by spinel, boundaries are straight and regular.	Predominantly anhedral grains with distinctive irregularly-shaped sub-parallel bands of undulose extinction. Extensive exsolution lamellae that have been deformed. Well-developed cleavage in grains adjacent to major fractures and alteration zones. Alteration to fibrous orthopyroxene is partially controlled by the orientation of both clinopyroxene

							lamellae and cleavage. Contain abundant fluid inclusions. Clear with pale green pleochroism in PPL, up to 1st order orange in XPL. Straight extinction.
Fibrous orthopyroxene	5	N/A	<0.025	<0.025	Subhedral to euhedral, elongate to fibrous	Cross-cuts all minerals, boundaries are generally straight and regular	Forms elongate, fibrous aggregates replacing primary mantle olivine, clinopyroxene and enstatite.
Clinopyroxene	5	0.5	3	1.7	Anhedral, equant	Self-boundaries not observed. Clinopyroxene-spinel boundaries are curved and irregular.	Very weak pale green pleochroism in PPL, up to 1st order greys in XPL. Inclined extinction that is often undulose. Strongly fractured and is replaced in and near fractures by fibrous orthopyroxene.
Spinel	3	<0.1	1	0.2	Subhedral to euhedral, short and prismatic	Self-boundaries not observed.	Dark brown/red in colour in PPL and isotropic in XPL; resistant to weathering and contains inclusions of primary orthopyroxene and olivine.
Pyrrhotite	1	<0.1	1	0.1	Subhedral to anhedral, equant	Grain boundaries tend to be defined by the surrounding minerals.	Fe-stained, associated with metasomatically altered regions in the thin section. Bright yellow-white under reflected light.
Overall Texture and Alteration:	Massive, no foliation or lineation. Cross-cut by a series of thin veins containing fibrous orthopyroxene. There is alteration of primary mantle minerals (with the exception of spinel) to very fine fibrous orthopyroxene and this is concentrated within a small ~2 mm vein running through the thin section. There are two episodes of fracturing evident – (1) open/clean fractures with little alteration and (2) commonly annealed fractures containing fibrous orthopyroxene and that develop in a perpendicular geometry often related to the orientation of the low-angle boundaries.						
Petrogenesis:	Grain boundary and cross-cutting relationships suggest initial crystallisation of olivine, followed by clinopyroxene, enstatite and lastly the coarser spinel grains under spinel peridotite facies conditions in the mantle. Clinopyroxene exsolution lamellae in enstatite and exsolved spinel grains in olivine (Franz and Wirth, 2000) suggest that there was a decompression event subsequent to crystallisation. Undulose extinction in both olivine and clinopyroxene suggest that the sample has been deformed to some degree by dislocation creep. The embayed nature of some olivine grain boundaries suggests some dynamic recrystallisation by grain boundary migration, and occasional straight grain boundaries parallel to internal microstructure suggests some subgrain rotation has also occurred. The relative timing of the recrystallisation is unclear. The peridotite was then fractured but the fractures were not associated with any metasomatic fluids. A second set of fractures subsequently developed, associated with alteration of primary mantle minerals to fibrous orthopyroxene and the development of fluid inclusions. The second set of fractures and fluid inclusions most likely developed synonymous with the deformation, as the fluid inclusions represent annealed fracture planes, and such annealing can only happen at depth where pressure and temperature conditions permit. The alteration of primary enstatite is also controlled by the orientation of deformed exsolution lamellae, thus these were present before alteration. The						

	most recent mineral to form is pentlandite, forming small crystals scattered throughout the sample, which may suggest a late influx of sulphidic fluids into the peridotite. The last event to occur was the exhumation of the sample to the Earth's surface through volcanic activity in a forearc volcano.

Sample 136063 Photomicrographs

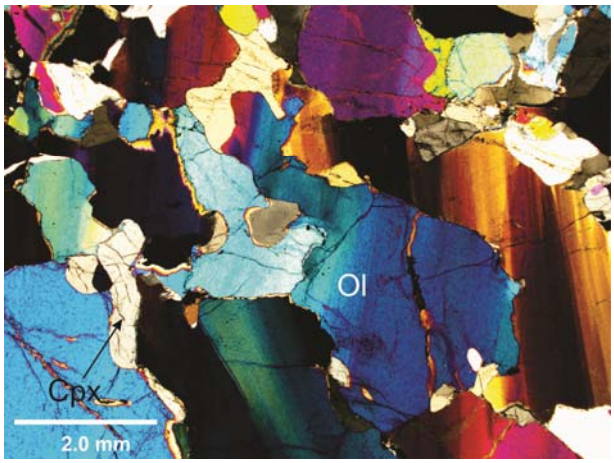

XPL image of the overall texture of sample. Olivine grains preserve low-angle boundaries associated with deformation of the sample.

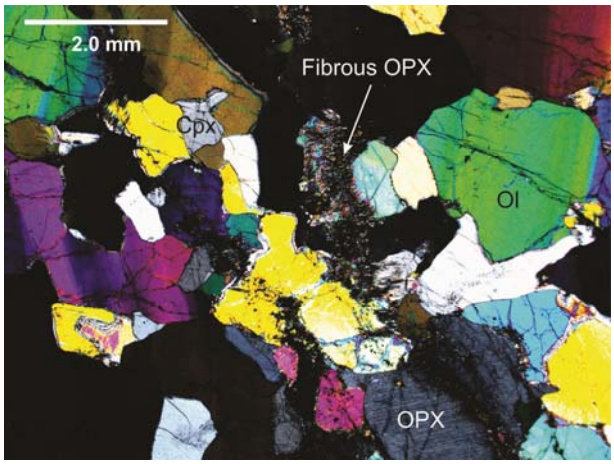

XPL image of an OPX vein cross-cutting the sample.

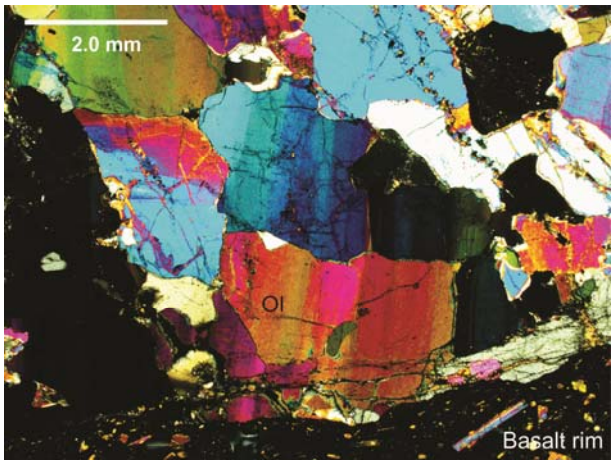

XPL image showing low-angle boundary preservation in olivine. The lower right edge of the image is the edge of the xenolith where the peridotite meets the host basalt.

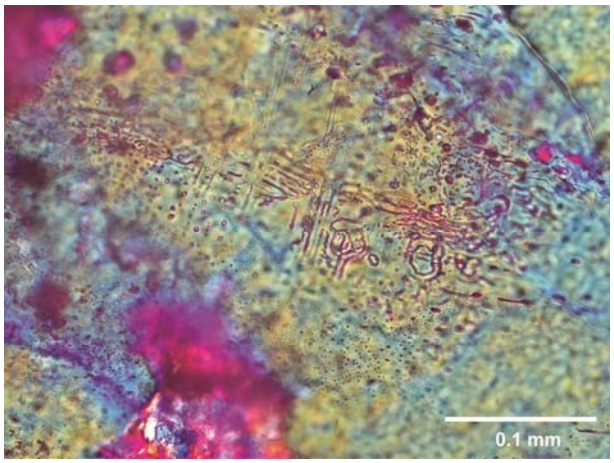

Vermicular morphology of fine fluid inclusions in olivine (XPL).

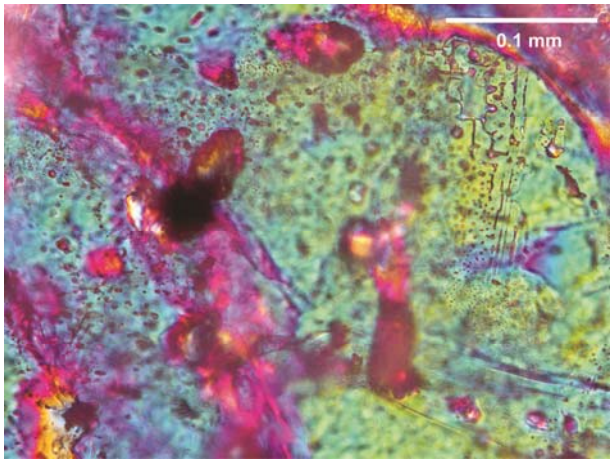

Coarse and fine fluid inclusions preserved in olivine (XPL).

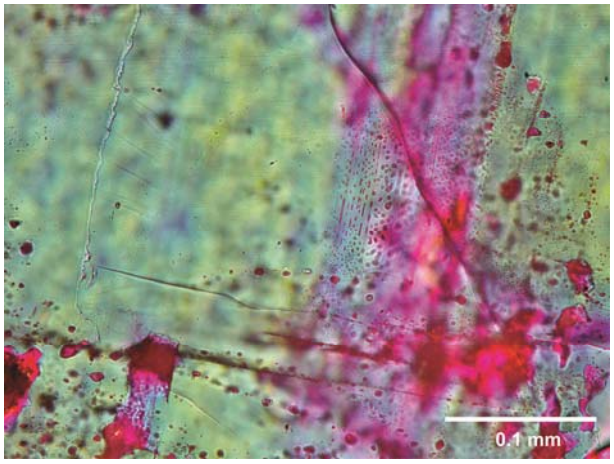

Coarse and fine fluid inclusions preserved in olivine (XPL). The fine inclusions form trails parallel to the low-angle boundaries.

THIN SECTION	**136065**	**OVERALL GRAIN SIZE:** Coarse-grained
ROCK NAME	Coarse-grained spinel harzburgite	
SAMPLE LOCATION	Tubaf seamount, Lihir Island, Papua New Guinea	
HAND SAMPLE	None available	

Mineral	%	Size (mm)			Morphology	Grain boundaries	Comments
		min.	max.	av.			
Olivine	84	0.1	2	2	Anhedral, equant	Self-boundaries are curved to straight and irregular. Boundaries with all other minerals are curved and regular.	Clear and moderate to high relief in PPL. Strongly deformed with prominent low-angle boundaries evident through intragrain variations in extinction angle. Contain abundant coarse fluid inclusions (~75 µm) and fine fluid inclusion trails (~1 µm) often running parallel to low-angle boundaries. Commonly fractured, with fractures also often seen to be parallel and/or orthogonal to low angle boundaries. Contains inclusions of aligned very fine-grained secondary spinel.
Enstatite	8	0.1	1.2	1	Anhedral, slightly elongate	Self-boundaries are curved to straight and regular. Boundaries with primary spinel and clinopyroxene are straight and regular.	Pale green to clear pleochroism in PPL, 2nd order interference colours and straight extinction. Displays undulose extinction across the grains. Contains extensive deformed exsolution lamellae of clinopyroxene. Generally has a weak cleavage.
Clinopyroxene	2	0.1	1.2	1	Anhedral, slightly elongate	Self-boundaries are not observed. Boundaries with primary spinel are straight and regular.	Pale green to clear pleochroism in PPL, 2nd order interference colours and inclined extinction. Well-formed cleavage, contains inclusions of primary olivine.
Spinel	2.5	0.01	0.9	0.5	Subhedral to anhedral, equant	Cross-cuts all other minerals	Red/brown in PPL, isotropic in XPL. Relatively unaltered and overgrows both primary olivine and enstatite.

Spinel	<0.5	<0.001	0.01	0.002	Subhedral to euhedral, prismatic	N/A	Red/brown colour in PPL. Isotropic in XPL. Occurs as small aligned, elongate inclusions within primary olivine grains, 1 - 2 microns in size.
Overall Texture and Alteration:	Massive, no obvious foliation, lineation or SPO. This sample is relatively pristine and unaltered, despite the presence of fluid inclusions suggesting interaction with fluids.						
Petrogenesis:	Grain boundary and cross-cutting relationships suggest initial crystallisation of olivine, followed by clinopyroxene, enstatite and lastly the coarser spinel grains under spinel peridotite facies conditions in the mantle. Clinopyroxene exsolution lamellae in enstatite and exsolved spinel grains in olivine (Franz and Wirth, 2000) suggest that there was a decompression event subsequent to crystallisation. Undulose extinction in both olivine and enstatite suggest that the sample has been deformed to some degree by dislocation creep, with some subsequent dynamic recrystallisation by subgrain rotation (relative timing unclear). Fracturing and fluid inclusions developed syn-deformation, as the fluid inclusions represent annealed fracture planes, and such annealing can only happen at depth where pressure and temperature conditions permit. The last event to occur was the exhumation of the sample to the Earth's surface through volcanic activity in a forearc volcano.						

Sample 136065 Photomicrographs

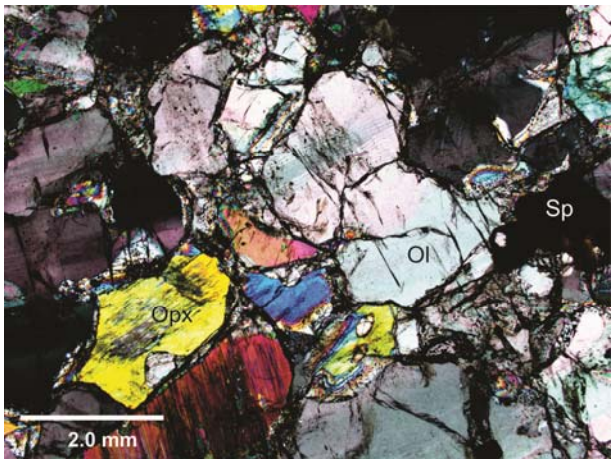

XPL image of the massive texture of sample 136065. Olivine grains show undulose extinction consistent with deformation. Orthopyroxene grains contain extensive clinopyroxene lamellae (yellow and red grains to the bottom left of the image).

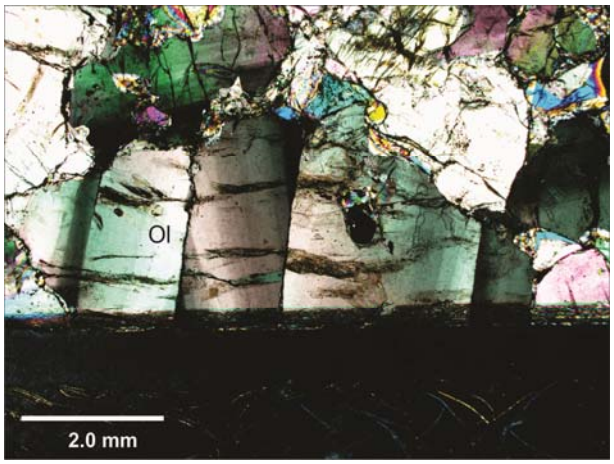

XPL image showing the complex low-angle boundary geometries preserved in olivine.

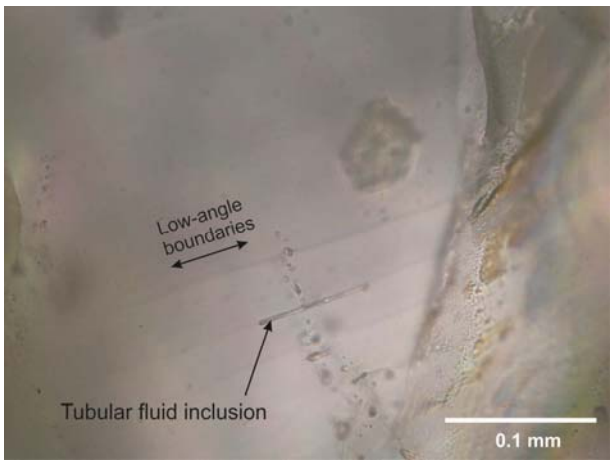

XPL image showing tubular fluid inclusions running parallel to low-angle boundaries in olivine.

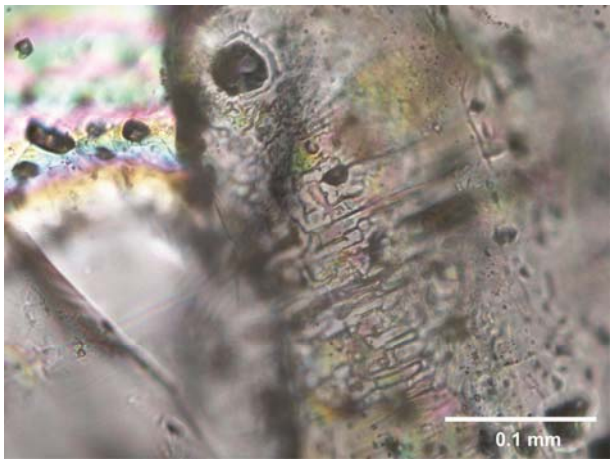

Coarse and fine fluid inclusions in olivine (XPL).

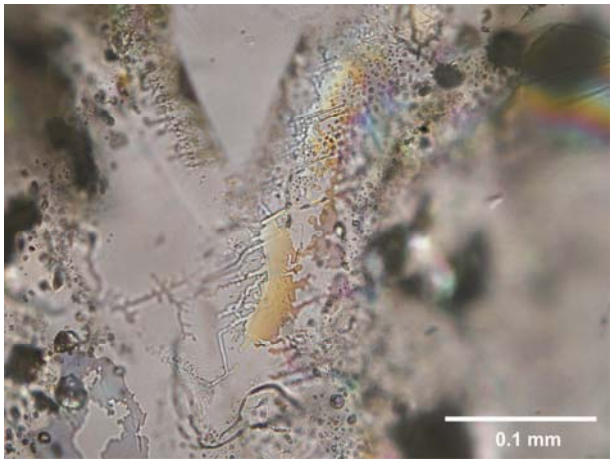

Coarse and fine fluid inclusions in olivine (XPL).

THIN SECTION	**136067**	**OVERALL GRAIN SIZE:** Coarse-grained
ROCK NAME	Coarse-grained spinel dunite	
SAMPLE LOCATION	Tubaf seamount, Lihir Island, Papua New Guinea	
HAND SAMPLE	None available	

Mineral	**%**	**Size (mm)**			**Morphology**	**Grain boundaries**	**Comments**
		min.	**max.**	**av.**			
Olivine	89	0.1	5	2	Anhedral, equant	Self-boundaries are irregular and straight to curved, with common triple point junctions. Olivine is overgrown by secondary spinel and boundaries are generally curved and regular.	Clear in PPL. Highly fractured grains with a bimodal grain size distribution. Smaller grains range from 0.1-1 mm and larger grains range from 1.5 – 5 mm. Grains contain abundant fluid inclusions and very small aligned spinel inclusions. Grains are deformed with prominent low angle boundaries as shown by parallel bands of undulose extinction under XPL.
Spinel	10	0.02	1	0.25	Subhedral, equant	Self-boundaries are curved and regular.	Opaque with a dark red/brown stain in PPL. Isotropic in XPL. Overgrows primary olivine and often delineates the olivine grain boundaries. In the finer section of the sample, spinel is more scattered and located both at olivine grain boundaries and also inside grains. In the coarser part of the sample the spinel growth appears to be more restricted to the olivine grain boundaries.
Spinel (inclusions)	1	<0.01	<0.01	<0.01	Subhedral to euhedral, short, prismatic	N/A	Opaque with a dark red/brown stain in PPL. Isotropic in XPL. Resistant to alteration and generally aligned. Occurs as an inclusion within primary olivine.
Overall Texture and Alteration:	The sample is bimodal, with 2 populations of olivine. Both are coarse-grained with respect to their grain size, but the larger grain population is substantially coarser. The olivine is extensively overgrown by small spinel grains, which often delineate olivine grain boundaries, and give the thin section a spotted appearance. There is no obvious foliation, lineation or shape-preferred orientation.						

Petrogenesis:	Grain boundary and cross-cutting relationships suggest initial crystallisation of olivine, followed by the coarser spinel grains under spinel peridotite facies conditions in the mantle. Exsolved spinel grains in olivine (Franz and Wirth, 2000) suggest that there was a decompression event subsequent to crystallisation. Undulose extinction in olivine suggest that the sample has been deformed to some degree by dislocation creep. Fluid inclusions were entrapped under mantle conditions (although there is not enough evidence to suggest relative timing), as the fluid inclusions represent annealed fracture planes, and such annealing can only happen at depth where pressure and temperature conditions permit. The last event to occur was the exhumation of the sample to the Earth's surface through volcanic activity in a forearc volcano.

THIN SECTION	**136068**	**OVERALL GRAIN SIZE:** Medium-grained
ROCK NAME	Medium-grained spinel lherzolite	
SAMPLE LOCATION	Tubaf seamount, Lihir Island, Papua New Guinea	
HAND SAMPLE	None available	

Mineral	%	Size (mm)			Morphology	Grain boundaries	Comments
		min.	max.	av.			
Olivine	81	0.1	2	0.5	Anhedral, equant	Self-boundaries are curved and irregular. Boundaries with enstatite, primary spinel and clinopyroxene are curved and regular.	Clear in PPL, with generally first order interference colours in XPL. Exhibits undulose extinction due to low angle boundaries indicating preservation of deformation microstructures. Highly fractured grains replaced by fibrous orthopyroxene along fractures. Contains abundant fluid inclusions representing annealed fracture planes.
Enstatite	6	0.5	3	1	Anhedral, slightly elongate	Self-boundaries are straight and regular. Boundaries with clinopyroxene are straight to curved and regular and with spinel are straight and regular.	Pale green to clear pleochroism in PPL, up to first order interference colours in XPL, parallel extinction. Contains sub-parallel bands of undulose extinction indicating deformation. Contains exsolution lamellae but not as prominent as is seen in other samples. Contains abundant fluid inclusion planes associated with annealed fractures that run parallel to the cleavage.
Orthopyroxene	4	N/A	N/A	<0.025	Subhedral to euhedral, acicular	Cross-cuts all other minerals (except spinel) and boundaries are generally straight.	Clear in PPL, up to first order greys in XPL. Forms fibrous aggregates replacing primary mantle olivine and pyroxenes.
Clinopyroxene	4	0.5	3	1	Subhedral to anhedral, equant	Self-boundaries are straight and regular. Boundaries with spinel are straight and regular.	Very pale green to clear pleochroism in PPL, up to first order greys in XPL with inclined undulose extinction. Has a weak ~90° cleavage. Strongly fractured and is replaced in and near fractures by

							fibrous orthopyroxene.
Spinel	4.5	0.01	1	0.5	Subhedral to euhedral, prismatic	Self-boundaries are straight to curved and regular.	Red/brown in PPL, extinct in XPL. Relatively unaltered and overgrows both primary olivine and enstatite.
Overall Texture and Alteration:	Massive, some veins running through the section. No obvious foliation, lineation or shape-preferred orientation. Alteration to fibrous orthopyroxene throughout the sample is linked to the presence of fluid inclusions within olivine and pyroxenes.						
Petrogenesis:	Grain boundary and cross-cutting relationships suggest initial crystallisation of olivine, followed by clinopyroxene, enstatite and lastly the coarser spinel grains under spinel peridotite facies conditions in the mantle. Clinopyroxene exsolution lamellae in enstatite suggests that there was a decompression event subsequent to crystallisation, but the lack of exsolved spinel in olivine and lesser degree of exsolution lamellae noted in the enstatite suggests that this sample did undergo decompression to the extent of other samples in the suite. Undulose extinction in both olivine and enstatite suggest that the sample has been deformed to some degree by dislocation creep, with some subsequent dynamic recrystallisation by grain boundary migration (relative timing unclear). Fracturing and fluid inclusions developed syn-deformation, as the fluid inclusions represent annealed fracture planes, and such annealing can only happen at depth where pressure and temperature conditions permit. The last event to occur was the exhumation of the sample to the Earth's surface through volcanic activity in a forearc volcano.						

Sample 136068 Photomicrographs

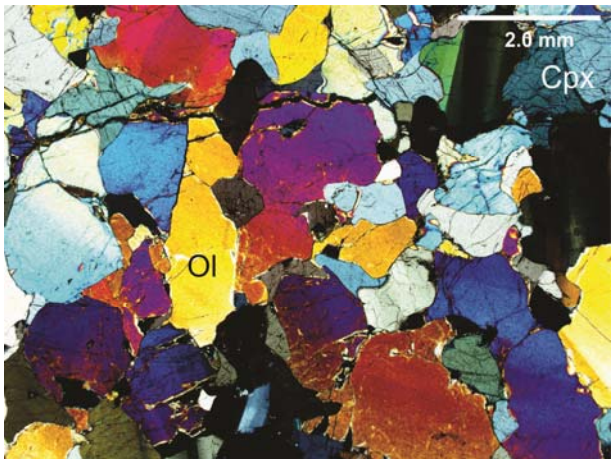

XPL image of the texture of sample 136068. Overall, the texture is massive. Olivine is deformed, with prominent low-angle boundaries preserved.

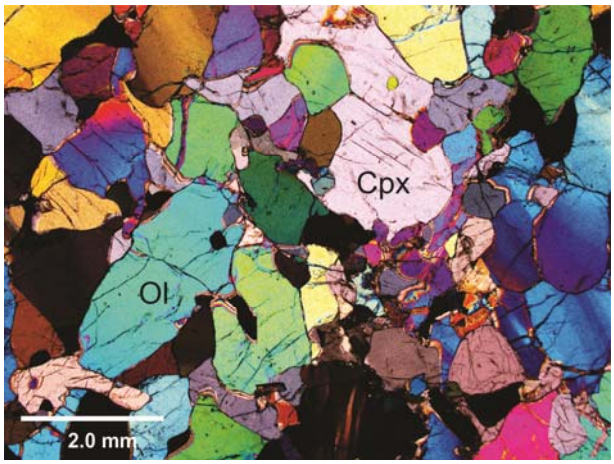

XPL image of the overall texture of sample 136068.

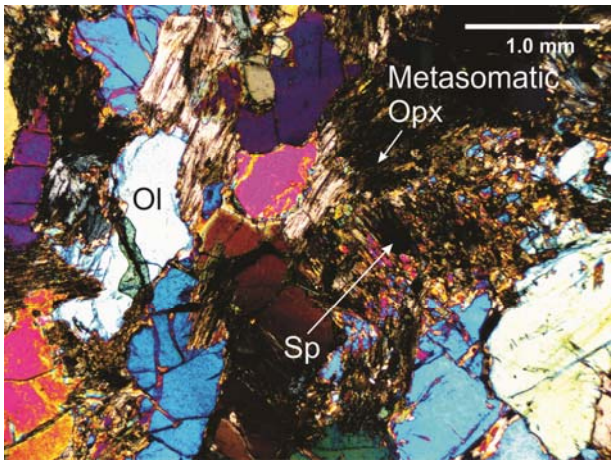

XPL image showing replacement of primary mantle minerals by metasomatic orthopyroxene along grain boundaries.

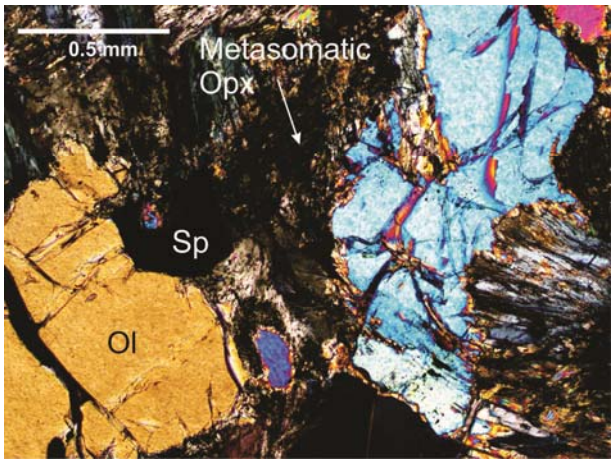

XPL image showing replacement of primary mantle minerals by metasomatic orthopyroxene along grain boundaries.

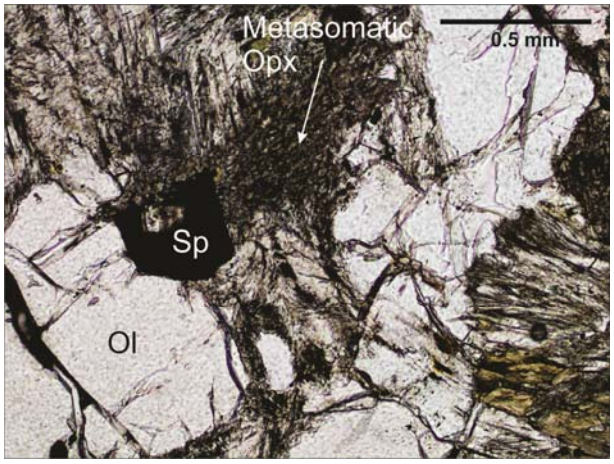

PPL image showing replacement of primary mantle minerals by metasomatic orthopyroxene along grain boundaries, and the lack of alteration of spinel.

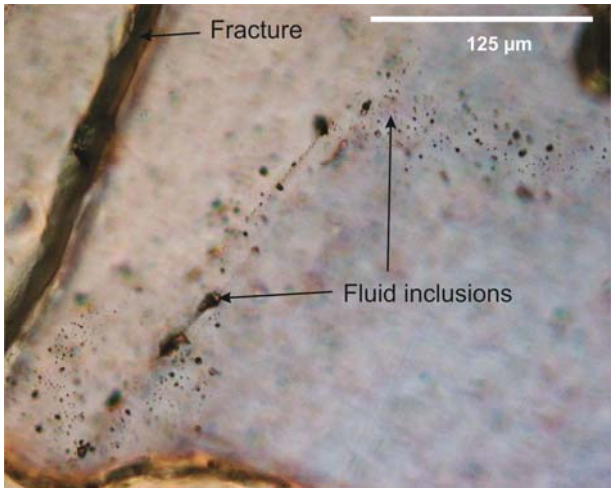

XPL image showing fine fluid inclusions preserved within an olivine grain.

THIN SECTION	**136069**	**OVERALL GRAIN SIZE:** Coarse-grained
ROCK NAME	Coarse-grained spinel dunite	
SAMPLE LOCATION	Tubaf seamount, Lihir Island, Papua New Guinea	
HAND SAMPLE	None available	

Mineral	%	Size (mm)			Morphology	Grain boundaries	Comments
		min.	max.	av.			
Olivine	85	0.1	2	1.5	Anhedral, equant	Self-boundaries are embayed to curved and irregular, but straight and parallel to internal microstructure on occasions. Olivine grain boundaries that terminate in triple junctions not uncommon. Enstatite-olivine boundaries are curved and regular. Boundaries with clinopyroxene and spinel are straight and regular.	Clear in PPL, 2nd order interference colours in XPL. Deformed grains with prominent low-angle boundaries highlighted by undulose extinction. Highly fractured and altered to fibrous orthopyroxene along fractures and grain boundaries. Contains abundant fluid inclusions near the main fractures that are sometimes parallel to low angle boundaries. Olivine contains abundant very fine aligned inclusions of spinel that are often seen to be oriented parallel to low-angle boundaries.
Enstatite	3	0.5	2	1.2	Subhedral to anhedral, slightly elongate to equant	Self-boundaries are curved and irregular. Boundaries with spinel are straight and regular. Boundaries with clinopyroxene are not observed.	Pale-green to clear pleochroism in PPL. Has a prominent widely spaced cleavage at ~90°. Abundant exsolution lamellae controlling the orientation of open and annealed fractures (as is evident in the presence of trails of fluid inclusions). Grains are deformed and show undulose, parallel extinction. Exsolution lamellae commonly show evidence for deformation.
Orthopyroxene	6	N/A	N/A	<0.025	Subhedral to euhedral, acicular	Cross-cuts all other minerals, boundaries are straight and regular.	Forms fibrous aggregates replacing primary mantle minerals. Interference colours range from light grey - light yellow under XPL.

Clinopyroxene	1	0.1	0.5	1.2	Subhedral to anhedral, equant	Clinopyroxene-spinel boundaries are straight and regular.	Pale green pleochroism in PPL. Rare and usually unaltered, and grains have a widely spaced cleavage.
Spinel	4	0.1	5	0.5	Subhedral to anhedral, short and prismatic	Self-boundaries are curved to straight and regular.	Dark red/brown in PPL and isotropic in XPL. Generally resistant to alteration, and are strongly fractured where it occurs near main alteration zones.
Spinel	1	N/A	N/A	<0.1	Subhedral to anhedral, short and prismatic	Contained within olivine, boundaries are straight and regular.	Dark red/brown in PPL and isotropic in XPL. Occurs as inclusions in both olivine and enstatite, and is generally resistant to alteration. Secondary spinel inclusions are often aligned.
Overall Texture and Alteration:	Massive, with no obvious structural fabric. Alteration is controlled by two ~0.5 mm thick parallel fractures associated with abundant fine-grained orthopyroxene. Fibrous orthopyroxene replaces primary mantle minerals (except spinel). Alteration of olivine to orthopyroxene is often controlled by the low-angle boundaries, as are fractures on a grain-scale.						
Petrogenesis:	Crystallisation of olivine followed by pyroxenes and spinel under spinel peridotite facies conditions in the mantle. Exsolved spinel grains in olivine and exsolution lamellae in enstatite suggest this was followed by a decompression of the peridotite (Franz and Wirth, 2000). This was followed by deformation of the peridotite producing low-angle boundaries in olivine and bending of the exsolution lamellae in enstatite. The olivine has also undergone a degree of dynamic recrystallisation by both subgrain rotation and grain boundary migration, as suggested by the nature of the grain boundaries. Alteration to fibrous orthopyroxene was subsequent to this and was accompanied by fracturing and fluid inclusion development. The latest event to affect the rock is it's exhumation as a result of forearc volcanic activity.						

Sample 136069 Photomicrographs

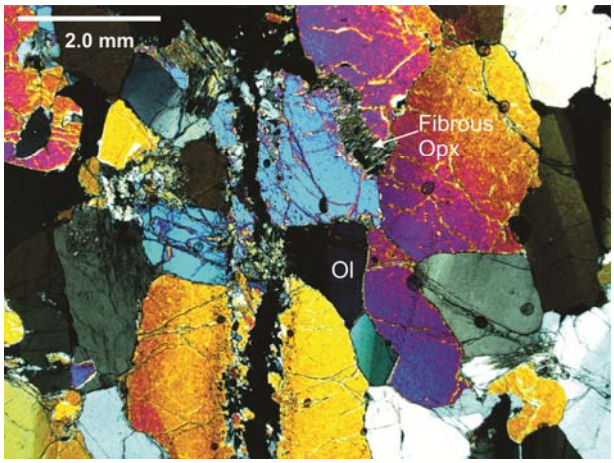

XPL image of a vein cross-cutting the massive fabric in sample 136069. Fibrous orthopyroxene replaces deformed olivine and clinopyroxene along grain boundaries.

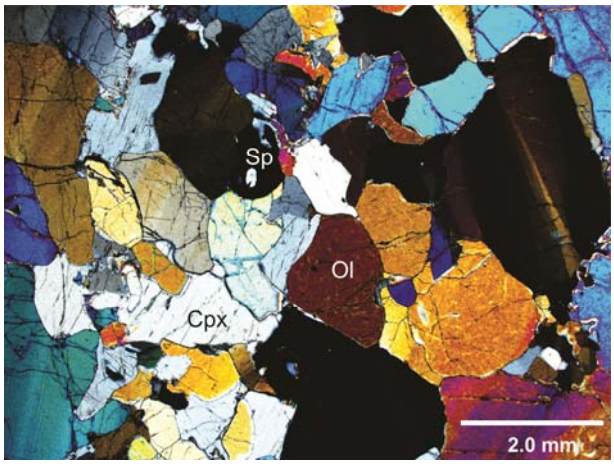

XPL image of olivine, clinopyroxene and spinel grains in sample 136069.

THIN SECTION	**136070**	**OVERALL GRAIN SIZE:** Coarse-grained
ROCK NAME	Coarse-grained spinel lherzolite	
SAMPLE LOCATION	Tubaf seamount, Lihir Island, Papua New Guinea	
HAND SAMPLE	None available	

Mineral	%	Size (mm)			Morphology	Grain boundaries	Comments
		min.	max.	av.			
Olivine	66	0.4	2.1	1	Subhedral to anhedral and equant	Self-boundaries are irregular and curved, and boundaries with enstatite and spinel are straight and regular.	Clear in PPL and fractured in appearance. Grains preserve low-angle boundaries related to deformation. Fluid inclusions commonly preserved, often running parallel to low angle boundary orientation.
Enstatite	30	1	4.2	2.1	Subhedral and equant	Self-boundaries are irregular and curved and boundaries with spinel are straight and regular.	Pale green to clear pleochroism, straight extinction in XPL. Often contains deformed clinopyroxene exsolution lamellae. Replaced in places by fine-grained orthopyroxene, and often contains fluid inclusions associated with major fractures running through the sample. Contains inclusions of primary olivine.
Orthopyroxene	1	<0.1	<0.1	<0.1	Fibrous to acicular	Cross-cut all other minerals.	Clear in PPL, straight extinction in XPL. Observed to be replacing primary olivine and enstatite along grain boundaries and fractures.
Spinel	3	0.25	1	0.5	Subhedral to euhedral, equant	Straight and regular	Very dark brown in PPL, isotropic in XPL. Resistant to alteration.

Overall Texture and Alteration:	Massive texture with parallel bands rich in pyroxene alternating with bands rich in olivine (a layered cumulate texture). No foliation or lineation observed. Some fine fractures cutting across the sample. Alteration of primary mantle minerals to fibrous orthopyroxene predominantly around grain boundaries but also within fractures. Alteration is associated with the presence of fluid inclusions preserved within olivine and pyroxenes.
Petrogenesis:	Crystallisation of olivine followed by enstatite and spinel under spinel peridotite facies conditions in the mantle. Exsolution lamellae in enstatite suggest this was followed by a decompression of the peridotite, although there is an absence of exsolved spinel in olivine as seen in the other samples. This was followed by deformation of the peridotite producing low-angle boundaries in olivine and bending of the clinopyroxene exsolution lamellae in enstatite. Alteration to fibrous orthopyroxene followed this and was accompanied by fracturing and fluid inclusion development. Fluid inclusions form trails and are likely to represent annealed fractures, suggesting that fracturing occurred in the mantle where conditions permitted fracture annealing. The latest event to affect the rock is it's exhumation as a result of forearc volcanic activity.

Sample 136070 Photomicrographs

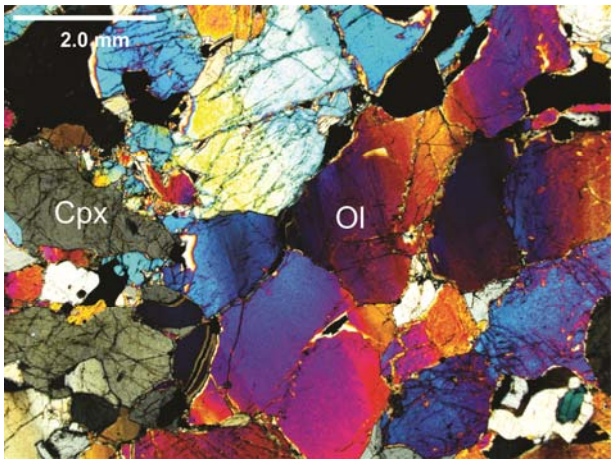

XPL image of the massive texture of sample 136070 comprised of deformed olivine, enstatite (not visible in this image) and clinopyroxene, with minor spinel.

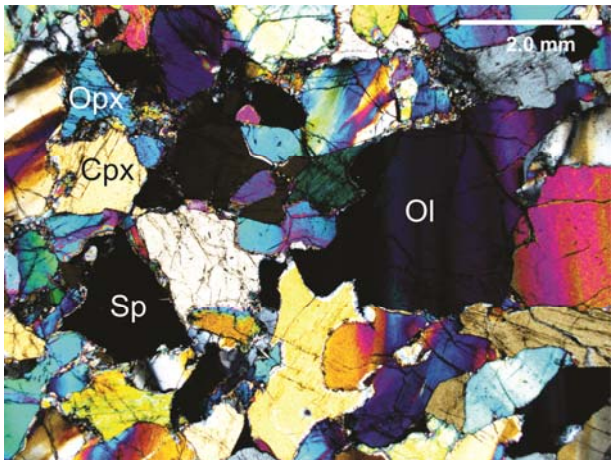

XPL image of the olivine-rich region of the sample.

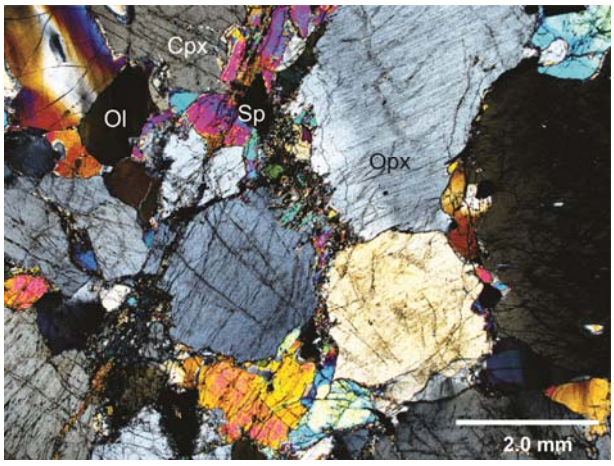

XPL image showing the pyroxene-rich region of the sample. Alteration is more pervasive in this part of the sample.

THIN SECTION	**136074**	**OVERALL GRAIN SIZE:** Coarse-grained
ROCK NAME	Coarse-grained spinel lherzolite	
SAMPLE LOCATION	Tubaf seamount, Lihir Island, Papua New Guinea	
HAND SAMPLE	None available	

Mineral	%	Size (mm)			Morphology	Grain boundaries	Comments
		min.	max.	av.			
Olivine	80	0.5	3	1	Anhedral, equant	Self-boundaries are straight and regular, often terminating at triple junctions (sometimes boundaries are also curved or straight and parallel to internal microstructure). Curved and irregular boundaries with enstatite and pyroxene. Curved and irregular with spinel.	Clear in PPL, high relief, up to 2nd order pink interference colours in XPL. Often highly fractured and deformed as shown by the prominent low-angle boundaries. Contains abundant fluid inclusions that are oriented parallel to low-angle boundaries, as are some fractures. Contains very small inclusions of aligned spinel.
Enstatite	10	0.5	4	1	Anhedral, equant	All grain boundaries tend to be curved and irregular.	Pale grey to yellow under XPL with straight extinction. Highly fractured grains with a prominent cleavage at ~90°. Highly altered in places and contains extensive exsolution lamellae.
Orthopyroxene	4	N/A	N/A	<0.1	Subhedral to euhedral, acicular	N/A (too fine to observe)	Very fine grains forming aggregates replacing primary mantle minerals (excluding spinel).
Clinopyroxene	4	1	4	1.5	Anhedral, equant	Curved and irregular.	Pale grey to yellow with inclined extinction. Highly fractured grains with a prominent cleavage at ~90°. Highly altered in places to fibrous orthopyroxene and contain extensive exsolution lamellae.
Spinel	2	0.1	0.5	0.35	Subhedral to euhedral, short and prismatic	Curved and irregular.	Dark red/brown in PPL, isotropic in XPL. Clearly overgrows olivine and orthopyroxene.

Overall Texture and Alteration:	Massive with occasional thin fractures traversing the thin section. No obvious foliation or lineation. Alteration is associated with prominent fracturing and fractures are often controlled by the low-angle boundary orientations. Fibrous orthopyroxene occurs in 0.5 mm veins cross-cutting the section, replacing olivine and primary orthopyroxene.
Petrogenesis:	Crystallisation of olivine followed by pyroxenes and spinel under spinel peridotite facies conditions in the mantle. Exsolved spinel grains in olivine and exsolution lamellae in enstatite suggest this was followed by a decompression of the peridotite (Franz and Wirth, 2000). This was followed by deformation of the peridotite producing low-angle boundaries in olivine and bending of the exsolution lamellae in enstatite. The olivine subsequently underwent a degree of dynamic recrystallisation by both subgrain rotation and grain boundary migration, as suggested by the nature of the grain boundaries (relative timing is unclear). Alteration to fibrous orthopyroxene occurred subsequent to this and was accompanied by fracturing and fluid inclusion development. The rock was subsequently exhumed within magmas related to forearc volcanism.

Sample 136074 Photomicrographs

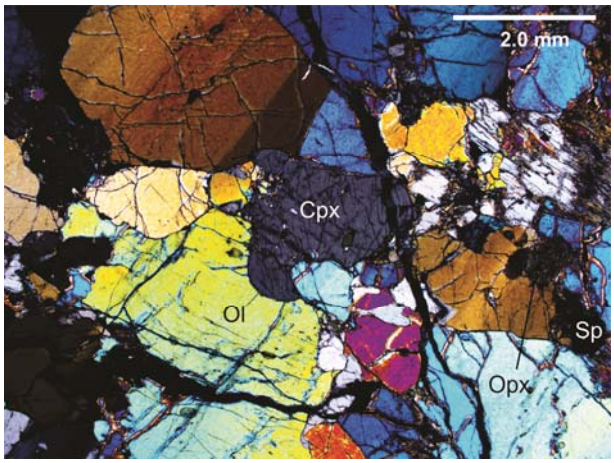

XPL image of olivine, clinopyroxene, fibrous orthopyroxene and spinel.

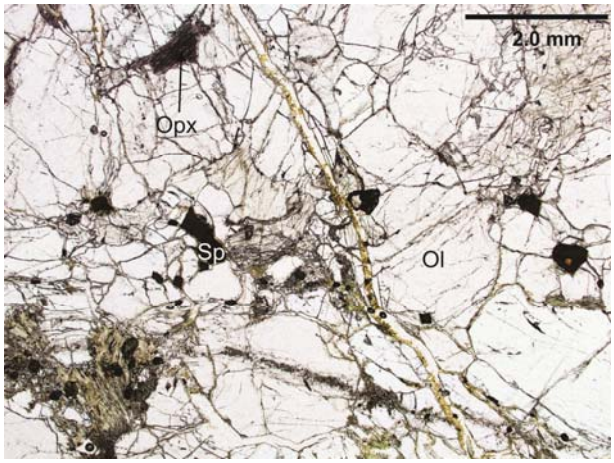

PPL image of olivine, clinopyroxene, fibrous orthopyroxene and spinel.

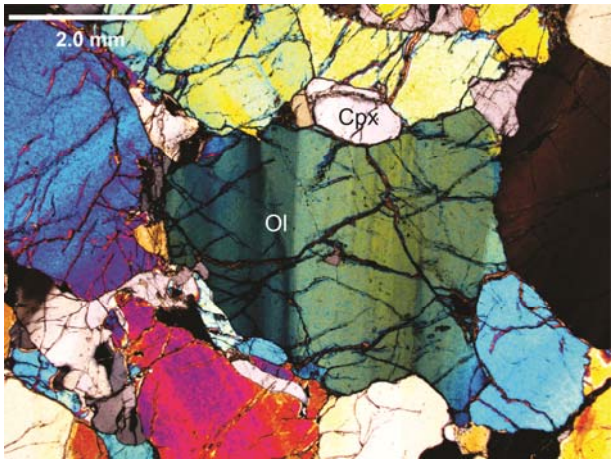

Deformed olivine grains in sample 136074 (XPL).

THIN SECTION	**136090**	**OVERALL GRAIN SIZE:** Coarse-grained
ROCK NAME	Coarse-grained metasomatised spinel dunite	
SAMPLE LOCATION	Tubaf seamount, Lihir Island, Papua New Guinea	
HAND SAMPLE	None available	

Mineral	**%**	**Size (mm)**			**Morphology**	**Grain boundaries**	**Comments**
		min.	**max.**	**av.**			
Olivine	80	0.5	2	1.5	Anhedral, equant	Mostly curved and irregular, with some triple junctions between olivine grains.	Clear in PPL, up to 3rd order green and pink interference colours in XPL. Deformed anhedral grains exhibiting prominent low angle boundaries. Grains are 0.5 – 2mm and contain abundant fluid inclusions often oriented parallel to the low-angle boundaries. Olivine is extremely altered to orthopyroxene.
Enstatite	5	0.5	1	0.7	Anhedral, slightly elongate	Curved/scalloped and irregular.	Clear in PPL, with weak pink/green pleochroism. Grey to pale yellow under XPL with parallel extinction. Altered 0.5 – 1 mm grains with strongly developed exsolution lamellae and a prominent ~90° cleavage. Highly fractured and these are controlled by the orientation of the lamellae.
Orthopyroxene	10	N/A	N/A	<0.1	Euhedral, acicular	N/A (too fine to observe)	Clear in PPL, prey in XPL. Lower relief than olivine. Subhedral grains forming fibrous aggregates replacing primary mantle olivine, clinopyroxene and orthopyroxene.
Clinopyroxene	3	0.1	0.5	0.3	Anhedral, slightly elongate	Curved and irregular	Clear in PPL, grey to yellow in XPL, inclined extinction. Altered 0.1 – 0.5 mm grains containing abundant fluid inclusions and a widely spaced ~90° cleavage.

Spinel	1.5	0.1	1	0.3	Subhedral to euhedral, stubby and prismatic	Curved and irregular	Dark red/brown subhedral to euhedral short prismatic grains <0.1 – 1 mm in size. Isotropic under XPL. Resistant to alteration and overgrows olivine and primary pyroxenes.
Pyrrhotite	<0.5	0.01	0.25	0.1	Subhedral to euhedral	Variable - sometimes straight and regular, sometimes curved and regular.	Very bright, light yellow under reflected light, opaque under PPL. Occurs in trace amounts as individual grains.
Overall Texture and Alteration:	Massive with no obvious foliation or lineation. Alteration of primary mantle minerals to orthopyroxene is associated with fluid influx and widespread fracturing of the grains. Fractures are commonly annealed and are parallel to low-angle boundaries.						
Petrogenesis:	Grain boundary and cross-cutting relationships suggest initial crystallisation of olivine, followed by pyroxenes and the coarser spinel grains under spinel peridotite facies conditions in the mantle. Clinopyroxene exsolution lamellae in enstatite suggest that there was a decompression event subsequent to crystallisation. Undulose extinction in both olivine and pyroxenes indicates that the sample has been deformed by dislocation creep. The peridotite was then fractured and metasomatised with alteration of primary mantle minerals to fibrous orthopyroxene accompanied by the development of fluid inclusions. The fractures and fluid inclusions most likely developed synonymous with the deformation, as the fluid inclusions represent annealed fracture planes, and such annealing can only happen at depth where pressure and temperature conditions permit. The most recent mineral to form is pentlandite, forming small sporadic crystals, which may suggest a late influx of sulphidic fluids into the peridotite. The last event to occur was the exhumation of the sample to the Earth's surface through volcanic activity in a forearc volcano.						

Sample 136090 Photomicrographs

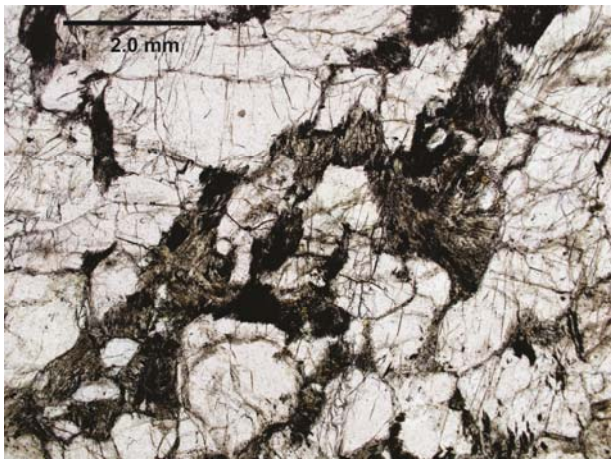

PPL image of a vein containing fibrous orthopyroxene cross-cutting the peridotite in sample 136090.

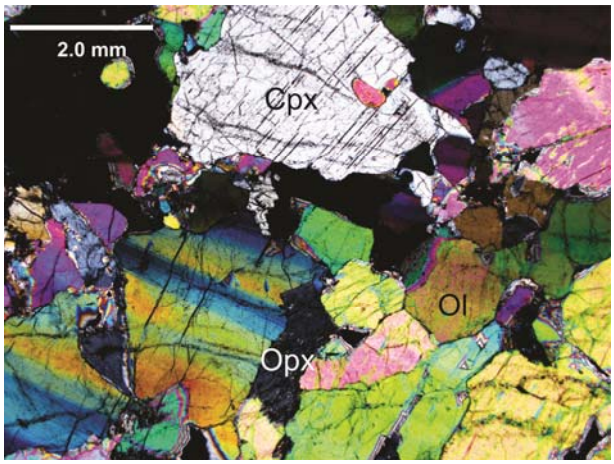

Olivine, enstatite (Opx) and clinopyroxene grains in sample 136090 (XPL).

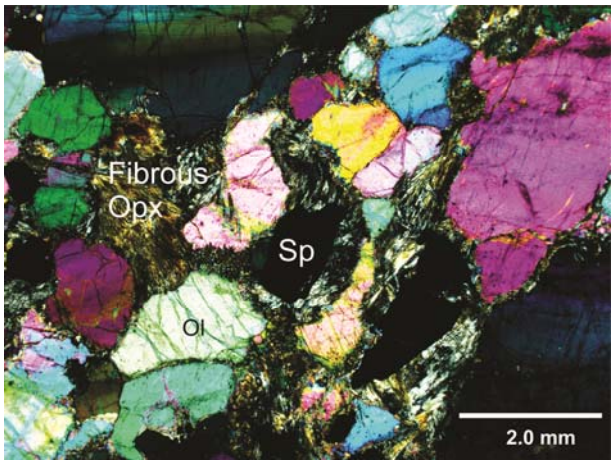

Replacement of olivine and pyroxenes by fibrous orthopyroxene (XPL).

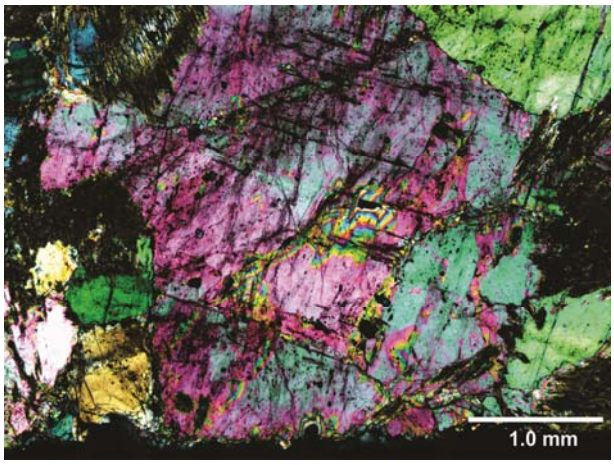

‘Dusty’ olivine grains filled with fluid inclusions in the more highly altered region of the sample (XPL).

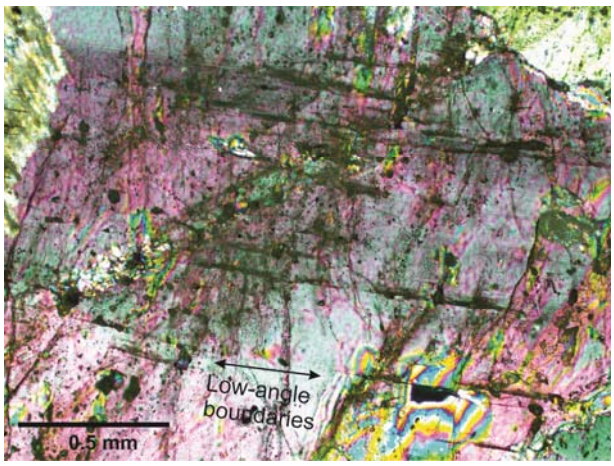

Close-up of the grain above showing fracture development parallel to low-angle boundaries (XPL).

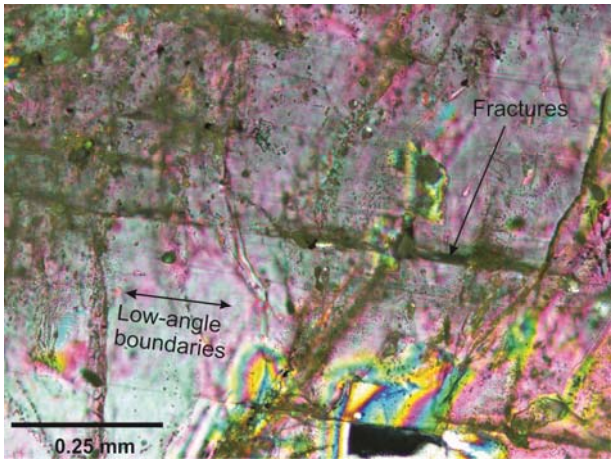

Close-up of the grain above showing the different types of fluid inclusions and fracture development parallel to low-angle boundaries (XPL).

Appendix 3. FTIR Absorbance Data from olivine in Lihir peridotite 136063

Absorbance Feature ID	Associated structure	Wavenumber	Absorbance (I)	Total Absorbance (Io)	I/Io	Intensity Error	Error
47_13	Grain Interior	3354	0.0033	0.0071	0.46479	0.0001	0.0141
47_14	Grain Interior	3354	0.0033	0.0071	0.46479	0.0001	0.0141
47_15	Grain Interior	3354	0.0032	0.0071	0.45070	0.0001	0.0141
47_16	Grain Interior	3354	0.0033	0.0071	0.46479	0.0001	0.0141
47_17	Grain Interior	3354	0.0033	0.0071	0.46479	0.0001	0.0141
47_18	Grain Interior	3354	0.0033	0.0071	0.46479	0.0001	0.0141
47_19	Grain Interior	3426	0.0014	0.0071	0.19718	0.0001	0.0141
47_20	Grain Interior	3426	0.0013	0.0071	0.18310	0.0001	0.0141
47_21	Grain Interior	3422	0.001	0.0071	0.14085	0.0001	0.0141
47_22	Grain Interior	3417	0.001	0.0071	0.14085	0.0001	0.0141
47_23	Grain Interior	3572	0.0012	0.0071	0.16901	0.0001	0.0141
47_24	Grain Interior	3572	0.0009	0.0071	0.12676	0.0001	0.0141
47_41	Grain Interior	3572	0.003	0.0071	0.42254	0.0001	0.0141
47_42	Grain Interior	3572	0.004	0.0071	0.56338	0.0001	0.0141
47_43	Grain Interior	3572	0.0011	0.0071	0.15493	0.0001	0.0141
47_44	Grain Interior	3572	0.0022	0.0071	0.30986	0.0001	0.0141
47_63	Grain Interior	3637	0.0044	0.0071	0.61972	0.0001	0.0141
47_64	Grain Interior	3637	0.0059	0.0071	0.83099	0.0001	0.0141
47_65	Grain Interior	3637	0.0026	0.0071	0.36620	0.0001	0.0141
47_69	Grain Interior	3185	0.00096	0.0071	0.13521	0.0001	0.0141
47_70	Grain Interior	3174	0.00097	0.0071	0.13662	0.0001	0.0141
47_71	Grain Interior	3184	0.00097	0.0071	0.13662	0.0001	0.0141
47_73	Grain Interior	3235	0.001	0.0071	0.14085	0.0001	0.0141
47_74	Grain Interior	3244	0.00097	0.0071	0.13662	0.0001	0.0141
47_75	Grain Interior	3250	0.001	0.0071	0.14085	0.0001	0.0141
47_76	Grain Interior	3241	0.00098	0.0071	0.13803	0.0001	0.0141
47_07	Mineral inclusions	3354	0.0026	0.0071	0.36620	0.0001	0.0141
47_11	Mineral inclusions (Spinel)	3354	0.0035	0.0071	0.49296	0.0001	0.0141
47_38	Mineral inclusions (Spinel)	3572	0.0038	0.0071	0.53521	0.0001	0.0141
47_60	Mineral inclusions (Spinel)	3637	0.0047	0.0071	0.66197	0.0001	0.0141
47_67	Mineral inclusions (Spinel)	3176	0.00097	0.0071	0.13662	0.0001	0.0141
47_72	Mineral inclusions (Spinel)	3254	0.00097	0.0071	0.13662	0.0001	0.0141
47_77	Mineral inclusions (Spinel)	3220	0.00098	0.0071	0.13803	0.0001	0.0141
47_01	Type I Fluid inclusions	3354	0.0053	0.0071	0.74648	0.0001	0.0141
47_02	Type I Fluid inclusions	3354	0.0048	0.0071	0.67606	0.0001	0.0141
47_03	Type I Fluid inclusions	3354	0.0032	0.0071	0.45070	0.0001	0.0141

47_04	Type I Fluid inclusions	3354	0.0029	0.0071	0.40845	0.0001	0.0141
47_10	Type I Fluid inclusions	3354	0.0035	0.0071	0.49296	0.0001	0.0141
47_12	Type I Fluid inclusions	3354	0.0026	0.0071	0.36620	0.0001	0.0141
47_25	Type I Fluid inclusions	3572	0.0026	0.0071	0.36620	0.0001	0.0141
47_26	Type I Fluid inclusions	3572	0.0029	0.0071	0.40845	0.0001	0.0141
47_27	Type I Fluid inclusions	3572	0.002	0.0071	0.28169	0.0001	0.0141
47_28	Type I Fluid inclusions	3572	0.0021	0.0071	0.29577	0.0001	0.0141
47_29	Type I Fluid inclusions	3572	0.0043	0.0071	0.60563	0.0001	0.0141
47_37	Type I Fluid inclusions	3572	0.0038	0.0071	0.53521	0.0001	0.0141
47_39	Type I Fluid inclusions	3572	0.0018	0.0071	0.25352	0.0001	0.0141
47_40	Type I Fluid inclusions	3572	0.0018	0.0071	0.25352	0.0001	0.0141
47_45	Type I Fluid inclusions	3637	0.0038	0.0071	0.53521	0.0001	0.0141
47_46	Type I Fluid inclusions	3637	0.0038	0.0071	0.53521	0.0001	0.0141
47_47	Type I Fluid inclusions	3637	0.003	0.0071	0.42254	0.0001	0.0141
47_48	Type I Fluid inclusions	3637	0.0012	0.0071	0.16901	0.0001	0.0141
47_49	Type I Fluid inclusions	3637	0.0026	0.0071	0.36620	0.0001	0.0141
47_50	Type I Fluid inclusions	3637	0.0064	0.0071	0.90141	0.0001	0.0141
47_59	Type I Fluid inclusions	3637	0.0054	0.0071	0.76056	0.0001	0.0141
47_61	Type I Fluid inclusions	3637	0.0024	0.0071	0.33803	0.0001	0.0141
47_62	Type I Fluid inclusions	3637	0.0016	0.0071	0.22535	0.0001	0.0141
47_68	Type I Fluid inclusions	3176	0.00095	0.0071	0.13380	0.0001	0.0141
47_78	Type I Fluid inclusions	3220	0.00098	0.0071	0.13803	0.0001	0.0141
47_05	Type II Fluid inclusions	3354	0.0023	0.0071	0.32394	0.0001	0.0141
47_06	Type II Fluid inclusions	3354	0.0022	0.0071	0.30986	0.0001	0.0141
47_08	Type II Fluid inclusions	3354	0.0033	0.0071	0.46479	0.0001	0.0141
47_09	Type II Fluid inclusions	3354	0.0026	0.0071	0.36620	0.0001	0.0141
47_30	Type II Fluid inclusions	3572	0.004	0.0071	0.56338	0.0001	0.0141
47_31	Type II Fluid inclusions	3572	0.0011	0.0071	0.15493	0.0001	0.0141
47_32	Type II Fluid inclusions	3572	0.003	0.0071	0.42254	0.0001	0.0141
47_33	Type II Fluid inclusions	3572	0.0045	0.0071	0.63380	0.0001	0.0141
47_34	Type II Fluid inclusions	3572	0.0028	0.0071	0.39437	0.0001	0.0141
47_35	Type II Fluid inclusions	3572	0.0026	0.0071	0.36620	0.0001	0.0141
47_36	Type II Fluid inclusions	3572	0.0025	0.0071	0.35211	0.0001	0.0141
47_51	Type II Fluid inclusions	3637	0.0052	0.0071	0.73239	0.0001	0.0141
47_52	Type II Fluid inclusions	3637	0.0042	0.0071	0.59155	0.0001	0.0141
47_53	Type II Fluid inclusions	3637	0.0016	0.0071	0.22535	0.0001	0.0141
47_54	Type II Fluid inclusions	3637	0.0051	0.0071	0.71831	0.0001	0.0141
47_55	Type II Fluid inclusions	3637	0.0066	0.0071	0.92958	0.0001	0.0141
47_56	Type II Fluid inclusions	3637	0.0037	0.0071	0.52113	0.0001	0.0141
47_57	Type II Fluid inclusions	3637	0.0042	0.0071	0.59155	0.0001	0.0141
47_58	Type II Fluid inclusions	3637	0.0033	0.0071	0.46479	0.0001	0.0141
47_66	Type II Fluid inclusions	3572	0.0019	0.0071	0.26761	0.0001	0.0141
70_02	Grain Interior	3355	0.00355	0.0045	0.78889	0.00005	0.0111

70_03	Grain Interior	3355	0.00335	0.0045	0.74444	0.00005	0.0111
70_06	Grain Interior	3354	0.00275	0.0045	0.61111	0.00005	0.0111
70_08	Grain Interior	3355	0.00235	0.0045	0.52222	0.00005	0.0111
70_09	Grain Interior	3356	0.00235	0.0045	0.52222	0.00005	0.0111
70_100	Grain Interior	3639	0.0031	0.0045	0.68889	0.00005	0.0111
70_101	Grain Interior	3644	0.0034	0.0045	0.75556	0.00005	0.0111
70_102	Grain Interior	3619	0.00115	0.0045	0.25556	0.00005	0.0111
70_106	Grain Interior	3630	0.0015	0.0045	0.33333	0.00005	0.0111
70_11	Grain Interior	3353	0.00225	0.0045	0.50000	0.00005	0.0111
70_12	Grain Interior	3355	0.00265	0.0045	0.58889	0.00005	0.0111
70_14	Grain Interior	3355	0.00235	0.0045	0.52222	0.00005	0.0111
70_16	Grain Interior	3356	0.0028	0.0045	0.62222	0.00005	0.0111
70_17	Grain Interior	3355	0.0026	0.0045	0.57778	0.00005	0.0111
70_18	Grain Interior	3354	0.00265	0.0045	0.58889	0.00005	0.0111
70_19	Grain Interior	3355	0.0028	0.0045	0.62222	0.00005	0.0111
70_20	Grain Interior	3355	0.0031	0.0045	0.68889	0.00005	0.0111
70_22	Grain Interior	3355	0.00285	0.0045	0.63333	0.00005	0.0111
70_23	Grain Interior	3355	0.0032	0.0045	0.71111	0.00005	0.0111
70_28	Grain Interior	3356	0.00295	0.0045	0.65556	0.00005	0.0111
70_29	Grain Interior	3356	0.0031	0.0045	0.68889	0.00005	0.0111
70_32	Grain Interior	3518	0.00125	0.0045	0.27778	0.00005	0.0111
70_34	Grain Interior	3488	0.00125	0.0045	0.27778	0.00005	0.0111
70_35	Grain Interior	3488	0.0011	0.0045	0.24444	0.00005	0.0111
70_36	Grain Interior	3521	0.00105	0.0045	0.23333	0.00005	0.0111
70_40	Grain Interior	3572	0.00185	0.0045	0.41111	0.00005	0.0111
70_42	Grain Interior	3576	0.00125	0.0045	0.27778	0.00005	0.0111
70_45	Grain Interior	3574	0.0019	0.0045	0.42222	0.00005	0.0111
70_47	Grain Interior	3574	0.003	0.0045	0.66667	0.00005	0.0111
70_51	Grain Interior	3573	0.00245	0.0045	0.54444	0.00005	0.0111
70_53	Grain Interior	3572	0.00145	0.0045	0.32222	0.00005	0.0111
70_54	Grain Interior	3574	0.00155	0.0045	0.34444	0.00005	0.0111
70_55	Grain Interior	3573	0.0033	0.0045	0.73333	0.00005	0.0111
70_56	Grain Interior	3574	0.0018	0.0045	0.40000	0.00005	0.0111
70_57	Grain Interior	3574	0.0017	0.0045	0.37778	0.00005	0.0111
70_58	Grain Interior	3574	0.0016	0.0045	0.35556	0.00005	0.0111
70_60	Grain Interior	3520	0.00135	0.0045	0.30000	0.00005	0.0111
70_61	Grain Interior	3537	0.0013	0.0045	0.28889	0.00005	0.0111
70_63	Grain Interior	3572	0.00175	0.0045	0.38889	0.00005	0.0111
70_64	Grain Interior	3573	0.0015	0.0045	0.33333	0.00005	0.0111
70_66	Grain Interior	3569	0.00125	0.0045	0.27778	0.00005	0.0111
70_72	Grain Interior	3525	0.0016	0.0045	0.35556	0.00005	0.0111
70_73	Grain Interior	3572	0.002	0.0045	0.44444	0.00005	0.0111
70_77	Grain Interior	3640	0.00255	0.0045	0.56667	0.00005	0.0111
70_79	Grain Interior	3638	0.002	0.0045	0.44444	0.00005	0.0111
70_81	Grain Interior	3639	0.0031	0.0045	0.68889	0.00005	0.0111

70_83	Grain Interior	3640	0.0026	0.0045	0.57778	0.00005	0.0111
70_85	Grain Interior	3640	0.00445	0.0045	0.98889	0.00005	0.0111
70_88	Grain Interior	3639	0.0034	0.0045	0.75556	0.00005	0.0111
70_91	Grain Interior	3604	0.0012	0.0045	0.26667	0.00005	0.0111
70_92	Grain Interior	3620	0.0017	0.0045	0.37778	0.00005	0.0111
70_93	Grain Interior	3640	0.0023	0.0045	0.51111	0.00005	0.0111
70_94	Grain Interior	3640	0.00335	0.0045	0.74444	0.00005	0.0111
70_95	Grain Interior	3644	0.0023	0.0045	0.51111	0.00005	0.0111
70_96	Grain Interior	3640	0.0027	0.0045	0.60000	0.00005	0.0111
70_98	Grain Interior	3640	0.0023	0.0045	0.51111	0.00005	0.0111
70_01	Low angle boundary	3356	0.00315	0.0045	0.70000	0.00005	0.0111
70_04	Low angle boundary	3356	0.0024	0.0045	0.53333	0.00005	0.0111
70_05	Low angle boundary	3354	0.0024	0.0045	0.53333	0.00005	0.0111
70_07	Low angle boundary	3355	0.00245	0.0045	0.54444	0.00005	0.0111
70_10	Low angle boundary	3355	0.00245	0.0045	0.54444	0.00005	0.0111
70_104	Low angle boundary	3620	0.0014	0.0045	0.31111	0.00005	0.0111
70_105	Low angle boundary	3619	0.00235	0.0045	0.52222	0.00005	0.0111
70_107	Low angle boundary	3621	0.0023	0.0045	0.51111	0.00005	0.0111
70_108	Low angle boundary	3639	0.00105	0.0045	0.23333	0.00005	0.0111
70_109	Low angle boundary	3355	0.0031	0.0045	0.68889	0.00005	0.0111
70_110	Low angle boundary	3644	0.0018	0.0045	0.40000	0.00005	0.0111
70_13	Low angle boundary	3354	0.0021	0.0045	0.46667	0.00005	0.0111
70_15	Low angle boundary	3354	0.00255	0.0045	0.56667	0.00005	0.0111
70_21	Low angle boundary	3355	0.003	0.0045	0.66667	0.00005	0.0111
70_24	Low angle boundary	3355	0.00305	0.0045	0.67778	0.00005	0.0111
70_25	Low angle boundary	3354	0.003	0.0045	0.66667	0.00005	0.0111
70_26	Low angle boundary	3356	0.00325	0.0045	0.72222	0.00005	0.0111
70_27	Low angle boundary	3354	0.00275	0.0045	0.61111	0.00005	0.0111
70_30	Low angle boundary	3319	0.0012	0.0045	0.26667	0.00005	0.0111
70_31	Low angle boundary	3220	0.00105	0.0045	0.23333	0.00005	0.0111
70_33	Low angle boundary	3483	0.00105	0.0045	0.23333	0.00005	0.0111
70_37	Low angle boundary	3470	0.00105	0.0045	0.23333	0.00005	0.0111
70_38	Low angle boundary	3485	0.001	0.0045	0.22222	0.00005	0.0111
70_39	Low angle boundary	3501	0.0012	0.0045	0.26667	0.00005	0.0111
70_41	Low angle boundary	3573	0.00105	0.0045	0.23333	0.00005	0.0111
70_43	Low angle boundary	3575	0.00245	0.0045	0.54444	0.00005	0.0111
70_44	Low angle boundary	3573	0.0023	0.0045	0.51111	0.00005	0.0111
70_46	Low angle boundary	3574	0.0033	0.0045	0.73333	0.00005	0.0111
70_48	Low angle boundary	3574	0.0014	0.0045	0.31111	0.00005	0.0111
70_49	Low angle boundary	3572	0.0015	0.0045	0.33333	0.00005	0.0111
70_50	Low angle boundary	3574	0.0029	0.0045	0.64444	0.00005	0.0111
70_52	Low angle boundary	3572	0.0022	0.0045	0.48889	0.00005	0.0111
70_59	Low angle boundary	3574	0.00175	0.0045	0.38889	0.00005	0.0111
70_62	Low angle boundary	3522	0.0011	0.0045	0.24444	0.00005	0.0111
70_65	Low angle boundary	3574	0.0013	0.0045	0.28889	0.00005	0.0111

70_67	Low angle boundary	3574	0.00155	0.0045	0.34444	0.00005	0.0111
70_68	Low angle boundary	3528	0.0011	0.0045	0.24444	0.00005	0.0111
70_69	Low angle boundary	3567	0.0018	0.0045	0.40000	0.00005	0.0111
70_70	Low angle boundary	3527	0.0012	0.0045	0.26667	0.00005	0.0111
70_71	Low angle boundary	3572	0.00125	0.0045	0.27778	0.00005	0.0111
70_74	Low angle boundary	3528	0.00265	0.0045	0.58889	0.00005	0.0111
70_75	Low angle boundary	3546	0.00105	0.0045	0.23333	0.00005	0.0111
70_76	Low angle boundary	3574	0.00105	0.0045	0.23333	0.00005	0.0111
70_78	Low angle boundary	3640	0.00145	0.0045	0.32222	0.00005	0.0111
70_80	Low angle boundary	3639	0.00365	0.0045	0.81111	0.00005	0.0111
70_82	Low angle boundary	3639	0.0021	0.0045	0.46667	0.00005	0.0111
70_84	Low angle boundary	3639	0.0038	0.0045	0.84444	0.00005	0.0111
70_86	Low angle boundary	3640	0.0015	0.0045	0.33333	0.00005	0.0111
70_87	Low angle boundary	3640	0.00365	0.0045	0.81111	0.00005	0.0111
70_89	Low angle boundary	3640	0.0036	0.0045	0.80000	0.00005	0.0111
70_90	Low angle boundary	3604	0.0011	0.0045	0.24444	0.00005	0.0111
70_97	Low angle boundary	3640	0.00185	0.0045	0.41111	0.00005	0.0111
70_99	Low angle boundary	3644	0.0024	0.0045	0.53333	0.00005	0.0111
70_103	Mineral inclusions	3620	0.0014	0.0045	0.31111	0.00005	0.0111
13a01	Coarse fluid inclusions	3576	0.0029	0.0063	0.46032	0.0001	0.0159
13a01	Coarse fluid inclusions	3638	0.0045	0.0063	0.71429	0.0001	0.0159
13a02	Coarse fluid inclusions	3576	0.0015	0.0063	0.23810	0.0001	0.0159
13a02	Coarse fluid inclusions	3638	0.0023	0.0063	0.36508	0.0001	0.0159
13a03	Coarse fluid inclusions	3576	0.0026	0.0063	0.41270	0.0001	0.0159
13a03	Coarse fluid inclusions	3638	0.0034	0.0063	0.53968	0.0001	0.0159
13a04	Fine fluid inclusions	3576	0.0015	0.0063	0.23810	0.0001	0.0159
13a04	Fine fluid inclusions	3638	0.0019	0.0063	0.30159	0.0001	0.0159
13a05	Fracture	3576	0.0024	0.0063	0.38095	0.0001	0.0159
13a05	Fracture	3638	0.0037	0.0063	0.58730	0.0001	0.0159
13a06	Fracture	3576	0.0021	0.0063	0.33333	0.0001	0.0159
13a06	Fracture	3638	0.003	0.0063	0.47619	0.0001	0.0159
13a07	Fracture	3576	0.002	0.0063	0.31746	0.0001	0.0159
13a07	Fracture	3638	0.0024	0.0063	0.38095	0.0001	0.0159
13a23	Mineral inclusions	3576	0.0012	0.0063	0.19048	0.0001	0.0159
13a23	Mineral inclusions	3638	0.0013	0.0063	0.20635	0.0001	0.0159
13a36	Coarse fluid inclusions	3356	0.0023	0.0063	0.36508	0.0001	0.0159
13a37	Coarse fluid inclusions	3356	0.00235	0.0063	0.37302	0.0001	0.0159
13a38	Coarse fluid inclusions	3356	0.00245	0.0063	0.38889	0.0001	0.0159
13a39	Coarse fluid inclusions	3356	0.0026	0.0063	0.41270	0.0001	0.0159
13a53	Mineral inclusions	3356	0.00235	0.0063	0.37302	0.0001	0.0159
13a08	Fracture	3576	0.0019	0.0063	0.30159	0.0001	0.0159
13a08	Fracture	3638	0.0027	0.0063	0.42857	0.0001	0.0159
13a09	Fracture	3576	0.0012	0.0063	0.19048	0.0001	0.0159
13a09	Fracture	3638	0.0018	0.0063	0.28571	0.0001	0.0159
13a10	Fracture	3576	0.0037	0.0063	0.58730	0.0001	0.0159

13a10	Fracture	3638	0.0057	0.0063	0.90476	0.0001	0.0159
13a12	Fine fluid inclusions	3576	0.0015	0.0063	0.23810	0.0001	0.0159
13a12	Fine fluid inclusions	3638	0.0024	0.0063	0.38095	0.0001	0.0159
13a13	Fine fluid inclusions	3576	0.0037	0.0063	0.58730	0.0001	0.0159
13a13	Fine fluid inclusions	3638	0.0063	0.0063	1.00000	0.0001	0.0159
13a14	Fine fluid inclusions	3576	0.003	0.0063	0.47619	0.0001	0.0159
13a14	Fine fluid inclusions	3638	0.0046	0.0063	0.73016	0.0001	0.0159
13a25	Grain Interior	3576	0.0014	0.0063	0.22222	0.0001	0.0159
13a25	Grain Interior	3638	0.0019	0.0063	0.30159	0.0001	0.0159
13a26	Fine fluid inclusions	3576	0.0015	0.0063	0.23810	0.0001	0.0159
13a26	Fine fluid inclusions	3638	0.0017	0.0063	0.26984	0.0001	0.0159
13a27	Coarse fluid inclusions	3576	0.001	0.0063	0.15873	0.0001	0.0159
13a27	Coarse fluid inclusions	3638	0.0015	0.0063	0.23810	0.0001	0.0159
13a28	Fracture	3576	0.002	0.0063	0.31746	0.0001	0.0159
13a28	Fracture	3638	0.0023	0.0063	0.36508	0.0001	0.0159
13a29	Fracture	3638	0.0032	0.0063	0.50794	0.0001	0.0159
13a29	Fracture	3576	0.0025	0.0063	0.39683	0.0001	0.0159
13a30	Coarse fluid inclusions	3638	0.003	0.0063	0.47619	0.0001	0.0159
13a30	Coarse fluid inclusions	3576	0.0023	0.0063	0.36508	0.0001	0.0159
13a31	Fracture	3576	0.0013	0.0063	0.20635	0.0001	0.0159
13a31	Fracture	3638	0.0014	0.0063	0.22222	0.0001	0.0159
13a32	Fracture	3576	0.0032	0.0063	0.50794	0.0001	0.0159
13a32	Fracture	3638	0.0044	0.0063	0.69841	0.0001	0.0159
13a33	Fracture	3576	0.0014	0.0063	0.22222	0.0001	0.0159
13a33	Fracture	3638	0.0017	0.0063	0.26984	0.0001	0.0159
13a40	Coarse fluid inclusions	3356	0.00265	0.0063	0.42063	0.0001	0.0159
13a42	Fracture	3356	0.00255	0.0063	0.40476	0.0001	0.0159
13a43	Fracture	3356	0.00255	0.0063	0.40476	0.0001	0.0159
13a44	Fine fluid inclusions	3356	0.00235	0.0063	0.37302	0.0001	0.0159
13a56	Grain Interior	3356	0.0024	0.0063	0.38095	0.0001	0.0159
13a57	Grain Interior	3356	0.0022	0.0063	0.34921	0.0001	0.0159
13a58	Grain Interior	3356	0.0022	0.0063	0.34921	0.0001	0.0159
13a59	Grain Interior	3356	0.0022	0.0063	0.34921	0.0001	0.0159
13a62	Grain Interior	3356	0.0022	0.0063	0.34921	0.0001	0.0159
13a63	Coarse fluid inclusions	3356	0.0021	0.0063	0.33333	0.0001	0.0159
13a64	Fine fluid inclusions	3356	0.0022	0.0063	0.34921	0.0001	0.0159
13a65	Fine fluid inclusions	3356	0.0021	0.0063	0.33333	0.0001	0.0159
13a11	Fracture	3576	0.0025	0.0063	0.39683	0.0001	0.0159
13a11	Fracture	3638	0.004	0.0063	0.63492	0.0001	0.0159
13a41	Fine fluid inclusions	3356	0.00235	0.0063	0.37302	0.0001	0.0159

13a60	Low angle boundary	3356	0.0022	0.0063	0.34921	0.0001	0.0159
13a61	Grain Interior	3356	0.0022	0.0063	0.34921	0.0001	0.0159
13a66	Fracture	3356	0.00305	0.0063	0.48413	0.0001	0.0159
13a15	Grain Interior	3576	0.0026	0.0063	0.41270	0.0001	0.0159
13a15	Grain Interior	3638	0.0035	0.0063	0.55556	0.0001	0.0159
13a16	Grain Interior	3576	0.0016	0.0063	0.25397	0.0001	0.0159
13a16	Grain Interior	3638	0.0029	0.0063	0.46032	0.0001	0.0159
13a17	Grain Interior	3576	0.0037	0.0063	0.58730	0.0001	0.0159
13a17	Grain Interior	3638	0.0049	0.0063	0.77778	0.0001	0.0159
13a18	Grain Interior	3576	0.0028	0.0063	0.44444	0.0001	0.0159
13a18	Grain Interior	3638	0.005	0.0063	0.79365	0.0001	0.0159
13a19	Fracture	3576	0.0033	0.0063	0.52381	0.0001	0.0159
13a19	Fracture	3638	0.0051	0.0063	0.80952	0.0001	0.0159
13a20	Fracture	3576	0.0029	0.0063	0.46032	0.0001	0.0159
13a20	Fracture	3638	0.0042	0.0063	0.66667	0.0001	0.0159
13a21	Grain Interior	3576	0.0015	0.0063	0.23810	0.0001	0.0159
13a21	Grain Interior	3638	0.0029	0.0063	0.46032	0.0001	0.0159
13a22	Mineral inclusions	3576	0.0029	0.0063	0.46032	0.0001	0.0159
13a22	Mineral inclusions	3638	0.0028	0.0063	0.44444	0.0001	0.0159
13a24	Mineral inclusions	3576	0.0018	0.0063	0.28571	0.0001	0.0159
13a24	Mineral inclusions	3638	0.0022	0.0063	0.34921	0.0001	0.0159
13a45	Grain Interior	3356	0.00225	0.0063	0.35714	0.0001	0.0159
13a46	Grain Interior	3356	0.0022	0.0063	0.34921	0.0001	0.0159
13a47	Grain Interior	3356	0.0022	0.0063	0.34921	0.0001	0.0159
13a48	Grain Interior	3356	0.0021	0.0063	0.33333	0.0001	0.0159
13a49	Fracture	3356	0.00235	0.0063	0.37302	0.0001	0.0159
13a50	Fracture	3356	0.0022	0.0063	0.34921	0.0001	0.0159
13a51	Grain Interior	3356	0.00245	0.0063	0.38889	0.0001	0.0159
13a52	Grain Interior	3356	0.00255	0.0063	0.40476	0.0001	0.0159
13a54	Mineral inclusions	3356	0.00255	0.0063	0.40476	0.0001	0.0159
13a55	Grain Interior	3356	0.0024	0.0063	0.38095	0.0001	0.0159
13b04	Fracture	3319	0.0015	0.0057	0.26316	0.0001	0.0175
13b05	Fracture	3354	0.0029	0.0057	0.50877	0.0001	0.0175
13b12	Fracture	3354	0.0035	0.0057	0.61404	0.0001	0.0175
13b13	Fracture	3437	0.0057	0.0057	1.00000	0.0001	0.0175
13b14	Fracture	3426	0.001	0.0057	0.17544	0.0001	0.0175
13b15	Fracture	3420	0.0011	0.0057	0.19298	0.0001	0.0175
13b18	Fracture	3526	0.0007	0.0057	0.12281	0.0001	0.0175
13b25	Fracture	3572	0.001	0.0057	0.17544	0.0001	0.0175
13b26	Fracture	3572	0.0014	0.0057	0.24561	0.0001	0.0175
13b27	Fracture	3572	0.0017	0.0057	0.29825	0.0001	0.0175
13b28	Fracture	3572	0.001	0.0057	0.17544	0.0001	0.0175
13b39	Fracture	3572	0.0008	0.0057	0.14035	0.0001	0.0175
13b40	Fracture	3638	0.0013	0.0057	0.22807	0.0001	0.0175
13b41	Fracture	3638	0.0011	0.0057	0.19298	0.0001	0.0175

13b46	Fracture	3638	0.0007	0.0057	0.12281	0.0001	0.0175
13b47	Fracture	3638	0.0008	0.0057	0.14035	0.0001	0.0175
13b48	Fracture	3638	0.0005	0.0057	0.08772	0.0001	0.0175
13b01	Grain Interior	3319	0.0015	0.0057	0.26316	0.0001	0.0175
13b02	Grain Interior	3319	0.001	0.0057	0.17544	0.0001	0.0175
13b03	Grain Interior	3319	0.0019	0.0057	0.33333	0.0001	0.0175
13b06	Grain Interior	3354	0.0044	0.0057	0.77193	0.0001	0.0175
13b07	Grain Interior	3354	0.0034	0.0057	0.59649	0.0001	0.0175
13b09	Grain Interior	3354	0.0026	0.0057	0.45614	0.0001	0.0175
13b10	Grain Interior	3354	0.0026	0.0057	0.45614	0.0001	0.0175
13b11	Grain Interior	3354	0.0023	0.0057	0.40351	0.0001	0.0175
13b17	Grain Interior	3420	0.0023	0.0057	0.40351	0.0001	0.0175
13b19	Grain Interior	3526	0.0006	0.0057	0.10526	0.0001	0.0175
13b20	Grain Interior	3526	0.0005	0.0057	0.08772	0.0001	0.0175
13b23	Grain Interior	3572	0.0009	0.0057	0.15789	0.0001	0.0175
13b24	Grain Interior	3572	0.0009	0.0057	0.15789	0.0001	0.0175
13b29	Grain Interior	3572	0.0009	0.0057	0.15789	0.0001	0.0175
13b32	Grain Interior	3572	0.0011	0.0057	0.19298	0.0001	0.0175
13b33	Grain Interior	3572	0.0014	0.0057	0.24561	0.0001	0.0175
13b34	Grain Interior	3572	0.0015	0.0057	0.26316	0.0001	0.0175
13b35	Grain Interior	3572	0.0015	0.0057	0.26316	0.0001	0.0175
13b36	Grain Interior	3572	0.0017	0.0057	0.29825	0.0001	0.0175
13b37	Grain Interior	3572	0.001	0.0057	0.17544	0.0001	0.0175
13b38	Grain Interior	3572	0.0011	0.0057	0.19298	0.0001	0.0175
13b44	Grain Interior	3638	0.0006	0.0057	0.10526	0.0001	0.0175
13b45	Grain Interior	3638	0.0005	0.0057	0.08772	0.0001	0.0175
13b49	Grain Interior	3638	0.0004	0.0057	0.07018	0.0001	0.0175
13b51	Grain Interior	3638	0.0006	0.0057	0.10526	0.0001	0.0175
13b52	Grain Interior	3638	0.0008	0.0057	0.14035	0.0001	0.0175
13b53	Grain Interior	3638	0.0009	0.0057	0.15789	0.0001	0.0175
13b08	Type II Fluid inclusions	3354	0.003	0.0057	0.52632	0.0001	0.0175
13b16	Type II Fluid inclusions	3420	0.0044	0.0057	0.77193	0.0001	0.0175
13b21	Type II Fluid inclusions	3572	0.0012	0.0057	0.21053	0.0001	0.0175
13b22	Type II Fluid inclusions	3572	0.0019	0.0057	0.33333	0.0001	0.0175
13b30	Type II Fluid inclusions	3572	0.0007	0.0057	0.12281	0.0001	0.0175
13b31	Type II Fluid inclusions	3572	0.0009	0.0057	0.15789	0.0001	0.0175
13b42	Type II Fluid inclusions	3638	0.0008	0.0057	0.14035	0.0001	0.0175
13b43	Type II Fluid inclusions	3638	0.0008	0.0057	0.14035	0.0001	0.0175
13b50	Type II Fluid inclusions	3638	0.0006	0.0057	0.10526	0.0001	0.0175
13b54	Type II Fluid inclusions	3638	0.0006	0.0057	0.10526	0.0001	0.0175
13c1	Fracture	3353	0.0011	0.005	0.22000	0.0001	0.02
13c14	Fracture	3570	0.0027	0.005	0.54000	0.0001	0.02
13c15	Fracture	3570	0.0028	0.005	0.56000	0.0001	0.02
13c2	Fracture	3353	0.001	0.005	0.20000	0.0001	0.02
13c25	Fracture	3637	0.0016	0.005	0.32000	0.0001	0.02

13c26	Fracture	3637	0.0019	0.005	0.38000	0.0001	0.02
13c27	Fracture	3637	0.0043	0.005	0.86000	0.0001	0.02
13c28	Fracture	3637	0.0042	0.005	0.84000	0.0001	0.02
13c3	Fracture	3353	0.0014	0.005	0.28000	0.0001	0.02
13c8	Fracture	3353	0.0015	0.005	0.30000	0.0001	0.02
13c16	Grain Interior	3570	0.0022	0.005	0.44000	0.0001	0.02
13c17	Grain Interior	3570	0.0023	0.005	0.46000	0.0001	0.02
13c19	Grain Interior	3637	0.0015	0.005	0.30000	0.0001	0.02
13c20	Grain Interior	3637	0.0048	0.005	0.96000	0.0001	0.02
13c29	Grain Interior	3637	0.003	0.005	0.60000	0.0001	0.02
13c30	Grain Interior	3637	0.0039	0.005	0.78000	0.0001	0.02
13c4	Grain Interior	3353	0.0013	0.005	0.26000	0.0001	0.02
13c5	Grain Interior	3353	0.0013	0.005	0.26000	0.0001	0.02
13c6	Grain Interior	3353	0.0014	0.005	0.28000	0.0001	0.02
13c7	Grain Interior	3353	0.0015	0.005	0.30000	0.0001	0.02
13c9	Grain Interior	3570	0.0029	0.005	0.58000	0.0001	0.02
13c10	Type II Fluid inclusions	3570	0.0023	0.005	0.46000	0.0001	0.02
13c11	Type II Fluid inclusions	3570	0.0023	0.005	0.46000	0.0001	0.02
13c12	Type II Fluid inclusions	3570	0.0023	0.005	0.46000	0.0001	0.02
13c13	Type II Fluid inclusions	3570	0.0017	0.005	0.34000	0.0001	0.02
13c18	Type II Fluid inclusions	3568	0.001	0.005	0.20000	0.0001	0.02
13c21	Type II Fluid inclusions	3637	0.0036	0.005	0.72000	0.0001	0.02
13c22	Type II Fluid inclusions	3637	0.0035	0.005	0.70000	0.0001	0.02
13c23	Type II Fluid inclusions	3637	0.0027	0.005	0.54000	0.0001	0.02
13c24	Type II Fluid inclusions	3637	0.0027	0.005	0.54000	0.0001	0.02
13c31	Type II Fluid inclusions	3619	0.0014	0.005	0.28000	0.0001	0.02
13c32	Type II Fluid inclusions	3637	0.0012	0.005	0.24000	0.0001	0.02
59a_78	Grain Interior	3526	0.00065	0.0033	0.19697	0.00005	0.0152
59a_04	Grain Interior	3233	0.0007	0.0033	0.21212	0.00005	0.0152
59a_05	Grain Interior	3246	0.00065	0.0033	0.19697	0.00005	0.0152
59a_06	Grain Interior	3149	0.0005	0.0033	0.15152	0.00005	0.0152
59a_07	Grain Interior	3159	0.00055	0.0033	0.16667	0.00005	0.0152
59a_08	Grain Interior	3228	0.00045	0.0033	0.13636	0.00005	0.0152
59a_09	Grain Interior	3355	0.00225	0.0033	0.68182	0.00005	0.0152
59a_10	Grain Interior	3355	0.0024	0.0033	0.72727	0.00005	0.0152
59a_15	Grain Interior	3355	0.002	0.0033	0.60606	0.00005	0.0152
59a_16	Grain Interior	3355	0.0022	0.0033	0.66667	0.00005	0.0152
59a_17	Grain Interior	3355	0.00255	0.0033	0.77273	0.00005	0.0152
59a_18	Grain Interior	3355	0.00245	0.0033	0.74242	0.00005	0.0152
59a_19	Grain Interior	3325	0.00125	0.0033	0.37879	0.00005	0.0152
59a_20	Grain Interior	3325	0.0013	0.0033	0.39394	0.00005	0.0152
59a_21	Grain Interior	3355	0.00295	0.0033	0.89394	0.00005	0.0152

59a_22	Grain Interior	3355	0.0028	0.0033	0.84848	0.00005	0.0152
59a_24	Grain Interior	3355	0.0024	0.0033	0.72727	0.00005	0.0152
59a_25	Grain Interior	3325	0.0008	0.0033	0.24242	0.00005	0.0152
59a_28	Grain Interior	3409	0.00075	0.0033	0.22727	0.00005	0.0152
59a_29	Grain Interior	3450	0.001	0.0033	0.30303	0.00005	0.0152
59a_30	Grain Interior	3427	0.0009	0.0033	0.27273	0.00005	0.0152
59a_31	Grain Interior	3398	0.0007	0.0033	0.21212	0.00005	0.0152
59a_32	Grain Interior	3437	0.00075	0.0033	0.22727	0.00005	0.0152
59a_34	Grain Interior	3573	0.00165	0.0033	0.50000	0.00005	0.0152
59a_35	Grain Interior	3568	0.001	0.0033	0.30303	0.00005	0.0152
59a_38	Grain Interior	3573	0.0016	0.0033	0.48485	0.00005	0.0152
59a_39	Grain Interior	3504	0.0007	0.0033	0.21212	0.00005	0.0152
59a_41	Grain Interior	3573	0.0011	0.0033	0.33333	0.00005	0.0152
59a_52	Grain Interior	3519	0.00095	0.0033	0.28788	0.00005	0.0152
59a_53	Grain Interior	3526	0.002	0.0033	0.60606	0.00005	0.0152
59a_55	Grain Interior	3638	0.00075	0.0033	0.22727	0.00005	0.0152
59a_56	Grain Interior	3638	0.00145	0.0033	0.43939	0.00005	0.0152
59a_59	Grain Interior	3638	0.00155	0.0033	0.46970	0.00005	0.0152
59a_60	Grain Interior	3629	0.00065	0.0033	0.19697	0.00005	0.0152
59a_69	Grain Interior	3629	0.001	0.0033	0.30303	0.00005	0.0152
59a_70	Grain Interior	3625	0.0033	0.0033	1.00000	0.00005	0.0152
59a_74	Grain Interior	3573	0.00095	0.0033	0.28788	0.00005	0.0152
59a_75	Grain Interior	3573	0.0027	0.0033	0.81818	0.00005	0.0152
59a_01	Low angle boundary	3220	0.00075	0.0033	0.22727	0.00005	0.0152
59a_27	Low angle boundary	3443	0.00075	0.0033	0.22727	0.00005	0.0152
59a_40	Low angle boundary	3573	0.00098	0.0033	0.29697	0.00005	0.0152
59a_46	Low angle boundary	3526	0.0006	0.0033	0.18182	0.00005	0.0152
59a_47	Low angle boundary	3573	0.0007	0.0033	0.21212	0.00005	0.0152
59a_65	Low angle boundary	3638	0.00065	0.0033	0.19697	0.00005	0.0152
59a_77	Low angle boundary	3313	0.0007	0.0033	0.21212	0.00005	0.0152
59a_79	Low angle boundary	3409	0.0006	0.0033	0.18182	0.00005	0.0152
59a_11	Low angle boundary	3355	0.00245	0.0033	0.74242	0.00005	0.0152
59a_12	Low angle boundary	3355	0.0022	0.0033	0.66667	0.00005	0.0152
59a_23	Low angle boundary	3355	0.00245	0.0033	0.74242	0.00005	0.0152
59a_33	Low angle boundary	3573	0.0015	0.0033	0.45455	0.00005	0.0152
59a_42	Low angle boundary	3573	0.00125	0.0033	0.37879	0.00005	0.0152
59a_45	Low angle boundary	3573	0.00165	0.0033	0.50000	0.00005	0.0152
59a_51	Low angle boundary	3519	0.00105	0.0033	0.31818	0.00005	0.0152
59a_54	Low angle boundary	3526	0.0013	0.0033	0.39394	0.00005	0.0152
59a_57	Low angle boundary	3638	0.0011	0.0033	0.33333	0.00005	0.0152
59a_61	Low angle boundary	3629	0.0015	0.0033	0.45455	0.00005	0.0152
59a_64	Low angle boundary	3638	0.0022	0.0033	0.66667	0.00005	0.0152
59a_68	Low angle boundary	3629	0.0018	0.0033	0.54545	0.00005	0.0152

59a_71	Low angle boundary	3632	0.0031	0.0033	0.93939	0.00005	0.0152
59a_72	Low angle boundary	3632	0.00195	0.0033	0.59091	0.00005	0.0152
59a_73	Low angle boundary	3573	0.00135	0.0033	0.40909	0.00005	0.0152
59a_76	Low angle boundary	3573	0.0014	0.0033	0.42424	0.00005	0.0152
59a_80	Low angle boundary	3434	0.0006	0.0033	0.18182	0.00005	0.0152
59a_81	Low angle boundary	3442	0.00055	0.0033	0.16667	0.00005	0.0152
59a_02	Mineral inclusions	3200	0.0006	0.0033	0.18182	0.00005	0.0152
59a_03	Mineral inclusions	3269	0.0006	0.0033	0.18182	0.00005	0.0152
59a_26	Mineral inclusions	3409	0.00055	0.0033	0.16667	0.00005	0.0152
59a_36	Mineral inclusions	3568	0.0012	0.0033	0.36364	0.00005	0.0152
59a_37	Mineral inclusions	3525	0.00065	0.0033	0.19697	0.00005	0.0152
59a_43	Mineral inclusions	3573	0.0009	0.0033	0.27273	0.00005	0.0152
59a_44	Mineral inclusions	3573	0.0011	0.0033	0.33333	0.00005	0.0152
59a_58	Mineral inclusions	3629	0.0013	0.0033	0.39394	0.00005	0.0152
59a_62	Mineral inclusions	3629	0.0007	0.0033	0.21212	0.00005	0.0152
59a_63	Mineral inclusions	3638	0.00125	0.0033	0.37879	0.00005	0.0152
59a_13	Mineral inclusions	3355	0.002	0.0033	0.60606	0.00005	0.0152
59a_14	Mineral inclusions	3355	0.00205	0.0033	0.62121	0.00005	0.0152
59a_82	Mineral inclusions	3488	0.0005	0.0033	0.15152	0.00005	0.0152
59a_48	Type I Fluid inclusions	3526	0.00065	0.0033	0.19697	0.00005	0.0152
59a_49	Type I Fluid inclusions	3573	0.00095	0.0033	0.28788	0.00005	0.0152
59a_50	Type I Fluid inclusions	3573	0.0008	0.0033	0.24242	0.00005	0.0152
59a_66	Type I Fluid inclusions	3629	0.00105	0.0033	0.31818	0.00005	0.0152
59a_67	Type I Fluid inclusions	3638	0.0008	0.0033	0.24242	0.00005	0.0152
59b_10	Fracture	3413	0.0012	0.0082	0.14634	0.0002	0.0244
59b_11	Fracture	3421	0.0016	0.0082	0.19512	0.0002	0.0244
59b_12	Fracture	3421	0.0008	0.0082	0.09756	0.0002	0.0244
59b_13	Fracture	3297	0.0006	0.0082	0.07317	0.0002	0.0244
59b_17	Fracture	3517	0.001	0.0082	0.12195	0.0002	0.0244
59b_18	Fracture	3514	0.001	0.0082	0.12195	0.0002	0.0244
59b_20	Fracture	3544	0.0006	0.0082	0.07317	0.0002	0.0244
59b_21	Fracture	3544	0.0006	0.0082	0.07317	0.0002	0.0244
59b_25	Fracture	3572	0.0008	0.0082	0.09756	0.0002	0.0244
59b_26	Fracture	3567	0.0008	0.0082	0.09756	0.0002	0.0244
59b_27	Fracture	3572	0.0018	0.0082	0.21951	0.0002	0.0244
59b_30	Fracture	3573	0.0016	0.0082	0.19512	0.0002	0.0244
59b_34	Fracture	3636	0.001	0.0082	0.12195	0.0002	0.0244
59b_35	Fracture	3631	0.001	0.0082	0.12195	0.0002	0.0244
59b_36	Fracture	3638	0.0024	0.0082	0.29268	0.0002	0.0244
59b_39	Fracture	3638	0.0024	0.0082	0.29268	0.0002	0.0244
59b_40	Fracture	3638	0.0038	0.0082	0.46341	0.0002	0.0244
59b_41	Fracture	3638	0.003	0.0082	0.36585	0.0002	0.0244
59b_44	Fracture	3600	0.0036	0.0082	0.43902	0.0002	0.0244
59b_45	Fracture	3600	0.0042	0.0082	0.51220	0.0002	0.0244

59b_46	Fracture	3600	0.004	0.0082	0.48780	0.0002	0.0244
59b_05	Mineral inclusions	3413	0.0006	0.0082	0.07317	0.0002	0.0244
59b_06	Mineral inclusions	3421	0.0006	0.0082	0.07317	0.0002	0.0244
59b_07	Mineral inclusions	3421	0.0008	0.0082	0.09756	0.0002	0.0244
59b_08	Mineral inclusions	3421	0.0008	0.0082	0.09756	0.0002	0.0244
59b_09	Mineral inclusions	3421	0.0008	0.0082	0.09756	0.0002	0.0244
59b_14	Mineral inclusions	3456	0.0006	0.0082	0.07317	0.0002	0.0244
59b_15	Mineral inclusions	3517	0.0006	0.0082	0.07317	0.0002	0.0244
59b_19	Mineral inclusions	3536	0.0006	0.0082	0.07317	0.0002	0.0244
59b_23	Mineral inclusions	3567	0.0024	0.0082	0.29268	0.0002	0.0244
59b_24	Mineral inclusions	3567	0.0006	0.0082	0.07317	0.0002	0.0244
59b_28	Mineral inclusions	3573	0.0026	0.0082	0.31707	0.0002	0.0244
59b_31	Mineral inclusions	3573	0.0014	0.0082	0.17073	0.0002	0.0244
59b_32	Mineral inclusions	3638	0.0034	0.0082	0.41463	0.0002	0.0244
59b_33	Mineral inclusions	3626	0.0006	0.0082	0.07317	0.0002	0.0244
59b_37	Mineral inclusions	3638	0.0054	0.0082	0.65854	0.0002	0.0244
59b_42	Mineral inclusions	3600	0.0026	0.0082	0.31707	0.0002	0.0244
59b_01	Type I Fluid inclusions	3354	0.0022	0.0082	0.26829	0.0002	0.0244
59b_43	Type I Fluid inclusions	3600	0.0026	0.0082	0.31707	0.0002	0.0244
59b_02	Type IFluid inclusions	3326	0.0006	0.0082	0.07317	0.0002	0.0244
59b_03	Type IFluid inclusions	3326	0.0008	0.0082	0.09756	0.0002	0.0244
59b_04	Type IFluid inclusions	3326	0.0004	0.0082	0.04878	0.0002	0.0244
59b_16	Type II Fluid inclusions	3517	0.0008	0.0082	0.09756	0.0002	0.0244
59b_22	Type II Fluid inclusions	3567	0.0006	0.0082	0.07317	0.0002	0.0244
59b_29	Type II Fluid inclusions	3573	0.0034	0.0082	0.41463	0.0002	0.0244
59b_38	Type II Fluid inclusions	3638	0.0064	0.0082	0.78049	0.0002	0.0244